BIOPHYSICAL CHEMISTRY 1 (1974) 141–151. © NORTH-HOLLAND PUBLISHING COMPANY

ENUMERATION OF INTERACTING SPECIES AND SEDIMENTATION PROPERTIES OF f_d-DNA AT LOW IONIC STRENGTH *

Paul W. CHUN‡, William P. HERSCHLEB†, Darryl J. DOWNING† and Mary L. KRISTA
Department of Biochemistry, College of Arts and Sciences, University of Florida, Gainesville, Florida 32610, USA

Received 27 July 1973
Revised manuscript received 8 October 1973

The ionic strength dependent aggregation of f_d-DNA was studied by ultracentrifugal field experiments. Compressibility studies indicate a conformational change in the f_d-DNA aggregates with a change in the ionic environment. Principal component or factor analysis, a technique to determine the number of linearly independent components, indicated that three aggregating species are present in the f_d-DNA system at low ionic strength.

1. Introduction

In studies on the self-assembly of f_d phage, it has long proven difficult to dissociate the coat protein gene 8 from f_d phage in viable form even under the most drastic conditions. Finding the aggregation of the coat protein to be highly ionic strength dependent, we have conducted studies of the self-assembly of f_d phage at very low ionic strength [1].

Therefore, although sedimentation studies to date on the conformational state of single-stranded DNA in a system such as f_d phage have been chiefly limited to analysis of the moving zone at high ionic strength, we have developed a new method for examining the aggregation of f_d-DNA in a low ionic environment. Our examination of f_d-DNA by the ultracentrifugal relaxation procedure at low ionic strength puts such conformational studies in a strikingly different light.

The filamentous, male specific bacterial phage f_d is a flexible, helical rod 8500 to 9500 Å in length with a diameter of 60 to 70 Å [2–5] which absorbs at the F-pili appendages of the male strain of *E. coli*. f_d phage (like M13, F1 and ZJ/2) has a circular single-stranded DNA genome [2, 6, 7] and a DNA replication process which somewhat resembles that of ϕX174 [8, 9].

Poon and Schumaker [10] have proposed that the aggregation of DNA is pressure-independent, arising from steric interaction as a result of brownian motion, where aggregation is related to sedimentation behavior as pressure is increased along the centrifugal field. This is in contrast to a second principal theory (Le Chatelier principle) of the pressure-dependent aggregation of macromolecules, which suggests that the change in the molecular volume of the reaction can be explained in terms of the pressure dependence of the thermodynamic equilibrium between protein monomers and polymers [11–13], as in the pressure-dependent depolymerization of myosin [14, 15] and sickle cell hemoglobin [16].

In our studies on the sedimentation behavior of single-stranded circular f_d-DNA, we found that DNA does form compressible states [17]. Our preliminary examination indicates that the aggregation of f_d-DNA is pressure-independent, as Poon and Schumaker [10] have proposed, but that the conformational state of the aggregates is pressure-dependent.

Partial molar compressibility measurements such as we report for f_d-DNA in this communication can give valuable information about DNA–solvent interaction, solvation of DNA by solvent, partial specific volume and interaction parameters between DNA molecules in

* This work was supported by the National Science Foundation Grant GB 28223-A*-1.
† Graduate students.
‡ Address all correspondence to Paul W. Chun.

a wide variety of biological systems.

Compressibility measurements and principal component analysis indicate there is a change in the conformational state of the DNA shown in the moving zone of the schlieren pattern and the highly aggregated material at the bottom of the cell (the gel-like state), upon field relaxation. The number of linearly independent aggregating species present in both cases has been enumerated by principal component analysis.

Principal component analysis, along with matrix rank analysis, determines the number and distribution of components in a biological system [18, 19]. These methods have wide application, and have been utilized to determine the number of components in a mixture of absorbing species [20, 21], to analyze the optical rotatory dispersion of TMV [22], and to determine the number of components in fluorescent spectroscopy [23, 24]. They have also been applied to the kinetics of the oxidation of hemoglobin [25], to gel filtration [26], and to the determination of components from a diffusion experiment in the ultracentrifuge [27].

In this communication, we report the use of principal component analysis to enumerate the interacting components in a single-stranded circular f_d-DNA system in the ultracentrifuge, and the pronounced effect of ionic environment on the sedimentation behavior of f_d-DNA.

Information on the conformational state and aggregation behavior of single-stranded DNA, such as is reported here, is a major step towards an understanding of its biological roles, as well as its reactions with enzymes and other molecules of biological interest.

2. Material and methods

2.1. Isolation of f_d phage

The *E. coli* K-38 (Su^-) host cells were grown at 37°C in standard media [28], infected with f_d phage (multiplicity of interaction: 50) at an optical density of 0.3 at 550 mμ and a cell density of 1×10^8 cells/ml (exponental growth), and incubated for 20 hours. Bacterial lysates were centrifuged to remove debris. The resulting supernatant was brought to 0.5 M NaCl concentration and the phage precipitated by addition of polyethylene glycol (PEG M_w 6000) at 2% PEG. Phage pellets were redissolved in Na_2EDTA–borate buffer (0.001 M Na_2EDTA – 0.086 M $Na_2B_4O_7$ – 10 H_2O, pH 9.2) and purified by CsCl density gradient centrifugation containing 5 to 8 layers of CsCl solution of appropriate densities in the same tubes for the Spinco SW 25.2 swinging bucket rotor. Banding of purified f_d phage occurred at a CsCl density of 1.30 [29]. The concentration of purified f_d phage was determined from the extinction coefficient, $E^{1\%}_{260m\mu} = 36.7$ [30]. In purified f_d phage, the optical density ratio of 260/280 mμ is 1.0. One optical density unit of 280 mμ is equal to 1.3×10^{13} plaque forming units/ml (PFU). PFU values are determined by plaque assay.

2.2. Isolation of f_d-DNA

f_d-DNA was obtained from purified f_d phage by a 6X phenol extraction method similar to that of Knippers and Hoffmann–Berling [6]. Twenty ml of Na_2EDTA–borate buffer, pH 9.2 (0.086 M $Na_2B_4O_7$-$10H_2O$ and 0.001 M Na_2EDTA) were added to 10 ml of purified f_d phage (approximately 100 mg of phage). Thirty ml of freshly distilled phenol, which had been previously saturated with the same buffer, were added and the mixture shaken at room temperature for 15 minutes. The solution was centrifuged at 6000 rpm using a Beckman fixed-angle JA-20 rotor for 10 minutes at 4°C. The resulting aqueous layer was re-extracted three times with 20 ml of EDTA–borate buffer saturated with phenol, and the process repeated three more times at room temperature. The aqueous layer was then dialyzed against water at 4°C for one week with several changes per day.

The volume was reduced to 20 ml by filtering through PM2 filter paper using an Amicon filtering apparatus. This DNA solution was further purified by 5–20% sucrose gradient centrifugation for 5 hours at 4°C using a swinging bucket rotor SW 25.2. The purified f_d-DNA was incubated at 42°C for 30 minutes after 10 μg/ml of pronase was added. The yield of purified f_d-DNA in solution was about 0.35 mg/ml, as determined by sulfuric acid testing [31]. We also performed the Lowry test [32] for protein contaminatio before pronase treatment. None was found. The optical density ratio (260/280 mμ) was 1.86. One optic density unit at 260 mμ is equivalent to 43 γg/ml of DNA ($E^{1\%}_{260m\mu} = 430$) [6]. The specific refraction index increment was found to be 0.01333 dl/g.

3. Ultracentrifugation

3.1. Ultracentrifugal field relaxation procedure

Sedimentation velocity experiments were performed at 20°C with a Spinco/Beckman Model E analytical ultracentrifuge equipped with the standard RTIC unit and interference/schlieren optical system. A solution of single-stranded circular f_d-DNA, at low ionic strengths of Na^+ and Mg^{2+} and at neutral pH, was examined by sedimentation velocity and by the ultracentrifugal field relaxation procedure of Kegeles and Sia [33]. Under the ultracentrifugal field relaxation procedure, a series of consecutive schlieren photographs are taken at maximum speed (50 740 rpm) and at descending speeds after relaxation of the field until a low speed of 12 590 to 5 225 rpm has been reached. Sedimentation velocity measurements were carried out in an aluminum centerpiece, and sapphire windows were used in the ultracentrifuge cell.

Sedimentation coefficients were computed from the movement of the maximum ordinates of the sedimenting zones and were not corrected for infinite dilution at 20°C. The photographic plates were measured with a two-coordinate microcomparator (Nikon 6C optical comparator, Model 7244) equipped with booster condensing lens, goniometer, zero-setting device for the micrometer and surface illuminator.

3.2. Sedimentation equilibrium measurements

Sedimentation equilibrium experiments were also performed with the Model E analytical ultracentrifuge as described previously [34]. The apparent weight average molecular weight was obtained from an IBM computer plot of ln C versus r^2 with a slope of $M_{w\ app}\, w^2(1-\bar{v}\rho)/2RT$. The partial specific volume used in the computation of molecular weight was 0.556 ml/g of calf thymus DNA [38].

3.3. Isothermal compressibility of f_d-DNA

All of our compressibility calculations were based on the following expression [35]

$$\beta = 6(\bar{y})\, n_p \tan\theta / La m_1 m_2 (n_p^2 + 2)(n_p^2 - 1)\rho w^2 x_p ,$$

where θ is the schlieren bar angle; L, the optical level; a, the cell thickness; $m_1 m_2$, the vertical magnification of the optical system; w, the angular velocity; and x_p, the distance from the center of rotation. The density of the solution at any given pressure is determined from $\rho_p = \rho_0(1+\beta P)$, and the refractive index n of the solution from $n_p = n_0$ + area under the schlieren pattern. Measurements of $\bar{y}$, the height of the schlieren pattern above the reference line, were taken at 0.01 cm intervals only in the liquid–gel interface of the schlieren pattern, that is, between the interface and the bottom of the cell, as shown in figs. 2B and 3C. The total compressibility of a solution is the sum of the partial compressibility of solvent and solute [35], i.e.,

$$\beta_T = \bar{\beta}_1\, c_1/\rho_1 + \bar{\beta}_2\, c_2/\rho_2 ,$$

where c_1 and c_2 are concentration of solvent and solute respectively, and ρ_1 and ρ_2 are the density of solvent and solute. Assuming $\rho_2 = 1.7023$, a value for the density of T-7 DNA as reported by Bauer et al. [36], we were able to determine the total compressibility, β_T, of f_d-DNA in 0.01 M or 0.005 M NaCl solution.

3.4. Factor or principal component analysis of f_d-DNA system

A comparison of methods for enumeration of components in a biological system has been described extensively by Magar and Chun [19]. With respect to factor analysis, the method can be outlined briefly as follows.

Factor analysis can be used to analyze any system which can be written in the form [37]

$$X_{ji} = \sum_{k=1}^{m} \varrho_{jk}\zeta_k + e_j , \qquad (j = 1, 2 \ldots p) .$$

The X_{ji} values are samples thought to be made up of m components denoted by ζ_k ($k = 1, 2 \ldots m$); ϱ_{jk} is the quantitative contribution of the kth factor to the jth sample; and e_j stands for the errors. For this method, the data matrix X is transformed into its standard form, given by the matrix Z, as follows, defining the sample variance of X_j by

$$S_j^2 = \sum_{i=1}^{m} (X_{ji}/n) .$$

The elements of Z are given by $Z_{ji} = X_{ji}/S_j$. From the matrix Z, the matrix of observed correlation (given by $R = ZZ'/n$) is obtained from n number of separate experimental measurements. In the above equation Z' is the transpose of Z. The eigenvalues of θ are then found, calling them $\theta_1, \theta_2 \ldots \theta_n$. There are as many significant factors as there are eigenvalues greater than unity. Thus, the number of eigenvalues approaching unity will be equivalent to the number of components operating in the system. This criterion of eigenvalue unity is one of the best methods available for enumerating the interacting species. The procedure for principal component analysis is similar, except that e_j is not considered.

Once the data matrix, X, for the height of the schlieren pattern above the reference line as a function of radical distance along the sedimentation boundary is set up, it is simply a matter of inserting matrix values into a biomedical computer program BMD 03M [46], which is available at most computer centers.

4. Results

4.1. The effect of ionic strength on sedimentation behavior of f_d-DNA

The ionic-strength dependent sedimentation coefficients of f_d-DNA in NaCl and $MgCl_2$ solutions are shown in fig. 1. It is apparent that aggregation of f_d-DNA in the presence of the divalent ion (Mg^{2+}) is greater than in the presence of equimolar amounts of the monovalent ion (Na^+). This conclusion is borne out by values determined for the sedimentation coefficients as a function of ionic strength and by the field relaxation behavior of the two solutions (figs. 1–5).

Upon field relaxation the Na^+–f_d-DNA exhibits a hypersharp boundary, seen in figs. 2B and 3C, between the liquid–liquid interface and the bottom of the cell. The Mg^{2+}–f_d-DNA, on the other hand, shows a broadening of the boundary upon field relaxation (fig. 4C) indicative of independent particle behavior. The total compressibility of Na^+–f_d-DNA, determined from figs. 2B and 3C, changes from approximately 73 to 56×10^{-6} bar^{-1} as the pressure changes from 22 to 23 bar [17]. The total compressibility of Mg^{2+}–f_d-DNA was found to be 84×10^{-6} bar^{-1} under comparable conditions.

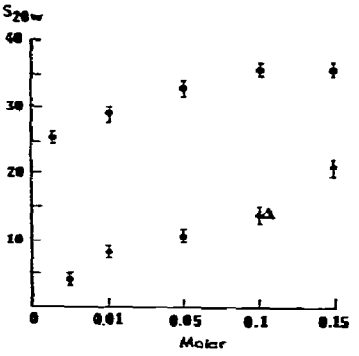

Fig. 1. Ionic strength dependent sedimentation coefficients of f_d-DNA (1.2 mg/ml) in NaCl and $MgCl_2$; (•) $MgCl_2$; (○) NaCl; (△) ϕX174-DNA.

We attempted to relate the compressibility to the partial specific volume in the gel-like interface, based on the following expression

$$(\beta_T - d\rho/\rho_1 dP_1)/(d\rho_2/dP_2) = \upsilon_2 .$$

We found a slight increase in υ_2 from 0.592 to 0.635 ml/g with increasing pressure, an error range of 8 to 12%. Normally, the partial specific volume of calf thymus DNA is 0.556, as reported by Halsall and Schumaker [38].

Figs. 2B and 3C, along with our computation of compressibility and partial specific volume at the interface and the bottom of the cell, indicate that there is a change in the conformational state of the gel-like material between the interface and the bottom of the cell. The molecular volume is small because the material is more compressed at the interface, while the volume increases at the bottom of the cell.

At the interface, therefore, the compressibility is much greater than at the bottom of the cell, while the partial specific volume is less.

Once the concentration of the Mg^{2+} or Na^+ ions exceeds 0.15 M, the relaxation phenomenon is no longer observable, as the schlieren patterns remain identical to those shown in figs. 5B and 5C up to the completion of our sedimentation runs. The width of the reference line at the bottom of the cell in fig. 5C is 1½ times that of fig. 5A, indicating that a great deal of aggregated material is present. Another striking effect of ionic environment appears with ionic strengths of Na^+ at 0.005, where at high speed (50 740 rpm)

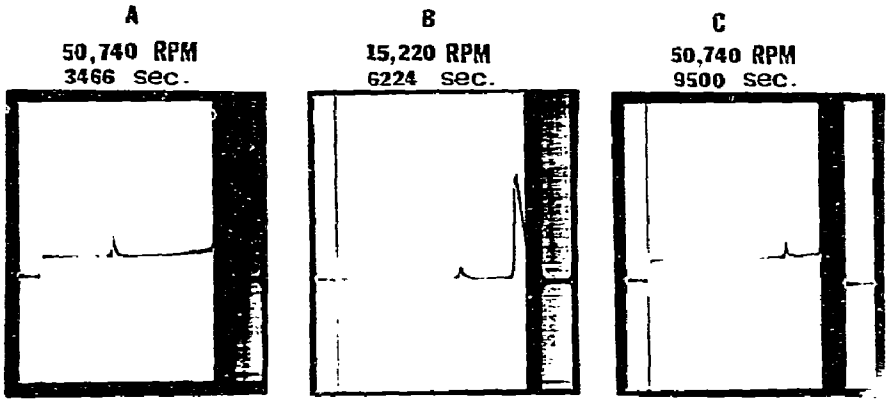

Fig. 2. Ultracentrifuge patterns of f_d-DNA in 0.01 M NaCl (1.2 mg/ml), using a standard 4° – 12 mm sector cell, bar angle 60°. Initial speed of 50 740 rpm lowered to 15 220 rpm, then raised to 50 740 rpm. Elapsed time after reaching speed given in sec.

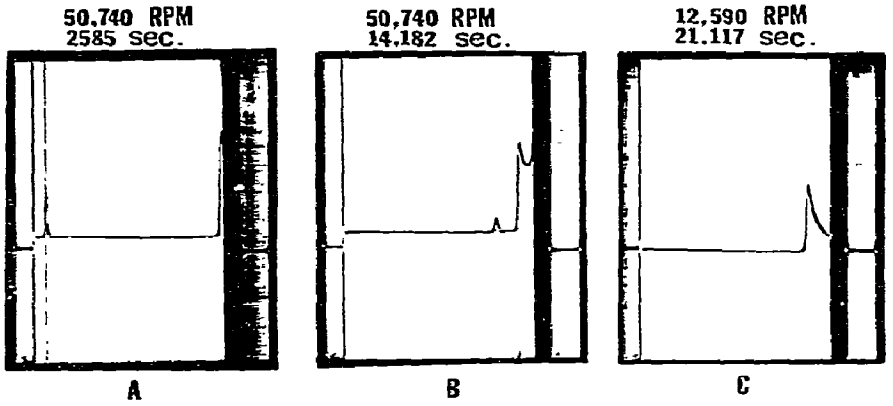

Fig. 3. Ultracentrifuge patterns of f_d-DNA in 0.005 M NaCl (1.2 mg/ml), using a standard 4° – 12 mm sector cell, bar angle 70°. Elapsed time after reaching speed given in sec.

without field relaxation, a hypersharp interface appears as shown in fig. 6. Our results would lead us to conclude that, at low ionic strength, the Na^+–f_d-DNA remains highly compressed.

The area under the moving zone of the sedimentation boundary for both Na^+–f_d-DNA and Mg^{2+}–f_d-DNA indicates that the aggregation of the f_d-DNA is pressure-independent. The observed values of the ratio of the area (A_t/A_0) under the schlieren curve after depletion of the moving zone as a function of time were constant, showing no significant pressure dependent depolymerization, as determined from the last three photos in the sequence of fig. 6.

For an interacting system, we would generally expect the aggregates at the bottom of the cell to increase asymptotically with increasing pressure. Upon field relaxation, this curve would level off in a plateau.

In the formation of a gel-like material, however, we observed the opposite effect. Even after prolonged field relaxation, no plateau was observed. Instead, the schlieren pattern for this gel-like material shows a hypersharp interface with a negative slope, rather than the asymptotic curve of positive slope which marks a pattern produced merely by the concentration gradient.

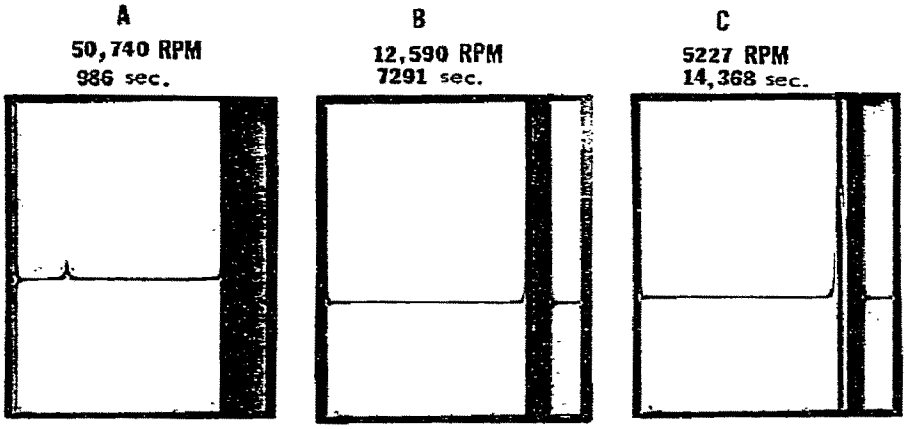

Fig. 4. Ultracentrifuge patterns of f_d-DNA (1.2 mg/ml) in 2.5×10^{-3}M $MgCl_2$. Initial speed of 50 740 rpm lowered to 12 590 rpm, then again lowered to 5227 rpm, using standard 4°–12 mm sector cell, bar angle 70°. Elapsed time after reaching speed given in sec.

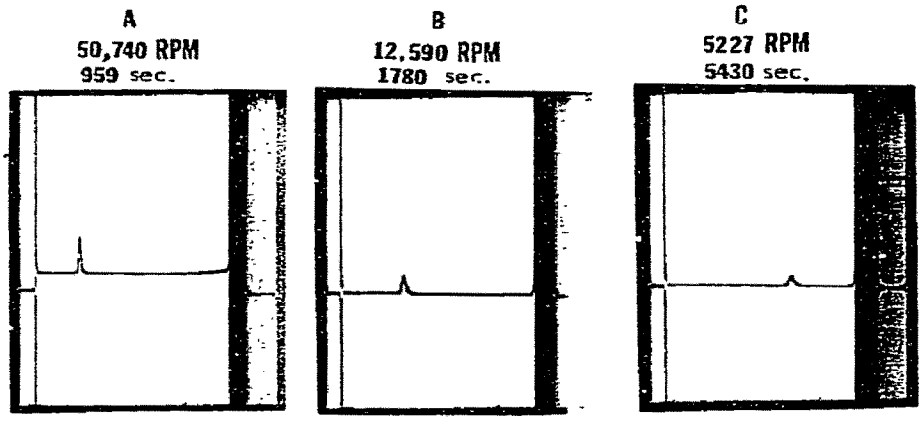

Fig. 5. Ultracentrifuge patterns of f_d-DNA (1.2 mg/ml) in 0.15 M NaCl. Initial speed of 50 740 rpm, lowered to 12 590 rpm, then again lowered to 5227 rpm, using standard 4°–12 mm sector cell, bar angle 70°. Elapsed time after reaching speed given in sec.

This is consistent witj Kegeles' findings on the reversible pressure-induced gel formation in T-2 bacteriophage DNA [39].

4.2. *Molecular weight distribution*

The weight average molecular weight of the f_d-DNA solution from low-speed sedimentation equilibrium measurements was found to be $1.83 \times 10^6 \pm 58\,000$. The number average molecular weight was $1.5 \times 10^6 \pm 37\,000$ and the z-average molecular weight was $2.04 \times 10^6 \pm 779\,000$ at infinite dilution.

The material for molecular weight determination was further fractionated using a 4°–12 mm partition cell run at 33 450 rpm for one hour. Only the top section of this solution was recovered; the remainder of the solution, consisting of most of the highly aggregated material, was discarded.

A typical plot of ln C versus r^2 for f_d-DNA weight average molecular weight determination is shown in fig. 7. The homogeneity of the solution is reflected by the linearity of this plot. Weight average molecular weight values were consistent with those reported by Halsall and Schumaker [38], based on zone diffusion and band sedimentation experiments.

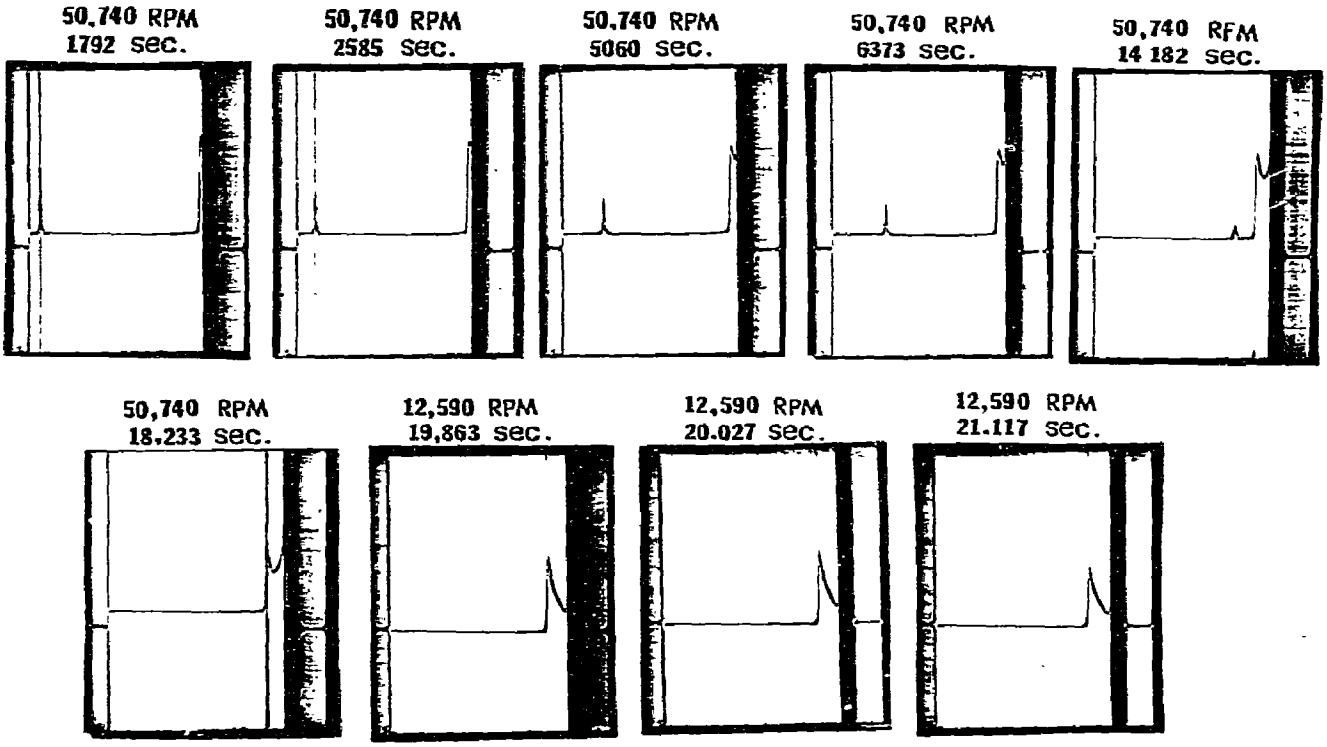

Fig. 6. Ultracentrifuge patterns for enumeration of aggregating species in f_d-DNA system (1.2 mg/ml in 0.005 M NaCl). Initial speed 50 740 rpm, lowered to 12 590 rpm. Elapsed time after reaching speed given in sec. Standard 4° –12 mm sector cell was used. Bar angle 70°.

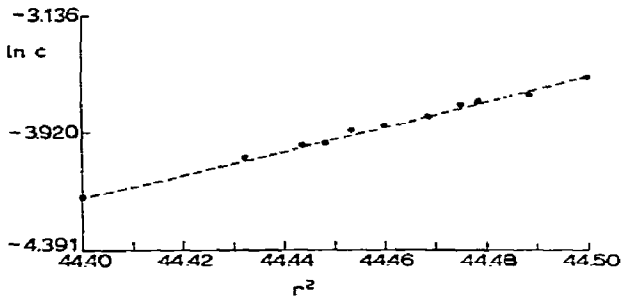

Fig. 7. A plot in ln C versus r^2 for evaluation of weight average molecular weight of f_d-DNA after repeated fractionation of f_d-DNA by partition cell (Spinco/Beckman, no. 6178), 4°–12 mm. Only top section of solutions were run at 6995 rpm for 26 hr in 0.1 M NaCl. Calculations limited to meniscus region of cell.

4.3. Enumeration of interacting components

The data matrix generated from fig. 6 is shown in table 1. The total length of time for this run at 0.005 ionic strength of NaCl is approximately 5 hours at 50 740 rpm. As may be seen from the schlieren patterns, a hypersharp boundary is visible at the bottom of the cell. This is a highly unusual phenomenon which is exhibited by f_d-DNA aggregates under these conditions.

Upon field relaxation after five hours, once the moving boundary has been depleted, we note a widening of the bottom boundary, which remains hypersharp even at lower speeds. These results, based on the final sequence of photographs at 12 590 rpm in fig. 6, were the basis for compressibility studies of f_d-DNA, as described in the text.

Our next question, to be answered by factor or

Table 1
Data matrix for principal component or factor analysis; $\bar{y}$ at 50 740 rpm [a], base line set at 2.0 cm

Distance r(cm)	Photo 1 [b]	Photo 2	Photo 3	Photo 4	Photo 5	Photo 6
6.5014	2.2180	2.2545	2.2589	2.2700	2.2700	2.2596
6.0393	2.7191	2.2543	2.2611	2.2702	2.2703	2.2613
6.0894	2.2188	2.7216	2.2616	2.2710	2.2701	2.2615
6.1349	2.2190	2.2553	2.2624	2.2709	2.2710	2.2618
6.1946	2.2207	2.2555	2.2667	2.2720	2.2711	2.2616
6.2549	2.2201	2.2542	2.6712	2.2746	2.2714	2.2605
6.3002	2.2208	2.2536	2.2604	2.2748	2.2700	2.2615
6.3471	2.2180	2.2541	2.2582	2.6220	2.2707	2.2588
6.3783	2.2196	2.2548	2.2576	2.2663	2.2708	2.2584
6.4243	2.2186	2.2526	2.2595	2.2628	2.2721	2.2596
6.4555	2.2188	2.2520	2.2586	2.2607	2.5776	2.2578
6.6310	2.2163	2.2522	2.2557	2.2618	2.2612	2.2576
6.9623	2.2247	2.2564	2.2615	2.3207	2.2185	2.4218
7.0329	2.2299	2.2620	2.2692	2.2779	2.2283	2.2724
7.1155	2.2401	2.2727	2.2796	2.2846	2.2892	3.5758
7.1455	2.2452	2.2732	2.3342	3.3192	3.5991	3.3528
7.1568	2.2468	2.2853	3.2770	3.6245	3.5478	3.3188
7.1644	2.2463	2.3078	3.6543	3.5677	3.4838	3.3051
7.1940	3.7170	3.7706	3.4811	3.4386	3.4022	3.3600
7.1996	3.7724	3.7408	3.4722	3.4644	3.4222	3.3896

[a] $\bar{y}$ is the height of the schlieren pattern above the reference line.
[b] Elapsed time after reaching speed in sec: photo 1, 1792 sec; photo 2, 2585 sec; photo 3, 5060 sec; photo 4, 6373 sec; photo 5, 10 560 sec; photo 6, 14 182 sec.

Table 2
Principal component and factor analysis based on table 1. Correlation coefficients of principal and factor components. Computed using Biomed Program BMD 03M [46]

1.00000	0.94319	0.62865	0.58488	0.49930	0.47654
0.94319	1.00000	0.64010	0.59556	0.50690	0.48276
0.62865	0.64010	1.00000	0.95676	0.81698	0.76570
0.58488	0.59556	0.95676	1.00000	0.82519	0.70864
0.49930	0.50690	0.81698	0.82519	1.00000	0.82101
0.47654	0.48276	0.76570	0.70864	0.82101	1.00000

principal component analysis, must be: "How many linearly independent aggregating species are present in this system?"

Using the data matrix from table 1, the correlation coefficients for principal and factor components were computed using Biomed Program BMD 03M [46] as shown in table 2.

The eigenvalues based on this correlation matrix were computed to be:

4.41349 0.97482 0.36991 0.14370
0.05671 0.04139

and cumulative proportions of the total variance were:

0.73558 0.89805 0.95970 0.98365
0.99310 1.0000

Based on these eigenvalues, we conclude that two components are present with a cumulative variance of 90%. Applying the principal of eigenvalue unity, we would deduce that this is a two-component system. However, since the third eigenvalue represents 6% of the total variance, there may be a third minor species present.

In order to confirm our results, we examined f_d-DNA in 0.01 ionic strength of NaCl, as shown in fig. 8. These patterns at various speeds were used to compute the correlation matrices shown in tables 3 and 4.

To accomplish this, we examined both the moving boundary and the bottom boundary. Data matrices were constructed based on $\bar{y}$, the height of the schlieren pattern above the reference line, as a function of radial distance. Table 3 shows the resulting correlation matrix for the moving zone of the sedimenting boundary, and table 4, the matrix for the bottom of the cell.

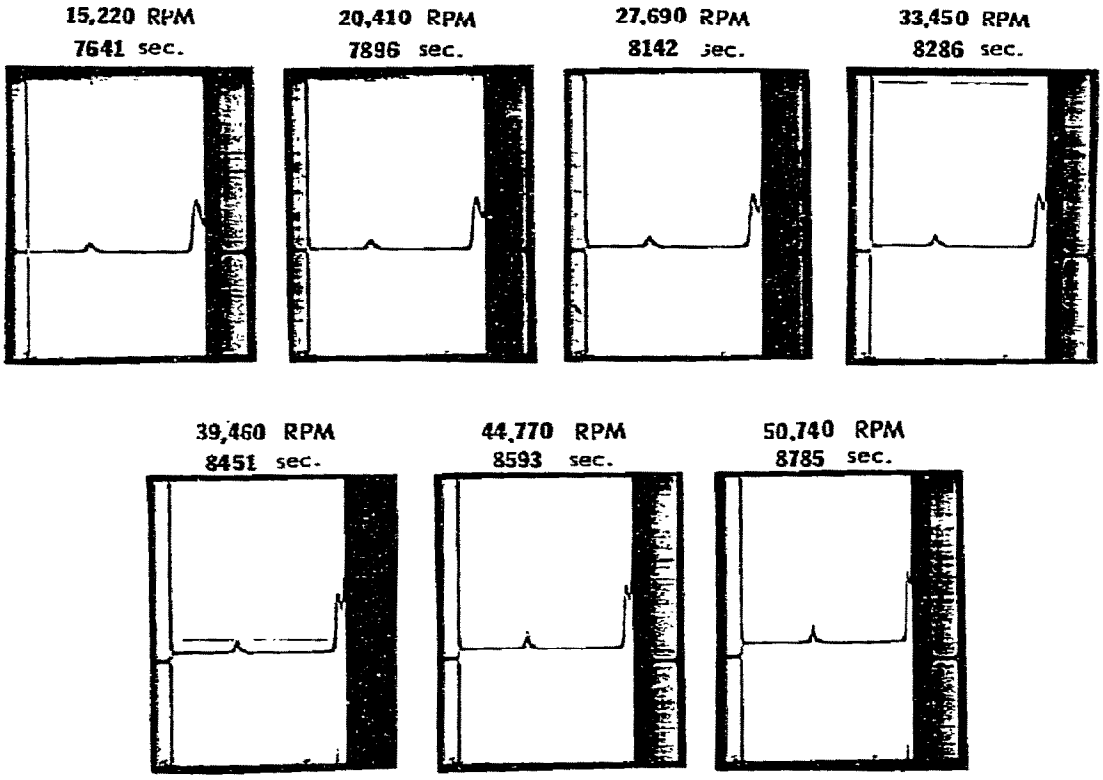

Fig. 8. Ultracentrifuge patterns for enumeration of aggregating species in f_d-DNA system (1.2 mg/ml in 0.01 M NaCl) using standard 4°–12 mm sector cell, bar angle 70°. Initially run at 50 740 rpm for 2407 sec after reaching speed, then lowered to 12 590 rpm. Speed was gradually increased to 50 740 rpm by steps as indicated.

Eigenvalues obtained from table 3 were:

6.24434 0.49714 0.20228 0.04208
0.00824 0.00462 0.00135

and cumulative proportions of the total variance:

0.89205 0.96306 0.99196 0.99797
0.99915 0.99981 1.00000

Thus, the moving zone consists of one component.

Eigenvalues obtained from table 4 were:

4.03949 2.27081 0.55360 0.10294
0.08245 0.01119 0.00253

Cumulative proportions of the total variance were:

Table 3
Correlation coefficients of principal and factor components in the moving boundary based on fig. 8. Computed using Biomed Program BMD 03M [46]

1.00000	0.89959	0.83556	0.84361	0.73263	0.64397	0.66095
0.89959	1.00000	0.98162	0.98446	0.91904	0.76132	0.86056
0.83556	0.98182	1.00000	0.99777	0.97052	0.82769	0.93320
0.84361	0.98446	0.99777	1.00000	0.96116	0.81139	0.92152
0.73263	0.91904	0.97052	0.96116	1.00000	0.87486	0.98385
0.64397	0.76132	0.82769	0.81139	0.87486	1.00000	0.88187
0.66095	0.86056	0.93320	0.92152	0.98385	0.88187	1.00000

Table 4
Correlation coefficients of principal and factor components in bottom boundary based on fig. 8. Computed using Biomed Program BMD 03M [46]

1.00000	0.09772	−0.24908	−0.34518	−0.66006	−0.66842	−0.63358
0.09772	1.00000	0.44109	0.39040	−0.68177	−0.69712	−0.70754
−0.24908	0.44109	1.00000	0.98254	−0.18240	−0.32588	−0.34030
−0.34518	0.39040	0.98254	1.00000	−0.07918	−0.23062	−0.25022
−0.66006	−0.68177	−0.18240	−0.07918	1.00000	0.92156	0.89664
−0.66842	−0.69712	−0.32588	−0.23062	0.92156	1.00000	0.99446
−0.63358	−0.70754	−0.34030	−0.25022	0.89664	0.99446	1.00000

0.57707 0.89247 0.97156 0.98626
0.99804 0.99964 1.00000

Based on these results we conclude that two components are present at the bottom of the cell. Thus, a total of three linearly-independent species are present for f_d-DNA in this ionic environment.

5. Discussion

Our results indicate that the aggregation of f_d-DNA is highly dependent on ionic strength, and will vary greatly with a slight change in ionic environment. It should be emphasized that an accurate measure of the compressibility of f_d-DNA must be made in a very particular ionic environment and under specific gelling conditions.

Compressibility measurements of Mg^{2+}–f_d-DNA and Na^+–f_d-DNA differ markedly, indicating a difference in f_d-DNA binding with monovalent and divalent ions. Such a difference in binding has been noted by Archer et al. [40] and Krakauer [41], in studies on the binding of Na^+ and Mg^{2+} to poly A, poly U·A, and poly A2·U. Electrophoretic mobility studies by Ross and Scruggs [42] indicate that approximately 0.62 ± 0.02 Na^+ ions are bound per nucleotide. We conclude that Mg^{2+}–f_d-DNA is more compressed and tightly folded, even at 0.005 ionic strength, while Na^+–f_d-DNA may exist in a more relaxed conformational state.

The ultracentrifugal field relaxation behavior of Na^+–f_d-DNA, that is the appearance of a moving zone and a hypersharp interface at the bottom of the cell, may be explained in terms of diffusion [43,44]. One factor operating here is a difference in the driving force. Thus, the driving force on the Na^+ ions is small, and they retard the Na^+–f_d-DNA molecules in the moving zone (figs. 6 and 8). On the other hand, if the driving force for the Na^+–f_d-DNA aggregates at the bottom of the cell is independent of particle size, then you would expect to observe a hypersharp interface.

As a general rule, the dilution of polyelectrolytes to a solution of very low ionic strength will increase the frictional coefficient [45]. As may be seen in figs. 6 and 8, a front with an extremely high concentration gradient forms at the bottom of the cell, from which the Na^+–f_d-DNA aggregates begin to diffuse into the solvent layer, producting a hypersharp interface.

In schlieren patterns of Mg^{2+} (fig. 4) at the same ionic strength as Na^+ (fig. 6), Mg^{2+}–f_d-DNA shows a broadening of the bottom boundary rather than a hypersharp interface at the bottom of the cell. We speculate that the magnitude of the driving force for this divalent ion, and for Mg^{2+}–f_d-DNA aggregates, differs from that of the monovalent Na^+ion.

Schlieren patterns along with compressibility and molecular volume measurements at the interface and bottom of the cell, therefore, lead us to conclude that there is a change in the conformational state of the gel-like f_d-DNA aggregates.

In enumerating the aggregating components for Na^+–f_d-DNA at 0.005 ionic strength within 90% confidence limits, we found two linearly-independent aggregating species definitely present in the system, with the possibility of a third species indicated. It should be noted that in this method of enumeration only linearly independent components are determined. All linearly dependent components appear as a single species.

Despite the effects of sedimentation and diffusion operating on a system at low ionic strength, this type of ionic environment is best suited for enumeration of interacting species by principal component or factor analysis.

Our conclusion is that the first component in this single-stranded f_d-DNA system may represent a fully relaxed conformation; the second species being more compressed, partially folded aggregates at the interface, and the third a tightly-packed, gel-like material at the extreme bottom of the cell.

Acknowledgement

We thank Dr. A.J. Richard for critically reviewing this manuscript prior to publication.

References

[1] P.W. Chun, W.P. Herschleb, R.L. Buckley, M.M. Bliziotes and U.T. Son, manuscript in preparation (1973).
[2] D.A. Marvin and H. Hoffmann–Berling, Z. Naturforsch. 186 (1963) 884.
[3] D.E. Bradley, J. Gen. Microbiol. 35 (1964) 471.
[4] L.G. Caro and M. Schnos, Proc. Natl. Acad. Sci. U.S. 56 (1966) 126.
[5] D.A. Marvin, J. Mol. Biol. 15 (1966) 8.
[6] B. Knippers and H. Hoffmann–Berling, J. Mol. Biol. 21 (1966) 281.
[7] D.A. Marvin and H. Schaller, J. Mol. Biol. 15 (1966) 1.
[8] W. Wickner, D. Brutlag, R. Schekman and A. Kornberg, Proc. Natl. Acad. Sci. U.S. 69 (1972) 965.
[9] R. Schekman, W. Wickner, D. Westergaard, D. Brutlag, K. Geider, L.L. Bertsch and A. Kornberg, Proc. Natl. Acad. Sci. U.S. 69 (1972) 2691.
[10] P.H. Poon and V.N. Schumaker, Biochemistry 6 (1967) 276.
[11] G. Kegeles, L. Rhodes and J. Bethune, Proc. Natl. Acad. Sci. U.S. 58 (1967) 45.
[12] L.F. TenEyck and W. Kauzmann, Proc. Natl. Acad. Sci. U.S. 58 (1967) 888.
[13] G. Kegeles, Federation Proc. 27 (1968) 799.
[14] R. Josephs and W.F. Harrington, Proc. Natl. Acad. Sci. U.S. 58 (1967) 1587.
[15] R. Josephs and W.F. Harrington, Biochemistry 5 (1967) 3474.
[16] M. Murayama, Clin. Chem. 13 (1967) 578.
[17] P.W. Chun, A.J. Richard, W.P. Herschleb and Mary L. Krista, Biopolymers 12 (1973) 1931.
[18] P.W. Chun and M.E. Magar, Federation Proc. 32 (1973) 2529.
[19] M.E. Magar and P.W. Chun, Biophys. Chem. 1 (1973) 18.
[20] R.M. Wallace, J. Phys. Chem. 64 (1960) 899.
[21] R.M. Wallace and S.M. Katz, J. Phys. Chem. 68 (1964) 3890.
[22] D.W. McMullen, S.R. Jaskunas and I. Tinoco, Biopolymers 5 (1967) 589.
[23] S. Ainsworth, J. Phys. Chem. 65 (1961) 1968.
[24] G. Weber, Nature 190 (1961) 27.
[25] S. Ainsworth and W.S.W. Bingham, Biochim. Biophys. Acta 160 (1968) 10.
[26] G.K. Ackers, J. Biol. Chem. 243 (1968) 2056.
[27] W. Godschalk, Biochemistry 10 (1971) 3284.
[28] D. Pratt, H. Tzagoloff and W.S. Erdahl, Virology 30 (1966) 397.
[29] K.R. Yamamoto, B.M. Alberts, R. Benzinger, L. Lawhorne and G. Treiber, Virology 4 (1970) 734.
[30] N. Zinder, R.C. Valentine, M. Roger and W. Stoeckenius, Virology 20 (1963) 638.
[31] P. Byvoet, Anal. Biochem. 13 (1965) 314.
[32] O. Lowry, J.S. Rosenbrough, A.L. Farr and R.J. Randall, J. Biol. Chem. 193 (1951) 265.
[33] G. Kegeles and C.L. Sia, Biochemistry 2 (1963) 906.
[34] D.A. Yphantis, Biochemistry 3 (1964) 297.
[35] J. Dayantis, Compt. Rend. Acad. Sci. Ser. 207 (1968) 223.
[36] W. Bauer, F. Prindaville and J. Vinograd, Biopolymers 10 (1971) 2615.
[37] H.A. Harman, Modern factor analysis (Univ. Chicago Press, Chicago, 1967).
[38] H.B. Halsall and V.N. Schumaker, Biochemistry 11 (1972) 4692.
[39] G. Kegeles, Federation Proc. 28 (1969) 866.
[40] B.G. Archer, C.L. Craney and H. Krakauer, Biopolymers 11 (1972) 781.
[41] H. Krakauer, Biopolymers 11 (1972) 811.
[42] P.D. Ross and R.L. Scruggs, Biopolymers 2 (1964) 231.
[43] O. Kedem and A. Katchalsky, J. Polymer Sci. 15 (1955) 321.
[44] H. Morawetz, Macromolecules in solution (Interscience, New York, 1966) p. 365.
[45] M. Nagasawa and H. Fujita, J. Am. Chem. Soc. 86 (1964) 3005.
[46] M. Dixon, Biomed Program BMD 03M, UCLA (1969).

BIOPHYSICAL CHEMISTRY 1 (1974) 152–160. © NORTH-HOLLAND PUBLISHING COMPANY

RHEOLOGY OF FIBRIN CLOTS. I. DYNAMIC VISCOELASTIC PROPERTIES AND FLUID PERMEATION

Wesley W. ROBERTS, Ole KRAMER, Robin W. ROSSER, F. Henry M. NESTLER and John D. FERRY

Department of Chemistry and Rheology Research Center, University of Wisconsin, Madison, Wisconsin 53706, USA

Received 5 November 1973

The storage and loss shear moduli (G', G'') of human fibrin clots have been measured in small oscillating deformations over a frequency range of 0.01 to 160 Hz with the modified Birnboim transducer apparatus. Most clots were prepared by the action of thrombin on purified fibrinogen, under various conditions of pH and ionic strength to produce networks ranging from coarse to fine structure; some were ligated by fibrinoligase. The fine, unligated clot showed very little mechanical loss or frequency dependence of G' over the experimental frequency range, though loss mechanisms evidently appear at higher frequencies; G' was proportional to the 1.5 power of fibrin concentration. The coarse, unligated clot showed a slight increase of G' with frequency, reflecting some relaxation mechanisms with time constants whose reciprocals lie in the experimental frequency range. Ligation did not greatly affect the magnitude of G'. However, clots prepared by dilution of solutions of fibrin monomer in 1 M sodium bromide had smaller moduli by a factor of ten than corresponding clots prepared by the action of thrombin of fibrinogen. Oscillatory measurements in the Birnboim apparatus with closed-end (annular pumping) geometry revealed a low-frequency anomaly which was shown to be due to permeation of fluid through the clot structure, and from these measurements the Darcy constants for coarse clots were calculated. From the Darcy constants, the average thicknesses of the fibrous elements of the structures were estimated to be from 300 to 700 Å.

1. Introduction

The mechanical properties of fibrin clots are obviously important in their physiological function and can also provide clues to their detailed structure and the mechanism of their formation from fibrinogen. A few studies of elasticity and viscoelasticity of fibrin have appeared in the literature [1–7]. In an earlier investigation [6], dynamic viscoelastic properties in the frequency range from 0.003 to 10 Hz and stress relaxation were measured with a Weissenberg rheogoniometer [8], with special attention to the effects of ligation (formation of primary chemical bonds between fibrin units, through the action of fibrinoligase [9]). Another rheological property of physiological importance which can be related to clot structure is the permeation of fluid through a clot under pressure. In the present study, information has been obtained about both dynamic viscoelastic properties and fluid permeation. The differences between clots of coarse and fine structure, as determined by the pH, ionic strength, and other variables during clotting, are of particular interest. The effect of clot ligation by fibrinoligase has been explored to some extent.

2. Materials

Lyophilized human fibrinogen was obtained from Kabi A.B., Stockholm. It was dissolved in tris hydroxymethylaminomethane buffer of the desired pH and dialyzed against a large volume of the same buffer overnight at 4°C to adjust its pH and ionic strength (μ), of which 0.05 was contributed by the buffer and the remainder by sodium chloride. Aliquots were frozen and stored at −10°C for future use. The protein concentration was determined spectrophotometrically from absorption at 2820 Å of aliquots diluted

with a solution containing 0.2 M sodium hydroxide and 40% urea by weight; the extinction coefficient was taken as 1.651 cm^{-1} $(g/\ell)^{-1}$ [10]. The protein was stated by the manufacturer to be either 90 or 95%; of the non-clottable moiety, 3% is attributable to fibrinopeptides and the remainder to other protein, which was ignored. All solutions were prepared with deionized, double-distilled water.

Bovine thrombin (topical) was obtained from Parke-Davis and company and dissolved in buffer of the same pH and ionic strength as the fibrinogen solvent. The concentration of thrombin in NIH units was determined by appropriate tests [11]; the stock solution which was added to fibrinogen solutions for clotting was usually 20 u/ml, although higher if an unusually high final concentration was required.

Fibrin stabilizing factor (FSF) prepared from human plasma [12] was generously furnished by Professor L. Lorand and Mr. A.J. Gray, Jr., of Northwestern University. It was kept at 4° in a tris buffer solution of pH 7.5, ionic strength 0.15, containing 0.001 M ethylene diamine tetraacetate. When used for clot ligation, it was incubated at room temperature with calcium chloride (including excess to combine with EDTA) and thrombin to activate to fibrinoligase, before adding this mixture to the fibrinogen, the volumes being adjusted to obtain the desired final concentrations of all components. In some cases, clot aliquots were subjected to analysis of polypeptide chain subunit patterns by gel electrophoresis [13] to determine whether ligation had actually taken place. These analyses were kindly performed by Professor Lorand and Mr. Gray.

Fibrin monomer prepared according to Donnelly et al. [14], dissolved in 1 M sodium bromide with pH adjusted to 5.3 by acetic acid, was generously provided by Professor Lorand and Mr. Gray.

Clotting mixtures were introduced into the apparatus as described below and allowed to clot in situ. Because of the importance of the coarseness of structure in determining rheological properties, an aliquot of the mixture was usually allowed to clot in a spectrophotometer cell and its opacity was measured at 6000 Å as a gauge of coarseness [15, 16]. Here, the opacity is defined as $(1/\ell) \log I_0/I$, where I_0 and I are the incident and transmitted light intensities for a path length of ℓ in cm. The measurement was made at the same elapsed time as the beginning of mechanical measurements. Often, syneretic fluid was expressed from a clot aliquot for a final check of pH.

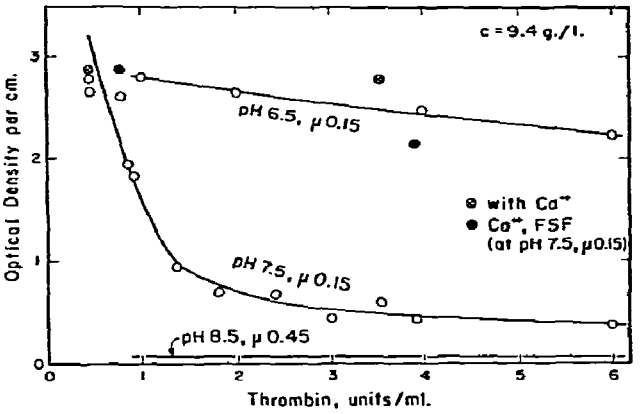

Fig. 1. Clot opacity in cm^{-1} plotted against thrombin concentration, for several pH and ionic strength conditions as shown, also with Ca^{2+} (0.0056 M) and FSF (0.002 mg/ml) as indicated; c = 9.4 g/ℓ.

It was found that, in addition to the well-known effects of pH and ionic strength [15, 16] on clot coarseness, the thrombin concentration during clotting had a strong influence at pH 7.5, μ0.15. This is shown in fig. 1, where the opacity decreases from 2.9 (white, opaque) to 0.4 (slightly hazy) with increasing thrombin and concomitant decreasing clotting time. At pH 6.5 and 8.5, on the other hand, the opacity is respectively very high (coarse) and very low (fine) over the entire range of thrombin concentrations. It may be noted that addition of calcium ion, with or without FSF, can increase the opacity at pH 7.5 when the thrombin concentration is high.

3. Methods

Measurements of dynamic storage and loss shear moduli (G', G'') were made over a frequency range from 0.01 to 160 Hz with the Birnboim transducer apparatus as modified by Massa and Schrag [17], with computerized data acquisition and processing system. A stainless steel cell and rod were used. Normally, the sample is deformed with annular pumping geometry by periodic motion of the inner rod along its axis with the cell end closed, as shown in fig. 2b. For samples with high mechanical impedance, however, an open-

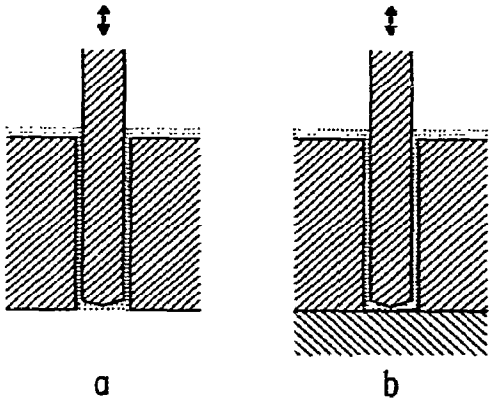

Fig. 2. Deformation in Segel–Pochettino (open-end) geometry (a) and annular pumping (closed-end) geometry (b).

ended cell can be used as shown in fig. 2a (Segel–Pochettino geometry). For linearly viscoelastic polymer solutions and gels, the choice is purely a matter of the magnitude of the sample impedance Z_M^S [17], which is the complex ratio of force to velocity contributed by the sample to the moving system. With the proper sample coefficient A or A_0, measurements of Z_M^S will provide G' and G'' in either case. For annular pumping, $Z_M^S = A\eta^* \equiv A(G' + iG'')\, i\omega$; for Segel–Pochettino, $Z_M^S = A_0\eta^*$. Here η^* is the complex dynamic viscosity and ω the radian frequency (2π times the frequency in Hz). The coefficients A and A_0 depend on the radii of rod (R_1) and cell (R_2) and the length of the annulus (L). For the cell dimensions used in this work, A = 24 400 cm and A_0 = 123 cm. (In these expressions for Z_M^S, a term involving the sample density [17] has been omitted because it is not significant except at the highest frequencies.)

Many measurements on clots were made with closed end cells before it was realized that pumping geometry can introduce an additional response besides viscoelastic deformation if the clot structure is permeable to fluid. For coarse clots, the pressure at the bottom forces fluid up through the clot annulus with consequent flow; this fluid may arise from syneresis of a very small volume of clot below the bottom of the rod. In an extreme case of a very permeable gel, the sample deformation would correspond to Pochettino geometry even with the end closed, with a very much smaller sample coefficient.

The apparent storage and shear moduli, G'_a and G''_a, which would be calculated from measurements of Z_M^S if permeation is not taken into account, can be derived from an analysis of the forces on the moving rod. The mechanical impedance Z_P corresponding to the flow through the annulus is the ratio of force to velocity:

$$Z_P = p\pi R_1^2/v_1, \tag{1}$$

where p is the pressure and v_1 the rod velocity (both periodic functions of time). In terms of a mechanical model, Z_P acts in series with an impedance $A_0(G' + G'')/i\omega$, and the combination is in parallel with an impedance $(A - A_0)(G' + G'')/i\omega$. Setting the total impedance equal to $A(G'_a + iG''_a)/i\omega$, we obtain the apparent moduli which would be calculated with the sample coefficient A if the permeation were ignored [18]:

$$G'_a = (A_0/A)G' + \frac{\omega^2}{A}\,\frac{Z_P^2(A-A_0)G'}{(A-A_0)^2G'^2 + [Z_P\omega + (A-A_0)G'']^2}, \tag{2}$$

$$G''_a = (A_0/A)G'' + \frac{\omega}{A}\,\frac{Z_P(A-A_0)^2G'^2 + Z_P(A-A_0)G''[Z_P\omega + (A-A_0)G']}{(A-A_0)^2G'^2 + [Z_P\omega + (A-A_0)G'']^2} \tag{3}$$

Several limiting cases of interest may be distinguished. If $Z_P \gg Z_M^S$, $G'_a = G'$ and $G''_a = G''$, so permeation can be ignored; this will be found to be the case for fine clots. At high frequencies, $G'_a = G'$ and $G''_a = G''$; permeation can be ignored even for coarse clots. At the limit of low frequency, $G'_a = (A_0/A)G'$ and $G''_a = (A_0/A)G'' + \omega Z_P/A$. Thus the apparent loss modulus G''_a gives a measure of permeability provided $\omega Z_P \gg A_0G''$, as is usually the case.

The permeability of a reticulate structure to fluid is conventionally expressed by the Darcy constant $\mathcal{D}$, which may be defined [19] as

$$\mathcal{D} = Q\eta_s L/Ftp, \tag{4}$$

where Q is the volume of fluid passing through a column of length L and cross-section area F in time t under a pressure p, and η_s is the viscosity of the fluid.

In our geometry, $F = \pi(R_2^2 - R_1^2)$ and Q/t is the rate at which the bottom of the rod expels fluid, viz., $Q/t = \pi R_1^2 v_1$. Combination with eq. (1) yields

$$\mathcal{D} = \pi\eta_s L R_1^4/(R_2^2 - R_1^2)Z_P. \quad (5)$$

Or, combining with the limiting from of eq. (3) at low frequencies and negligible $(A_0/A)G''$,

$$\mathcal{D} = \pi\eta_s L R_1^4/(R_2^2 - R_1^2)A \lim_{\omega \to 0} (G_a''/\omega). \quad (6)$$

From the Darcy constant, calculated in this manner from G_a'' at low frequencies, the average diameter of the fibrous elements of the gel structure can be estimated [19]. If the volume fraction φ_2 of the gel structure is less than 3%,

$$\mathcal{D} = k\varphi_2^{-1} d^2, \quad (7)$$

and, from hydrodynamic calculations of Emersleben [20] and model experiments of Kuhn [21], the proportionality constant k can be assigned a value of 0.105 ± 0.01.

The Darcy constant of a clot can also be determined from the rate of flow of buffer through a cylindrical sample of known dimensions under moderate pressure, and a few such measurements were made with a simple apparatus to check the results from eq. (6).

For measurements in the Birnboim apparatus, the clotting mixture was normally prepared in a plastic test tube and poured into the cell, which was then raised to its proper place around the rod and locked. The rod and drive coil were then unclamped so the moving system could assume its equilibrium position. A small amount of mineral oil was layered on the clot surface with a hypodermic needle to avoid evaporation. Before clotting occurred, the transducer housing was sometimes closed and the assembly was immersed in a water bath for temperature regulation at 25.0°C; though sometimes measurements were made at the ambient temperature of about 23°C. The clotting time was usually from 3 to 15 min, and 2 to 2½ h were allowed to elapse for the full clot rigidity to develop [1, 15]. Measurements at 1.0 Hz were then repeated at 15 min intervals until the force/amplitude ratio (a measure of modulus) was constant within 1%. After a series of measurements at different frequencies, the initial measurements were repeated to make sure that the modulus had not changed by more than a few per cent during the sequence.

When the clotting time was very short (< 2 min), the mixture without thrombin was placed in the cell and the required thrombin in a solution volume of 0.05 cc was placed on the tip of the rod. The cell was then raised and pumped manually several times to complete the mixing, and afterwards the rod and drive coil were quickly unclamped. In this case, the transducer could not be moved to the water bath because the clot, once formed, might be damaged or dislodged from the cell or rod surface; measurements were made at the ambient temperature of about 23°C.

For open-end geometry, the glass bottom of the cell was removed after the clot had formed. This was facilitated by previously coating the glass with a thin layer of silicone grease. The exposed clot was coated with a drop of mineral oil to reduce evaporation.

In a few cases, clots were formed by diluting fibrin monomer, dissolved in 1 M sodium bromide at pH 5.3 [14], with tris buffer of pH 7.5; the transducer was left at ambient temperature.

4. Results

4.1. Dynamic measurements: Open-end geometry

The maximum axial displacement of the rod used in oscillatory shear measurements was about 1.3×10^{-4} cm, and with open-end geometry the corresponding maximum shear strain was (for an annular gap of 0.037 cm) only 0.35%. The wave forms for both force and displacement, as viewed on an oscilloscope, were sinusoidal.

The storage and loss shear moduli (in dynes cm^{-2}) of a typical fine and a typical coarse clot are plotted logarithmically against radian frequency in fig. 3. The upper end of the frequency range is limited by incipient shear wave propagation across the gap [17]. The fibrin concentration is 9.4 g/ℓ. For the fine clot (opacity 0.039 cm^{-1}), G' is remarkably independent of frequency over nearly four logarithmic decades, indicating absence of relaxation mechanisms with time constants whose reciprocals lie in this region; such nearly perfect elasticity is rarely if ever observed in polymeric systems. The loss modulus G'' is very low at low

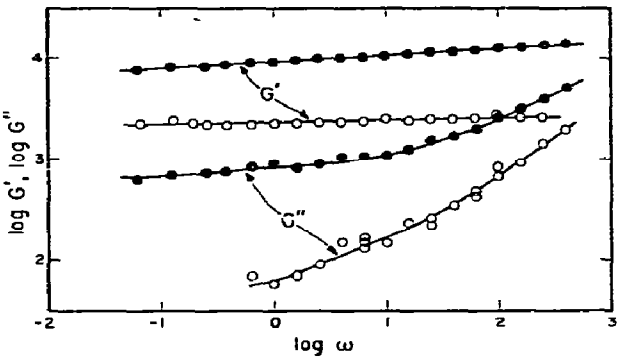

Fig. 3. Logarithmic plots of G' and G'' (in dyne/cm^2) against radian frequency for deformation in Segel–Pochettino geometry. Open circles, fine clot (pH 8.5, μ 0.45, fibrin 9.4 g/ℓ, thrombin 4 u/ml); black circles, coarse clot (pH 7.5, μ 0.15, fibrin 9.4 g/ℓ, thrombin 0.8 u/ml).

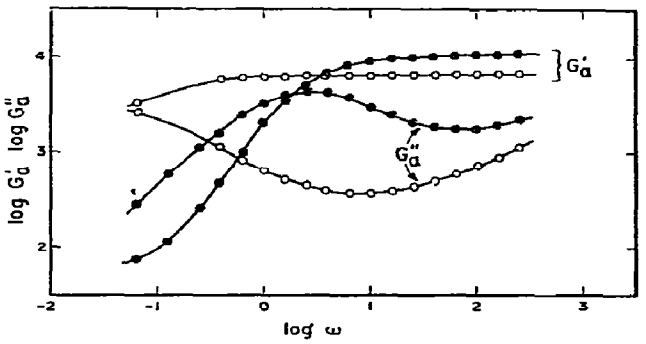

Fig. 4. Logarithmic plots of apparent G'_a and G''_a(in dyne/cm^2) against radian frequency for deformation in annular pumping geometry. Open circles, fine clot (pH 7.5, μ 0.45, fibrin 9.4 g/ℓ, thrombin 6 u/ml); black circles, coarse clot (pH 7.5, μ 0.15 fibrin 9.4 g/ℓ, thrombin 0.25 u/ml).

frequencies (corresponding to a loss tangent, G''/G', of 0.025), but at higher frequencies it increases almost directly proportional to frequency, reflecting a substantial relaxation mechanism whose reciprocal time constant lies at a frequency above the experimental range. For the coarse clot (opacity 2.63 cm^{-1}), G' is somewhat higher and increases somewhat with frequency, reflecting a finite relaxation spectrum. Correspondingly, G'' is relatively considerably higher (minimum loss tangent about 0.1), but it too increases more rapidly at frequencies above log $\omega = 2$, indicating a substantial relaxation mechanism operative at higher frequencies.

4.2. Dynamic measurements: Closed-end geometry

For the closed-end geometry, the maximum rod displacement was also usually 1.3×10^{-4} cm; in this case, the maximum shear strain calculated from a formula given elsewhere [22] was about 10%. Despite this rather large strain, no effects attributable to alteration of clot structure were observed. In several experiments, much smaller strains (down to 2%) were employed, with essentially the same values of G' and G'' at a given frequency. Check measurements after completion of a series of frequencies revealed no progressive alteration of structure; and rapid alternation of measurements at low and high frequencies gave values in respective agreement so that a steady state was evidently quickly reached with no thixotropic effects. However, for coarse clots, the wave form for the displacement signal showed departures from sinusoidal shape; at low frequencies, the maxima and minima were unsymmetrical, revealing some kind of hysteresis within the cycle, and at higher frequencies there were irregularities near the peaks. The values of G' and G'' calculated by the cross-correlation analysis of the computer [17] do not correspond exactly to the quantities defined for sinusoidal deformations, therefore, but emphasis is placed on G' at higher frequencies which is probably affected very little by these irregularities.

The apparent storage and loss shear moduli of a typical coarse clot (opacity 2.7 cm^{-1}) and a relatively fine clot (opacity 0.4 cm^{-1}) are plotted in fig. 4. At the highest frequencies, the behavior is similar to that observed with open-end geometry. However, with decreasing frequency, the clots show very different behavior. For the coarse clot, G' falls by more than two orders of magnitude; G'' passes through a minimum and maximum, and at low frequencies approaches direct proportionality to ω (slope of unity). This indicates an energy-dissipating process with a time constant of the order of one second, but the absence of such a process in fig. 3 demonstrates that it is not viscoelastic. It is due to permeation of fluid through the clot annulus.

According to the low-frequency limiting form of eq. (3) (with negligible $(A_0/A)G''$ term), $G''_a/\omega = Z_P/A$. If this ratio as observed at low frequencies for the

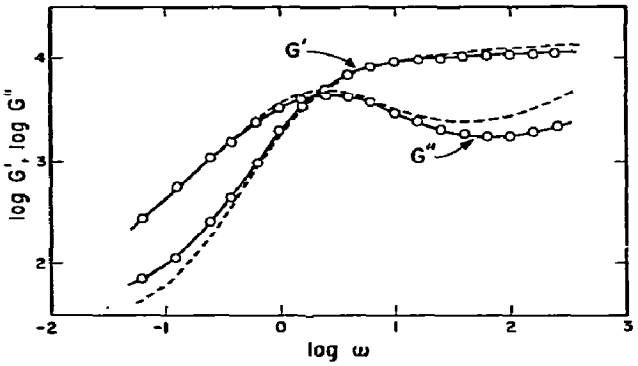

Fig. 5. Data for coarse clot of fig. 4 (points) compared with calculation of apparent G'_a and G''_a taking permeation of fluid into account, with data for coarse clot of fig. 3 and eqs. (2) and (3) (dashed curves).

coarse clot in fig. 4 is attributed to permeation, we obtain $Z_P = 1.1 \times 10^8$ dyne sec/cm. From this value together with the actual frequency dependence of G' and G'' measured on a clot prepared under identical conditions (fig. 3), eqs. (2) and (3) can be used to predict the values of G'_a and G''_a which would be measured under closed-end conditions. This calculation is compared in fig. 5 with the data of fig. 4, and the agreement is quite good. In particular, G'_a at low frequencies approaches the expected limiting value of $(A_0/A)G'$.

From the above value of Z_P and eq. (5), we obtain for the Darcy constant of the coarse clot $\mathcal{D} = 1.8 \times 10^{-10}$ poise cm^4 dyne^{-1} sec^{-1}. To compare this with a more direct measurement, the flow of buffer through a clot prepared under identical conditions in a cylindrical tube was measured by applying hydrostatic pressure to one end. From measurements at different pressures and application of eq. (4), $\mathcal{D}$ was found to be 2.3×10^{-10}, in quite reasonable agreement. (Further details concerning this procedure and data for different types of clots will be reported subsequently.)

The fine clot of fig. 4 offers much greater resistance to permeation and the effect on G'_a and G''_a is therefore shifted to lower frequencies; the expected maximum in G''_a lies below the experimental frequency range, and Z_P cannot be calculated. For still finer clots (prepared at pH 8.5), the frequency dependence of closed-end data closely resembles that of open-end data but for a slight rise in G''_a at lowest frequencies.

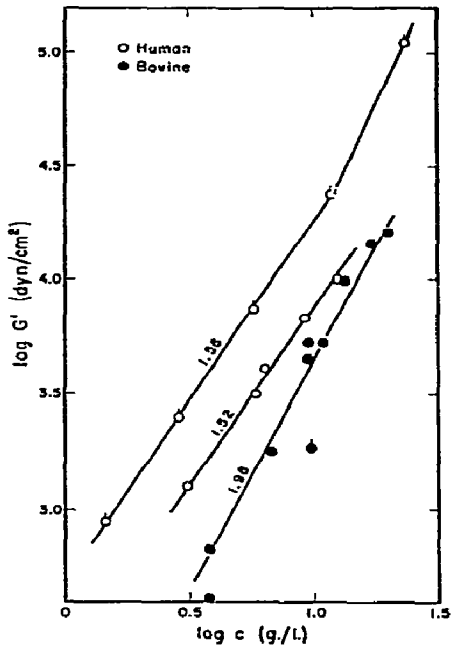

Fig. 6. Logarithmic plots of G' of clots at frequencies at or above 63 rad/sec against fibrin concentrations in g/ℓ; numbers denote slopes. ○, human, data of fig. 7 and additional concentrations under same conditions; ◇, human, Ferry and Morrison [1], pH 6.8, μ 0.30, thrombin 4 u/ml; ●, bovine, Miller et al. [3], pH 7, μ 0.45, thrombin 1 u/ml; ◆, bovine, Kaibara and Fukada [4], pH 6.8, μ 0.37, thrombin 1.7 u/ml.

4.3. Plateau moduli and Darcy constants

At the upper end of the experimental frequency range, G' is nearly independent of frequency and unaffected by fluid permeation in closed-end geometry. This value is a measure of the rigidity of the structure and is listed in table 1 for clots formed under various conditions at pH 7.5, ionic strength 0.15. They are not always reproducible for different preparations of fibrinogen, as previously noted in wave propagation measurements in a similar frequency range [3]. However, measurements on the same preparation are comparable.

Results for a series with different fibrin concentrations are plotted logarithmically against concentration (c) in fig. 6, giving a straight line with a slope of 1.52. The concentration dependence is close to that ob-

Table 1
Limiting modulus data, pH 7.5, μ 0.15 (annular pumping geometry)

F'gen Stock	Fibrin (g/ℓ)	Thrombin (u/ml)	Opacity (cm^{-1})	log G' ($dyne/cm^2$) high ω	log (G''/ω) low ω	$\mathcal{D}$ ($\times 10^{10}$)	d (Å)
A	3.1	6		3.10			
A	5.9	6		3.50			
A	6.3	6		3.61			
A	9.3	6	0.38	3.83			
A	12.5	6		4.00			
	9.2	0.25	2.7	3.80	3.52	2.5	400
	9.4	0.45	2.8	3.72			
B	9.4 a)	0.6	2.9	4.23	3.06	7.1	670
	9.4	0.65	2.7	3.78			
B	9.4	0.8	2.6	4.05	3.65	1.8	340
B	9.4 b)	0.8	2.9	4.33	3.40	3.3	470
B	9.4	3.5	0.61	4.06			
B	9.4 b)	3.5	2.6	4.05	3.80	1.3	290

a) 0.006 M calcium ion added.
b) Ligated with 0.006 M calcium and FSF (0.002 mg/ml).

served for human fibrin many years ago [1] under slightly different conditions, though the magnitudes differ. Earlier data on bovine fibrin [3] give a slope near 2, though it is questionable whether there can be a real species difference. A single point on bovine fibrin from Kaibara and Fukada [4] is included for comparison.

Table 1 also provides some comparisons of the effect of varying thrombin concentration and ligation by fibrinoligase, both of which affect the shear modulus relatively little in this frequency range.

Measurements were also made on a few clots formed by diluting fibrin monomer solutions with tris buffer. The modulus G', measured at higher frequencies where it is nearly frequency-independent, is compared in table 2 with that for corresponding clots formed by the usual action of thrombin on fibrinogen. Since the clots from fibrin monomer inevitably contain residual sodium bromide (0.15 M after dilution in our case), which is known to modify clot structure in the direction of fineness, the clots from fibrinogen were made in the presence of the same concentration of sodium bromide. Thrombin was also added in making the clots from fibrin monomer (needed to activate FSF in the case of ligation). For the clots to which fibrinoligase was added, ligation was confirmed by end-group analysis.

It is evident that the clots formed from fibrin monomer have lower moduli of rigidity by about a factor of ten, indicating a much weaker structure when polymerization takes place in this manner. The effect of ligation, however, is again very slight whether the precursor is fibrin monomer or fibrinogen.

Since G' is nearly proportional to $c^{1.5}$ at higher frequencies, it is of interest to examine both $G'_a/c^{1.5}$ and $G''_a/c^{1.5}$ over the entire frequency range at various fibrin concentrations. The moduli reduced in this manner are plotted logarithmically against frequency in fig. 7, with the somewhat surprising result that the curves coincide almost exactly. Although they do not extend to low enough frequencies to define the permeation effect clearly, it should follow from eqs. (2)

Table 2
Moduli of clots from fibrinogen and from fibrin monomer (fibrin concentration 3.0 g/ℓ, pH 7.3, ionic strength 0.28 including 0.15 M sodium bromide, thrombin 1.1 u/ml)

Precursor	Calcium ($M\times10^3$)	Fibrinoligase	Clotting time (min)	log G'
Fibrinogen	0.5	absent	3	2.6
Fibrin monomer	0.5	absent	4	1.7
Fibrinogen	1.0	present	3	2.8
Fibrin monomer	1.0	present	0.3	1.8

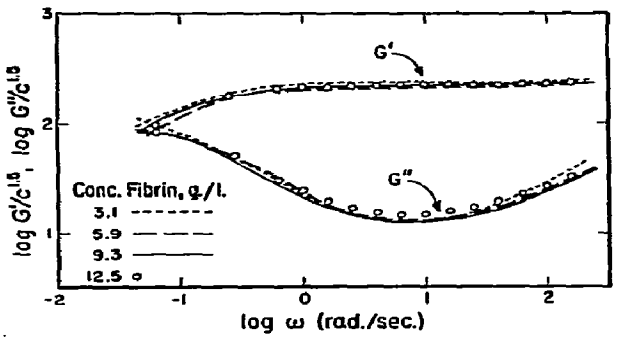

Fig. 7. Logarithmic plots of apparent $G'/c^{1.5}$ and $G''/c^{1.5}$ against radian frequency for annular pumping geometry; clots with four fibrin concentrations (c) as indicated; pH 7.5, μ 0.15, thrombin 6 u/ml, temperature 25°.

and (3) that the impedance is also proportional to $c^{1.5}$ and therefore [eq. (5)] that the Darcy constant is proportional to $c^{-1.5}$.

Darcy constants, obtained from G_a'' at low frequencies, are also given in table 1 for several clots. They appear to be correlated with opacity as expected, the highest opacity (coarest structure) having the highest permeability. At equal opacity, ligation perhaps decreases permeability slightly.

5. Discussion

5.1. Concentration dependence of modulus

The magnitude of G' in the present experimental frequency range reflects the elasticity of a network structure relatively free of relaxation processes. It must depend on the resistance of the individual fibrous elements (which can be seen in the electron microscope [23]) to extension and bending, as well as torsional deformations at the junctions.

The elastic behavior of a random two-dimensional network of fibrous elements has been treated by Sternstein [24]. It is assumed that in deformation the individual fibers extend and that twisting occurs at the junctions, to a degree which minimizes the elastic free energy. Unfortunately, this treatment has not yet been extended to a three-dimensional network.

5.2. Relaxation in fine clots at higher frequencies

In the region of log ω = 2.5, the fine clot of fig. 3 shows G' nearly independent of ω and G'' nearly directly proportional. This behavior corresponds to the presence of one or more relaxation mechanisms with modulus contributions G_i, and relaxtion times τ_i all of which are smaller than $1/\omega$ in the experimental range, such that

$$G''/\omega = \sum_i G_i \tau_i = \eta_v. \qquad (8)$$

The viscosity η_v may be regarded also as the viscosity of a Voigt model in parallel with the (frequency-independent) modulus G'; in fig. 3, η_v = 5 poise. In coarse clots, similar behavior appears to be approached at higher frequencies. To the extent that the form of the frequency dependence is independent of concentration as suggested by fig. 6, the viscosity η_v is proportional also to $c^{1.5}$, and the relaxation times are independent of concentration. It is tempting to associate the mechanical loss with bending deformations of the fibrous elements. Measurements at higher frequencies are needed to elucidate the mechanism.

5.3. Relaxation at very low frequencies or long times

Measurements at long times, such as creep and stress relaxation, are needed to elucidate mechanisms which reflect readjustments in the clot structure. It has already been observed that such measurements, as well as sinusoidal measurements at low frequencies [6] (in contrast to data in the upper frequency scale of the present experiments) differentiate clearly between ligated and unligated clots [3, 6], and the distinction is now being studied in more detail.

5.4. Estimation of fiber diameters from Darcy constants

By eq. (7), estimates of the average fiber diameter d can be made from the Darcy constants, and these are also listed in table 1. For coarse clots, the range of 300–700 Å agrees remarkably well with observations in the electron microscope [23]. The fluid permeation method has the advantage, of course, of studying the intact three-dimensional clot without alterations by drying, etc. The proportionality of Φ to $c^{-1.5}$ implies, together with eq. (7) and the fact that $v_2 = cp/1000$

where ρ is the density of the protein, that d is proportional to $c^{-0.5}$. Thus, dilution produces a mild coarsening effect.

Acknowledgements

This work was supported in part by Grant HL-13760 from the National Institutes of Health. We are much indebted to Professor L. Lorand and Mr. A. J. Gray, Jr. of Northwestern University for their advice, help, and cooperation in various aspects of these studies.

References

[1] J.D. Ferry and P.R. Morrison, J. Am. Chem. Soc. 69 (1947) 388.
[2] H. Wagreich and I.M. Tarlov, Arch. Biochem. 7 (1945) 345.
[3] J.D. Ferry, M. Miller and S. Shulman, Arch. Biochem. Biophys. 34 (1951) 424.
[4] M. Kaibara and E. Fukada, Biorheology 6 (1970) 329.
[5] E. Fukada and L. Dintenfass, Biorheology 8 (1971) 149.
[6] W.W. Roberts, L. Lorand and L.F. Mockros, Biorheology 10 (1973) 29.
[7] W.W. Roberts, Ph.D. Dissertation, Northwestern University (1970).
[8] K. Weissenberg, The testing of materials by means of the rheogoniometer (Farol Research Engineers, Bognor Regis, Sussex, England, 1964).
[9] L. Lorand, Ann. N.Y. Acad. Sci. 202 (1972) 6.
[10] B. Blombäck, Arkiv Kemi 12 (1958) 99.
[11] D.J. Baughman, Methods in Enzymology 19 (1970) 145.
[12] L. Lorand and T. Gotoh, Methods in Enzymology 19 (1970) 770.
[13] P. McKee, P. Matlock and R.L. Hill, Proc. Natl. Acad. Sci. U.S. 66 (1970) 738.
[14] T.H. Donnelly, M. Laskowski, Jr., N. Notley and H.A. Scheraga, Arch. Biochem. Biophys. 56 (1955) 369.
[15] J.D. Ferry and S. Shulman, J. Am. Chem. Soc. 71 (1949) 3198.
[16] S. Shulman and J.D. Ferry, J. Phys. Coll. Chem. 54 (1950) 66.
[17] D.J. Massa and J.L. Schrag, J. Polymer Sci. A-2 10 (1972) 71.
[18] R.W. Rosser, forthcoming thesis, University of Wisconsin.
[19] R. Signer and H. Egli, Rec. Trav. Chim. 69 (1950) 45.
[20] V.O. Emersleben, Physik. Z. 26 (1925) 601.
[21] H. Kuhn, Thesis, Basel (1946).
[22] T.L. Smith, J.D. Ferry and F.W. Schremp, J. Appl. Phys. 20 (1949) 144.
[23] S. Szalontai, in: Fibrinogen, ed. K. Laki (Marcel Dekker, New York, 1968) p. 137.
[24] S.S. Sternstein, in: Cellulose and cellulose derivatives, Vol. 5, eds. N. Bikales and L. Segal (Wiley, New York, 1971) p. 649.

BIOPHYSICAL CHEMISTRY 1 (1974) 161–174. © NORTH-HOLLAND PUBLISHING COMPANY

ON SITE HETEROGENEITY IN STURGEON MUSCLE GPDH: A KINETIC APPROACH

François SEYDOUX* and Sidney BERNHARD
Institute of Molecular Biology and Department of Chemistry, University of Oregon, Eugene, Oregon 97403, USA

Received 5 September 1973

The kinetics and stoichiometry of the reaction of sturgeon muscle glyceraldehyde-3-PO_4-dehydrogenase (GPDH) with the disulfide interchange reagent bis(2,2′ dithio-bis (5-nitrobenzoate) (DTNB) has been studied in detail. The native enzyme, a tetramer of covalently identical subunits, reacts relatively rapidly with precisely four equivalents of reagent, although there are three cysteine residues per subunit (12 per tetramer). Reaction of these four cysteines leads to total catalytic inactivation; the extent of inactivation is proportional to the fractional reaction. The rate of reaction is dependent on the extent of bound NAD: reactivity being very much greater at unliganded sites. The reaction with apo-enzyme is fastest, bimolecular and monophasic. Over a wide range of NAD concentration, however, the reaction of enzyme with a large molar excess of reagent is precisely biphasic, and each individual kinetic experiment can be analytically described by two pseudo first-order (NAD concentration-dependent) rate constants and two unequal NAD concentration-insensitive amplitudes. The biphasicity in rate is quantitatively explainable on the basis of a C_2 symmetry for the tetrameric subunits with a tighter binding of NAD at two of the four sites, if high reactivity is exclusively dependent on the absence of bound NAD. The *inequality* in the two amplitudes, however, requires either a more complex or a more dynamic model. Arguments are presented for the appropriateness of a C_2 symmetry model in which intramolecular transconformational isomerization of tight and loose NAD binding sites is possible. The equilibrium constant for the isomerization is estimable from the macroscopic specific rates and amplitudes. This "flip-over" C_2 symmetry model is apropos to all situations of negative cooperativity in ligand binding to tetramers, as is discussed.

1. Introduction

Considerable interest has recently centered on the active-site specific ligand binding properties of oligomeric enzymes composed of identical monomers, particularly in regard to the relationship between such ligand interactions and the regulatory functions of the enzyme [1–3]. Muscle GPDH enzymes from a variety of sources, as well as other oligomeric enzymes, exhibit two interesting phenomena: *negative cooperativity* (progressive decrease in ligand affinity with increasing extent of ligation) and *half-site reactivity* (stoichiometric limitation of an irreversible reaction to one half of the potential active sites of the molecule). These phenomena must each arise as a consequence of ligand-dependent variations in subunit interactions within the oligomer; although the precise mechanism of the ligand-mediated quaternary conformational changes is a matter of considerable controversy. Negative cooperativity can be a consequence of either site heterogeneity or of the extra stability of quaternary structures which contain a variety of ligand induced tertiary conformational subunits over an oligomer composed of subunits of identical conformation. Half-site reactivity may, according to either hypothesis be an extreme consequence of negative cooperativity. Its origin may also be a consequence of kinetic limitations.

Until now negative cooperativity has been studied primarily by equilibrium titration experiments [4,5]. Although titration experiments are suited to the detection of substantial site heterogeneity (i.e., when the ratio of the dissociation constants ≥ 10), extreme-

* Visiting research scientist from CNRS, France. Present address: EPCM, Bat. 430, Université Paris Sud, Orsay 91, France.

ly accurate data are required to differentiate among less variant sites [6]. The inherent inaccuracy in polyphasic titration analysis arises from the errors in estimation of free ligand concentration, especially in the stoichiometrically interesting concentration region where both the total *ligand* and *site* concentrations are comparable to the dissociation constants.

NAD^+ binding to sturgeon muscle GPDH, a tetrameric enzyme [7], has been previously shown to be quantitatively describable by a model involving *equal* numbers of two non-equivalent NAD^+ binding sites (i.e., negative cooperativity via site heterogeneity) [5]. Moreover, the chromophoric acyl phosphate β-(2-furyl)acryloyl phosphate, [8,9] acylates only two of the four potentially available active sulfhydryl sites of the enzyme (half-site reactivity). In contrast, 2,2'dithio-bis-(5-nitrobenzoic acid), a specific thiol reagent [10] reacts specifically, and very rapidly, with *four* active site cysteines of the enzyme tetramer [5].

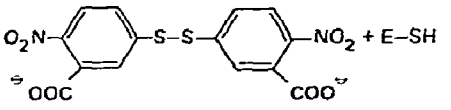

2, 2' dithio-bis (5-nitrobenzoate) (1)

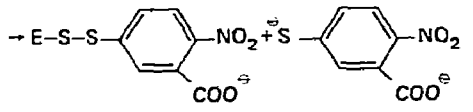

2-thiolate-5-nitrobenzoate

Our present concern is to examine the kinetics of this fast reaction.

Irreversible specific reaction kinetics at the active site of an oligomeric enzyme can be utilized to investigate for heterogeneity among otherwise liganded and unliganded sites, provided that the irreversible reagent is structurally oriented enough to discriminate the actual heterogeneity. Kinetic data (i.e., signal change versus *time*) can in principle, discriminate site heterogeneity more sensitively than titration data (signal change versus *concentration*) because of the *exponential* nature of the decay in reaction rate in each step of the polyphasic process. Moreover, all the heterogeneous kinetic parameters are obtainable from a *single* kinetic experiment.

Unfortunately, kinetic polyphasicity can also be a consequence of the reaction complexity (e.g., a multi-step reaction mechanism within a given subunit). The experiments we describe utilize a spectrophotometrically interpretable reaction (eq. (1)) which does not suffer from chemical kinetic complexity.

2. Materials and methods

2.1. Reagents

DTNB* (Calbiochem) was recystallized from glacial acetic acid. Fresh DTNB solutions contained less than 1% of TNB as impurity on the basis of absorbance measurements at 412 nm using $\epsilon = 13.600\ M^{-1}cm^{-1}$ for TNB [10].

Exact concentrations of DTNB stock solutions (up to 2 mM) were determined by absorbance at 412 nm after addition of excess dithiothreitol (5 mM) to the diluted DTNB solution (10 to 50 μM) in standard EDA buffer, pH 7.0. Two molecules of TNB were produced per DTNB molecule in these conditions. NAD^+ (Sigma, Grade III) was assayed as previously described [5]. All other chemicals used were analytical grade.

2.2. Enzyme

Highly purified sturgeon apo-GPDH was prepared and assayed as previously described [5]. The maximum specific activity of this enzyme was 340 ± 10 units/mg of enzyme under Ferdinand [11] assay conditions. A maximum of four active site cysteines per enzyme molecule were titrated by DTNB as previously described [5]. Standard EDA buffer (10 mM EDA, 0.1 M KCl, 1 mM EDTA, pH 7.0) was used as solvent in all experiments reported herein.

2.3. Isolation of the DTNB modified enzyme

Sturgeon holo-GPDH (21 or 67 μM) was reacted with an excess of DTNB (0.24 or 0.57 mM) at room temperature for 5 minutes. The resulting inactive

* Abbreviations used: GPDH: glyceraldehyde-3-phosphate dehydrogenase; DTNB: 2,2'dithio-bis-(5-nitrobenzoic acid); TNB: 2-thiol-5-nitrobenzoic acid; EDA: ethylene diamine.

enzyme was Bio-gel-P-10 filtered at 5°. UV spectra of the modified, DTNB free enzyme was recorded immediately after elution.

2.4. Kinetic measurements

The stopped flow apparatus used in this work was redesigned from the original apparatus described by Gutfreund [12]. The mixer and the observation chamber consisted of eight mixing jets and 1 cm light path built into a single quartz block cast into a plastic mounting. The dead time of the instrument was about 1 msec. Monochromatic light was obtained from a 24 volt quartz–tungsten–iodine lamp (Atlas), and a Schoeffel prism monochromator (model AMP30) with a bandwidth of ± 4 nm at 412 nm. Optical detection of the transmitted light was monitored with an EMI 9529B photomultiplier operated with 11 dynodes stages. The photomultiplier signal was amplified and filtered using a time constant from 0.1 to 1 msec depending on the half-life of the reaction under observation. Light transmission was recorded simultaneously on a Tektronix storage oscilloscope and on an Ampex tape deck recorder. The analogue signal (i.e., voltage versus time) recorded on tape was transformed and plotted in digital form (i.e., absorbance versus time) using a Varian 620i computer. A detailed description of this apparatus is forthcoming [36].

2.5. Analysis of kinetic data

Transformed kinetic data (i.e., absorbance versus time) were analyzed numerically with a computer program based on the iterative fitting procedure described by Cleland [13]. 30 data points per kinetic recording (absorbance at 412 nm versus time) covering at least 90–95% of the total reaction were fitted to either a single or a double exponential equation

$$\Delta A(t) = A\,[1-\exp(-kt)]\,, \qquad (2)$$

$$\Delta A(t) = A_f\,[1-\exp(-k_f t)] + A_s\,[1-\exp(-k_s t)]\,, \qquad (3)$$

where $\Delta A(t)$ is the time-dependent absorbance change and A, A_f and A_s the reaction amplitudes associated with the rate constants k, k_f and k_s respectively. The relative goodness of fit to the preceding equations was estimated by comparing the experimental variances σ^2 obtained in each case. In most cases σ^2 values were decreased by at least one order of magnitude when eq. (3) was used to fit the biphasic data instead of the single exponential of eq. (2). As shown in fig. 1, deviations between the calculated and the experimental absorbance values for each data set occurs randomly when the double exponential of eq. (3) is used to fit the data. The average deviation between calculated and experimental value is close to the observed random noise of the signal (from about 10^{-4} to 10^{-3} absorbance units at an average absorbance of 0.1, depending on the time constant used). Thus, no further refinement of the fitting equation (eq. (3)) was required.

3. Results

3.1. Isolation and characterization of DTNB reacted GPDH

The DTNB modified enzyme (TNB-enzyme) has an absorbance maximum at 327 nm, a characteristic of mixed thio-nitrobenzoate disulfide [14] (fig. 2). Immediate addition of 5 mM dithiothreitol displaces TNB from the enzyme as is indicated by the appearance of the nitro-thiophenolate absorbance maximum at 412 nm (fig. 2). Following dithiothreitol treatment, at least 99% of the initial activity of the enzyme is

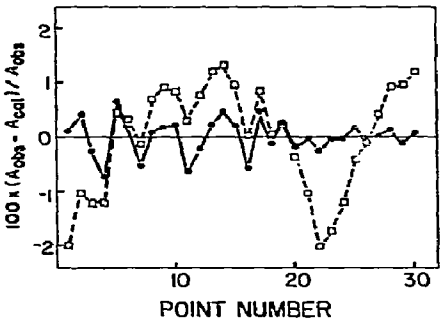

Fig. 1. Computer fit of the experimental data to a monophasic reaction model (eq. (2), squares) and a biphasic reaction model (eq. (3), circles): % deviation between the observed and calculated data (absorbance at 412 nm). Data (30 points) are those of kinetic experiment 7 as given in table 1. Average deviations are 0.85% and 0.26% for the data fitted to eqs. (2) and (3) respectively. The deviations for the fit to eq. (3) are random.

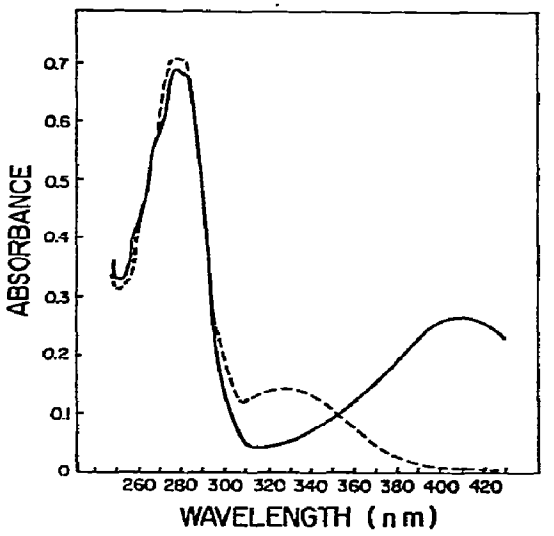

Fig. 2. Absorption spectra of TNB-Sturgeon-GPDH before (– – –) and after (——) treatment with dithiothreitol. Absorbance at 280 and 260 nm for the enzyme–coenzyme system can be corrected for the TNB contribution from the known nitro-thiophenolate absorbances at 412, 280 and 260 nm. The enzyme concentration (4.9 μM) was estimated either from the corrected absorbance at 280 nm using $E_{280}^{1\%,1\ cm} = 0.9$ or by the Biuret method [33] using untreated holoenzyme as standard. These estimates agree to ± 5%. A total of 3.90 ± 0.1 mole of TNB was released per mole of enzyme (i.e., 145 000 daltons of protein material) upon dithiothreitol treatment.

recoverable. From the visible absorbance, the contribution of the thiophenolate to the total UV absorbance can be calculated and consequently the UV absorbance of the residual protein and coenzyme chromophores is determinable. An absorbance ratio A_{280}/A_{260}, of 1.90 ± 0.1 was found indicating that under the conditions of Bio-gel chromatography less than 0.5 mole of NAD^+ was eluted with the DTNB modified enzyme. Since the holo-enzyme still retains 3.9 ± 0.1 NAD^+ per enzyme molecule (A_{280}/A_{260} = 1.13 ± 0.02, [5]) under identical elution, NAD^+ binding to the TNB-enzyme is considerably looser than in the native enzyme.

The 412 nm absorbance appears spontaneously in the isolated DTNB modified enzyme within several hours, indicating the slow disulfide interchange already mentioned by several authors [15, 16]. This slow reaction was accompanied by an irreversible loss of enzyme activity and further precipitation of the enzyme.

3.2. Kinetics of the reaction of DTNB with sturgeon apo-enzyme

The reaction of fresh *apo*-sturgeon GPDH at pH 7.0 with an excess of DTNB is a clean, extremely fast, *first order* process (see fig. 3a). The *pseudo* first-order rate constant, k, (eq. (2)) is linearly related to the DTNB concentration. From the linear plot of k versus [DTNB], a bimolecular rate constant of 0.55 ± 0.05 $\mu M^{-1} sec^{-1}$ was calculated. The observed kinetic homogeneity in the reaction of DTNB with the apo-enzyme is not in agreement with a previous report wherein partially purified sturgeon GPDH was used [17]. In this regard we have noted that aged preparations of apo-GPDH were inhomogeneous in the reaction kinetics with DTNB, especially when the total reaction stoichiometry was less than 3.5 mole of DTNB per enzyme molecule.

3.3. Inhibition of the DTNB-enzyme reaction by NAD^+

Apo-enzyme (about 1 μM) was preincubated with varying amounts of NAD^+ and then mixed in the stopped flow apparatus with an excess of DTNB (usually 0.25 mM). The time-course of absorbance change at 412 nm was discernably *biphasic* under these conditions, as shown in fig. 3. Accordingly, we have separated our analysis into a *fast* and a *slow* phase, each with a variable rate and amplitude. The rate constants and *relative* amplitudes (the *total* amplitude corresponds to the formation of *four* TNB per enzyme, except as specifically noted below) of each of these phases are dependent on NAD^+ concentration (fig. 4). Three distinct regions of NAD^+-concentration dependent phenomena (corresponding to different extents of NAD^+ binding) are separable from the kinetic data. These are describable as follows.

3.3.1. Enzyme containing less than two bound NAD^+ per tetramer

The rate constants for both the fast and the slow phases are independent of NAD^+-concentration. The fast phase *amplitude* decreases almost linearly with

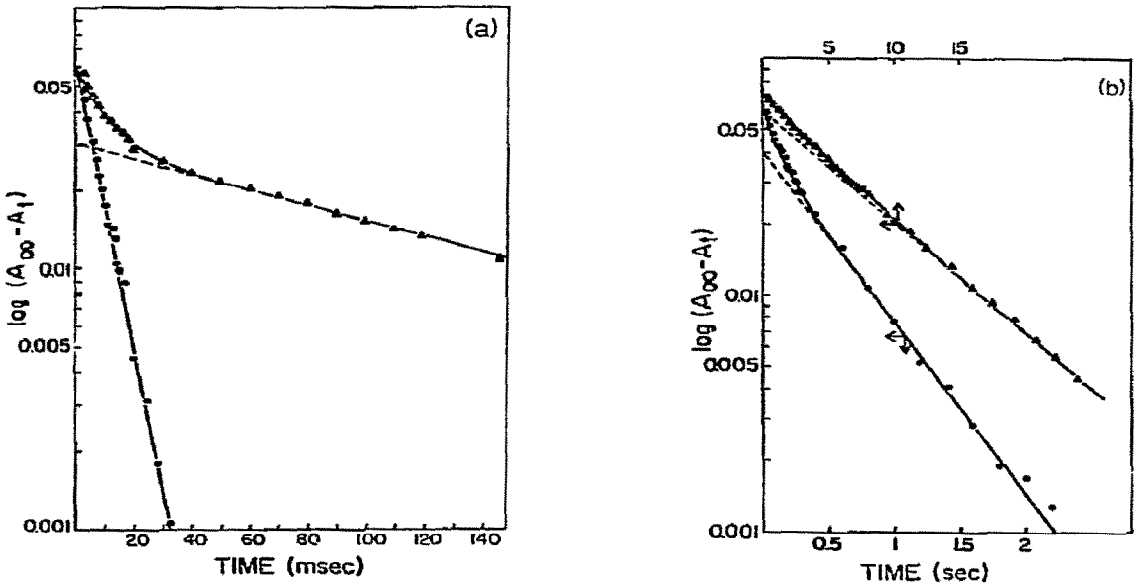

Fig. 3. Kinetics of the reaction of sturgeon GPDH with excess DTNB at various NAD^+ concentrations. Semi-log plots of the data fitted to eqs. (2) or (3) as given in the text. Points are experimental. Curves are calculated using the corresponding kinetic parameters values as given in table 1.

(a) Reactions of the apo-enzyme (•), and at $NAD^+/E \approx 2$ (▲). 1.24 μM enzyme, other conditions are as given in table 1 (experiments 1 and 3 respectively).

(b) Reaction at 21.6 μM (•) and 740 μM (▲) NAD^+. Enzyme concentrations were 1.24 and 1.34 μM respectively. Other conditions as given in table 1 (experiments 7 and 10 respectively).

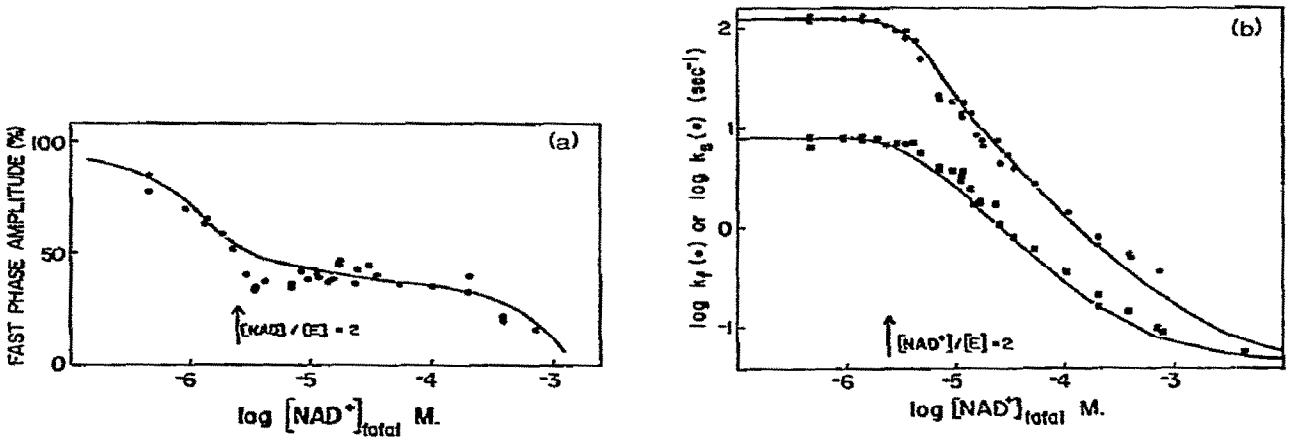

Fig. 4. Biphasic reaction of DTNB with sturgeon GPDH at various NAD^+ concentrations. Points are experimental, solid curves are calculated according to eqs. (5), (6), (9), (10) and (12) as discussed in the text. DTNB: 0.25 mM, enzyme: 1.29 ± 0.05 μM. Standard EDA buffer pH 7.0, 25°.

(a) Amplitude of the fast phase (A_f) in % of the total reaction amplitude versus total NAD^+ concentrations. The amplitude of the slow phase is $A_s\% = 100\% - A_f\%$.

(b) Rate constants for the fast (k_f, •) and slow (k_s, ▪) phases versus total NAD^+ concentration. The two lowest points in the k_s graph were obtained from kinetic measurements in a conventional spectrophotometer (for these two NAD^+ concentrations the overall reaction is nearly monophasic).

Table 1
Kinetic parameters of the DTNB reaction with sturgeon GPDH at various NAD^+ concentrations[a]

Exp no.	$[NAD^+]$ [b]	k_f [c]	A_f(%) [d]	k_s [c]	A_s(%) [d]	AD(%) [e]	DTNB/E [f]
1	0	127.4 ± 2.3	100	–	–	0.57	3.75
2 [g]	0.72	55.2 ± 1.6	71.3 ± 1.7	7.5 ± 1.0	28.7 ± 1.1	0.60	3.60
3	0.86	128.5 ± 2.7	69.8 ± 0.7	7.8 ± 0.4	30.2 ± 0.4	0.23	3.78
4	2.16	112.4 ± 3.2	52.5 ± 0.7	6.7 ± 0.2	47.5 ± 0.7	0.17	3.73
5	5.55	21.3 ± 1.4	35.0 ± 2.1	4.1 ± 0.17	65.0 ± 2.1	0.19	3.77
6	10.8	13.2 ± 1.1	39.4 ± 3.3	2.87 ± 0.2	60.6 ± 3.1	0.21	3.74
7	21.6	7.55 ± 0.8	36.0 ± 4.1	1.66 ± 0.13	64.0 ± 3.8	0.26	4.01
8	54.0	2.75 ± 0.07	35.9 ± 1.0	0.63 ± 0.01	64.1 ± 1.0	0.08	4.00
9	200	0.81 ± 0.05	32.5 ± 3.1	0.22 ± 0.01	67.5 ± 2.8	0.12	4.01
10 [h]	740	0.39 ± 0.03	16.2 ± 1.5	0.103 ± 0.002	83.8 ± 1.3	0.05	3.86

a) Kinetic parameters were obtained by fitting the kinetic data to eq. (3) except for the apo-enzyme reaction (exp 1) where eq. (2) was used (see text). Enzyme, 1.28 ± 0.05 μM; DTNB, 0.25 mM. Standard EDA buffer pH 7.0, 25°.
b) Units: μM.
c) Pseudo first-order rate constants for the fast (k_f) and slow (k_s) phases. Units: sec^{-1}.
d) Relative amplitudes for the fast (A_f) and slow step (A_s) are given in % of the total reaction amplitude.
e) Average deviation in % between the observed and calculated absorbance values for each kinetic experiment. The decrease in the average deviation with increasing NAD^+ concentration is due to the better resolution in absorbance when the reaction becomes slower.
f) Moles of DTNB reacted per mole of enzyme as determined from the total amplitude of the reaction using $\epsilon = 13600\ M^{-1}\ cm^{-1}$ for TNB dianion at 412 nm.
g) At 0.078 mM DTNB and 0.8 μM enzyme.
h) At 4.5 mM NAD^+ and 0.18 mM DTNB, kinetic data are well fitted to eq. (2) (i.e., monophasic reaction) with $k = 0.044\ sec^{-1}$ but the total amplitude of the reaction corresponds to only 3.15 DTNB molecules reacted per mole of enzyme.

increasing bound NAD^+. The *fast* rate constant is dependent on DTNB concentration (table 1), whereas the *slow* rate constant is invariant to a three-fold change in DTNB concentration (table 1).

3.3.2. Enzyme containing more than two but less than four bound NAD^+

At higher extents of saturation, both fast and slow rate constants (k_f and k_s) decrease with increasing NAD^+ concentrations, their ratio (5 ± 0.5) being constant. Both amplitudes, A_f and A_s, remain constant at about 40 and 60% of the total amplitude respectively. k_f and k_s are dependent on DTNB concentration; both rates however, show a less than linear dependence on reagent concentration. The ratio of the two rate constants and the relative amplitudes of the phases are invariant to DTNB concentration.

3.3.3 Enzyme nearly saturated with bound NAD^+

At very high NAD^+ concentration (from about 200 μM NAD^+), the relative amplitude of the fast phase decreases and the slow phase rate constant k_s approaches a minimum value. The overall reaction is nearly monophasic at 4.5 mM NAD^+, the amplitude of the slow phase representing more than 90% of the total reaction amplitude. Unlike results at lesser extents of saturation, the total reaction amplitude is dependent on the DTNB concentration (as is the slow step rate constant), indicating that the reaction is no longer quasi-irreversible.

Observed rate constants and amplitudes for various $[NAD^+]/[E]$ ratios are listed in table 1.

3.4. Quantitative analysis of the kinetic results

On the basis of the results reported herein and for reasons detailed below we have chosen to analyze these kinetic data according to an explicit simple model. The essential feature of this model is that the observed biphasicity of the reaction is assumed to arise only as a consequence of the heterogeneity of NAD^+ binding to the four sites of a tetrameric enzyme with maximal two-fold symmetry. The biphasic reaction of DTNB with the holo-enzyme is describable

in terms of the two different and relatively slow rates of desorption of NAD^+ from the loose and the tight sites. In order to calculate the "microscopic" parameters associated with each of these discrete processes, we shall first consider the rate of reaction of DTNB at a single site.

3.4.1. Reaction at a single site

The irreversible DTNB reaction at a *non-interacting* active site in the presence of NAD^+ can be described formally by scheme 1. Accordingly, the rate of product (*TNB*) formation can be biphasic (see appendix A). However, the *amplitude* of the fast step decreases as the NAD^+ concentration increases (at fixed DTNB concentration). At moderate NAD^+ concentrations this amplitude can become negligible, and hence a monophasic linear decay rate will be observed (see discussion below; in essence, the condition for linear decay is that k_1 [A] exceeds the other pseudo first order rates of scheme 1). An approximate expression for the macroscopic observable rate constant, k_{II}, under these conditions (cf. eq. (A.1)) is given by

$$k_{II} = (k_1 k_3 [A][B] + k_{-1} k_2 [B] + k_2 k_3 [B]^2) / (k_1 [A] + k_{-1} + k_2 [B] + k_3 [B]). \quad (4)$$

Scheme 1
Irreversible modification of a reversibly liganded site [a]

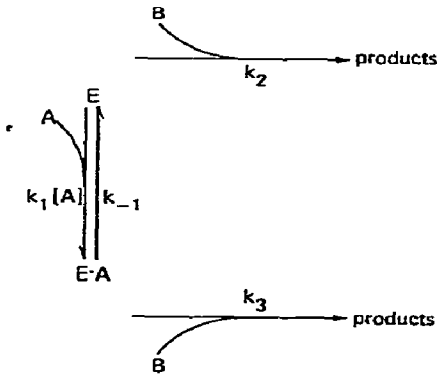

a) k_1 [A] and k_{-1} are the first order rate constants for absorption and desorption of ligand (A = NAD^+) to the enzyme active site (E). k_2 and k_3 are the bimolecular rate constants for the irreversible reaction with reagent (B = DTNB) at the liganded and unliganded site respectively. Inhibition of the irreversible reaction by ligand A occurs if $k_3 < k_2$.

The relationship between the rate constant k_{II} and DTNB concentration is not necessarily linear (eq. (4)) as has been pointed out previously [17]. Note that non-linear rate-dependence on the reactant concentration does not require a prior substantial binding of DTNB to the enzyme. The extent of the inhibition of the irreversible reaction by NAD^+, according to this single-site analysis, is related to the particular site affinity for NAD^+; NAD^+-occupied loose sites should react more rapidly than NAD^+-occupied tight sites.

3.4.2. The individual rate constants for reaction at tight and loose sites

Among the *four* rates constants figuring in scheme 1, only the NAD^+ dissociation rate constant (k_{-1}) is assumed to differ between tight and loose sites. The corresponding rate constants are denoted by k^T_{-1} and k^L_{-1} respectively. Thus, 5 distinct individual rate constants are required to fit the experimental data according to our model (i.e., k_1, k^T_{-1}, k^L_{-1}, k_2 and k_3). Three of these, k_2, k_3 and k^T_{-1}, can be estimated directly from the limiting values of the observed rate constants for apo- and holo-enzyme as is described in table 2. At lower NAD^+ levels ($[NAD^+]/[E] < 2$) the rate of the slow reaction component k_s is invariant to DTNB concentration over a three-fold range. This follows from eq. (4) if the pseudo-first order constants are in the sequence $k_2[B] >> k_{-1} \approx k_1[A] >> k_3[B]$. Under these conditions the macroscopic (concentration independent) specific rate is equal to the microscopic specific rate of desorption of NAD^+ from the tight binding site (k^T_{-1}). From this value and the previously obtained NAD^+ dissociation constant, K^T_d, for the tight binding sites [5], the association rate k_1, for NAD^+ can be calculated, according to the relation $k_1 = k^T_{-1}/K^T_d$. This calculated bimolecular specific rate, 40 $\mu M^{-1} sec^{-1}$, is reasonable for a diffusion controlled process [18], and is in good agreement with the value obtained by direct observation of the fluorescence quenching upon NAD^+ binding to the apo-enzyme [37]. The remaining kinetic constant to be estimated k^L_{-1} is the NAD^+ "off"-rate for the "loose" binding site. This was estimated by a trial and error best fit of the experimental data to our model (see next page).

Table 2
Individual kinetic constants of scheme 1 for the reaction of sturgeon GPDH loose and tight NAD^+ binding sites with DTNB [a,b]

k_1 ($\mu M^{-1} sec^{-1}$)	k^T_{-1} (sec^{-1})	k^L_{-1} (sec^{-1})	K^T_d (μM)	K^L_d (μM)	$k_2[B]$ (sec^{-1})	$k_3[B]$ (sec^{-1})
40	8	40	0.2	1	130	0.05

a) The pseudo first-order rate constant $k_2[B]$ for the reaction of an unliganded tight or loose site with DTNB(= B) is equal to the rate constant of the apo-enzyme reaction under pseudo first order conditions. Similarly, $k_3[B]$, the rate constant for the reaction of an NAD^+ occupied tight or loose site is obtained from the pseudo first-order rate constant of the reaction at $[NAD^+] \geq 1$ mM. k^T_{-1} and k^L_{-1}, the NAD^+ *off*-rate constants for tight and loose sites respectively, were estimated as discussed in the text. k_1, the NAD^+ *on*-rate constant for both classes of sites was deduced from k^T_{-1} and K^T_d as discussed in the text. K^T_d and K^L_d are the dissociation constants for NAD^+ at the tight and loose sites.

b) Experimental conditions: at 25°, pH 7, Standard EDA buffer, 0.25 mM DTNB.

3.4.3. "Microscopic" kinetic parameters of the functional dimer reaction

In our model, each "tight" and "loose" NAD^+ binding site of the functional dimer reacts with DTNB as described in scheme 1. The overall reaction rate should be at least *biphasic*, if one class of sites react faster than the other. Over a limited range of NAD^+ concentration, namely when $k_1[A] < k_2[DTNB]$, the reaction of *each* particular class of sites should also be biphasic (see appendix A)*. This leads to the prediction of an overall polyphasicity to the reaction kinetics over a limited but important range of NAD^+ concentration. Phenomenologically, we observe a simpler biphasic kinetic pattern (i.e., a time-dependence which can always be fit to eq. (3)). Hence, we use an approximation to calculate the "microscopic" fast step amplitude and rate constant (A_L and k_L respectively). In our simple model there is no distinction between "loose" and "tight" binding sites provided that they contain no NAD^+. Thus a normal approximation for A_L and k_L is to sum the individual amplitudes and average the rate constants corresponding to the reaction of unliganded loose and tight sites (A^L_I, k^L_I and A^T_I, k^T_I respectively) *and* NAD^+ occupied loose sites (A^L_{II} and k^L_{II}), as given in the following equations

$$k_L = (A^L_I k^L_I + A^L_{II} k^L_{II} + A^T_I k^T_I)/A_L, \quad (5)$$

$$A_L = A^L_I + A^L_{II} + A^T_I. \quad (6)$$

For $[NAD^+]/[E] > 10$ the contributions of A^L_I and A^T_I to A_L can be neglected, thus leading to the prediction of simple relations between the phenomenological and the microscopic kinetic parameters

$$k_L = k^L_{II}, \quad (7) \quad \text{and} \quad A_L = A^L_{II}. \quad (8)$$

The "tight" site microscopic reaction parameters, k_T and A_T are consequently defined by

$$k_T = k^T_{II}, \quad (9) \quad \text{and} \quad A_T = A^T_{II}. \quad (10)$$

Thus, for any particular NAD^+ concentration[‡], we can calculate the miscroscopic parameters k_L, A_L, A_T and k_T utilizing eqs. (5), (6), (9) and (10) (see appendix A) with the numerical values of the individual constants of scheme 1 (table 2). The calculated values of k_T and k_L are in good agreement with the observed rate constants k_f and k_s (see fig. 4b) obtained by fitting the experimental data to eq. (3) (see section 2) over the large range of NAD^+ concentrations where substantial biphasicity of the reaction kinetics is observed. This agreement provides an a posteriori justification for the approximations discussed[†].

* The kinetic parameters for each fast and slow components of the discrete reaction of one particular site (k_I, A_I, k_{II} and A_{II} as given in eq. (A.1) are superscripted by the index "T" and "L" for "tight" and "loose" sites respectively.

‡ The *free* NAD^+ concentrations, required for calculating kinetic parameters k^L_I, k^L_{II}, A^L_I, A^L_{II}, etc. (see appendix A), were determined by solving the cubic equation for $[NAD^+]_{free}$ obtained by assuming two classes of sites for NAD^+ binding within the tetrameric enzyme molecule. The dissociation constants values listed in table 2 were used in these calculations. Since the DTNB reaction decreases NAD^+ affinity for both sites (see above), the free NAD^+ concentration for the slow tight-site reaction was assumed to be equal to the initial free NAD^+ concentration *plus* the NAD^+ initially bound at the loose site.

† Another approximation is the assumption of constant free NAD^+ concentration during the time course of the DTNB reaction with tight and loose sites at low NAD^+/E ratio. Since this reaction displaces bound NAD^+, free NAD^+ concentration should increase continuously during the reaction. Numerical computer simulation showed this effect to be of almost negligible kinetic consequence, however.

The simulation of the macroscopic fast and slow amplitudes (A_f and A_s) from the "microscopic parameters" depends on the particular reaction mechanism for the functional dimer. This simulation according to a specific model is discussed below.

4. Discussion

4.1. Preliminary considerations

A striking feature of the DTNB reaction with sturgeon GPDH is the observed substantial kinetic *biphasicity* over a wide range of NAD^+ concentration, even when virtually *all* coenzyme binding sites are saturated. Under extreme conditions, namely with the *apo*-enzyme or in presence of an extreme excess of NAD^+, kinetic monophasicity is observed. Kinetic biphasicity, with nearly equal amplitudes of transformation in each step of the DTNB reaction, persists over two order of magnitude of variation in the NAD^+ concentration. This kinetic result is in contrast to the kinetic behavior of *yeast* GPDH in the same reaction at pH 8.5 and 20°. According to the elegant study of Ellenrieder et al. [19], the amplitude of the fast step yeast-enzyme reaction decreases *continuously* when NAD^+ concentration is increased, whereas there is no significant variation in either the fast or the slow step rate constant. These observations with the yeast enzyme are fully consistent with the NAD^+-induced displacement from a reactive "T"-state conformation to a less reactive "R"-state, as postulated in the concerted transition model [19,20]. Our results with *sturgeon* GPDH at pH 7.0 cannot be explained by the simple "concerted" model (which allows for *only* two classes of sites). This is not surprising since *negative cooperatively* is observed in NAD^+ binding to sturgeon GPDH; a phenomenon incompatible with the simplest formulation of the "concerted" model [4]. This simplest model assumes a single transition between two maximally *symmetrical* oligomeric conformations [20]. A reasonable extension of the model for the case of a tetramer is to consider a transition from a maximally-symmetrical D_2 conformation to a disymmetrical C_2 conformation. Indeed, conformations of less than maximal symmetry have recently been reported with a variety of coenzyme-bound dehydrogenases [21–24]. Although such a concerted "D_2–C_2" transition can explain NAD^+-dependent biphasicity in the DTNB reaction, the model predicts a mixed *negative* and *positive* cooperativity in NAD^+-binding [25]. We observe *only negative cooperativity* in ligand-binding with sturgeon GPDH [2,5,37]. This extension of the concerted model is hence not apropos to our present results.

An alternative to the concerted model is a "DTNB-*induced* dissymmetry in the oligomeric enzyme", similar to the model previously proposed for interpretation of "half of the site's reactivity" [26]. Such a model neglects the necessity for enzyme-bound NAD^+ in order to observe kinetic biphasicity. Moreover, in its most general formulation the "induced-fit" model [27] predicts a *tetraphasic* kinetic reaction in our particular case.

4.2. A simple consistent model

We have previously demonstrated two classes of sites, equal in number, but differing in affinity for NAD^+ binding to sturgeon GPDH [5]. This is in agreement with a C_2 symmetry for the enzyme tetramer [2], as reported for human holo GPDH [24]. Thus we can describe the enzyme molecule as formed of two *functional dimers* each containing one "tight" and one "loose" site for NAD^+ binding (fig. 5).

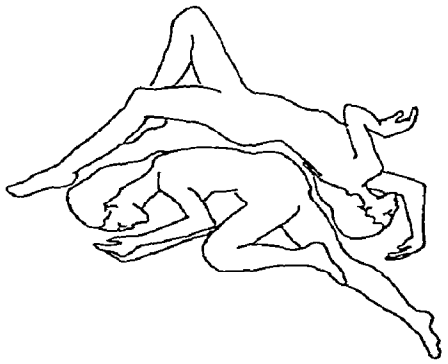

Fig. 5. An illustration from everyday life, following Kendrew and Crick [34], of an asymmetric dimer with point group symmetry C_1. Note the nonequivalent tertiary structures for the two "covalently-identical protomers", presumably arising from the tight-heterologous binding domains.

Obviously, biphasicity in the DTNB reaction might arise from such site heterogeneity. However, apo-enzyme lacks this biphasicity, and holo-enzyme kinetics are still NAD^+-concentration-dependent. The observed biphasicity is still predicted however, if NAD^+ inhibits the otherwise identical reaction at *each* enzyme active site: Reaction of DTNB with the "apo-dimer" is monophasic because the structurally non-specific reagent (DTNB) does not differentiate between unliganded "loose" and "tight" sites. On the other hand, the differently bound NAD^+ sites can lead to kinetic differentiation due to the different rates of NAD^+ desorption, as predicted by eq. (4). The reaction is faster with NAD^+-occupied "loose" sites than with "tight" sites because of the faster NAD^+ dissociation rate at the former, provided that the DTNB reaction pathway involving prior dissociation of bound NAD^+ is favored (cf. $k_1k_2 >> k_1k_3[A]$ in eq. (4)). With this provision, the overall reaction will remain *biphasic* and both fast and slow steps rate constants will decrease with increasing NAD^+ concentration, even at virtual saturation, due to the competitive rates of NAD^+ absorption and DTNB (bimolecular) reaction. At very high NAD^+ concentrations, however, reaction of DTNB with NAD^+ occupied sites may exceed the alternative reaction pathway (if $k_1k_3[A] > k_{-1}k_2$ in eq. (4)). Accordingly, the biphasicity of the overall reaction will disappear provided that NAD^+-occupied "loose" and "tight" sites react at similar rates. Our rate data can be fitted to this model over the entire range of NAD^+ concentrations investigated (from 0.5 to 4500 μM),

4.3. Amplitudes of the fast and slow reaction components

The irreversible modification of a *functional* dimer, a model fully in accord with both the above-mentioned rate phenomena and with the crystallographic symmetry [24] can be formally described either by the simplest kinetic pathway illustrated in scheme 2 or by scheme 3. In scheme 2 (the "random" mechanism), the reactions of loose and tight sites are independent. In scheme 3 (the "sequential" mechanism), reaction at loose sites occur prior to any reaction at the tight sites. From scheme 2, a biphasic kinetic equation similar to eq. (3) can be derived in which the equalities

Scheme 2
"Random" mechanism for the irreversible modification of an asymmetric dimer [a]

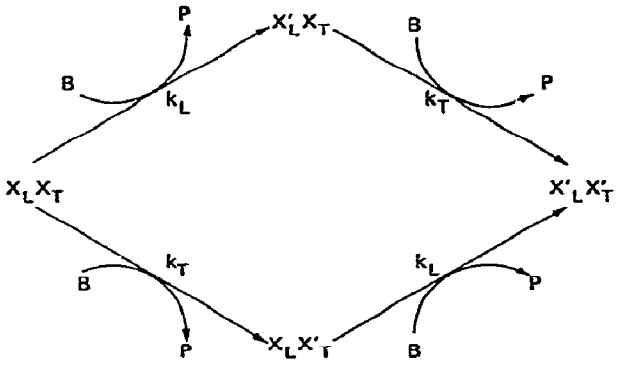

a) The irreversible reagent B reacts randomly with the asymmetric dimer X_LX_T containing one fast reacting loose site (X_L) and one slow reacting tight site (X_T). The "microscopic" reaction rate constant for tight and corresponding loose sites are k_T and k_L respectively. Reacted sites are primed.

summarized in the following equation must obtain.

$$k_f = k_L, \quad k_s = k_T, \quad A_f = A_L, \quad A_s = A_T \qquad (11)$$

Most importantly, scheme 2 predicts equal amplitude for the fast and slow phases of reaction (provided that the loose and tight site concentrations, as defined by eqs. (6) and (10) are equal).

The observed kinetic behavior is not in *complete* agreement with this prediction. The amplitude of the fast phase is significantly smaller than that of the slow phase in the range of NAD^+ concentrations where $A_L = A_T$ (fig. 4a).

The rate of product formation according to scheme 3 is given by eq. (3) with the following equalities

$$\begin{aligned} k_f &= k_L, & A_f &= A_L(k_L - 2k_T)/(k_L - k_T), \\ k_s &= k_T, & A_s &= A_T k_L/(k_L - k_T). \end{aligned} \qquad (12)$$

Scheme 3
"Sequential" mechanism for the irreversible modification of an asymmetric dimer [a]

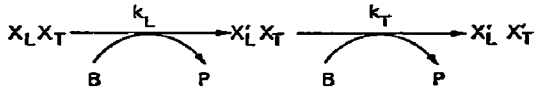

a) Same notation as in scheme 2. The fast reacting loose site (X_L) reacts prior to any reaction at the tight site (X_T).

Accordingly, the observed amplitudes for the "fast" and "slow" phases are not necessarily equal: For example, even when fast and slow reacting sites are equally distributed within the functional dimer ($A_L = A_T$), if k_L is $5k_T$, the macroscopic fast amplitude (A_f) will be 38.5% of the total amplitude. A nearly exact simulation of our amplitude data can be achieved on the basis of scheme 3 utilizing the analytically derived microscopic rate constants k_L and k_T (see section 3 for the calculations). On these bases, we are confident of the appropriateness of scheme 3, or some analogous model in describing the real system.

4.4. Mechanistic interpretations

Although scheme 3 is merely a formality, it is suggestive of the "induced fit" model of Koshland et al. [35] within the *functional dimer*. Two mechanisms might be envisaged for the dissymmetric reaction of an originally symmetric holo-enzyme (with DTNB): (i) Sequential "induced fit" wherein chemical modification of one subunit by reaction affects subsequent reaction at the other subunit. (ii) Redistribution of NAD^+ binding sites as a consequence of partial chemical modification; reaction at one site inducing "tight NAD^+ binding" at the unmodified site. As already pointed out the apparent monophasic kinetics observed for the apo-enzyme and at very high NAD^+ concentration rules out the reagent-induced alternative (i). The latter alternative is qualitatively consistent with all of our present kinetic results. Indeed, it is an appealing mechanism in light of the observed "negative cooperativity" in NAD^+ binding [4]. However, strong evidence has been presented elsewhere [5,24,28] that the unmodified holo-enzyme is asymmetric; consisting of a pair of dimers with an overall maximal two-fold symmetry. We can allow for these findings, which are once again suggestive of the kinetically unacceptable scheme 2, by introducing a plausible modification.

4.5. The "flip over" mechanism

Within the functional (heterogeneous) dimer two energetically identical conformations are expected for the apo-, holo-, and fully reacted (apo or holo) enzyme, namely

(13)

where X represents NAD, TNB or *both*. By contrast, a *half-reacted* (or liganded) species need not have an energetically equivalent conformer

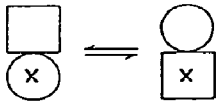

(14)

The selectivity of conformer depends on the relative stability of ligation in each state. As an extremum, consider that reaction (enzyme-TNB formation) is nonselective but that NAD^+-binding is tertiary conformation dependent

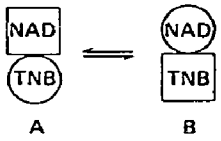

(15)

If NAD^+ binding is favored in A, DNTB reaction of the half-reacted "species" will tend to proceed via NAD^+ desorption from B, the conformer of lower probability. This reactive conformer is available by isomerization ("flip over", [29]) from A. The general mechanism for complete reaction is given in scheme 4. One important parameter of this "flip-over" mechanism is the equilibrium constant K. This constant is simply given by the ratio of the NAD^+ dissociation constants at the loose (conformer B) and tight (conformer A) sites. Previously we found a value of about 10 for this ratio from equilibrium titration studies. It is of importance to compare this value with the ratio of the microscopic rate constants, k_L/k_T, for the DTNB reaction. According to our model, these ratios should be equal over a wide range of NAD^+ concentration (see section 3). In the "flip-over" mechanism, however, as discussed in appendix B, the microscopic ratio, k_L/k_T, is not equal to the *observed* ratio, k_f/k_s. A ratio of k_f/k_s equal to five (the observed ratio) should be smaller than the ratio

Scheme 4
The "flip-over" mechanism for the reaction of an asymmetric dimer with an irreversible reagent a)

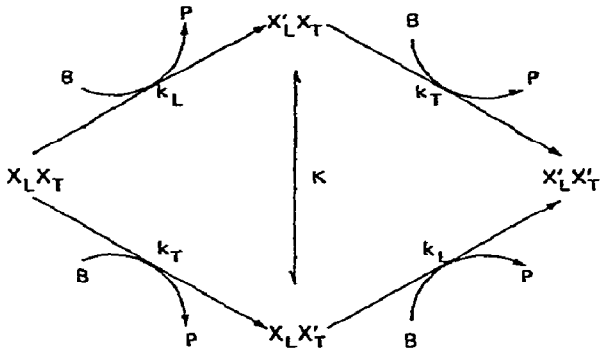

a) Same notation as in scheme 2. The two half-reacted enzyme species $X'_L X_T$ and $X_L X'_T$ are rapidly convertible via a "flip-over" isomerization in which the reacted sites are exchanged. K, the equilibrium constant for this isomerization is defined as $K = [X'_L X_T]/[X_L X'_T]$.

k_L/k_T *. For example, a microscopic ratio (k_L/k_T) of ten leads to a macroscopic ratio (k_f/k_s) of six (see appendix B). Thus the "flip-over" mechanism leads to good agreement between the present kinetic data and previous equilibrium titration results.

Utilizing the formalism of scheme 4, we can interpret all kinetic phenomena on the basis of a simple physical model. According to this model, the kinetic biphasicity of the DTNB reaction is solely a consequence of the heterogeneous binding of NAD^+ within a functional dimer. "Flip-over" isomerization of the *half*-reacted enzyme allows a faster reaction at an otherwise slowly reacting site, giving rise to unequal amplitudes for the fast and slow phases of reaction.

The consequence of such a mechanism for the functionally specific active-site acylation reaction may be still more dramatic. For example, since NAD^+ binding at a particular site has a pronounced effect on its acylation rate [8] the "flip-over" isomerization of the half reacted enzyme might allow subsequent reaction at an otherwise unreactive site. Thus complete tetra-acylation of the enzyme can be achieved, as previously reported with the physiological substrate, 1-3 diphosphoglycerate [5,30]. On the other hand, if this "flip-over" isomerization is blocked, then the acylation reaction might be limited to half of the "active-sites" of the enzyme molecule, as has been extensively reported with β-(2-furyl)acryloyl phosphate [5,8,9,27,31].

* In the simulation of the rate constant data given in section 3, we implicitly assumed that $k_L = k_f$ and $k_T = k_s$ as predicted by scheme 3. These equalities are not apropos to the "flip-over" mechanism (scheme 4). However, exact simulation of the rate constant data according to this mechanisms requires only minor change in the values of the parameters listed in table 2. Thus we do not report these simulations herein.

Acknowledgement

This work was supported by grants from the U.S. National Science Foundation (No. GB31375X) and the U.S. National Institutes of Health (GM1045-10).

We have benefited from frequent discussions with Dr. O.P. Malhotra and from a manuscript dealing with negative cooperativity and "flip-over isomerization" kindly sent to us by Dr. E. Whitehead prior to publication.

Appendix A

To obtain the integral equation for the concentration–time dependence of the reaction of scheme 1, a set of two independent first-order linear differential equations is solved using the Laplace–Carson transform method [32]. The concentration of either reagent B or ligand A are assumed to be much greater than the enzyme site concentration (E_T). The time dependent appearance of the product is consequently given by

$$P(t)/[E_T] = A_I[1-\exp(-k_I t)] + A_{II}[1-\exp(-k_{II} t)]. \quad (A.1)$$

The rate constants, k_i (k_I and k_{II}) are defined by

$$k_i = \tfrac{1}{2}(b + (-1)^{i+1}\sqrt{b^2-4c}), \text{ with } i = \text{I or II}, \quad (A.2)$$

where

$$b = k_1[A] + k_{-1} + k_2[B] + k_3[B],$$

$$c = k_1 k_3[A][B] + k_{-1}k_2[B] + k_2 k_3[B]^2;$$

and the amplitudes A_i (A_I and A_{II}) by

$$A_i = [(k_i - k_1[A] - k_{-1})(k_{-1}k_2[B] + k_1k_3[B][A]) + k_2k_3[B]^2(k_{-1} + k_1[A])]/k_i(k_i - k_f)(k_{-1} + k_1[A]). \quad (A.3)$$

An approximate expression for k_I and k_{II} can be obtained from eq. (A.2) by using the binomial expansion for the square root in eq. (A.2). Accordingly, the phenomenological rate constants are given by

$$k_I = b, \qquad k_{II} = c/b. \quad (A.4)$$

Substituting the exact expression for b and c (eq. A.2) into eq. (A.4) we obtain eq. (4) as given in the text.

Appendix B

The time-dependent consequence of the "flip-over" mechanism of scheme 4 can be solved using the same method as given in appendix A. The rate of isomerization of half reacted species is assumed to be extremely rapid compared to other reaction rates. The time-dependent appearance of product P is biphasic as given in eq. (3) of the text. The parameters, A_f and k_f, of the fast phase and A_s and k_s of the slow phase of reaction are given by

$$A_f = A_L(k_L + k_T - 2\bar{k})/(k_L + k_T - \bar{k}), \quad (B.1)$$

$$A_s = A_T(k_L + k_T)/(k_L + k_T - \bar{k}), \quad (B.2)$$

$$k_f = k_L + k_T, \quad (B.3)$$

$$k_s = \bar{k} = k_L/(1+K) + k_TK/(1+K), \quad (B.4)$$

where A_L and A_T are the concentration-associated amplitudes of the fast and slow reacting sites. K is the equilibrium constant for the isomerization of the half reacted species and is given by the ratio k_L/k_T as discussed in the text. By substituting k_L/k_T for K in eq. (B.4), the ratio k_f/k_s is given by

$$k_f/k_s = (k_T + k_L)^2/2k_Tk_L. \quad (B.5)$$

Hence, the ratio of the macroscopic rate constants (k_f/k_s) should be smaller than the ratio of the microscopic rate constants (k_L/k_T).

References

[1] K. Kirschner, Current Topics in Cellular Regulation 6 (1972) 167.
[2] B.W. Matthews and S.A. Bernhard, Ann. Rev. Biophys. Bioeng. 2 (1973) 257.
[3] D.E. Koshland and K.E. Neet, Ann. Rev. Biochem. 37 (1968) 359.
[4] A. Conway and D.E. Koshland, Jr., Biochemistry 7 (1968) 4011.
[5] F. Seydoux, S.A. Bernhard, O. Pfenninger, M. Payne and O.P. Malhotra, Biochemistry 12 (1973) 4290.
[6] H. Uchida, J. Heystek and M.H. Klapper, J. Biol. Chem. 246 (1971) 2031.
[7] W.S. Allison and N.O. Kaplan, J. Biol. Chem. 239 (1964) 2140.
[8] O.P. Malhotra and S.A. Bernhard, J. Biol. Chem. 243 (1968) 1243.
[9] O.P. Malhotra and S.A. Bernhard, Proc. Nat. Acad. Sci. U.S. 70 (1973) 2077.
[10] G.L. Ellman, Arch. Biochem. Biophys. 82 (1959) 70.
[11] W. Ferdinand, Biochem. J. 92 (1964) 578.
[12] H. Gutfreund, in: Fractions no. 2, Beckman Instruments, Inc., Palo Alto, California (1968).
[13] W.W. Cleland, Advan. Enzymol. 29 (1968) 1.
[14] R.F. Colman, Biochemistry 8 (1969) 888.
[15] L. Boross, Act. Biochim. Biophys. Acad. Sci. Hung. 4 (1969) 57.
[16] P.M. Wassarman and J.P. Major, Biochemistry 8 (1969) 1076.
[17] P.J. Harrigan and D.R. Trentham, Biochem. J. 124 (1971) 573.
[18] M. Eigen and G.G. Hammes, Advan. Enzymol. 25 (1963) 1.
[19] G. Ellenrieder, K. Kirschner and I. Schuster, Eur. J. Biochem. 26 (1972) 220.
[20] J. Monod, J. Wyman and J.P. Changeux, J. Mol. Biol. 12 (1965) 88.
[21] M.J. Adam, A. McPherson, Jr., M.G. Rossmann, R.W. Scheritz and A.J. Wonacott, J. Mol. Biol. 51 (1970) 31.
[22] C.I. Brändeu, H. Eklund, B. Nordström, T. Boive, G. Söderlund, E. Zeppezauer and I. Ohlelson, Proc. Nat. Acad. Sci. U.S. 70 (1973) 2439.
[23] D. Tsernoglou, E. Hill and L.J. Banaszak, J. Mol. Biol. 69 (1972) 75.
[24] H.C. Watson, E. Duée and W.D. Mercer, Nature New Biol. 240 (1972) 130.
[25] H. Buc, K.J. Johannes and B. Hess, J. Mol. Biol. 76 (1973) 199.
[26] A. Levitzki, W.B. Stallcup and D.E. Koshland, Jr., Biochemistry 10 (1971) 3371.
[27] W.B. Stallcup and D.E. Koshland, Jr., J. Mol. Biol. 80 (1973) 41.
[28] S.A. Bernhard and R.A. MacQuarrie, J. Mol. Biol. 74 (1973) 73.
[29] E. Whitehead (1973) in press.
[30] D.R. Trentham, Biochem. J. 122 (1971) 59.

[31] R.A. MacQuarrie and S.A. Bernhard, J. Mol. Biol. 55 (1971) 181.
[32] N.M. Rodiguin and E.N. Rodiguina, in: Consecutive chemical reactions, ed. R.F. Schneider (Van Nostrand Princeton, 1964).
[33] E. Laynes, in: Methods in enzymology, Vol. 3, eds. S.P. Colowick and N.O. Kaplan (Academic Press, New York, 1963) 447.
[34] F.H.C. Crick and J.C. Kendrew, Advan. Protein Chem. 12 (1957) 133.
[35] D.E. Koshalnd, G. Nemethy and D. Filmer, Biochemistry 5 (1966) 365.
[36] G. de Wilde, E. Swanson and S.A. Bernhard, to be published.
[37] O. Pfenninger, unpublished results.

BIOPHYSICAL CHEMISTRY 1 (1974) 175–183. © NORTH-HOLLAND PUBLISHING COMPANY

PHYSICAL CHEMICAL STUDIES OF SHORT-CHAIN LECITHIN HOMOLOGUES. I. INFLUENCE OF THE CHAIN LENGTH OF THE FATTY ACID ESTER AND OF ELECTROLYTES ON THE CRITICAL MICELLE CONCENTRATION

R.J.M. TAUSK, J. KARMIGGELT, C. OUDSHOORN and J.Th.G. OVERBEEK
Van 't Hoff Laboratory, State University, Utrecht, The Netherlands

Received 2 August 1973

The critical micelle concentration (CMC) of four synthetic phosphatidylcholines (containing two hexanoyl, heptanoyl, octanoyl or nonanoyl residues respectively) in aqueous solutions have been determined by surface tension measurements. The dependence of the CMC on the chain length is discussed on the basis of the mass action model for micelle formation. For the three higher homologues a contribution of 1.08 kT per CH_2 group to the standard free energy of micellisation is found. The change in this free energy in going from the dihexanoyl- to the diheptanoyllecithin is somewhat larger (1.2 kT per CH_2 group).

The influence of high concentrations (several moles per liter) of simple electrolytes on the CMC is interpreted as a salting-out of nonpolar solutes in water. Contrary to expectations the effects of NaCl and LiI on the CMC of dioctanoyllecithin are not additive.

1. Introduction

Studies of the enzymatic breakdown of lecithins continue to yield information on protein–lipid interactions of great potential value for the study of living systems [1–8]. From the recent work of de Haas and co-workers [1, 2] it appeared that the mode of aggregation of lecithins plays an essential role in their interaction with porcine pancreatic phospholipase A. This enzyme catalyses the hydrolysis of the 2 fatty acid ester bonds. It was found to be very weakly active on dispersions of natural or synthetic lecithins, when aggregated in the form of smectic liquid crystals. The activity is greatly increased when these lecithins form micelles after addition of soap-like substances, such as deoxycholate. A similar effect is produced by organic solvents which by solubilisation may profoundly change the aggregate structure.

With lecithins containing shorter acyl chains normal micellisation processes occur. Dioctanoyllecithin (diC_8)*, the highest homologue to show this phenomenon, is an excellent substrate for the enzyme, even in the absence of additives. At concentrations slightly above the critical micelle concentration (CMC) a phase separation occurs by formation of a coacervate (in the terminology of Bungenberg de Jong [9]: a unicomplexcoacervate). Shorter lecithin homologues behave like normal soaps. They form small Hartley micelles [10] at least at low concentrations. When aggregated in small micelles they are hydrolysed more slowly by the enzyme than the dioctanoyl homologue. When dissolved as single molecules they are broken down extremely slowly. It was found, that the activity of the enzyme does not primarily depend on the chain length of the lecithins but on their state of aggregation. Such conclusions could also be drawn from monolayer studies [2, 11].

Apart from this special aspect, the study of micelle formation of short-chain lecithins (diC_6–diC_9) is important from a more classical physical chemical point of view. The molecules contain two nonpolar carbon chains and a zwitter-ionic polar group. Few studies have been published on surfactants with two carbon chains [12–14]. Molecules with a zwitter-ionic head group have received much less attention than the more common ionic- or nonionic surfactants. The most important contributions come from Swarbick, Daruwala and coworkers

* Abbreviation for 1,2-dioctanoyl-sn-glycero-3-phosphorylcholine. This type of abbreviation will be used throughout this paper.

[15], Tori and Nakagawa [16, 17], Hermann [18] and Corkill and coworkers [19, 20]. Roholt and Schlamowitz [21] studied the CMC and the micellar weight of diC_6-lecithin. The micellar weight of diC_7-lecithin was reported by Smink [22]. Pugh measured the micellar weight of the diC_8 homologue [23].

In this paper we are mainly interested in the CMCs and in the standard free energy of micelle formation. One of the questions is: Does each carbon chain in the monomer molecule, containing two acyl chains, contribute independently to the micellisation energy? Moreover, the knowledge of the CMCs is very useful for the interpretation of micellar weight determinations.

For several reasons we became interested in the possible effects of electrolytes on our systems. These effects may provide information on the interactions between the polar groups in the micellar interface and thereby on the orientation of these groups, which has been debated [24–28]. Electrolytes can also produce salting-out or salting-in [29–33]. Finally by addition of salt we might be able to change the micellar structure and interactions between solute molecules without changing the lecithin molecule at all. This might open another way to study the factors, which control lipid–protein interactions. In the specific case of the hydrolysis by phospholipase A, large salt effects have been observed [1].

The first paper in this series will be devoted to the CMC of the short-chain lecithin homologues (diC_6–diC_9). The CMC of the dinonanoyl lecithin (which forms a liquid crystalline dispersion) is defined by the break-point in the plot of the free monomer concentration versus the total lipid concentration.

In later publications micellar weights of the diC_6-, diC_7- and diC_8-lecithin system and some peculiarities of the phase separation in the diC_8-lecithin–water system will be discussed.

2. Materials and methods

The short-chain lecithins* were prepared from egg yolk lecithin according to the procedure of Cubero Robles and DeJongh [34]. The egg lecithin was extracted from chicken eggs with $CHCl_3$–MeOH (2:1) and purified according to the procedure of Pangborn [35]. The 3-sn glycerylphosphorylcholine, obtained after hydrolysis of the natural lecithin with tetrabutylammonium hydroxide [36], was purified by repeated precipitation by diethylether from a methanol solution. Next the glycerylphosphorylcholine was esterified with the appropriate acid anhydride.

The resulting lipids were purified by the following steps:

(a) Column chromatography on silicic acid (Merck 70–230 mesh or Malinckrodt 60–100 mesh), elution with chloroform and increasing concentrations (up to 70%) of methanol.

(b) Column ion exchange chromatography with mixed-bed amberlite (IR 45, IRC 50 from BDH), elution with methanol–water (75:25). The ion exchange resins were purified extensively with 1M acetic acid, 1M ammonia and hot and cold methanol [37].

(c) Silicic acid chromatography, at least twice.

(d) Column chromatography on aluminum oxide (Woelm) with chloroform and chloroform–methanol (90:10) elution.

Depending on the results obtained with thin layer chromatography an extra batchwise ion exchange treatment was introduced between the two treatments in step (c). Between step (c) and (d) we often performed an extraction of the lecithin in methanol and water with hexane. When we used large amounts in the esterification reaction (for ten grams resulting lecithin or more) the main purification difficulty resulted from the formation of byproducts. These were extremely difficult to eliminate by column chromatography or other purification methods, such as $CdCl_2$ complex precipitation, charcoal treatment and chromatography with sephadex LH 20 in methanol. Fractional crystallisation was never successful. One of the main drawbacks of column chromatography is the need of large elution volumes which inevitably contain contaminants from the solvents, even when we used spectroscopic quality, which sometimes had been passed through an aluminum oxide column for further purification. The aluminum oxide step (d) was largely intended to remove these solvent contaminants. Traces of fatty acids are also removed in this step. Silicic acid may cause hydrolysis of the lecithin and ion exchange resins will nearly always release contaminants. The lipid obtained was usually colorless and was stored in ethylalcohol at −20°C. On thin layer chromatography (elution with chloroform–

* The diC_9-lecithin was kindly supplied by dr. W.A. Pieterson of the Department of Biochemistry, University of Utrecht.

methanol–water, 65:35:4) often a small spot at the elution front showed up, when large quantities of lecithin were applied.

All chemicals used were of p.a. or equivalent quality except for the organic solvents in the preliminary steps of the synthesis and in step (d) (where spectroscopic quality was used). Sodium chloride was heated at 500°C for at least 5 hours. Lithium iodide was heated under vacuum to 120°C. Aqueous solutions were filtered through millipore filters (0.05μ), which were washed with boiling water. Water was double distilled, the second time from an all quartz system, through heating from above with an IR lamp. All aqueous electrolyte solutions were checked for organic impurities by surface tension measurements. The surface tension values were always equal to or higher than the value for water.

Aqueous lecithin solutions were prepared in the following manner. An appropriate amount of an alcoholic solution of the lecithin was pipetted into a small pre-weighed glass bottle and taken to dryness with a rotavapor. Then the lecithin was dried at 80°C in vacuum (10^{-2} mm Hg), for 20 hours in the presence of phosphorus pentoxide. After reweighing, solvent was added and concentrations were calculated on a weight basis. Phosphor analysis [38] agreed to within 1% of the calculated value for monohydrate. The lecithin solutions mostly contained a phosphate buffer (10^{-2}M, pH = 6.9 ± 0.2) in order to suppress possible influences of traces of charged surface active impurities. We never found any effect of the buffer on the CMC and on micellar weights.

2.1. Surface tension measurements

The surface tensions of dihexanoyllecithin solutions were measured with the drop-weight method [39,40]. A stalagmometer was mounted directly above the pan of a Mettler balance. The tip with an effective radius of 0.404 cm, as obtained by calibration with water, was placed in a small erlenmeyer containing the solvent. The dropping time was always greater than one minute, which proved long enough for adsorption to be complete within the experimental accuracy of 0.1 dyne cm^{-1} or better. The measurements on solutions of diC_7-, diC_8- and diC_9-lecithin were performed with the drop-volume method [41], as the dropping times had to be much longer (5 to 30 min) owing to the lower CMCs. A stainless steel tip with a radius of 0.307 cm was used.

3. Results

In fig. 1 surface tension values are plotted against the logarithm of the lecithin concentration in 10^{-2}M phosphate buffer. In some cases especially at low surfactant concentrations of diC_8- and diC_9-lecithin the amount of solute adsorbed at the air–water interface was not negligible in relation to the amount within the bulk of the drop. We corrected for this by calculating the amount on the surface from the total drop area and the area/molecule, $1/\Gamma_i$, as found from the Gibbs adsorption isotherm:

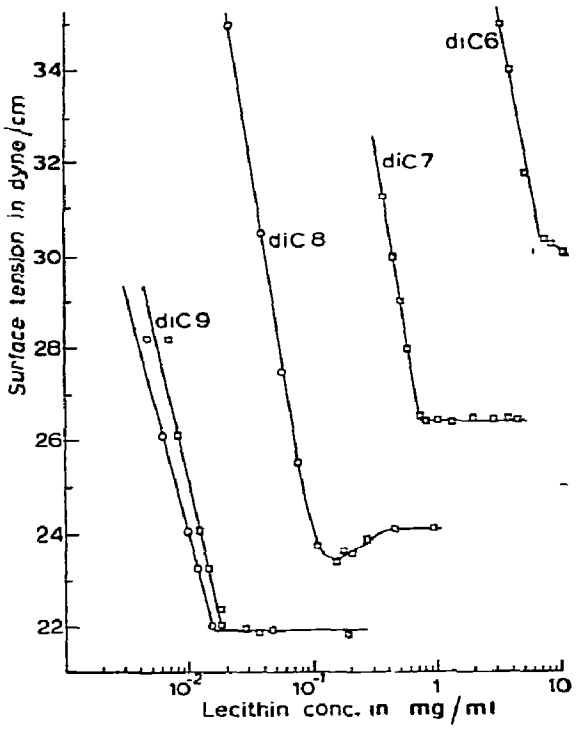

Fig. 1. Surface tension values (in dyne cm^{-1}) for several short-chain lecithin homologues at different lecithin concentrations (in mg ml^{-1}) in aqueous solutions containing 10^{-2}mole ℓ^{-1} phosphate buffer, pH = 6.9 ± 0.2. In the data indicated with □ the initial bulk concentrations were used, while in the data indicated with ○ the bulk concentrations were corrected for adsorption at the air–water interface (see section3).

$$\partial\gamma/\partial\mu_i = (RT)^{-1}\partial\gamma/\partial \ln c_i = -\Gamma_i, \quad (1)$$

where γ is the surface tension, μ_i is the chemical potential, c_i is the concentration (activity coefficient assumed to be constant) and Γ_i is the surface excess of the surfactant (component i). Assuming that the diffusion through the capillary hole of the tip was negligible we were able to calculate the decrease in the bulk concentration. It is evident, that this correction method will only be valid if the concentration change in the bulk is not too large. Moreover, at the lowest concentrations the dropping-time dependence of the drop-volume causes an extra inaccuracy in the γ measurements and especially in the calculation of the area per molecule. In fig. 1 initial (□) and calculated concentration (○) of diC_9-lecithin are both plotted.

From the γ versus log c plots the critical micelle concentrations are found by the intersection of straight lines. The γ versus log c curve for diC_8-lecithin showed a minimum. In this case we assumed the CMC to be within a concentration range around the minimum. This minimum indicates a surface-active impurity [43], which we were not able to remove. It was present in three samples synthetised and purified separately and also in a sample kindly given to us by dr. W.A. Pieterson of the Department of Biochemistry. The values of the CMCs are given in table 1 together with the results obtained from lightscattering (to be published) and the values obtained by de Haas and coworkers [1, 42], and by Roholt and Schlamowitz [21]. Limiting area's per molecule are also included in this table.

Table 1

CMC in mg(monohydrate) ml^{-1} and area per molecule in A^2 $molec.^{-1}$ [eq. (1)] for several lecithins in aqueous solutions (10^{-2}M phosphate buffer)

Compound	Surface tension	Light scattering	Literature value [1, 21, 42]	Area/molec.[a]
diC_6	6.9	6.5	6.5–5.8	66 ± 1
diC_7	0.71	0.8 ± 0.04	1.0 ± 0.9	60 ± 1
diC_8	0.12–0.16	0.13	0.10	63 ± 3
diC_9	0.016[b]			85 ± 2[b]

a) From surface-tension data.

b) These values were obtained by using the corrected concentrations; using initial concentrations a CMC of 0.018 mg ml^{-1} and an area of 77 ± 3 A^2 $molec.^{-1}$ was found.

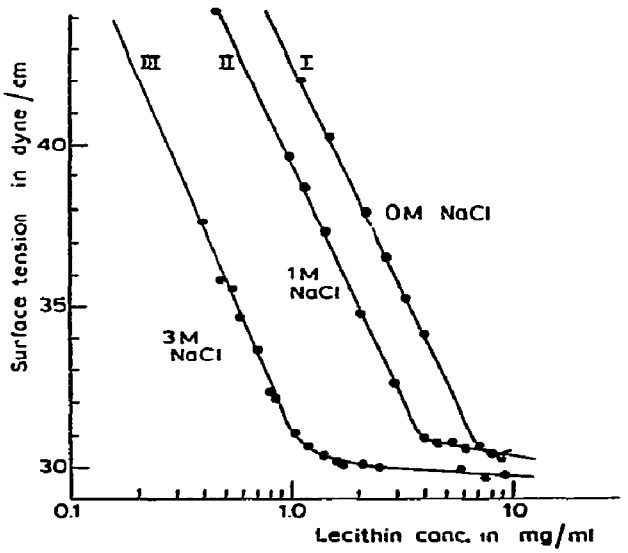

Fig. 2. Surface tension (in dyne cm^{-1}) of diC_6-lecithin (in mg ml^{-1}) in aqueous solutions containing 10^{-2} mole ℓ^{-1} phosphate buffer pH = 6.9 ± 0.2, and varying concentration of NaCl. Curve I: 0 mole ℓ^{-1} NaCl; curve II: 1 mole ℓ^{-1} NaCl; curve III: 3 mole ℓ^{-1} NaCl.

Some of the γ versus log c curves, in aqueous solutions containing high electrolyte concentrations, are plotted in figs. 2 and 3. The influence of the salt concentration on the CMC is also summarized in fig. 4 and table 2.

4. Discussion

4.1. Effect of acyl chain length on the standard free energy of micellisation

For the association equilibrium $M_1 \rightleftarrows (1/n)M_n$ between monomers (M_1) and monodisperse micelles (M_n) with association numbers n, the standard free energy per mole for micelle formation ΔG^0 is given by

$$\Delta G^0 = -RT\ln K = -(RT/n)\ln[M_n] + RT\ln[M_1]. \quad (2)$$

In eq. (2) the association constant is called K and symbols in square brackets represent mole fractions. If the micelles have a distribution in aggregation number,

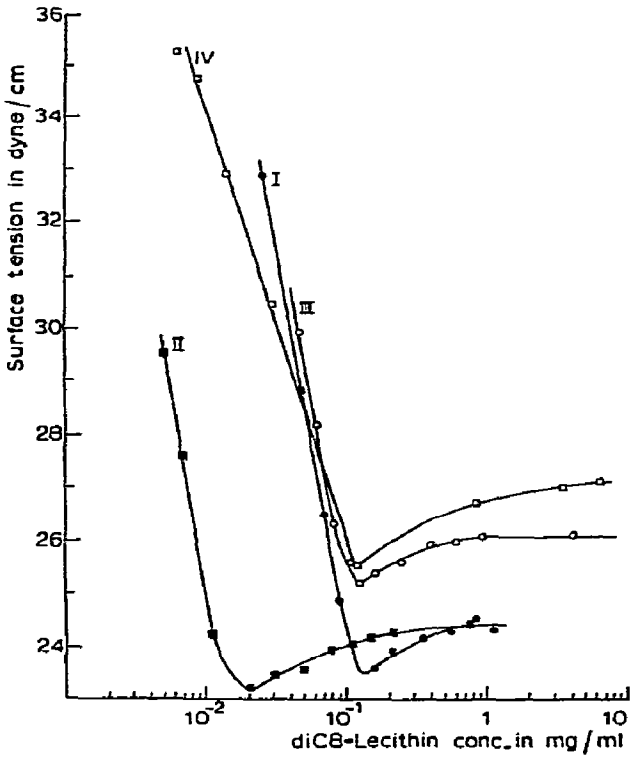

Fig. 3. Surface tension (in dyne cm^{-1}) for different concentrations (in mg ml^{-1}) of diC_8-lecithin in aqueous solutions containing, in addition to 10^{-2} mole ℓ^{-1} phosphate buffer (pH = 6.9 ± 0.2), variable concentrations of electrolytes. Curve I (•) no extra added electrolyte; II (▪) 1 mole ℓ^{-1} NaCl; III (○) 1 mole ℓ^{-1} LiI; IV (□) 1 mole ℓ^{-1} NaCl + 3 mole ℓ^{-1} LiI.

Table 2

Influence of salt concentrations (in mole ℓ^{-1}) on the CMC (in mg ml^{-1}) of diC_6-, diC_7-, diC_8-lecithin

Lecithin	Salt	Concentration (mole ℓ^{-1})	CMC (mg ml^{-1})	Area/molec. (A^2/molec.)
diC_6	–	–	6.9	66 ± 1
	Na_2SO_4	0.310	3.29	67 ± 1.5
		0.657	1.62	65 ± 1.5
		0.727	1.12	61 ± 1
		1.715	0.29[5]	70 ± 2
	NaF	0.595	3.01	64 ± 3
	NaCl	1.00	3.74	62 ± 1
		3.00	1.10	58 ± 2.5
	LiI	1.18	5.91	68 ± 1
		3.68	4.63	69 ± 1.5
		4.82	6.20	76 ± 1
	NaCl + LiI	1.00 1.85	3.6	73 ± 1
diC_7	–	–	0.71	60 ± 1
	NaCl	1.00	0.43	75 ± 1
		1.98	0.2	74 ± 2
diC_8	–	–	0.12–0.16	60 ± 3
	NaCl	1.00	0.02	61[5] ± 1
	LiI	1.00	0.11–0.14	59 ± 2
		3.00	0.1 –0.14	67 ± 2
	NaCl + LiI	1.00 3.00	0.14–0.16	118 ± 2

average concentrations and association numbers have to be used and an average free energy will be obtained [20]. For large association numbers the term containing the micellar concentration will vanish and the free energy change per monomer may be approximated by

$$\Delta G^0 = RT \ln [M_1] = RT \ln [CMC]. \quad (3)$$

In cases where the micellar species have to be taken into account we have followed Mukerjee [44]. At a total concentration of C_t = CMC the micelle concentration equals 2% of the monomer concentration. In table 3 the change in standard free energy of the monomers, when associating in micelles, is given for the different lecithins in 10^{-2}M phosphate buffer. Column I was calculated on the basis of eq. (3), from surface tension data (table 1). The results based on eq. (2) are given in column II and III. In column II Mukerjee's approximation was made, while the values in column III were calculated from light scattering and ultracentrifugation data (to be published). The latter techniques in principle allow for an independent evaluation of $[M_1]$ and $[M_n]$, so that Mukerjee's approximation can be avoided. Comparison of column II and III indicates how well Mukerjee's approximation applies to our systems.

In fig. 5 we have plotted $\Delta G^0/RT$ against the chain length of the lecithin. The slope of this graph gives for the increase in free energy per mole CH_2 a value of 1.08 ± 0.02. This magnitude agrees with the hydrocarbon

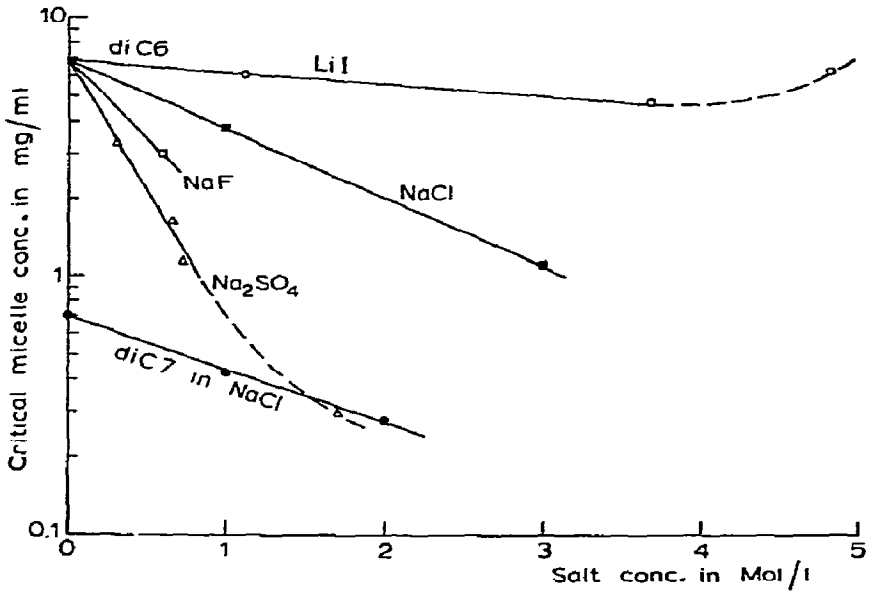

Fig. 4. The influence of varying concentrations in mole ℓ^{-1} of several electrolytes on the CMC (in mg ml^{-1}) of diC_6-lecithin and of NaCl on the CMC of diC_7-lecithin.

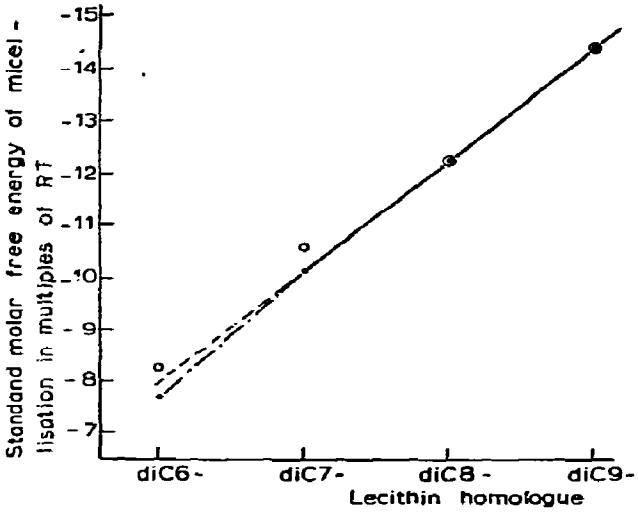

Fig. 5. Standard free energy of micellisation for the four lecithin homologues. The points indicated by an open circle (o) are calculated from eq. (3) (from CMC values only); dots (•) are calculated by eq. (2) (with the help of Mukerjee's approximation). Values from table 3 column I and II respectively.

Table 3

Standard molar free energy of micellization in multiples of RT

Compound	I [a]	II [b]	III [c]
diC_6 ($n \approx 30$)	− 8.2[5]	− 7.7	− 7.8
diC_7 ($n \geq 40$)	−10.5[5]	−10.12	−10.15 (to −10.30)
diC_8 ($n \geq 470$)	−12.3 ± 0.15	−12.3±0.15	−12.3 ± 0.15
diC_9 (liquid crystals)	−14.4 ± 0.06	−14.4±0.06	–

a) $\Delta G^0/RT = \ln[CMC]$; [CMC] in mole fraction = CMC (in g ml^{-1}) × $18/M_1$.
b) $\Delta G^0/RT = \ln[M_1] - (1/n)\ln[M_n]$, where M_n was calculated as 2% of the CMC on a gram basis.
c) $\Delta G^0/RT = \ln[M_1] - (1/n)\ln[M_n]$, calculated from light-scattering or ultracentrifugation (to be published).

contributions found for many other surfactants containing one hydrocarbon chain [45, 46]. From this agreement we may conclude that the two relatively short chains in our molecules are independent of each other in the monomer molecule, i.e., there is no substantial association of the chains in the single molecule.

Similar conclusions for other surfactants can be drawn from the data of Williams et al. [13] and Ralston [14], when taking the CMC values given by Shinoda [46]. On the other hand the extensive data of Evans [12] on alkylsulphates with varying sulphate position have been interpreted by Smith and Tanford [47] by assuming an interaction of the alkylchains in the single molecule. The associated part in the molecule is already shielded from the water and contributes less to the hydrophobic bond than free hydrocarbon chains. This interpretation is based on data concerning compounds with two chains of unequal lengths. An estimate (with the help of eq. (2) and Mukerjee's approximation) of the standard free energy of micellisation using the data of Evans [12] on sulphates with two equal chains gives a value for the micellisation free energy per mole methylene group of 0.6 RT. When eq. (3) is used, 0.5 RT/mole CH_2 is obtained. The value for the soaps with the sulphate in the 1 position is about 0.7 RT/mole CH_2, which is a normal value for an ionic micellar system [45, 46]. Although these values are expressed per mole CH_2 they do in fact also account for changes in the contributions of the polar group, since these values are calculated from the slope of ΔG^0 versus chainlength (as in fig. 5). In spite of the approximations and uncertainties it seems fair to conclude, from the difference between 0.6 and 0.7 RT/mole CH_2, that at least in this system there is some interaction between the alkyl-groups in the single dissolved molecule.

Smith and Tanford [47] determined the CMC of dipalmitoyllecithin to be 4.6×10^{-10}M ($\equiv \ln[\text{CMC}] = -25.5$). If we combine this value with ours for the CMC of diC_9 ($\ln[\text{CMC}] = -14.4$) by drawing a straight line between these two points as in fig. 5, we arrive at a calculated value of 0.8 RT/mole CH_2. This might be an indication that with longer carbon chains ($c > 9$) there is some association of the chains on the monomer.

4.2. Effects of electrolytes on the critical micelle concentrations

The change in the critical micelle concentration, on addition of an inert electrolyte to a nonionic or zwitterionic surfactant, can often be expressed by the equation

$$\log \text{CMC} = -k_s C_s + (\log \text{CMC})_{C_s=0}, \qquad (4)$$

where k_s is a constant, which depends on the salt and the soap studied, and C_s is the electrolyte concentration [17, 32, 33]. Mukerjee [32] has given a theoretical explanation for this relation by using the McDevit–Long theory [29, 30] for salting-out effects of electrolytes on nonpolar solutes in water and the mass action equilibrium for micelle formation. He made the following approximations:

(a) The influence of the salt on the polar group of the single dissolved monomer equals the effect on that group in the micellar interface.

(b) The apolar part of the surfactant in the micelle exposed to the water is very small.

(c) The term $(1/n)\ln[M_n]$ from eq. (2) does not change significantly with the salt concentration. With these approximations the following equation was derived,

$$k_s = \overline{V}_i(V_s - \overline{V}_s)/2.3\,RT\beta_0, \qquad (5)$$

where $\overline{V}_i$ is the partial molal volume of the apolar part of the monomer, $(V_s - \overline{V}_s)$ equals the electrostriction of the electrolyte in solution and β_0 is the compressibility of water at temperature T. We could in principle substitute the value for k_s from eq. (5) in eq. (4), but this generally leads to an overestimate of salt effects by about a factor of 3 [29, 30, 33, 48]. However, on comparing different systems the relative values are often found to correlate well with one another. If for example we take the coefficient of NaCl and benzene ($k_{\text{NaCl,benz.}}$) as a reference we can estimate values for the salting-out coefficients in other systems by using a modified form of eq. (5):

$$k_s = (\overline{V}_i/\overline{V}_{\text{benz.}})\,[(V_s - \overline{V}_s)/(V_{\text{NaCl}} - \overline{V}_{\text{NaCl}})]\,k_{\text{NaCl,benz.}} \qquad (6)$$

The influence of different salts on the CMC of diC_6-lecithin and of NaCl on diC_7-lecithin is shown in fig. 4 and the data are given in table 2. In tables 4 and 5 our results of k_s values for different salts with diC_6- and of NaCl with different lecithins are presented, together with values calculated on the basis of eq. 6. We used the same values for the volumes as Ray and Nemethy [33], i.e., $\overline{V}_{CH_3} = 25.5$ cm^3/mole [49, 50], $\overline{V}_{CH_2} = 15.9$ cm^3/mole [49, 50], $\overline{V}_{\text{benz.}} = 86$ cm^3/mole [48], and the $(V_s - \overline{V}_s)$ values from Deno and Spink [48] and Mukerjee [51]. The coefficient for LiI was obtained by assuming additivity of the electrostrictions for ions.

Table 4
Salting-out effects on diC_6-lecithin

Salt	k_s(obs.)	k_s [eq. (6)]
Na_2SO_4	1.04 ± 0.08	1.14
NaF	0.6	0.58
NaCl	0.26[6] ± 0.01	0.414
LiI	0.05 ± 0.01	0.08

From table 4 we see that the results for diC_6-lecithin are in qualitative agreement with the theory. Table 5, however, indicates that the theory is not satisfactory when comparing the effects of one salt (NaCl) on various surfactants.

Very surprising was the effect of a mixture of NaCl and LiI on diC_8-lecithin. The theory assumes additivity of the salt effects and this apparently does not apply since LiI, which by itself has hardly any influence on the CMC of an electrolyte free solution, counteracts the lowering of CMC due to added NaCl (see table 2). This increase in CMC is parallelled by an increase in the area per molecule (table 2). The reason for this increase may be an association of the lecithin at concentrations below the CMC (for instance a nearly complete dimerisation), or an increase in the hydration of the polar group. This latter assumption was proposed by Kurzendörfer [52] as an explanation for the increase in area/molecule of alcohols at the air–water interface when adding high concentrations of urea and sodium benzoate.

In this connection a few remarks about the area per molecule, given in table 2, should be made. The limiting areas for insoluble higher homologues in a monolayer are about 35 to 40 Å^2 per molecule [53, 54]. The areas in the L–α lamellar liquid crystalline phase, however, are about 60 Å^2 [55]. An area per molecule of around 60 Å^2 is also found for lecithin in the rodlike structures H, Q and R, where the paraffin chains are also in the liquid state. These phases occur at high temperatures and lipid concentrations [55, 56]. The monolayers of the soluble short-chain lecithins probably have the same packing as the higher homologues in the L–α phase.

Table 5
Salting-out effects for NaCl on diC_6-, diC_7-, diC_8-lecithin

Compound	k_s(obs.)	k_s [42]	k_s [eq. (6)]
diC_6	0.26[6] ± 0.01	0.26[7] ± 0.01	0.414
diC_7	0.21 ± 0.01	0.24 ± 0.04[a)]	0.488
diC_8	0.8		0.562

[a)] CMC values for 0.1, 1, and 2 M NaCl were used; if only the value for 0.1 and 1 M NaCl are used a k_s of 0.3 is found.

The effect of the salts on the area/molecule is small and barely above the experimental error except in the case of LiI + NaCl. This unexpected non-additivity deserves further experiments.

Acknowledgement

The authors are indebted to Professor G.H. de Haas and Professor L.L.M. van Deenen (Department of Biochemistry, Utrecht) for suggesting this research project and the helpful advice given during synthesis and purification of the lecithins. Part of the experimental work has been performed in their laboratory. We would also like to thank Mr. G. Voordouw and Miss J.C. Hopman for their skilful assistance in some of the surface tension measurements.

References

[1] G.H. de Haas, P.P.M. Bonsen, W.A. Pieterson and L.L.M. van Deenen, Biochim. Biophys. Acta 239 (1971) 252.
[2] R. Verger, M.C.E. Mieras and G.H. de Haas, J. Biol. Chem. 248 (1973) 4023.
[3] D. Attwood, L. Saunders, D.B. Gammack, G.H. de Haas and L.L.M. van Deenen, Biochim. Biophys. Acta 102 (1965) 301.
[4] Ph.R. Bird, G.H. de Haas, C.H.Th. Heemskerk and L.L.M. van Deenen, Biochim. Biophys. Acta 98 (1965) 566.
[5] R.M.C. Dawson, Biochim. Biophys. Acta 70 (1963) 697.
[6] R.A. Shipolini, G.L. Callewaert, R.C. Cottrell, S. Doonen, C.A. Veron and B.E.C. Banks, Eur. J. Biochem. 20 (1971) 459.
[7] J. Olive and D.G. Dervichian, Bull. Soc. Chim. Biol. 50 (1968) 1409.
[8] M.A. Wells, Biochem. 11 (1972) 1030.
[9] H.G. Bungenberg de Jong, Koninkl. Ned. Akad. Wetenschap. Proc. XLI (1938) 776.
[10] H.L. Booy, in: Colloid science, Vol. II ed. H.R. Kruyt (Elsevier, Amsterdam, 1949) p. 689.
[11] G. Zografi, R. Verger and G.H. de Haas, Chem. Phys. Lipids 7 (1971) 185.

[12] H.C. Evans, J. Chem. Soc. (1956) 579.
[13] E.F. Williams, N.T. Woodberry and J.K. Dixon, J. Colloid Sci. 12 (1957) 452.
[14] A.W. Ralston, D.N. Eggenberger and P.L. Du Brow, J. Am. Chem. Soc. 70 (1948) 977.
[15] J. Swarbrick and J. Daruwala, J. Phys. Chem. 74 (1970) 1293, 73 (1969) 2627;
J. Daruwala, Thesis, Univ. of Connecticut (1969);
P. Molyneux, C.T. Rhodes and J. Swarbrick, Trans. Farad. Soc. 61 (1965) 1043.
[16] K. Tori and T. Nakagawa, Kolloid Z.Z. Polym. 187 (1963) 44, 188 (1963) 47, 191 (1963) 42, 191 (1963) 47.
[17] K. Tori and T. Nakagawa, Kolloid.Z.Z. Polym. 189 (1963) 50.
[18] K.W. Hermann, J. Coll. Interf. Sci. 22 (1966) 352; J. Phys. Chem. 66 (1962) 295.
[19] J.M. Corkill, J.F. Goodman, T. Walker and J. Wyes, Proc. Roy. Soc. A312 (1969) 243.
[20] J.M. Corkill, K.W. Gemmell, J.F. Goodman and T. Walker, Trans. Farad. Soc. 66 (1970) 1817.
[21] O.A. Roholt and M. Schlamowitz, Arch. Biochem. Biophys. 94 (1961) 364.
[22] D.A. Smink, Thesis, Leiden (1969).
[23] W.J. Pugh, Thesis, London (1970).
[24] T. Hanai, D.A. Haydon and J. Taylor, J. Theoret. Biol. 9 (1965) 278.
[25] B.A. Pethica, Surface activity and the microbial cell, Soc. Chem. Ind. Symp. London (1965) p. 85.
[26] D.O. Shah and J.H. Schulman, J. Lipid Res. 8 (1967) 227.
[27] D.A. Cadenhead, R.J. Demchak and M.C. Phillips, Kolloid Z.Z. Polym. 220 (1967) 59.
[28] H.T. Tien, J. Theoret. Biol. 16 (1967) 97.
[29] W.F. McDevit and F.A. Long, J. Am. Chem. Soc. 74 (1952) 1773.
[30] F.A. Long and W.F. McDevit, Chem. Rev. 51 (1952) 119.
[31] P.H. van Hippel and T. Schleich, in: Structure and stability of biological macromolecules, eds. S.N. Timasheff and G.D. Fasman (Marcel Dekker, New York, 1969) p. 417.
[32] P. Mukerjee, J. Phys. Chem. 69 (1965) 4038.
[33] A. Ray and G. Nemethy, J. Am. Chem. Soc. 93 (1971) 6787.
[34] E. Cubero Robles and H. de Jongh, Anal. Biochem. 31 (1969) 246.
[35] M.C. Pangborn, J. Biol. Chem. 188 (1951) 471.
[36] H. Brockenhoff and M. Yurokowski, Can. J. Biochem. 43 (1965) 1777.
[37] J.W. Vanderhoff, H.J. van den Hul, R.J.M. Tausk and J.Th.G. Overbeek, in: Clean surfaces, ed. G. Goldfinger (Marcel Dekker, New York, 1970) p. 15.
[38] C.H. Fiske and Y. Subbarow, J. Biol. Chem. 66 (1925) 375.
[39] W.D. Harkins and F.E. Brown, J. Am. Chem. Soc. 41 (1919) 499.
[40] J.F. Lando and H.T. Oakley, J. Coll. Interf. Sci. 25 (1967) 526.
[41] N.D. Weiner and G. Zografi, J. Pharm. Sci. 54 (1965) 436.
[42] P.P.M. Bonsen, G.H. de Haas, W.A. Pieterson and L.L.M. van Deenen, Biochim. Biophys. Acta 270 (1972) 364.
[43] P.H. Elworthy and K.J. Mysels, J. Colloid Sci. 21 (1966) 331.
[44] P. Mukerjee, Kolloid Z.Z. Polym. 236 (1970) 76.
[45] I.J. Lin and P. Somasundaran, J. Coll. Interf. Sci. 37 (1971) 731.
[46] K. Shinoda, in: Colloidal surfactants, eds. E. Hutchinson and P. van Rysselberghe (Academic Press, New York, 1963) p. 47.
[47] R. Smith and L. Tanford, J. Mol. Biol. 67 (1972) 75.
[48] N.C. Deno and C.H. Spink, J. Phys. Chem. 67 (1963) 1347.
[49] W.L. Masterton, J. Chem. Phys. 22 (1954) 1830.
[50] E.E. Schrier and E.B. Schrier, J. Phys. Chem. 71 (1967) 1851.
[51] P. Mukerjee, J. Phys. Chem. 65 (1961) 744.
[52] C.P. Kurzendörfer and H. Lange, VIth Intern. Congr. Surface Active Substances, Zürich (1972).
[53] P. Joos and R.A. Demel, Biochim. Biophys. Acta 183 (1969) 447.
[54] D. Chapman, N.F. Owens, M.C. Phillips and D.A. Walker, Biochim. Biophys. Acta 183 (1969) 458.
[55] F.C. Reman, Thesis, Utrecht (1971).
[56] V. Luzzati, T. Gulik-Krzywicki and A. Tardieu, Nature 218 (1968) 1031.

BIOPHYSICAL CHEMISTRY 1 (1974) 184–203. © NORTH-HOLLAND PUBLISHING COMPANY

PHYSICAL CHEMICAL STUDIES OF SHORT-CHAIN LECITHIN HOMOLOGUES. II. MICELLAR WEIGHTS OF DIHEXANOYL- AND DIHEPTANOYLLECITHIN

R.J.M. TAUSK, J. VAN ESCH, J. KARMIGGELT, G. VOORDOUW and J.Th.G. OVERBEEK
Van 't Hoff Laboratory, State University, Utrecht, The Netherlands

Received 2 August 1973

The micellar weights of dihexanoyl- and diheptanoyllecithin in aqueous solutions are calculated from light scattering and ultracentrifugation data. A monomer–micelle assocation model is used and corrections for the thermodynamic nonideality, on the basis of rigid noninteracting particles, are applied. A few experiments on the influence of high NaCl concentrations (up to 3 M) are described. Dihexanoyllecithin forms micelles with micellar weight of 15 000 to 20 000 and with rather narrow weight distributions. Diheptanoyllecithin micelles however, have broad size distributions with micellar weights of 20 000 up to about 100 000 in the concentration range studied. Micelles are assumed to be spherical or to have sphero-cylindrical shapes depending on the molecular weights. Two models are used: (1) a compact structure, where no attention is paid to the hydrocarbon–water contact (2) micelles with as little hydrocarbon–water contact as possible.

1. Introduction

In the first paper of this series [1] we outlined the importance of the knowledge of the aggregation properties of short-chain lecithins for the understanding of certain biochemical processes. In one of these processes, the enzymatic hydrolysis of lecithins by phospholipase A [2], it appeared that the kinetics are profoundly influenced by the micellar structure.

In this paper we describe micellar weight determinations of dihexanoyl- and diheptanoyllecithin, performed by light scattering and analytical ultracentrifugation. In order to estimate the micellar weight distribution the thermodynamic nonideality of the solutions has to be taken into account. The second virial coefficients will be discussed in some detail on the basis of the excluded volume of rigid noninteracting molecules.

2. Methods and materials

The preparation and purification of dihexanoyl- and diheptanoyllecithin as well as the preparation of the aqueous solutions, containing 10^{-2}M phosphate buffer (pH = 6.9 ± 0.1) and variable concentrations of NaCl have been described in part I of this series [1]. In all mass per unit volume concentrations we assume the lecithin to be present as monohydrate.

2.1. Ultracentrifugation

Low speed sedimentation–diffusion equilibrium experiments [3] were performed with Beckman Spinco E analytical ultracentrifuges, equipped with Rayleigh- and Schlieren optics and RTIC units. The optical parts were aligned according to the procedure of Brinkhuis et al. [4]. The photographs of the Rayleigh interference pattern were read on a comparator (Aus Jena). The photographs of the Schlieren pattern were enlarged photographically and redrawn. The resulting curves were graphically smoothed. The aluminum, Kel F or Al-filled epon cells contained an oil layer (FC-43), which we added after it was shown that this oil did not disturb the micellar equilibrium. Experiments were performed at 24 ± 1°C. The individual runs for diC_6- and diC_7-lecithin took about 20 hours and 40 hours respectively.

2.2. Light scattering

Two light scattering instruments, manufactured by the Société Française d'Instruments de Contrôle et d'Analyses, were used. The measurements on diC_6-lecithin were performed with the Sofica Photo-Gonio-Diffusomètre model 40 000 B, which had been modified by Huisman [5]. Experiments on diC_7-lecithin were done with the Fica 50.

The solutions were filtered, mostly under pressure, through millipore filters (50 nm or 20 nm) directly into measuring cells [5]. The cells were then centrifuged in a Beckman preparative centrifuge (Model Spinco L) at 20 000 rpm, while floating in a mixture of carbontetrachloride and petroleum ether or in nearly saturated aqueous solutions of sodium nitrate. This last solution is preferable since organic vapors are easily solubilized in the micelles.

2.3. Refractive index increments

The refractive index increments were measured with a Rayleigh interferometer (Aus Jena) at $\lambda = 546$ nm and at room temperature (22 ± 1°C). When experiments were performed in aqueous solutions containing high concentrations of NaCl, the cell walls were first treated with dichloro-dimethylsilane to render the glass hydrophobic and prevent creeping of the salt.

2.4. Density measurement

The densities of the aqueous lecithin solutions were measured with the digital density measuring device DMA-02/C from Anton Paar (Graz) [6]. The system was checked with KCl solutions [7] and the experiments were performed at 25°. During every dilution series temperature stability was about ± 0.003°C. Reproducibility was within $\pm 3 \times 10^{-6}$ g ml^{-1}.

2.5. Vapor pressure osmometry

A few molecular weight measurements by vapor pressure osmometry were performed on diC_6-lecithin using the Hitachi Perkin Elmer Molecular Weight Apparatus Model 115 at 48.5°C and 60°C. The lecithin was dissolved in pure water or in 10^{-4}M phosphate buffer. The osmometer was calibrated with mannitol and sucrose. In the concentration range of 5×10^{-3}–1.5×10^{-1} M sugar reproducibilities of 0.2–0.5% were achieved.

3. Light scattering and ultracentrifugation equations

In order to interpret the measurements in terms of an association process we assume the lecithin to be composed of several species: monomers and several types of micelles with different micellar aggregation numbers. We start from multicomponent light scattering or ultracentrifugation equations and relate the concentrations of the different lecithin components (species) to each other by association constants afterwards. Thermodynamically lecithin is of course only one component.

One of the equations used [8–12] for the light scattered by a solution in excess over the solvent scattering for a multicomponent system composed of isotropic particles with dimensions and interaction distances small compared to the wavelength is

$$\frac{K'c}{R_{90}} = \frac{1}{\sum_i f_i M_i n_i^2} + c \frac{\sum_i \sum_j f_i f_j n_i n_j A_{ij}}{(\sum_i f_i M_i n_i^2)^2} + \ldots\ldots\ldots \quad (1)$$

where K' stands for the constant $2\pi^2 n_0^2 \lambda_v^{-4} N_0^{-1}$, n_0 is the refractive index of the solvent, λ_v is the wavelength in vacuum and N_0 is Avogadro's constant. R_{90} stands for the excess Rayleigh ratio at an angle perpendicular to the incident beam ($R_{90} = (3/16\pi) \times$ turbidity) and c is the total concentration in mass per unit volume ($c = \Sigma_i c_i$). f_i equals the weight fraction ($= c_i/c$) of a solute component i, with molecular weight M_i and refractive index increment n_i

$$n_i = (\partial n/\partial c_i)_{P,T,c'} \quad (2)$$

This differentiation is performed at constant pressure, temperature and concentrations of all solute components except i. The summations in eq. (1) are performed over all solute components i and j. For an incompressible solution the interaction parameter A_{ij} is found from the change of the activity coefficient γ_i of component i with the concentration of component j.

$$A_{ij} = (\partial \ln \gamma_i/\partial C_j)_{\mu_0,T,C'} \quad (3)$$

The differentiation to concentration C_j (in amount per unit volume) is performed at constant temperature, concentrations of solute components (except j) and chemical potential of the solvent (μ_0). The activity coefficient γ_i stems from the chemical potential of solute component i according to

$$\mu_i = \mu_i^0(\mu_0, T, C') + RT \ln C_i\gamma_i. \tag{4}$$

The ultracentrifugation equilibrium equation reads [12, 13]

$$\left(\frac{RT}{\omega^2 rc}\frac{dc}{dr}\right)^{-1} = \frac{1}{\sum_i f_i M_i \rho_i} + c\,\frac{\sum_i\sum_j f_i f_j \rho_j A_{ij}}{(\sum_i f_i M_i \rho_i)^2}. \tag{5}$$

R and T are the gas constant and the absolute temperature respectively, ω is the angular velocity and ρ_i equals the density increment

$$\rho_i = (\partial\rho/\partial c_i)_{P,T,c'}. \tag{6}$$

All other symbols in eq. (5) have the same meaning as in eq. (1). The measured quantities $R_{90}/K'c$ and $(RT/\omega^2 rc)$ (dc/dr) will be called the *reduced total apparent weight average molecular weights:* $\langle M(\partial n/\partial c)^2\rangle_{w.app.}$ or $\langle M(\partial\rho/\partial c)\rangle_{w.app.}$.

It is impossible to distinguish between association and thermodynamic nonideality from thermodynamic data alone. This means that one can only get detailed information about the association phenomenon after accepting a model for the nonideality. In order to calculate the real weight average molecular weight $\langle M\rangle_{w.id.} = \Sigma_i f_i M_i$ from measured quantities we will have to estimate:

(1) The second terms on the right hand side of eqs. (1) and (5). To obtain these virial terms we need estimates of (i) the interaction parameter A_{ij}, and (ii) the weight fractions f_i of the different lecithin species. Both subjects will be discussed in section 6.

(2) The mean density increment or the refractive index increment squared. These are a kind of Z-averages as can be seen from the following relation

$$\langle\partial\rho/\partial c\rangle_z = \sum_i f_i M_i \rho_i / \sum_i f_i M_i, \tag{7}$$

a further interpretation of these increments is given in the next section.

From the total average molecular weight and the monomer concentration the micellar weight can be obtained. Relations for estimating the monomer concentration are also given in the next section.

4. Association equilibrium

In this section we assume all lecithin species to be in equilibrium with one another. This implies that relations between the concentrations (or activities) of the various species exist.

An impression of the micellar weight distribution can be obtained if the weight and number average micellar weights $[\langle M\rangle_{n.id.mic.} = (\Sigma_{i=2} f_i/M_i)^{-1}]$ are known. The lecithin species are denoted with a subscript i, whose value equals the association number.

If the chemical potential of a species is given by the relation

$$\mu_i = \mu_i^0(P, T, c') + RT \ln a_i$$
$$= \mu_i^0 + RT\,[\ln c_i + M_i(B_1 c + B_2 c^2 + \ldots)], \tag{8}$$

in which a_i is the activity of a solute species i, and B_1, B_2, etc., are independent of i, one can easily prove that the following relation between the concentration of that species and the total concentration holds

$$dc_i/dc = c_i M_i / c\langle M\rangle_{w.id.} \tag{9}$$

Using this equation one readily obtains the well known [14–18] relations for calculating the monomer weight fraction, f_1, and the number average molecular weight from the dependence of the weight average molecular weight on the total concentration

$$\ln f_1 = \int_0^c (M_1/\langle M\rangle_{w.id.} - 1)\, c^{-1}\, dc, \tag{10}$$

and

$$c/\langle M\rangle_{n.id.} = \int_0^c \langle M\rangle_{w.id.}^{-1}\, dc. \tag{11}$$

These equations apply irrespective of the relations between the different association constants between the various associating species.

Other types of averages can also be calculated. The Z-average molecular weight is obtained from

$$\langle M\rangle_{z.id.} = \sum_i f_i M_i^2 / \sum_i f_i M_i = \frac{d}{dc}(c\langle M\rangle_{w.id.}). \tag{12}$$

The Z-average density increment likewise follows from

$$\langle \partial\rho/\partial c\rangle_z = \frac{\mathrm{d}}{\mathrm{d}c}\left[\sum_i c_i(\partial\rho/\partial c_i)_{R,T,c'}\right] = \frac{\partial\rho}{\partial c}. \qquad (13)$$

It can thus be seen that this mean increment, at concentration c, that has to be inserted into eq. (5) equals the measured density increment. The mean refractive index increment squared should be calculated from the definition

$$\langle(\partial n/\partial c)^2\rangle_Z = \sum_i f_i M_i n_i^2 / \sum_i f_i M_i. \qquad (14)$$

Due to the high association numbers in micellar systems the transition at the CMC is rather sharp. At concentrations outside the small transition region the Z-average increments become indistinguishable from the limiting values for monomers and micelles.

The equations given above apply only for systems at constant pressure. In ultracentrifugation, however, pressure is not constant in the cell and varies from one experiment to the other. For each separate experiment eqs. (9–12) do hold for systems in which the partial specific volume of each species is concentration independent, if the reduced molecular weights (thus including the factor $\partial\rho/\partial c$) are substituted.

If apparent weight average molecular weights are used eq. (11) yields the apparent number average molecular weight and eqs. (10) and (9) provide us with the first estimates of the true activities a_1 or a_i (defined with the help of eq. (8).

In general relation (8), however, does not apply [8, 10]. Using classic thermodynamics one can derive for an incompressible system the relation (15) between the chemical potentials and the coefficients $A_{\bar{i}}$ introduced in eq. (3).

$$\mu_i = \mu_i^0(P,T,c') + RT\ln c_i + RT\sum_j M_j^{-1}(A_{\bar{i}\bar{j}} - \bar{V}_i)c_j + \ldots\ldots \qquad (15)$$

$\bar{V}_i$ equals the partial molal volume of species i. In section 6 dealing with the *second virial coefficient* a simple model for calculating $A_{\bar{i}\bar{j}}$ will be described. The model is based on rigid non-interacting solute molecules. It has often been realized [19–22], that eq. (15) (neglecting $\bar{V}_i$) reduces to eq. (8) for rigid long cylinders with equal radii. In the case of spherical solute molecules B_1 in eq. (8) is inversely proportional to the molecular weight. It can however be shown that the errors involved in using eq. (9) through (13) are often small, especially in micellar systems.

5. Micellar weight distribution

In the preceding section an equation (11) has been given to obtain the number average from the weight average molecular weight. This equation holds for the total molecular weight and for the micellar weight. The ratio $Q = \langle M\rangle_{\mathrm{w.id.mic.}}/\langle M\rangle_{\mathrm{n.id.mic.}}$ for the real (often called ideal) micellar weights is a measure of the width of the distribution. The standard deviation σ_n around the number average molecular weight for an arbitrary distribution is given by [23]

$$\sigma_n/\langle M\rangle_n = (Q-1)^{1/2}. \qquad (16)$$

The actual weight distribution depends on all association constants, but these are generally unknown unless experiments of extremely high accuracy and a very detailed model of the association behaviour are available.

Wide molecular weight distributions are expected if the association constant K for different micelles are about equal

$$K = C_{n+1}/C_nC_1. \qquad (17)$$

C_n stands for the molar concentration of a micelle containing n monomers. Equal values of K are likely to appear, if the micellar structure strongly departs from the spherical shape and lead to Q values of 2, as has been shown in several papers [18, 21, 24, 25]. This model also leads to a linear increase of the micellar weight with the square root of the micellar concentration.

In the calculations of the second virial coefficients we would like to use actual values for the concentrations of the various micelles. Instead of making assumptions about the various association constants we assume that the Schulz distribution function [13, 26] applies. This is a two parameter function which is easy to integrate. One of the variables can be expressed as $\langle M\rangle_w/\langle M\rangle_n$

$$f(M) = (y^{z+1}/\Gamma_{z+1})M^z\exp[-yM], \qquad (18)$$

where $f(M)$ stands for the weight fraction of the molecules with a molecular weight M;

$y = (z + 1)/\langle M\rangle_w$; $\quad z = \langle M\rangle_n/(\langle M\rangle_w - \langle M\rangle_n)$;

Γ_{z+1} is the gamma function.

6. Second virial coefficient

Details of the micellisation phenomenon can only be obtained after estimation of the coefficients of the second terms on the right hand side of eqs. (1) and (5). These terms contain next to the weight fractions the interaction parameters A_{ij}. Evaluation of this last quantity is actually the basic problem.

6.1. Interaction parameter A_{ij}

As the electrostatic dipole intermicellar interactions are probably quite small one may visualize the micelles as rigid noninteracting particles. A_{ij} is related to the pair correlation function [8, 10] and can in this simplified case be calculated from the mutual pair excluded volume. Isihara solved this problem for molecules of arbitrary size and shape. The relation for A_{ij} (defined in our concentration units) reads

$$A_{ij} = N_0[v_i + v_j + (1/4\pi)(x_i s_j + x_j s_i)], \qquad (19)$$

where v_i stands for the volume of a molecule i with surface s_i, and x_i equals the integral over all orientations ω of H_i, called the supporting function.

$$x_i = \int H_i \, d\omega. \qquad (20)$$

For simplicity's sake we will assume the lecithin monomers to be spheres and the micelles to be spheres or spherocylinders. The geometry of these molecules is given in fig. 1 and the definition of H_i and the relations needed to calculate A_{ij} are given in table 1. If there is a distribution in micellar weights we assume the spherocylinders to have equal radii and different lengths and the spheres to have different radii. These models will be discussed in more detail in section 9.

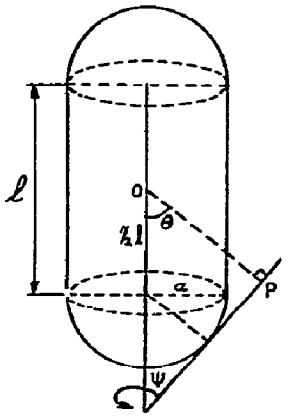

Fig. 1. Geometry of a spherocylinder.

6.2. Weight fractions of the various species

The monomer concentrations and the total micellar concentrations can be evaluated with the help of eq. (10). The weight fractions of the different types of micelles can be estimated from an assigned distribution function. We have assumed the Schulz distribution (eq. (18)) to apply. The two independent parameters in that relation can be obtained from the weight and the number average micellar weight.

It will be important that the value of the second virial coefficient is not too sensitive to the actual applied distribution function. The influence of the width of the distribution can readily be found by solving the second terms of eqs. (1) and (5) for different geometric models (different relations for A_{ij} in eq. (19)) and polydispersities. The virial coefficient for mixtures of spherocylinders with equal radii and weight average molecular weights is independent of the width of the distribution.

Table 1
Size and shape parameters for the calculation of the interaction parameter A_{ij}

	Sphere	Spherocylinder
v	$\frac{4}{3}\pi a^3$	$\frac{4}{3}\pi a^3 + \pi a^2 l$
s	$4\pi a^2$	$4\pi a^2 + 2\pi a l$
H	a	$a + \frac{1}{2} l \cos\theta$
x	$4\pi a$	$4\pi a + \pi l$

For mixtures of spheres with equal partial specific volumes $\bar{v}$ the nonideality coefficient decreases with increasing width. Assigning a value of $8\,M_w\,\bar{v}$ to the total excluded volume of a monodisperse system we find at $M_w/M_n=2$ a volume of $7.39\,M_w\bar{v}$ and at $M_w/M_n=\infty$ a value of $6.84\,M_w\bar{v}$.

7. Procedure for calculating micellar weights

7.1. Light scattering

We will now discuss the actual procedure for calculating the micellar weights from light scattering data. We start from the plot of the reduced total apparent weight average molecular weight ($R_{90}/K'c \equiv \langle M(\partial n/\partial c)^2\rangle_{w.app.}$) versus the total concentration and divide these "molecular weights" by the average refractive index increment squared and obtain the values for $\langle M\rangle_{w.app.}$. The values for $\langle(\partial n/\partial c)^2\rangle_z$ near the CMC are calculated using eq. (14) from estimates of the monomer concentration (eq. (10)), micellar concentrations, association numbers and the refractive index increments measured at concentrations well outside the CMC region.

The values from the resulting curve of $\langle M\rangle_{w.app.}$ versus c are now used in eqs. (10) and (11), since these equations can also be used when substituting apparent values, as stated there. We now arrive at the monomer activity f_{1a}, the apparent weight average micellar weight $\langle M\rangle_{w.app.mic.}$ and the apparent number average micellar weight $\langle M\rangle_{n.app.mic.}$. The following approximation was used:

$$\langle M\rangle_{w.app.mic.} = (\langle M\rangle_{w.app.} - M_1 f_{1a})/(1-f_{1a}). \qquad (21)$$

The values of $\langle M\rangle_{w.app.mic.}$ should provide us with the information necessary to estimate the shapes and sizes of the micelles, while the values for $\langle M\rangle_{w.app.mic.}/\langle M\rangle_{n.app.mic.}$ give us an estimate of the polydispersity of the micelles. Using the Schulz distribution (eq. (18)), the monomer concentration and the values for A_{ij} from geometric models (eq. (19)), the summations in the second virial coefficient of eq. (1) can be carried out. In most cases the summations can be replaced by integrals.

After the reduced total ideal weight average molecular weights are calculated we start micellar weight estimations by again using eqs. (7), (10) and (11). The resulting micellar weights provide us with a better estimate of the second virial coefficient and weight average micellar weights are obtained using a sufficient number of iterations. This whole procedure is schematically given in fig. 2.

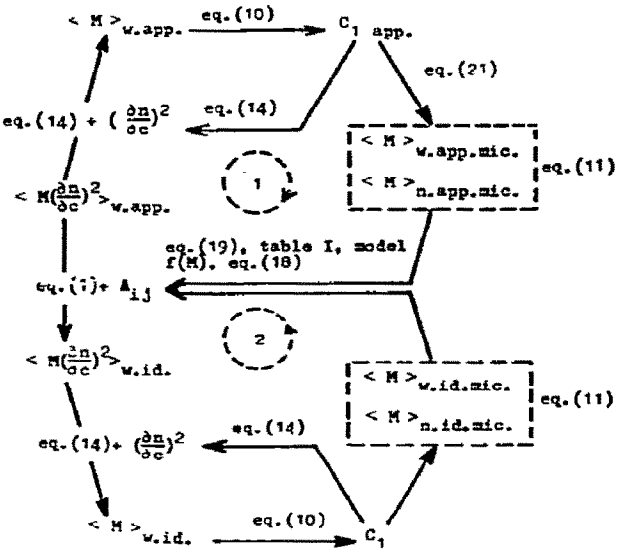

Fig. 2. Procedure for calculating the ideal micellar weights from reduced apparent total weight average molecular weights.

Cycle 1. The apparent weight and number average micellar weights are obtained from the total apparent molecular weights with the help of eqs. (10) and (11). At concentrations near the CMC an iteration procedure is used to calculate $(\partial n/\partial c)$ from eq. (14). From the weight average micellar weights the micellar shape and size is estimated. This leads to the first approximation of the interaction parameter A_{ij} (eq. (19)). The parameters of the distribution function $f(M)$ (eq. (18)) are obtained from a comparison of the number and weight average micellar weights.

Cycle 2. Introduction of the weight fractions, the values of A_{ij} and $(\partial n/\partial c)$ in eq. (1) leads to estimates of the ideal total molecular weights from which the micellar weights are obtained. An iteration procedure provides us with better estimates of A_{ij}.

7.2. Ultracentrifugation

Evaluation with the help of eq. (10) of the micellar weight at a certain concentration above the CMC requires the knowledge of the total average molecular weight at all lower concentrations.

If we want to keep the time to reach equilibrium within reasonable limits we have to use small solution columns (around 3 mm), which allow only a modest concentration range in one experiment. Experiments

with various starting concentrations but with overlapping equilibrium concentration ranges are performed. At the lowest concentrations the highest speeds are required in order to get an optimal resolution.

The hydrostatic pressure in the solution columns therefore varies from one experiment to the other. Since the partial specific volume of monomers and micelles differ the association equilibrium is pressure dependent. This leads to a nonsuperposition of the plots of $\langle M\, \partial\rho/\partial c\rangle_{w,app.}$ against c from different experiments [32]. In this case the micellar weights should be calculated for every experiment separately, but this demands an extremely high accuracy. Moreover, the theoretical pressure effects in our case result in a nonsuperposition of a few percent at most, as follows from some estimated numerical data for diC_6- under our experimental conditions. At the lowest concentration and at the bottom positions in the cells a maximal pressure of 17 atm prevailed. The measured total average molecular weights are smaller than the molecular weights if obtained at 1 atm pressure [32]. At total concentrations of 8 mg ml^{-1}, 11 mg ml^{-1} and 20 mg ml^{-1} the decrease of the molecular weight due to the pressure is only 4%, 2% and 0.5% respectively. The calculated effects for diC_7- are even much smaller. We therefore neglect the pressure effects and plot $\langle M\, \partial\rho/\partial c\rangle_{w,app.}$ values versus c from different experiments on one curve and analyse this curve in a manner completely analogous to the method used in interpreting the light scattering data.

8. Results

8.1. Refractive index increment

The change in the refractive index of the solution with increasing lecithin concentration can be described by two straight lines, intersecting near the CMC. The curvature near the CMC extended only over a very small concentration range. The expression for the refractive index change above the CMC is given by

$$\Delta n = (\partial n/\partial c)_{P,T} c + a, \qquad (22)$$

and we may identify this increment with the micellar refractive index increment $(\partial n/\partial c)_m$. The increment for monomers will be abbreviated with $(\partial n/\partial c)_1$. In table 2 the values of the increments and of the constant a are given for diC_6-lecithin in aqueous solutions containing various NaCl concentrations and for diC_7-lecithin. The value for diC_8-lecithin is also included for comparison. In this special case it is not possible to measure the increment at room temperature in electrolyte free (or dilute buffer) solutions, due to the appearance of a phase separation (to be published).

The decrease of the refractive index increment $(\partial n/\partial c)_s - (\partial n/\partial c)_0$ of the lecithin with increasing salt concentrations can be explained by taking the increase of the refractive index of the medium $n_s - n_0$ into account. Assuming the refractive index of a solution to be a linear function of the volume composition of the various components the following relation holds [12, 33]

$$(\partial n/\partial c)_s - (\partial n/\partial c)_0 = -(n_s - n_0)\bar{v}, \qquad (23)$$

$\bar{v}$ equals the partial specific volume of the lecithin. In table 2 we also give the values for the refractive index increments calculated from this equation, using the partial specific volumes and the refractive index increments both measured in 10^{-2}M phosphate buffer.

8.2. Density measurements

In plotting density values ρ versus lecithin concentrations straight lines intersecting near the CMC were obtained. As in refractive index measurements only a slight curvature near the CMC was found. From the slopes of the lines the partial specific volumes $\bar{v}$ and the partial molal volumes $\overline{V}$ were calculated [12]. The data for diC_6- and diC_7-lecithin are given in table 3.

By subtraction of appropriate values from each other the volume of a mole CH_2 and the volume change during micellisation are found. These values compare favorably with data for other soaps studied by Corkill [34].

In the last column of table 3 we added for comparison the molar volumes calculated from data of longer chain lecithin homologues in the L–α liquid crystalline phase [35–37].

8.3. Vapor pressure osmometry

We only succeeded in measurements of molecular weights by vapor pressure osmometry at concentrations below the CMC for diC_6-lecithin. Up to a concentration of about 6 mg ml^{-1} a molecular weight of 471 ± 2 was

Table 2
Refractive index increments for three lecithin homologues

Lecithin	M NaCl	observed $\partial n/\partial c$ (ml g^{-1})		$a \times 10^6$	$\partial n/\partial c$ [eq. (23)]	
		$c <$ CMC	$c >$ CMC	$c >$ CMC	$c >$ CMC	$c >$ CMC
diC_6-	0	0.132(0.001) [a]	0.126(0.001)	37		
	1	0.122(0.001)	0.113(0.001)	31	0.124	0.118 [d]
	2	0.117(0.002)	0.1073(0.001)	19	0.116	0.110 [d]
	3	0.111(0.002)	0.0997(0.001)	12	0.109	0.102 [d]
diC_7-	0	0.136(0.002)	0.125(0.001)	11		
diC_8-	0 [b]		0.125(0.002)			
	0 [c]		0.118(0.001)			0.119 [e]

[a] The numbers between brackets are the standard deviations from least square straight lines.
[b] This value was obtained by extrapolating measurements from high temperatures (50–90°C).
[c] Measured in solutions containing 0.2 M LiI.
[d] Calculated on the basis of measured values in salt free solutions.
[e] Corrected for the LiI effect from extrapolated measurements at high temperatures (to be published, see also ref. [1]).

obtained, which is in perfect agreement with the monohydrate monomer molecular weight (471.5). This means that there is no substantial preassociation. At higher concentrations measurements were progressively less reliable, probably due to decomposition of the lecithin and the formation of the more volatile caproic acid at the high temperatures: 48.5°C and 60°C. The osmometer signals became unstable and the calibration constant showed sudden jumps, leading to too small apparent molecular weights.

8.4. Calibration of the light scattering instrument

The following systems were used in the calibration.

(a) Lysozyme (Boehringer & Soehne, for analytical purposes). The protein was dissolved in a Na_2HPO_4 (0.056 M) – citric acid (0.071 M) buffer (pH = 3.7) to suppress dimerisation [38]. The molecular weight was found from ultracentrifugation equilibrium experiments and was in agreement with other physical analyses [39] and with the chemical analysis [40].

Table 3
Density increments and molal volumes of dihexanoyl- and diheptanoyllecithin

Lecithin	$\partial\rho/\partial c$		$\bar{V}_2$ (ml $mole^{-1}$)		$\bar{V}_{CH_2}$ (ml $mole^{-1}$)		$\Delta\bar{V}_2$	V_2
	$c <$ CMC	$c >$ CMC	$c <$ CMC	$c >$ CMC	$c <$ CMC	$c >$ CMC	micellisation	L–α
diC_6-	0.1513(0.0007)	0.1324(0.0007)	401.3(0.4)	410.3(0.4)			9.0(0.6)	411.3
diC_7-	0.139 (0.003)	0.1103(0.0005)	431.4(1.5)	445.8(0.3)	15(1.6)	17.7(0.5)	14.4(1.6)	443.8

(b) β-Lactoglobulin*. Crystalline bovine lactoglobulin was dissolved in 10^{-3} M EDTA (pH = 6.0), 0.2 M NaCl and dialyzed for 24 hours. The concentrations were determined by absorption measurements ($E^{1\%}_{278} = 9.1$) [41]. The refractive index increment was taken [41, 42] to be 0.182 ml g^{-1}. The dimer molecular weight [41] was found by ultracentrifugation (36700).

(c) 12-Tungstosilicic acid (Merck, p.a.). The calibration constant from TSA in aqueous solutions containing 0.3 M or 1M NaCl was obtained by extrapolation to infinite dilution. The refractive index increments from literature were used [43] (0.100 ml g^{-1} and 0.0972 ml g^{-1} respectively in 0.3 M and 1 M NaCl). The water content was determined with the help of Karl Fischer titrations.

(d) Sucrose (BDH aristar). The measurements on sucrose were also extrapolated to infinite dilution, using the same dependence of K' (eq. (1)) on the refractive index of the solution as Maron and Lou [44] did. Contrary to Maron and Lou and Mijnlieff [45] we found no substantial depolarisation ($\rho_u \leqslant 0.01$).

All calibration constants agreed within 1.5%. Comparison of the calibration constants obtained from the aqueous solutions and from benzene leads to the conclusion that the influence of the refractive index of the solution on the calibration constant is much less than the theoretically expected [46–48] n^2 (actually we obtained a value quite close to n). This might partially be caused by the fact that the photomultiplier does see past the incident beam [49].

8.5. Micellar weight determinations

8.5.1. Ultracentrifugation equilibrium

In analysing the data from equilibrium experiments use is made of the interference and the Schlieren pattern. The fringes and the refractive index gradients were converted to concentrations or concentration gradients respectively with the help of eq. (22). We thus ignore the influence of the pressure on the refractive indices and index increments. The reduced total apparent weight average molecular weights at concentrations above the CMC and at different positions in the cell were calculated with the help of a computer program of Ketellapper [50].

* The β-lactoglobulin was a generous gift of Dr. T.A.J. Payens of the Netherlands Institute of Dairy Research, Ede, The Netherlands.

The results for diC_6- and diC_7-lecithin are plotted in figs. 3 and 4. The experiments on diC_7- were very poorely reproducible. This large nonsuperposition of the curves cannot be explained on the basis of the pressure influence on the association equilibrium and is probably due to traces of impurities or to decomposition of the lecithin during the 40 hours centrifugation. When analysing average molecular weights of diC_7- at the meniscus and the bottom of the cell at shorter time intervals (Archibald method) this "decomposition effect" has in fact a few times been observed. The direction of the change of the molecular weights was, however, not always the same. In two experiments a slight increase, while in one other a larger decrease was found. Seven experiments, indicated with dots in fig. 4, show a molecular weight–concentration dependence basically different from the results of the other nine experiments. These deviating lines are curved upwards or have a very pronounced S-shape. Such plots are often obtained in experiments where the sedimentation equilibrium is not reached or in cases where the micellar equilibria are disturbed by impurities.

The measured values of $\langle M\, \partial\rho/\partial c\rangle_{w,app.}$ from all experiments were averaged and a smooth curve was drawn. The standard deviation of the experimental points around this mean curve is 5 to 7%. An other average curve was obtained by excluding the seven experiments marked with dots. The standard deviation now is around 3%.

The resulting mean curves of diC_6- and diC_7- were graphically extrapolated into the CMC region. As a guide in this extrapolation CMC values from surface tension measurements [1] were used. These values are indicated by arrows in figs. 3 and 4. After analysis of the entire curves with the help of eqs. (10) (modified so as to contain apparent quantities), (13) and (21) the apparent *micellar* weight–concentration dependence is obtained. The results are plotted in figs. 5 and 6. The broken lines in fig. 6 from ultracentrifugation were obtained by taking all results from fig. 4 into account. If only the nine more well behaved experiments are used the micellar weights equal the data from light scattering. At micellar concentrations below 4 mg ml^{-1} the micellar weights are dramatically influenced by slight changes in the extrapolation of the total average molecular weight to the monomeric region. By trial and error extrapolations were found that yield acceptable micellar weight against concentration plots. The sudden increase in micellar weight going to very low micelle concentrations

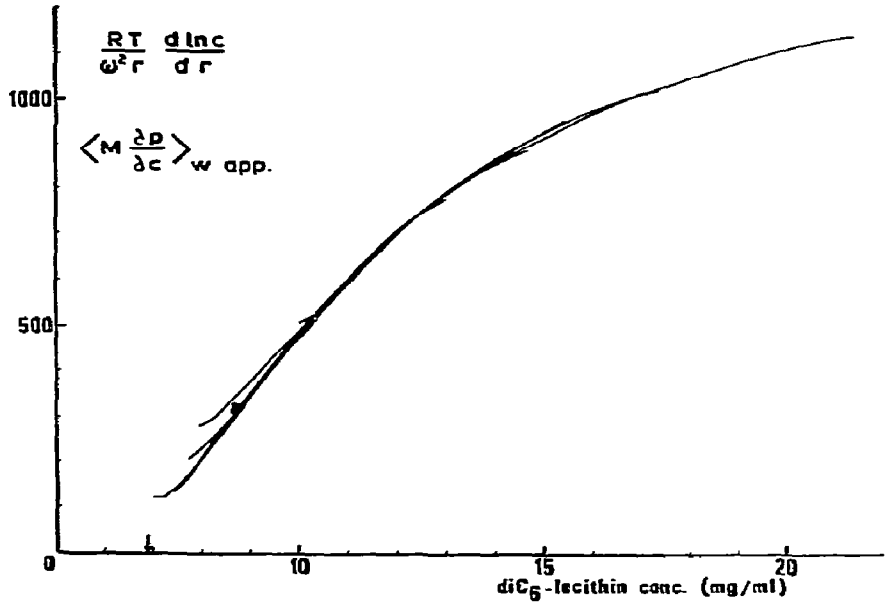

Fig. 3. Results from five ultracentrifugation experiments on diC_6-lecithin in aqueous solutions containing 10^{-2}M phosphate buffer (pH = 6.9 ± 0.1). In this figure and in figs. 4 and 7–10 the arrows indicate the CMC obtained by surface tension measurements [1].

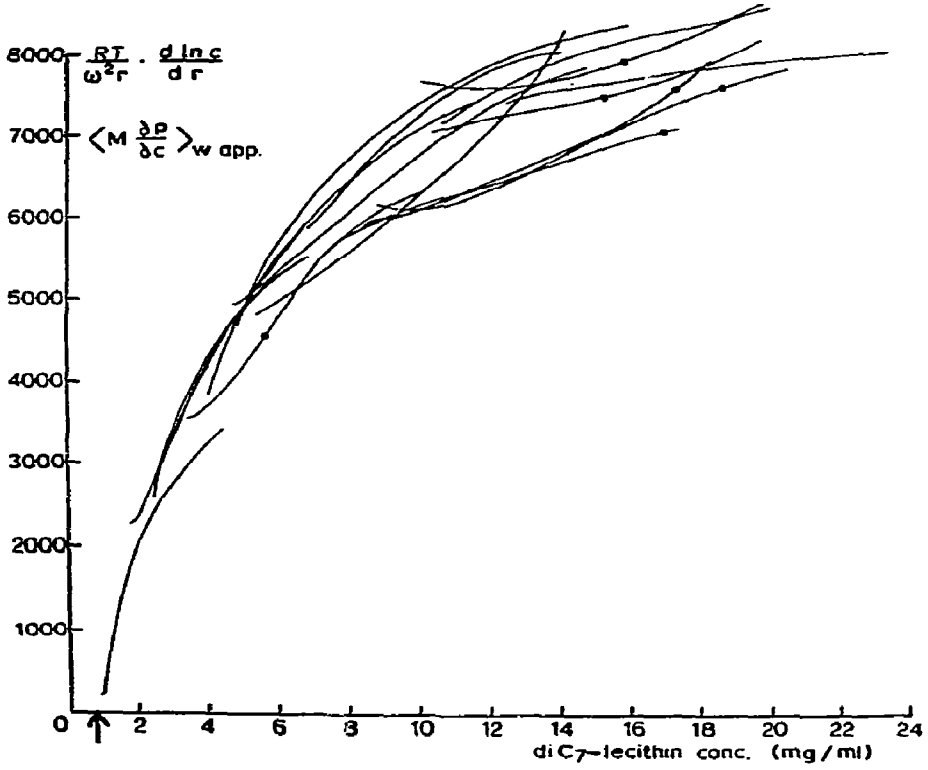

Fig. 4. Results from sixteen ultracentrifugation experiments on diC_7-lecithin in aqueous solutions containing 10^{-2} M phosphate buffer (pH = 6.9 ± 0.1).

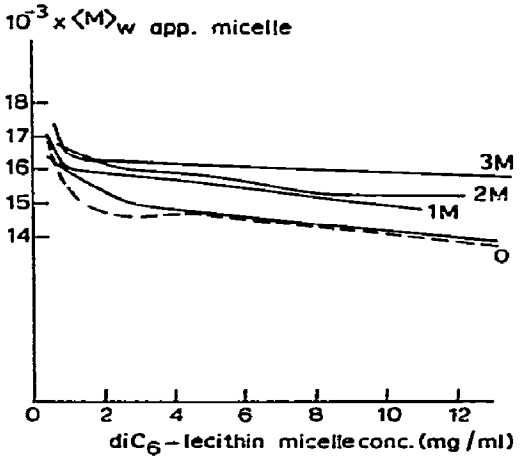

Fig. 5. Apparent weight average micellar weights as a function of the diC_6-micellar lecithin concentration. The broken line is derived from ultracentrifugation experiments (dilute buffer solutions). The fully drawn lines are obtained from light scattering, the solutions contained various NaCl concentrations next to the phosphate buffer.

is caused by mathematical difficulties in the numerical integration in eq. (10) and has no physical significance.

8.5.2. Light scattering

In fig. 7 the R_{90} values for diC_6-lecithin in 0, 1, 2 and 3 M NaCl are shown and in fig. 8 R_{90} for diC_7- in 0 and 3 M NaCl is plotted. Owing to the limited quantity of diC_7-lecithin, we calculated the value for the refractive index increments in 3 M NaCl, with the help of eq. (23): $(\partial n/\partial c)_1 = 0.112$ and $(\partial n/\partial c)_m = 0.101$. This may have introduced systematic errors of a few percent.

The plots of $R_{90}/K'c$ for concentrations above the CMC are shown in figs. 9 and 10. The values for concentrations below the CMC are consistently too high, probably due to some dust. Owing to the limited quantities of the lecithins we used as little material as possible and prepared stock solutions in the light scattering cuvettes. Dilutions were carried out in the cells and by the time the CMC was reached, after three to five dilutions, the dust level was mostly too high (dissymmetry $z \approx 1.03$ to 1.04). The curves were extrapolated to the CMC in a manner completely analogous to the procedure used in analysing the ultracentrifugation data. The apparent micellar weights were obtained with the help of eqs.

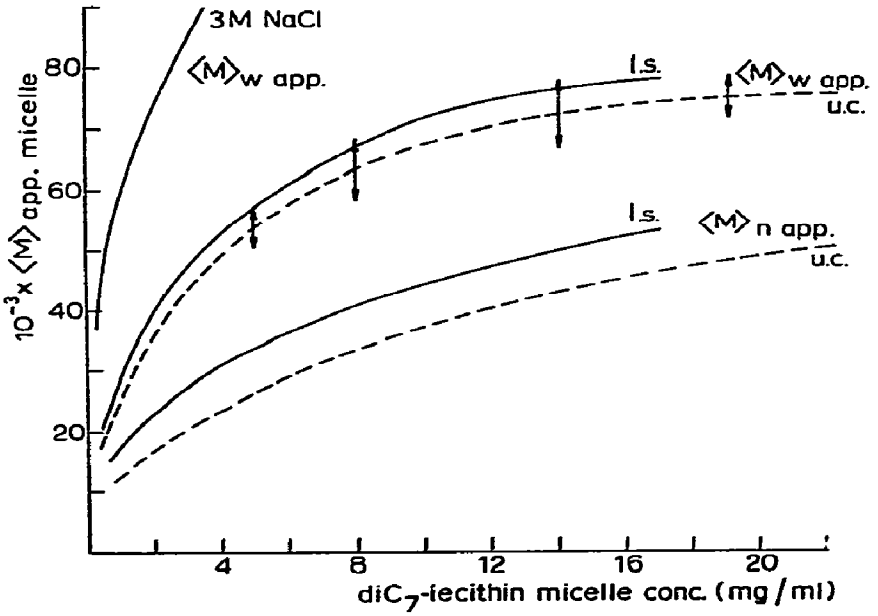

Fig. 6. Apparent weight and number average micellar weights of diC_7-lecithin as derived from light scattering (l.s.——) and ultracentrifugation (u.c. ····). The arrows (↕) indicate the standard deviation of the ultracentrifugation data around the mean values.

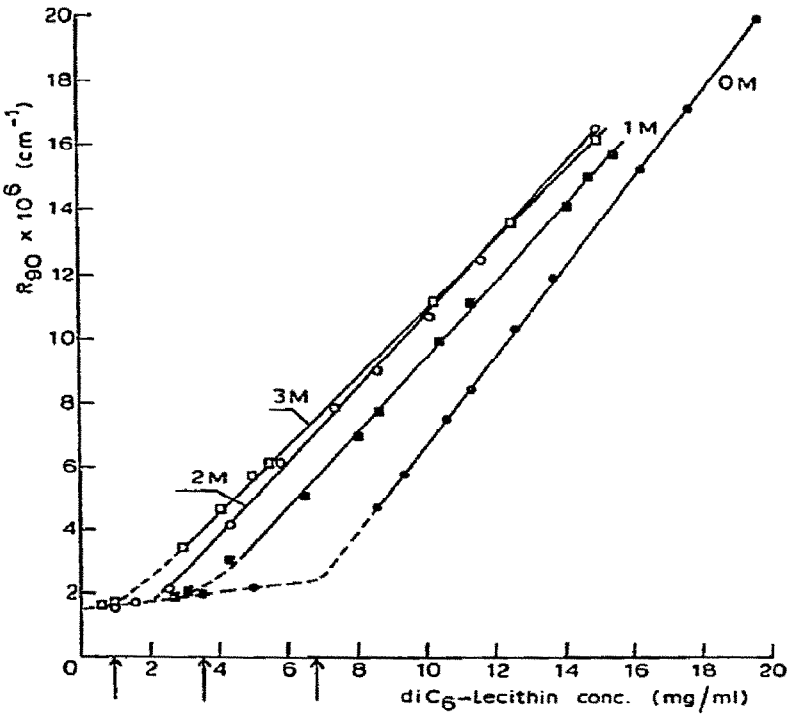

Fig. 7. Rayleigh ratio (R_{90}) as a function the diC$_6$-lecithin concentration in aqueous solutions containing in addition to the phosphate buffer (10^{-2} M, pH = 6.9 ± 0.1) various concentrations of NaCl. (•): 0 M, (▪): 1 M, (○): 2M, (□): 3M NaCl.

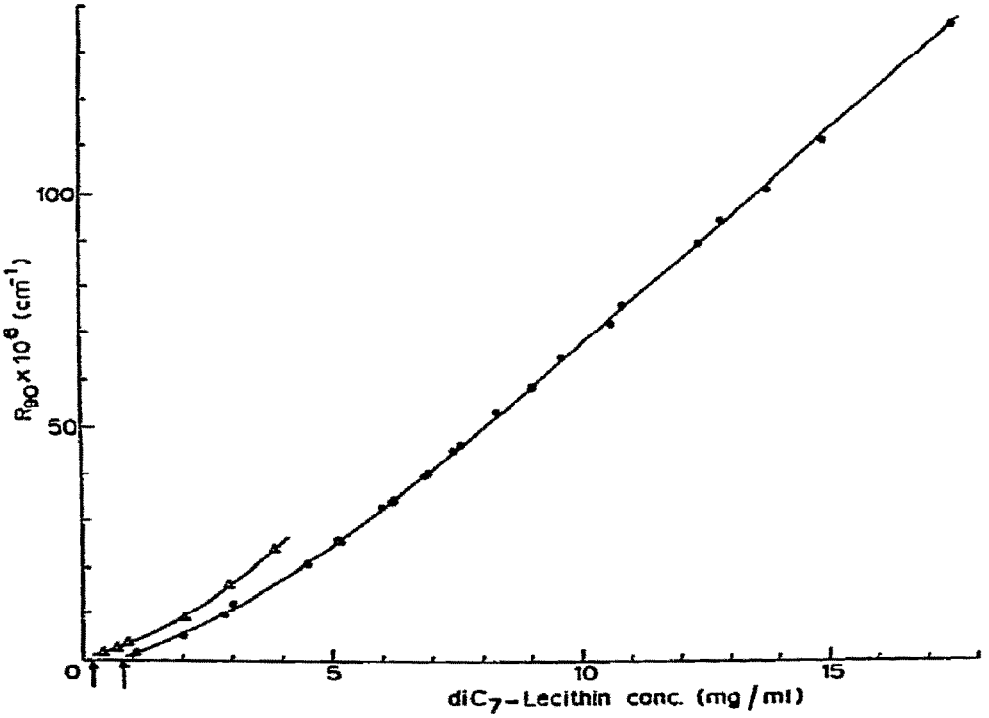

Fig. 8. Rayleigh ratio (R_{90}) as a function of the diC$_7$-lecithin concentration in aqueous buffer solutions containing 0 M (•) and 3M NaCl (△).

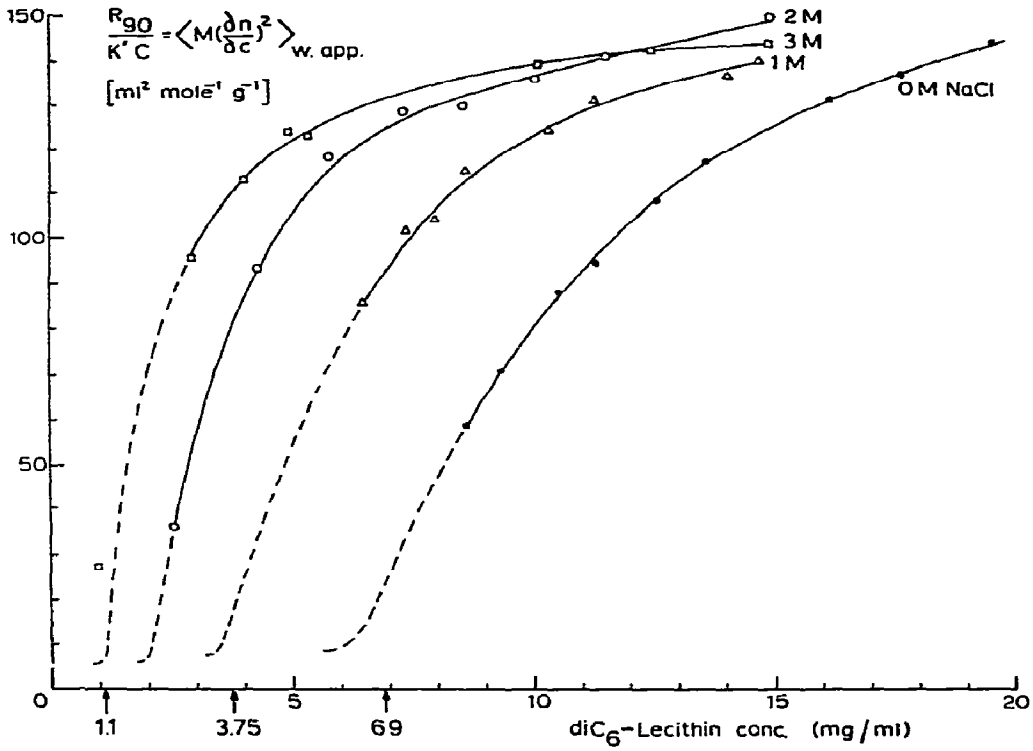

Fig. 9. Reduced apparent total weight average molecular weight of diC_6-lecithin as a function of the lecithin concentration in buffer solutions containing various NaCl concentrations. (•): 0 M, (△): 1 M, (○): 2 M, (□): 3 M NaCl.

(10), (13) and (21) and are also plotted in figs. 5 and 6.

9. Micellar models

9.1. diC_6-Lecithin

The apparent micellar weight of diC_6- (fig. 5) shows a slight decrease with increasing concentrations, due to nonideality. Applying eq. (11) to these apparent micellar weights then leads immediately to $\langle M \rangle_{w,app,mic.} / \langle M \rangle_{n,app,mic.} < 1$. A further analysis is only possible after correction for nonideality. As a first approximation we assume the micelles to be monodisperse. For the shape of the micelles we use two simple and rather extreme models: (I) a compact sphere, in which the whole lecithin molecules are accomodated, (II) a spherocylinder with a pure hydrocarbon center [51]. The length of the molecule depends to a great extent on the unknown orientation of the polar group (see, e.g., Cadenhead et al. [52] and their references). We will use a length, in the radial direction, of the polar part of 8 to 11 Å. This polar part includes the carboxylic groups and the glycerylphosphorylcholine and has a maximal extended length of about 14 Å, as determined from molecular models.

9.1.1. Model I: Compact sphere

From the measured partial specific volume of the lecithin micelles and the micellar weight (≈ 15 000) a radius of 18 Å is found. This value is quite reasonable in view of the length of the monomer. To calculate the excluded volume of the lecithin species we also have to take the hydratation of the polar groups into account [53], with the help of

$$\bar{v}_{\text{fh}} = \bar{v}_i + \delta, \qquad (24)$$

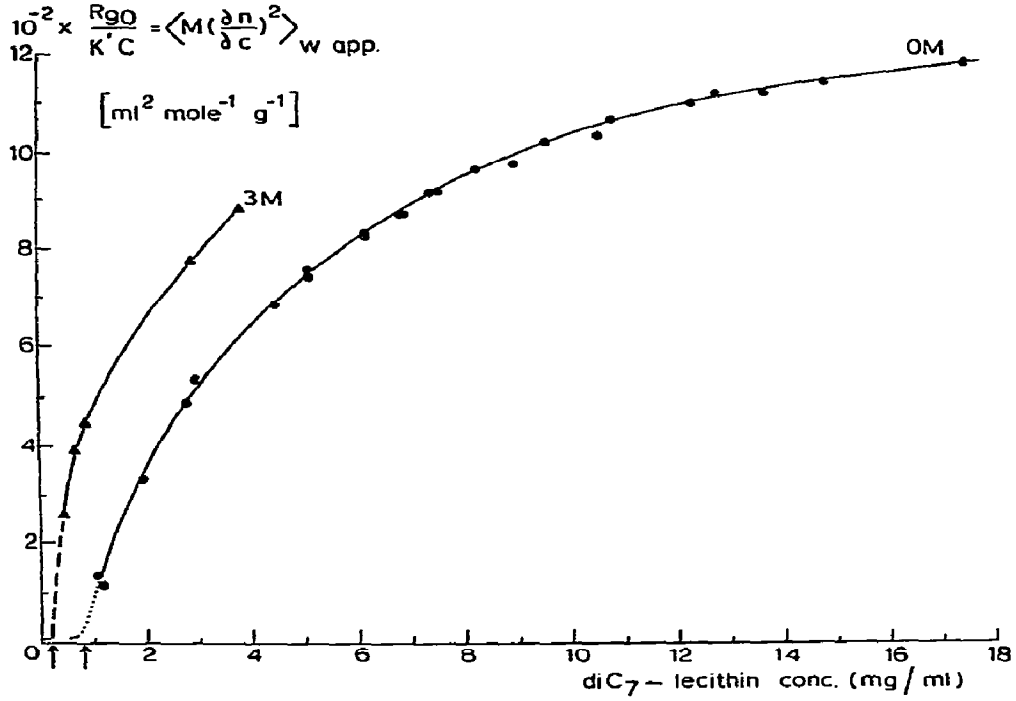

Fig. 10. Reduced apparent total weight average molecular weight of diC_7-lecithin as a function of the lecithin concentration in aqueous buffer solutions containing 0 M (•) and 3 M (▲) NaCl.

where $\bar{v}_{\bar{lh}}$ is the volume per gram hydrated lecithin, $\bar{v}_l$ is the partial specific volume and δ is the hydration in gram water of density 1 per gram lecithin. The literature values of the hydration vary from 7 to 20 water molecules per lecithin molecule, depending on the method used (see, e.g., refs. [54–57] and references quoted therein). A value of 10 water molecules per molecule lecithin seems quite reasonable. The influence of the hydration layer on the calculated values for the ideal micellar weights is small (a few percent at the highest lecithin concentration). Using this model of hydrated spherical monomers and monodisperse micelles the real weight average micellar weights were calculated and plotted in fig. 11.

9.1.2. Model II: Spherocylinders

One can visualise the micelles in an alternative model, where the contact between the hydrocarbon part of the molecules and water and the polar parts is avoided [51]. Using the equations [51] for the hydrocarbon volume v (eq. (25)) and the maximal radius r of the hydrocarbon

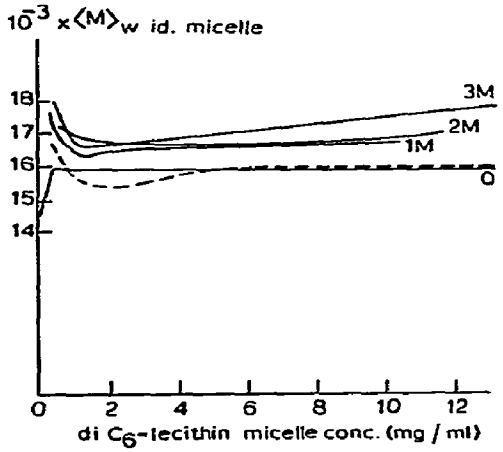

Fig. 11. diC_6-Lecithin ideal micellar weights as a function of the micellar concentrations. The apparent micellar weights are idealised using the compact sphere model (see section 9). The broken line represents ultracentrifugation data, the full lines stem from light scattering.

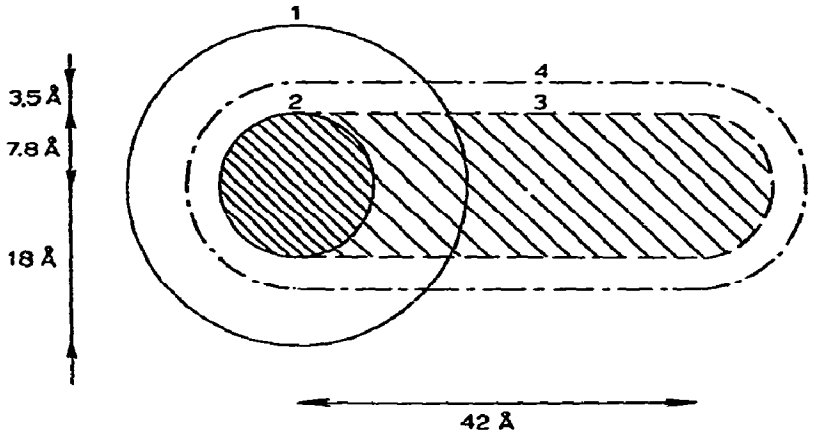

Fig. 12. Section through the diC_6-lecithin micelle model. Circle 1 represents the contour of the compact sphere (radius = 18 Å). Circle 2 is the contour of the hydrocarbon core with radius 7.8 Å and a volume large enough to contain 6.8 monomers. Within the volume surrounded by 3 the hydrocarbon parts of 34 monomers (micellar weights 16 000) can be situated. The volume within 4 is the minimum to contain 34 hydrated lecithin molecules.

core (eq. (26)) one finds that a spherical micelle of diC_6 can accomodate only 6 to 7 monomers.

$$v = 27.4 + 26.9 \times 2 \times n \text{ Å}^3, \quad (25)$$

$$r = 1.5 + 1.265 \times n \text{ Å}, \quad (26)$$

n is the number of carbon atoms per chain participating in the hydrocarbon core (for diC_6: $n = 5$, $v = 296.4$ Å^3, $r = 7.8$ Å). As the micelles however contain about 35 monomers the geometry has to depart from the spherical. For simplicity's sake we introduce the spherocylindrical model. We now have to choose the outer radius R of the spherocylinder. We use two values $R = 15$ Å and $R = 18$ Å. From the molal volume a value for a of 11.2 Å would suffice, but this seems impossible without a great strain on the chemical bonds in the lecithin molecule. The spherocylindrical model is shown in fig. 12 and the calculated ideal micellar weights are shown in figs. 13 and 14.

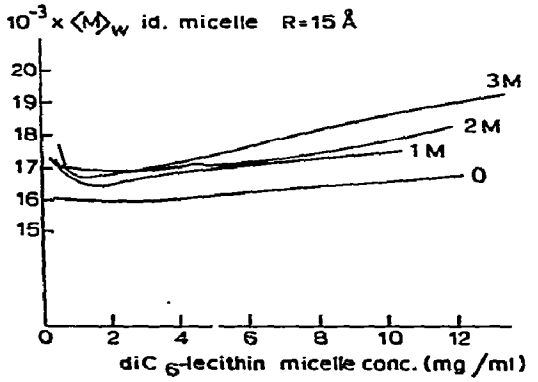

Fig. 13. Weight average micellar weights, from light scattering, as a function of the diC_6-lecithin micellar concentration, in aqueous solutions containing various NaCl concentrations. The micellar weights are corrected for non-ideality using the spherocylinder model (see section 9.1.2) with a radius of 15 A.

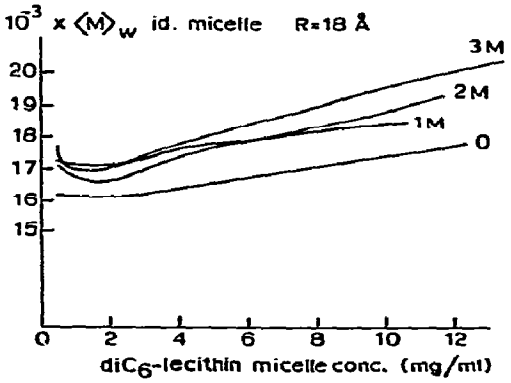

Fig. 14. Same as fig. 13, now for $R = 18$ A.

9.2. diC_7-Lecithin

The apparent micellar weight increases with concentration (fig. 6). This system is clearly polydisperse: $\langle M\rangle_{w.app.mic.}/\langle M\rangle_{n.app.mic.} \approx 1.5$, as calculated with eq. (11). The ratio for the ideal average molecular weights will be higher and we use as a first approximation $\langle M\rangle_{w.id.mic.}/\langle M\rangle_{n.id.mic.} = 2$. This simplifies the Schulz distribution function eq. (18). Again we use two models for estimating the interaction parameter A_{ij}.

9.2.1. Model I

In analogy to the compact sphere of diC_6-lecithin we assume the maximal compact sphere of diC_7-lecithin micelles to have a radius of 19 Å. These micelles can accommodate about 40 monomers ($\langle M\rangle_{w.mic.} \approx 20\,000$). As the micelles grow far beyond this value, we assume the larger micelles to be spherocylinders with radii of 19 Å and different lengths. Again a hydration of 10 water molecules per lecithin molecule is added. We also assume spherical micelles with association numbers between 2 and 40 to be present. This last assumption has a very minor effect on the second virial coefficients. The calculated ideal weight average micellar weights are shown in fig. 15.

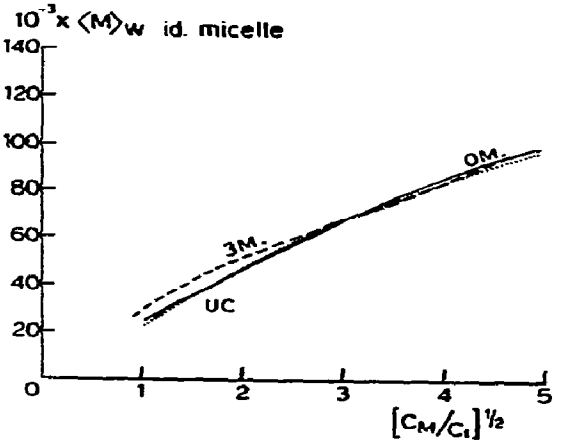

Fig. 16. Ideal weight average micellar weights of diC_7-lecithin as a function of the root of the ratio of micellar and monomer concentration. The molecular weights are idealised using the compact micelle model (see section 9.2.1). The dotted line (····) is derived from ultracentrifugation (only buffer present). The full line (——) and the broken line (– – – –) were obtained from light scattering in 0 M and 3 M NaCl respectively.

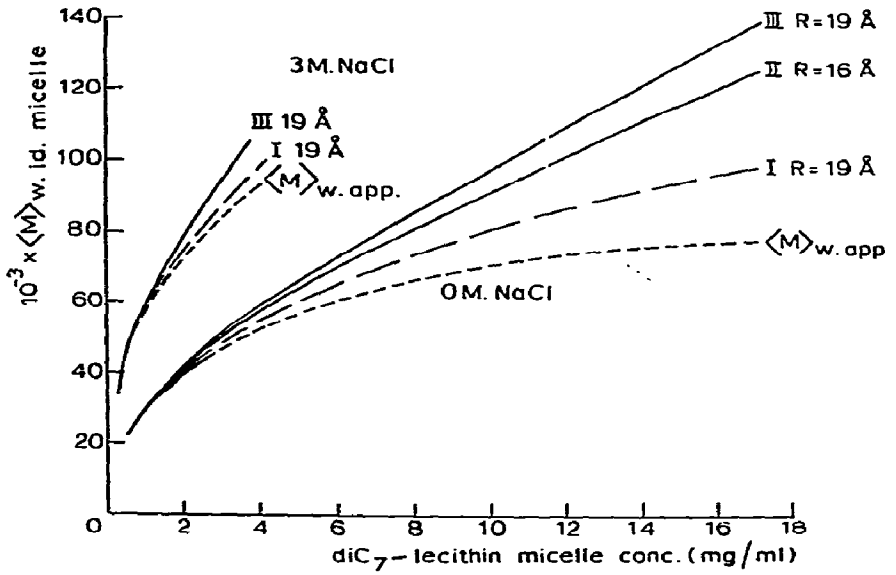

Fig. 15. Weight average micellar weights of diC_7-lecithin as a function of the micellar concentration. In 0 M and 3 M NaCl (upper set of curves). The dotted lines represent the apparent weights. The broken lines I are obtained from the compact micelle model (type I) and the full drawn lines II and III are derived from the spherocylinder model (type II) with radii of 16 Å and 19 Å respectively and with as little hydrocarbon–water contact as possible.

9.2.2. Model II

Avoiding the hydrocarbon–water contact in spherocylinders with hydrocarbon core radii of 9.1 Å leads to much longer micelles and greater second virial coefficients. In analogy to the diC_6-micelle we assume an outer radius of 16 Å and 19 Å. Results for the ideal molecular weights are shown in fig. 16.

10. Discussion

10.1. Micellar weights

In analysing micellar weights the association model is seldom used, partly due to the complication of the slight increase of the monomer concentration at total concentrations above the CMC. Usually micellar weights are evaluated with the assumption of a constant monomer concentration, for example in the so called Debye-plot [58] in light scattering $H(c - \mathrm{CMC})/(\tau - \tau_{\mathrm{CMC}})$ versus $c - \mathrm{CMC}$. This last method does give accurate results at high micellar concentrations in respect to the CMC.

The results of diC_6-lecithin, where the CMC is relatively high, are, however, significantly different when calculated by both methods, as can be seen from table 4. The second virial coefficients given there are calculated from the apparent micellar weights (fig. 5) with the help of the relation

$$\langle M\rangle^{-1}_{\mathrm{w.id.mic.}} = \langle M\rangle^{-1}_{\mathrm{w.app.mic.}} + 2Bc_{\mathrm{mic.}} \qquad (27)$$

Table 4

Micellar weights of dihexanoyllecithin in aqueous solutions containing various NaCl concentrations

NaCl conc. (M)	$\langle M_w(c_{\mathrm{mic.}} \to 0)$ Debye-plot	$\langle M_w(c_{\mathrm{mic.}} \to 0)$ Association model	Virial coeff. $2B \times 10^4$ (mole ml g^{-2}) Association model
0	13200	15400	5.7 ± 0.1
1	14100	16200	5.0 ± 0.2
2	14700	16350	4.7 ± 0.3
3	15500	16300	1.6 ± 0.1

In this equation $\langle M\rangle_{\mathrm{w.id.mic.}}$ equals the micellar weight, linearly extrapolated to micellar concentration zero. In this case the weight average loses its significance, since calculating the virial coefficient in this manner implies a monodisperse system. Analysis from the Debye-plots reveals no significant virial coefficient ($2B < 10^{-5}$ mole ml g^{-2}), because the plots of the turbidities versus the total concentrations are straight lines (fig. 7). This situation is also found in other micellar systems, especially with nonionic or zwitter-ionic surfactants [59–61].

DiC_7-lecithin gives Debye-plots with a negative virial term, which implies a polydisperse system.

It is essential to have a model for calculating the second virial coefficients. In this article we have used the simplest possible model: an excluded volume based on rigid noninteracting particles. The geometric models for the micelles have been discussed in detail in section 9. Our simplified approach does seem to give answers in the right order of magnitude as can be seen from the diC_6-lecithin results (figs. 5, 11, 13, 14) where the decrease in the apparent molecular weight completely disappears upon idealising the molecular weights.

From the graphs we may conclude that the *diC_6-lecithin* micelles have rather narrow weight distributions, at least compared to the diC_7-micelles (to be discussed below). An impression of the width of the distribution can also be obtained from the ratio $Q = \langle M\rangle_{\mathrm{w.id.mic.}}/\langle M\rangle_{\mathrm{n.id.mic.}}$, as has been discussed in section 5. The lowest significant value for Q that can be obtained with our experimental methods is around 1.04. The highest values for Q are obtained for the spherocylinder (model II) with a radius of 18 Å: at a total concentration of 19 mg ml^{-1} (micellar concentration = 12 mg ml^{-1}) we obtain $Q = 1.06$ for the NaCl free solutions and $Q = 1.1$ in the presence of 3 M NaCl.

diC_7-Lecithin micelles are clearly very polydisperse with Q values around 2 (see figs. 6, 15). Using the spherocylinder (model II) with little hydrocarbon–water contact and radii of 16 Å and 19 Å we find at a total concentration of 16 mg ml^{-1} (micellar concentration = 15.2 mg ml^{-1}) $Q = 2.1$ and $Q = 2.0$ respectively. For the more compact and shorter micelles (model I) we find $Q = 1.7$. As pointed out previously (section 5) these wide distributions are obtained if all association constants leading to different types of micelles are about equal. The micellar weight is then proportional to the square root of the micellar concentration. In figs. 16 and 17

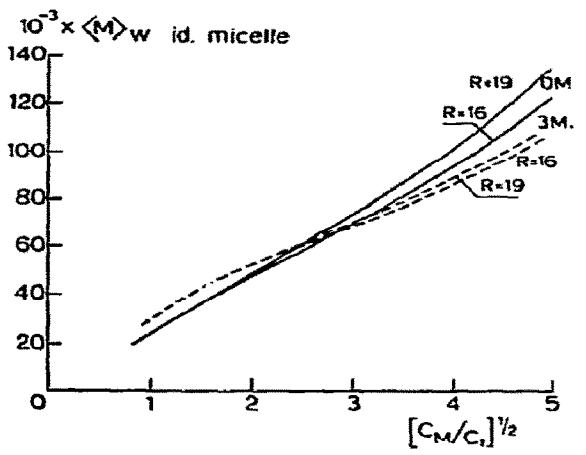

Fig. 17. Idealised weight average micellar weight of diC_7-lecithin from light scattering. The full lines are derived from NaCl free and the broken lines from aqueous solutions containing 3 M NaCl. Two different radii of the spherocylinders (R = 16 Å and R = 19 Å) with as little hydrocarbon–water contact as possible are used (see section 9.2.2).

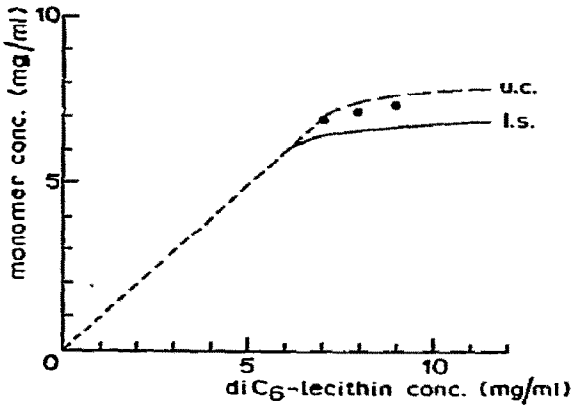

Fig. 18. The monomer concentration of diC_6-lecithin as a function of the total lecithin concentration. The full line is calculated from light scattering, the broken line from ultracentrifugation. The three dots were obtained from surface tension measurements [1].

we have plotted the ideal micellar weights calculated from our different models against $(C_{mic.}/C_{mon.})^{1/2}$.

The results of the experiments performed in 3 M NaCl, where micellar weights increase much more steeply with the micellar concentration than in 0 M NaCl (figs. 13 and 14) are now very close to the data obtained in NaCl free solutions. This could mean that all association constants increase in the same way with increasing salt concentrations, by a kind of salting-out mechanism [1, 62].

10.2. Monomer concentration of diC_6-lecithin

Although the micellar weights obtained from light scattering and ultracentrifugation agree very well with each other the monomer concentrations differ significantly. The calculated results are shown in fig. 18. The CMC obtained from ultracentrifugation is 7.0 mg ml^{-1} and is in fair agreement with the CMC as obtained from surface tension measurements [1] (6.9 mg ml^{-1}). Light scattering gives a CMC of 6.2 mg ml^{-1}. The three points in fig. 18 have been calculated from surface tension measurements [1] by extrapolation of the linear part of the γ versus log c curve below the CMC. To explain the differences between these data several hypotheses can be proposed in connection with the presence of dust in light scattering or decomposition of the lecithin in centrifugation experiments, but no definite opinion can yet be given.

If the monomer concentration as a function of the total concentration is accurately known micellar weights can be estimated. We made some calculations for diC_6-lecithin in 3 M NaCl using the surface tension data [1] and the monodispers micellar model with no thermodynamic nonideality. After curve fitting a micellar weight of 17 000 ± 1 000 was obtained, which is in remarkable agreement with the light scattering data.

11. Conclusion

The association of dihexanoyllecithin leads to the formation of micelles with an apparent measured micellar weight of about 15 000 to 14 000 in solutions of low electrolyte content (fig. 5). The slight decrease of these values with increasing lipid concentration completely disappears after introduction of a thermodynamic nonideality correction based on the excluded volume of the lecithin. The micellar weights corrected for this effect range from 16 000 to 17 500 (figs. 11, 13 and 14). A rather narrow size distribution is observed. The results are rather insensitive to the details in the numerical assumptions involved in the analysis. Roholt and

Schlamowits [63] obtained a somewhat larger micellar weight.

Diheptanoyllecithin, however, associates into much larger aggregates with wide weight distributions. The apparent micellar weights range from 20 000 to 80 000 (fig. 6). The influences of the assumptions, concerning the geometric model of the micelles, on the nonideality correction are much greater than in the case of the shorter homologue (figs. 15, 17). Smink [64] reported a micellar weight of 30 000. He, however, gives no further details and we presume that he calculated this molecular weight after extrapolation to infinite dilution.

Addition of NaCl to the dihexanoyl compound has only a very limited effect on the micellar weight (fig. 5). It therefore seems fair to conclude that the electrostatic zwitterionic dipole interactions are of minor importance to the lecithin micellar size in a monodisperse system. The large increase in the association number of the higher homologue on addition of NaCl (fig. 15) is expected if all association constants from this multiple equilibrium system are increased, for instance by a salting out mechanism, which also explains the strong decrease of the CMC.

Acknowledgements

The authors are indebted to Mr. L.W. Ketellapper for the many helpful suggestions and discussions and to Miss J.C. Hopman for her skilful assistance in the ultracentrifugation experiments. We would also like to thank Mr. A.A. Caljé for his useful contribution with vapor pressure osmometry. The authors are indebted to Dr. H.A.M.G. Vaessen of the National Institute of Public Health, Laboratory for Chemical Analysis of Foodstuffs, Bilthoven, and to Miss T.A. Schippers of the Pharmaceutical Laboratories, Utrecht, for their Karl Fischer titrations on tungstosilicic acid.

References

[1] R.J.M. Tausk, J. Karmiggelt, C. Oudshoorn and J.Th.G. Overbeek, Biophys. Chem. 1 (1974) 175.
[2] H.G. de Haas, P.P.M. Bonsen, W.A. Pieterson and L.L.M. van Deenen, Biochim. Biophys. Acta 239 (1971) 252.
[3] K.E. van Holde, Fractions 1 (1967), Beckman Instruments Inc.
[4] J.A. Brinkhuis, H.J. Vreeman and L.W. Ketellapper, J. Electroanal. Chem. 37 (1972) 343.
[5] H.F. Huisman, Koninkl. Ned. Akad. Wetensch. Proc. Ser. B 67 (1964) 367.
[6] O. Kratky, H. Leopold and H. Stabinger, Z. Angew. Physik 27 (1969) 273.
[7] L.J. Gostings, J. Am. Chem. Soc. 72 (1950) 4418.
[8] H. Yamakawa, Modern theory of polymer solutions, Harper & Row, New York, 1971 ch. 5.
[9] W.H. Stockmayer, J. Chem. Phys. 18 (1950) 58.
[10] T.L. Hill, Statistical mechanics (McGraw-Hill, New York, 1956).
[11] T.L. Hill, J. Chem. Phys. 30 (1959) 93.
[12] E.F. Cassasa and H. Eisenberg, Advan. Protein Chem. 19 (1964) 287.
[13] H. Fujita, Mathematical theory of sedimentation analysis, eds. E. Hutchinson and P. van Rysselberghe (Academic Press, New York, 1962).
[14] E.T. Adams and J.W. Williams, J. Am. Chem. Soc. 86 (1964) 3454.
[15] E.T. Adams and D.L. Filmer, Biochemistry 5 (1966) 2971.
[16] J.M. Corkill, J.F. Goodman, T. Walker and J. Wyer, Proc. Roy. Soc. A 312 (1969) 243.
[17] J.M. Corkill and J.F. Goodman, Advan. Coll. Interf. Sci. 2 (1969) 297.
[18] P. Mukerjee, J. Phys. Chem. 76 (1972) 565.
[19] B.H. Zimm, J. Chem. Phys. 14 (1946) 164.
[20] C. Tanford, Physical chemistry of macromolecules (Wiley, New York, 1965) p. 196.
[21] H. Reerink, J. Colloid. Sci. 20 (1965) 217.
[22] H.G. Elias, R. Bareiss and J.G. Watterson, Advan. Polymer Sci. 11 (1973) 111.
[23] G. Herdan, Nature 163 (1949) 139.
[24] J.G. Watterson and H.G. Elias, Kolloid Z.Z. Polym. 249 (1971) 1136.
[25] J.M. Corkill, K.W. Gemmel, J.F. Goodman and T. Walker, Trans. Faraday Soc. 66 (1970) 1274.
[26] G.V. Schulz, Z. Phys. Chem. B 47 (1940) 155.
[27] A. Isihara, J. Chem. Phys. 18 (1950) 1446.
[28] A. Isihara, J. Chem. Phys. 19 (1951) 397.
[29] A. Isihara, J. Phys. Soc. Japan 6 (1951) 40.
[30] A. Isihara, J. Phys. Soc. Japan 6 (1951) 46.
[31] T. Kihara, J. Phys. Soc. Japan 8 (1953) 686.
[32] G.J. Howlett, P.D. Jeffrey and L.W. Nichol, J. Phys. Chem. 76 (1972) 777.
[33] W. Heller, Rec. Chem. Progr. 20 (1959) 209.
[34] J.M. Corkill, J.F. Goodman and T. Walker, Trans. Faraday Soc. 63 (1967) 768.
[35] F.C. Reman, Thesis, Utrecht (1971).
[36] T. Gulik–Krzywicki, E. Rivas and V. Luzzati, J. Mol. Biol. 27 (1967) 303.
[37] V. Luzzati, T. Gulik–Krzywicki and A. Tardieu, Nature 218 (1968) 1031.
[38] M.R. Bruzzesi, E. Chiancone and E. Antonini, Biochemistry 4 (1965) 1796.
[39] R.C. Deonier and J.W. Williams, Biochemistry 9 (1970) 4260.
[40] R.E. Canfield, J. Biol. Chem. 238 (1963) 2698.
[41] J. Visser, R.C. Deonier, E.T. Adams and J.W. Williams, Biochemistry 11 (1972) 2634.

[42] M. Halwer, G.C. Nutting and B.A. Brice, J. Am. Chem. Soc. 73 (1951) 2786.
[43] J.P. Kratohvil, L.E. Oppenheimer and M. Kerker, J. Phys. Chem. 70 (1966) 2834.
[44] S.H. Maron and R.L.H. Lou, J. Phys. Chem. 59 (1955) 231.
[45] P.F. Mijnlieff, H. Zeldenrust, J. Phys. Chem. 69 (1965) 689.
[46] J.J. Hermans and S. Levineson, J. Opt. Soc. Am. 41 (1951) 460.
[47] D.J. Coumou, J. Colloid. Sci. 15 (1960) 408.
[48] E. Ahad and B.R. Jennings, J. Phys. D3 (1970) 1509.
[49] H.J. Cantow, J.U.P.C., Intern Symp. Macromol. Chem. p. 504, Milano, Torino (1954).
[50] L.W. Ketellapper, to be published.
[51] C. Tanford, J. Phys. Chem. 76 (1972) 3020.
[52] D.A. Cadenhead, R.J. Damchak and M.C. Phillips, Kolloid Z.Z. Polym. 220 (1967) 59.
[53] C. Tanford, Physical chemistry of macromolecules (Wiley, New York, 1965) p. 339.
[54] D.M. Small, J. Lipid Res. 8 (1967) 551.
[55] W.V. Walten and R.G. Hayes, Biochim Biophys. Acta 249 (1971) 528.
[56] C. Horwitz, L. Krut and L.S. Kaminsky, Chem. Phys. Lipids 8 (1972) 185.
[57] J.L. Rigaud, Y. Lange, C.M. Carry–Bobo, A. Samson and M. Ptak, Biochem. Biophys. Res. Commun. 50 (1973) 59.
[58] P. Debye, Ann. N.Y. Acad. Sci. 51 (1949) 575.
[59] K.W. Herrmann, J. Coll. Interf. Sci. 22 (1966) 352.
[60] J.B. Daruwala, Thesis, Connecticut (1969).
[61] J. Swarbrick and J.B. Daruwala, J. Phys. Chem. 74 (1970) 1293.
[62] P. Mukerjee, J. Phys. Chem. 69 (1965) 4038.
[63] O.A. Roholt and M. Schlamowitz, Arch. Biochem. Biophys. 94 (1961) 364.
[64] D.A. Smink, Thesis, Leiden (1969).

BIOPHYSICAL CHEMISTRY 1 (1974) 204–213. © NORTH-HOLLAND PUBLISHING COMPANY

GROWTH RATES OF YEAST COLONIES ON SOLID MEDIA

B.F. GRAY and N.A. KIRWAN*
School of Chemistry, University of Leeds, Leeds LS2 9JT, UK

Received 8 October 1973

Previous measurements of growth rates of giant yeast colonies on solid media are shown to be unreliable as they depend strongly on extraneous factors such as the proximity of other colonies and the dimensions of the apparatus used. The hitherto unexplained dependence of the growth rate on the square root of the growth limiting nutrient concentration is explained by constructing a theory based on the diffusion of nutrient towards the colony which makes use of many ideas used in the theory of flame propagation. The theory also explains why the temperature dependence of the homogeneous growth constant is different from that observed in the surface colony, and it requires the existence of a lag phase in the homogeneous culture kinetics if the velocity of propagation of the culture is to be independent of inoculum size and shape. Both phenomena are known to occur.

1. Introduction

The growth of bacteria, moulds and yeasts in colonies on the surface of solid nutrient media is an experimental technique which has been in common use for many years, but it is not until recently that any quantitative studies have been made on the process [1, 2]. It has been found experimentally [2] that after a brief initial period of exponential growth rate, a phase is entered in which the radius of the colony is a linear function of the time of incubation. Later the so-called "radial law" gives way to a slower phase in which the area of the colony increases linearly with time. Previous workers [1, 2] have made growth rate measurements on several colonies growing together in a single 9 cm diameter Petri dish. The significance of boundary effects (i.e., the size of the dish and the proximity of neighbouring colonies) does not appear to have been realized and investigated. Experiments have therefore been carried out to examine the effect of the size of the dish used for the culture of single colony at the centre of the dish on the growth rate of that colony.

A theory has been developed to describe the growth of a single colony on the surface of a solid nutrient medium, which takes account of the diffusion of nutrients through the medium. This theory is in many ways analogous to the theory of one dimensional flame propagation [3, 4]. Laminar flame theory shows how, if an ignition is initiated at some point in a large body of gas, the disturbance will propagate, as a result of the conduction of heat, or diffusion of radicals, as a wave satisfying highly non-linear equations. These non-linear equations arise as a result of the coupling of transport processes and positive feedback from the products of the reaction. Similar non-linear waves have been studied in biological systems, a classic example being the study of the propagation of a dominant gene through a given population, according to a non-linear diffusion equation [5]. Another example is the Hodgkin–Huxley theory of nerve transmission [6], where many concepts formally similar to flame theories are discussed, for example, excitation threshold (parallel to flame extinction limits), hysteresis and so on. In fact, many concepts responsible for a great clarification of the phenomenological basis of nerve transmission have obvious parallels in combustion. A more recent example is the observation and theory of travelling waves in bacteriology [7]. Bands of motile bacteria placed at one end of a capillary tube containing oxygen and a source of energy have been observed to travel along the tube at constant velocity. The phenomenon of chemotaxis (the ability to move towards or away from a particular chemical) is used to explain the experimental facts, and again a threshold is appar-

* Department of Chemical Pathology.

ent. The theory developed again shows many similarities to flame theory.

2. Apparatus

Colonies were grown on the surface of nutrient agar in circular dishes of diameter 5, 9, 12.5 and 21 cm. The dishes did not have optically clear lids, and so it was necessary to remove the lids to make measurements of the colony diameters. Therefore, in order to prevent contamination of the cultures by airborne bacteria during measurement, the dishes were contained throughout the experiment in a polythene "dry bag", supplied by Townson and Mercer. This was a polythene bag of size approximately 85 by 70 cm which was fitted with a pair of rubber gloves to enable operations to be carried out inside the bag, and a gas inlet tube for inflation. The mouth of the bag was sealed by folding over several times and securing with clips. A 7 by 5 cm section of the bag was removed and replaced by a glass window to enable measurements of colony diameters to be made from outside the bag, using a travelling microscope. The bag was kept inflated by filtered compressed air from a cylinder. The air was filtered through a grade HP/EKS asbestos bacteriological filter pad (Griffin S25-812).

3. Materials and methods

The nutrient medium was quite orthodox, containing D-glucose, disodium hydrogen orthophosphate, ammonium sulphate, yeast energiser and agar. Nine tubes of prepared medium (each containing 35 ml) were warmed to melt the agar, and placed in the bag. Also into the bag were put the four sterilised growth dishes, a Petri dish containing a 13 day old yeast culture, sterile measuring cylinders of 10, 25, and 100 ml capacity and a sterile platinum needle. The mouth of the bag was then sealed and the bag inflated with sterile air. The following operations were then carried out inside the bag. Volumes of nutrient agar of 10.8, 35.0, 67.4, and 190.5 ml. were measured and put into the 5, 9, 12.5, and 21 cm dishes respectively, giving an agar thickness of 0.137 cm in each dish. The plates were left to dry for a period of 24 hours. The plates were inoculated at their centres, using the platinum needle, with yeast from the periphery of the two week old colony. Measurements of the diameters of the colonies were taken from the outside of the bag using a travelling microscope. The mean of two diameters at right angles was taken in each case. The experiments were carried out in a room which was thermostatted at a temperature of 23.0 ± 0.5°C.

4. Experimental results

Several runs were carried out under the above conditions. It was found that the inoculation technique was not exactly reproducible, in that there was some variation in the amount of yeast transferred to the agar plate by the platinum needle. This was reflected in the range of diameters measured 18 hours after inoculation of from 0.51 to 0.84 mm, in different runs. The results presented in table 1 and in fig. 1 are taken from three separate runs, selected so that the diameters of the colonies in the different dishes, measured 18 hours

Table 1

Time (days)	Mean colony diameter (mm)			
	a	b	c	d
0.75	0.61	0.60	0.61	0.60
1.00	0.69	0.69	0.69	0.69
1.75	1.21	1.24	1.25	1.25
2.00	1.50	1.51	1.50	1.50
2.75	1.94	1.98	2.04	2.07
3.00	2.20	2.21	2.24	2.26
3.75	2.74	2.80	2.81	2.88
5.75	3.69	3.90	4.08	4.24
6.00	3.81	4.08	4.27	4.48
7.00	4.18	4.56	4.80	5.09
7.75	4.40	4.90	5.16	5.51
9.00	4.78	5.39	5.69	6.18
9.75	4.97	5.68	6.08	6.60
12.75	5.65	6.56	7.06	8.00
15.00	6.02	7.21	7.74	8.94
16.00	6.17	7.45	8.12	9.33
17.00	6.34	7.72	8.39	9.78
20.00	6.64	8.46	9.14	10.89

a) Colony in 5 cm diameter dish.
b) Colony in 9 cm diameter dish.
c) Colony in 12.5 cm diameter dish.
d) Colony in 21 cm diameter dish.

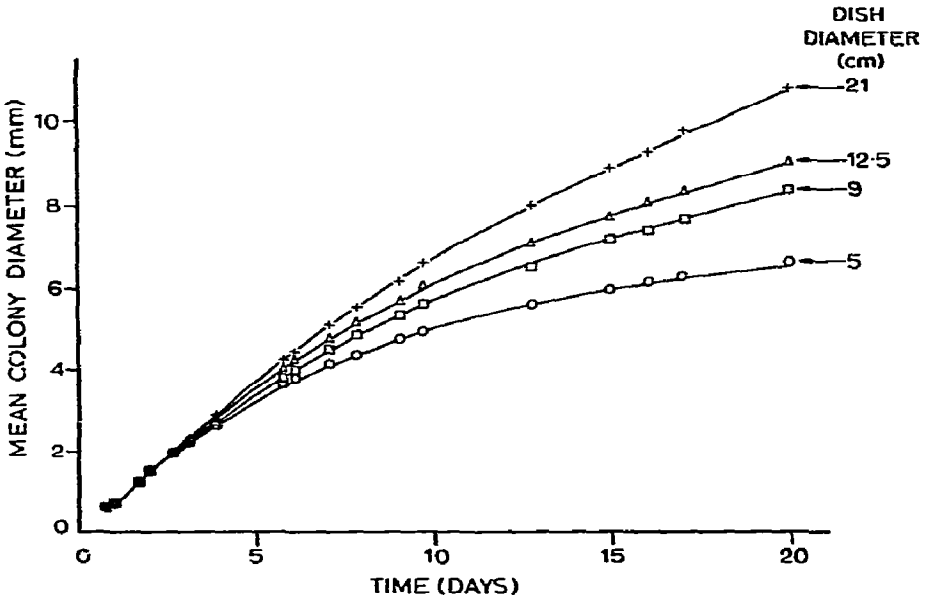

Fig. 1. Radial growth curves for yeast colonies grown in dishes of different diameters.

after inoculation, were as close together as possible. Table 2 and fig. 2 show the reproducibility of growth rates measured in dishes of the same diameter, when the 18 hour colony diameters are similar (columns a and b of table 2), and also the variation brought about by differing inoculum sizes, as reflected by the different 18 hour diameter measurements. The rate of colony growth does not appear to be affected by differences in inoculum size, as shown by the parallel growth curves in fig. 2.

Table 2

Time	Mean colony diameter (mm)			
(days)	a	b	c	d
0.75	0.61	0.60	0.51	0.84
1.00	0.69	0.69	0.60	0.95
1.75	1.23	1.24	1.15	1.56
2.00	1.52	1.51	1.36	1.75
2.75	1.99	1.98	1.84	2.33
3.00	2.23	2.21	2.06	2.48
3.75	2.80	2.80	2.56	3.03
5.75	3.93	3.90	3.75	4.23
6.00	4.11	4.08	3.88	4.28
7.00	4.59	4.56	4.37	4.82
7.75	4.94	4.90	4.68	5.17
9.00	5.42	5.39	5.16	5.62
9.75	5.72	5.68	5.39	5.94

a, b, c and d are all colonies grown in 9 cm diameter dishes. Column b corresponds to column b of table 1.

In fig. 3 the colony area is plotted against time for growth of colonies in dishes of different diameters, using the data of table 1. The previously observed transition form radial to area growth law [2] can clearly be seen to be dependent upon the size of the dish in which the colony is grown. It is perhaps significant that the so called area growth rate law is observed most markedly in the 9 cm dish, the size of Petri dish most commonly used by other workers. It would appear that the area growth rate law is an artefact produced by limitations on the colony growth due to depletion of nutrients in the medium, which is most apparent in the 9 cm diameter dish. Fig. 3 shows that the area of the colony in the 21 cm dish increases more rapidly with time, and that of the colony in the 5 cm. dish less rapidly with time, than the linear case of the colony in the 9 cm dish.

The period over which the radial growth rate law holds is longer, the larger the diameter of the dish. It would be interesting to perform an experiment in which the concentrations of nutrients at the boundary

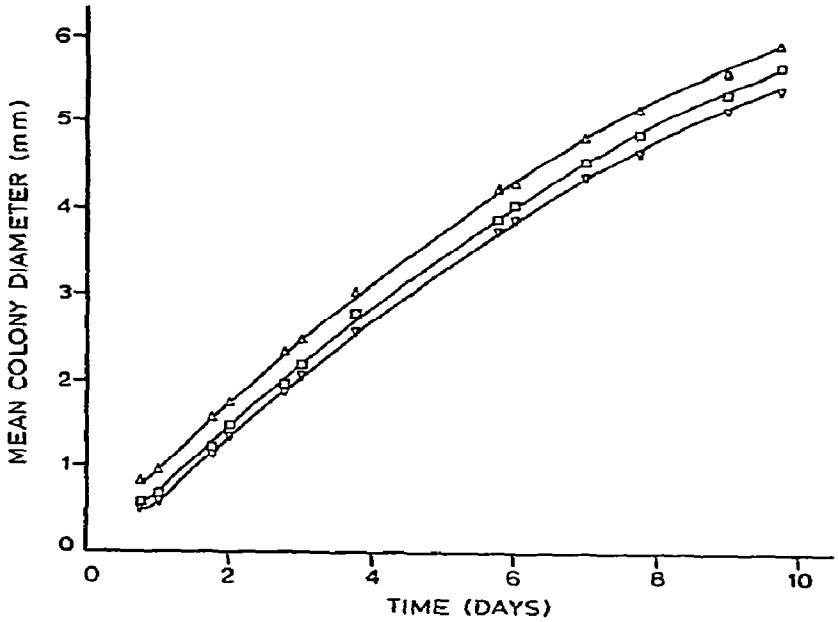

Fig. 2. Radial growth rates for yeast colonies grown in 9 cm diameter dishes.

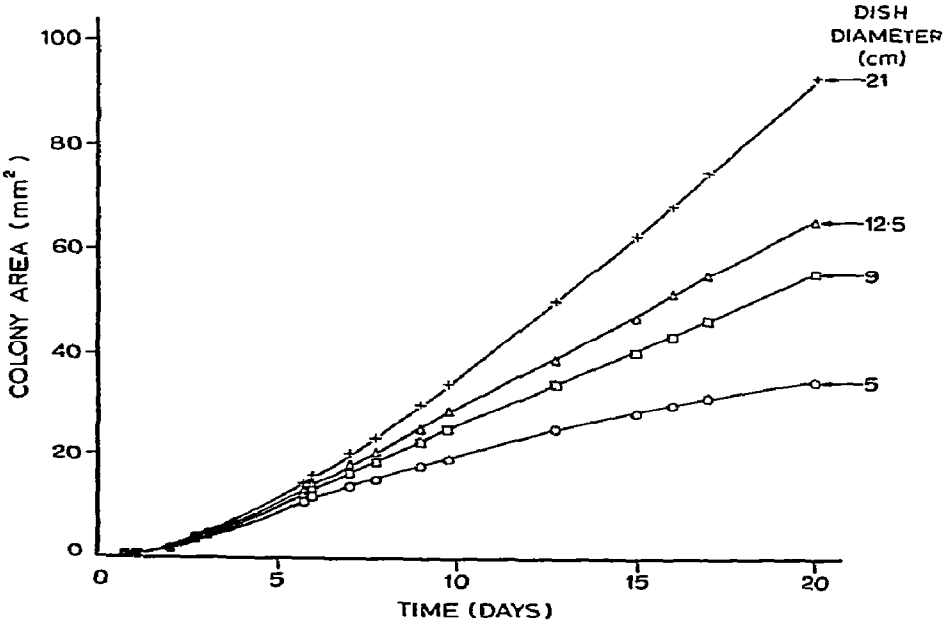

Fig. 3. Area growth curves for yeast colonies grown in dishes of different diameters.

of a large dish were held constant by some means (i.e., using the equivalent of a dish of infinite diameter), and to see whether this would produce a true radial growth rate law. There are theoretical grounds for supposing that for a colony grown in a dish of infinite diameter the radial growth rate law would hold, as explained in the next section.

5 Theory

In liquid culture, if all nutrients are present in excess, bacterial growth rate is described by the equation [8]

$$dn/dt = kn, \tag{1}$$

where n is the number of cells present at time t, and k is the specific growth rate constant. Integration of this equation gives

$$\ln n = kt + \ln n_0, \tag{2}$$

where n_0 is the number of cells at zero time. In solid culture, if the flow of nutrients into the colony were unrestricted, the growth rate of the colony should conform to eq. (1). If the colony grew as a disc of radius r and constant height h, then

$$n = \pi r^2 h\rho, \tag{3}$$

where ρ is the density of the colony, expressed in cells per unit volume, and it is easily shown that

$$\ln r = 0.5\ kt + \ln r_0 \tag{4}$$

where r_0 is the radius at zero time. The radius should therefore increase exponentially with time. This is in fact observed in the initial stages of growth (for approximately $r < 0.1$ mm.).

During the phase of constant radial growth, the radius r, of the colony at time t, is described by the equation

$$r = Kt + r_0, \tag{5}$$

where K is the radial growth rate constant. The constant, K, has been found experimentally [1] to be related to other parameters by the equation

$$K = k'(\sqrt{g_0} - \sqrt{g_1})\sqrt{k}, \tag{6}$$

where g_0 is the initial concentration of glucose in the medium, g_1 is the minimum glucose concentration required for growth, and is known as the lag concentration, k is the specific growth rate constant in liquid culture and k' is a constant of proportionality.

Previous attempts to develop a mathematical model for the growth of surface colonies run as follows [1]. Growth in the circular colony is assumed to be restricted to an annulus of width a. The growth law of eq. (1) then becomes

$$dn/dt = kn_g \tag{7}$$

where n_g is the number of cells in the growing zone. If $a \ll r$ then we have

$$n \simeq \pi r^2 h\rho, \tag{8}$$

and

$$n_g \simeq 2\pi r^2 \Delta\rho. \tag{9}$$

If Δ approximates to a triangle of area $0.5\ ah$, then the result is obtained that

$$r = 0.5\ akt + r_0. \tag{10}$$

Hence the observed rate constant K from eq. (5) is given by

$$K = 0.5\ ak. \tag{11}$$

This is obviously not in agreement with the experimental observations described in eq. (6).

The faults in this theory lie in the fact that diffusion of nutrients through the medium is not considered. Growth is in fact assumed not to be limited by diffusion. An improved theory should consider the diffusion processes.

We consider the one dimensional propagation of a colony along the x axis from right to left, the plane front of the colony moving with velocity G. We assume a rate law for the consumption of glucose

(fuel) to be of the form

$$-\mathrm{d}g/\mathrm{d}t = kn(g - g_l), \tag{12}$$

where g is the glucose concentration at time t, g_l is the lag concentration required for growth), k is the homogeneous specific growth rate constant and n is the number of cells.

The diffusion equations for this system are analogous to the equations describing the thermal propagation of a flame with Lewis number infinity [9]. The equations are, for glucose

$$D\,\mathrm{d}^2g/\mathrm{d}x^2 - G\,\mathrm{d}g/\mathrm{d}x - kn(g - g_l) = 0, \tag{13}$$

and for cells, assuming that the cells are non-motile

$$-G\,\mathrm{d}n/\mathrm{d}x + ckn(g - g_l) = 0, \tag{14}$$

where D is the diffusion coefficient of glucose through the medium and c is a conversion factor, the number of cells produced per unit mass of glucose consumed.

We now define a dimensionless glucose concentration, γ, by

$$\gamma = (g - g_l)/(g_{-\infty} - g_l), \tag{15}$$

where $g_{-\infty}$ is the glucose concentration at $x = -\infty$ and g_l is the glucose concentration at $x = +\infty$ (assumed to be equal to the lag concentration). From eq. (15) it can be seen that $\gamma = 1$ at $x = -\infty$ and $\gamma = 0$ at $x = +\infty$.

Expressing cell concentration in the same units as glucose concentration by putting $y = n/c$, we define a dimensionless cell concentration, σ, by

$$\sigma = (y - y_{-\infty})/(y_\infty - y_{-\infty}) = y/y_\infty, \tag{16}$$

since $y_{-\infty}$, the cell concentration at $x = -\infty$, is zero. We thus have $\sigma = 0$ at $x = -\infty$ and $\sigma = 1$ at $x = +\infty$.

The dimensionless concentrations are now as represented in fig. 3a. Substituting the dimensionless concentration parameters in the diffusion eqs. (13) and (14), we obtain

$$D\,\mathrm{d}^2\gamma/\mathrm{d}x^2 - G\,\mathrm{d}\gamma/\mathrm{d}x - cky_\infty\gamma\sigma = 0, \tag{17}$$

and

$$-G\,\mathrm{d}\sigma/\mathrm{d}x + ck\sigma(g - g_l) = 0. \tag{18}$$

From consideration of the conservation of mass within the system, we have

$$g_l + y_\infty = g_{-\infty} + y_{-\infty} = g_{-\infty}\,. \tag{19}$$

Hence

$$y_\infty = g_{-\infty} - g_l\,. \tag{20}$$

We can now write eqs. (17) and (18) as

$$\mathrm{d}^2\gamma/\mathrm{d}x^2 - (G/D)\,\mathrm{d}\gamma/\mathrm{d}x - (ck/D)(g_{-\infty} - g_l)\gamma\sigma = 0, \tag{21}$$

and

$$-(G/D)\,\mathrm{d}\sigma/\mathrm{d}x + (ck/D)(g_{-\infty} - g_l)\gamma\sigma = 0. \tag{22}$$

We now introduce the dimensionless distance pa-

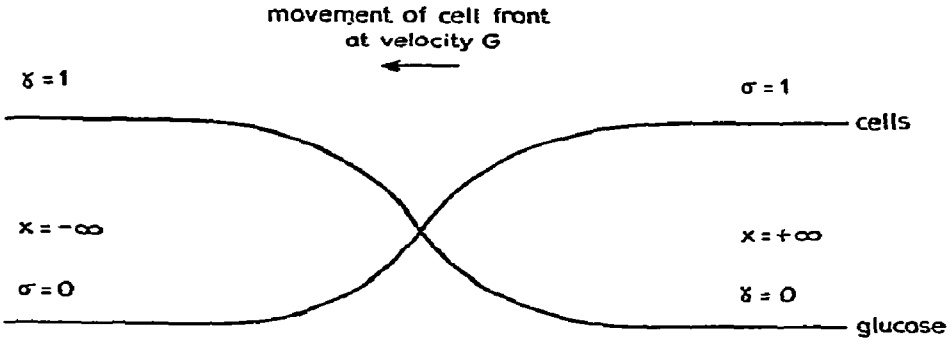

Fig. 3a. Geometrical arrangement of one-dimensional theoretical model.

ameter, $z = x/l$, where

$$l^{-2} = (ck/D)(g_{-\infty} - g_1), \tag{23}$$

transforming eqs. (21) and (22) into

$$d^2\gamma/dz^2 - (Gl/D)\, d\gamma/dz - \gamma\sigma = 0, \tag{24}$$

and

$$-(Gl/D)\, d\sigma/dz + \gamma\sigma = 0. \tag{25}$$

If we introduce the dimensionless velocity, $\mu = Gl/D$, we have the two diffusion equations in the completely dimensionless forms:

$$d^2\gamma/dz^2 - \mu\, d\gamma/dz - \gamma\sigma = 0, \tag{26}$$

and

$$-\mu\, d\sigma/dz + \gamma\sigma = 0. \tag{27}$$

The problem now is to determine whether this pair of equations has an eigenvalue solution in μ, i.e., whether there is a unique value or a set of discrete values of μ for which the pair of equations has a solution.

We integrate eqs. (26) and (27) from $-\infty$ to z, using the boundary conditions $\gamma = 1$ and $\sigma = 0$ at $z = -\infty$, to give

$$d\gamma/dz - \mu(\gamma - 1) - \int_{-\infty}^{z} \gamma\sigma\, dz = 0, \tag{28}$$

and

$$-\mu\sigma + \int_{-\infty}^{z} \gamma\sigma\, dz = 0. \tag{29}$$

Adding eqs. (28) and (29) to eliminate the integral, we obtain

$$d\gamma/dz - \mu(\gamma + \sigma - 1) = 0, \tag{30}$$

and using eq. (27) gives us

$$d\gamma/d\sigma = \mu^2(\gamma + \sigma - 1)/\gamma\sigma, \tag{31}$$

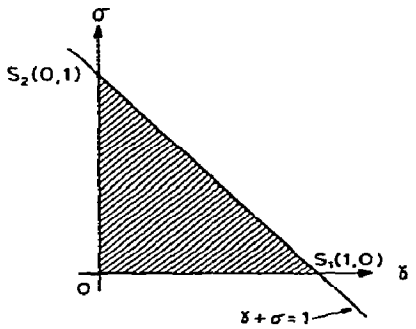

Fig. 4. The (γ, σ) phase plane for eq. (31). Physical solutions must lie within the shaded area.

which can be studied conveniently in the (γ, σ) phase plane.

The behaviour of the solutions of eq. (31) can be mapped out by using Liopounoff's stability theorem [10] to investigate the nature of the singularities of the equation. Any solution must pass through the points $\gamma = 1$, $\sigma = 0$ (the initial point, at $z = -\infty$), and $\gamma = 0$, $\sigma = 1$ (final point, at $z = +\infty$). These are the only two singularities. In the phase plane a physically acceptable solution must link these two singularities and also remain in the positive quadrant, bounded by the γ and σ axes, and the lines $\gamma = 1$ and $\sigma = 1$. In addition, from eq. (30) and the fact that γ is a monotonically decreasing function of z (i.e., $d\gamma/dz < 0$), the solutions must also satisfy the condition

$$\gamma + \sigma - 1 < 0. \tag{32}$$

Such solutions are therefore restricted to the shaded area of fig. 4.

The nature of the singularities is determined by the solutions of the characteristic equation

$$\begin{pmatrix} A - \lambda & B \\ C & D - \lambda \end{pmatrix} = 0, \tag{33}$$

where

$$A = \partial[\mu^2(\gamma + \sigma - 1)]/\partial\gamma = \mu^2, \tag{34}$$

$$B = \partial[\mu^2(\gamma + \sigma - 1)]/\partial\sigma = \mu^2, \tag{35}$$

$$C = \partial[\gamma\sigma]/\partial\gamma = \sigma, \tag{36}$$

$$D = \partial[\gamma\sigma]/\partial\sigma = \gamma, \tag{37}$$

evaluated at the singular point. If one root of the characteristic equation is positive, then the singularity will be unstable, i.e., a perturbation away from the equilibrium position will tend to increase with time. If the second root is also positive, then the singularity will be an unstable nodal point, i.e., an infinite number of integral curves leave the singularity. If the second root is negative, then the singularity is a saddle point and has only two integral curves entering and two leaving the point [10].

For the initial point ($\gamma = 1$, $\sigma = 0$), the characteristic equation is

$$\lambda^2 - (\mu^2 + 1)\lambda + \mu^2 = 0, \tag{38}$$

which has roots $\lambda = 1$ and $\lambda = \mu^2$. The initial point is therefore an unstable nodal point.

For the final point ($\gamma = 0$, $\sigma = 1$), the characteristic equation is

$$\lambda^2 - \mu^2\lambda - \mu^2 = 0, \tag{39}$$

which has roots $\lambda = \mu^2$ and $\lambda = -1$. This point is therefore a saddle point.

The situation in the (γ, σ) phase plane is therefore as shown in fig. 5. For a given value of μ there will always be one integral curve from the infinite set of curves leaving the initial singularity which enters the final singularity. This will be true for any value of μ. In this situation therefore the system does not have an eigenvalue solution. This means that any value of μ will satisfy the equations describing the system. In physical terms, the implication is that the system would be extremely sensitive to the initial conditions, and any variation in, for example, the profile of the inoculum, would result in different values of the observed growth velocity. This is obviously not the case, as measurements of growth velocity are reproducible, even for colonies grown from inoculi of different sizes, and so it would appear necessary to impose some additional restriction on the growth equations in order to obtain an eigenvalue solution.

It has been shown by Johnson*, in the consideration of the mathematically analogous one dimensional flame propagation equations, that if the rate function, $\phi(\gamma, \sigma)$, for the consumption of glucose or the generation of cells in this case, is such that $\phi(\gamma, \sigma)$ becomes zero in some finite neighbourhood of the initial singularity ($\gamma = 1$, $\sigma = 0$), then a system of this type will have a unique eigenvalue solution. With this restriction, the initial singularity becomes a degenerate type of saddle-node, with only one integral curve leaving the singular point into the positive quadrant. For general values of the dimensionless growth velocity μ, the phase plane diagram will take the form of fig. 6(a) or fig. 6(b). For one particular value of μ, there will be an integral curve which joins the initial and final singularities, as shown in fig. 7. This curve gives the eigenvalue solution of the problem. The condition that $\phi(\gamma, \sigma)$ becomes zero in some finite neighbourhood of the initial singularity is easily satisfied by consideration of the lag phase of bacterial growth. The lag phase is the period of time immediately following inoculation during which no growth occurs [8], i.e., $\phi(\gamma, \sigma) = 0$. After the lag phase, growth proceeds according to the rate law given in eq. (12).

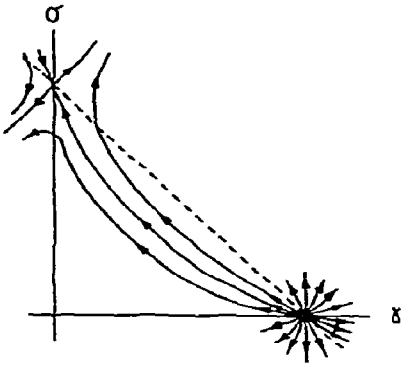

Fig. 5. Integral curves in the (γ, σ) phase plane for solutions of eq. (31). Arrows indicate motion in time.

Having shown that an eigenvalue solution exists for this system, we can now examine the relationship between the eigenvalue dimensionless velocity, μ, and the real velocity, G. From the definition of μ ($\mu = Gl/D$), and eq. (23), we obtain

* See ref. [9], p. 109.

$$G = \mu\sqrt{kcD(g_{-\infty} - g_1)} \,. \tag{40}$$

This equation may now be compared with the experimental observations [1] given by eq. (6). The growth velocity, G, is equivalent to the radial growth rate constant, K. The glucose concentration, $g_{-\infty}$, at $x = -\infty$, corresponds to the initial glucose concentration, g_0. Eq. (40) may be expressed as

$$K = \mu\sqrt{cD}\,\sqrt{g_0 - g_1}\sqrt{k} \,. \tag{41}$$

We can thus see that the constant k' of eq. (6) is equal to $\mu\sqrt{cD}$. The fact that the dependence on the initial glucose concentration, g_0, and the lag concentration, g_1, does not correspond exactly between eqs. (6) and (41) may well be due to the fact that g_1 is much smaller than g_0. With this condition the approximation holds that

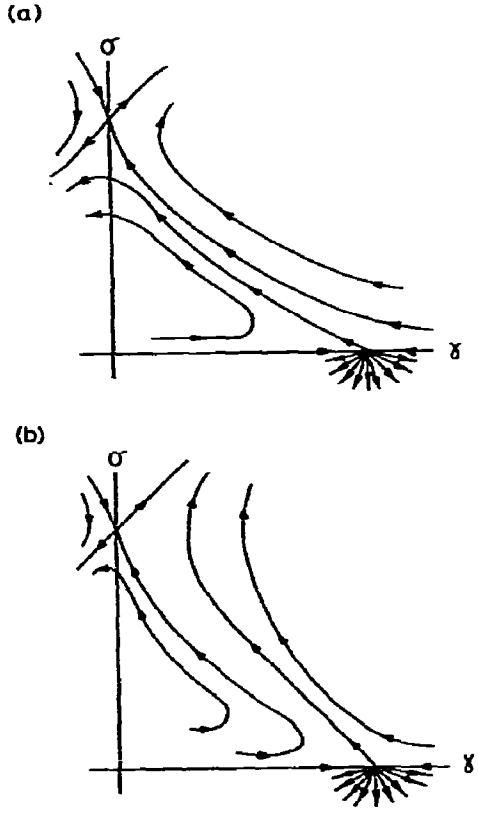

Fig. 6. Integral curves in the (γ, σ) phase plane for general values of μ with the additional restriction (lag phase) on $\phi(\gamma, \sigma)$.

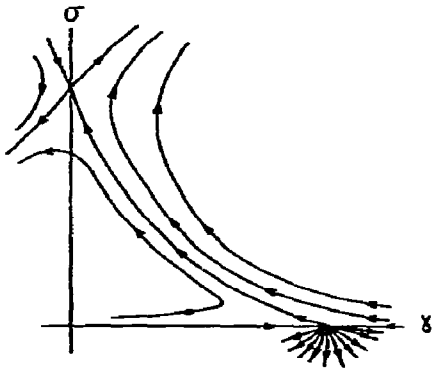

Fig. 7. Integral curves in the (γ, σ) phase plane for the eigenvalue of μ (with lag phase).

$$\sqrt{g_0} - \sqrt{g_1} \simeq \sqrt{g_0 - g_1} \,. \tag{42}$$

It is therefore quite possible that the experimentally observed dependence of the radial growth rate constant on the glucose concentrations [1] only approximately obeys eq. (6), and may be more accurately described by eq. (41).

Another experimentally observed feature [1] which this theory can explain is the fact that the temperature dependence of K, the radial growth rate constant, is different from the temperature dependence of k, the homogeneous growth rate constant. We can see from eq. (41) that K depends not only on $\sqrt{k}$ but also on $\sqrt{D}$. The diffusion coefficient of glucose, D, is itself temperature dependent, and so we would predict a different temperature dependence of K from that of k (or $\sqrt{k}$).

References

[1] S.J. Pirt, J. Gen. Microbiol. 47 (1967) 181.
[2] A.L. Cooper A.C.R. Dean and C. Hinshelwood, Proc. Roy. Soc. B171 (1968) 175.
[3] D.A. Frank-Kamenetaskii, Diffusion and heat exchange in chemical kinetics (Princeton Univ. Press, 1955).
[4] Y.B. Zeldovich and D.A. Frank-Kamenetskii, Zhur. Fiz. Khim. 12 (1938) 100.
[5] A. Kolmogoroff, I. Petrovsky and N. Piscounoff, Bull. de l'Univ. D'Etat à Moscou, I.A., 1 (1937).
[6] A.L. Hodgkin and A.F. Huxley, J. Physiol. 117 (1952) 500.

[7] E.F. Keller and L.A. Segal, J. Theoret. Biol. 30 (1971) 235.
[8] A.C.R. Dean and C. Hinshelwood, Growth function and regulation in bacterial cells (Clarendon Press, Oxford, 1966).
[9] F.A. Williams, Combustion theory (Addison Wesley, Reading, Mass., 1965).
[10] H.T. Davis, Introduction to non-linear differential and integral equations (Dover, New York, 1962).

BIOPHYSICAL CHEMISTRY 1 (1974) 214–221. © NORTH-HOLLAND PUBLISHING COMPANY

CALORIMETRIC INVESTIGATIONS OF THE HELIX–COIL CONVERSION OF PHENYLALANINESPECIFIC TRANSFER RIBONUCLEIC ACID

Diedrich BODE, Ulrich SCHERNAU and Theodor ACKERMANN
Institut für Physikalische Chemie der Universität Freiburg, 78 Freiburg, West-Germany

Received 22 October 1973

The enthalpy of the helix–coil conversion of phenylalaninespecific transfer ribonucleic acid from brewer's yeast ($tRNA^{Phe}_{brewer's\ yeast}$) has been measured using both an LKB 10700-2 batch microcalorimeter and an adiabatic differential scanning calorimeter. In the mixing calorimeter the conversion from coil to helix was induced by mixing a $tRNA^{Phe}$ solution with a solution containing an excess of $MgSO_4$. We measured the enthalpy of this reaction stepwise in the temperature range from +9 to +60°C. For the enthalpy of folding of $tRNA^{Phe}$ from coil to helix this method yielded the remarkably high value of −310 kcal/mole of $tRNA^{Phe}$. With the differential scanning calorimeter in which the helix–coil conversion is simply induced by raising the temperature we found a value of +240 kcal/mole of $tRNA^{Phe}$ at a T_m value of 76°C and a value of +200 kcal/mole of $tRNA^{Phe}$ at a T_m value of 50°C. A comparison of the apparent van't Hoff enthalpies with the calorimetrically measured enthalpies shows, that the cooperativity of the system increases continually with rising melting temperatures – which are achieved by increasing Mg^{2+} concentrations – reaching a constant value at about 57°C. Above this temperature value the thermodynamic behaviour of the helix–coil conversion of $tRNA^{Phe}$ may be approximately described by the model of an all-or-none process.

1. Introduction

The thermodynamic behaviour of the unfolding of tRNA has been studied by several authors with different indirect methods such as UV absorption, viscosity and fluorescence measurements. Except for one experiment performed by Levy et al. [1] no direct calorimetric investigations of the helix–coil conversion of specific tRNAs have been reported. Römer et al. [2,3] have studied the unfolding reaction of $tRNA^{Phe}_{yeast}$ comparing the differentiated UV-melting curves of separated half molecules with the melting curve of the intact molecule. Including fluorescence measurements they could resolve the melting process of $tRNA^{Phe}_{yeast}$ into five reactions. To evaluate the enthalpy of the whole unfolding process the authors treated the single reactions as all-or-none processes constructing van't Hoff plots and summarized the apparent van't Hoff enthalpies of the partial reactions. They obtained 180 kcal/mole of tRNA for the unfolding of $tRNA^{Phe}$. These investigations were made in buffer solutions free of Mg^{2+} ions. The results have been reproduced by *T*-jump experiments. When extending kinetic investigations to tRNA solutions containing Mg^{2+} the authors found that with increasing Mg^{2+} concentrations the spectrum of relaxation times degenerated to one single relaxation time. These kinetic results led to the conclusion that only at sufficiently high Mg^{2+} concentrations the unfolding of $tRNA^{Phe}$ may be described as a single all-or-none process. Levy et al. on the other hand treated the whole helix–coil conversion of $tRNA^{Phe}$ as a single all-or-none process independent of the experimental conditions. They claim that the enthalpy of conversion of $tRNA^{Phe}$ can be evaluated from a single van't Hoff plot in any case, and found that their theory is sufficiently supported by one mixing experiment in an LKB flow microcalorimeter, by mixing a Mg^{2+}–$tRNA^{Phe}$ solution at 57°C (tRNA in the folded state) with an isothermal solution of excess ethylene-diamine-tetra-acetic acid (EDTA) to complex the Mg^{2+} ions. By that procedure $tRNA^{Phe}$ unfolds spontaneously.

The experiment yielded a value of +125 kcal/mole of $tRNA^{Phe}$, which was exactly the same value the authors obtained from a van't Hoff plot of a UV-melting curve at a melting temperature of 57°C. In the face of these two different opinions we thought that a systematic calorimetric investigation should bring some clearness into the thermodynamic description of the helix–coil conversion of $tRNA^{Phe}_{yeast}$.

2. Experimental

2.1. Materials

$tRNA_{brewer's\ yeast}$ was purchased from Boehringer–Mannheim. $tRNA^{Phe}$ was purified by column chromatography with benzoylated DEAE-cellulose [4] using the procedure as described by Schneider et al. [5]. The final purity of the $tRNA^{Phe}$, characterized by aminoacylation assay [6] with radioactive STAN Star ^{14}C-phenylalanine (Schwarz Bio Research) was 1.6 to 1.7 nmole phenylalanine incorporated to one OD_{260} unit* of $tRNA^{Phe}$. All solutions used were prepared with double distilled water and with chemicals of analytical reagent grade.

2.2. Methods

The concentrations of $tRNA^{Phe}$ solutions were calculated on the basis of gravimetric phosphorous determinations [7] which were made with aliquots of the solutions after all organic material had been destroyed by evaporation with $HClO_4$. All tRNA solutions prepared for the various measurements were buffered with sodium citrate (5×10^{-3} M) pH = 6.5.

UV-melting curves were measured with a Hitachi–Perkin–Elmer spectrophotometer 124 using standard quartz cuvettes of 1 cm pathlength. The temperature of the thermostatted cell holder was regulated with the aid of a Lauda Kryomat K2R. Using an X–Y recorder (Hewlett Packard, Palo Alto) absorbance was recorded as a function of the EMF of a copper–constantan thermocouple (hot junction inside the sample cell and cold junction inside a bath of ice-water).

The adiabatic differential scanning calorimeter which was developed by Grubert [8] employing solid state electronics is able to operate in the temperature range from −10 to +110°C. It is an improved version of the apparatus described by Ackermann [9]. Each calorimeter vessel contains 25 ml of solution. The sensitivity of the apparatus is such that heat effects of 12 cal/ℓ occurring over a temperature range of 5°C can be determined with a precision of ± 3%.

Mixing experiments were performed with an LKB batch microcalorimeter (10700-2). A detailed description of this apparatus has been given by Wadsö [10]. As the standard version of the LKB 10700-2 works only in the temperature range from +20 to +40°C the calorimeter was modified for operation in the range from 0 to +60°C.

3. Results

3.1. UV-absorption measurements

As we found the point of inflexion and the general shape of the UV-melting curves of $tRNA^{Phe}$ solutions to be invariant with respect to the wavelength we measured the temperature course of the absorbance at 260 nm where the hyperchromicity reaches its maximum value.

Fig. 1 shows a series of melting curves of $tRNA^{Phe}$

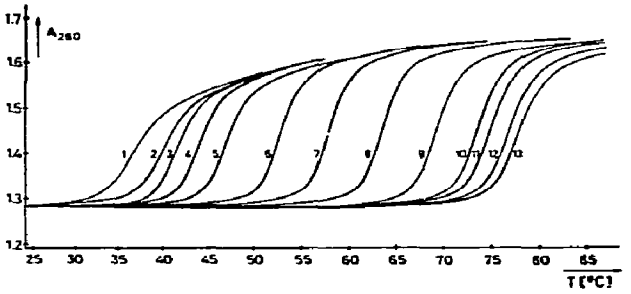

Fig. 1. Melting curves of $tRNA^{Phe}$ recorded at 260 nm. The solutions were buffered with 5×10^{-3} M citrate at pH 6.5. The concentration of tRNA was 2.5×10^{-6} M. Concentrations of $MgSO_4$ were as follows: 1: 2×10^{-4} M; 2: 4×10^{-4} M; 3: 6×10^{-4} M; 4: 8×10^{-4} M; 5: 10^{-3} M; 6: 2×10^{-3} M; 7: 3×10^{-3} M; 8: 4×10^{-3} M; 9: 5×10^{-3} M; 10: 6×10^{-3} M; 11: 8×10^{-3} M; 12: 10^{-2} M; 13: 2×10^{-2} M.

* One OD_{260} unit is the amount of material, which in 1 ml of solution produces the absorbance 1 when measured at 260 nm in a cuvette of 1 cm pathlength.

obtained from solutions of different Mg^{2+} concentrations. If we define the points of inflexion with respect to the temperature axis as melting temperature – independent of the problem whether there are one or more melting processes – we can construct a phase diagram of tRNA^{Phe}. For this purpose the melting temperatures of fig. 1 were plotted versus the corresponding Mg^{2+} concentrations (see fig. 2). At the upper left part of the curve tRNA^{Phe} is stable in its unfolded state and at the lower right part it is stable in its folded state. Passing this curve means that a transition of tRNA^{Phe} from the folded to the unfolded form or vice versa takes place. As can be seen from fig. 2 this transition can be induced either by changing the concentration of Mg^{2+}, which allows one to measure the enthalpy of the reaction with the LKB batch microcalorimeter, or by changing the temperature, which allows one to follow the reaction with the differential scanning calorimeter.

Besides these direct methods to determine the enthalpy of conversion an apparent van't Hoff enthalpy of the unfolding reaction can be estimated. For this purpose the reaction is regarded as a two-state process according to Levy et al. [1]. The enthalpy of such a simple reaction can be evaluated with the aid of the equation

$$(d\theta/dT)_{T_m} = \tfrac{1}{4}\Delta H_c'/RT_m^2, \qquad (1)$$

where $\Delta H_c'$ is the apparent enthalpy of conversion and $(d\theta/dT)_{T_m}$ is the slope of the temperature course of the degree of conversion $\theta(T)$ at T_m.

The function $\theta(T)$ can be easily constructed normalizing the UV-melting curves by setting the original absorbance value to zero and the final absorbance value to one.

Fig. 3 shows the apparent enthalpies $\Delta H_c'$ evaluated by applying eq. (1) to the experimental data given in fig. 1. In contradiction to the curve published by Levy et al. [1] we find no straight line but, instead, a curve rising up to 55°C and then remaining at a nearly constant level. Levy et al. [1] explained the constant slope of their curve by the assumption, that a relatively large ΔC_p value causes the growth of $\Delta H_c'$ with increasing temperature according to the equation

$$\Delta H_c'(T) = \Delta H_c'(T_0) + \int_{T_0}^{T} \Delta C_p \mathrm{d}T. \qquad (2)$$

Our interpretation of fig. 3 is, that the cooperativity of the melting of tRNA^{Phe} increases with increasing melting temperatures up to 55°C. At this temperature the cooperative length [11] has nearly reached the length of the molecule so that no further increase of cooperativity can occur. In this view the application of eq. (1) is only justified at T_m values above 55°C. As will be shown later even in these cases this procedure is only an approximation.

3.2. *Differential scanning calorimetry*

The excess heat capacity versus temperature plots

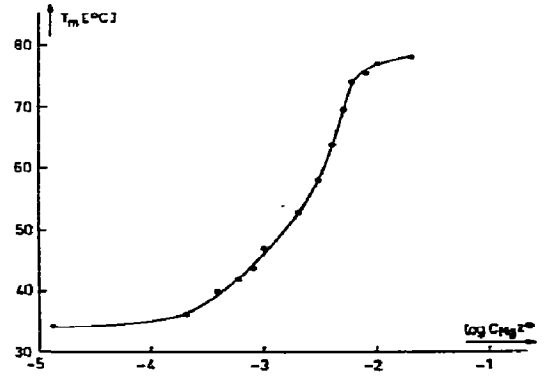

Fig. 2. Phase diagram of tRNA^{Phe}. The diagram is constructed using the melting temperatures of the curves in fig. 1 for the corresponding Mg^{2+} concentrations.

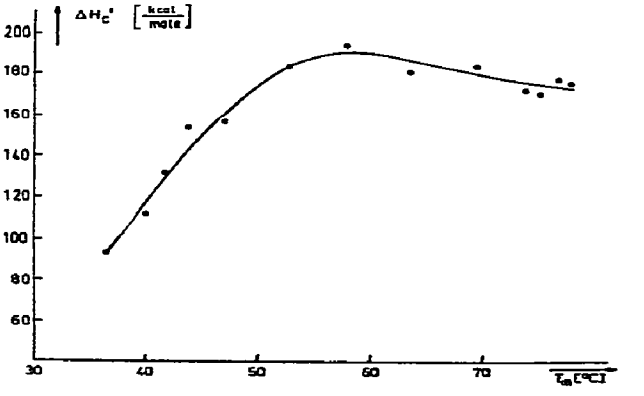

Fig. 3. Apparent enthalpies of conversion of tRNA^{Phe}, $\Delta H_c'$, as function of the melting temperature T_m.

of two typical measurements with the differential scanning calorimeter are presented in fig. 4. The slight rise of the base lines may not be interpreted in terms of a permanent increase of the heat capacity of $tRNA^{Phe}$. It is rather due to the imperfect shielding of the calorimeter vessels [8]. The measurement presented in fig. 4a was performed with a $tRNA^{Phe}$ solution containing a small amount of Mg^{2+}. The advantage of using such solutions is that the melting process occurs at relatively low temperatures. The disadvantage is that the measurement yields only a flat and broad peak of excess heat capacity, the computation of which is rather difficult on account of the long distance of base line under the peak which is obtained by interpolation. The result given in fig. 4a was found to be easily reproducible – within the margins of error – when a new measurement was performed on the same $tRNA^{Phe}$ solution.

When we tried to reproduce the result of fig. 4b with the identical solution it turned out that the peak became more flat after each measurement and the area of the peak diminished. For example, a second measurement with the solution of fig. 4b yielded only 200 and a third one only 170 kcal/mole of $tRNA^{Phe}$. We believe that this effect is due to degradation of tRNA taking place at such high temperatures (up to 90°C) to which the solution had to be heated to get a reliable base line at temperatures above the conversion. Both the high temperature and the rather high concentration of Mg^{2+} cause degradation of polynucleotides, a phenomenon which is well known from the literature [12].

In addition to Mg^{2+} ions we need in most cases a rather high content of NaCl to prevent precipitation of $tRNA^{Phe}$ at high temperatures. By doing several UV-absorption experiments with special cuvettes

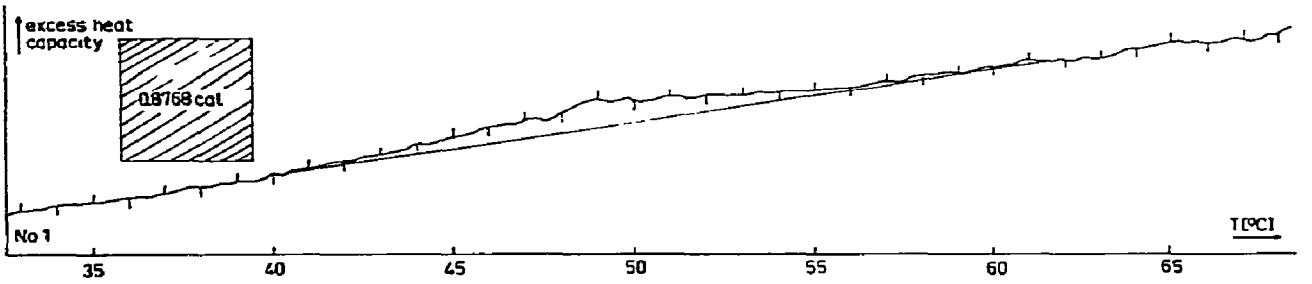

Fig. 4a.

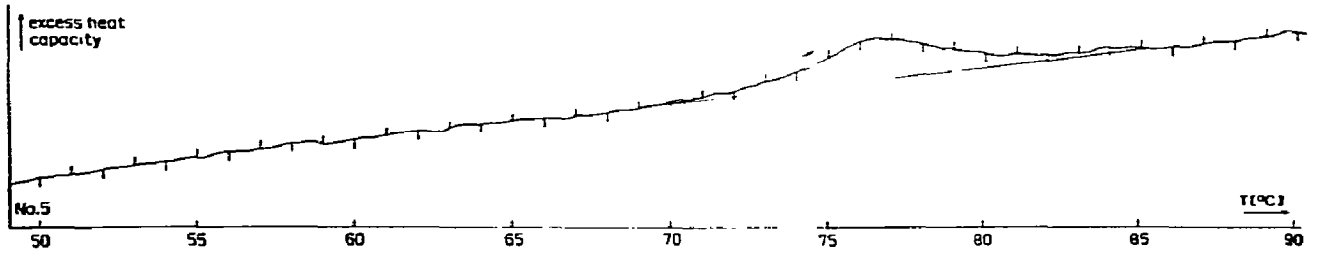

Fig. 4b.

Fig. 4. Typical temperature courses of the additional heat capacity of $tRNA^{Phe}$ solutions recorded with the differential scanning microcalorimeter (measurements no. 1 and no. 5 of table 1). A relative calibration of the ordinates can be obtained using the standard area of 0.8768 cal. The energy represented by this standard area was determined by a series of electrical calibration experiments [8].

Table 1
Results of the measurements obtained with the differential scanning calorimeter. (Concentration of $tRNA^{Phe}$: 6×10^{-5} to 8×10^{-5} M)

No.	Salt concentrations	T_m(°C)	ΔH_c (kcal/mole of $tRNA^{Phe}$)
1	10^{-3} M $MgSO_4$	49	200 ± 30
2	5×10^{-3} M $MgSO_4$	70	250 ± 20
3	8×10^{-2} M $MgSO_4$ 0.5 M NaCl	76.5	240 ± 20
4	8×10^{-3} M $MgSO_4$ 1 M NaCl	76.5	240 ± 20
5	8×10^{-2} M $MgSO_4$ 1 M NaCl	76.5	240 ± 20
6	8×10^{-2} M $MgSO_4$ 1 M NaCl	76.5	220 ± 20
7	2×10^{-2} M $MgSO_4$	79	230 ± 20

(pathlength = 0.3 mm) we were able to establish that $tRNA^{Phe}$ at concentrations needed for calorimetry (about 7×10^{-5} mole/ℓ of $tRNA^{Phe}$) tends to precipitate during the helix–coil conversion at high Mg^{2+} concentrations. That means we found the folded form to be soluble under all conditions tested but the unfolded form precipitating from 2.2×10^{-2} M Mg^{2+} upwards. We found the precipitation to be entirely reversible on cooling the suspensions.

In table 1 the results obtained from measurements performed with the adiabatic scanning calorimeter are listed. As can be seen hardly any temperature dependence of the ΔH_c values is detectable. This is perhaps the most striking argument against the concept of Levy and Biltonen [13]; who interpreted the increase of the apparent enthalpy of conversion (see fig. 3) with rising melting temperature by an increase of the true enthalpy of conversion due to a rather large ΔC_p value.

3.3. Mixing calorimetry

With the aid of the batch microcalorimeter we measured the heat liberated when $tRNA^{Phe}$ is converted from its unfolded to its folded state by a change of the composition of the solution. This change resulted from mixing the tRNA solution with a solution of $MgSO_4$ having the same temperature. To compensate the heat of dilution of $MgSO_4$ we took advantage of the differential principle of the LKB calorimeter mixing in the reference cell 2 ml of buffer with 2 ml of $MgSO_4$ solution and in the reaction cell 2 ml of $tRNA^{Phe}$ solution with 2 ml of $MgSO_4$ solution*. This general arrangement of the mixing experiment as explained by scheme 1 was used during the whole series of measurements. The scheme shows the reference and the reaction cell of the LKB batch microcalorimeter. Each cell is divided into two compartments for part of its height. Mixing is initiated by rotating the calorimeter unit.

The lowest temperature at which the calorimeter could be operated – cooled by a Lauda Kryomat K2R – was +9°C (see fig. 5). The highest temperature at which we could measure the folding reaction of $tRNA^{Phe}$ was 60°C. The results of our measurements in the temperature range mentioned are given in fig. 5. At low temperatures the course of the enthalpy values, referred to one mole of $tRNA^{Phe}$, reaches a rather constant level at about +12 kcal/mole. These small positive enthalpies can be associated with the binding of Mg^{2+} to the negatively charged phosphate residues.

* The heat of dilution of $tRNA^{Phe}$ was measured in a separate experiment and was found to be neglegible small.

Scheme 1
The mixing experiments

Reference cell		Reaction cell	
2ml 5×10^{-3} M sodium citrate, pH 6.5	2ml 5×10^{-3} M sodium citrate, pH 6.5 2×10^{-2} M $MgSO_4$	2ml 5×10^{-3} M sodium citrate, pH 6.5 5–10 mg of $tRNA^{Phe}$	2ml 5×10^{-3} M sodium citrate, pH 6.5 2×10^{-2} M $MgSO_4$

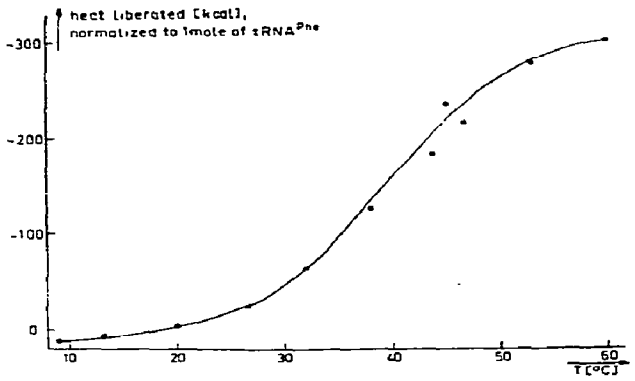

Fig. 5. Heat liberated on mixing $tRNA^{Phe}$ solutions with Mg^{2+} solutions as a function of temperature. The values on the ordinate are normalized to one mole of $tRNA^{Phe}$.

The stoichiometry and the binding constants of this reaction have been investigated by several authors by NMR relaxation studies [14] and electron spin resonance [15] in the case of Mn^{2+}, and by mixing calorimetry [16] and cation specific electrodes [17] in the case of Mg^{2+}. Krakauer [18] has measured the heat of binding of Mg^{2+} to the phosphate groups of synthetic polynucleotides and has found a positive value of about 1 kcal/mole Mg^{2+} bound in all cases with the exception of polyadenylic acid.

In the case of $tRNA^{Phe}$ we measured +12 kcal/mole of $tRNA^{Phe}$ at +9°C. With a mean value of about 30 binding sites for one tRNA molecule, found by the authors mentioned above, one obtains 0.4 kcal/mole of Mg^{2+} bound. But this value may not be simply interpreted by the association reaction alone. UV-absorption experiments showed, that at +9°C the absorbance value at 260 nm of a $tRNA^{Phe}$ solution free of Mg^{2+} decreases upon addition of $MgSO_4$. (We found a decrease of about 3% at a final concentration of 10^{-2} M Mg^{2+}.) From this we conclude that even at this temperature tRNA is present in a structure of higher order (for example a higher degree of base stacking in the loops) in the presence than in the absence of Mg^{2+}. On account of this phenomenon our value of +12 kcal/mole of $tRNA^{Phe}$ must be considered to be composed of the positive heat of binding of Mg^{2+} to the phosphate groups and of a small negative enthalpy resulting from enhanced base staking. At 60°C the enthalpy values for the reaction of $tRNA^{Phe}$ and Mg^{2+} have reached an upper constant level, indicating that they represent the enthalpy difference between completely unfolded and folded $tRNA^{Phe}$. We wish to point out that our results do not agree with those obtained by Levy et al. [1]. These authors found for the unfolding reaction of $tRNA^{Phe}$ at 57°C initiated by complexing Mg^{2+} with EDTA a value of +123 ± 25 kcal/mole of $tRNA^{Phe}$. Our value at that temperature is 290 kcal/mole of $tRNA^{Phe}$. Hence, our results obtained with the batch microcalorimeter are in contradiction to the concept of Levy et al. who postulated the apparent van't Hoff enthalpy to be equal to the calorimetrical value at any melting temperature.

To get the true enthalpy of the conformational conversion of $tRNA^{Phe}$ from fig. 5 we must subtract the value of the lower level from that of the upper one. By this procedure we can eliminate the heat of binding of Mg^{2+} to $tRNA^{Phe}$, provided that this heat of binding does not depend on temperature. According to this procedure we obtain 310 kcal/mole of $tRNA^{Phe}$ for ΔH_c.

4. Discussion

Throughout this paper we have repeatedly pointed out that our experimental results and interpretations are different from those of Levy et al. The main differences can be summarized as follows:

(1) The van't Hoff enthalpy calculated by using eq. (1) does not rise linearly with temperature as found by Levy et al. but reaches a constant level at 57°C. We attribute this behaviour to an increasing cooperativity which reaches a maximum value at 57°C which approximately represents the true enthalpy of conversion above that temperature.

(2) The enthalpy of conversion of $tRNA^{Phe}$ determined with the differential scanning calorimeter hardly shows any temperature dependence. This clearly shows that there is not such a considerable difference as high as 3 kcal/mole deg between the heat capacities of folded and unfolded $tRNA^{Phe}$ as postulated by Levy et al. The absolute values of ΔH_c being 240 kcal/mole of $tRNA^{Phe}$ at 76°C and 200 kcal/mole of $tRNA^{Phe}$ at 49°C are considerably higher than those predicted by Levy et al. who found values as low as 160 kcal/mole of $tRNA^{Phe}$ at 76°C and 100 kcal/mole

of $tRNA^{Phe}$ at 49°C.

(3) The reliability of the calorimetrical mixing experiment performed by Levy et al. at 57°C yielding a suspiciously low value of 123 ± 25 kcal/mole of $tRNA^{Phe}$ for ΔH_c is open to question, since our systematic investigation of this reaction over a broad temperature region yielded 290 ± 25 kcal/mole of $tRNA^{Phe}$ at 57°C (see fig. 5).

The difference between the results we obtained with the differential scanning calorimeter and those we measured with the LKB batch microcalorimeter can be explained at least in part by the following hypothesis: If there occurred any non-cooperative increase in the heat capacity of $tRNA^{Phe}$ during heating the solution, for example, due to unstacking of the bases in the unfolded state, this would influence the enthalpy change determined with the mixing calorimeter. However, this would not influence the ΔH_c value measured with the adiabatic calorimeter. In this case there would result only a shift of the base line to higher values. We have also observed a difference of the same magnitude when we measured the enthalpies of the helix–coil conversion of polyuridylic acid using the two calorimetric methods without finding a satisfactory explanation [19]. Because the reaction taking place in the differential scanning microcalorimeter is more distinct than that in the mixing calorimeter we think the results we have obtained by the first method are more realistic.

If we compare our calorimetric results with those obtained from UV-absorption experiments by Römer et al. [2] there is a moderately good agreement with respect to the numerical values of ΔH_c determined with the differential scanning calorimeter (240 kcal/mole) and to those estimated by Römer et al. from transitions of isolated half molecules and of resolved transitions from the whole molecule (180 kcal/mole). Our interpretation of increasing cooperativity with increasing melting temperatures is not in contradiction to their concept of evaluating van't Hoff enthalpies from resolved transitions which may be assigned to different parts of the molecule. But neither adiabatic scanning calorimetry nor mixing calorimetry are sensitive enough to resolve the conversion of $tRNA^{Phe}$ into distinct transitions under appropriate conditions and to give direct support to the findings of Römer et al.

The difference between our calorimetrically determined value (240 kcal/mole) and that estimated by Römer et al. (180 kcal/mole) is probably due to the fact that the van't Hoff enthalpies and the true calorimetric enthalpies are not identical even for rather small helical segments.

It is rather difficult to discuss the enthalpy of conformational conversion on the basis of the experimental data of model compounds and of the primary and secondary structure evaluated by Raj Bhandary et al. [20]. According to the cloverleaf structure which was confirmed by the X-ray diffraction analysis of Kim et al. [21] $tRNA^{Phe}$ should have 12 GC pairs, 8 AU pairs and 1 GU pair. The enthalpy of the helix–coil conversion of the poly(A+U) double helix was determined to be 9 kcal/mole of base pairs at $T_m = 75$°C [22].

Calorimetric measurements of the helix–coil conversion of poly(G+C) have not yet been performed, not to mention the poly(G+U) double helix. Even if such data were available it would not be clear whether one has to take into consideration all 21 base pairs or only 21 minus 2. The problem is that each first base pair of the two continuous stacks proposed by Kim et al. [21] does not contribute to the stacking enthalpy which represents the main contribution to the helix–coil enthalpy.

Acknowledgements

We are deeply indebted to Dr. F. von der Haar (Max-Planck-Institut für experimentelle Medizin, Abteilung Chemie, 34 Göttingen) for a generous gift of phenylalanyl-tRNA synthetase and for helpful advice concerning the isolation of $tRNA^{Phe}$ by column chromatography. We thank Miss Ch. Rühaak for skilful technical assistance. This work was supported by the Deutsche Forschungsgemeinschaft.

References

[1] J. Levy, G. Rialdi and R. Biltonen, Biochemistry 11 (1972) 4138.
[2] R. Römer, D. Riesner, G. Maass, W. Wintermeyer, R. Thiebe and H.G. Zachau, FEBS Letters 5 (1969) 15.
[3] R. Römer, D. Riesner and G. Maass, FEBS Letters 10 (1970) 352.

[4] J. Gillam, S. Millward, D. Blew, M. von Tigerstrom, E. Wimmer and G.M. Tener, Biochemistry 6 (1967) 3043.
[5] D. Schneider, R. Solfert and F. von der Haar, Hoppe–Seylers Z. Physiol. Chem. 353 (1972) 1330.
[6] E. Schlimme, F. von der Haar and F. Cramer, Z. Naturforsch. 24b (1969) 631.
[7] E. Asmus and H.-P. Baumert, Z. Analyt. Chem. 233 (1967) 252.
[8] M. Grubert, Thesis, Freiburg (1973).
[9] T. Ackermann, in: Biochemical microcalorimetry, ed. H.D. Brown (Academic Press, New York. 1969).
[10] J. Wadsö, Acta Chem. Scand. 22 (1968) 927.
[11] J. Engel and G. Schwarz, Angew. Chem. 82 (1970) 468.
[12] J.J. Butzow and G.L. Eichhorn, Biopolymers 3 (1965) 95.
[13] J. Levy and R. Biltonen, Biochemistry 11 (1972) 4145.
[14] M. Cohn, A. Danchin and M. Grunberg–Manago, J. Mol. Biol. 39 (1969) 199.
[15] A. Danchin and M. Guéron, Eur. J. Biochem. 16 (1970) 532.
[16] G. Rialdi, J. Levy and R. Biltonen, Biochemistry 11 (1972) 2472.
[17] Ch. Sander and P.O.P. Ts'o, J. Mol. Biol. 55 (1971) 1.
[18] H. Krakauer, Biopolymers 11 (1972) 811.
[19] M. Heinecke, D. Bode and U. Schernau, Biopolymers, submitted for publication.
[20] U.L. Raj Bhandary, S.H. Chang, A. Stuart, R.D. Faulker, R.M. Hoskinson and H.G. Khorana, Proc. Natl. Acad. Sci. U.S. 57 (1966) 751.
[21] S.H. Kim, G.J. Quigley, F.L. Suddath, A. Mc Pherson, D. Sneden, J.J. Kim, J. Weinzierl and A. Rich, Science 179 (1973) 285.
[22] E. Neumann and Th. Ackermann, J. Phys. Chem. 73 (1969) 2170.

BIOPHYSICAL CHEMISTRY 1 (1974) 222–226. © NORTH-HOLLAND PUBLISHING COMPANY

THE ORIGIN OF ROTATIONAL BARRIERS IN AMIDES AND ESTERS

Joel F. LIEBMAN

Department of Chemistry, University of Maryland Baltimore County, Baltimore, Maryland, USA

and

A. GREENBERG

Department of Chemistry, Frostburg State College, Frostburg, Maryland, USA

Received 11 June 1973
Revised manuscript received 1 October 1973

We discuss in this article the origin and magnitude of the single bond rotational barrier in amides and esters. The high rotational barrier of amides is biochemically manifested in the limited conformational freedom of proteins, since there are only two instead of three bonds to rotate about per amino acid residue. On the basis of thermochemical estimates with model compounds, we find that the resonance energy of esters is somewhat higher than that of amides. However, the experimental rotational barrier for the former is considerably lower than the latter. We suggest esters have lower rotational barriers than the corresponding amides because they retain a large fraction of the resonance energy in the transition state. Justification is offerred using an orbital delocalization argument.

1. Introduction

The purpose of this article is to discuss the origin and magnitude of the single bond rotational barriers in amides and esters. The high rotational barrier of amides is biochemically manifested in the limited conformational freedom of proteins, since there are only two instead of three bonds to rotate about per amino acid residue [1–3]. The conformational energies of proteins and their components has been the subject of active quantum chemical investigation. (See ref. [4] and literature cited therein.) Qualitatively, the high rotational barrier to rotating around the C–N bond in amides has usually been rationalized in terms of a large ground-state double-bond contribution from resonance structure *1b*.

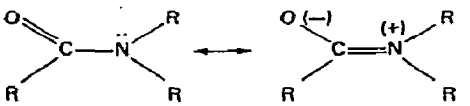

1a 1b

This explanation is also consistent with the considerably lower rotational barriers in esters. In esters, the higher electronegativity of oxygen relative to nitrogen should considerably decrease the resonance contribution of *2b* in the ground state since it requires positive oxygen. Accordingly, there should be less double-bond character to the carbon–oxygen bond in question.

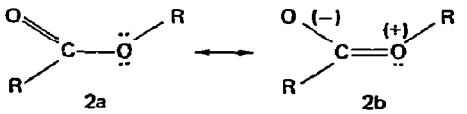

2a 2b

In this paper, we intend to show that this interpretation involving comparison of C–N and C–O multiple bonding is incorrect, or at best, markedly incomplete.

2. Results and discussion

The rotational barriers of amides, ca. 21 kcal/mol [5] reflect their resonance energies. (The resonance energy of a compound is defined here as the differ-

ence of its heat of formation determined experimentally and theoretically by use of model compounds, bond additivity, or related thermochemical schemes.) In eq. (1), the heat of formation [6, 7] of N,N-dimethylacetamide is calculated on the basis of model compounds [8]. Comparison with the calculated value, $\Delta H_f = -58$ kcal/mol yields a resonance energy of about 21 kcal/mol.

$$\Delta H_f(CH_3CON(CH_3)_2) = \Delta H_f(CH_3COCH_3) + \Delta H_f((CH_3)_3N) - \Delta H_f(C_2H_6), \quad (1)$$

$$-37.5 \text{ kcal/mol} = (-51.90) + (-5.81) - (-20.24).$$

For those compounds where neither resonance nor strain considerations are anticipated, these calculations of heat of formations are reliable to within 1 or 2 kcal/mol. In eq. (2), the heat of rormation of 1,1-dimethylacetone (3-methyl-2-butanone) is estimated:

$$\Delta H_f(CH_3COCH(CH_3)_2) = \Delta H_f(CH_3COCH_3) + \Delta H_f((CH_3)_3CH) - \Delta H_f(C_2H_6), \quad (2)$$

$$-64.1 \text{ kcal/mol} = (-51.90) + (-32.41) - (-20.24).$$

The experimental heat of formation is −62.8 kcal/mol in close agreement with our result. Enamines display slightly lower rotational barriers than those of amides [9, 10]. The thermochemistry of few enamines is available. Comparison of the calculated heat of formation [eq. (3)] of aminoethylene with the suggested value, 5.5 kcal/mol [11], yields a resonance energy of about 14 kcal/mol. This value (to be compared with the value of 21 kcal/mol in amides) is consistent with a smaller contribution from *3b* since carbon is not as electronegative as oxygen.

$$\Delta H_f(CH_2{=}CHNH_2) = \Delta H_f(CH_2{=}CHCH_3) + \Delta H_f(CH_3NH_2) - \Delta H_f(C_2H_6), \quad (3)$$

$$19.6 \text{ kcal/mol} = (4.88) + (-5.50) - (-20.24).$$

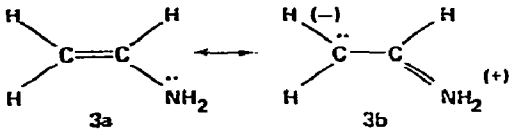

3a 3b

Equation (4) estimating the heat of formation of the saturated ethylamine again shows good agreement between theory and experiment as neither resonance nor strain considerations are applicable here.

$$\Delta H_f(CH_3CH_2NH_2) = \Delta H_f(CH_3CH_2CH_3) + \Delta H_f(CH_3NH_2) - \Delta H_f(C_2H_6), \quad (4)$$

$$-10.09 \text{ kcal/mol} = (-24.83) + (-5.50) - (-20.24).$$

The experimental value for this quantity is −11.35 kcal/mol*.

Let us now consider esters. The intrinsic isomerization barrier about the carbon–oxygen bond in esters for *cis–trans* interconversion is about 7–10 kcal/mol [12]. However, comparison of the calculated [eq. (5)] and experimental, −99.2 kcal/mol, heats of formation of methyl acetate yields a resonance energy of approximately 24 kcal/mol.

* The reader may have noted that there are atomic hybridization problems inherent in eq. (1) not found in eq. (2). That is, we do not precisely conserve the number and types of bonds. In (1), there is an sp^2–sp^2 C–N in the left-hand compound. In the right-hand compounds, there is one bond each of sp^2–sp^3 C–C and sp^3–sp^3 C–N and one sp^3–sp^3 C–C bond has been removed. In (2), there are equal numbers of sp^2–sp^3 and sp^3–sp^3 C–C bonds on both sides of the equal sign. Analogous to (1), in (3), there is an sp^2–sp^2 C–N in the left-hand compound while with the right-hand compounds, we have an sp^2–sp^3 C–C bond and an sp^3–sp^3 C–N bond and the removal of a sp^3–sp^3 C–C bond. Analogous to (2), in (4) there is no such hybridization problem. However, we may estimate the hybridization effects by appying our logic to $\Delta H_f(CH_3CH{=}CH_2)$:

$$\Delta H_f(CH_3CH{=}CH_2) = \Delta H_f(CH_3CH_2CH_3) + \Delta H_f(CH_2{=}CH_2) - \Delta H_f(C_2H_6),$$

$$7.86 \text{ kcal/mol} = (-24.83) + (12.45) - (-20.24).$$

The experimental value is 4.88 kcal/mol, an energy difference of 3.0 kcal/mol. This difference combines the effect of a change from sp^3–sp^3 to sp^3–sp^2 C–C bonding and hyperconjugative stabilization. Since the later effect is inseparable from the former, the 3 kcal/mol is "merely" an upper bound to the hybridization effects which we wished to estimate. However, in comparison to the 21 or 24 kcal/mol resonance energy, this 3 kcal/mol is a small, but admittedly non-negligible quantity that we will continue to ignore.

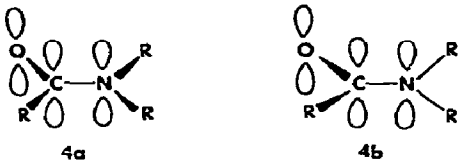

Fig. 1. Rotamers of amides.

$$\Delta H_f(CH_3COOCH_3) = \Delta H_f(CH_3COCH_3) + \Delta H_f(CH_3OCH_3) - \Delta H_f(C_2H_6), \quad (5)$$

$$-75.66 \text{ kcal/mol} = (-51.90) + (-44.00) - (-20.24).$$

Accordingly, the resonance energy of the ester is greater than that of the amide, 21 kcal/mol. As such, resonance energies and rotational barriers for amides and esters do not correspond when analogous model calculations are used for both. The reader should note we have not assumed that the fraction of the π-contribution to resonance stabilization is the same. That is, we have not assumed the relative importance nor estimated the absolute importance of structures *1a*, *1b*, *2a* and *2b*.

The high rotational barrier of an amide results from a loss of resonance stabilization in the transition state. This may be envisioned as being due to removal of the nitrogen p-orbital from the π-system of *4a* to yield *4b* (fig. 1).

Alternatively, one might envision overlap of the carbonyl system with the antisymmetric linear combination of the two nitrogen sp^2-orbitals bound by two substituents as shown in *4c* (fig. 2) [13, 14].

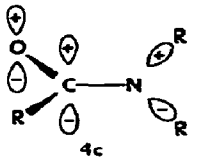

Fig. 2. Delocalization of the antisymmetric conbination of the two nitrogen bond pairs into the carbonyl group of an amide.

These bound electrons are delocalized onto the carbonyl group to a much smaller extent than lone-pair electrons. This is analogous to the relative magnitude of lone pair–lone pair and lone pair–bond pair repulsions in Valence-Shell Electron Pair Repulsion theory [15]. Accordingly, the delocalization or resonance contribution, is insignificant. This difference in the ability to participate in resonance or delocalization between lone pair electrons has been used to explain the surprising quantum chemical prediction that the rotational barrier of methylene immonium, *5* is greater than that of methylene imine, *6* [16]. (Isomerization barriers for substituted methylene imines are discussed in reference [17].)

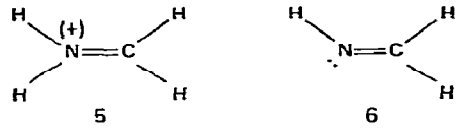

The low energy barrier for *isomerization* about the carbon–oxygen bond in esters is explicable in a number of ways. Two are presented here. A low rotational barrier may be rationalized as the result of overlap of the carbonyl group with the antisymmetric linear combination of oxygen sp^2-orbitals in the transition state, *7*, (fig. 3).

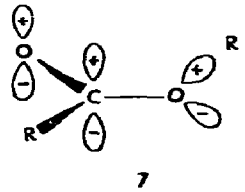

Fig. 3. Delocalization of the antisymmetric combination of the oxygen bond and lone pairs into the carbonyl group of an ester.

Only one substituent is bound to oxygen and the electron pair in the orbital shown is more readily delocalized than the pair in the corresponding orbital of an amide. Alternatively, by analogy to imines [17], esters may be isomerized through inversion as depicted in scheme I (fig. 4).

In the linear C–O–R transition state, the central oxygen is formally hybridized sp but this does not prevent resonance stabilization of the ester. Accordingly, the barrier to isomerization for esters is lowered.

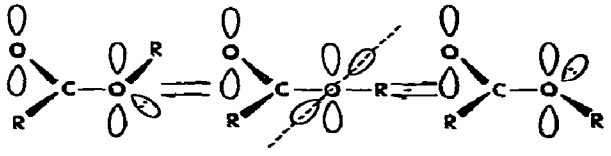

Fig. 4. Inversion pathway for esters.

There is no corresponding process for amides. We may make one C–N–R group of an amide, but not both. Were both linear, the substituents would be directly superposed.

The most crucial difference, therefore, in the isomerization pathways in esters and amides is the ability of the former to retain a large fraction of the ground-state stabilization in the transition states of rotation. Furthermore, inversions which maintain resonance are possible only in esters. Amides apparently lose most of their resonance stabilization in the transition state of the rotation mechanism.

The barriers to rotation in protonated aldehydes [18], protonated ketones [19], and methylated ketones [20], are higher than those of unprotonated esters. In the first three cases, resonance delocalizes a positive charge, while resonance in esters separates opposite charges. Protonated imines have resonance through delocalization of a positive charge while amides have separation of charges. Accordingly, we should not be surprised that the former have higher rotational barriers [21] than the latter. Protonated imines most probably have higher rotational barriers than protonated ketones and aldehydes for the reasons discussed above. Finally, one would speculate that protonated ester *8* might have a rotational barrier comparable to that of an amide, since only one lone pair is available for delocalization. However, resonance contributor *9* would be high in energy and the barrier might well be lower than that of an unprotonated ester.

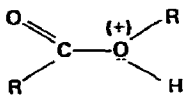

8

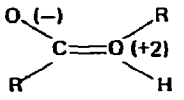

9

Experimentally, however, it is known that esters are protonated on the carbonyl group, *10* [22].

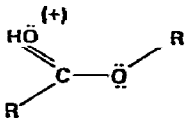

10

Esterification of mesitoic acid [23] and hydrolysis of mesitoates [24] most probably proceed through protonated esters such as *8*. As such, these structures should not be summarily dismissed.

3. Conclusion

In summary, we find that the resonance energy of esters is somewhat greater than that of amides even though the rotational barrier for the former is considerably lower than the latter. The reason why esters have lower rotational barriers than the corresponding amides is that they retain a large fraction of the resonance energy in the transition state. This is justified by an orbital delocalization argument.

4. Acknowledgements

We wish to thank Drs. J.S. Taylor and J.B. Hays for many fruitful discussions and one of us (J.F.L.) acknowledges the donors of the Petroleum Research Fund, administered by the American Chemical Society, for support for this research.

References

[1] L. Pauling, R.B. Corey and H.R. Branson, Proc. Natl. Acad. Sci. U.S. 37 (1951) 205.
[2] C. Rama'krishnan and G.N. Ramachandran, Biophys. J. 5 (1965) 909.
[3] J.T. Edsall, P.J. Flory, J.C. Kendrew, A.M. Liquori, G. Nemethy, G.N. Ramachandran and H.A. Scheraga, J. Mol. Biol. 15 (1966) 399; 20 (1966) 589.
[4] L.C. Shipman and R.E. Christoffersen, J. Am. Chem. Soc. 95 (1973) 4733.
[5] H.S. Gutowsky, J. Jones and T.H. Sidall, J. Am. Chem. Soc. 89 (1967) 4300.
[6] D.R. Stull, E.F. Westrum Jr. and G.C. Sinke, The chemical thermodynamics of organic compounds (Wiley, New York, 1969).
[7] J.D. Cox, Thermochemistry of organic and organometallic compounds (Academic Press, New York, 1970).
[8] J.F. Liebman and A. Greenberg, Estimation of thermal small-ring systems by bond-additivity schemes, J. Org. Chem., in press.
[9] A. Mannschreck and U. Koelle, Tetrahedron Letters (1967) 863.
[10] Y. Shvo, E.C. Taylor and J. Bartulin, Tetrahedron Letters (1967)3259.

[11] J.L. Franklin, J.G. Dillard, H.M. Rosenstock, J.T. Herron, K. Draxl and F.H. Field, Ionization potentials, appearance potentials, and heats of formation of gaseous positive ions, Nat. Stand. Ref. Data Ser., Nat. Bur. Stand. (U.S.), 26 (1969).
[12] J. Bailey and A.M. North, Trans. Faraday Soc. 65 (1968) 1499.
[13] R.B. Woodward and R. Hoffmann, The conservation of orbital symmetry, (Academic Press, New York, 1970) p. 29.
[14] J.F. Liebman, J. Fluor. Chem. 3 (1973/4) 27.
[15] R.J. Gillespie, J. Chem. Educ. 40 (1963) 295.
[16] P.A. Kollman, W.F. Trager, S. Rothenberg and J.E. Williams, J. Am. Chem. Soc. 95 (1973) 458.
[17] M. Raban, Chem. Commun. (1970) 1415.
[18] G. A. Olah, D.H. O'Brien and M. Calin, J. Am. Chem. Soc. 89 (1967) 3582.
[19] G.A. Olah, M. Calin and D.H. O'Brien, J. Am. Chem. Soc. 89 (1967) 3586.
[20] G.A. Olah and J.M. Bollinger, J. Am. Chem. Soc. 89 (1967) 2993.
[21] G.A. Olah and P. Kreibühl, J. Am. Chem. Soc. 89 (1967) 4756.
[22] G.A. Olah and A.M. White, J. Am. Chem. Soc. 89 (1967) 3591.
[23] M.S. Newman, J. Am. Chem. Soc. 63 (1941) 2431.
[24] H.P. Treffers and L.P. Hammett, J. Am. Chem. Soc. 59 (1937) 1708.

BIOPHYSICAL CHEMISTRY 1 (1974) 227–235. NORTH-HOLLAND PUBLISHING COMPANY

STUDY OF THE INTERACTION OF POLYNUCLEOTIDE CHAINS WITH OLIGOMERS BY MEANS OF CHROMATOGRAPHY. II. EFFECT OF MAGNESIUM IONS AND NONCOMPLEMENTARY BASES ON THE STABILITY OF COMPLEXES

V.M. CHERNAJENKO and S.E. BRESLER

Institute of Nuclear Physics, Academy of Science of USSR, Leningrad, USSR

Received 25 June 1973

The interaction of the oligonucleotides ApA, ApApA, ApApC and ApApU with poly(U) and $(Ip)_5I$ and $(Ip)_6$ with poly(C) has been studied by means of equilibrium gelfiltration through Sephadex.

From sorption isotherms the free energies, energies and entropies of complexing have been computed for different concentrations of magnesium ions in the medium.

The stoichiometric ratio of polymers to oligomers has been measured and found equal to 2 in the case of ApApA and ApApC. This shows that the cytidylic acid residue is included in the ternary complex. But in the case of ApApU the noncomplementary base is partly squeezed out of the complex.

The stacking free energy of neighbouring oligomers has been found to be in the range 1000–3000 cal/mole depending on the conditions.

The stoichimetric ratio has been found to be 1 in the case of poly(C): oligo(I), the stacking energy is equal to 1.2 kcal/mole. The effect of magnesium is somewhat different in the case of double and triple helices and probably reflects the formation of coordination compounds with the nitrogen bases of nucleotides.

1. Introduction

Simple polynucleotide complexes can be regarded as models of nucleic acids. In particular, they can be used to simulate the thermodynamic properties of the codon–anticodon interaction. This is relevant for the role of ions and hydrogen bonds in protein synthesis and the origin of the free energy barrier which protects translation against errors.

Recently, a series of papers has been published, dealing with the interaction of homopolynucleotides with complementary oligomers [1–8]. This process was studied by means of hypochromicity measurements. The thermodynamic characteristics were found by complicated calculations because in every run the concentration and temperature of the solution were varied simultaneously.

Another method was used by Ts'o and Davidson [9–11]. They applied equilibrium dialysis and obtained directly the sorption isotherm.

In our previous paper [12], we described a direct method of measuring soprtion isotherms for oligonucleotides on polynucleotides by means of gelfiltration through Sephadex. This method has an important advantage as compared with equilibrium dialysis. It enables one to study the interaction for a much broader class of different oligomers.

In our first paper we applied it to the study of the interaction of polyuridylic acid with the triplets ApApA in the absence of magnesium ions. This paper is devoted to the comparison of the interaction of ApA, ApApA, ApApU and ApApC with poly(U) and $(Ip)_5I$ and $(Ip)_6$ with poly(C) at various magnesium concentrations.

2. Materials and methods

We used ADP, UDP, CDP, poly(A) of Reanal (Hungary), poly(I) of Calbiochem (USA), Sephadexes G-50, G-75, G-100, G-200 of Pharmacia (Sweden).

The oligonucleotides were prepared by hydrolysis of the corresponding homopolymers and copolymers

by pancreatic RNase in the case of $(Ap)_nU$ and $(Ap)_nC$ or by alcali in the case of $(Ap)_n$ [13] and $(Ip)_n$ [14]. After completion of hydrolysis the solutions were incubated for 4 hours at pH 1, and 37°C.

Neutralized hydrolisates were purified of RNase by phenol, and fractionated on a DEAE cellulose column under conditions described by Tomlinson and Tener [15].

The cleavage of end phosphate groups in the oligonucleotides was effected by means of alcali phosphatase from E. coli (We are much obliged to R.J. Tatarskaja for supply of this enzyme). After this procedure ApA, $(Ap)_2A$, $(Ap)_2U$ and $(Ap)_2C$ were rechromatographed on DEAE cellulose (elution in NaCl gradient from 0.0 to 0.3 M in 0.005 Tris-HCl, pH 7.5–8.0). Finally desalting of the preparations was effected on DEAE-cellulose columns by means of ionic exchange with LiCl and subsequent extraction of the lithium salt with ethanol from the samples. $(Ip)_6$ and $(Ip)_5I$ were desalted by means of gelfiltration through Biogel P-2 columns.

The analysis of the sequence of the oligomers was performed by complete alcaline hydrolysis in 0.3 M KOH at 37°C during 18 hours and subsequent separation of the products on a DEAE-cellulose column. The results are presented in table 1.

Molar extinction of oligonucleotides were found by means of comparison of the optical density of the oligomers in buffer (0.005 M Tris-HCl, pH 7.2; 0.005 EDTA; 0.1 M NaCl) with their alcaline hydrolysate neutralized to pH 2. The values found are in agreement with published data (table 2).

Molar extinction of poly(U) at $\lambda = 260$ nm was taken as 9.2×10^3 units/mole cm [16, 17], and of poly(C) as 6.3×10^3 units/mole cm ($\lambda = 268$ nm) [8]. Data for the molar extinction of the nucleotides and nucleosides were adopted from [18].

Poly(U), poly(AU) and poly(AC) were synthesized by means of polynucleotidephosphorylase of E. coli,

Table 1

Analysis of structure of oligonucleotides. Molar ratio of nucleotides to nucleosides in the alcaline hydrolysate of oligonucleotides

ApA	ApApA	ApApU	ApApC	$(Ip)_5I$
0.99	2.1	1.95	2.18	4.8

Table 2

Extinction of oligonucleotides per mole of monomeric unit

Oligonucleotide	λ (nm)	Exp. value of $\epsilon \times 10^{-3}$	Figures taken from literature	
			$\epsilon \times 10^{-3}$	Ref.
ApA	260		13.6	[4]
ApApA	260		12.6	[4]
ApApU	260	11.5	12.0	[16]
ApApC	260	10.6	10.0	[16]
$(Ip)_5I$	250	10.6		
$(Ip)_6$	248		10.8	[8]

purified according to [19].

The reaction was performed in the following solution: 5 μmole/ml of $MgCl_2$, 1μmole/ml of EDTA, Tris-HCl (pH 8.2) 100 μmole/ml. The nucleosidediphosphates were taken in concentrations: UDP, 10 μmole/ml; ADP, 5 μmole/ml; together with UDP, 5 μmole/ml or with CDP, 5 μmole/ml. After completion of the reaction, the mixture was purified twice by phenol extraction, the polynucleotides were precipitated twice with 70% ethanol in the presence of 0.1 M Na-acetate. The precipitate was washed with alcohol, redissolved in water and dried in vacuo.

The control of molecular weights of polyuridylic acid was effected by gelfiltration through Sephadex G-200 in the presence of 7 M urea. For the main part of the product it was higher than 200000 dalton. Some low molecular weight impurities were detected, mostly unreacted UDP.

Immediately before the experiments the poly(U) sample was purified by gelfiltration through a G-75 or G-100 column to get rid of low molecular weight material.

The sorption isotherms were obtained by means of a column 0.5 x 12 cm filled with Sephadex G-50, G-75 or G-100. The buffer was 0.1 M NaCl; 0.0005 M EDTA; 0.005 M Tris-HCl (pH 7.2). The concentration of $MgCl_2$ varies within broad limits.

The following method of measurement was adopted. A long zone of an equilibrium mixture of oligonucleotide with polynucleotide was passed through a Sephadex

column. The zone was divided into two. In front was the zone of the complex, which contained an equilibrium concentration of free oligomers, behind it was the zone of free oligomers. From the extinction of the back zone we found the concentration of free oligomers and determined (knowing its initial concentration) the amount complexed with the polymer. A series of measurements at a constant temperature and different initial concentrations of the oligomers gave us a complete sorption isotherm [12].

3. Control experiments

It was noticed that different nucleotides are eluted from Sephadex with a retention volume exceeding the geometric volume of the gel column [20]. It is due to some interaction of the heterocyclic compounds with dextrane. To make sure that this effect has no measurable influence on the sorption isotherms of polynucleotides with oligomers, we undertook special control experiments.

If the Sephadex matrix interacts to some degree with the oligomers the sorbate must be distributed between the polynucleotide chains and the gel matrix. Therefore the sorption isotherm measured under our conditions must appear shifted to higher oligomer concentrations. This shift is expected to be proportional to the amount of dextran gel in a unit of volume.

Taking Sephadex with different swelling coefficients, i.e., G-50 and G-100, which differ by a factor of two with respect to this property, we could expect a significant difference in sorption isotherms.

The results of measurements are presented in fig. 1a. We see that all experimental points obtained with both Sephadexes are coincident on the same curve. Therefore

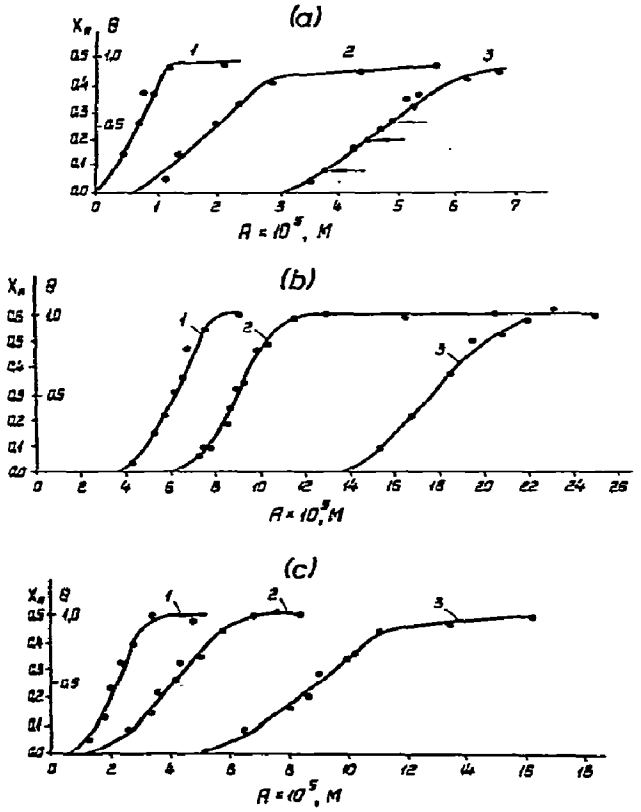

Fig. 1. Sorption isotherms of oligonucleotides on polyuridylic acid.
(a) Sorption isotherms of ApApA on poly(U): 0.01 M Mg^{2+}, 0.1 M Na^{+}, 0.0005 M EDTA, 0.005 M Tris-HCl (pH 7.2). Sephadex G-50 and G-100. Arrows indicate the points obtained on a column of G-100. Curve 1: 13°C, curve 2: 21°C, curve 3: 26°C. Concentration of poly(U) is 5 and 10 × 10^{-5} M of monomer units.
(b) Sorption isotherms of ApApU on poly(U). 0.1 M Mg^{2+}, Sephadex G-75 A. Concentration of poly(U) is 6 and 12 × 10^{-5} M of monomer units. Curve 1: 4.5°C, curve 2: 8.5°C, curve 3: 13°C. All other conditions as under (a).
(c) Sorption isotherms of ApApC on poly(U). Concentration of poly(U) is 10^{-4} M of monomer units. All other conditions and designations same as for (b).

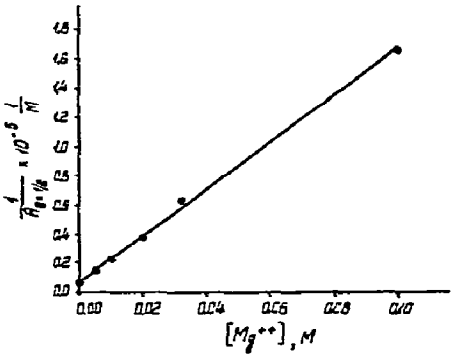

Fig. 2. Dependence of the binding constant of the complex ApApA:2 poly(U) on Mg^{2+} concentration. Buffer same as for fig. 1. T = 26°C. The value of the dissociation constant at 26°C and at zero Mg^{2+} concentration was obtained by extrapolation of measured values for 0, 6.6, 11 and 17°C to 26°C.

Table 3

Thermodynamic characteristics of the interaction of oligonucleotides with polynucleotides computed from experimental sorption isotherms [a]

Oligonucleotide	Mg^{2+} [b] (mole)	T (°C)	$A_{\theta=1/2} \times 10^5$ (mole)	X_A	$-\Delta f$ (cal/mole)	$-\Delta(E+\epsilon)$ [c] (kcal/mole)	$-\Delta S$ [c] (cal/mole deg)	$-(\Delta F)_{13}$°C (kcal/mole)
ApApA [d]	0.000	0.0	1.2	0.5	1100	14.8 ± 1.5	37 ± 5	4.2
		6.6	2.4		1200			
		11.0	2.9		1300			
		17.0	6.1		1350			
ApApA	0.010	13.0	0.6	0.5	1000	27.5 ± 1.5	73 ± 5	6.6
		21.0	2.0		1300			
		26.0	4.9		2400			
ApApA	0.100	26.0	0.7	0.5	1500	35.5 ± 2.5	95 ± 8	8.2
		31.0	1.5		2200			
		37.0	5.6		2200			
ApA	0.100	8.4	0.87	0.5	1300	24.2 ± 1.0	63 ± 3	6.30
		14.0	1.85		2100			
		19.8	4.63		3450			
ApApU	0.100	4.5	6.1	0.6	2400	20.0 ± 3	52 ± 11	5.0
		8.5	9.0		2800			
		13.0	17.7		3000			
ApApC	0.100	4.5	2.25	0.5	1700	26.0 ± 1.7	67 ± 6	6.7
		8.5	4.1		1600			
		13.0	9.0		2100			
ApApA	0.003	0.0	0.36	0.5	1900			6.8 [e]
ApApU	0.003	0.0	68		2600			4.0 [e]
ApApA	0.035	26.0	1.65	0.5	2000			
	0.020	26.0	2.6		1700			
	0.005	26.0	6.63		3600			
$(Ip)_5I$	0.100	0.0	1.25	0.95	1100	25 ± 1.8	68 ± 6.8	5.4
		8.0	4.75	0.92	1200			
		14.0	11.00		1250			
$(Ip)_6$	0.100	0.0	1.25	0.95	1100	25 ± 1.8	68 ± 6.8	5.4
		8.0	4.70	0.92	1200			
		14.0	11.00		1250			
$(Ip)_5I$	0.001	0.0	15.0		700			
	0.003		5.35		1500			
	0.010		2.35		1000			
$(Ip)_6$	0.001	0.0	19.5		1200			
	0.003		7.0		1400			
	0.005		5.0		1800			
	0.010		2.35		1300			
	0.025		1.35		900			
	0.050		1.35		900			

[a] The study of the complex formation was performed in the buffer: 0.1 M NaCl, 0.0005 M EDTA, 0.005 M Tris-HCl (pH 7.2)

[b] Designations: Mg^{2+} total concentration of magnesium in the medium; $A_{\theta=1/2}$ equilibrium concentration of the oligomers in the solution at half saturation of the polymer sites; X_A molar ratio of the oligomer to the polymer in the complex at saturation; f stacking free energy; E binding energy of single oligomer to the polymer; ϵ the stacking energy; S binding entropy of the oligomer to polymer; $(\Delta F)_{13}$°C free binding energy of the oligomer to polymer, computed for 13°C.

[c] The computation of $\Delta(E+\epsilon)$ and ΔS was performed according to eq. (1) by the least squares method.

[d] Data taken from [12].

[e] In this case ΔF is calculated at 0°C.

we can be sure that the isotherms are not distorted by the interaction of oligonucleotides with the gel.

Another control was performed by the variation of the concentration of polynucleotides. Obviously the sorption isotherms must not depend on the concentration of the polymers. This was confirmed by experiments, changing the concentration of the polymer 3 times.

4. Results

Examples of sorption isotherms of the oligomers on polyuridylic acid are given for ApApA in fig. 1a, for ApApU in fig. 1b and for ApApC in fig. 1c, and in fig. 2 (sorption of $(Ip)_5I$ and $(Ip)_6$ on poly(C). Quantitative characteristics of studies of all 37 combinations are listed in table 3.

The binding energy was calculated from

$$A_{\theta=1/2} = k \exp[(E+\epsilon)/RT], \quad (1)$$

where $A_{\theta=1/2}$ is the equilibrium concentration of free oligomers at half saturation of the polymer sites, k is the entropy factor, E the binding energy of a single oligomer to the polymer, ϵ the stacking energy, and θ the fraction of occupied sites on the polymer chain. The free binding energy is

$$\Delta F = RT \ln(A_{\theta=1/2}).$$

The free energy of stacking Δf is computed from

$$(4A\, d\theta/dA)_{\theta=1/2} = \exp[-\Delta f/2RT]. \quad (2)$$

These formulas were derived from the statistical theory of the cooperative sorption isotherm [12, 21, 22].

4.1. Effect of magnesium ions on the interaction of ApApA with poly(U)

From table 3 we see that the stoichiometry of interaction of ApApA with poly(U) remains unchanged, always 1(A):2(U), at different Mg^{2+} concentrations. This is different from the polymeric complex poly(A):poly(U), which changes its composition when the ionic strength increases [22, 23].

We conclude from the same data, that the energy of interaction increases considerably with the concentration of magnesium ions. Simultaneously the entropy decreases.

From the data of table 3 a plot of $1/A_{\theta=1/2}$ for the complex ApApA with poly(C) versus the magnesium concentration C_{Mg} at 26°C was constructed (fig. 2). $1/A_{\theta=1/2}$ has the meaning of the binding constant of oligomers with polynucleotides. The linear dependence of $1/A_{\theta=1/2}$ on magnesium concentration shows that magnesium gets bound to the complex and stabilizes it. It is obvious from this plot that until 0.1 M Mg^{2+} does not saturate the complex because the binding constant goes on increasing proportionally to magnesium concentration. Therefore it is impossible to estimate the dissociation constant of the magnesium complex. It must be larger than 0.1 M.

4.2. Interaction of $(Ip)_5I$ and $(Ip)_6$ with poly(C)

The interaction of $(Ip)_5I$ and $(Ip)_6$ with poly(C) at varying magnesium concentration in solution was also studied.

These complexes are very interesting because they are binary and therefore seem to be adequate models of nucleic acid double helices. It is interesting to compare the adsorption isotherms in the presence of the phosphate end group and in its absence on the 3' end of the oligonucleotides. This allows us to evaluate the contribution of the phosphate groups to the interaction energy and entropy of polynucleotides with oligonucleotides.

The formation of the complex oligo(I):poly(C) at varying magnesium concentration was studied. In fig. 3 are presented adsorption isotherms of $(Ip)_5I$ and $(Ip)_6$ on poly(C) in the presence of 0.1 M Mg^{2+}. The stoichiometry of the complexes is 1(I):1(C) in accord with previous findings [5, 8]. The isotherms of both oligomers on poly(C) coincide entirely at this high magnesium concentration. From these data the values of the energy $\Delta(E+\epsilon)$ and entropy ΔS of complex formation were computed. They are presented in table 3. The value $\Delta(E+\epsilon) = -24.5$ kcal/mole is in agreement with that of Ts'o [8] obtained from melting curves of this complex, analyzed according to [24]. In accord with the data of Ts'o [8] the complex oligo(I):poly(C) proved much less stable than oligo(A):poly(U).

From the curves of fig. 3 free energies of stacking were obtained, which are listed in table 3. They are of

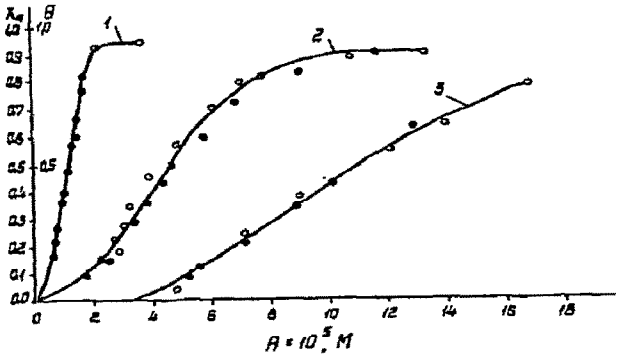

Fig. 3. Sorption isotherms of $(Ip)_5I$ and $(Ip)_6$ on poly(C). Concentration of poly(C) 8×10^{-5} M of monomer units. All other conditions same as for fig. 1b; (•) experimental points for $(Ip)_5I$:poly(C) interaction; (○) experimental points for $(Ip)_6$: poly(C) interaction. Curves 1, 2 and 3 correspond to 0, 8 and 14°C, respectively.

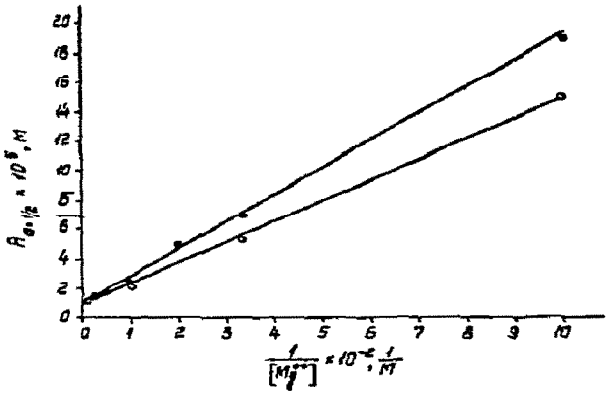

Fig. 5. Plot of dissociation constants of $(Ip)_5I$ and $(Ip)_6$ with poly(C) versus the reciprocal values of magnesium concentration. (○) $(Ip)_5I$:poly(C) interaction; (•) $(Ip)_6$:poly(C) interaction.

the same order as the values found for the triple complex 2 poly(U):oligo(A) and equal to 1.2 kcal/mole.

We measured also sorption isotherms of $(Ip)_5I$ and $(Ip)_6$ on poly(C) at 0°C and different magnesium concentrations in the buffer. The plot of $1/A_{\theta=1/2}$ versus C_{Mg} is presented in fig. 4. Fig. 4 shows that in this case we obtain a curve of the Langmuir type showing saturation. This curve can be described by

$$1/A_{\theta=1/2} = aC_{Mg}/(b + C_{Mg}). \qquad (3)$$

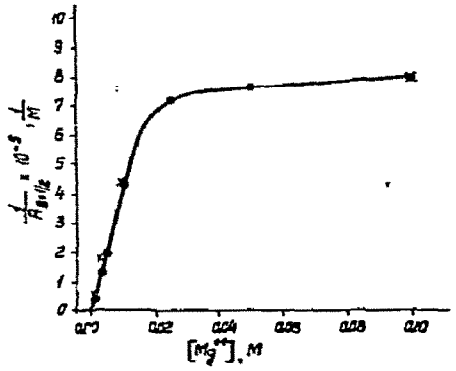

Fig. 4. Plot of reciprocal values of dissociation constants of $(Ip)_5I$ and $(Ip)_6$ with poly(C) versus the total concentration of magnesium in the medium. This curve was constructed according to data from table 3. $T = 0$°C. (×) $(Ip)_5I$:poly(C) interaction; (•) $(Ip)_6$:poly(C) interaction.

Here C_{Mg} is the concentration of Mg^{2+} in solution, and b the dissociation constant of magnesium in a complex with double-stranded oligo(I):poly(C).

In this case we can make a rectilinear plot of the inverse values, i.e., $A_{\theta=1/2}$ versus $1/C_{Mg}$ (fig. 5).

From table 3 and fig. 5 we see that the strength of complexes is the same for $(Ip)_5I$:poly(C) and $(Ip)_6$: poly(C) at high magnesium concentration (0.1 M), but becomes different when the concentration of Mg^{2+} decreases. At 0.001 M Mg^{2+} the contribution of the end phosphate group of $(Ip)_6$ to the binding constant is about 20%.

4.3. Influence of the oligomer size on the thermodynamic characteristics of the complex with polynucleotides

Comparing energies and entropies of the complex of poly(U) with ApApA and ApA in 0.1 M NaCl, 0.1 M $MgCl_2$ at pH 7.2 we find that $\Delta(E + \epsilon)$ and ΔS for one A group are the same and equal to $\Delta(E + \epsilon) = -12$ kcal/mole, and $\Delta S = -31$ cal/mole degree.

4.4. Effect of noncomplementary bases at the 3′ end of the oligonucleotides on the complexing with poly(U)

One of the most interesting points in the interaction of polynucleotides is the behaviour of noncomplementary bases. From data on melting of complexes of poly(U) with the copolymer poly(AG) Uhlenbeck concluded

that up to a definite amount of guanylic acid in the copolymer, the noncomplementary bases are included into the complex [25].

To the same conclusion came Podder, who studied the interaction of two pairs of oligomers: GpGpGpC with GpCpCpC and GpGpGpU with GpCpCpC. He assumed that there is complexing between noncomplementary bases G and U [26].

On the other hand there exist many data showing that the noncomplementary bases are squeezed out of the complex, if they are situated at the end of the oligonucleotide [1, 3, 6].

Our data for the sorption isotherms of ApApC on poly(U) and ApApU on poly(U) in 0.1 M NaCl and 0.1 M $MgCl_2$ (pH 7.2) are presented in fig. 1b and 1c.

The molar ratio of the oligomers to the polymer X_A at saturation, computed for one chain link is 0.6 for ApApU and 0.5 for ApApC. Therefore the stoichiometric ratio of the complex poly(U):ApApC is the same as in poly(U):ApApA, i.e., 2:1. But for the complex poly(U):ApApU the stoichiometric ratio is different, namely 1.67:1.

From these data we conclude that in the case of poly(U):ApApC a perfect ternary complex is formed. Obviously there exist molecular forces binding the cytidylic acid residue in the complex. This reminds one of the rules of wobbling, discovered by Crick. They allow hydrogen bonding of a cytidylic residue at the end of the oligomer with polyuridylic acid [27].

In the case of poly(U):ApApU, the stoichiometric ratio 1.67:1 shows that the complexing of the noncomplementary base is effected partially. At many points the "erroneous" base is squeezed out of the chain. If this were complete, we would have expected a stoichiometric ratio 1.335:1 because each triplet ApApU would then bind a doublet UpUp in each poly(U) chain. Obviously this is not the case and the noncomplementary bases must be partly included into the ternary complex.

If we compare the binding energies $\Delta(E+\epsilon)$ of ApApA, ApApC and ApApU with poly(U), we see that in standard conditions (at 0.1 M $MgCl_2$) the binding energy of the perfectly complementary complex is much larger than that of the erroneous triplets ApApC and ApApU. In the last case the decrease of binding energy is more pronounced (−26 kcal/mole and −20 kcal/mole, respectively, instead of −35.5 kcal/mole). This result is in qualitative agreement with the data of Bautz and Uhlenbeck concerning the dependence of the melting temperature of the complexes poly(U):$(Ap)_nX$ on the specificity of the "wrong" base X [3, 25].

From table 3 the values of ΔS for the three complexes poly(U):ApApA, poly(U):ApApC and poly(U):ApApU are respectively −92, −67, −52 cal/mole degree. The interpretation of these data is not unambiguous. The difference in energy and in entropy losses by the formation of the complexes investigated, reflects the different solvation of the 3′ end bases of the oligonucleotides [28] and a different degree of perfection of the complexes.

4. Discussion

On the basis of eq. (3) the stacking free energy Δf was calculated for all sorption isotherms (table 3). We see that the free energy increases with temperature due to the entropy variation.

It is important to emphasize that in all conditions studied the free energy of stacking is several times smaller than the free energy of complex formation (ΔF is near −8 kcal/mole).

The average value of Δf in our experiments is about −2 kcal/mole, which agrees fairly well with the data obtained by equilirbium dialysis [9−11].

It would be interesting to know the stacking energy, but we cannot obtain it because our measurements are limited to a very narrow temperature range.

The stacking free energy, which is the difference of two much larger terms $\Delta f = \Delta\epsilon - T\Delta S$ is not known with a sufficient degree of precision for the computation of the energy term.

But in any case the stacking is due to hydrophobic interaction of bases and it is well known from the work of Nemethy and Scheraga [29] that the hydrophobic forces are the result of entropy increase of water in the case when hydrophobic parts of molecules come together. The energy change in the case of hydrophobic interactions is small or even positive. Therefore the value −1000, −3000 cal/mole found for the stacking free energy is mainly of an entropy nature. This is important because the energy of complex formation found to be about −13000 cal/mole per nucleotide residue is practically totally explained by hydrogen bonding of the bases; the contribution of stacking energy must be insignificant.

It was estimated earlier from the temperature depen-

dence of CRD spectra of the oligomers ApA and ApApA [30, 31] that there must be an energy barrier of the magnitude of 7000 cal/mole separating both states, the stacked and freely rotating ones. But this is a different situation. In the case of an oligomer surrounded by water the hydrogen bonds of bases are not saturated by interaction with complementary bases. Therefore the energy found in these last experiments is not of a purely hydrophobic interaction. It is connected with the solvation of polar groups and is similar to the hydration energy of bases starting from the crystalline state.

What results from these measurements is that the triplets are already stacked before their sorption on the polymers.

In fact some free rotation inside the oligomers is allowed at the temperatures of our experiments. Computing the contribution of internal rotation to the stacking energy from the data of Brahms et al. [31], we find a small correction of 10–15% to the value discussed above.

We see from table 3 and figs. 2 and 3 that the binding of oligomers to polynucleotide chains depends strongly on magnesium. Obviously electrostatic interaction makes a significant contribution to the energy of the complexes.

There are two modes of binding magnesium to nucleotides. One is ionic exchange with sodium on the phosphate groups, the second is by coordination bonding of nitrogens in adjacent bases. The ionic exchange equilibrium was studied by Krakauer et al. [32, 33]. Obviously the apparent equilibrium constant is strongly dependent on the sodium concentration. For the polynucleotide triple complex poly(A): 2 poly(U) at 0.1 M Na^+, the apparent dissociation constant of Mg^{2+} is about 10^{-2} M. We see that the entire straight line in fig. 3 is above this concentration. We conclude therefore that it is the second equilibrium of magnesium with the nitrogen bases which is important for the formation of the triple helix.

With some metallic ions the formation of bridges between nitrogen atoms of the bases was demonstrated in a straightforward way by X-ray analysis [34]. Up to now this has not been accomplished in the case of magnesium but it seems quite plausible. It is interesting to note that the investigation of the interaction of magnesium with tRNA showed the existence of two kinds of sites for Mg^{2+} binding [35]. It was found that the binding constants for these sites differ by about a factor of 100. It is quite possible that this difference reflects two kinds of magnesium binding with polynucleotides discussed above. In our case a direct measurement of the dissociation constant of the bases with magnesium has to be done. We expect it to be higher than 0.1 M. In the case of the double complex oligo(I):poly(C) the probable value of the dissociation constant of magnesium with the complex is 10^{-2} M, which is not so far from the dissociation constant of Mg^{2+} with the phosphates in the double complex poly(A):poly(U) [32, 33] (in the case for the complex poly(I):poly(C) no data are available, but different complexes must be similar in this respect).

It is seen from fig. 5 that the phosphate group at the end of the oligomers gives a negative contribution to the binding constant of oligo(I) and poly(C), depending on the magnesium concentration.

We have seen that the energy contribution of an adenylic acid residue with 2 uridylic acids is $\Delta(E + \epsilon) = -12$ kcal/mole and $\Delta S = -30$ cal/mole degree at 0.1 M Mg^{2+}. Davidson and Damle [7, 11] obtained for the complex poly(U):adenosine (2U:1A) $\Delta H = -19$ kcal/mole and $\Delta S = -30$ cal/mole degree. The energy of interaction of the poly(U) with adenosine is higher by 6 kcal/mole. This is due to the absence of phosphate groups in adenosine and shows that the repulsion energy is not completely compensated even in the presence of magnesium ions.

Finally we will discuss the effect of an "erroneous" base on the dissociation constant of the complex.

In table 3 the characteristics of sorption for ApApA and ApApU at 0°C and ionic conditions similar to physiologic ones are compared (0.1 M NaCl; 0.003 M $MgCl_2$; pH 7.2). $A_{\theta=1/2}$ is equal to 0.36×10^{-5} M for ApApA:poly(U) and 68×10^{-5} M for ApApU:poly(U). The ratio of binding constants for the "right" and "erroneous" triplets is 200:1. It was shown that the probability of spontaneous mistakes in translation is about 10^{-4} [36]. This high fidelity of the translation mechanism is not accounted for by the molecular forces, which bind the triplet to the complementary polynucleotide. Probably the ribosome participates actively in the interaction of the anticodon with the codon and acts as an additional filter against erroneous binding. Possibly the squeezing of the noncomplementary bases out of the complex becomes very unfavorable in conditions of the ribosomal site, because of steric hindrance.

In any case it is important to know the origin of the free energy barrier, which protects translation against random error.

References

[1] M.N. Lipsett, L.A. Heppel and D.F. Bradley, J. Biol. Chem. 236 (1961) 857.
[2] M.N. Lipsett, J. Biol. Chem. 239 (1964) 1256.
[3] E.K.F. Bautz and F.A. Bautz, Proc. Natl. Acad. Sci. U.S. 52 (1964) 1476.
[4] C.R. Cantor and W.M. Chin, Biopolymers 6 (1968) 1745.
[5] A.M. Michelson and C. Monny, Biochem. Biophys. Acta 149 (1967) 107.
[6] S.K. Podder, Biopolymers 11 (1972) 1395.
[7] V.N. Damle, Biopolymers 11 (1972) 1789.
[8] I. Tazawa, S. Tazawa and P.O.P. Ts'o, J. Mol. Biol. 66 (1972) 115.
[9] W.M. Huang and P.O.P. Ts'o, J. Mol. Biol. 16 (1966) 523.
[10] P.M. Pitha, W.M. Huang and P.O.P. Ts'o, Proc. Natl. Acad. Sci. U.S. 61 (1968) 932.
[11] R.J. Dawies and W. Davidson, Biopolymers 10 (1971) 1455.
[12] S.E. Bresler, V.M. Chernajenko and E.M. Saminsky, Biopolymers 11 (1972) 1541.
[13] J.D. Smith, J. Mol. Biol. 8 (1964) 772.
[14] S. Tazawa, I. Tazawa, J. Alderfer and P.O.P. Ts'o, Biochem. 11 (1972) 3544.
[15] R.V. Tomilinson and G.M. Tener, J. Am. Chem. Soc. 84 (1962) 2644.
[16] C.K. Cantor and I. Tinoco, Biopolymers 5 (1967) 821.
[17] M. Riley, B. Mling and H. Chamberlin, J. Mol. Biol. 20 (1966) 359.
[18] Data for biochemical Research (Oxford University Press, Oxford, 1969).
[19] S.E. Bresler, L.M. Firsov and V.M. Chernajenko, Prikladnaya Biokhimija and Microbiologija (1973) in press.
[20] J. de Bersagues, J. Chromatography 31 (1967) 222.
[21] T. Hill, An introduction in statistical mechanics (Addison-Wesley, Reading, Mass., 1960).
[22] R.F. Stainer and R.F. Beers, Polynucleotides (Elsevier, Amsterdam, 1960) p. 216.
[23] G. Felsenfeld, D.R. Davies and A. Rich, J. Am. Chem. Soc. 79 (1957) 2023.
[24] D.M. Crothers, Biopolymers 10 (1971) 2147.
[25] O. Uhlenbeck, R. Harrison and P. Doty, in: Molecular associations in biology (Academic Press, New York, 1968) p. 107.
[26] S.K. Podder, Nature (New Biology) 232 (1971) 115.
[27] F.H.C. Crick, J. Mol. Biol. 19 (1966) 548.
[28] R.L. Scruggs, E.K. Achter and P.D. Ross, Biopolymers 11 (1972) 1961.
[29] G. Nemethy and H.A. Scheraga, J. Phys. Chem. 66 (1962) 1773.
[30] M.J. Lowe and J.A. Chellman, J. Mol. Biol. 65 (1972) 91.
[31] J. Brahms, A.M. Michelson and K. van Holde, J. Mol. Biol. 15 (1966) 467.
[32] H. Krakauer, Biopolymers 10 (1971) 2459.
[33] B.G. Archer, C.L. Ganey and H. Krakauer, Biopolymers 11 (1972) 781.
[34] P. De Meester, D. Goodgame, D.J. Richman and A.C. Skapsi, Nature 242 (1973) 257;
J.M. Rosenberg, N.C.Seeman, J.J.P. Kim, F.L. Suddath, H.B. Nicholas and A. Rich, Nature 243 (1973) 150.
[35] A. Dauchin, Biopolymers 11 (1972) 1317.
[36] C.L. Loftfild, Biochem. J. 89 (1963) 82.

BIOPHYSICAL CHEMISTRY 1 (1974) 237–241. © NORTH-HOLLAND PUBLISHING COMPANY

SELF-ASSOCIATION STUDIES OF TWO ADENINE DERIVATIVES BY EQUILIBRIUM ULTRACENTRIFUGATION*

Rolf BRETZ, Ariel LUSTIG and Gerhard SCHWARZ**

Department of Biophysical Chemistry, Biocentre of the University of Basel, CH- 4056 Basel, Switzerland

Received 20 September 1973
Revised manuscript received 7 November 1973

Among the purine derivatives, N-6-dimethyladenosine [6-(dimethylamino)-purine-ribonucleoside] and N-6,9-dimethyladenine [6-(methylamino)-9-methyl-purine] show an exceptionally high self-association tendency. The self-association of these two substances was studied by equilibrium ultracentrifugation at several concentrations and temperatures. Thus, the thermodynamic quantities ΔH^0 and ΔS^0 as well as the nonideality parameters could be evaluated. In both cases, the equilibrium constants at 25°C were found to be higher than the values reported in the literature. This may be due to the fact that in our work the influences of nonideality were taken into account.

1. Introduction

Various purine nucleosides and nucleobases were studied by Ts'o et al. [1] as well as Poerschke and Eggers [2]. Among these, N-6-dimethyladenosine [6-(dimethylamino)-purine-ribonucleoside] and N-6, 9-dimethyladenine [6-(methylamino)-9-methyl-purine] exhibit the highest tendency to form linear self-aggregates by "vertical stacking". The thermodynamics of their association was investigated by vapor pressure osmometry, and the results were not corrected for nonideality, although very high concentrations (up to 1 M) had to be used.

As these substances are of high interest, e.g., as model systems in non-enzymic base recognition studies [3], it was desired to obtain more exact parameters describing their thermodynamic behaviour. Hence, the series of ultracentrifugation experiments described below was performed, following the technique of Van Holde and Rossetti [4], which is based on theoretical calculations done by Adams and Williams [5, 6] and takes into account deviations from thermodynamic ideality.

* This work was supported by the Swiss National Foundation (grant No. 3.522.71, Schweizerischer Nationalfonds zur Förderung der wissenschaftlichen Forschung).
** To whom correspondence should be addressed.

2. Experimental

N-6-dimethyladenosine (Merck-Schuchardt) and N-6, 9-dimethyladenine (Cyclo Chemical Co.) were found to be chromatographically pure by thin layer chromatography in two solvent systems (*n*-butanol/acetic acid/water and *n*-butanol/methanol/ammonia/water). Elemental analysis confirmed these results (theoretical values in brackets): 48.88 (48.80)%C, 5.73 (5.80)%H for N-6-dimethyladenosine, 51.55 (51.52)%C, 5.47 (5.56)%H for N-6,9-dimethyladenine. Thus, both substances were used without further purification. All solutions were prepared in bidistilled water on a weight per volume basis. The concentration was controlled each time by diluting an appropriate aliquot and determining the concentration spectrophotometrically. (N-6-dimethyladenosine: ϵ_{275}=18 800 M^{-1} cm^{-1} [7]; N-6,9-dimethyladenine: $\epsilon_{267.5}$ = 17 400 M^{-1} cm^{-1} according to the manufacturer's specifications.)

Partial specific volumes were determined with a digital density measuring device DMA 02 C (Anton Paar KG, Graz, Austria). Repeated experiments gave values of 0.688 ml/g for N-6-dimethyladenosine and 0.731 ml/g for N-6,9-dimethyladenine.

Equilibrium sedimentation was carried out in a Beckman Model E analytical ultracentrifuge equipped

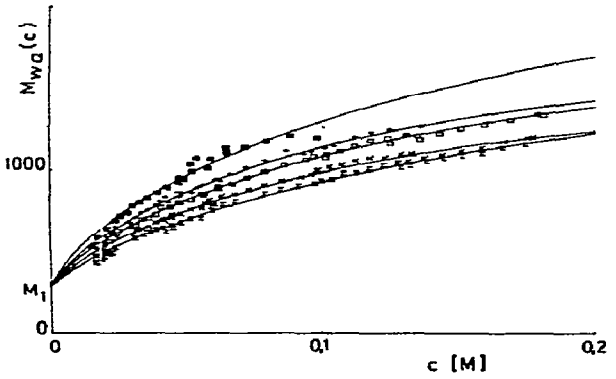

Fig. 1. Apparent weight average molecular weight $[M_{wa}(c)]$ of N-6-dimethyladenosine as a function of the total local concentration (c). Experimental points: ▪ (15°C), + (20°C), □ (25°C), × (30°C), I (35°C). Least squares fit curves at the following temperatures (from top to bottom): 15, 20, 25, 30, and 35°C.

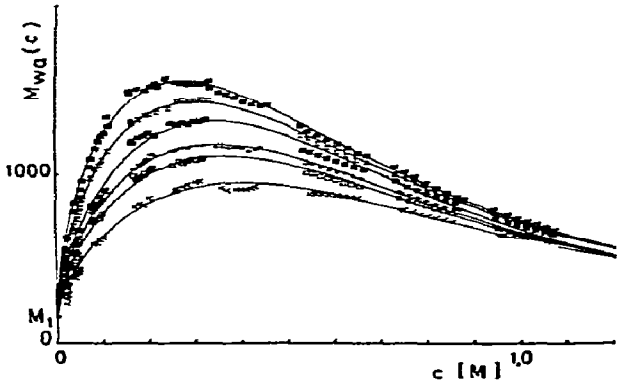

Fig. 2. Apparent weight average molecular weight $[M_{wa}(c)]$ of N-6,9-dimethyladenine as a function of the total local concentration (c). Experimental points: ⧈ (6°C), I (10°C), ▪ (15°C), + (20°C), □ (25°C), × (32°C). Least squares fit curves at the following temperatures (from top to bottom): 6, 10, 15, 20, 25, and 32°C.

with Schlieren optics. To achieve better photographs at high concentrations, the 12 mm Epon Double Sector cell was assembled with a 1° negative radial wedge window.

An An–D aluminium rotor was used for more exact temperature control by means of the RTIC unit. Normally, solution columns of 2 mm length and rotor speeds between 30 000 and 60 000 rpm were used, and sedimentation equilibrium was approached within about 6 hours.

The areas of photographic plates were calibrated in terms of initial concentrations by synthetic boundary experiments in a double sector cell at various concentrations.

3. Results

The apparent molecular weights are shown as a function of the total (local) concentrations in fig. 1 for N-6-dimethyladenosine and in fig. 2 for N-6,9-dimethyladenine. The values were calculated at several radial positions for each run with a WANG 700 desk-top computer by numerical integration of the wire image displacements recorded on the photographic plates. It may be noticed that all points at a certain temperature lie on a single curve (within experimental accuracy), although they are collected from different runs with various starting concentrations.

In the case of N-6,9-dimethyladenine, the curves show a pronounced tendency to fall at higher concentrations, which indicates a strongly nonideal behaviour. Because of the lower solubility of N-6-dimethyladenosine, an analogous curvature is more difficult to observe, although the following analysis of the data proves the influences of nonideality here, too.

In order to explain our data, we use the model of noncooperative, infinite linear association proposed by Ts'o [1], Poerschke and Eggers [2] and Van Holde and Rossetti [4], in which all association steps occur with the same equilibrium constant K

$$A_{n-1} + A \overset{K}{\rightleftharpoons} A_n \qquad (n = 2, 3, \ldots).$$

In addition, we make three assumptions, following the proposal of Van Holde [4]:

(a) The partial specific volume, and

(b) the specific refractive index increment of the solute is not changed by aggregation. The latter assumption is confirmed by the fact that the synthetic boundary experiments did not yield any detectable concentration dependence in the normalized Schlieren signal.

(c) The activity coefficient of the ith species, γ_i, can be expressed as a function of the total concentration in terms of monomeric units by the equation

$$\ln \gamma_i = iB_1M_1c, \quad (1)$$

where M_1 is the molecular weight of the monomer and B_1 is a constant. This expression is consistent with the theory of the virial coefficient in rodlike molecules.

As Adams and Williams [5] show, one gets the equation for the apparent weight average molecular weight $M_{wa}(c)$

$$M_1/M_{wa}(c) = M_1/M_w(c) + B_1M_1c. \quad (2)$$

Herein, $M_w(c)$ is the true weight average molecular weight, which can be expressed as a function of the total (local) concentration c*

$$M_w(c) = \sum_i c_iM_i^2 / \sum_i c_iM_i = 2M_1\sqrt{Kc + \tfrac{1}{4}}. \quad (3)$$

Here, c_i is the molar concentration and M_i the molecular weight of the ith species. This relationship (3) can be derived from the mass conservation law

$$\sum_i ic_i = c, \quad (4)$$

and the mass action equations for every step:

$$a_i/a_{i-1}a_1 = (c_i/c_{i-1}c_1)(\gamma_i/\gamma_{i-1}\gamma_1) = K, \quad (5)$$

where a_i is the activity and γ_i the activity coefficient of the ith species. It may be noticed that the term $\gamma_i/\gamma_{i-1}\gamma_1$ becomes unity according to eq. (1).

In the case of N-6-dimethyladenosine, each set of data points at a single temperature can be fitted by the functional dependency [$M_{wa}(c)$ versus c] resulting from (2) and (3), according to the method of least squares, using a Hewlett–Packard 9810 A desktop computer. The least squares lines obtained are shown in fig. 1, and the resulting values of the equilibrium constant K and B_1M_1 are summarized in table 1(a). Standard errors of estimate of $M_{wa}(c)$ on c were evaluated according to the definition

$$S_{M.c} = \left\{ \sum_{k=1}^{N} [M_{wa}(c_k) - M_k]^2/N \right\}^{1/2}, \quad (6)$$

in which c_k and M_k are the measured data belonging to the kth data pair, N is the number of data pairs at one temperature, and $M_{wa}(c_k)$ means the apparent molecular weight value at the concentration c_k, calculated from eq. (2). The $S_{M.c}$ values (in molecular weight units) are listed in table 1(a).

Table 1
Least squares fit results for N-6-dimethyladenosine

Method of fit	T (°C)	K (M^{-1})	B_1M_1 (M^{-1})	Standard error	Average of the M_k
(a) K and	15	49.6	0.093	37.7	877.3
B_1M_1	20	39.8	0.170	24.1	882.1
varied	25	34.5	0.136	22.5	915.9
	30	28.7	0.178	25.5	835.9
	35	23.5	0.088	20.7	790.3
(b) K varied,	15	50.4	0.133	37.8	877.3
B_1M_1 fixed	20	38.9	0.133	24.4	882.1
(average)	25	34.4	0.133	22.5	915.9
	30	27.6	0.133	26.2	835.9
	35	24.4	0.133	22.3	790.3

The nonideality parameter B_1M_1 does not seem to show any decreasing or increasing temperature dependence. In order to check whether the differences in B_1M_1 are real or just due to experimental scattering, we tried a somewhat modified fit, in which only K was varied, whereas B_1M_1 was taken as a fixed number (equal to the average of the values resulting from the first approach).

As one can see from the $S_{M.c}$ values in table 1(b), an almost equally good fit could be achieved by this procedure, and the differences in the equilibrium constants obtained by both methods are always less than 4%.

The N-6,9-dimethyladenine data cannot be fitted by the model mentioned above, based on eq. (2), but show a remarkable downward deviation from the theoretical curves at higher concentrations, thus indicating even stronger nonideality. Following a proposal of Adams and Williams [5], eq. (1) can be extended to a quadratic term in c:

* The eqs. (1) and (2), as well as eqs. (7) and (8) following below, were originally formulated in terms of weight-per-volume concentrations [5]. As the molecular weight of the monomeric unit is known, they can be easily converted to molar concentrations (moles of monomers/liter), which are used in this work. Thus, the resulting equilibrium constants are directly obtained in the more common (M^{-1}) units.

Table 2
Least squares fit results for N-6,9-dimethyladenine

Method of fit	T (°C)	K (M^{-1})	B_1M_1 (M^{-1})	B_2M_1 (M^{-2})	Standard error	Average of the M_K
(a) K, B_1M_1 and B_2M_1 varied	6	160.7	0.080	0.052	27.3	1150.4
	10	119.6	0.068	0.057	19.1	996.7
	15	82.5	0.036	0.075	31.1	893.5
	20	68.0	0.060	0.063	24.7	875.0
	25	56.4	0.057	0.064	34.2	780.2
	32	38.0	0.063	0.059	29.2	716.4
(b) K varied, B_1M_1 and B_2M_1 fixed	6	149.6	0.061	0.062	33.8	1150.4
	10	117.4	0.061	0.062	19.6	996.7
	15	88.4	0.061	0.062	36.6	893.5
	20	67.5	0.061	0.062	25.0	875.0
	25	56.8	0.061	0.062	34.4	780.2
	32	37.9	0.061	0.062	29.3	716.4

$$\ln \gamma_i = iB_1M_1c + iB_2M_1c^2. \quad (7)$$

This leads to the modified equation

$$M_1/M_{wa}(c) = M_1/M_w(c) + B_1M_1c + 2B_2M_1c^2, \quad (8)$$

whereas the relationships (3), (4), and (5) remain unchanged. Eqs. (8) and (3) can be combined to give an extended expression for $M_{wa}(c)$. The N-6,9-dimethyladenine data can be fitted to this relationship by a least-squares treatment (curves shown in fig. 2), and the resulting parameters and standard errors are listed in table 2(a).

Again, no systematic temperature dependence in B_1M_1 and B_2M_1 could be detected. The results of a second fit with fixed (average) B_1M_1 and B_2M_1 values [cf. table 2(b)] show randomly distributed deviations in K, which are somewhat greater (up to 7.5%) than in the case of N-6-dimethyladenosine. The changes in $S_{M,c}$, however, which represent the quality of the fit, are small.

In order to obtain further thermodynamic information, and also as an additional test for the two models, ln K can be plotted against $1/T$, and in both cases, linear van't Hoff plots are obtained (fig. 3). Thermodynamic parameters ΔH^0 and ΔS^0 for the aggregation process (related to a single step) may be evaluated from the slopes and intercepts of the regression lines. Results are given in table 3.

It may be noticed that the resulting enthalpies and entropies are only slightly changed, if the various B_1M_1 and B_2M_1 values are replaced by their (temperature independent) averages. Especially in the case of N-6,9-dimethyladenine, the K values obtained with fixed coefficients seem to scatter much less with respect to the regression line in the van't Hoff plot.

4. Discussion

The comparison made in table 3 shows that our data for $K_{25°C}$ are consistently higher than those of other authors, although the differences are not very large. It may be seen from eq. (2) [or (8), respectively] for positive B_1 (and B_2) that $M_{wa}(c) < M_w(c)$. The

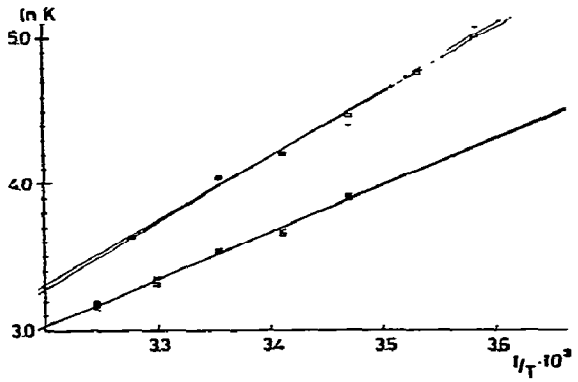

Fig. 3. Van't Hoff plots, ln K versus $1/T$. N-6-dimethyladenosine: (×) K values from fit with B_1M_1 varied; (⊠) K values from fit with B_1M_1 fixed. N-6,9-dimethyladenine: (+) K values from fit with B_1M_1 and B_2M_1 varied; (□) K values from fit with B_1M_1 and B_2M_1 fixed.

Table 3
Thermodynamic parameters

Substance	Method of fit	ΔH^0 (kcal/mole)	ΔS^0 (e.u.)	$K_{25°C}$ $(M^{-1})^{a)}$
N-6-dimethyl-adenosine	K and B_1M_1 varied	−6.4	−14.5	33.8
	K varied, B_1M_1 fixed	−6.3	−14.3	33.9
	cf. Ts'o [1]	–	–	22.2
N-6,9-di-methyladenine	K, B_1M_1, and B_2M_1 varied	−9.0	−22.4	53.5
	K varied, B_1M_1 and B_2M_1 fixed	−8.7	−21.4	54.0
	cf. Poerschke and Eggers [2]	−8.7	−21.6	45.6

a) Value calculated from thermodynamic data.

same relation holds for the number average molecular weights used in vapor pressure osmometry: $M_{na}(c) < M_n(c)$. Thus, if nonideality is neglected, too small values for $M_n(c)$ are employed and consequently too low K values are found by both methods, although the weight average molecular weight is more sensitive to nonideality of the solution [6] as well as to heterogeneity of the solute.

As shown above, the virial coefficients do not exhibit a measurable temperature dependence. On the more common g/ml scale, we find as an average value for N-6-dimethyladenosine: $B_1M_1 = 0.45$ ml/g, and for N-6,9-dimethyladenine: $B_1M_1 = 0.37$ ml/g.

This is of the same order of magnitude as the value of 1.2 ml/g found for purine by Van Holde and Rossetti [4], but is too small to be entirely explained in terms of excluded volume.

The maximum values of the apparent molecular weight obtained for both substances are much higher than the corresponding dimer values. (In the case of N-6,9-dimethyladenine, $M_{wa}(c) \approx 1600$ corresponds to an average chain length of 10.) Thus, a simple monomer–dimer association model can be ruled out directly. As there is no obvious physical reason for an abrupt termination of the association process somewhere beyond the decamer state, a model with infinite association seems to be the most adequate to describe the data.

Certainly, the simplest assumption of equal equilibrium constants for each step is not the only possible one, although it describes the measured data very well. On the other hand, there is neither experimental evidence (e.g., all-or-none behaviour) nor an obvious physical reason for strong cooperativity (or anticooperativity), whereas a possible weak chainlength dependence of the association constant may hardly be detected within the experimental accuracy of the method. In the latter case, the thermodynamic quantities listed in table 3 may serve as average values.

Like many other purine derivatives, N-6-dimethyladenosine and N-6,9-dimethyladenine show negative association enthalpies and entropies, in contrast to other "hydrophobic" compounds (like certain detergents).

As pointed out by Ts'o [8], this different behaviour of the purines cannot be explained by the concept of hydrophobic interactions developed by Kauzmann [9]. Instead, the effect of the reduced surface tension described by Sinanoğlu [10] seems to be a major contribution to the thermodynamic quantities of the two compounds studied in this work.

Acknowledgement

We wish to thank Dr. Maarten P. Heyn for many helpful discussions and Dr. John C. Shepherd for carefully reading the manuscript.

References

[1] A.D. Broom, M.P. Schweizer and P.O.P. Ts'o, J. Am. Chem. Soc. 89 (1967) 3612.
[2] D. Poerschke and F. Eggers, Eur. J. Biochem. 26 (1972) 490.
[3] G.M. Hoffman and D. Poerschke, Biopolymers 12 (1973) 1611 and 1625.
[4] K.E. Van Holde and G.P. Rossetti, Biochemistry 6 (1967) 2189.
[5] E.T. Adams Jr. and J.W. Williams, J. Am. Chem. Soc. 86 (1964) 3454.
[6] E.T. Adams Jr., Biochemistry 4 (1965) 1646.
[7] L.B. Townsend, R.K. Robins, R.N. Loeppky and N.J. Leonard, J. Am. Chem. Soc. 86 (1964) 5320.
[8] P.O.P. Ts'o, in: Fine structure of proteins and nucleic acids, eds. G.D. Fasman and S.N. Timasheff (M. Dekker, New York, 1970) p. 49.
[9] W. Kauzmann, Adv. Prot. Chem. 14 (1959) 1.
[10] O. Sinanoğlu, in: Molecular association in biology, ed. B. Pullman (Academic Press, New York, 1968) p. 427.

BIOPHYSICAL CHEMISTRY 1 (1974) 242–256. © NORTH-HOLLAND PUBLISHING COMPANY

CONFORMATIONAL TRANSITIONS IN A MODEL POLYMER CHAIN WITH SECONDARY AND TERTIARY STRUCTURES

T.M. BIRSHTEIN, A.M. ELYASHEVICH and L.A. MORGENSTERN

Institute of Macromolecular Compounds, the USSR Academy of Sciences, Leningrad, USSR; and the Erevan State University, Erevan, USSR

Received 25 May 1973

The conformational properties of a simulated polymer chain with secondary and tertiary structures are calculated. The calculation is carried out by a Monte-Carlo procedure for a chain on the cubic lattice consisting of 64 links with Zimm–Bragg parameters $s = 0.8–1.3$, $\sigma = 1/64$ and an energy of attraction between links $\epsilon = 0–1.0$.

Different conformational transitions are investigated: helix–coil, coil–globule, coil–crystal, globule–crystal. It is shown that in all cases formation (or destruction) of a crystal-like structure occurs as a jump-like transition.

The results obtained for a model chain are discussed in relation with conformational transitions in globular proteins.

1. Introduction

The characteristic property of polymeric systems is the presence of several levels of molecular ordering. In particular, globular proteins possess both a secondary structure, characterizing a short-range order in a polymer chain, and a tertiary one, determining the spatial arrangement of individual chain segments, given the short-range order. With a change in external conditions proteins may undergo conformation transitions accompanied by a change in the secondary and tertiary structures (denaturation).

Up to the present, however, theoretical consideration has been given only to the transitions in which either the change of the secondary structure alone is taken into account with the possible change of the tertiary structure neglected (the helix–coil transition theories [1, 2]), or else the tertiary structure changes, with the secondary structure invariable (the theory of globule–coil transition [3–5]).

In the present paper we consider a model polymer chain in which the change in characteristic parameters corresponding to the change in the external conditions can lead to the transitions which involve the secondary and the tertiary structure simultaneously.

2. The model description of a macromolecule

Consider a polymer chain whose links may be in either of the two states: that of the helix and that of the coil. The contribution of the secondary structure to the statistical weight of each state of the macromolecule can be taken into account through the Zimm–Bragg parameters s and σ. The statistical weight $s = \exp[-(F_h - F_c)]$ (F_h and F_c are the free energies of a link in the helical and coiled states respectively) is ascribed to each helix-state link, and the statistical weight $\sigma = \exp(-F_{in})$ takes into account the free energy of initiation of a helical region (the values of the free energy and energy are expressed in terms of kT). A decrease in s indicates that the stabilization energy of the secondary structure decreases, which leads to destruction of the structure, while a decrease in σ denotes an increase in co-operativeness of secondary-structure formation.

The contribution of the tertiary structure to statistical weights of different states is associated with the interactions of the links which are widely separated in the chain sequence yet close to one another in space. Here an essential part is played both by the repulsive forces at small distances (the finite volume of links) and the gain in energy on direct contact.

For calculating the partition function and the physical properties of a polymer chain the computer simulating

method was used. Chain links were positioned in cubic lattice points. The helical state of a link corresponded to one step forward on the lattice (the link addition at a valence angle of 180°), the coiled one, each of the four side steps (the link addition at a valence angle of 90°). Thus, the partially helical chain was represented as a sequence of rigid (helical) and flexible (coiled) regions. The step aside was given a statistical weight value of 1/4 (here the total weight of the coiled state is unity as is usually assumed in the theories of helix–coil transition), the step forward was given the statistical weight s, the first step forward after a step aside, the weight σs.

The spatial interactions in the macromolecule were simulated by forbidding two links to occupy one lattice point (self-avoiding walks) and taking into account the interaction of the links occupying neighbouring lattice points. Such a pair of links was assigned an attraction energy $(-\epsilon)$, i.e., a statistical weight $\exp \epsilon$. An increase in ϵ must give rise to formation of intramolecular contacts in the macromolecule, i.e., to the setting-in of a certain tertiary structure. Therefore we shall treat ϵ as the stabilization energy of the tertiary structure.

It should be noted that the contributions of the secondary and tertiary structures to the partition function of the system under consideration are described in terms of the theories of the helix–coil and globule–coil transitions. Therefore at certain values of the parameters our model is reduced to the ones considered earlier. Thus, at $\epsilon = 0$ and "allowedness" of self-intersections, when only the interaction along the chain (parameters s and σ) is taken into account, we obtain a linear co-operative chain undergoing the helix–coil transition, and numerical computation must give the same results that follow from the analytical theory of the helix–coil transition. On the other hand, at $\sigma = 1$ we obtain a chain with random breaks whose rigidity is determined by the value of s. The coil-globule transition associated with the growth of volume interactions in this system was considered earlier [6].

3. Method of computation

To obtain the mean characteristics of the chain for the particular values of the parameters of the secondary (s, σ) and tertiary (ϵ) structures it is necessary to perform an averaging over the ensemble of all self-avoiding conformations of the chain. This ensemble is common for all values of s, σ and ϵ; however, the statistical weights ascribed to various conformations are dependent on s, σ and ϵ. The major contribution to the partition function in each set of s, σ and ϵ is made by a small part of conformations. Therefore appropriately selecting conformations with maximum weight by the Monte-Carlo method we can obtain average characteristics by investigating but a relatively small number (10^4 – 10^5) of different states of the chain. Here sampling can be performed in various ways:

(a) For each set of s, σ, ϵ a separate sampling can be performed [7]. For other sets of parameters this procedure does not give reliable results.

(b) Sampling can be performed for fixed values of s and σ without assigning any determined value to ϵ. For this sampling to be sufficiently representative over a particular range of ϵ variation it is necessary to include in it conformations with a significantly different number of contacts. Such a sampling was performed in [6] using the technique of enriching the ensemble with conformations having a great number of contacts [8].

(c) Sampling can be performed for a fixed value of σ without giving the values of the parameters s and ϵ. Such a sampling should include conformations not only with a varying number of contacts but also with a different degree of helicity. Here the enrichment technique has proved to be insufficient, and so we have developed a subensemble summation method described below. In this method a number of independent samplings are performed yielding conformations with various degrees of helicity, and a sampling ensemble is composed from them in a specified way. The ensemble thus obtained permits the chain characteristics to be calculated over a sufficiently large range of variation of stabilization parameters of the secondary and tertiary structures. We believe this method to be the most adequate for solving the problem of interrelation between the secondary and tertiary structures in conformation transitions.

In order that summation of subensembles should give meaningful results we classified the states of the chain by the degree of helicity θ, the number of contacts m and the number of helical segments n. The partition function of the system Z is written then as follows:

$$Z(s, \sigma, \epsilon) = \sum_{N_h=0}^{N-2} \sum_{n=0}^{N/2} \Omega(N_h, n) s^{N_h} \sigma^n \times \sum_{m=0}^{m_{max}} p_{\theta,n}(m) \exp[m\epsilon], \quad (1)$$

where N is the number of links in the molecule, $N_h = N\theta$ is the number of links in the helical state,

$$\Omega(N_h, n) = \frac{(N_h-1)!\,(N-N_h-1)!}{(N_h-n)!\,(n-1)!\,(N-N_h-n-1)!\,n!} \quad (2)$$

is a combinatory factor taking into account the entropy of mixing of the helical and coiled regions along the chain; $p_{\theta,n}(m)$ is the portion of conformations with the given values of θ and n and with m number of contacts which was approximately calculated by the Monte-Carlo method using the subensemble summation technique.

A number of subensembles consisting of conformations with different values of θ, n and m were generated. The conformations belonging to a particular subensemble were generated via a Markovian process with the stochastic matrix of transition probabilities W:

$$W = \begin{pmatrix} W_{c-c} & W_{c-h} \\ W_{h-c} & W_{h-h} \end{pmatrix}. \quad (3)$$

The conditional probablities W_{c-c}, W_{c-h}, W_{h-c}, W_{h-h} determine the probabilities of annexing a new link in the helical (h) or the coiled (c) state depending on the state of the preceding link. The subensemble generated with the use of the W matrix (for $N \gg 1$) has the same distribution of chains in θ and n characteristic of a statistical ensemble at parameter values $s = \bar{s}$, $\sigma = \bar{\sigma}$ related [2] with the elements of the stochastic matrix:

$$W_{c-c} = 1 - W_{c-h} = 1/(1 + r - q),$$
$$W_{h-h} = 1 - W_{h-c} = (1 - 2q)/(1 + r - q), \quad (4)$$

where

$$r = [\tfrac{1}{4}(1 - \bar{s})^2 + \bar{\sigma}\bar{s}]^{1/2}, \quad q = \tfrac{1}{2}(1 - \bar{s}).$$

The mean values of the degree of helicity and the number of helical segments $\langle\bar{\theta}\rangle$, and $\langle\bar{n}\rangle$ corresponding to the values of $\bar{s}$ and $\bar{\sigma}$ are determined from the formulae

$$\langle\bar{\theta}\rangle = (r - q)/2r,$$
$$\langle\bar{n}\rangle = N(r^2 - q^2)/2r(1 + r - q). \quad (5)$$

In constructing conformations in a subensemble the elimination of the conformations with self-intersections and the enrichment with conformations having a great number of contacts was attained by methods which have been used earlier [8, 9]. At each step of the Markovian chain the analysis of the next possible steps leading to conformations without self-intersections was carried out. Since the number of these steps was different for different conformations, the generated noninteresting chains proved to be nonequiprobable. Therefore each generated conformation is assigned a factor p_R inversely proportional to the probability of this particular conformation generating in this method, and, consequently, the generated chains have the statistical weight corresponding to independent construction.

We also used the enrichment technique. After a definite number of steps (16, 32, 48) the number of contacts between the links was calculated, and if it exceeded the preset values of m_{16}, m_{32}, m_{48}, the conformations were multiplied to T copies. As a result of the procedure the number of generated conformations with a great number of contacts increased sharply, and each conformation obtained by multiplication was to be assigned an additional statistical weight $p_{enr} = 1/T^r$, where r is the number of reproductions. Upon generating individual subensembles their joining together was carried out. To do this, conformations with definite values of θ and n were picked out of all subensembles. The values of $p_{\theta,n}(m)$ were calculated from

$$p_{\theta,n}(m) = \sum_{j=1}^{G_{\theta,n}(m)} p_{R(j)} p_{enr(j)} \Big/ \sum_{j=1}^{G_{\theta,n}} p_{enr(j)}. \quad (6)$$

Here $G_{\theta,n}$ is the total number of generated conformations with definite θ and n, and $G_{\theta,n}(m)$ the number of those among them having m contacts.

Two independent realizations were carried out for a chain consisting of 64 links at $\sigma = 1/64$. The data characterizing the subensembles in these realizations are given in table 1. As analysis has shown, the θ and n distribution functions in generated subensembles overlapped so that the generated chains filled the θ–n phase plane

Table 1
Subensemble characteristics

	$\langle\tilde{\sigma}\rangle$	$\langle\tilde{n}\rangle$	$\tilde{s}$	$\tilde{\sigma}$	m_{16}, m_{32}, m_{48} I	m_{16}, m_{32}, m_{48} II	Number of enrichments in subensembles ($T=50$) I	Number of enrichments in subensembles ($T=50$) II	Number of chains I	Number of chains II	Number of independent chains I	Number of independent chains II [b]
1	0.165	2.5	0.8	0.0156	13, 29, 60	12, 30, 58	9, 24, 0	59, 17, 0	8192	16384	6575	12660
2	0.306	3.2	0.9	0.0156	13, 29, 60	12, 32, 58	5, 60, 1	32, 41, 3	8192	16384	4958	12660
3	0.5	3.6	1.0	0.0156	11, 30, 60	10, 32, 64 [a]	4, 28, 20	63, 83, 64	5504	16384	2956	6125
4	0.67	3.3	1.1	0.0156	13, 30, 60	11, 31, 60	3, 0, 0	18, 0, 0	10880	8192	10733	7310
5	0.795	2.8	1.2	0.0156	13, 30, 60	11, 31, 60	0	11, 0, 0	8192	8192	8192	7653
6	0.875	3.8	1.86	0.07	12, 15, 30	–	0, 32, 50	–	16384	–	10737	–
7	0.825	5.3	1.8	0.11	12, 15, 30	12, 15, 30	0, 16, 10	1, 52, 49	8192	24576	5688	14618
8	0.062	2.0	0.51	0.03	12, 27, 43	12, 27, 43	51, 24, 48	87, 44, 77	16384	24576	10401	14384
Total number of chains									81920	114688	60240	75410

a) The enrichment has been carried out by the total number of contacts and helical links.
b) I, II – two independent realizations.

over the whole range of θ and $n \lesssim 10$. The total ensemble obtained is sufficiently representative within the parameter variation range $0 \leqslant \epsilon \leqslant 1$, $0.8 \leqslant s \leqslant 1.3$. (The limitation on n is inessential, because we consider short chains with $N = 64$ and $\sigma = 1/64$ when the appearance of a greater number of helical regions is scarcely probable.) For this region we calculated the values of free energy and other thermodynamic quantities, mean values of $\langle\theta\rangle$, $\langle n\rangle$, $\langle m\rangle$, and geometric characteristics of the chain: the mean square of the end-to-end distance, $\langle h^2\rangle$, and the mean square radius of gyration, $\langle R^2\rangle$. The θ and m distribution functions were plotted. The evaluation of the accuracy of results obtained was carried out by comparison of the results of two independent realizations. The quantitative discrepancy between them forms a small percentage at $\epsilon = 0$ and somewhat increases with increased ϵ. All the physical effects discussed below are retained in both realizations.

4. The limiting states of the system

We shall begin with analysis of the conformations associated with the limiting values of the parameters s and ϵ under consideration in the present work. These conformations are shown in fig. 1 and their averaged characteristics in table 2.

As is seen from table 2, at $\epsilon = 0$, that is, in the absence of interactions stabilizing the tertiary structure, it is uncoiled conformations with a small number of intermolecular contacts that prove to be the most probable ones. These conformations and the transitions between them are close to those described by conventional theory of helix–coil transitions. A certain difference is due to taking into account the effect of the excluded volume in the system involved (self-intersections are forbidden) so that the characteristics obtained at $\epsilon = 0$ relate to a macromolecule in a good solvent. For comparison table 2 gives the values of conformation characteristics for a chain unperturbed by volume interactions.

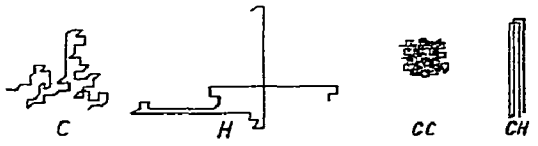

Fig. 1. The limiting conformations of the system.

At a small value of the secondary-structure stabilization parameter $s = 0.8$ the system under study has a low degree of helicity and constitutes a flexible swelled coil. The coefficient of swelling, $\alpha^2 = \langle h^2\rangle/\langle h_0^2\rangle$, i.e., the ratio between the mean square end-to-end dimensions of the chain and the mean square dimensions of the unperturbed chain (index "0") at the same degree of helicity, is equal to 1.5 (for details see appendix). Some deviation from gaussian statistics is also attested by the relation $\langle h^2\rangle/\langle R^2\rangle$ being equal to 6.5, while for the gaussian coil it should be equal to 6. As seen from table 2, a part of this deviation manifests itself also in the absence of volume effects ($\langle h_0^2\rangle/\langle R_0^2\rangle = 6.25$) and is due to the presence of rigid helical regions whose length is comparable to that of the whole chain [10]. The other part of the deviation is associated with the influence of volume effects. For a model chain with $\vartheta = 0$, free from helical regions, with self-intersections forbidden and $\epsilon = 0$, calculation gives $\langle h^2\rangle/\langle R^2\rangle = 6.3$ [11].

At another limiting value of $s = 1.3$ the system is characterized by a high degree of helicity and represents a set of several rigid helical regions with flexible joints. In this case the mean square end-to-end dimensions are greater by an order of magnitude than in the case of macromolecules with $s = 0.8$, and the large value of the relation $\langle h^2\rangle/\langle R^2\rangle$ is an indication of a sharp deviation from gaussian statistics. The values of this relation for the swelled and unperturbed chains being close to each other indicates that such a deviation is mainly due to a high rigidity of the short chain. From now on both the above conformations associated with the assumed limiting values of the secondary-structure stabilization parameter s at $\epsilon = 0$ will be referred to as the coil conformation (C) and the helix conformation (H).

Now consider conformations of the system at a high stabilization energy of the tertiary structure. As is seen from table 2, the common property of these conformations is a high degree of compactness, i.e., small dimensions of the system and a great number of intramolecular contacts. Thus the great value of ϵ determines the formation of compact globular conformations. The average number of intramolecular contacts proves to be practically the same at both the limiting values of the secondary-structure parameter s, whereas the secondary structure in globules is strongly dependent on s. At $s = 0.8$ the degree of helicity is practically zero, i.e., the system does not possess a secondary structure, although at the

Table 2
Conformational characteristics of limiting states

	$\epsilon = 0$		$\epsilon = 1$ [a]	
	$s = 0.8$	$s = 1.3$	$s = 0.8$	$s = 1.3$
$\langle\theta\rangle$	0.23	0.84	0.02 – 0.025	0.78 – 0.86
$\langle n\rangle$	3	2.5	0.8 – 1.0	4.2 – 4.9
$\langle m\rangle$	11	1.8	56 – 59	54 – 57
$\langle h^2\rangle$ [b]	260 (175)	2000 (1630)		
$\langle R^2\rangle$	41 (28)	225 (190)	5.3 – 5.4	18 – 22
$\langle h^2\rangle/\langle R^2\rangle$	6.5 (6.25)	8.9 (8.6)		
S/N [c]	1.3	0.4	1.0	0.2
Structure	expanded, of low helicity	expanded, of high helicity	globular, of low helicity	globular, of high helicity
Structure designation	C	H	GC	GH

[a] For $\epsilon = 1$ values obtained in two realizations are given. For $\epsilon = 0$ both realizations yield the same values.
[b] Bracketed are the values of $\langle h_0^2\rangle$, $\langle R_0^2\rangle$, calculated from the formulae for finite chains [10] and relating to an unperturbed chain at a given $\langle\theta\rangle$.
[c] S stands for the entropy of chain.

same s an expanded conformation C had a helicity degree of 0.23. We shall refer to such a structureless globule whose links feature coil conformations as GC. The geometrical parameters of the GC conformation also indicate that it is nearly spherical in shape. Thus, the magnitude of $\langle R^2\rangle = 5.3$–5.4 is near to the minimum value 4 which corresponds to a close packing of 64 links in a spheric volume.

At the upper limiting value of the stabilization parameter of the secondary structure, $s = 1.3$, the globule designated as GH is of a structure with a high degree of helicity, the same as found in an expanded ($\epsilon = 0$) conformation H. However, in this case, too, we observe a rearrangement of the secondary structure in transition from the expanded to the globular structure: the number of helical regions $\langle n\rangle$ increases.

The globule GH has an asymmetric structure with $\langle R^2\rangle$ greater than that of the globule GC. It is a compact three-dimensional small crystal of four, five rigid rods stuck together (average lengths of the rods are 10 to 13 monomers). For an ideal structure of this kind (4 rigid rods of 14 monomers each, see fig. 1) the number of contacts between the rigid regions would be 61 and $\langle R^2\rangle = 17$.

The results obtained permit some conclusions to be drawn as to the properties of the system under study. They show that there is a strong correlation between the secondary and tertiary structures in macromolecules. Formation of a compact conformation at $\epsilon = 1$ may be accompanied by a marked rearrangement of the secondary structure. At the same time, the initial secondary structure determines the structure of the globule, with the same degree of compactness established in the structureless (GC) and crystal-like (GH) globules, i.e., with equal $\langle m\rangle$.

For more detailed analysis of the behaviour of the system consider the transitions between the limiting states with varying stabilization parameters s and ϵ of the secondary and tertiary structures. We shall consider the transitions due to variation of either parameter, the value of the other parameter fixed.

5. Conformational transitions due to increase of ϵ (s = const)

We shall begin with analysis of the averaged characteristics of the system. Fig. 2 shows the number of contacts $\langle m\rangle$ and the mean square radius of gyration $\langle R^2\rangle$ as functions of ϵ at the two limiting values of s, i.e., the curves of transitions from expanded structures C and H with a small number of contacts to compact

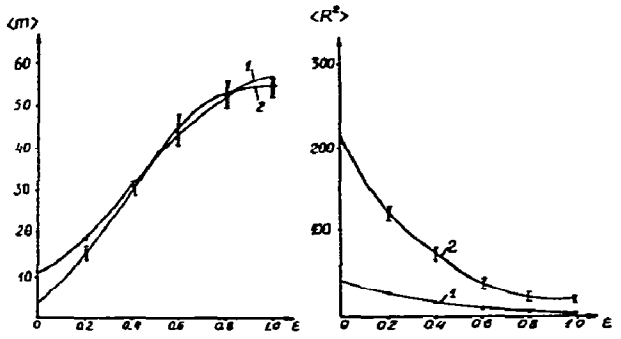

Fig. 2. Plots of the average number of contacts $\langle m \rangle$ and the mean square radius of gyration $\langle R^2 \rangle$ against the stabilization energy of the tertiary structure ϵ at different values of the secondary-structure stabilization parameter s. Curve 1: $s = 0.8$; curve 2: $s = 1.3$.

structures GC and GH with a great number of contacts, respectively.

Fig. 3 shows the degree of helicity characterizing the secondary structure of a molecule as a function of the tertiary-structure stabilization energy. It can be seen that the formation of the tertiary structure caused by increase in ϵ affects the secondary structure of the macromolecule, although the parameters s and σ of the secondary structure remain constant. As has been noted, the degree of helicity $\langle \theta \rangle$ diminishes with the transition C–GC. Formation of compact globules is accompanied by decrease in $\langle \theta \rangle$ also for all molecules with the initial

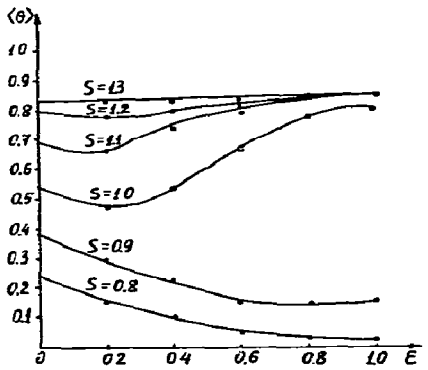

Fig. 3. The mean degree of helicity $\langle \theta \rangle$ versus the tertiary-structure stabilization energy ϵ at different values of the secondary-structure stabilization parameter s.

degree of helicity $\langle \theta \rangle \lesssim 0.5$. On the contrary, for the molecules with an initial value of $0.5 \lesssim \langle \theta \rangle \lesssim 0.8$ ($1.0 \leqslant s \leqslant 1.2$) the degree of helicity increases. In this case the change in $\langle \theta \rangle$ with increasing ϵ is nonmonotonic. At small interaction energies (up to 0.2) the degree of helicity somewhat diminishes with increasing ϵ (it is easier for a more flexible chain to increase the number of contacts), and only for great values of ϵ the requirement for the maximum ordering becomes of crucial importance, leading to an increase in the degree of helicity. For the H–GH transition the degree of helicity is practically constant, and the rearrangement of the secondary structure amounts to a change in the number of helical regions in the chain, this change occuring within a narrow range of ϵ variation (see fig. 4).

More comprehensive data on the nature of transitions is given by the distribution functions for the degree of helicity θ and for the number of intramolecular contacts m. Figs. 5 and 6 present these functions obtained for the whole variation range of stabilization parameters of the secondary and tertiary structures. The upper line in each figure represents the C–GC transition; the lower one, the H–GH transition.

As is seen from fig. 5, there is a radical difference between the C–GC and H–GH transitions. When ϵ increases and a flexible molecule C folds itself into a compact low-helicity conformation GC, a gradual shifting if the distribution function for the number of contacts $\Omega(m)$ in the direction of a greater number of contacts is observed, and, consequently, the C–GC transition is a continuous one.

For H molecules with a high degree of helicity an initial increase in the contact energy up to $\epsilon = 0.4$ also leads to a gradual shift of $\Omega(m)$ in the direction of

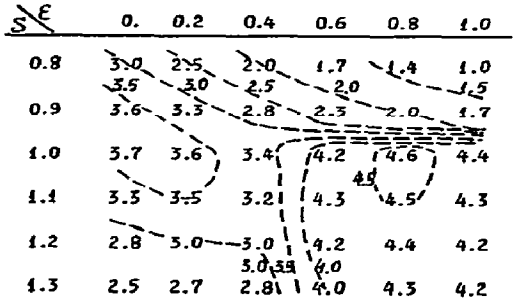

Fig. 4. Average numbers of rigid segments in macromolecules $\langle n \rangle$. The isolines $\langle n \rangle$ are drawn at 0.5 intervals.

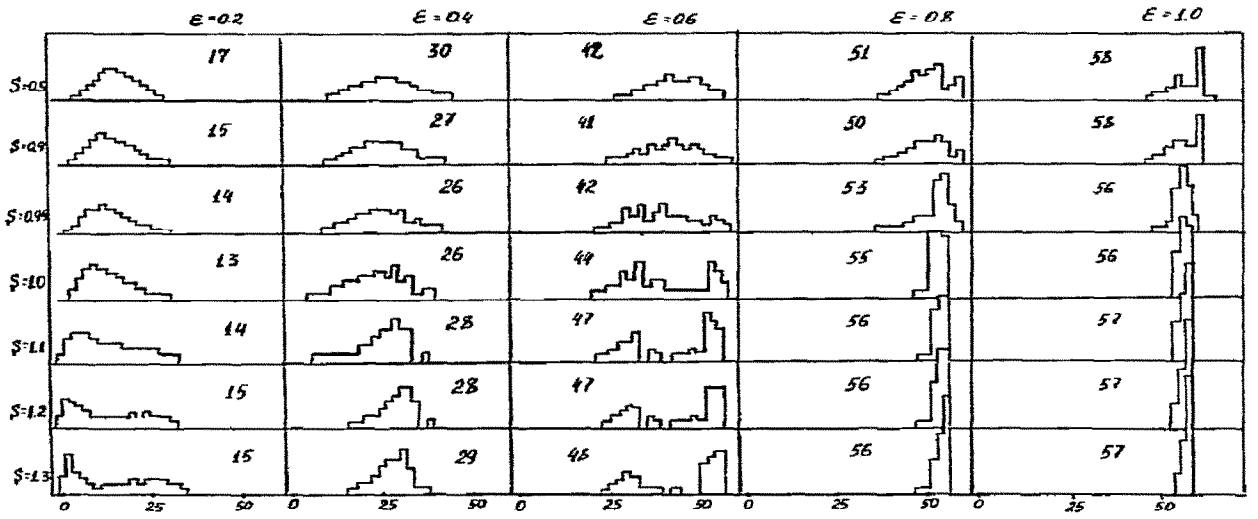

Fig. 5. Distribution functions for the number of contacts $\Omega(m)$. Indicated are the values of $\langle m \rangle$.

greater values of m. The increase in ϵ from 0 to 0.4 involves a gradual transition from the expanded structure H with a small number of contacts $\langle m \rangle = 1.8$ to a more compact partially folded structure H′ with a moderate number of contacts $\langle m \rangle \approx 30$. However, as ϵ increases further, the behaviour of the distribution function $\Omega(m)$ changes drastically. At $\epsilon = 0.6$ alongside the first maximum $\Omega(m)$ corresponding to the conformation H′ and practically retaining the position which it had at $\epsilon = 0.4$, there appears a second maximum in the region of high-compact structures GH with a great number of contacts. Still further increase in energy results in

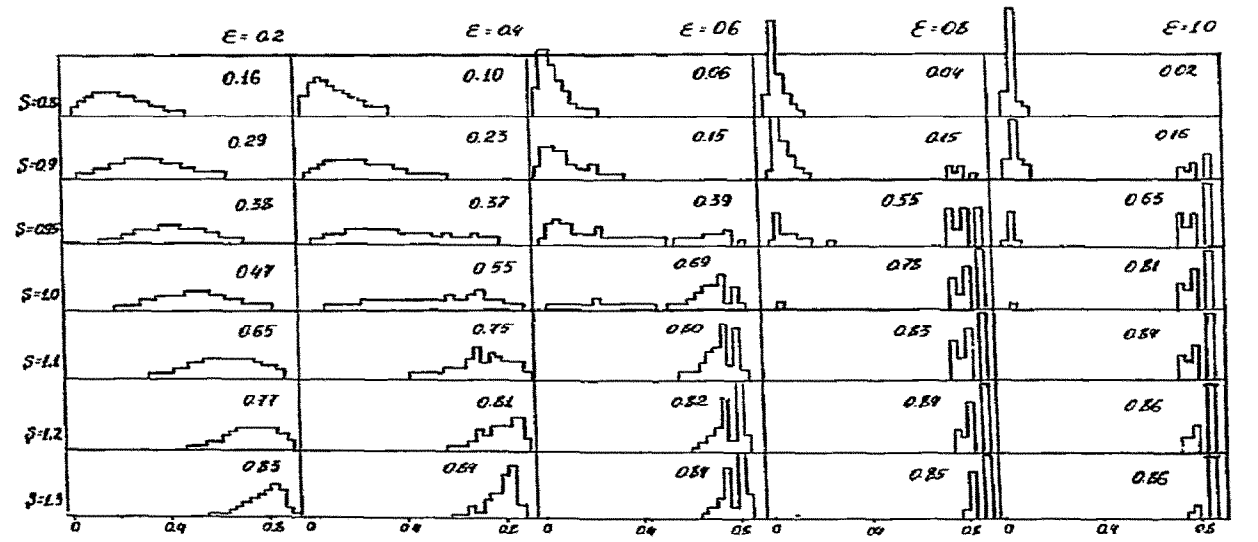

Fig. 6. Distribution functions for the degree of helicity $\Omega(\theta)$. Indicated are the values of $\langle \theta \rangle$.

complete disappearance of the first maximum and sharpening of the second one.

Thus the formation of the GH structure as a result of the chain folding due to an increase in the tertiary-structure stabilization energy, occurs through a jumplike transition which for a small system is an analogue of the first kind phase transition in a large system ($N \to \infty$).

A comparison of the distribution functions $\Omega(m)$ for the two compact structures GC and GH shows that although the average numbers of the contacts are practically the same for both structures, the distribution function $\Omega(m)$ is narrower for the high-helicity GH structure than for the low-helicity GC structure. This points to a lower entropy of the GH conformation, which is due to its crystallike nature. The values of the entropy of the limiting states per monomeric link are given in table 1. They confirm the above conclusion.

As has been noted, the C–GC and H–GH transitions involve a change in average characteristics of the secondary structure. Thus, in transition H–GH the number of rigid helical regions, $\langle n \rangle$, increases. As is seen from fig. 4 this rearrangement of the secondary structure goes along with the jumplike formation of the crystallike structure. The formation of a moderately compact structure H′ during the initial growth of ϵ is not attended with variation of $\langle n \rangle$.

Finally, as fig. 6 shows, formation of compact structures GC and GH is also accompanied by a significant narrowing of the distribution function for the degree of helicity $\Omega(\theta)$. While for the expanded structures C and H the distribution functions $\Omega(\theta)$ are almost overlapping, for the compact structures GC and GH there exist extremely narrow distribution functions for θ according to which an overwhelming majority of the molecules of each given class in compact state are characterized by the same degree of helicity $\theta \approx 0$ in the case of low-helicity molecules GC and $\theta \approx 0.85$ in the case of high-helicity molecules GH.

The influence of the tertiary structure on the secondary structure manifests itself most pronouncedly in the cases when the molecules in the initial expanded state (at $\epsilon = 0$) have a moderate degree of helicity. The behaviour of the distribution functions $\Omega(m)$ and $\Omega(\theta)$ in formation of the compact structures in such molecules can be traced in lines 2–6 in figs. 5 and 6. As is seen from fig. 5, as the secondary-structure stabilization parameter increases, one observes a change in the character of transition to a compact structure with ϵ increasing. At $s = 0.9 - 0.95$, when the initial (at $\epsilon = 0$) degree of helicity $\langle \theta \rangle = 0.38 - 0.46$, there occurs a continuous transition to compact structure, much like the transition C–GC. At $s = 1.0$ ($\langle \theta \rangle = 0.54$ at $\epsilon = 0$) there is a region of ϵ where $\Omega(m)$ has two overlapping maxima. A further increase of s and $\langle \theta \rangle$ leads to separation of the maxima in the transition region and, consequently, for the molecules with the initial degree of helicity $\langle \theta \rangle \geqslant 0.5$ the transition to compact structure with ϵ increasing is always jumplike. It should be noted that for such molecules in a compact conformation the distribution functions for the number of contacts $\Omega(m)$ are narrow and practically coincide with the distribution functions $\Omega(m)$ for a high-helicity conformation GH. This circumstance is directly connected with the results shown in fig. 3 according to which for the molecules with the initial degree of helicity $\langle \theta \rangle \geqslant 0.5$, the degree of helicity in a compact structure grows, approaching the value observed for the conformation GH.

The course of rearrangement of the secondary structure can be analyzed from the data in fig. 6. As is seen, in an intermediate region of $s = 0.95 - 1.0$ ($\langle \theta \rangle = 0.46 - 0.54$ at $\epsilon = 0$), the growth of ϵ results first in broadening of the distribution function $\Omega(\theta)$ (at $\epsilon = 0.4 - 0.6$) and then (at $\epsilon = 0.8 - 1.0$) in its separation into two isolated peaks, corresponding to the high-helicity GH and low-helicity GC structures. Thus it turns out that in a compact state the model molecules under consideration can have but one of the two conformations: a globular one, GC, practically free from the secondary structure, or a crystallike conformation, GH. At extreme values of s only one of these conformations exists; at intermediate values their co-existence is possible.

6. Conformational transitions due to variation of s (ϵ = const)

Now consider transitions at varying s and ϵ = const, i.e., the transitions corresponding to different columns in figs. 5 and 6. The variations in average characteristics of the secondary and tertiary structures in such transitions are shown in figs. 7 and 8.

At $\epsilon = 0$ the $\langle \theta \rangle$ versus s curve, that is, the curve of the transition C–H, corresponds to a usual coil–helix

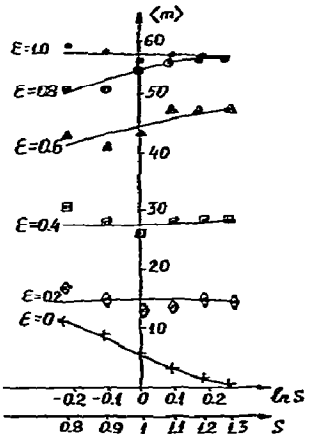

Fig. 7. The average number of contacts $\langle m \rangle$ versus the secondary-structure stabilization parameter s at different values of the tertiary-structure stabilization energy ϵ.

transition. As noted above, however, in contrast to analytical theories which do not take into account volume interactions, the model under consideration retains even at $\epsilon = 0$ the volume interactions due to the chain selfintersections being forbidden. In other words, the analytical theories consider a molecule in the θ-solvent, whereas our model at $\epsilon = 0$ represents a molecule in a good solvent. As is seen from fig. 8 the curve obtained for the C–H transition at $\epsilon = 0$ is

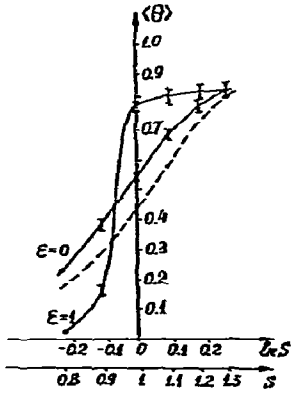

Fig. 8. The mean degree of helicity $\langle \theta \rangle$ versus the secondary-structure stabilization parameter s. The theoretical dependence [10] for $N = 64$ is shown by a dotted line.

displaced from the theoretical curve by a magnitude of the order of 0.1 in ln s units. This displacement is due to the fact that the volume effects, i.e., the forbiddenness of self-intersections limits mainly the set of the effect serves the mean number of contacts at $\epsilon = 0$ which decreases from $\langle m \rangle = 11$ for the C conformation down to $\langle m \rangle = 1.8$ for the H conformation.) Eventually, the free energy of the coil increases and so does the relative stability of the helical state, which leads to displacement of the transition curve. This effect of the solvent quality on the midpoint of the transition should be taken into account in the quantitative treatment of experimental data on helix–coil transitions in polypeptides.

The obtained data concerning the dependence of the size of a macromolecule on $\langle \theta \rangle$ in the presence of volume effects, are discussed in the appendix.

Now consider the transition $\langle \theta \rangle = \langle \theta \rangle (s)$ at a nonzero stabilization energy of the tertiary structure. It follows from fig. 8 that as ϵ increases the transition curve sharpens and shifts to the region of smaller s. The change in the steepness of the transition curve, as seen from fig. 6, is associated with a radical change in the nature of transition. In the C–H transition one observes a gradual displacement of the distribution function for the degree of helicity in the direction of greater θ: the helix–coil transition in an expanded structure is not a phase transition. In the course of the GC–GH transition the distribution functions are divided into two separate peaks corresponding, respectively, to the globular structure GC with a low degree of helicity and the globular structure GH with a high degree of helicity, and consequently the intramolecular crystallization in a compact structure follows the principle "all or none" (cf. ref. [4]). Thus the distinction between the transition curves shown in fig. 8 is due to the fact that the curve for $\epsilon = 0$ describes transitions in a one-dimensional system, whereas the curve for $\epsilon = 1$ describes transitions in a three-dimensional system.

The displacement of the transition curve at $\epsilon = 1$ with respect to the one at $\epsilon = 0$ cannot be explained as a pure energetic effect because the structures GC and GH possess approximately equal numbers of intramolecular contacts. More essential is the fact that the set of conformations corresponding to the GC structure is limited as compared to the one for the C structure. As a result, the crystal-like structure GH arises even at $s = 0.9$ when the probability of the high-helicity state

of the chain in the absence of long-range interactions is negligibly small.

7. The diagram of states

Using the data obtained we can plot the diagram of the states of the system involved over the whole range of variation of the secondary- and tertiary-structure stabilization parameters s and ϵ. Such a diagram is shown in fig. 9. The corners of the diagram correspond, by definition, to the states C, GC, H, and GH schematically shown in fig. 1.

The expanded coiled and helical conformations C and H on the one hand, and the low-helicity expanded and compact conformations C and GC on the other hand, can gradually convert into each other with change in the energy of stabilization of the secondary or the tertiary structure, respectively. A compact high-helicity conformation GH occupies a peculiar position in the diagram of states. Firstly, this conformation proves to be the only stable conformation over a certain range of the s and ϵ parameters. Secondly, the region of stability of the GH conformation borders on transition regions Tr_1 and Tr_2 (see fig. 9) in which the distribution functions $\Omega(\theta)$ or/and $\Omega(m)$ have two separated peaks, i.e., in which the co-existence of the GH conformation with the compact low-helicity conformation GC or the partially folded high-helicity conformation H′ is observed. Thus, no matter in what manner the stabilization parameters of the structures s and ϵ are

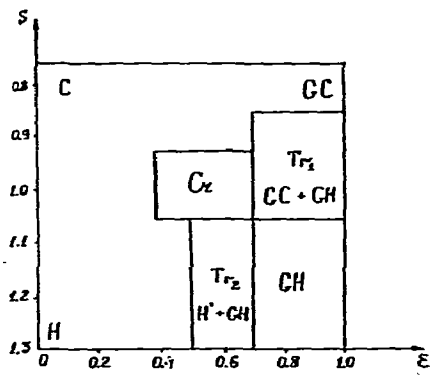

Fig. 9. Diagram of states. Tr_1 and Tr_2 are the regions of co-existence of the GC and GH structures, and the H′ and GH structures, respectively. Cr is the region of critical parameters.

changing, the formation (or destruction) of the high-helicity compact conformation GH occurs via a jump-like transition, and, consequently, the transition to the GH conformation is always of a phase nature.

Consider in more detail the regions (Tr_1 and Tr_2) of co-existence of the structures of different types. We shall begin with the Tr_1 region of co-existence of the GC and GH structures.

From the above data it follows that the tertiary structure of a macromolecule has a marked effect on its secondary structure. At the same time at a high tertiary-structure stabilization energy the average number of intramolecular contacts is practically independent of the secondary-structure stabilization parameter s, i.e., of the initial secondary structure of the macromolecule in an expanded state. This indicates that in the range of high energies of stabilization of the tertiary structure a macromolecular conformation is principally determined by the requirement of the intramolecular packing.

In our treatment of the lattice model for a short chain the requirement for the close packing is fulfilled by compact structures of two types: symmetrical structures with random distribution of the links over the lattive and extended crystal-like structures of several (no less than four) rigid rods. It is these conformations GC and GH that are formed in folding-up of the initially low-helicity and high-helicity macromolecules.

At the same time a short chain consisting of some rigid helical rods alternating with flexible coiled regions of comparable length cannot be effectively packed in the model involved. This leads to variation of the secondary structure with increasing ϵ, that is, to forbiddenness of the states with a medium degree of helicity and co-existence of the GC and GH structures in the Tr_1 region.

As noted above, the intersection of the Tr_1 region owing to an increase in the secondary-structure stabilization parameter s, i.e., in rigidity of the macromolecule, corresponds to the process of intramolecular crystallization due to a change in the character of interactions along the chain. As would be expected, in a three-dimensional globular structure such a transition occurs as a phase one.

We now turn to consideration of the Tr_2 region (fig. 9) where the co-existence of the H′ and GH structures is observed. The phase nature of the transition to a crystal-like structure in rigid chains was first discovered

and comprehensively analyzed in [6]. The H conformations with a high degree of helicity correspond generally to short rigid chains with infrequent breaks. It is the crystal-like GH structure consisting of several (no less than four) rigid segments stuck together that constitutes a stable compact conformation for such chains. As is seen from fig. 5 and the data of [6] the states corresponding to this structure have proved to be separated from the states of an expanded or partially folded chain, i.e., the transition to a crystal-like structure with increase in the energy of stabilization of the tertiary structure is of a jump-like phase nature.

At the same time, as follows from comparison of our data with the data of [6] the distance between the two maxima of the $\Omega(m)$ function in the Tr_2 region is significantly different for different models, i.e., can be strongly dependent from the properties of the macromolecule. Thus in [6] the first maximum is shifted in the direction of a smaller number of contacts ($m \approx 20$) as compared with its position in our case ($m \approx 30$), i.e., in [6] the maxima are separated by a wider distance, which involves a greater steepness of the transition $\langle m \rangle = \langle m \rangle(\epsilon)$ than that observed in our work (cf. fig. 2 with fig. 1 from [6]).

The analysis shows that this is determined by the following differences in the models involved: ref. [6] deals with a non-co-operative ($\sigma = 1$) rigid chain with random breaks (a step aside) having, on the average, 8 breaks at $\epsilon = 0$. In such a chain the folding of the neighbouring rods is only possible on condition that two successive steps at the bending between them be side steps, i.e., on conditions of two breaks merged into one. It is evident that, the probability of each break being small, such an occurrence will be rare enough, owing to which the initial rise in ϵ will not practically lead to any increase in $\langle m \rangle$, and the first maximum of the distribution function will lie within the range of small m.

On the other hand, the crystal-like compact structure is the most favourable structure of the chain from the viewpoint of energy. Also, the formation of this structure in [6] requires only a redistribution of the breaks along the chain without changing their number. In consequence, as is seen from fig. 6 in [6], the formation of a crystal-like structure has proved to be possible beginning with $\epsilon = 0.4$, and at $\epsilon = 0.5$ practically all chains possess such a structure.

Another situation exists in our system. The co-operativeness of the linear structure brings about the fact that the individual side steps are not independent but integrated into flexible coiled regions. Thus, in the H conformation when the mean degree of helicity $\langle \theta \rangle = 0.84$ and the chains comprise 2–3 helical regions on the average (see table 2), each flexible region consists, on the average, of 3–4 links. So the rigid helical regions (rods) are bound by sufficiently flexible joints, which enables then to form contacts with one another easily enough. Therefore, even a small rise in ϵ involves an appreciable increase in $\langle m \rangle$, and the first maximum of the distribution function $\Omega(m)$ corresponding to the H′ conformation lies within the region of greater m than in the above case.

At the same time, formation of the most advantageous (from the energy standpoint) crystal-like structure requires a rearrangement of the secondary structure of the chain. Indeed, in the H and H′ conformations the chain comprises 2–3 helical segments (see table 2 and fig. 4), while for formation of a three-dimensional crystal at least 4 rigid regions are needed. The necessity of an additional break (fig. 4) causes the displacement of the jump-like transition to a crystal-like structure in direction of greater values of ϵ (see fig. 5). It should be noted that the contour $\langle n \rangle = 4$ is practically identical with the border of the GH state in the phase diagram (fig. 9). It is evident that a relatively small change in the parameters of our system (the growth of $N\sqrt{\sigma}$) involving the increase in $\langle n \rangle$ up to a value of 4 at $\epsilon = 0$ led to the adjustment of the initial secondary structure H to the requirements imposed by intramolecular packing in the GH conformation. One can suggest that in this case the formation of the GH conformation would start at a smaller value of ϵ, and the transition $\langle m \rangle = \langle m \rangle(\epsilon)$ would have a steeper curve.

In conclusion of this section it should be noted that in the diagram of states, in the vicinity of the bimodal Tr_1 and Tr_2 regions of the distribution functions $\Omega(\theta)$ and $\Omega(m)$ there exists a region Cr, of the critical values of the parameters ($\epsilon = 0.4$–0.6; $s = 0.95$–1.0), whose distinguishing feature for the systems with finite N is a greater width of the distribution functions [13]. In our system it is most pronounced for the distribution function $\Omega(\theta)$ (fig. 6), broadening markedly in this region and giving an almost equiprobable distribution over the whole range of θ.

8. Conclusion

Now we shall discuss some consequences of the above calculation as applied to real systems.

Although the model under consideration is sufficiently simple and describes the molecule of a homopolymer whose links are located in a regular lattice, the crystal-like structure obtained can serve as a model of a unique structure of globular proteins. An analysis has shown that in compact conformations the main requirements upon the molecular ordering are those imposed by intramolecular packing. These space requirements can dictate to the polymer chain a secondary structure which is disadvantageous from the standpoint of linear short-range interactions. In globular proteins the stable conformation is, of course, not associated with any close packing, but with the packing taking into account the tendency of hydrophobic groups to avoid contact with water and of polar groups to select a water environment. Based upon the space requirements, it has been possible [14, 15] to predict the secondary structure, in particular the position of α-helical regions in globular proteins. And the interesting thing is that α-helixes are generated just in those places along the chain where their formation is advantageous from the viewpoint of linear short-range interactions as well [16]. Thus, in globular proteins one observes a certain co-ordination in the effects of the short-range and long-range interactions which is apparently the result of the evolutionary selection of primary structures. This co-ordination seems to be "redundant" for the globular structures, and a special mechanism responsible for its origination is yet to be found (see [15]).

In our model the process of destruction of a crystal-like conformation due to the change in stabilization parameters of the secondary and tertiary structures may be treated as a simulated process of denaturation of the globular proteins. The different ways of leaving the GH state and, respectively, the different final states, correspond to the action of different agents in denaturation. Thus (see [17]) the increase in temperature seems primarily to weaken the hydrogen bonds and brings about the transition of the GH–GC type in the phase diagram (fig. 9); the organic solvents cause the transition of the GH–H type, urea and guanidine chloride, the transition of the GH–C type, etc. As follows from the data obtained, denaturation always occurs through jump-like destruction of the native structure, though the resultant state may be capable of further substantial rearrangements under the action of the denaturating agent. In our system a similar situation existed with decreasing energy of stabilization of the tertiary structure in a high-helicity chain. The jump-like transition GH–H′ was accompanied by the gradual H′–H transition. As has been shown, the extent of this effect depends on the properties of polymeric chains, so that the quantitative estimate for the proteins calls for a special consideration. At the same time, according to our data the destruction of the secondary structure due to the decrease in its stabilization parameters s (thermal denaturation), is bound to occur by the "all or none" principle, i.e., via the transition between two states. This is in good agreement with the experimental data [17].

The results of our work can also be used for interpreting the experimental data on formation of polymer–oligomer complexes [18, 19]. In [18] the formation is described of 1:1 complexes between matrix molecules of polymetacrilic acid PMAA (M = 190000) and low-molecular polyethyleneglycol PEG (M = 6000–15000). As a result of binding, the matrix assumed a compact conformation. One of the interesting results obtained in [18] is the fact, that in deficiency of PEG an irregular distribution of oligomers over the matrix is observed: one part of PMAA molecules proves to be entirely filled with PEG (about 8–10 molecules of PEG per one PMAA molecule), the other part is practically free of them, i.e., the process of sorption on the matrix is of a phase nature.

The data obtained in the present work together with the data of [20] on simulation of conformational transitions in macromolecules under the action of a binding agent make it possible to formulate the following two conditions which are essential for the process of sorption on a linear flexible matrix to be of a phase nature: (1) the bound region of the matrix must become more rigid with sorption, and (2) there must exist volume attraction between the filled regions, i.e., the sorption must result in formation of compact structures. If these conditions are fulfilled the nature of sorption will be determined by requirements of intramolecular packing which, as shown above, lead to concentration of rigid regions in some macromolecules. It should be noted that in our model the energy ϵ is equal for all the links of the chain. The increase in energy of interaction between rigid filled regions will result in a more pro-

nounced effect of separation of complexes into fractions with filled and vacant matrices.

Acknowledgement

The authors wish to thank V.A. Kabanov, O.B. Ptitsyn, A.M. Skvortsov for helpful discussions.

Appendix

The quality of the solvent influences the mean square end-to-end chain distance $\langle h^2 \rangle$ and its dependence on $\langle \theta \rangle$ (see fig. 10, curve $\epsilon = 0$). For a finite chain in θ-solvent, in the absence of volume effects, the theory of helix–coil transitions taking into account the terms of the order of $1/N\sqrt{\sigma}$ gives [10]

$$\frac{\langle h^2 \rangle}{Nb_0^2(1-\langle\theta\rangle)} = 1 + \frac{2}{\sqrt{\sigma}}\left(\frac{b_1}{b_0}\right)^2 \left(\frac{\langle\theta\rangle}{1-\langle\theta\rangle}\right)^{3/2}, \qquad (7)$$

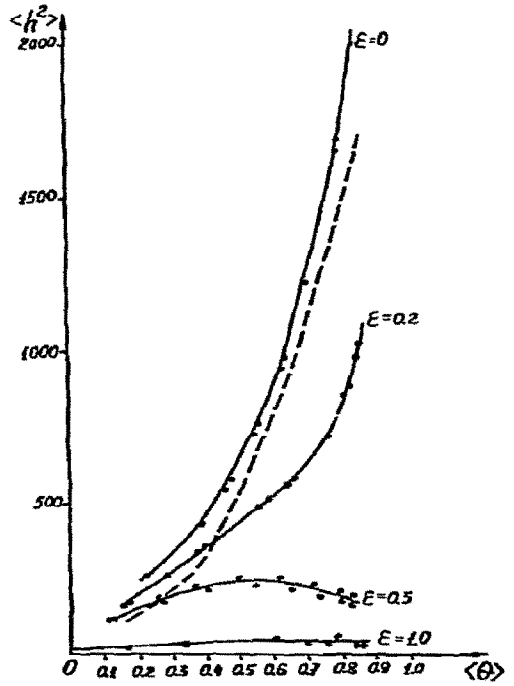

Fig. 10. The mean square end-to-end chain distance $\langle h^2 \rangle$ versus degree of helicity $\langle \theta \rangle$ at different values of the tertiary-structure stabilization energy ϵ. The theoretical dependence [10] for $N = 64$ is shown by a dotted line.

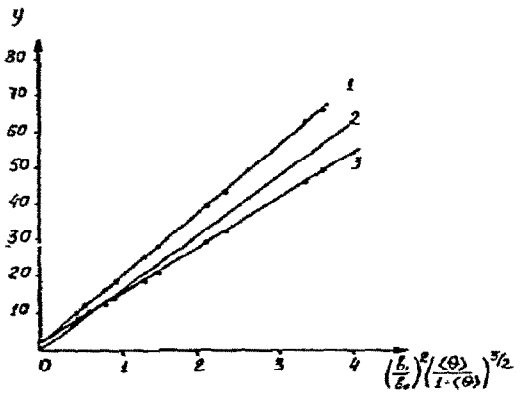

Fig. 11. Plots of the mean square end-to-end chain distance $\langle h^2 \rangle$ (curves 1 and 2) and the mean square radius of gyration $\langle R^2 \rangle$ (curve 3) against the degree of helicity $\langle \theta \rangle$. (1) Calculated values of $\langle h^2 \rangle$, and straight line given in eq. (9). (2) Theoretical plot, eq. (7), for the $\langle h^2 \rangle$ chain free of volume effects. (3) Calculated values of $\langle R^2 \rangle$ and straight line given in eq. (10).

where b_0 is the length of a statistical segment in the coiled chain and b_1 is the projection of a link on the helical axis in the helical chain; in our case $b_0 = b_1 = 1$. Expression (7) is valid in the range of not too large values of $\langle \theta \rangle$. For interpretation of experimental data on helix–coil transitions in polypeptides in good solvents an approximated relation is used which has been obtained by Hagenauer and Miller [12] substituting $\alpha^2 b_0^2$ for b_0^2 in (7), where α^2 is the coefficient of swelling for a pure coiled chain

$$\frac{\langle h^2 \rangle}{N\alpha^2 b_0^2(1-\langle\theta\rangle)} = 1 + \frac{2}{\sqrt{\sigma}}\left(\frac{b_1}{\alpha b_0}\right)^2 \left(\frac{\langle\theta\rangle}{1-\langle\theta\rangle}\right)^{3/2}. \qquad (8)$$

The way of taking into account volume interactions in eq. (8) is based on the assumption that the swelling of the chain consisting of the coiled and helical regions is only associated with the interactions inside the coiled regions, these interactions manifesting themselves through the increasing length of statistical segments in the coil.

To test the validity of eq. (8) the function $\langle h^2 \rangle / N(1-\langle\theta\rangle)$ versus $[\langle\theta\rangle/(1-\langle\theta\rangle)]^{3/2}$ is plotted in fig. 11 from the data obtained for the case $\epsilon = 0$. The results of the computations are well described by the linear dependence

$$\frac{\langle h^2 \rangle}{N(1-\langle\theta\rangle)} = \alpha^2 + 17.5\left(\frac{\langle\theta\rangle}{1-\langle\theta\rangle}\right)^{3/2}, \qquad (9)$$

in agreement with eq. (8) at a value of $\alpha^2 = 2 \pm 0.2$,

although the slope of this curve is somewhat greater than follows from eq. (8), which in our case gives $2/\sqrt{\sigma} = 16$. The obtained value of $\alpha^2 = 2$ agrees well with the value obtained in [11] for a chain with coiled conformations.

A similar result has been obtained for the mean square radius of gyration $\langle R^2 \rangle$. The curve calculated in this work $\langle R^2 \rangle / \frac{1}{6} N(1 - \langle \theta \rangle)$ versus $[\langle \theta \rangle / (1 - \langle \theta \rangle)]^{3/2}$ lies somewhat above the theoretical curve calculated from the formulae equivalent to eqs. (7) and (8) (in the approximation involved,

$$\langle R^2 \rangle = \tfrac{1}{6} \langle h^2 \rangle \left[1 + \frac{2\langle \theta \rangle}{N\sqrt{\sigma}} \left(\frac{\langle \theta \rangle}{1 - \langle \theta \rangle} \right)^{1/2} \right]$$

holds), and can be represented with good accuracy in the form of

$$\frac{6\langle R^2 \rangle}{N(1 - \langle \theta \rangle)} = 2 + 14 \left(\frac{\langle \theta \rangle}{1 - \langle \theta \rangle} \right)^{3/2}. \qquad (10)$$

References

[1] B. Zimm and J. Bragg, J. Chem. Phys. 28 (1958) 1246.
[2] T.M. Birshtein and O.B. Ptitsyn, Conformation of macromolecules (Interscience, NY, 1966).
[3] O.B. Ptitsyn and Yu.E. Eizner, Biofizika 10 (1965) 3.
[4] I.M. Lifshits, Zh. Eksp. Teor. Fiz. 55 (1968) 2408.
[5] Yu.E. Eizner, Vysokomolek. Soyed. A11 (1969) 364.
[6] A.M. Elyashevich and A.M. Skvortsov, Molek. Biol. 5 (1971) 204.
[7] A.K. Kron, O.B. Ptitsyn, A.M. Skvortsov and A.K. Fedorov, Molek. Biol. 1 (1967) 576.
[8] M.N. Rosenbluth and A.W. Rosenbluth, J. Chem. Phys. 23 (1956) 356.
[9] Markov chains and Monte Carlo calculations in polymer chains, ed. G.G. Lowry (Marcel Dekker, New York, 1970).
[10] A. Teramoto, T. Norisuye and H. Fujita, Polymer J. 1 (1970) 55.
[11] A.M. Elyashevich, A.K. Kron and A.K. Fedorov, Vysokomolek. Soyed. A11 (1969) 1875.
[12] G. Hagenauer and W.G. Miller, Biopolymers 9 (1970) 589.
[13] T. Hill, Thermodynamics of small systems (W.A. Benjamin, Inc., Publishers, New York, 1963).
[14] V.I. Lim, IVth Intern. Biophys. Congr., Abstracts of Papers, Moscow, 1972.
[15] O.B. Ptitsyn, IVth Intern. Biophys. Congr., Abstracts of Papers, Moscow, 1972.
[16] O.B. Ptitsyn and A.V. Finkelshtein, Biofizika 15 (1970) 757.
[17] C. Tanford, Advan. Protein Chem. 24 (1969) 45.
[18] I.M. Papisov, V.Yu. Baranovsky, V.Ya. Chernyak, A.D. Antipina and V.A. Kabanov, Dokl. Akad. Nauk SSSR 199 (1971) 1364.
[19] T.M. Birshtein, A.M. Elyashevich and L.A. Morgenstern, Vysokomolek. Soyed. B14 (1972) 487.
[20] T.M. Birshtein, A.M. Elyashevich and A. Melenevsky, Biofizika 18 (1973) 797.

BIOPHYSICAL CHEMISTRY 1 (1974) 257–265. © NORTH-HOLLAND PUBLISHING COMPANY

STRUCTURAL FLEXIBILITY AND FAST PROTON TRANSFER REFLECTED BY THE DIELECTRIC PROPERTIES OF POLY-L-PROLINE IN AQUEOUS SOLUTION*

Gerhard SCHWARZ and Paul-Jörg BAUER
Department of Biophysical Chemistry, Biocentre of the University of Basel, CH-4056 Basel, Switzerland

Received 15 October 1973
Revised manuscript received 16 November 1973

Dielectric dispersion curves for the helix-II form of poly-L-proline in aqueous solution have been determined for various pH in the acid range of zwitterion formation. The results could be excellently described by means of a Cole–Cole dispersion function involving the three parameters $\Delta\epsilon^0$ (total dielectric increment), τ_r (effective rotational relaxation time) and h (characterizing the width of the dispersion region). The quantities τ_r and h were found to be clearly independent of pH and added inert electrolyte. An analysis of the data permits an evaluation of the dipole moments and leads to the conclusion that the molecule cannot be considered to be a completely stretched rigid rod but must be more or less bent. Addition of formic acid slightly below pH 4 caused a distinct broadening of the experimental curves which could be quantitatively interpreted by a second dielectric relaxation process due to orientation of zwitterions by means of fast proton transfer.

1. Introduction

If the dipole moment of a molecule is changed by a chemical reaction, application of an electric field will displace the chemical equilibrium towards greater dielectric polarization. This effect provides another means of dielectric relaxation in addition to the well-known rotational mechanism. It should actually contribute to dielectric dispersion behavior provided the chemical rate process is about as fast or faster than the rotational movement [1]. Such a situation can naturally be expected for fast reactions of macromolecules. As a matter of fact chemically induced dielectric relaxation could indeed be demonstrated with the extremely rapid helix–coil transitions of polyamino acids [2–4].

As was pointed out in a previous article, an analogous effect should occur in a system involving zwitterion formation due to the exchange of protons [5].

* This work was supported by grant Nr. 3.131.69 from the Schweizerischer Nationalfonds zur Förderung der wissenschaftlichen Forschung.

A process of this kind at low pH may be written

$$\underset{(a)}{HZH^+} + A^- \underset{k_{21}}{\overset{k_{12}}{\rightleftharpoons}} \underset{(b)}{ZH^+} + HA \qquad (1)$$

i.e., the non-zwitterion state (a) transfers a proton to the anion A^- thus turning it to the zwitterion state (b) and producing the acid HA. The phenomenon in question requires that at equilibrium appreciable concentrations of all the reaction partners exist. Thus it will be necessary to have a $pH \approx pK_1 \approx pK_A$ (the pK values refer to HZH^+ and HA, respectively). Under these circumstances both rate constants can be assumed to be of an order of magnitude of 10^9 M^{-1} sec^{-1} since the proton transfer is ordinarily diffusion controlled [6]. The theory predicts for the complex dielectric increment

$$\Delta\epsilon^* = \Delta\epsilon_1^0/(1+i\omega\tau_1) + \Delta\epsilon_2^0/(1+i\omega\tau_2), \qquad (2)$$

where the first term is caused by rotational diffusion with a reciprocal relaxation time

$$1/\tau_r = 2D_r, \tag{3}$$

(D_r = rotational diffusion coefficient) while the second one is due to the chemical process. The respective relaxation time is found according to

$$1/\tau_2 = 1/\tau_r + 1/\tau_{ch}, \tag{4}$$

where

$$1/\tau_{ch} = k_{12}c_{A^-} + k_{21}c_{HA} \tag{5}$$

refers to the chemical relaxation time of (1). Furthermore it follows

$$\Delta\epsilon_r^0 = g(N_A c_0/3\epsilon_0 kT)\,(x_1\mu_1 \pm x_2\mu_2)^2, \tag{6}$$

$$\Delta\epsilon_2^0 = g(N_A c_0/3\epsilon_0 kT)\,x_1 x_2(\mu_2 \mp \mu_1)^2, \tag{7}$$

where g is a factor taking into account the effects of the reaction and directing fields, N_A is Avogadro's number, ϵ_0 is the permittivity of vacuum, $c_0 = c_1 + c_2$ is the total weighing-in concentration of the zwitterion forming substance, and $x_1 = c_1/c_0$ and $x_2 = c_2/c_0$ denote the mole fractions of the two individual states. It is assumed here that the dipole moments of both states (having the magnitude μ_1 and μ_2 respectively) are parallel to each other. If they point in the same direction the upper sign in eqs. (6) and (7) holds while the lower one applies to the case of oppositely directed dipoles. We note that the total static dielectric increment

$$\Delta\epsilon^0 = g(N_A c_0/3\epsilon_0 kT)\,(x_1\mu_1^2 + x_2\mu_2^2), \tag{8}$$

turns out to be independent of the chemical effect. The latter can only influence the dispersion properties of the system.

Rod-like macromolecules are known to exhibit rather slow rotational diffusion. If a zwitterion can be formed parallel to the long axis the circumstances would be especially well suited to expect — under proper conditions — a chemically induced contribution to dielectric relaxation which is observable experimentally. Poly-L-proline in aqueous solution appeared to be such a system since this polymer is supposed to be of a fairly rigid helical structure (the so-called helix-II which is characterized by all peptide bonds in the trans configuration) [7].

2. Technical details

2.1. Substances

Three different samples of fairly monodisperse poly-L-proline have been used in the experiments. These were

(i) purchased from Sigma Chem. Co., St. Louis, Miss. (P 2129 Type I lot 49 B-5350): molecular weight 14000;

(ii) donated by Dr. J. Engel, Max-Planck-Institut für Eiweiss- und Lederforschung, Munich: molecular weight 13500;

(iii) synthesized by P. Bader of our laboratory during a visit at Dr. Engel's laboratory: molecular weight 18500;

They are to be denoted by PLP 14000, 13500 and 18500 respectively.

The molecular weight was determined on the basis of equilibrium sedimentation in the ultracentrifuge employing the Yphantis method. Solutions of 1, 0.66, and 0.33% PLP in 0.1 M NaCl showed a slight concentration dependence which was extrapolated to infinite dilution. The thus determined weight average resulted in practically the same values as the number average determined by dielectric end group titration (within the accuracy of measuring of ±5%). This clearly indicates a rather uniform distribution of molecular weight.

The original material was purified by means of gel chromatography (Sephadex G 15, G 25, and G 50) and finally freeze dried. The preparation of the solution was performed by weighing-in of the PLP as a freeze dried substance. An aqueous solution of 10 mg/ml displayed a pH of 4.5 and an electric conductivity of about 1.4×10^{-3} S m^{-1}. Below 5°C and at low salt concentration the helix-II form is well soluble in water (up to about 70 mg/ml). For storage the aqueous solution was frozen and kept at −30°C in order to avoid degradation by germ attack.

Most measurements had to be conducted at the fairly high concentration of 0.4 M (= 38.85 mg/ml). Because of the small supply of polymer it had to be recovered frequently after the measurements by chromatography. This, however, did not affect the quality of the material as was shown by dielectric control ex-

periments.

2.2. Apparatus

The measuring cell was especially designed to utilize the full measuring range of the impedance bridges (filling volume: 6 ml, capacity when empty: 1.32 pF). Both coaxial cylindrical electrodes were made of 0.5 mm sheet platinum with an inner diameter of 19 mm (height: 34.5 mm) for the outer electrode and an outer diameter of 8 mm (height: 19.5 mm) for the inner electrode. All insulating and sealing material was Teflon.

The outer electrode was thermostated by means of a Haake R 20 thermostat (which was cooled by a Lauda TK 30 K cryomat). This permitted a constancy of temperature within ±0.01°C. The temperature (of the outer electrode) was registered by means of a thermistor–resistance measuring bridge.

Depending on the respective frequency range, different impedance measuring equipments had to be employed, namely for

(i) 200 Hz–50 kHz: a Wayne Kerr impedance bridge B 221 plus a Hewlett–Packard 200 CD wide range oscillator and a Rhode and Schwarz UBM tunable resonance amplifier;

(ii) 100 kHz–5 MHz: a Wayne Kerr impedance bridge B 201 plus a Hewlett–Packard 651 B test oscillator and a Rhode and Schwarz USVH selective microvoltmeter;

(iii) 500 kHz–ca. 20 MHz: a Boonton (Hewlett–Packard) RX-Meter 250 B.

Above 50 kHz the measuring cell was connected to the bridges by means of a low inductivity plug which could be opened on one side by an electric screw contact for balancing the bridge.

2.3. Measuring technique

The true capacitance C and conductance G of the completely filled cell can in principle be related to the complex dielectric constant ϵ^* of the solution according to

$$Y = G + i\omega C = G_0 + i\omega\epsilon^* C_0, \tag{9}$$

where G_0 is the static conductance (at $\omega \to 0$) and C_0 the dead capacitance (this neglects the self-inductance of the cell which is justified since even at the highest frequency used the error can be estimated to be a few percent at the most). Due to $\epsilon^* = \epsilon' - i\epsilon''$ the real dielectric constant ϵ' and dielectric loss ϵ'' would then be found as

$$\epsilon' = C/C_0, \qquad \epsilon'' = (G - G_0)/\omega C_0. \tag{10a,b}$$

However, because of possible stray capacitances this was not directly applied in the evaluation of our experimental data. The latter was based on a calibration of the cell by means of an aqueous KCl solution of known conductivity and dielectric constant. This procedure also showed that at lower frequencies (about 10–100 kHz depending on conductivity) electrode polarization may affect the final results. Appropriate means to correct such effects [8] had fortunately not to be employed since the phenomena of interest occurred at higher frequencies where according to the calibration no appreciable polarization exists. The lower frequency values could be extrapolated unambiguously my means of the Cole–Cole function method discussed below.

At higher frequencies (> 100 kHz) the lead inductance L_0 between the bridge and the cell causes deviations of the true values of C and G from the measured ones (C_m, G_m). These have been corrected by means of the relations [9]

$$C = C_m + L_0 G_m^2, \qquad G = G_m(1 - \omega^2 L_0 C_m). \tag{11a,b}$$

In our case, calibration yielded $L_0 = (4.0 \pm 0.2) \times 10^{-8}$ H. With this value the application of (11) is permitted up to about 20 MHz which was indeed the upper bound of frequencies here.

Good measuring accuracy essentially depends on a sufficiently small ratio of the ohmic and capacitive components. We found it necessary to have

$$\tan\delta = G/\omega C \lesssim 10^2, \tag{12}$$

where δ is the loss angle. This clearly demonstrates that small frequencies as well as high conductivity lead to unfavorable condition. Typical values (for the polymer plus acid/base system) were $G = 6$ mS and $C = 100$ pF which apparently implies a $\tan\delta$ around $10^7/\nu$. Thus a frequency $\nu \gtrsim 100$ kHz would be required. Under these circumstances the poly-L-proline already dis-

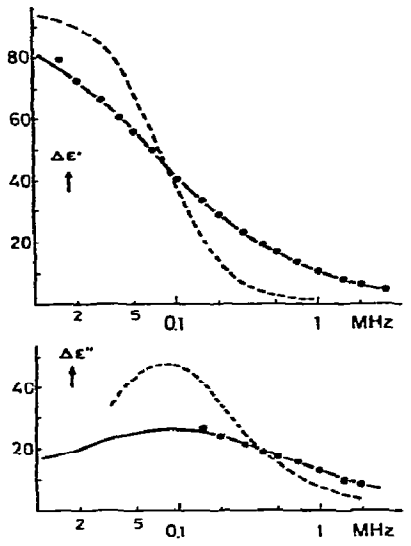

Fig. 1. Dielectric dispersion curves of 0.4 M PLP 18500 in aqueous solution at 25°C. The solid curves represent a Cole–Cole function with $\Delta\epsilon^0 = 96$, $\nu_r = 1/2\pi\tau_r = 80$ kHz and $h = 0.35$. The dashed curves are equivalent Debye functions ($h = 0$).

plays appreciable dispersion so that the question of extrapolation towards the low-frequency limits of dielectric properties arises. This problem could be satisfactorily solved by means of the special evaluation method described below.

The (real) dielectric constant ϵ' is comparatively easy to measure at higher frequencies (> 300 kHz). The experimental values can be reproduced with very little error (< 0.4%). On the other hand, the dielectric loss ϵ'' of conductive solutions is usually much more difficult to obtain with reasonable accuracy.

2.4. Evaluation of experimental data

The polymer in solution without any additional electrolyte exhibits a fairly low conductivity. This made it possible to conduct measurements also at lower frequencies (≳ 10 kHz). As is obvious from the results shown in fig. 1 the dielectric dispersion cannot be described by a simple Debye function. Using a desk computer the data can, however, be excellently fitted with the Cole–Cole function

$$\epsilon^* - \epsilon_\infty = \Delta\epsilon^* = \Delta\epsilon_r^0/[1 + (i\omega\tau_r)^{1-h}], \qquad (13)$$

with ϵ_∞ the high-frequency limit of the dielectric constant. The three parameters $\Delta\epsilon_r^0$, τ_r, and h are determined by the magnitude, position and width of the dispersion step, respectively. For this reason they can be evaluated rather accurately from the experimental curves (an error in one of them cannot be balanced by adjusting the other ones).

It must be emphasized that according to experimental tests the addition of inert electrolyte (measurements up to 0.02 M were possible) as well as strong acid (to regulate the pH) had absolutely no effect on τ_r and h, i.e., the distribution of relaxation times is not altered. Only $\Delta\epsilon_r^0$ is affected provided a variation of pH occurs which changes the number of zwitterions. A chemical contribution to dielectric relaxation as discussed in the introduction should, however, at least result in an apparent broadening of the dispersion range (if there is no clear splitting in two separate ranges). Thus the experimental curves must no longer be expected to be fitted with the original τ_r and h if a suitable partner for proton transfer is added at appropriate pH. Such a phenomenon has indeed been observed by us. As far as the quantitative analysis is concerned the eqs. (2)–(8) are apparently not direcly applicable since they do not take into account the actual distribution of relaxation times.

We have reason to believe that the observed relaxation spectrum is due to a certain – though comparatively limited – distribution of lengths of the polymer molecules (see further below). We assume that the rotational part of $\Delta\epsilon^*$ is still described by the same τ_r and h as determined without the special admixture. This seems to be justified in view of the above mentioned fact that a variety of added substances did not affect these parameters. Thus we put

$$\Delta\epsilon^* = \Delta\epsilon_r^0/[1 + (i\omega\tau_r)^{1-h}] + \Delta\epsilon_2^0/(1 + i\omega\tau_2), \qquad (14)$$

with the eqs. (4) as well as (6)–(8) still applicable, though the τ_r as well as μ_1, μ_2 are taken as mean values. Since τ_2 is essentially determined by τ_{ch} which is not affected by the particle lengths, no relaxation spectrum has been taken into account regarding the second term.

Now we may determine τ_r, h, μ_1 (at low pH where only protonated PLP exists, i.e., $x_1 = 1$) and μ_2 (at

high pH where only zwitterionic pH PLP is encountered, i.e., $x_2 = 1$) under the condition that no proton transfer partner is added. After its addition extrapolation of the dielectric increment towards $\omega = 0$ can be performed using (14) with only order of magnitude knowledge about τ_2 (since it has little effect on the dispersion at lower frequencies). The result of this extrapolation (i.e., $\Delta\epsilon^0$) is used to determine x_1 (and $x_2 = 1 - x_1$) by means of eq. (8). This method yields much more accurate values than a calculation based on a pH measurement which was found to be difficult to conduct without affecting the essential properties of the system.

Once all the above mentioned parameters are known the entire experimental dispersion curve can be fitted by means of eq. (14) with τ_2 as the only adjustable parameter. This procedure proved to be very successful in the evaluation of the chemically induced relaxation effect at various weighing-in concentrations of the added acid–base material and a number of different pH values (with corresponding values of x_1). At first glance it may appear to be more appropriate to evaluate the effect in question by subtracting the $\Delta\epsilon^*$ without the admixture from the total $\Delta\epsilon^*$ measured after its addition. This, however, was practically not feasible since upon such operation some change of pH (which affects $\Delta\epsilon^0$!) cannot be avoided.

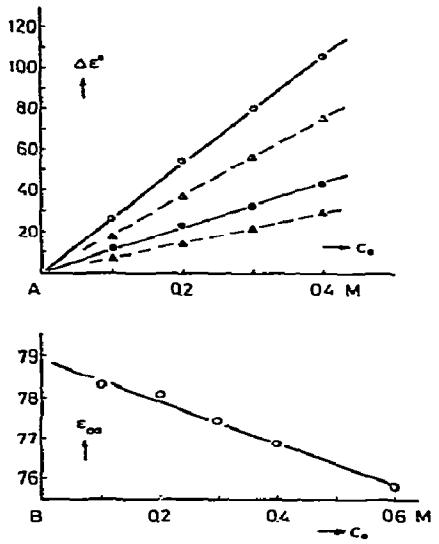

Fig. 2. (A) Concentration dependence of the total dielectric increment at neutral pH ≈ 4.5 (open points) and acidic pH ≈ 3.0 (solid points) for PLP 18500 (circles) and PLP 13500 (triangles). (B) Concentration dependence of the high-frequency limit of the dielectric constant for PLP 13500.

3. Results and discussion

3.1. Dielectric constants of the pure polymer system

First the real dielectric constant ϵ' of the polymer by itself in aqueous solution was measured as a function of frequency (between 10 kHz and 20 MHz) for various pH and concentrations ($c_0 = 0.1, 0.2, 0.3$, and 0.4 M) at 25°C. At given pH the static dielectric increment $\Delta\epsilon^0$ proved to be strictly proportional to c_0 within measuring accuracy. This can be seen in fig. 2A for the upper and lower limiting values of $\Delta\epsilon^0$ at neutral ($\gtrsim 5$) and acidic ($\lesssim 3$) pH, respectively. Such pH dependence of $\Delta\epsilon^0$ is of course associated with the dissociation of the carboxylic end group and the formation of the zwitterion dipole.

The high-frequency limit of the dielectric constant, ϵ_∞, is reached at about 20 MHz. As is shown in fig. 2B there is a linear decrease with increasing c_0 which can be written

$$\epsilon_\infty = \epsilon_w - \beta c_0. \tag{15}$$

The quantity ϵ_w agrees quite well with the dielectric constant of pure water while we obtain $\beta = 5.1\ \mathrm{M}^{-1}$. This effect can readily be interpreted by the exclusion of water because of the presence of the polymer. If the fraction of excluded water is denoted α and we simply assume a superposition of the dielectric polarizations of polyproline and water it follows that

$$\epsilon_\infty = \alpha\epsilon_p + (1-\alpha)\epsilon_w = \epsilon_w - \alpha(\epsilon_w - \epsilon_p). \tag{16}$$

With $\bar{v}$ and M_p being the partial specific volume and the residue molecular weight, respectively, we have apparently

$$\alpha = M_p \bar{v} c_0, \tag{17}$$

so that

$$\beta = M_p(\epsilon_w - \epsilon_p)\,\bar{v}. \qquad (18)$$

Using the recently determined value of $\bar{v} = 0.74\,cm^3/g$ (which is believed to be quite accurate because of the especially careful measurements) [10] we obtain

$$\epsilon_p \approx 8.$$

This appears to be somewhat greater than could be explained by purely atomic and electronic polarization. There seems to be some solvent effect which leads to an increased apparent dielectric constant of the polymer. Actually we must expect the water structure in the vicinity of the polymer to be enhanced by hydrophobic interaction. Since this would be accompanied by an increase of volume which is included in the measured value of $\bar{v}$, the actual $\bar{v}$ to be inserted in eq. (18) should be less than the value used above. Indeed we obtain the more plausible result

$$\epsilon_p \approx 3-4,$$

if $\bar{v} = 0.70\ cm^3/g$ is employed (which also agrees better with the X-ray data of the polyproline structure [11]).

The pH dependence of $\Delta\epsilon^0$ provides an excellent means to determine the pK value of the carboxylic end group of the polymer. According to (8) we have

$$\Delta\epsilon^0 = \Delta\epsilon_n^0 + (\Delta\epsilon_z^0 - \Delta\epsilon_n^0)x_2, \qquad (19)$$

with the subscripts n and z referring to the pure non-zwitterionic and zwitterionic states, respectively. Since

$$\log [x_2/(1-x_2)] = \mathrm{pH} - \mathrm{pK}, \qquad (20)$$

we may evaluate the pK from the experimental data as demonstrated in fig. 3. The pH measurements have been carried out with a Polymetron pH meter which was calibrated with pH standards of pH 4.00 and 6.88 (accuracy being ± 0.07 pH units). For the two samples PLP 13500 and PLP 18500 we consistently found

$$\mathrm{pK} = 3.90 \pm 0.07,$$

while in the case of PLP 14000 the rather low value of 3.55 was indicated. Potentiometric titration by means of a Polymetron automatic pulse burette Type

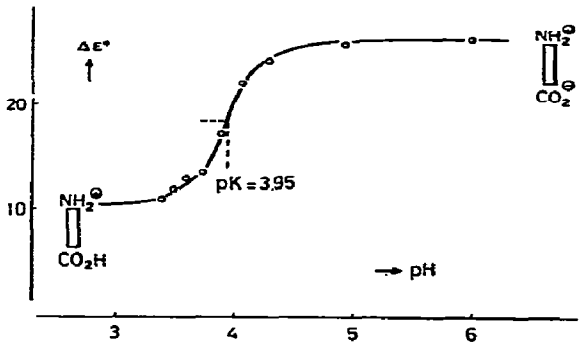

Fig. 3. Dielectric titration curve of a 0.1 M solution of PLP 18500.

111 confirmed these results, though this method proved to be much less sensitive than the dielectric titration.

Assuming that all polymer molecules have one acidic group, the amount of acid required to turn the zwitterion into the non-zwitterion state permits a determination of the degree of polymerization. There is very good agreement with the results of ultracentrifugation as far as the PLP 13500 and PLP 18500 are concerned. In these cases we may therefore be certain that we really deal with polyprolin chains carrying only one acidic group of a pK = 3.90. For the molecular weight of the PLP 14000 the much lower value of 11500 was obtained by means of the end group titration method. Obviously an appreciable fraction of the polymer molecules must have more than one acidic group in this case. This also explains the low pK of 3.55 mentioned above. A comparatively small number of defects during synthesis leading to the incorporation of some acidic groups with a pK $\lesssim$ 3 could indeed cause such effects while it would practically not affect most of the other properties of the macromolecule.

3.2. Rotational diffusion coefficients and dipole moments

An average rotational diffusion coefficient of the polymer can be immediately determined on the basis of the relation [5]

$$D_r = 1/2\tau_r\,. \qquad (21)$$

It is known that D_r decreases at higher concentrations due to macromolecular interactions [12]. With an extrapolated value

$$D_r^0 = \lim_{c_0 \to 0} D_r , \tag{22}$$

we may write

$$D_r = D_r^0 f(N, c_0), \tag{23}$$

where N denotes the degree of polymerization. On the basis of our data for PLP 13500 and PLP 18500 in aqueous solution at 25°C we were able to fit the experimental points (up to $c_0 = 0.8$ M) within less than 1% by the empirical function

$$f(N, c_0) = 1 - a_1 N c_0 + a_2 N^{3.5} c_0^2, \tag{24}$$

where c_0 is measured in mg/ml and

$$a_1 = 8.46 \times 10^{-5} \text{ ml/mg}, \tag{25}$$

$$a_2 = 1.26 \times 10^{-12} (\text{ml/mg})^2. \tag{26}$$

The extrapolated D_r^0 values can be assumed to be essentially determined by the length of the particle. If we approximate it by an extremely extended rotational ellipsoid we may set [13]

$$D_r^0 = (3kT/2\pi\eta_0 L^3)(2 \ln 2p - 1), \tag{27}$$

where η_0 (= 0.89 cP at 25°C) stands for the viscosity of the solvent (water), L denotes the total length and p the ratio of the axes (here we have $p = L/d$, d being the diameter). Clearly this is very sensitive to the extent to which the polymer is stretched out. The maximum vlue of $L = Nl_0$ ($l_0 = 3.12$ Å being the length per residue according to X-ray analysis [11]) is naturally to be expected for a completely rigid rod. Actually we have found considerably smaller effective lengths by applying eq. (27) to our extrapolated D_r^0. The quantity

$$q = D_r^0(\text{eff})/D_r^0(\text{rigid}) \tag{28}$$

turned out as 10 (PLP 14000), 6.5 (PLP 13500), and 4.5 (PLP 18500), respectively. Recalling the obvious deviations from a Debye relaxation behavior we must conclude that a distribution of effective lengths of the polyproline molecules exists with an average value of 60% of the theoretical maximum (PLP 18500) or less. Since we know that this effect can hardly be due to a distribution of molecular weight it obviously indicates a certain degree of flexibility of the helical structure. The particularly large q for PLP 14000 may well be accounted for by breaks in the structure due to defects during synthesis as pointed out above. Minor structural deficiencies because of insufficient quality of synthesis cannot be excluded completely for the two other samples and may possibly have a slight effect on the measured q values. However, the observed flexibility is doubtless an intrinsic property even of the ideal helix-II structure. The theory indeed predicts that at least for sufficiently long chains appreciable bending must occur. This is quantitatively expressed by the so-called characteristic ratio [14]

$$r = \langle l^2 \rangle / N l_0^2 , \tag{29}$$

where $\langle l^2 \rangle$ is the mean square of the individual end-to-end distances. This r would be equal to N at low molecular weight (rigid rod) and approach an asymptotic value at $N \to \infty$ (complete flexibility). Numerical calculations of $r(N)$ for the polyproline helix-II have led to quite different results [15, 16] because of different assumptions on basic structural data. We obtain for PLP 18500 $r = 67$ (if we put $\langle l^2 \rangle = L^2$) which agrees fairly well with the theoretical curve of Schimmel and Flory [15] while it is in clear contrast to the results of Mattice and Mandelkern [16].

Turning now to the question of dipole moments we note that even the isolated non-zwitterionic state of poly-L-proline should have a permanent dipole moment becuase of the charge distribution about the peptide bond. On the basis of the atomic coordinates of the helix-II structure a dipole moment of 3.1 D per residue was calculated [17]. It points from the carbon to the nitrogen atom at an angle of 73.1° from the helix axis. The axial component thus amounts to 0.9 D.

Experimental values of the dipole moments in aqueous solutions can be evaluated from the measured $\Delta\epsilon^0$ using relation (8). Because of the approximately rod-like nature of the polymer we may assume $g = 1$. Then we obtain for

PLP 13500: $\mu_1 = 409$ D, $\mu_2 = 652$ D,

PLP 18500: $= 578$ D, $= 903$ D. (30)

Dividing these values by N (= 140 and 190, respectively) yields apparent dipole moments per residue which are certainly much smaller than the real values because of the pronounced flexibility of the macromolecules. This may be approximately corrected by employing an effective number of residues, $N' = L/l_0$, resulting in $\mu_1 = 5.2$ D per residue (±5%) and $\mu_2 = 8.2$ D per residue (±5%), no matter which of the two polymer samples is used. At any rate, it is quite obvious that the dipole moment contributed by the polymer must be considerably greater than the 0.9 D predicted in vacuum. This can only be due to interaction with the solvent.

As is to be pointed out below, μ_1 and μ_2 have the same direction, so that $\mu_2 - \mu_1$ is identical with the zwitterion dipole (C→N). The moment of this dipole is now readily evaluated as 243 D (PLP 13500) and 325 D (PLP 18500). These values are evidently much smaller than the theoretical maximum (i.e. one elementary charge times L) of 1126 D and 1645 D, respectively, indicating rather strong electrostatic screening.

3.3. Chemically induced dielectric relaxation

According to the theory, dielectric relaxation due to proton transfer can be expected here around a pH of 3.9 (= pK) if a suitable acid/base system (of similar pK) is added. We have chosen formic acid ($pK_A = 3.75$). For the sake of good measuring accuracy, only experiments at a high concentration (0.4 M) of polyproline (PLP 13500 and PLP 18500) have been carried out. The necessary variations of pH and c_A^0 (= $c_A + c_{HA}$, i.e., weighing-in concentration of formic acid) turned out to be restricted by the fact that the conductivity of the system must not be too high in order to permit sufficiently accurate measurements. Under the circumstances we were able to work within the ranges of pH 3.2 – 3.85 and $c_A^0 \lesssim 10^{-2}$ M.

As a matter of fact we did not observe a distinctly separated second dispersion step but only a significant broadening of the dispersion curves. This implies that the two dipole moments μ_1 and μ_2 must have the same direction because otherwise a quite spectacular effect would have to be observed.

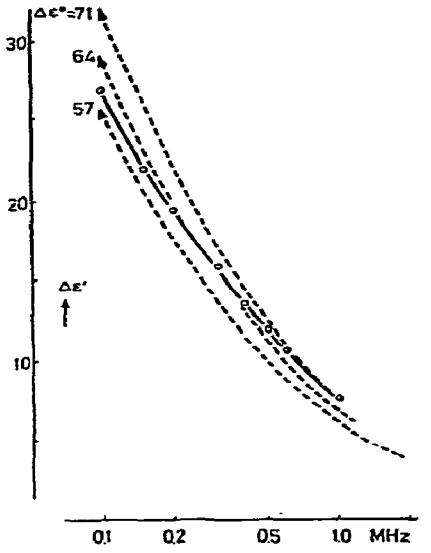

Fig. 4. Broadening of the dispersion curve for 0.4 M PLP 18500 at pH 3.8 after addition of 10^{-2} M formic acid. The dashed curves correspond to $\nu_r = 80$ kHz and $h = 0.35$ as well as assuming $\nu_{ch} = (2\pi\tau_{ch})^{-1} = 0$. Adjusting ν_{ch} appropriately yields the solid curve.

The broadening effect is demonstrated in fig. 4. It must be emphasized that it is absolutely beyond the inaccuracy of measuring and cannot be induced by electrolytes not able to exchange a proton with the zwitterion (as was stated already before, see the section on evaluation of experimental data). Since all the parameters to be inserted in (14) are known except τ_2 we may attempt to fit the experimental curves with $\nu_{ch} = (2\pi\tau_{ch})^{-1}$ as an adjustable parameter. As can be seen in fig. 5 this is very well possible, although mostly only with ϵ' because of the greater uncertainty in the determination of ϵ''.

Owing to pH ≈ pK ≈ pK_A we may put $k_{12} \approx k_{21}$ so that the reciprocal chemical relaxation time

$$1/\tau_{ch} = k_{12} c_A^0 \tag{31}$$

must be expected to be proportional to c_A^0. Our data actually comply with this relationship within the accuracy of evaluation as is shown by the example in fig. 6. Taking into account the experiments with both

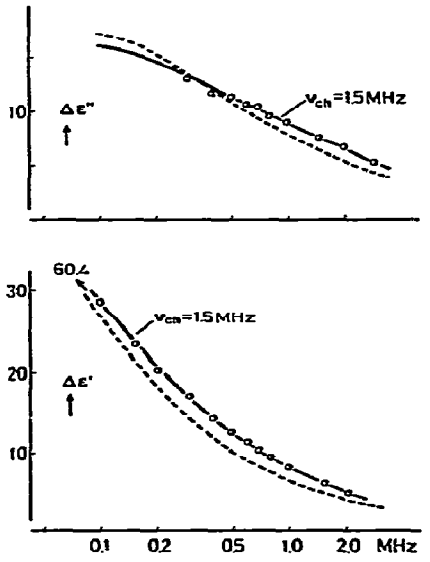

Fig. 5. Fitting of the dispersion curves for a 0.4 M solution of PLP 18500 with $c_A^0 = 10^{-2}$ M at pH 3.8 using the theoretical function (14) with a ν_{ch} = 1.5 MHz. The unaffected curves are indicated by the dashed lines.

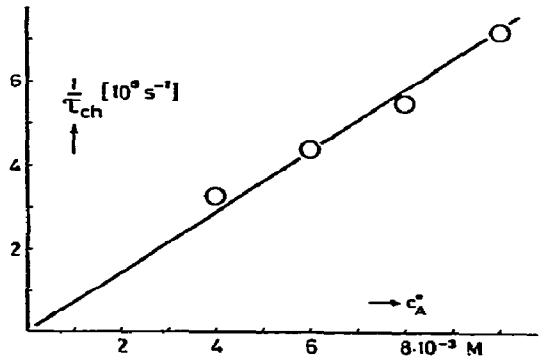

Fig. 6. Reciprocal chemical relaxation times as evaluated from the broadening of dielectric dispersion versus weighing-in concentration of the formic acid.

samples of polyproline we obtain

$$k_{12} = 1 \times 10^9 \text{ M}^{-1} \text{ sec}^{-1}, \quad (\pm 25\%), \tag{32}$$

which is in very good agreement with the order of magnitude of rate constants observed for similar proton transfer processes [6].

Acknowledgement

The authors would like to express their thanks for the excellent technical assistance of Mr. P. Bader (synthesis of PLP 18500) and Mr. A Lustig (ultracentrifugation work). They also acknowledge their gratitude to Dr. J. Engel for stimulating discussions, donation of the PLP 13500 and allowing the synthesis of PLP 18500 in his laboratory.

References

[1] G. Schwarz, J. Phys. Chem. 71 (1967) 4021.
[2] G. Schwarz and J. Seelig, Biopolymers 6 (1968) 1263.
[3] A. Wada, Chem. Phys. Letters 8 (1971) 211.
[4] A. Wada, T. Tanaka and H. Kihara, Biopolymers 11 (1972) 587.
[5] G. Schwarz, J. Phys. Chem. 74 (1970) 654.
[6] M. Eigen, Discussions Faraday Soc. 39 (1965) 7.
[7] L. Mandelkern, in: Poly-α-amino acids, ed. G.D. Fasman (M. Dekker, New York, 1967) p. 675.
[8] H.P. Schwan, in: Physical techniques in biological research, Vol. VI/B (Academic Press, New York, 1963).
[9] H. Pauly, L. Packer and H.P. Schwan, J. Biophys. Biochem. Cytol. 7 (1960) 589.
[10] S. Knof and J. Engel, Israel J. Chem., in press.
[11] P.M. Cowan and S. McGavin, Nature 176 (1955) 501.
[12] M. Joly, Kolloid-Z. 126 (1951) 77.
[13] R. Gans, Ann. Physik 86 IV. Folge (1928) 652.
[14] P.J. Flory, Statistical mechanics of chain molecules (Interscience, New York, 1968).
[15] P.R. Schimmel and P.J. Flory, Proc. Natl. Acad. Sci. U.S. 58 (1967) 52.
[16] W.L. Mattice and L. Mandelkern, J. Am. Chem. Soc. 93 (1971) 1769.
[17] G. Krause, Ph.D. Thesis, Univ. Munich (1970).

BIOPHYSICAL CHEMISTRY 1 (1974) 266–278. © NORTH-HOLLAND PUBLISHING COMPANY

THE FLUORESCENCE ANISOTROPY DECAY DUE TO ENERGY TRANSFERS OCCURRING IN THE ETHIDIUM BROMIDE–DNA COMPLEX. DETERMINATION OF THE DEFORMATION ANGLE OF THE DNA HELIX

D. GENEST, Ph. WAHL and J.C. AUCHET
Centre de Biophysique Moléculaire, 45045 Orléans Cedex, France

Received 9 May 1973

It has been shown in a preceding work that the fluorescence anisotropy decay of ethidium bromide–DNA complex is accelerated by energy migration between dyes bound to the same DNA molecule. In the present work, this result is confirmed. A quantitative analysis has been performed in the following way. The spectroscopic term of the transfer rate constant has been accurately reevaluated by quantum yield and spectral measurements. One assumes that the dye intercalates between two adjacent base pairs and that its distribution is random along the DNA molecule. One introduces the deformation angle δ of the DNA helix induced by the ethidium bromide intercalation. For several values of δ, the energy migration contribution to the anisotropy decay is computed by a Monte Carlo method. In multiplying these computed functions by the measured brownian anisotropy, one obtains the anisotropy decay curve. Comparison with the experimental data leads to the conclusion that the ethidium bromide molecule unwinds the DNA helix by an angle $\delta = -16°$. This result is in agreement with the work of other authors. We think that the method used here may provide accurate information on the spatial distribution of an array of chromophores bound to a rigid structure.

1. Introduction

Lerman [1] has proposed an intercalation model for dye–DNA complexes, which supposes an unwinding of the double helix of DNA. Fuller and Waring [2], Crothers [3] and Bauer and Vinograd [4] have specified this model. A dye molecule is inserted between two adjacent base pairs of DNA, which causes a separation of these two base pairs, and two adjacent chromophores must be separated by at least two base pairs. More recently, Paoletti and Le Pecq [5] have put this model in doubt. They measured the static polarization of the ethidium bromide–DNA complex as a function of the P/D ratio (number of nucleotides per bound dye). These experiments have been interpreted in calculating the influence of energy migration on the fluorescence polarization by an interesting Monte Carlo method. Comparison of experiment with computation leads the authors to conclude that the DNA helix is wound with a winding angle of 13°.

In a previous work [6, 7] we have shown that there was an increase in fluorescence anisotropy decay of ethidium bromide bound to DNA when the P/D ratio decreased. We attributed this phenomenon to migration of the energy between dye molecules bound to the same DNA molecule. We are able to interpret the data obtained with values of P/D equal to or greater than 20, by calculation based on a Förster-type approximation, the energy migration occurs only between the two neighbouring chromophores, and a continuous dye distribution along the DNA helix is assumed. A discrepancy was noted between the calculated curves and experiment when P/D became smaller than 20. Evidently the approximation is not sufficient in these cases, and a more accurate model is needed.

In the present work, we extend our measurements to a still smaller range of P/D values. Some preliminary results have already been given [7].

We have also reevaluated accurately the spectroscopic term of the transfer rate constant.

In order to interpret the experimental data, we

adopt the model used by Paoletti and Le Pecq [5] which takes into account the torsional angle of the DNA helix induced by ethidium bromide intercalation. We too use a Monte Carlo method of calculation but our method of simulation is different. To compute the anisotropy decay, we must simulate the time course of the energy migration, whereas a time average determination only was performed in Paoletti and Le Pecq's calculations.

2. Theory

2.1. Geometrical model of ethidium bromide–DNA complex

The intercalation model has been adopted [1, 2, 5]. A dye molecule is inserted between two adjacent base pairs, with the restriction that two successive sites cannot be occupied. This model is schematized in fig. 1. It is supposed that the phenanthridinium plane is perpendicular to the helix axis [8], and that the transition moment of ethidium bromide lies in the phenanthridinium ring. This assumption is supported by a recent theoretical work of Giacomoni and Le Bret [9]. If no chromophore is inserted between two base pairs, the distance between these pairs is 3.4 Å, and they make an angle $\alpha = 36°$. When a dye molecule inserts, the distance becomes 6.8 Å and the angle becomes $\beta = \alpha + \delta$. If β is smaller than α, then δ is negative and we will say that there is unwinding of the DNA helix. If β is greater than α, then δ is positive and we will say that there is winding of the helix.

These angles must be considered as average angles since we know that the ethidium bromide molecules and probably also the base pairs perform a local brownian motion [10]. It is also assumed that all the chromophores have an identical position in the DNA helix.

2.2. The rate constant of energy transfer

When a chromophore A is excited by a photon, the excitation energy may migrate to another chromophore B [11–14]. The rate of transfer has been given by Förster [12, 13]

$$V = (c/n_1^4)\,(\kappa^2/R_{AB}^6)\,(J/\tau_0), \qquad (1)$$

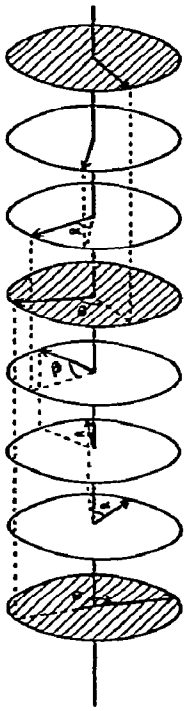

Fig. 1. Model of the ethidium bromide–DNA complex. The shaded discs represent ethidium bromide molecules. The clear discs are the base pairs of DNA. The distance between two adjacent discs is 3.4 Å.

where $c = \frac{9000}{128} \log 10/\pi^5 N$ is a universal constant, N being Avogadro's number; n_1 is the refractive index of the medium; J/τ_0 is a factor which depends only on the spectral properties of the dye: τ_0 is the natural lifetime of the excited state and J is the overlap integral defined by

$$J = \int_0^\infty \bar{\nu}^{-4} F(\bar{\nu})\, \epsilon(\bar{\nu})\, d\bar{\nu}\,, \qquad (2)$$

where $F(\bar{\nu})$ is the fluorescence intensity at wavenumber $\bar{\nu}$. $F(\bar{\nu})$ is such that $\int_0^\infty F(\bar{\nu})\, d\bar{\nu} = 1$. $\epsilon(\bar{\nu})$ is the molar extinction coefficient. The factor κ^2/R_{AB}^6 depends only on the relative position of the two chromophores A and B. R_{AB} is the distance between the two dye molecules and κ is an angular factor defined by

$$\kappa = \cos\theta - 3\cos\theta_A \cos\theta_B, \qquad (3)$$

where θ is the angle between the dipolar moments of

transition of A and B, and θ_A and θ_B are respectively the angles made by these moments with the line joining A and B. With the model defined above, eq. (3) becomes: $\kappa = \cos\theta$, since $\cos\theta_A = \cos\theta_B = 0$.

We can write expression (1) as follows

$$V = k_T \cos^2\theta / R_{AB}^6, \tag{4}$$

with

$$k_T = (c/n_1^4)(J/\tau_0), \tag{5}$$

k_T is a constant for a given chromophore in a given medium.

In order to compare our data with the data found in the literature, we shall compute the critical distance of transfer R_0, which is defined as the distance where the frequency of transfers is equal to the frequency of deactivation by the other processes. This condition gives $V = \tau^{-1}$, where τ is the actual lifetime of fluorescence. In addition, one usually assumes $\kappa^2 = \frac{2}{3}$. Then the eqs. (1) and (5) immediately lead to the relation

$$R_0 = (\tfrac{2}{3} k_T \tau)^{1/6}.$$

One must point out that the factor n_1^4 which enters in the expressions (1) and (5) has been obtained under the following conditions: the chromophores are dispersed in an homogeneous, isotrope and continuous medium. These conditions are not fulfilled in the cases studied here. However, it seems reasonable to admit that the expression is still valuable, if n_1 is taken as the average refractive index of the DNA molecule.

2.3. Definition of the anisotropy of fluorescence for excitation by polarized light

Let a fluorescent solution be excited by a horizontal light beam polarized vertically. If one observes the emitted light at right angles to the direction of excitation one can measure $I_\parallel(t)$ and $I_\perp(t)$ which are the components of the fluorescence parallel and perpendicular to the direction of polarization of the exciting light. The anisotropy is then defined by

$$r(t) = [I_\parallel(t) - I_\perp(t)]/[I_\parallel(t) + 2I_\perp(t)].$$

In our model, two factors influence the time course of the fluorescence depolarization: (1) local brownian motion of the dye, and (2) energy transfer between dyes bound to the same DNA molecule. We assume that these two factors may be separated and that the anisotropy decay may be written as [15]

$$r(t) = r_B(t) r_T(t), \tag{6}$$

where $r_B(t)$ is the brownian anisotropy decay and $r_T(t)$ the anisotropy decay due to transfers.

2.4. The Monte Carlo method

The Monte Carlo method is used to determine $r_T(t)$. One first generates a configuration of the ethidium bromide–DNA complex characterized by a given distribution of the dye molecules on the DNA helix. Then, the time course of the energy migration is simulated for this configuration and the emission anisotropy calculated. The process is repeated a great number of times and the value of the average anisotropy computed. We now describe the calculation in more detail (fig. 2).

2.4.1. Generation of a configuration

The principle has been described by Paoletti and Le Pecq [5]. A DNA segment containing 200 sites is considered. The probability that a site j is occupied, is

$$p_j = (D/P)/(\tfrac{1}{2} - D/P),$$

if there is the restriction that two successive sites cannot be occupied. Each site is tested by comparing its probability of occupation p_j to a random number η_j picked out of the interval [0, 1]. If $\eta_j > p_j$, we impose the condition that site j is not occupied and we test the site $j + 1$ in the same way. If $\eta_j \leq p_j$, we impose the condition that site j is occupied and that the site $j + 1$ is not occupied. Then we test the site $j + 2$.

2.4.2. Simulation of the migration for a given configuration

2.4.2.1. Initiation of the migration. It is assumed that at time zero, the chromophore occupying the most central site absorbs a photon. The location of this dye is taken as the origin of distances on the DNA chain. Its transition moment defines the origin of the angles which characterize the angular positions of chromophores L.

2.4.2.2. A step in the migration. Let us assume that at

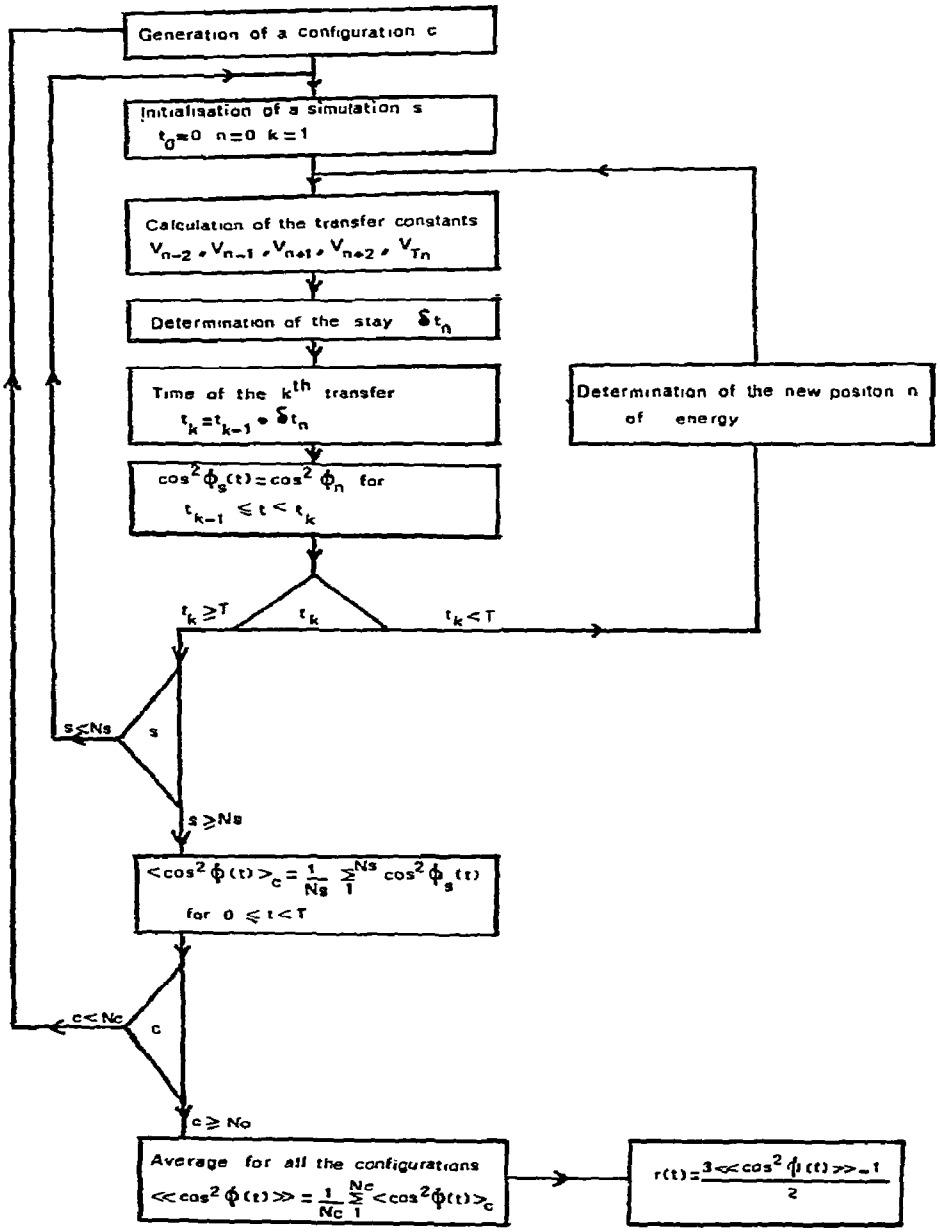

Fig. 2 (taken from ref. [7]). Scheme of the calculation of $r_T(t)$ by the Monte Carlo method. Notation used:

c = index of a configuration,
s = index of a step for a given configuration,
N_C = maximum number of configurations,
N_S = maximum number of steps for a configuration,
k = index of a transfer in a step,
n = index of the position of energy.

time t_K, the excitation is on the chromophore n after the Kth transfer. We now impose that this excitation may only go to the chromophores $n-2, n-1, n+1$ or $n+2$. This implies in particular that the excitation energy may come back on the chromophore which has been the donor in the previous step.

The corresponding rates of transfer V_{n-2}, V_{n-1}, V_{n+1}, and V_{n+2} may be calculated by formula (4) as function of the distances R_{n+i} and the angles θ_{n+i} between the chromophore n and the chromophore $n+i$ ($i=-2,-1,+1$ or $+2$). It is easy to see that for $i=\pm1$

$$\theta_{n+i} = M\alpha + \delta, \qquad R_{n+i} = (M+1) \times 3.4 \text{ Å};$$

and, for $i=\pm2$

$$\theta_{n+i} = M\alpha + 2\delta, \qquad R_{n+i} = (M+2) \times 3.4 \text{ Å};$$

M being the number of base pairs separating the chromophore n from the chromophore $n+i$. The total rate of transfer is then

$$V_{T_n} = V_{n-2} + V_{n-1} + V_{n+1} + V_{n+2}.$$

The probability that the excitation remains a time δt_n on the chromophore n is

$$p(\delta t_n) = \exp(-V_{T_n}\delta t_n).$$

Following the standard procedure in Monte Carlo calculations [16, 17], δt_n is determined by picking a random number ξ_n equally distributed in the interval [0, 1], and by putting $p(\delta t_n) = \xi_n$. The time of the $(k+1)$th transfer is then

$$t_{k+1} = t_k + \delta t_n.$$

For the first step in particular, one has obviously

$$t_1 = \delta t_0, \text{ since } t_0 = 0.$$

Location of the energy after the $(k+1)$*th migration step:* The relative probabilities of migration to each possible site are

$$P(n+i) = V_{n+i}/V_{T_n}.$$

The interval [0,1] is then divided into four segments of respective lengths $P(n-2), P(n-1), P(n+1)$ and $P(n+2)$. A random number is picked out and accordingly as its value is in the 1st, 2nd, 3rd or 4th segment, we stipulate that the energy has migrated to the chromophore $n-2, n-1, n+1$ or $n+2$.

Calculation of $\cos^2\phi_s(t)$: In this expression the index s designates a given simulation. During the time interval δt_n, the energy remains on the chromophore n. Then one may put

$$\cos^2\phi_s(t) = \cos^2\phi_n, \qquad \text{for } t_k \leqslant t < t_{k+1},$$

where ϕ_n is the angle between the transition moments of the chromophore n and the initially excited chromophore. We can also write

$$R_s^2(t) = R_n^2, \qquad \text{for } t_k \leqslant t < t_{k+1},$$

where R_n is the distance between chromophore n and the initially excited one. In particular

$$\cos^2\phi_s(t) = 1, \qquad \text{for } 0 \leqslant t < t_1.$$
$$R_s^2(t) = 0,$$

2.4.2.3. Completion of the migration. The chromophore on which the energy is located after the $(k+1)$th transfer is now taken as the starting chromophore for a new migration. The process described in section 2.4.2.2 is repeated. The migration is terminated when t_k happens to be equal to or greater than a fixed time T.

2.4.2.4. Determination of $\langle\cos^2\phi(t)\rangle_c$. The index c is characteristic of a configuration. In order to obtain a good statistical value of the distribution of the excitation energy, the processes described from sections 2.4.2.1 to 2.4.2.3 are repeated N_s times. The following mean values are then calculated

$$\langle\cos^2\phi(t)\rangle_c = \frac{1}{N_s}\sum_{s=1}^{N_s}\cos^2\phi_s(t),$$

$$\langle R^2(t)\rangle_c = \frac{1}{N_s}\sum_{s=1}^{N_s}R_s^2(t).$$

2.4.3. Determination of the anisotropy decay due to transfer

To determine this quantity, it is necessary to repeat all the calculations of section 2.4.2 for a set of configurations generated according to section 2.4.1. Then one may compute the average values

$$\langle\langle\cos^2\phi(t)\rangle\rangle = \frac{1}{N_c}\sum_{c=1}^{N_c}\langle\cos^2\phi(t)\rangle_c,$$

$$\langle\langle R^2(t)\rangle\rangle = \frac{1}{N_c}\sum_{c=1}^{N_c}\langle R^2(t)\rangle_c,$$

where N_c is a predetermined number of configurations.

The contribution of energy migration to the decay of anisotropy is then given by

$$r_T(t) = \tfrac{1}{2}(3\langle\langle\cos^2\phi(t)\rangle\rangle - 1).$$

3. Materials and methods

DNA was obtained from calf thymus and was kindly supplied by Mme G. Aubel-Sadron. It was used in an aqueous solution of 0.15 M NaCl. Ethidium bromide was a gift of Dr. Le Pecq.

Decays of fluorescence have been determined by the single photon counting technique in the same manner as previously described [6, 7, 18]. Experimental curves $i_{\parallel}(t)$, $i_{\perp}(t)$, $d(t)$, $s(t)$ and $g(t)$ are obtained, where

$$s(t) = i_{\parallel}(t) + 2\,i_{\perp}(t),$$
$$d(t) = i_{\parallel}(t) - i_{\perp}(t),$$

and $g(t)$ is the distribution in time of the exciting light pulse, and is obtained by reflecting the exciting light towards the measuring PM.

The experiments are analysed by numerical computation of the following convolution products

$$s'(t) = g(t) \otimes S(t),$$
$$d'(t) = g(t) \otimes D(t),$$

and comparison of these curves with the experimental curves $s(t)$ and $d(t)$. $S(t)$ and $D(t)$ are the true decay curves. $D(t)$ is assumed to be of the form

$$D(t) = S(t)r(t),$$

where $r(t)$ is given by formula (6).

In order to compare the experimental curve $d(t)$ with a series of computed curves $d'(t)$, we used a method described by Knight and Selinger [19]. For an experimental decay defined by a set of discrete values $f(k)$, one introduces the weighed mean variance estimate

$$\mathrm{SSQP} = \frac{1}{\frac{1}{n}\sum_{k=1}^{n}\frac{1}{f(k)}}.$$

If $f_0(k)$ is a computed curve, the weighted estimate of the fit is given by

$$\mathrm{SSQR} = \frac{\sum_{k=1}^{n}\frac{1}{f(k)}[f(k)-f_0(k)]^2}{\sum_{k=1}^{n}\frac{1}{f(k)}}.$$

The best computed curve is the curve which has the smallest value of the ratio $\rho = \mathrm{SSQR}/\mathrm{SSQP}$. ρ is equal to the sum of squares of the weighted residuals divided by the number of channels

$$\rho = \frac{1}{n}\sum_{k=1}^{n}\frac{[f(k)-f_0(k)]^2}{f(k)}.$$

Knight and Selinger [19] have pointed out that the goodness of the calculated curve fit is characterized by a value of ρ close to one. This is only true, however, on the assumption that the experimental count $f(k)$ obeys Poisson's statistics, with no systematic errors, and that no errors are introduced when including experimental data in the calculated curves.

Since the curves $d(t)$ are obtained by a difference between two experimental curves, the error on their points is sensibly greater than the error corresponding to Poisson statistics. On addition, it has recently been shown that the usual method of light reflection introduces a systematic error in the determination of $g(t)$ [20, 21]. For these reasons one expects that ρ is somehow greater than one, even for the best calculated curve which can be found.

A sensible improvement in the fit should be obtained by using the determination of $g(t)$, which has been described in a recent work [21].

The fluorescence spectra were measured with a Jobin–Yvon spectrofluorometer modified in this laboratory with an EMI 9558QB photomultiplier. Its quantum efficiency as a function of wavelength was taken to be that given by the manufacturer. Corrections were made for the monochromator dispersion and the quantum efficiency of the photomultiplier. Absorption spectra were measured with a Cary 14 spectrophotometer.

The different concentrations of DNA and of ethidium bromide were obtained by measuring optical densities with the Cary 14. The DNA concentration being very high ($> 10^{-3}$M), practically all the ethidium bromide is bound to DNA.

The natural lifetime of the excited state of ethidium bromide bound to DNA, τ_0, was obtained by several methods.

First, we have directly computed τ_0 using the formula of Stricker and Berg [22]

$$\frac{1}{\tau_0} = 2.88\times10^{-9} n_2^2 \frac{\int_0^\infty I(\bar{\nu})\,d\bar{\nu}}{\int_0^\infty \bar{\nu}^{-3} I(\bar{\nu})\,d(\bar{\nu})} \int_0^\infty \bar{\nu}^{-1}\epsilon(\bar{\nu})\,d\bar{\nu},$$

n_2 is the refractive index of the medium where the absorbed and emitted electromagnetic radiations propagate. This is essentially water, and we took $n_2 = 1.33$. $I(\bar{\nu})$ is the intensity of fluorescence at wavenumber $\bar{\nu}$ and $\epsilon(\bar{\nu})$ the molar extinction coefficient.

Secondly, we have measured the fluorescence quantum yield Q according to the technique described by Parker and Rees [23], by comparison of the fluorescence spectra of the ethidium bromide–DNA complex and some compounds whose quantum yield is known. The standards used were Rhodamine B dissolved in ethanol and quinine sulfate dissolved in 1 N H_2SO_4. We took 0.55 as the quantum yield of quinine sulfate [24, 25] and verified that Rhodamine B had a quantum yield of 0.69 as given by Parker and Rees [23]. The measurements were made at different excitation wavelengths (490, 510 and 520 nm for Rhodamine B, 325 and 365 nm for quinine sulfate).

The difference of the refractive index of water and ethanol was taken into account. After determination of the fluorescence quantum yield of bound ethidium bromide, τ_0 is given by the relation

$$Q = \tau/\tau_0,$$

where τ is the mean lifetime of the decay of fluorescence determined by the single photoelectron counting technique.

The overlap integral J of formula (2) was computed from measurements of the absorption and emission spectra of ethidium bromide, and then k_T was computed using formula (5).

The Monte Carlo calculations were performed with an IBM 370/165 computer. The energy migration was simulated up to the time $T = 80$ nsec. The curves $r_T(t)$ were computed with a time increment of 0.1 nsec during the first 8 nsec, and then 1 nsec. The number of simulations for a given configuration was $N_s = 100$ for each computed curve. For two values of δ($\delta = -20°$ and $\delta = -45°$), the number of configurations N_c was equal to or greater than 1000. For other values of δ, N_c was taken as 100.

The computation time for $N_s = 100$ and $N_c = 100$ varied from 1 to 10 min according to the value of δ and the value of P/D.

4. Results

The decays $S(t)$ corresponding to the different samples were somewhat variable (table 1), which must be attributed to experimental imprecision.

We have determined the brownian anisotropy $r_B(t)$ by analysis of the sample no. 0($P/D = 115$), since in this case energy transfer is negligible [6]. One finds

$$\sqrt{r_B(t)} = \tfrac{1}{2} r_0 [\exp(-t/\mu) + 1],$$

with $r_0 = 0.32$ and $\mu = 25$ nsec. These results are in good agreement with those previously obtained in the laboratory [6, 10].

The different methods which have been used for measuring τ_0 gave similar values. The results of these measurements are presented in table 2. With Rhodamine B as standard, we found a mean value of 74 nsec, and with quinine sulfate, a mean value of 71 nsec. The direct determination of τ_0 has been obtained using the spectra $\epsilon(\bar{\nu})/\bar{\nu}$ and $F(\bar{\nu})/\bar{\nu}^3$ necessary for this calculation. These spectra are given in fig. 3. The Strickler and Berg formula gave 73.2 nsec as mean value of τ_0. We used $\tau_0 = 73$ nsec in our calculations.

We found that J was difficult to determine accurately with the spectrofluorimeter we used. The small dispersion of this apparatus in the 600 nm wavelength range entails an insufficient mechanical reproducibility of the spectra. In addition, the corrections introduced in order to calculate the absolute spectrum, may also be a cause of error. After a number of measurements and an independent determination made with an absolute spectrofluorimeter (Cary special product 50–903), we adopted the value $J = (1.46 \pm 0.25)\times10^{-15}\,cm^3M^{-1}$.

According to Beardsley and Cantor [26], the refractive index n_1 of polynucleotides is equal to 1.4. Introducing this value in formula (1) gives $k_T = (0.46 \pm 0.07)\times10^7$ Å^6/nsec. On the other hand, from the value of the index increment and the specific volume of the DNA, one would predict a somehow higher

Table 1
Different samples of ethidium bromide–DNA complex used in the experimental study. $S(t)$ is the decay of fluorescence

Sample	P/D	$S(t)$	DNA concentration (M)	Concentration of bound ethidium bromide (M)
6	16.4	$0.12\exp(-t/10)+0.88\exp(-t/23)$	1.18×10^{-3}	0.72×10^{-4}
5	14.9	$0.07\exp(-t/10)+0.93\exp(-t/23)$	3.08×10^{-3}	2.07×10^{-4}
4	11.25	$0.12\exp(-t/10)+0.88\exp(-t/23)$	2.42×10^{-3}	2.15×10^{-4}
3	10.1	$0.12\exp(-t/10)+0.88\exp(-t/23)$	2.51×10^{-3}	2.49×10^{-4}
2	8.6	$0.26\exp(-t/10)+0.74\exp(-t/22.5)$	1.18×10^{-3}	1.37×10^{-4}
1	7.35	$0.12\exp(-t/10)+0.88\exp(-t/23)$	1.53×10^{-3}	2.08×10^{-4}
0	115	$0.16\exp(-t/10)+0.84\exp(-t/23.5)$	1.555×10^{-3}	1.005×10^{-5}

Table 2
Determination of the fluorescence quantum yield Q of ethidium bromide bound to DNA by comparison with standards. The quantum yields were taken equal to 0.69 for Rhodamine B and to 0.55 for quinine sulfate.

	λ_{exc}(nm)	Q	$\langle Q\rangle$	τ_0(nsec)
Rhodamine B	490	0.323		
	510	0.275	0.291	74
	520	0.291		
	520	0.275		
Quinine sulfate	325	0.332	0.304	71
	365	0.275		

value of the order of 1.6 [27]. In this case $k_T = (0.27 \pm 0.04)\times10^7$ Å^6/nsec. These two values of k_T lead to critical transfer distances of 20.2 Å and 18.5 Å respectively.

We computed the anisotropy of transfer $r_T(t)$ for different values of δ and for the two values of k_T corresponding to the two values of n_1, with $P/D = 7.35$. The following values of δ (in degrees) have been tried: $+14, 0, -6, -12, -14, -16, -18, -20, -24, -26, -36$ and -45. Some of the curves obtained are given in fig. 4. In fig. 5, an experimental decay curve $d(t)$ corresponding to $P/D = 7.35$ is compared with com-

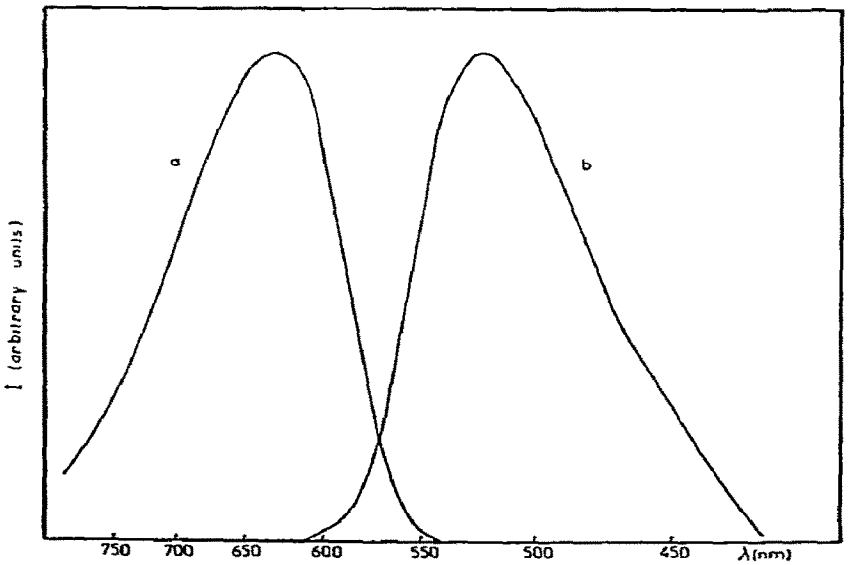

Fig. 3. Spectra (a) $F(\bar\nu)/\bar\nu^3$ and (b) $\epsilon(\nu)/\nu$ of ethidium bromide bound to DNA, used for the calculation of τ_0.

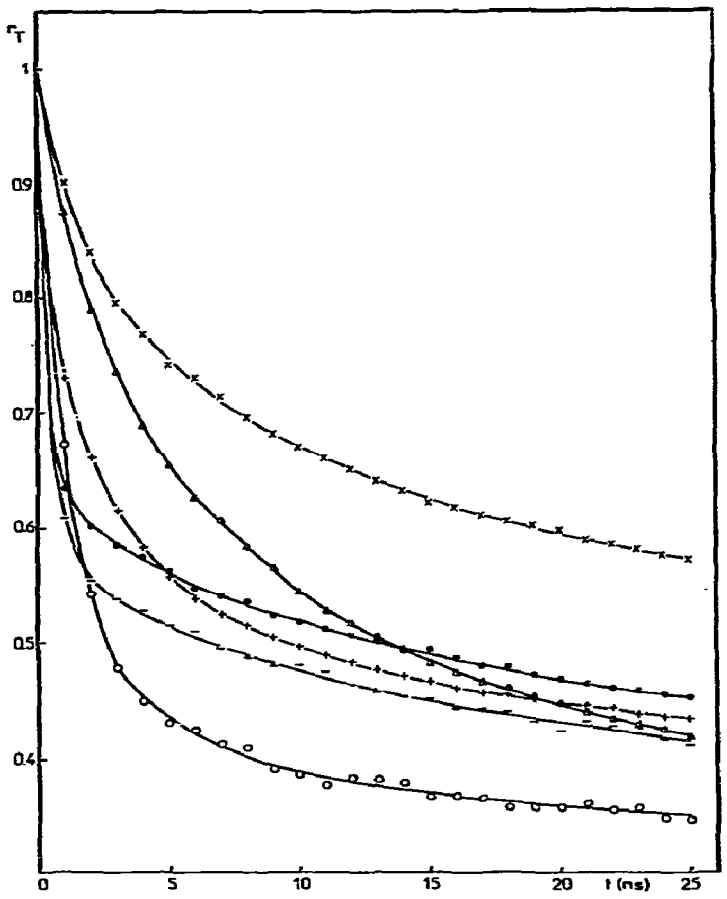

Fig. 4. Curves $r_T(t)$ for $P/D = 7.35$, computed by the Monte Carlo method with $k_T = 0.53 \times 10^7$ A^6 show the comparison between (×)$\delta = +20°$; (△)$\delta = +14°$; (+) $\delta = -45°$; (•)$\delta = -20°$; (–)$\delta = -12°$; (○)$\delta = 0°$.

Table 3

Values of ρ giving the fit between an experimental $d(t)$ curve ($P/D = 7.35$) and curves $d'(t)$ computed with different values of k_T and for different values of δ. k_T is given in A^6 nsec^{-1}.

k_T \ δ	−45°	−36°	−26°	−24°	−20°	−18°	−16°	−14°	−12°	−6°	−0°	+ 14°
0.53×10^7	103		82	69	74	81	92	123	169	355	505	248
0.46×10^7	85	96	66	59	58	64	71	93	130	282	410	253
0.40×10^7	82.5	89	61	59	54	60	66	83	111	252	372	291
0.31×10^7	93	94	65	72	53	61	62	69	83	188	289	420
0.27×10^7	110	109	77	87	59	67	66	68	72	158	250	523
0.24×10^7	128	125	88	100	65	74	70	70	67	142	229	605

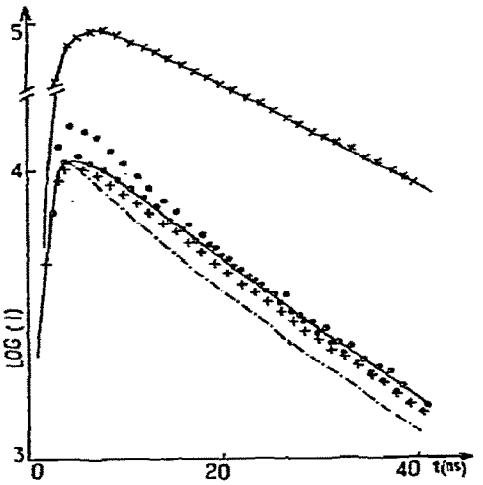

Fig. 5. Comparison between an experimental curve $d(t)$ (○) corresponding to $P/D = 7.35$ and curve $d'(t)$ computed with different values of δ; (●)$\delta = +14°$; (——)$\delta = -20°$; (+)$\delta = -12°$; (–·–·–)$\delta = 0°$; with $k_T = 0.40 \times 10^7$ Å^6/nsec. The upper curves show the comparison between experimental $s(t)$ (×) and computed $s'(t)$ (——) curves.

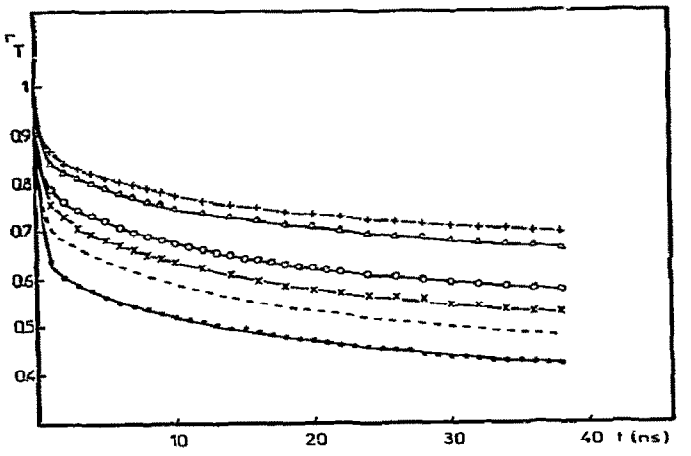

Fig. 6. Curves $r_T(t)$ computed by the Monte Carlo method with $k_T = 0.53 \times 10^7$ Å^6/nsec for $\delta = -20°$, corresponding to different values of P/D: (+) $P/D = 16.8$; (△) $P/D = 14.9$; (○) $P/D = 11.25$; (×) $P/D = 10$; (–) $P/D = 8.6$; (●) $P/D = 7.35$.

puted decays $d'(t)$ determined as discussed in section 3. Each $d'(t)$ curve corresponds to a different value of δ.

Table 3 gives the fit between the experimental curve and the computed ones. It can be seen in this table, that the best fit is obtained with $\delta = (-21 \pm 5)°$ when $k_T = 0.46 \times 10^7$ ($n_1 = 1.4$); and with $\delta = (-16 \pm 4)°$ when $k_T = 0.27 \times 10^7$ ($n_1 = 1.6$). We also included in table 3 the results of the calculations performed with the values of k_T corresponding to the limits of inaccuracy on J. It can be seen that this inaccuracy does not change the δ value giving the best fit.

We have also computed the values of $r_T(t)$ for the other experimental values of P/D with $\delta = -20°$ and

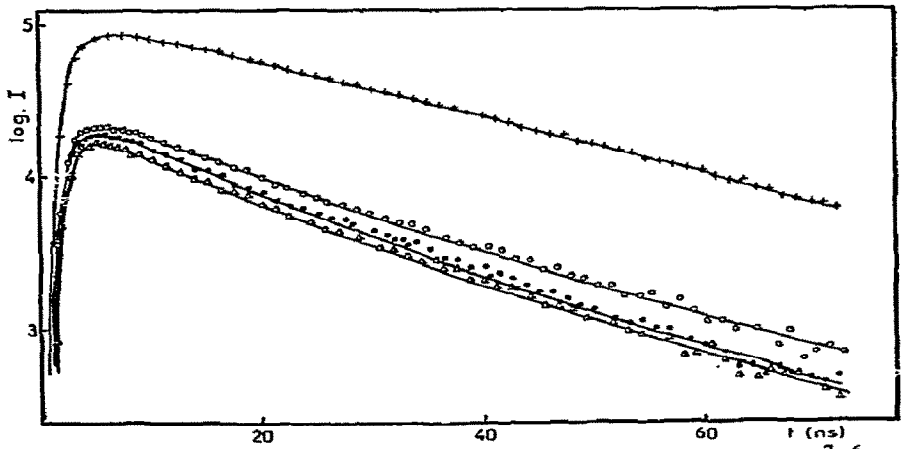

Fig. 7. Comparison of some experimental curves $d(t)$ with curves $d'(t)$ computed with $k_T = 0.53 \times 10^7$ Å^6/nsec and $\delta = -20°$ for different values of P/D. The continuous lines are computed curves. Experimental curves correspond to $P/D = 14.9$ (○), $P/D = 10$ (●), and $P/D = 7.35$ (△). The upper curves show the comparison between the experimental curve $s(t)$ (+), and the computed one $s'(t)$ (——) for $P/D = 14.9$.

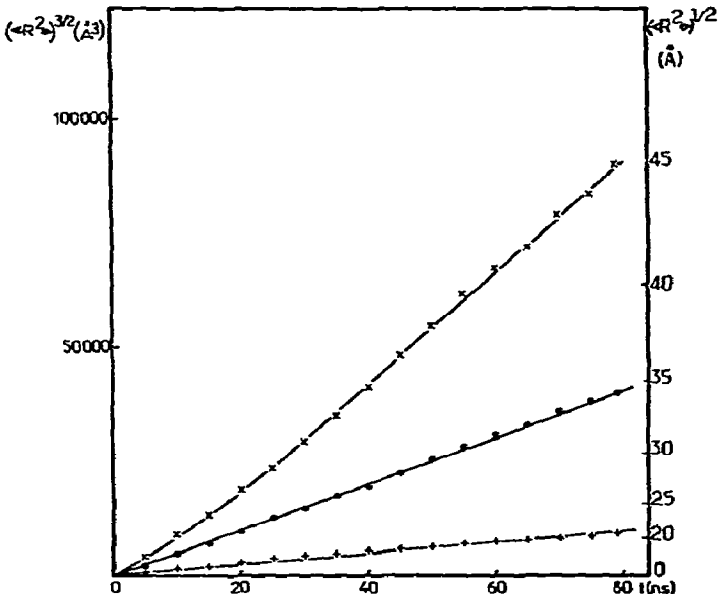

Fig. 8. Curves $\langle\langle R^2\rangle\rangle^{3/2}$ versus time computed by the Monte Carlo method with $\delta = -20°$ for different values of P/D: (X) $P/D = 7.35$; (•) $P/D = 10$; (+) $P/D = 20$. k_T was taken equal to 0.53×10^7 Å^6/nsec. On the right scale we have plotted $\langle\langle R^2\rangle\rangle^{1/2}$.

$k_T = 0.53\times10^7$ Å^6/nsec. These curves are given in fig. 6. Some $d'(t)$ curves are compared with the corresponding experimental ones (fig. 7), and one can see that a good fit is obtained.

In some of our Monte Carlo calculations, we have determined $\langle\langle R^2\rangle\rangle$, the mean square of the distance covered by the energy during its migration. We found empirically that $\langle\langle R^2\rangle\rangle^{3/2}$ varies linearly with t in most of the variable range explored. In order to evaluate the average distance of the energy migration, we plotted an example of this variation in fig. 8. The distance of migration after a given time increases when P/D decreases.

One can see that after 80 nsec $\langle\langle R^2\rangle\rangle^{1/2}$ is equal to 21.2, 34.3 and 45 Å for P/D values respectively equal to 20, 10 and 7.35. The corresponding numbers of base pairs are 5.7, 8.4 and 10.4. This means that the energy migration takes place only over a relatively short segment of the DNA molecule.

Discussion

We begin this discussion by considering the various causes which might lead to some errors in the estimate of the unwinding angle δ. The notion of the unwinding angle δ implies that all the sites occupied by an ethidium bromide molecule rotate with the same angle.

The model adopted in this work contains the additional assumption that the ethidium bromide molecules occupy identical positions in their sites. Thus the transition moments of two chromophores make an angle between them which only depends on the respective angular positions of their sites. This assumption could appear to be too restrictive since the nature and the sequence of the pyrimidine and purine bases bring about a variety of sites. However, 88% of the ethidium bromide molecules bound to DNA fluoresce with a decay time of 23 nsec. Therefore, the fluorescence emission appears to be relatively homogeneous. Then the assumption that the majority of chromophores occupy the same position in their sites seems to be a reasonable one.

As we already showed in a previous work [10], there is an angular brownian motion of the ethidium bromide molecules bound to DNA. From the value of the correlation time of the motion (25 nsec), one may reasonably assume that the length of the DNA

taking part in the motion is about 100 Å long. On the other hand, the DNA–ethidium bromide complex with $P/D = 7.35$ allows the most accurate determination of δ. In this case, the average distance between two nearest inserted chromophores is about 15 Å. Therefore, the brownian rotations of these two chromophores are in phase, and no change in their relative angular position occurs.

The value of k_T determined in the present work is different from values previously published by others [5] and ourselves [6]. As we have already discussed, there are some difficulties in obtaining an accurate value of the overlap integral J. We think that these measurements could be improved in future works. However, we have seen that the inaccuracy of J does not entail a perceptible change in the determination of δ. On the other hand, the calculations are very sensitive to the values of n_1. With $n_1 = 1.4$: $\delta = (-21 \pm 5)^\circ$, whereas with $n_1 = 1.6$, its value is $(-16 \pm 4)^\circ$. $n_1 = 1.6$ is probably closer to the true value of the DNA refractive index than $n_1 = 1.4$.

A winding of $+14^\circ$, as proposed by Paoletti and Le Pecq [5], gave computed anisotropy decays inconsistent with our experimental decays. The decay curve $d'(t)$ computed with $\delta = +14^\circ$ is first higher, then lower than the experimental one $d(t)$. This could explain Paoletti and Le Pecq's results.

These authors measured the time-average anisotropy using a continuous source of excitation, which corresponds to the decay curve integrals. Though experimental decays and decays computed with $\delta = +14^\circ$ are different, the integrated values can be similar.

On the other hand, our results are in fair agreement with the model first proposed by Lerman [1, 8], which supposes a local unwinding of the double helix of DNA when a dye is inserted. It is generally assumed [28] that the unwinding angle is comprised between -12° as proposed by Fuller and Waring [2], and -45° as proposed by Lerman [1]. These two values are deduced from studying molecular models.

It has been shown that intercalation of ethidium bromide leads to strong changes in sedimentation velocity [29, 30] and buoyant density [30] in cesium chloride of closed circular DNA molecules. This observation has been attributed to the unwinding of DNA duplex which entails an unwinding of the superhelix turns naturally occurring in these molecules. From these experiments, the superhelix density σ may be calculated when δ is known. In using the δ value of Fuller and Waring ($\delta = -12^\circ$), Bauer and Vinograd [30] found a fair agreement between the values of σ calculated by means of the ethidium bromide method and determined by the early alkaline titration method of Vinograd et al. [31].

However, we may point out that $\delta = (-15 \pm 3)^\circ$ will give a better agreement between these two methods. That last value is practically identical to the value obtained in the present work when the value 1.6 is taken for DNA refractive index.

We think that our experimental method provides a good evaluation of the unwinding angle of the ethidium bromide–DNA complex.

More generally, this method should be useful for determining the spatial distribution of any arbitrary array of identical chromophores.

Acknowledgements

We wish to thank Professor Charles Sadron for the interest he showed in this work and for several fruitful discussions with him about it. We thank Dr. De Witt for the use of the absolute spectrofluorimeter. Finally we thank Reidel Publishing Company for the permission to reproduce fig. 2 taken from ref. [7].

References

[1] L.S. Lerman, J. Mol. Biol. 3 (1961) 18.
[2] W. Fuller and M.J. Waring, Ber. Bunsenges. Phys. Chem. 68 (1964) 805.
[3] D.M. Crothers, Biopolymers 6 (1968) 575.
[4] W. Bauer and J. Vinograd, J. Mol. Biol. 47 (1970) 419.
[5] J. Paoletti and J.B. Le Pecq, J. Mol. Biol. 59 (1971) 43.
[6] D. Genest and Ph. Wahl, Biochim. Biophys. Acta 259 (1972) 175.
[7] D. Genest and Ph. Wahl, in: Dynamical aspects of conformation changes in biological macromolecules, ed. Ch. Sadron (Reidel, Dordrecht, 1973) p. 367.
[8] L.S. Lerman, Proc. Natl. Acad. Sci. US 49 (1963) 94.
[9] P.U. Giacomoni and M. Le Bret, FEBS Letters 29 (1973) 227.
[10] Ph. Wahl, J. Paoletti and J.B. Le Pecq, Proc. Natl. Acad. Sci. US 65 (1970) 417.
[11] A. Jablonski, Acta Phys. Pol. 14 (1955) 295.
[12] Th. Förster, Ann. Physik 2 (1948) 55.
[13] Th. Förster, Discussions Faraday Soc. 27 (1959) 7.
[14] R.S. Knox, Physica 39 (1968) 361.

[15] Ph. Wahl, Decay of Fluorescence Anisotropy, to be published in: Concepts in biochemical fluorescence, eds. R.F. Chen and H. Edelhoch (Dekker, New York).
[16] J.M. Hammersley and D.C. Handscomb, Les methodes de Monte Carlo (Dunod, Paris, 1967).
[17] J. Von Neumann, Collected works, Vol. V (Pergamon, Oxford, 1963) p. 751.
[18] Ph. Wahl, Biochim. Biophys. Acta 175 (1969) 55.
[19] A.E.W. Knight and B.K. Selinger, Spectrochim. Acta 27 A (1971) 1223.
[20] C. Lewis, W.R. Ware, L.J. Doemeny and T. Nemzek, Rev. Sci. Instr. 44 (1973) 107.
[21] Ph. Wahl, J.C. Auchet and B. Donzel, Rev. Sci. Instr., to be published.
[22] S.J. Strickler and R.A. Berg, J. Chem. Phys. 37 (1962) 814.
[23] C.A. Parker and W.T. Rees, Analyst (London) 85 (1960) 587.
[24] W.H. Melhuish, J. Phys. Chem. 65 (1961) 229.
[25] J.N. Demas and G.A. Crosby, J. Phys. Chem. 75 (1971) 991.
[26] K. Beardsley and Ch.R. Cantor, Proc. Natl. Acad. Sci. US 65 (1970) 39.
[27] R.E. Harrington, J. Am. Chem. Soc. 92 (1970) 6957.
[28] D.M. Neville, I. Davies and D.R. Davies, J. Mol. Biol. 17 (1966) 57.
[29] L.V. Crawford and M.J. Waring, J. Mol. Biol. 25 (1967) 23.
[30] W. Bauer and J. Vinograd, J. Mol. Biol. 33 (1968) 141.
[31] J. Vinograd, J. Lebowitz and R. Watson, J. Mol. Biol. 33 (1968) 173.

BIOPHYSICAL CHEMISTRY 1 (1974) 279–291. © NORTH-HOLLAND PUBLISHING COMPANY

ANOMALIES IN SEDIMENTATION. IV. DECREASE IN SEDIMENTATION COEFFICIENTS OF CHAINS AT HIGH FIELDS

Bruno H. ZIMM

Department of Chemistry, Revelle College, University of California (San Diego), La Jolla, California 92037, USA

Received 8 August 1973
Revised manuscript received 23 October 1973

A theory is presented for the decrease of sedimentation coefficient at high centrifugal fields recently reported for samples of DNA by Rubenstein and Leighton and others. The theory uses the model of a chain of beads and springs to represent the molecule. Kirkwood's approximation is used for the sedimentation coefficient. The decrease in sedimentation coefficient with field comes about as a result of the uneven frictional forces in the chain, which on the average are less on segments near the center of the chain than on those near the ends. As a result the ends of the chain tend to drag behind the center, and the average intersegment distances are increased; consequently the hydrodynamic shielding of one segment by another is reduced, and the average friction is increased. The effect is thus characteristic of single molecules; intermolecular interaction is not involved. The sedimentation coefficient, S, varies as a power series in a parameter y that measures the distortion produced by the uneven friction:

$$S = S^0(1 - D_2y^2 + D_4y^4 - \ldots) ,$$

where S^0 is the limiting value of S at zero centrifugal field and D_2 and D_4 are constants; y is proportional to the centrifuge speed squared times the molecular weight squared divided by S^0. It has been observed that the effects of centrifuge speed on S are negligible below certain critical values of the speed and molecular weight, but increase dramatically immediately above these values; this follows naturally from the high powers of the speed and molecular weight that appear in the above equation.

1. Introduction

With macromolecules it is usually assumed that the sedimentation coefficient is independent of the strength of the centrifugal field. This is usually a safe assumption, since the sedimenting forces are not usually great enough to appreciably orient or distort the macromolecules, or to affect their distribution relative to one another. However, as larger and larger molecules have come under investigation in the last few years, the assumption of velocity independence has become questionable. In the previous three papers [1–3] of this series we have discussed a concentration-dependent anomaly which appears as an increase in sedimentation coefficient at high centrifugal fields. Now we turn to a decrease in sedimentation coefficient of large chain molecules at high fields; this effect was first observed, as far as we are aware, by Rubenstein and Leighton with large DNA molecules [4]. The decrease was seen at very low concentrations, less than one part per million by weight, and was therefore apparently distinct from the concentration-dependent anomaly.

This effect is important to the practice of macromolecular science, since it appears to set the upper limit on the molecular weights of DNA molecules that can be measured by present sedimentation techniques. Moreover it presents the theory of the hydrodynamic properties of chain molecules with a new challenge.

The probable explanation of the effect, as suggested in 1969 by Rubenstein in a private communication to the author, is an increase in friction resulting from distortion of the chain molecules by uneven forces. The unevenness in the forces appears to be caused mainly by inequality in the friction, the average friction at the ends of the chain

being greater than the average friction at the middle because of the greater hydrodynamic shielding around the middle. As a result, the ends tend to drag behind the middle, and the chain becomes distorted. If the distortion is great enough, the amount of hydrodynamic shielding of the various parts of the chain by one another is lessened, and the sedimentation coefficient can be expected to decrease.

The rest of this paper is devoted to working out these ideas in detail.

2. Sedimentation and distortion

2.1. The model and the Kirkwood formula for the sedimentation coefficient

The model we use is the familiar beads-and-springs model [5–7]. There are $N+1$ beads, numbered from 0 to N, connected through universal joints by N springs. When there are no external forces, the root-mean-square length of each spring is b, a constant. Since the springs are connected by universal joints, random-flight statistics apply to the chain, i.e., the mean square distance, $\langle r_{ij}^2 \rangle$, between the ith and jth beads is

$$\langle r_{ij}^2 \rangle = \langle x_{ij}^2 \rangle + \langle y_{ij}^2 \rangle + \langle z_{ij}^2 \rangle = |i-j|b^2 \,. \tag{1}$$

Each bead interacts with the surrounding fluid (the solvent) with a friction coefficient ρ', and there is a sedimenting force, g, a constant, driving each bead toward the negative z-direction of a Cartesian frame of reference. Let u_i be the velocity of the ith bead, v_i the velocity that the solvent at the position of bead i would have if that bead were not there, and F_i the sum of the spring forces and the sedimenting forces acting on bead i; then

$$F_i = \rho'(u_i - v_i) \,. \tag{2}$$

(In this section bold-face type indicates vectors in three-dimensional space.) We assume that the solvent is generally at rest, except for currents created by the forces acting on the chain molecule. These currents are given by the Oseen–Burgers [8] formula, which is, in the notation of Kirkwood and Riseman [9]

$$v_i = \sum_0^N{}' \mathbf{T}_{ij} \cdot F_j \,, \tag{3}$$

where the prime on the summation sign indicates that $j \neq i$, and where the tensor $\mathbf{T}_{ij}$ is given by

$$\mathbf{T}_{ij} = (1/8\pi\eta r_{ij})(\mathbf{1} + \mathbf{r}_{ij}\mathbf{r}_{ij}/r_{ij}^2) \,. \tag{4}$$

Here η is the viscosity of the solvent, $\mathbf{r}_{ij}$ the vector between i and j, and the operator in parentheses is a dyadic which transfers the location of its operand (the force F_j) from j to i as well as performing the operations indicated by $\mathbf{1}$ (the unit operator) and by the dyad $\mathbf{r}_{ij}\mathbf{r}_{ij}$.

The force, F_j, on the jth bead is the sum of the sedimenting force, g, and the forces in the two springs connected to j; these latter forces we call $f_{j,j-1}$ and $f_{j,j+1}$. If we combine (2) and (3) we then have

$$u_i = (1/\rho')F_i + \sum_0^N{}' \mathbf{T}_{ij} \cdot g + \sum_0^N{}' \mathbf{T}_{ij} \cdot (f_{j,j-1} + f_{j,j+1}) \,. \tag{5}$$

The average velocity, u, of the whole molecule is the average over all beads of the time average of the velocity of each bead, $\langle u_i \rangle$. (The symbol $\langle\ \rangle$ denotes a time average, or, which is equivalent, an average over all configurations.)

$$u = [1/(N+1)] \sum_0^N {}_i \langle u_i \rangle = [1/(N+1)\rho'] \sum_0^N {}_i \langle F_i \rangle + [1/(N+1)] \sum_0^N {}_i \sum_0^N {}'_j \langle \mathsf{T}_{ij} \rangle \cdot g$$
$$+ [1/(N+1)] \sum_0^N {}_i \sum_0^N {}'_j \langle \mathsf{T}_{ij} \cdot (f_{j,j-1} + f_{j,j+1}) \rangle . \tag{6}$$

To obtain a useful approximation, due to Kirkwood [10], one neglects the last summation. (Kirkwood's original derivation [10] was much less specific; for this reason we have rederived the formula.) As partial justification, we note that $f_{j,j-1} = -f_{j-1,j}$, these quantities being the forces at the opposite ends of the same spring, while T_{ij} usually varies slowly with j, so that there is surely much near cancellation of terms in the summation. In contrast, in the second summation, involving g, the terms are all of the same sign. Further, since the total external force is $(N+1)g$ and the sum of the internal forces must vanish on the average, we have

$$\sum_0^N {}_i \langle F_i \rangle = (N+1)g . \tag{7}$$

In Kirkwood's approximation, then, the sedimentation velocity is

$$u = g/\rho' + [1/(N+1)] \sum_0^N {}_i \sum_0^N {}'_j \langle \mathsf{T}_{ij} \cdot \rangle g . \tag{8}$$

If the sedimenting force has a component only in the z-direction, u must have also a non-vanishing z-component only, and

$$\langle \mathsf{T}_{ij} \cdot \rangle = (1/8\pi\eta) \langle 1/r_{ij} + z_{ij}^2/r_{ij}^3 \rangle . \tag{9}$$

In a centrifuge, the magnitude of the sedimenting force on each bead, g, is

$$g = M(1 - \bar{v}\rho)\Omega^2 x/(N+1)N_a , \tag{10}$$

where M is the molecular weight of the chain molecule, $\bar{v}$ is its partial specific volume, ρ is the density of the solvent, Ω is the angular velocity of the centrifuge rotor of radius x, and N_a is Avogadro's number. The definition of the sedimentation coefficient, S, expressed in Svedberg units, is

$$10^{-13} S = u/\Omega^2 x . \tag{11}$$

These formulas may now be combined with (8) to give an expression for the sedimentation coefficient in molecular terms. One simplification remains, however. The value of N, the number of springs in the model, is rather arbitrary, there being no straight-forward way of relating this to some property of the real molecule. In (8) only the first term depends directly on N through g; the summation turns out to be largely independent of N. Also the first term is usually small in comparison to the summation. For these reasons we will neglect the first term. (We are in effect adopting what is usually called the "non-draining" approximation.) The result is Kirkwood's formula in the form

$$10^{-13} S = [M(1 - \bar{v}\rho)/8\pi(N+1)^2 N_a \eta] \sum_0^N {}_i \sum_0^N {}'_j \langle 1/r_{ij} + z_{ij}^2/r_{ij}^3 \rangle . \tag{12}$$

Kirkwood's formula, though admittedly approximate, has the great advantage of being well adapted for calculation, requiring only the evaluation of a sum or an integral over molecular conformations. Its accuracy has been

discussed by Zwanzig [11], using Tchen's [12] exact calculation of the friction tensor of an infinitely thin circular ring. The discrepancy is nine percent between the exact result and Kirkwood's formula for this ring. On the other hand, for an infinitely thin long rod, the agreement between the two formulas is perfect. For a chain molecule at low centrifugal fields the value of S is given in Kirkwood's approximation by eq. (53) below; the numerical constant in this equation is $\frac{4}{9}\pi^{3/2} = 0.0798$. Some time ago [4] the same constant was evaluated for the same model but without the neglect of the internal force terms of eq. (6) above, although with the use of pre-averaged T_{ij} factors, instead of averaging after multiplying (i.e., $\langle \mathsf{T}_{ij} \rangle \cdot f_{j,j-1}$ instead of $\langle \mathsf{T}_{ij} \cdot f_{j,j-1} \rangle$) as would be perfectly correct. The result was $\Gamma(\frac{5}{4})/3\pi^{1/2}\Gamma(\frac{1}{2})\,\Gamma(\frac{3}{4}) = 0.0784$, only two percent different from that above.

Thus Kirkwood's approximation appears to give results only a few percent away from more exact calculations. Probably the comparison between two calculations on similar models, both by Kirkwood's approximation, is more satisfactory than either calculation would be alone. For example, Bloomfield and Zimm [13] made a calculation of the ratio of the sedimentation coefficients of circular and linear chain molecules using Kirkwood's approximation; this ratio came out to be 1.16 for a DNA-like structure, in good agreement with experimental measurements, which range from 1.1 to 1.2.

For these reasons we feel hopeful that the present calculation, if not exact, should at least be within a few percent of a calculation that took full account of the internal forces.

2.2. The diffusion equation

It is now necessary to derive the amount of molecular distortion resulting from the sedimenting forces so that the correct distances can be inserted in Kirkwood's formula, eq. (12). Even though the sedimenting forces on each bead are equal and of value g, the frictional forces are not equal because of the differing values of the solvent currents, v_i, at each bead. Since the total frictional force at each bead must equal F_i according to eq. (2), obviously the internal (spring) forces are not all equal. As a result, the springs are unequally distorted by an amount that depends on the sedimenting force, g.

For this calculation we use the method already developed years ago [5, 7, 14] for viscoelastic and other problems in chain dynamics. The methods, fundamental equations, and most of the symbols used are the same as those discussed at length in a previous paper [7]; except for the following few remarks we must refer the reader thither.

From this point on we use bold-face type to designate $(N+1)$-dimentionsl matrices and column vectors, not the ordinary three-vectors of the preceding paragraphs.

Each element of one of these $(N+1)$-dimensional vectors is a certain quantity (such as the z-coordinate) pertaining to a particular bead; the vector thus represents the set of such quantities of the whole chain. The distribution of the chain among its conformations is described by the probability density function, ψ, which obeys a diffusion equation similar to eq. (17) of ref. [7]. This equation is to be obtained from the expressions for the force vectors; these are the same as eq. (6) of ref. [7] except for the z-component, which has the additional term representing the sedimenting force, $-ge$, where e is a $(N+1)$-dimensional vector all of whose elements are unity. (For format, compare eq. (99) of ref. [7].) The diffusion equation is greatly simplified by transformation to the normal coordinates, ξ, η, and ζ, according to the linear transformation $\mathbf{Q}$, defined in ref. [7].

We begin work with the diffusion equation in normal coordinates. Since we are interested in the steady-state rate of sedimentation, we can set $\partial\psi/\partial t = 0$. Analogous to eq. (38) of ref. [7], the diffusion equation now appears in the form

$$\sum_0^N{}_k \left[(g/\rho')\nu_k \epsilon_k \partial\psi/\partial\xi_k + 3\sigma\lambda_k\psi + \sum_{u=\xi,\eta,\zeta} (D\nu_k \partial^2\psi/\partial u_k^2 + \sigma\lambda_k u_k \partial\psi/\partial u_k) \right] = 0 . \tag{13}$$

Here σ is the ratio of the spring force constant to the resistance coefficient; $\sigma = 3k'T/b^2\rho'$, where k' is Boltzmann's constant, T is the absolute temperature, and b is the root-mean-square length of a spring in the molecule at rest; D, the bead diffusion coefficient, is $k'T/\rho'$. The index k is an integer running from 0 to N and denoting which normal coordinate is under consideration, and ν_k and λ_k are the kth diagonal elements of the hydrodynamic mo-

bility matrix, **H**, and of the product matrix **H·A**, respectively (where **A** is the matrix that converts a bead-position vector into a spring-force vector). ϵ_k is the kth element of the transform of the unit vector, e, that is,

$$\epsilon_k = \sum_{0}^{N}{}_j Q_{jk} , \tag{14}$$

where Q_{jk} are the elements of the transformation matrix, **Q**. (Compare eq. (106) in ref. [7].)

The physical meanings of the various terms in eq. (13) are simple. The first term is the divergence of the currents of bead flow produced by the sedimenting forces; the third term is the divergence of the corresponding currents produced by diffusion, and the second and fourth terms together represent the divergence of the currents resulting from the spring forces. In steady state, the sum of these divergences must be zero.

The solution of eq. (13) is easily found to be a product of exponential functions, one for each normal coordinate. For the coordinates ξ_k and η_k these functions are

$$\exp[-3\mu_k(\xi_k^2 + \eta_k^2)/2b^2] , \tag{15}$$

while for ζ_k they are

$$\exp(-3\mu_k\zeta_k^2/2b^2 - g\epsilon_k\zeta_k/k'T) , \tag{16}$$

where μ_k is equal to λ_k/ν_k. We now wish to express these in terms of the original coordinates of the beads, x_i, y_i, z_i. According to the transformation equations (eq. (34) of ref. [7]) a quadratic form in the normal coordinates becomes a quadratic form in the original coordinates. Since the functions in the exponentials of eqs. (15) and (16) are quadratic forms of the normal coordinates, they transform into quadratic forms of the original coordinates. We wish now to reduce this to the distribution function of the components of the distance between two beads, say i and j. Write

$$x_j = x_i + x_{ij} , \qquad y_j = y_i + y_{ij} , \qquad z_j = z_i + z_{ij} , \tag{17}$$

and integrate over all coordinates except those of bead j. The integration of the distribution function consists of successive integrations of the following type:

$$\int_{-\infty}^{\infty} \exp(-ax_\varrho^2 + bx_k x_\varrho)\mathrm{d}x_\varrho = \sqrt{\pi/a}\exp b^2 x_k^2/4a , \tag{18}$$

where a and b are constants and b may or may not be zero. The only thing that remains from the original exponential of quadratic forms is then the following function of x_{ij}, y_{ij}, z_{ij}, which is the function that was sought:

$$\psi(x_{ij}, y_{ij}, z_{ij}) = K\exp[-\alpha(x_{ij}^2 + y_{ij}^2 + z_{ij}^2) + \beta z_{ij}] , \tag{19}$$

where K α, and β are constants to be determined later.

2.3. The sedimentation coefficient in terms of average distances

Returning now to eq. (12) for the sedimentation coefficient, we see that the averages in the right-hand member of the equation are to be taken with the distribution function (19); that is,

$$\langle 1/r_{ij} + z_{ij}^2/r_{ij}^3 \rangle$$
$$= \iiint (1/r_{ij} + z_{ij}^2/r_{ij}^3) \exp(-\alpha r_{ij}^2 + \beta z_{ij})\, dx_{ij} dy_{ij} dz_{ij} \Big/ \iiint \exp(-\alpha r_{ij}^2 + \beta z_{ij})\, dx_{ij} dy_{ij} dz_{ij} . \quad (20)$$

The constants α and β are easily related to the averages $\langle x_{ij}^2 \rangle$ and $\langle z_{ij} \rangle$ by the equations

$$\langle x_{ij}^2 \rangle = \int x_{ij}^2 \exp(-\alpha x_{ij}^2)\, dx_{ij} \Big/ \int \exp(-\alpha x_{ij}^2)\, dx_{ij} = 1/2\alpha , \quad (21)$$

$$\langle z_{ij} \rangle = \int z_{ij} \exp(-\alpha z_{ij}^2 + \beta z_{ij})\, dz_{ij} \Big/ \int \exp(-\alpha z_{ij}^2 + \beta z_{ij})\, dz_{ij} = \beta/2\alpha . \quad (22)$$

The quantity α, and correspondingly $\langle x_{ij}^2 \rangle$, measures the size of the chain at rest and is not affected by the presence of the centrifugal field; on the other hand, β, and correspondingly $\langle z_{ij} \rangle$, measures the distortion of the chain caused by the field.

Equations (20), (21) and (22) give the quantity of interest, $\langle 1/r_{ij} + z_{ij}^2/r_{ij}^3 \rangle$, as a function of the averages $\langle x_{ij}^2 \rangle$ and $\langle z_{ij} \rangle$. To express this functional form most conveniently, we define a new variable, υ_{ij}, which is proportional to the square of the amount of distortion, $\langle z_{ij} \rangle$, of the chain from its resting form:

$$\upsilon_{ij} = \beta^2/2\alpha = \langle z_{ij} \rangle^2 / \langle x_{ij}^2 \rangle . \quad (23)$$

If we transform eq. (20) to polar coordinates, we can now perform the integrations over the angles to obtain a form that is conveniently written as

$$\langle 1/r_{ij} + z_{ij}^2/r_{ij}^3 \rangle = \tfrac{4}{3}(2/\pi \langle x_{ij}^2 \rangle)^{1/2} V(\upsilon_{ij}) , \quad (24)$$

where the function $V(\upsilon)$ is defined by

$$V(\upsilon) = \frac{3\, e^{-\upsilon/2}}{2\upsilon} \int_0^\infty \exp(-\omega^2/2\upsilon) \left(\sinh \omega - \frac{\cosh \omega}{\omega} + \frac{\sinh \omega}{\omega^2} \right) d\omega . \quad (25)$$

(Here ω has replaced βr_{ij}.) Expansion of the integrand in (25) and integration term by term leads to a power series in υ,

$$V(\upsilon) = \sum_0^N{}_n C_n \upsilon^n = 1 - \frac{\upsilon}{10} + \frac{3\upsilon^2}{280} - \dots , \quad (26)$$

where the coefficients C_n are given by

$$C_n = \frac{3}{2^n} \sum_0^N{}_\varrho \frac{(-1)^{n-\varrho} 2^{2\varrho} (\varrho + 1)!}{(n - \varrho)!(2\varrho + 3)!(2\varrho + 1)!} \quad (27)$$

and are tabulated in table 1.

2.4. Evaluation of the averages

The first term obtained by substituting eq. (26) into eq. (24) is a familiar form which is easy to sum over all pairs, ij. We replace i and j by continuous variables s and t defined by

$$s = -1 + 2i/N , \qquad t = -1 + 2j/N , \quad (28)$$

Table 1
The first four power-series coefficients

n	C_n	I_n	D_{2n}
1	−1/10	0.7698	-2.887×10^{-2}
2	3/280	1.361	2.051×10^{-3}
3	−1/1008	2.667	-1.550×10^{-4}
4	1/12672	5.460	1.105×10^{-5}

and approximate the summation over i and j in eq. (2) by integration over s and t. A further conversion into variables p and q is useful, where

$$p = \tfrac{1}{2}(s + t), \qquad q = \tfrac{1}{2}(s - t). \tag{29}$$

We then proceed to sum the first term in (24), obtaining $\langle x_{ij}^2 \rangle$ from eq. (1) (and noting that $\langle x_{ij}^2 \rangle$ is not affected by the centrifugal field);

$$\Sigma_i \Sigma_j \langle x_{ij}^2 \rangle^{-1/2} = (3^{1/2}/b) \Sigma_i \Sigma_j |i - j|^{-1/2} = (3^{1/2}/b)(N/2)^{3/2} \int_{-1}^{1} \int_{-1}^{1} |s - t|^{-1/2} \mathrm{d}s \mathrm{d}t$$

$$= 2(3^{1/2}/b)N^{3/2} \int_{0}^{1} \int_{0}^{1-q} q^{-1/2} \mathrm{d}p \, \mathrm{d}q = 8N^{3/2}/3^{1/2}b . \tag{30}$$

The next term of eq. (24) with (26) involves $\langle z_{ij} \rangle$. From eq. (34) of ref. [7] we have

$$\langle z_{ij} \rangle = \Sigma_k (Q_{jk} - Q_{ik}) \langle \zeta_k \rangle . \tag{31}$$

The matrix elements Q_{jk} and Q_{ik} can be represented in terms of the eigenvectors of the matrix $\mathbf{H \cdot A}$, as explained in previous papers [7, 15]. We can express these eigenvectors by continuous functions of s and t, $\alpha_k(s)$ and $\alpha_k(t)$,

$$Q_{ik} = (2/N)^{1/2} \alpha_k(s), \qquad Q_{jk} = (2/N)^{1/2} \alpha_k(t) . \tag{32}$$

The functions α_k are represented [15] conveniently as Fourier series, in particular, those of even k, the only ones that we will have need of, are given by

$$\alpha_k(s) = {}^k a_0 + \sum_{\substack{m \\ m \text{ even}}}^{\infty} {}^k a_m \cos(\pi m s/2) , \tag{33}$$

where ${}^k a_0$ and ${}^k a_m$ are coefficients which depend on both the indices k and m. Most of our work will involve the second eigenfunction, α_2; in this eigenfunction only the first two terms give numerically significant contributions, so that we may write

$$\alpha_2(s) = {}^2 a_0 + {}^2 a_2 \cos(\pi s) + \ldots , \tag{34}$$

and correspondingly for $\alpha_2(t)$.

The averages of the z-axis normal coordinates, $\langle \zeta_k \rangle$, which appear in eq. (31), can be evaluated by averaging with the distribution function, (16):

$$\langle \zeta_k \rangle = -g v_k \epsilon_k / \rho' \sigma \lambda_k \,. \tag{35}$$

The vector elements ϵ_k were defined by eq. (14). We can now complete the evaluation of these, using (32) and (33):

$$\epsilon_k = (2N)^{1/2}\, {}^k a_0 \,. \tag{36}$$

From the prescriptions given before [15] we can now estimate the ϵ_k, and from them show that only $\langle \zeta_2 \rangle$ contributes enough to eq. (31) to be worth evaluating carefully at present. The magnitudes of the other $\langle \zeta_k \rangle$ are all less than fifteen precent of $\langle \zeta_2 \rangle$, and their contributions to this calculation are further diminished by the rapid oscillations of the eigenfunctions, α_k, of k greater than two. For k equal to two, then, we have from the previous work [15],

$${}^2 a_0 = (3.052/-12.87)\, {}^2 a_2 \,. \tag{37}$$

We combine this with the normalization condition

$$\int_{-1}^{1} \alpha_2^2(s)\, ds = 1 = 2({}^2 a_0)^2 + ({}^2 a_2)^2 + \ldots \tag{38}$$

to generate two simultaneous equations for the coefficients ${}^2 a_0$ and ${}^2 a_2$. The results for the coefficients are ${}^2 a_0 = -0.2235$ and ${}^2 a_2 = 0.9428$. For the evaluation of $\langle \zeta_2 \rangle$ we need in addition the quantity ν_2/λ_2. In refs. [7] and [15] it was shown that this ratio was equal to the element μ_2, which is found from ref. [15] to be $3.5648\pi^2/N^2$. Putting all this together into eq. (35), we can evaluate the quantity of interest, $\langle \zeta_2 \rangle$:

$$\langle \zeta_2 \rangle = 0.02956\, N^{5/2} g b^2 / \pi^2 k' T \,. \tag{39}$$

From eqs. (31), (32) and (34) we get

$$\langle z_{ij} \rangle = (2/N)^{1/2}\, {}^2 a_2 \langle \zeta_2 \rangle (\cos \pi s - \cos \pi t) = 2(2/N)^{1/2}\, {}^2 a_2 \langle \zeta_2 \rangle \sin[\tfrac{1}{2}\pi(s-t)]\, \sin[\tfrac{1}{2}\pi(s+t)] \,. \tag{40}$$

We are now ready to sum the second term of eq. (24) with eq. (26) substituted into it. Proceeding as before, we have

$$\Sigma_i \Sigma_j \langle z_{ij} \rangle^2 / \langle x_{ij}^2 \rangle^{3/2} = (16/N^{1/2})(3/b^2)^{3/2} ({}^2 a_2)^2 \langle \zeta_2 \rangle^2 I_1 \,, \tag{41}$$

where I_1 is an integral,

$$I_1 = \int_0^1 \int_0^{1-q} q^{-3/2} [\sin(\pi q) \sin(\pi p)]^2 dp\, dq \,. \tag{42}$$

This integral may be evaluated by reduction to tabulated Fresnel integrals or by numerical integration as it stands. Its value is listed in table 1.

We can proceed in a similar way with the succeeding terms of eq. (26) substituted into eq. (24). The result is a power series in a parameter, y, as follows *

* In an earlier account of this work, circulated privately, a similar variable u was used, where $u = y^2/8$.

$$\Sigma_i \Sigma_j \langle 1/r_{ij} + z_{ij}^2/r_{ij}^3 \rangle = \tfrac{32}{9}(6/\pi)^{1/2}(N^{3/2}/b)\, Y(y) . \tag{43}$$

where

$$Y(y) = 1 + \sum_{n=1}^{\infty} D_{2n} y^{2n} , \tag{44}$$

y is given by

$$y = 4\sqrt{3}\langle \zeta_2 \rangle ({}^2a_2)/Nb , \tag{45}$$

and the D_{2n} are constant coefficients. The D_{2n} are given by

$$D_{2n} = \tfrac{3}{2}(2n)!\, C_n I_n / 8^n (n!)^2 , \tag{46}$$

with C_n defined in eq. (27) and the integrals I_n are

$$I_n = \frac{2^{2n-1}(n!)^2}{(2n)!} \int_0^1 \int_0^{1-q} \frac{[\sin(\pi q)\sin(\pi p)]^{2n}}{q^{(2n+1)/2}}\, dp\, dq$$

$$= \int_0^1 \frac{[\sin(\pi w^2)]^{2n}}{w^{2n}} \left[1 - w^2 + \frac{\cos(\pi w^2)}{\pi} \sum_{k=0}^{n-1} \frac{4^k (k!)^2 [\sin(\pi w^2)]^{2k+1}}{(2k+1)!} \right] dw . \tag{47}$$

(The last transformation was accomplished by a change of variable, $q = w^2$.) The first four of these integrals, evaluated by numerical integration, are listed in table 1, along with the coefficients D_{2n}.

The convergence of the series (44) turns out to be rather slow when y is large; for example, the four terms given converge to within one percent only when y is less than 2.6. For another alternative when y is large we can go back to eqs. (24) and (25). From eqs. (1) and (40) for $\langle x_{ij}^2 \rangle$ and $\langle z_{ij} \rangle$ respectively, and with (23) and (29), we can write v_{ij} as

$$v_{ij} = 24({}^2a_2)^2\langle \zeta_2 \rangle^2 \sin^2\pi q \sin^2\pi p / b^2 N^2 q = y^2 \sin^2\pi q \sin^2\pi p / 2q . \tag{48}$$

If we substitute this in eq. (25), and with (28), (29), etc., we obtain eq. (43) again, but with $Y(y)$ now expressed as a triple integral:

$$Y(y) = \frac{9}{4y^2} \int_0^1 \int_0^{1-q} \frac{q^{1/2} \exp(-y^2 PQ/4q)}{PQ} \int_0^{\infty} \exp(-q\,\omega^2/y^2 PQ) \left(\sinh\omega - \frac{\cosh\omega}{\omega} + \frac{\sinh\omega}{\omega^2} \right) d\omega\, dp\, dq , \tag{49}$$

where

$$PQ = \sin^2\pi p \sin^2\pi q . \tag{50}$$

Numerical integration of eq. (49) becomes useful as a means of evaluating $Y(y)$ when y is large.

2.5. Relation to experimental variables

Substitution of eq. (43) in eq. (12) will yield the sedimentation coefficient. First, however, we need to relate the parameters N and b to experimental quantities.

The mean square radius of the molecule at rest, R_0^2, which can be measured by light scattering, is defined (if N is large) by

$$R_0^2 = (1/2N^2)\Sigma_i \Sigma_j' r_{ij}^2 = \tfrac{1}{6} b^2 N \,. \tag{51}$$

Alternatively N and b can be related to the sedimentation coefficient at zero centrifugal field, S^0, as will be apparent in a moment.

If we put eq. (43) into eq. (12), the result is

$$S = S^0 Y(y) \,, \tag{52}$$

where S^0, using eq. (51), is given by

$$S^0 = 4M(1 - \bar{v}\rho) 10^{13} / 9\pi^{3/2} R_0 N_a \eta \,. \tag{53}$$

(Equation (53) is also the formula that Kirkwood obtained [9, 10] for S^0.) The variable y may be expressed in terms of either R_0 or S^0 [see eqs. (45) and (39)]:

$$y = 0.4729\, R_0\, M(1 - \bar{v}\rho)\Omega^2 x/\pi^2 RT \,, \tag{54}$$

$$= 3.825 \times 10^{10} M^2 (1 - \bar{v}\rho)^2 \Omega^2 x / N_a RT \eta S^0 \,, \tag{55a}$$

$$= 8.374 \times 10^{-24} M^2 (1 - \bar{v}\rho)^2 (\mathrm{rpm})^2 x / T \eta S^0 \,. \tag{55b}$$

S^0 is here expressed in Svedberg units (10^{-13} cgs); Ω is in radians per second *. In the last equation the values of the physical constants have been introduced and the angular velocity expressed in revolutions per minute (rpm).

3. Conclusions

The function $Y(y)$ thus turns out to equal the ratio, S/S^0, expressing the decline of sedimentation coefficient with centrifuge speed and other variables. This ratio is a function only of the dimensionless parameter, y. The parameter y has a simple physical meaning; from eqs. (1), (40) and (45) we can show that

$$y = \langle z_{0,N/2} \rangle / \langle x_{0,N/2}^2 \rangle^{1/2} \,, \tag{56}$$

where $\langle z_{0,N/2} \rangle$ is the average z-component of the distance between one end (index 0) and the mid-segment (index $N/2$) of the chain, and $\langle x_{0,N/2}^2 \rangle^{1/2}$ is the root mean square of the x-component of the same distance (which is equal to the root mean square of the corresponding z-component in the molecule at rest). The x-component does not change with the centrifugal field, while $\langle z_{0,N/2} \rangle$ vanishes at zero field and is proportional to the field. Thus y is a measure of the distortion of the molecule caused by the centrifugal field.

Figure 1 is a plot of $S/S^0 = Y(y)$ against $y^{1/2}$; since $y^{1/2}$ is proportional to Ω, this is effectively a plot of S versus centrifuge speed. The points show the predicted effect of speed on typical samples of DNA. Since rotors capable of 60 000 rpm have only recently come into general use, it is not surprising that this effect of speed on viral DNA escaped notice for many years. For unbroken bacterial DNA, however, the effect could obviously be serious.

The points shown in fig. 1 for T2 DNA can be compared with measured values, in particular, those of Schumaker [2]. The observed values were $S_{60\,000} = 55.1 \pm 1.3$ S and $S_{30\,000} = 61.8 \pm 0.9$ S, giving $S_{60\,000}/S_{30\,000} =$

* If S^0 is expressed as $S^0_{20,w}$, then the $(1 - \bar{v}\rho)$ in eq. (53) and one of the two factors $(1 - \bar{v}\rho)$ in eqs. (55) must correspond to water at 20°C.

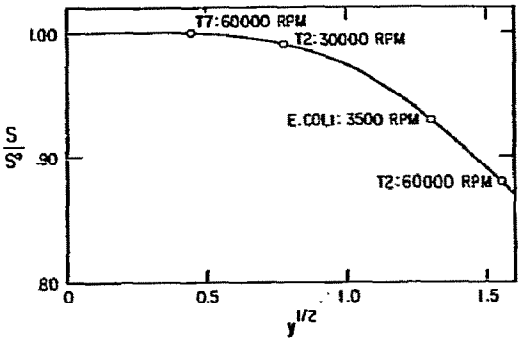

Fig. 1. Change of sedimentation coefficient with centrifuge speed according to eq. (52). The abscissa, $y^{1/2}$, is proportional to the centrifuge speed. The points shown were calculated by eqs. (52), (44), and (55b) for T7 DNA, $M = 25 \times 10^6$ and $S^0_{20,w} = 32$; T2 DNA, $M = 120 \times 10^6$ and $S^0_{20,w} = 61.8$, and *E. coli* DNA, $M = 2.7 \times 10^9$ and $S^0_{20,w} = 150$ (estimated), assuming the conditions given in table 1 of ref. [2] [$T = 293°$, $x = 5.2$ cm, $1 - \bar{v}\rho = 0.436$ (for 10% sucrose), $1 - \bar{v}\rho = 0.457$ (for 0.2 M NaCl), $\eta(H_2O) = 0.01$].

0.891 ± 0.024. We calculate from the numbers in the caption of fig. 1 that $y_{30\,000} = 0.620$ and $y_{60\,000} = 2.48$, leading to the points shown in the figure, and giving a ratio by eq. (44) of 0.884, in startlingly good agreement with the experiments. This agreement must be somewhat accidental, however, since the calculation is very sensitive to the values chosen for the molecular weight and for $1 - \bar{v}\rho$ in the sucrose gradient; neither of these quantities is known with much accuracy.

It is noteworthy that S^0 depends on y^2 and thus varies with high powers of the molecular weight, M, and of the centrifuge speed, Ω; this circumstance explains the observation that the effects on S of centrifuge speed are negligible below certain critical values of M and Ω, and then rise rapidly at higher values. This situation is well illustrated also in fig. 1.

The large amount of molecular distortion that accompanies a moderate change in the sedimentation coefficient is also noteworthy. The average form of the distortion, as given by eq. (40), is a displacement of the two ends of

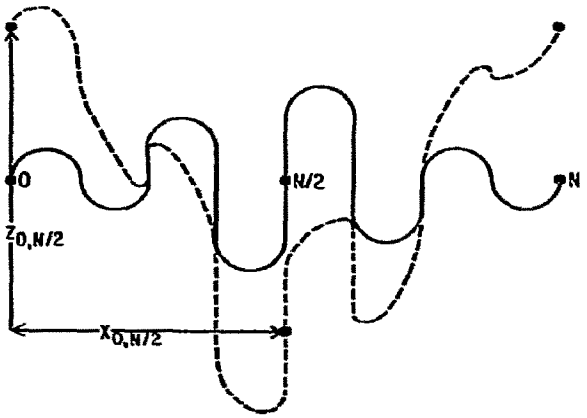

Fig. 2. Diagram of the distortion induced in a chain molecule by uneven friction according to eq. (40). A typical configuration of the undistorted molecule is shown by the solid curve; the same configuration with distortion is shown by the dashed curve. The direction of sedimentation is downward.

the chain "upward" (opposite to the direction of sedimentation) with respect to the middle of the chain, the displacement interpolating in a sinusoidal fashion between the middle and the ends. From eq. (44) we can calculate the amount of distortion, as measured by y, for a given value of $S/S^0 = Y(y)$; for example, when S/S^0 is 0.90, y is 2.15. Figure 2 is a diagram of this distortion.

It should probably be emphasized at this point that the molecular distortion that we deal with here is not caused by differences between the sedimenting forces on different parts of the molecule as the result of the dependence of the centrifugal acceleration on the centrifuge radius. That source of distortion was considered by Singer [16], who found it to be smaller than the effect discussed here by the ratio, R_0/x, approximately.

One remaining question comes to mind: If the sedimentation anomaly discussed here is a result of the differential in average forces between the middle and the ends of the chain, would it occur if the chain had no ends, that is, if it were a circle? Clearly, a calculation along the lines used here, in which average forces only are used, could never predict speed dependence of the sedimentation coefficient for a symmetrical circle. Perhaps an effect would appear from the consideration of momentary fluctuations in conformation, but one would expect it to be much smaller than that discussed here.

Acknowledgement

This work developed out of conversations with Irwin Rubenstein, whose contributions to the development of the basic ideas is hereby gratefully acknowledged. I am also indebted to Carl Zimm and to Verne Schumaker for computing the integrals I_n.

Appendix

In the text we have not considered the coordinate of the center of mass. The referee of this paper has pointed out that there are some useful remarks that can be made concerning it.

Considering only the z-coordinates, we find from eq. (13) two possible solutions (noting that $\lambda_0 = 0$),

$$\psi = A\psi_{\text{int}} \exp(-g\epsilon_0\zeta_0/D\rho') , \tag{A–1}$$

and

$$\psi = A\psi_{\text{int}} , \tag{A–2}$$

where A is the normalization constant, and ψ_{int}, the internal distribution function, is the product over all $k \neq 0$ of the exponential functions of eqs. (15) and (16). The coordinate ζ_0 measures, in a rather complicated way, the position of the center of mass. Equation (A–1) is then the solution corresponding to sedimentation equilibrium, and eq. (A–2) is the solution corresponding to a sedimentation velocity experiment, where a uniform concentration of solute sediments at a constant rate. It is the latter with which we deal in this paper.

Let us examine the part of the exponent in eqs. (A–1) and (A–2) that is linear in the ζ-coordinates. From eq. (16) we see that this involves

$$\sum_{k=0}^{N} \epsilon_k \zeta_k \tag{A–3}$$

in the equilibrium case [eq. (A–1)], and

$$\sum_{k=1}^{N} \epsilon_k \zeta_k \tag{A-4}$$

in the velocity case, [eq. (A–2)]. If we use eq. (14) for ϵ_k and eq. (43a) of ref. [7], we can transform (A–3) into

$$\sum_{k=0}^{N} \epsilon_k \zeta_k = e^{\dagger} \cdot \zeta = e^{\dagger} \cdot \mathbf{\Omega} \cdot \zeta = e^{\dagger} \cdot z = \sum_{i=0}^{N} z_i \,, \tag{A-5}$$

where e is the unit vector. Thus the exponent of the equilibrium solution, (A–1), depends linearly on the coordinate of the center of mass, $(1/N)\Sigma_{i=0}^{N} z_i$, as it should.

On the other hand, for the velocity case, the same transformation converts (A–4) into

$$\sum_{k=1}^{N} \epsilon_k \zeta_k = (e^{\dagger} - N^{1/2}\beta_0^{\dagger}) \cdot z \,. \tag{A-6}$$

Here e is the unit vector, but β_0 is the force vector corresponding to translation at uniform velocity; according to P.L. Auer and C.S. Gardner (private communication cited in ref. [7]) its ith element is (approximately)

$$\beta_{0i} = \frac{2\,\Gamma(\frac{5}{4})}{N^{1/2}\Gamma(\frac{1}{2})\,\Gamma(\frac{3}{4})\,[1-(1-2i/N)^2]^{1/4}} \,. \tag{A-7}$$

Thus the exponent in this steady-state solution does not depend simply on the coordinate of the center of mass, but involves a more complicated function expressing the fact of molecular distortion.

These results might be useful as the basis of an alternative method of calculating the distortion of the molecule, using the right-hand side of (A–6) as the starting point, instead of the normal coordinate form on the left-hand side, as was done in this paper. We have not yet looked into the feasibility or possible advantages of such an approach.

References

[1] B. Goldstein and B.H. Zimm, Biopolymers 12 (1973) 857.
[2] V.N. Schumaker and B.H. Zimm, Biopolymers 12 (1973) 869.
[3] V.N. Schumaker and B.H. Zimm, Biopolymers 12 (1973) 877.
[4] I. Rubenstein and S.B. Leighton, Biophys. Soc. Abstr. 209a (1971).
[5] P.E. Rouse, Jr., J. Chem. Phys. 21 (1953) 1272.
[6] F. Bueche, J. Chem. Phys. 22 (1954) 603.
[7] B.H. Zimm, J. Chem. Phys. 24 (1956) 269.
[8] J.M. Burgers, Second Report on Viscosity and Plasticity of the Amsterdam Academy of Sciences (Nordemann, New York, 1938).
[9] J.G. Kirkwood and J. Riseman, J. Chem. Phys. 16 (1948) 565.
[10] J.G. Kirkwood, J. Polymer Sci. 12 (1954) 1.
[11] R. Zwanzig, J. Chem. Phys. 45 (1966) 1858.
[12] C.M. Tchen, J. Appl. Phys. 25 (1954) 463.
[13] V. Bloomfield and B.H. Zimm, J. Chem. Phys. 44 (1966) 315.
[14] B.H. Zimm and R.W. Kilb, J. Polymer Sci. 37 (1959) 19.
[15] B.H. Zimm, G.M. Roe and L.F. Epstein, J. Chem. Phys. 24 (1956) 279.
[16] S.J. Singer, J. Polymer Sci. 2 (1947) 290.

BIOPHYSICAL CHEMISTRY 1 (1974) 292–299. © NORTH-HOLLAND PUBLISHING COMPANY

THE INFLUENCE OF ROTOR SPEED ON THE SEDIMENTATION BEHAVIOR IN SUCROSE GRADIENTS OF HIGH MOLECULAR WEIGHT DNA'S

Irwin RUBENSTEIN * and Sara B. LEIGHTON
Department of Molecular Biophysics and Biochemistry, Yale University, New Haven, Connecticut 06520, USA

Received 8 August 1973

Anomalous sedimentation behavior has been observed for high molecular weight duplex DNA's in sucrose gradients. The sedimentation rate of DNA's having molecular weights of 10^8 or higher is influenced by high centrifugal fields. The change in the sucrose sedimentation coefficient due to this effect, $S_{suc}^{RPM} - S_{suc}^{0}$, is equal to $1 \times 10^{-48} M^{3.65} (RPM)^4$. The anomalous behavior is not influenced by DNA concentration at sufficiently low concentrations. Because of the smallness of the coefficient this effect has not been previously detected for DNA's the size of T2 or smaller at rotor speeds below 40 000 RPM. For example, the relative sedimentation coefficient of T2 DNA at 65 000 RPM is only 9% less than at 10 000 RPM. However, the sedimentation profile of heterogeneous high molecular weight [$(100 - 350) \times 10^6$] *E. coli* DNA is severely altered even at moderate rotor speeds (37 000 RPM). Therefore, it seems advisable to use low rotor speeds when sedimenting high molecular weight DNA's.

1. Introduction

Sucrose gradient sedimentation is a useful tool for the characterization of DNA by means of its sedimentation velocity. In the course of some studies with *E. coli* DNA we discovered that its sedimentation behavior was affected by the strength of the sedimentation field. This effect becomes significant for DNA's whose molecular weights are greater than 10^8. To systematically study this phenomena we carried out a series of experiments with T2, T5 and T7 DNA's and studied the effect of rotor speed on their sedimentation behavior. In this paper we will report the results of these studies together with some of the data we have gathered on the sedimentation behavior of high molecular weight *E. coli* DNA.

2. Materials and methods

2.1. Bacteriophage

The growth and purification of the bacteriophage T2H, T5st+ and T7M has been previously described [1, 2].

2.2. DNA

The bacteriophage DNA's were isolated by phenol extraction as previously described [1, 2]. The bacterial DNA was isolated from *E. coli* using a technique developed by Lash [5] which is a modification of the procedure of Hoffman and Rubenstein [6]. The *E. coli* DNA is quantitatively isolated by this procedure and is heterogeneous in molecular weight [$(100 - 350) \times 10^6$].

2.3. Sucrose gradient sedimentation

E. coli, T2H, and T5st+ DNA's were sedimented in linear sucrose gradients and their relative sedimentation coefficients calculated using T7M DNA as a sedimentation standard according to procedures previously described [1, 2]. All sedimentation runs in the SW65 rotor employed polyallomer tubes because nitrocellulose tubes often failed at rotor speeds greater than 50 000 RPM. To form a gradient in the polyallomer tubes, which do not have the wetting properties of nitrocellulose, it was necessary to support the tubes at about a 45° angle to the horizon, and let the sucrose

* Present address: Department of Genetics and Cell Biology, University of Minnesota, St. Paul, Minnesota 55101.

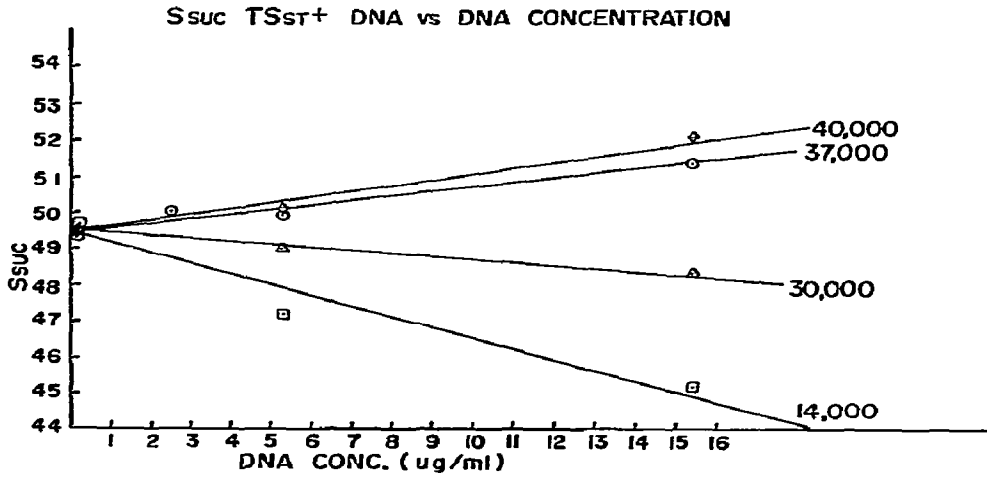

Fig. 1. Change of sedimentation coefficient of T5st+ DNA with concentration at various rotor speeds. The ^{32}P labeled T5st+ DNA was sedimented in 5–20% sucrose gradients in 0.1 M NaCl, 0.05 M PO_4, pH 6.7 at 10° in a SW39 rotor. ^{32}P labeled T7 DNA (0.1 μg/ml) was included as a reference. (S_{suc} = 32.6 *S*.) All points are the average of two determinations except those at 40 000 RPM for which only one determination was made.

solution run down a thin glass rod placed in the tube. After the gradient had been formed the rod was removed.

2.4. *Growth of radioactively labeled E. coli and bacteriophage*

The incorporation of ^{32}P or ^{3}H label into bacterial and bacteriophage DNA's and the counting of radioactive samples was carried out according to procedures previously described [1, 2, 6]. The dpm/μg DNA were determined from the known specific activity of the growth medium.

3. Results

3.1. *Effect of rotor speed on sedimentation velocity at high concentrations of DNA*

It has long been known [3] that at high concentrations the sedimentation behavior of high molecular weight DNA in sucrose gradients is strongly influenced by rotor speed. Fig. 1 shows the data we have obtained showing this effect for T5st+ DNA. The effect is complex in that at low rotor speeds the S_{suc} increases with decreasing DNA concentration, while at high rotor speeds the S_{suc} decreases with decreasing DNA concentration. At high rotor speeds (37 000 RPM) a similar effect is seen with T2 DNA; S_{suc} decreases as the DNA concentration is decreased (table 1). However, at DNA concentrations below about 0.5 μg/ml in the sample load the sedimentation behavior of T5 or T2 DNA for the rotor speeds indicated appears to be constant. For the remainder of the work described in this paper we have used low concentrations of DNA and have checked that these are not affecting the sedimentation behavior.

Table 1
Sedimentation behavior of T2 DNA [1)]

DNA concentration (μg/ml)	Time (min)	S_{suc}
5.5	120	59.5
5.5	150	58.9
1.1	150	56.9
0.5	120	56.8
0.5	150	56.3
0.3	120	56.8

[1)] T7 DNA (0.1 μg/ml) was used as an internal standard ($S^0_{20,w}$ = 32.6 *S*). Conditions of sedimentation: SW39 rotor; nitrocellulose tubes; 5–20% sucrose gradient in 0.1 M NaCl, 0.05 M PO_4, pH 6.7, 4.8 ml; 0.2 ml sample load; 37000 RPM, 10°.

Table 2
Sedimentation behavior of T2 DNA at high rotor speeds [1)]

	RPM	Time (hours)	S_{suc}	σ	n	Concentration (μg/ml)
A. Nitrocellulose tubes	14 000	14	57.6	–	2	0.10
			57.3	–	2	0.50
	25 000	4.4	56.6	–	2	0.01
			56.8	–	2	0.10
			57.8	–	2	0.50
	30 000	2.0	56.0	–	1	0.01
			56.6	–	2	0.50
	45 000	1.4	54.4	–	2	0.01
			54.1	–	3	0.10
			54.7	–	3	0.50
	50 000	1.4	54.7	0.7	6	0.01
			54.3	0.6	7	0.10
			54.0	0.8	7	0.50
B. Polyallomer tubes	37 000	2.0	58.9	0.1	3	
		2.83	58.0	0.7	4	
	50 000	1.08	57.3	0.5	3	
		1.58	57.7	0.5	6	
	60 000	0.75	56.4	0.3	3	
		1.17	53.9	0.3	3	
	65 000	0.67	53.8	1.1	7	
		1.0	54.3	0.3	5	

[1)] All runs employed ^{32}P labeled T7 DNA as an internal sedimentation standard; n refers to the number of runs; σ is the standard deviation of the experimental values. The runs in polyallomer tubes at the various rotor speeds each used a series of ^{32}P labeled T2 DNA concentrations, 0.05, 0.1 and 0.2 μg/ml and were carried out in a SW65 rotor at 10°, in 5–20% sucrose gradients in 0.1 M NaCl, 0.05 M PO_4, pH 6.7, 0.001 M EDTA.

3.2. The effect of high rotor speeds in the sedimentation behavior of DNA at very low concentrations

3.2.1. Bacteriophage DNA's

The sedimentation behavior of T2 DNA at high rotor speeds is shown in tables 2 and 3. The sedimentation runs were carried out in either nitrocellulose or polyallomer tubes with varying rotor speeds, lengths of time of centrifugation and DNA concentrations. The rotor speed had no effect on the gaussian shape of the T2 DNA peak, but as the rotor speed was increased the S_{suc} of the T2 DNA relative to T7 DNA progressively decreased.

At DNA concentrations below about 0.5 μg/ml the sedimentation coefficient seems to be independent of DNA concentrations and lengths of centrifugation at a given RPM. The longer times of centrifugation subjects the sedimenting DNA to higher hydrostatic pressures. This apparently has little or no effect on the sedimentation rate. The curious finding that the nature of the centrifugation tube influences the sedimentation coefficient of T2 DNA is completely unexpected and unexplained. A similar result was found for T5st+ DNA in that the S_{suc} in nitrocellulose is 49.2 S [1].

Table 3 summarizes the sedimentation data for T2 and T5 DNA. These values of S_{suc} are plotted in fig. 2 versus the fourth power of the rotor speed.

This plot of our experimental values was suggested by the form of the equation developed by Zimm [4] in which

Table 3
Sedimentation behavior of T2 and T5 DNA's at high rotor speeds [1)]

RPM	T2 DNA nitrocellulose			T2 DNA polyallomer			T5 DNA polyallomer		
	S_{suc}	σ	n	S_{suc}	σ	n	S_{suc}	σ	n
10 000	58.2	0.3	3						
12 000	57.7	0.3	3						
13 000	57.4	0.3	5						
14 000	57.1	0.6	11	59.4	0.3	5	51.1	0.3	8
15 000	57.5	0.5	3						
16 000	57.4	0.4	3						
25 000	57.1	0.5	15						
30 000	56.8	0.2	5						
37 000	56.6	0.5	16	58.4	0.7	7	50.4	0.3	8
45 000	54.4	0.5	8						
50 000	54.3	0.6	20	57.6	0.5	9	50.2	0.4	12
55 000				57.3	0.3	6	49.6	0.5	6
60 000				55.1	1.4	6	49.6	0.3	6
65 000				54.0	0.8	11	49.6	0.5	14

[1)] The sedimentation conditions were as described in table 2. For the series of runs at each rotor speed a range of DNA concentrations was used. The high (0.5 μg/ml) and the low (0.05 μg/ml) concentrations for each of the DNA's (T2 and T5) has the same relative sedimentation coefficients and are therefore grouped together in this table.

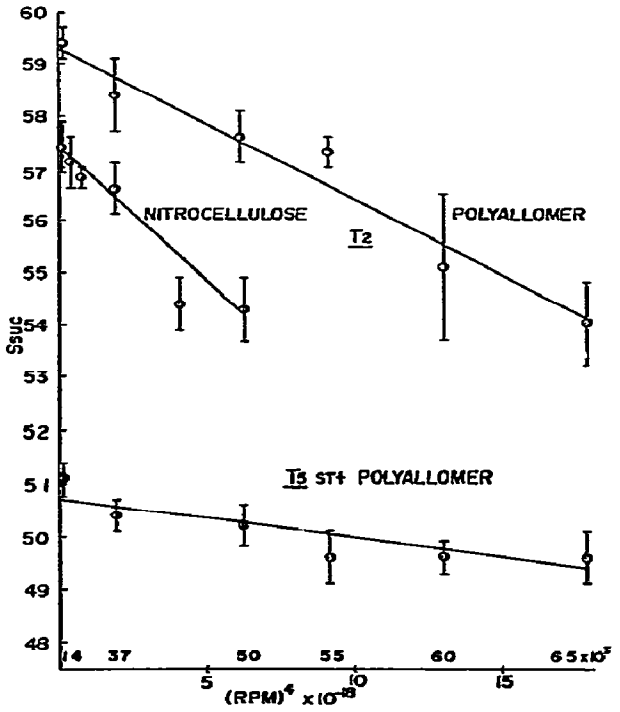

Fig. 2. The S_{suc} of T2 and T5st+ DNA's as a function of the fourth power of the rotor speed. The data used in this figure and the sedimentation conditions used are given in table 3. The standard deviations of the experimental values are indicated.

$$S_{20,w} = S^0_{20,w}\left\{1 - 2.024 \times 10^{-48} \times \frac{(1-\bar{v}\rho_{suc})^2(1-\bar{v}\rho_{20,w})^2 x^2 M^4 (\mathrm{RPM})^4 + \ldots}{T^2 \eta^2_{20,w} (S^0_{20,w})^2}\right\}, \quad (1)$$

where M is the molecular weight of the DNA, $\bar{v}$ its partial specific volume, ρ_{suc} is the density of the sucrose gradient at the radius x in cm, $\rho_{20,w}$ is the density and $\eta_{20,w}$ is the viscosity of water at 20°, RPM is the angular velocity in revolutions per minute of the centrifuge rotor, $S^0_{20,w}$ is expressed in svedberg units (10^{-13} sec) and T is the absolute temperature.

In most centrifugation runs which are carried out at 10° the larger DNA molecules are sedimented to about the mid-point of the rotor tube. For the SW65 rotor the mean value of x for such runs would occur at 5.32 cm where the sucrose concentration would be about 8.8% and its ρ_{suc} = 1.05 gm/cm^2. If we assume that $\bar{v}$ for DNA in sucrose is 0.56 cm^3/gm and that $S^0_{suc20,w} = 0.0833\, M^{0.35}$ (ref. [2]) and consider only the first term in Zimm's equation (1) the equation becomes

$$\Delta S_{suc20,w} = S^0_{suc20,w} - S^{RPM}_{suc20,w} = 2 \times 10^{-48} M^{3.65} (\mathrm{RPM})^4 . \quad (2)$$

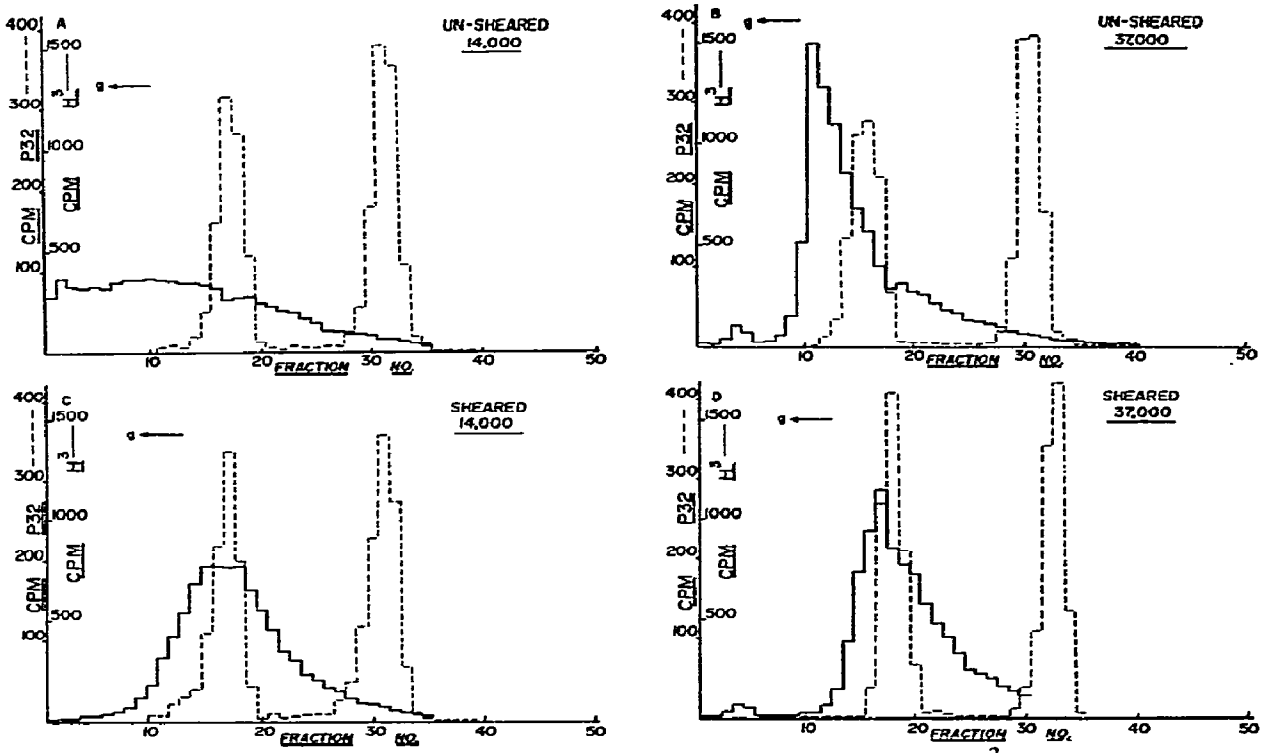

Fig. 3. The effect of rotor speed and DNA size on the sedimentation behavior of *E. coli* DNA. The ^{3}H labeled *E. coli* DNA (0.2 μg/ml) was sedimented in 5–20% sucrose gradients in 0.15 M NaCl, 0.015 M NaCit at 10° in a SW50 rotor. ^{32}P labeled T2 DNA (0.4 μg/ml) and T7 DNA (1 μg/ml) are included as sedimentation references. (A) 14000 RPM for 16 hours, (B) 37000 RPM for 2.5 hours. The DNA mixture placed in a shear gradient (see text) before sedimentation: (C) 14000 RPM for 16 hours, (D) 37000 RPM for 2.5 hours.

We can compare the constant 2×10^{-48} to the values of the constant generated from the data shown in fig. 2 for sedimentation of T2 and T5 DNA's in polyallomer tubes.

The observed $\Delta S_{\text{suc}20,w}$ for T2 DNA is 5.2 *S*. If we let the molecular weight of T2 DNA be equal to 120×10^6 [2, 7] then the calculated constant is about equal to 1×10^{-48}. The observed $\Delta S^0_{\text{suc}20,w}$ for T5st+ DNA is equal to 1.3 *S*. If we let the molecular weight of T5st+ DNA be equal to 80×10^6 [2, 7] then the calculated constant is once more approximately equal to 1×10^{-48}. These constants are in fair agreement with the constant calculated from Zimm's theory. We therefore propose the following empirical equation

$$\Delta S_{\text{suc}20,w} = 1 \times 10^{-48} M^{3.65} (\text{RPM})^4 . \qquad (3)$$

Because eq. (3) ignores the higher terms of Zimm's equation (1) (which can be significant) it is of limited usefulness in theoretically predicting the actual ΔS. But it does allow a ready calculation to be made as to whether or not a given rotor speed is significantly altering the sedimentation coefficient of a high molecular weight DNA.

We have also used the more complete form of Zimm's theory (ref. [4]; eqs. (44, 52, 55b)) which includes the higher power terms to predict the expected decrease in the sedimentation coefficient for a rotor speed of 65 000 RPM. For T2 DNA, using the following values: $M = 120 \times 10^6$, $S^0_{\text{suc}20,w} = 59.3$, and the above values of $\bar{v}$, T, and x, we obtain a calculated ratio of $S^{65\,000}/S^0 = 0.87$. The experimental ratio is 0.91.

It is interesting to note that the sedimentation data for the nitrocellulose tubes was gathered in SW39, SW50 or SW50.1 rotors. These have an average radius

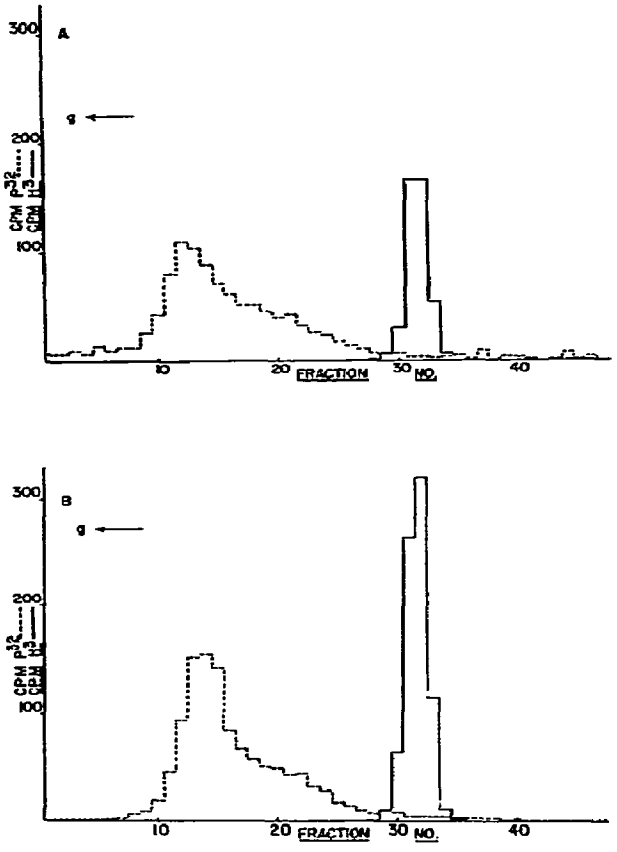

Fig. 4. The effect of rotor speed on the sedimentation behavior of *E. coli* DNA. The ^{32}P labeled *E. coli* DNA (0.016 μg/ml) was sedimented in 5–20% sucrose gradients in 0.1 M NaCl, 0.05 M PO_4, pH 6.7, 0.001 M EDTA at 10° in a SW50.1 rotor. ^{3}H labeled T7 DNA (0.3 μg/ml) is included as a sedimentation reference. (A) 14000 RPM for 14 hours, (B) 25000 RPM for 4.38 hours, (C) 37000 RPM for 2.0 hours.

about 1 cm greater than does the SW65 rotor. From Zimm's equation we would expect a steeper slope for the decrease of the sedimentation coefficient of T2 DNA in the former rotors and this is what was found. If we again use the complete form of Zimm's theory to predict the expected decrease in the sedimentation coefficient from these data for a rotor speed of 50 000 RPM, $S^0_{suc\ 20,w} = 57.4$ and mean $x = 6.3$ cm, we obtain a ratio of $S^{50000}/S^0 = 0.90$. The observed ratio is 0.94.

This agreement of the experimental values with the theory is in part accidental. The results are very sensitive to the values chosen for the molecular weight and $(1 - \bar{v}\rho)$ of the DNA's, neither of which are known with great decision. Moreover, by treating x, η and ρ of the gradient as constants we have ignored the fact that they do vary during sedimentation. However, fig. 2 does clearly indicate that the S_{suc} of T2 and T5 DNA's is affected by the rotor speed and that the dependence is a function of the rotor's RPM, mean radius and the DNA's molecular weight.

Finally, these values of S_{suc} for T2 and T5 DNA were determined using T7 DNA as a reference. How much would one expect the sedimentation behavior of T7 DNA to be affected by rotor speed of 65 000 RPM? Using eq. (3) we calculate that $\Delta S_{suc} = 0.02$ and therefore the effect of rotor speed can be ignored.

3.2.2. *E. coli* DNA

The effect of rotor speed in the sedimentation behavior of high molecular weight *E. coli* DNA is drastic.

Fig. 3 shows the same preparation of *E. coli* DNA sedimented at rotor speeds at 14 000 and 37 000 RPM; T2 and T7 DNA's are included as references. Using eq. (3) we calculate that T2 DNA has its S_{suc} reduced about 0.6*S* at 37 000 RPM. However, the *E. coli* DNA that sediments to fraction 5 in the 14 000 RPM (fig. 3A) would have a molecular weight of about 3×10^8 and its S_{suc} should be reduced about 16*S* at 37 000 RPM (at 14 000 RPM, $\Delta S_{suc} = 0.3S$ for 3×10^8 amu DNA) or about 10 gradient fractions. Therefore, we see in fig. 1B what appears to be a "piling up" of *E. coli* DNA and a drastic alteration of the sedimentation pattern seen in fig. 3A. The amount of *E. coli* DNA loaded on the gradient in the two runs and the amount recovered from the gradients are similar.

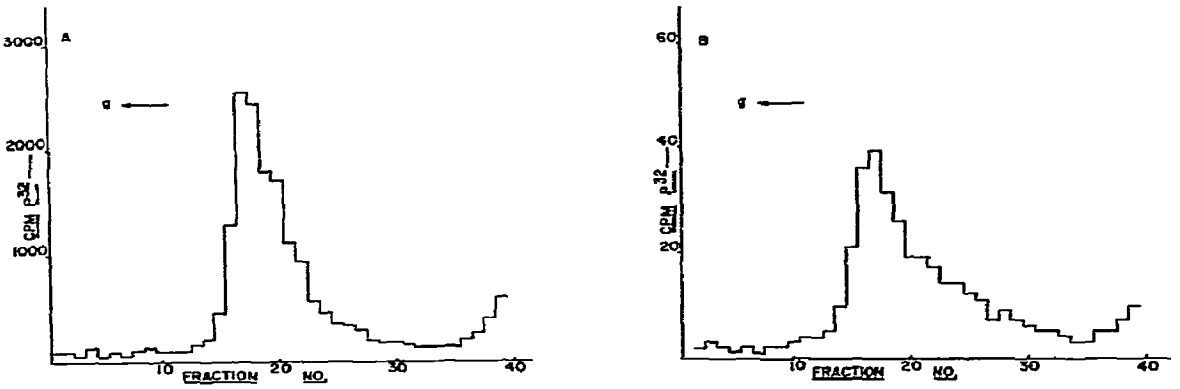

Fig. 5. The effect of low DNA concentrations on the sedimentation behavior of *E. coli* DNA at high rotor speeds. The ^{32}P labeled *E. coli* DNA was sedimented in 5–20% sucrose gradients in 0.1 M NaCl, 0.05 M PO_4, pH 6.7, 0.001 M EDTA at 10° in SW50.1 rotor at 37000 RPM for 2 hours. (A) 0.5 μg/ml *E. coli* DNA, 0.1 μg total, (B) 0.005 μg/ml *E. coli* DNA, 0.001 μg total.

The sedimentation profiles shown in figs. 3C and 3D indicate that the property of the *E. coli* DNA that gives it its odd sedimentation behavior is sensitive to a shear gradient. When the *E. coli* DNA preparation is subjected to a mild shear gradient (800 RPM in the apparatus described in ref. [1]) which should break high molecular weight DNA and produce fragments about the size of T2 DNA we see that the *E. coli* DNA does sediment with the T2 DNA at rotor speeds of either 14 000 or 37 000 RPM. Even here there is some indication that the larger DNA fragments of *E. coli* DNA seen in the gradients sedimented at 14 000 RPM are being retarded compared to gradients sedimented at 37 000 RPM.

Fig. 4 shows a series of *E. coli* DNA sedimentation runs at rotor speeds of 14 000, 25 000 and 37 000 RPM using T7 DNA as a sedimentation reference. These figures show the progressive alteration in the sedimentation behavior of the heterogeneous molecular weight distribution of the *E. coli* DNA. As the rotor speed is increased an artificially sharper and slower sedimenting peak is produced.

Evidence that this effect is independent of DNA concentration is presented in fig. 5. Samples of the same *E. coli* DNA preparation are sedimented at two different concentrations, 0.5 μg/ml and 0.05 μg/ml at 37 000 RPM. This DNA showed a much broader distribution of molecular weights such as is seen in figs. 3 and 4 at lower RPM's. Here in fig. 5 we see that the artificial sharpening of the DNA peak is independent of DNA concentration.

4. Discussion

The main conclusion of this work is that the sedimentation behavior of high molecular weight DNA at low concentrations is sensitive to rotor speed. This effect is noticeable with T2 DNA (120×10^6 amu) and is just noticeable with T5st+ DNA (80×10^6 amu) at rotor speeds higher than are normally used. The effect severely distorts the sedimentation behavior of high molecular weight *E. coli* DNA [$(100–300) \times 10^6$] even at relatively low rotor speeds (37 000 RPM). This strong dependence of the sedimentation behavior on rotor speed and molecular weight is predicted by the theory of Zimm [4] which hypothesizes a reduction in S proportional to approximately the 4th power of the RPM and the 3.65 power of the molecular weight [at least in the simplified formulations shown in eq. (3)]. This anomalous behavior in the sedimentation of high molecular weight DNA's has been confirmed by other investigators [8–10].

The sedimentation velocity of a macromolecule is a function of its molecular weight, partial specific volume and frictional coefficient. Since there is no reason to believe that the high sedimentation rates produced by high rotor speeds should alter the mole-

cular weight or the partial specific volume of the DNA then they must be affecting its frictional coefficient. This supposition is strongly supported by the theoretical derivations in the accompanying paper by Zimm [4].

Acknowledgements

This research was supported by the National Science Foundation Research Grants No. GB–26126. A preliminary report of this work was presented at the Biophysical Society Meetings [11].

References

[1] I. Rubenstein, Virology 36 (1968) 356.
[2] S.B. Leighton and I. Rubenstein, J. Mol. Biol. 46 (1969) 313.
[3] E. Burgi and A.D. Hershey, Biophys. J. 3 (1963) 309.
[4] B.H. Zimm, Biophys. Chem. 1 (1974) 279.
[5] T. Lash, Thesis, Yale University (1971).
[6] D.B. Hoffman, Jr. and I. Rubenstein, J. Mol. Biol. 35 (1968) 375.
[7] D. Lang, J. Mol. Biol. 54 (1970) 557.
[8] R. Kavenoff, J. Mol. Biol. 72 (1972) 801.
[9] D. Levin and F. Hutchinson, J. Mol. Biol. 75 (1973) 455.
[10] V.N. Schumaker and B.H. Zimm, Biopolymers 12 (1973) 869
[11] I. Rubenstein and S.B. Leighton, Biophys. Soc. Abstr. 11 (1971) 209a.

BIOPHYSICAL CHEMISTRY 1 (1974) 300–307. © NORTH-HOLLAND PUBLISHING COMPANY

CHEMICAL RELAXATION STUDIES ON BOVINE SERUM ALBUMIN. I. REACTIONS OF THE IMIDAZOLE GROUPS AT pH 6 TO 8

Herbert B. SILBER
Department of Chemistry, University of Maryland, Baltimore County Baltimore, Maryland 21228, USA

Received 20 June 1973
Revised manuscript received 5 September 1973

In the pH range of 6 to 8, the proton transfer reactions of BSA were measured using the temperature jump relaxation technique. The rate data were compared to the results using imidazole itself to establish that the observed reactions were those of the imidazole groups in the BSA. Upon the addition of calcium and gadolinium to the BSA solutions, no metal ion complexation was observed for either cation at the imidazole sites.

1. Introduction

The determination of the binding sites for metal ions in proteins is an extremely important and difficult problem. Although the binding of the first row transition metal ions can be studied using spectroscopic and magnetic techniques, this is of much greater difficulty when the binding cation is an alkaline earth ion such as calcium. In recent years several groups have attempted to determine the calcium binding sites through the isomorphous replacement by lanthanide (III) ions, which have magnetic and spectroscopic properties which can provide a handle for monitoring the cation binding [1–5]. In effect, the lanthanides successfully compete for these binding sites and hence act as "super calcium ions". However, in the case of bovine serum albumin (BSA), a protein of little selectivity, there is a question of whether or not these cations bind at the same sites [6–10].

Birnbaum et al. [6] used difference absorption spectra in the visible region to study the binding of Nd(III) to BSA. At pH = 5.6 they found that the Nd binding occurs through the carboxyl groups. At pH 7 or greater, other spectral changes occurred which the authors suspected arose from Nd binding to the imidazole groups in the BSA. This study was extended to investigate the Nd(III) binding to histidine and substituted histidines using proton magnetic resonance spectroscopy and analyzing the isotropic shifts caused by Nd binding [7]. At pH's below 5.0, a 1:1 monodentate histidine–Nd(III) complex was observed, with coordination through the carboxyl group. At a pH greater than 6 a bidentate histidine–Nd(III) complex was observed and attributed to Nd(III) coordination to the carboxyl group and the imidazole nitrogen. These results are similar to those reported for calcium binding to human serum albumin [8], where all of the bound Ca(II) was at the carboxyl site at or below pH 5.5. Significant bidentate binding with the carboxyl group in conjunction with imidazole and amino groups in serum albumin was found starting at a pH above 6. At pH 7, 0.22 mole of Ca was bound in this bidentate fashion per mole of albumin. However, as the pH exceeded 8, this figure rose rapidly reaching 1.4 at pH 8 and 10.5 mole at pH 10.5. Thus, these equilibrium measurements tend to support the notion that Nd(III) and Ca(II) bind at the same sites under similar conditions in serum albumins and similar molecules. However, in an alternate study of the binding of Gd(III) with BSA, Reuben reports that the binding sites for Gd(III) seem to be different than for Ca(II) [9]. In that NMR paper, Reuben used Scatchard plots to determine the existence of four Gd(III) binding sites, with an apparent Gd(III) binding dissociation constant of 1.3×10^{-4}M at 300°K and pH = 6.3. Further evidence for Gd(III) binding to BSA came

from a second study utilizing the electron spin resonance technique, in which Reuben concluded that the environment of Gd(III) is more symmetric when bound to the protein, compared to the aquo ion [10].

We have carried out our initial investigations in this field to determine if kinetic techniques can be utilized to determine binding sites in proteins, especially when competing cations are present in the solution, and thereby helping to eliminate the literature discrepancies. By carrying out the investigation within the pH range of approximately 6 to 8, and by using the temperature jump technique in conjunction with an additional pH indicator, we hoped to focus attention on cation binding to the imidazole groups. This is possible because cation binding at the ionized carboxyl groups would not be observable via a proton indicator. We observed chemical relaxation phenomena in our temperature jump investigations on BSA with or without the presence of an additional complexing cation. Furthermore, as a check to determine that the reactions corresponded to those of the imidazole groups, similar measurements were carried out on imidazole, which were then compared to earlier results [11].

2. Experimental

2.1. Reagents and solutions

The BSA, purchased in the crystallized form from Miles Laboratory (Kankakee, Illinois), was used without further preparation. Stock solutions were made up by weight (MW assumed to be 65 000) [12], mixed with other reagents and then stored in the refrigerator. No BSA solutions were used which had been around for longer than one week. The stock solutions of the metal ions were made up from $Ca(NO_3)_2$ (Baker, Analyzed) and from lanthanide oxides (Lindsay Rare Earths) dissolved by the addition of perchloric acid. The pH indicators used were chlorophenol red at the lower pH's and metacresol purple at the higher ones. The pK of chlorophenol red had been determined to be 6.08 [13]. Using common spectroscopic techniques the pK of metacresol purple was determined to be 8.15 at 0.2 ionic strength and 25°C. Over the small temperature intervals investigated, these values were used without further corrections. The imidazole used in the comparison studies was obtained from Aldrich (99% pure) and was also used without further purification. All solutions had an ionic strength of 0.2 with $NaClO_4$ as the inert electrolyte, which was made by neutralizing weighed portions of Na_2CO_3 with $HClO_4$, heating to expel CO_2, and then by dilution to volume of the stock solution.

2.2. Instrumentation and experimental procedure

The kinetic measurements were carried out using a temperature jump spectrophotometer from Messanlagen Studiengesellschaft mbh (Göttingen, Germany). The cell compartment was regulated at constant temperature using a Lauda Ultra Kryomat, equipped with a R20 digital thermoregulator, which was reproducible in temperature to 0.02°. After discharging a 0.05 μF capacitor charged to 40 KW through the solution, causing a 5.0° temperature rise, the changes in optical density were monitored using a Tektronix 545A Oscilliscope in conjunction with a Polaroid CR-9 camera. Both the theory and techniques of the temperature jump technique have been well characterized elsewhere [14].

Before making the T-jump measurements, the solutions were thermostated at the given temperature within the cell. Measurements were carried out at 575 nm with chlorophenol red and 563 nm with the metacresol purple. At least 15 minutes were allowed to elapse between successive jumps so as to insure that the solution returned to the same initial temperature, with a minimum of two measurements carried out on each test solution. After the completion of the relaxation measurements, the pH of each test solution was measured with a Corning 112 digital pH meter equipped with a combination micro electrode. All numerical analyses were carried out on a Wang 720 programmable calculator.

The optical density as a function of time is read from the oscilloscope picture. The relaxation data is plotted in the form of $\ln[(X_0-X_f)/(X_t-X_f)]$ versus time, where X is the voltage which is proportional to the optical density and X_0 is the initial voltage, X_f is that after equilibrium is re-established and X_t is the voltage at a given time. Since the relaxation equation, $X = X_0 \exp[-t/\tau]$, is always a first order equation, X_0 need not correspond to the true initial condition at the temperature rise, but may be any convenient

starting point. The slope of the straight line obtained is equal to $1/\tau$ where τ is the characteristic relaxation time of the test solution. When $1/\tau$ is graphed using the concentration dependence characteristic of a given mechanism, the mechanism is said to be possible if the predicted curve, usually a straight line, goes through most of the experimental data. The errors usually associated with $1/\tau$ are of the order of 10 to 15%, excluding concentration errors, and often some of the data points lie more than the relaxation time error away from the least squares curve. If the assumed mechanism is not valid, no correlation can be seen between the experimentally determined relaxation data and the appropriate concentration dependence.

3. Results

The initial relaxation times measured using BSA indicated that the relaxation times increased in an irregular manner with BSA concentration and with increasing pH, with no simple correlation observed with either quantity. This provides evidence that the reaction must involve more than one BSA reaction step coupled to the indicator relaxations. This observation is similar to those made in the imidazole study [11]. The relaxation data for the BSA and imidazole systems are summarized in tables 1 and 2. The functional dependence of ϕ and θ will be described later after possible mechanisms are described.

The general mechanism operating in these systems involves at least the following four steps:

$$\mathrm{ImH^+} \underset{k_{21}}{\overset{k_{12}}{\rightleftharpoons}} \mathrm{Im} + \mathrm{H^+}, \tag{1}$$

$$\mathrm{ImH^+} + \mathrm{OH^-} \underset{k_{32}}{\overset{k_{23}}{\rightleftharpoons}} \mathrm{Im} + \mathrm{H_2O}, \tag{2}$$

Table 1
Relaxation data at 7°C for BSA

10^6 $\mathrm{Im}_{\mathrm{total}}$ BSA data	pH	10^6 $[\mathrm{H^+}]$ (M)	10^6 [Im] (M)	10^6 $[\mathrm{In^-}]$[a] (M)	$10^{-3}\tau^{-1}$ ($\mathrm{sec^{-1}}$)	$10^{-9}\tau^{-1}\theta^{-1}$ ($\mathrm{M^{-1}\ sec^{-1}}$)	ϕ ($\mathrm{M^{-1}}$)
0.317	6.03	1.24	0.0237	1.66 C	7.2 ± 0.1	5.3	0.81
3.17	6.10	1.07	0.272	18.1 C	17.3 ± 0.3	14.5	0.94
3.17	6.19	0.867	0.328	20.2 C	12.6 ± 2.3	12.7	1.15
3.17	6.95	0.148	1.28	35.2 C	9.5 ± 1.0	33.6	6.76
3.17	7.58	0.0347	2.35	6.95 M	20.6 ± 2.3	152.	28.8
4.04	7.08	0.112	1.91	0.611M	9.4 ± 0.9	42.7	8.95
4.04	7.34	0.0611	2.51	1.06 M	14.3 ± 1.6	86.9	16.4
4.04	7.52	0.0400	2.89	1.54 M	12.5 ± 0.7	88.2	25.0
4.04	7.67	0.0286	3.14	2.03 M	10.3 ± 0.1	79.5	35.0
6.23	5.32	6.403	0.0959	2.38 C	19.2 ± 0.4	2.9	0.16
6.23	7.32	0.0648	3.80	1.02 M	14.6 ± 0.4	86.0	15.6
6.34	6.35	0.593	0.914	24.2 C	28.1 ± 3.8	38.6	1.69
16.0	5.80	2.09	0.732	5.90 C	19.9 ± 0.3	8.2	0.48
16.0	6.35	0.589	2.33	12.1 C	20.9 ± 2.8	22.4	1.70
16.0	6.91	0.164	6.07	17.3 C	27.9 ± 1.6	47.0	6.09
16.0	7.51	0.0411	11.4	3.01 M	17.4 ± 2.1	118	24.3
16.0	7.87	0.0181	13.6	5.77 M	18.3 ± 0.8	153	55.3
16.0	7.87	0.0179	13.6	5.82 M	21.8 ± 2.8	183	55.9
20.6	5.93	1.58	1.23	7.17 C	22.0 ± 3.5	11.1	0.64
20.6	6.38	0.553	3.16	12.5 C	27.0 ± 0.6	27.9	1.81
20.6	7.38	0.0559	13.2	2.31 M	17.7 ± 2.9	104	17.9
20.6	7.65	0.0299	15.9	3.93 M	21.2 ± 0.9	157	33.5
20.6	7.79	0.0217	16.9	5.04 M	18.7 ± 2.1	150	46.0
20.6	7.95	0.0148	18.0	6.63 M	18.8 ± 1.9	162	67.4
25.4	6.06	1.16	2.01	17.2 C	26.8 ± 0.3	18.2	0.86

a) C = chlorophenol red; M = metacresol purple.

Table 2
Relaxation data at 7°C for imidazole

10^6 Im_{total} (M)	pH	10^6 $[H^+]$ (M)	10^6 [Im] (M)	10^6 $[In^-]$ a) (M)	$10^{-3}\tau^{-1}$ (sec^{-1})	$10^{-9}\tau^{-1}\theta^{-1}$ ($M^{-1}sec^{-1}$)	ϕ (M^{-1})
4.40	6.53	0.397	0.889	14.0 C	8.7 ± 0.6	15.3	2.52
4.40	8.19	0.00858	4.06	10.6 C	55.8 ± 2.0	262	117
6.70	8.11	0.0103	6.07	8.37 M	26.9 ± 1.0	244	97.4
11.0	6.19	0.870	1.14	20.3 C	15.9 ± 0.4	15.0	1.13
11.0	6.89	0.174	4.02	8.49 C	23.9 ± 1.6	34.3	5.75
16.7	7.28	0.0691	9.90	3.81	36.9 ± 4.8	102	14.5
16.7	7.69	0.0274	13.1	8.43 M	28.3 ± 0.8	157	36.5
16.7	8.01	0.0131	14.8	14.4 M	37.9 ± 3.3	284	76.3
22.0	5.86	1.85	1.13	12.9 C	16.3 ± 2.8	7.6	0.54
22.0	7.11	0.102	10.9	0.665M	25.6 ± 1.1	105	9.79
44.0	6.39	0.549	6.79	12.5 C	24.0 ± 0.6	18.1	1.82
88.1	6.35	0.595	12.7	12.1 C	30.5 ± 2.8	15.0	1.68

a) C = chlorophenol red; M = metracresol purple.

$$HIn \rightleftharpoons H^+ + In^- , \quad (3)$$

$$H^+ + OH^- \rightleftharpoons H_2O . \quad (4)$$

Here ImH^+ represents the protonated imidazolium ion and Im, the imidazole species. Similar definitions are employed for the indicators, represented by HIn and In^-, respectively. A very rapid relaxation, which could not be characterized, was present and was attributed to reactions (3) and (4). When BSA was added to solutions containing the indicators and inert electrolyte, an additional slower relaxation was observed. Our first attempt to fit the experimental data assumed that reaction (1) was rate determining and the other three reactions were treated as rapid equilibrium reactions. This mechanism was chosen because in the imidazole system reactions (2) through (4) were more rapid than (1) [11]. When the experimental data were plotted according to the relaxation equations that were derived, there was no correlation between the experimental data and the calculated concentration dependence relationship, thereby eliminating this mechanism from further consideration.

The next attempt assumed that the observed relaxation was characteristic of a combination of reactions (1) and (2), with the others being in rapid equilibrium. When this assumption is made, and suitable algebraic manipulations are carried out, the following equations result:

$$\tau^{-1}/\theta = k_{21} + k_{32}\,\phi , \quad (5)$$

where

$$\theta = K_{Im} + [H^+] + [Im]/\gamma , \quad (6)$$

$$\phi = (1 + [Im]/\gamma[H^+] + K_{Im}/[H^+])/\theta , \quad (7)$$

$$\gamma = 1 + [In^-]/(K_{In} + [H^+]) + K_w/[H^+]^2 , \quad (8)$$

and K_{Im} represents the acid dissociation constants of BSA or imidazole and K_{In} is the acid dissociation constant of the indicator which was present in a given solution. When $\tau^{-1}\theta^{-1}$ is plotted as a function of ϕ, a straight line can be drawn through most of the BSA data as is shown in fig. 1. The vertical bars represent only the observed experimental range of the calculated relaxation times. Since errors of unknown magnitude are also present in θ and ϕ, the actual experimental error is greater than that obtained only from the relaxation measurements, and thus it is not surprising that some points deviate from the least squares line by more than the experimental relaxation error. The line drawn in the figure only corresponds to that for the BSA system in the absence of Ca(II) or Gd(III). A weighted least squares program, with a $1/y^2$ weighting factor was used to obtain this least squares line. At 7° the slope which equals k_{32} was calculated to be $(3.5 \pm 1.4) \times 10^3$ sec^{-1}, and the intercept which is k_{21} equals $(4.0 \pm 3.4) \times 10^9$ $M^{-1}sec^{-1}$. Similar results

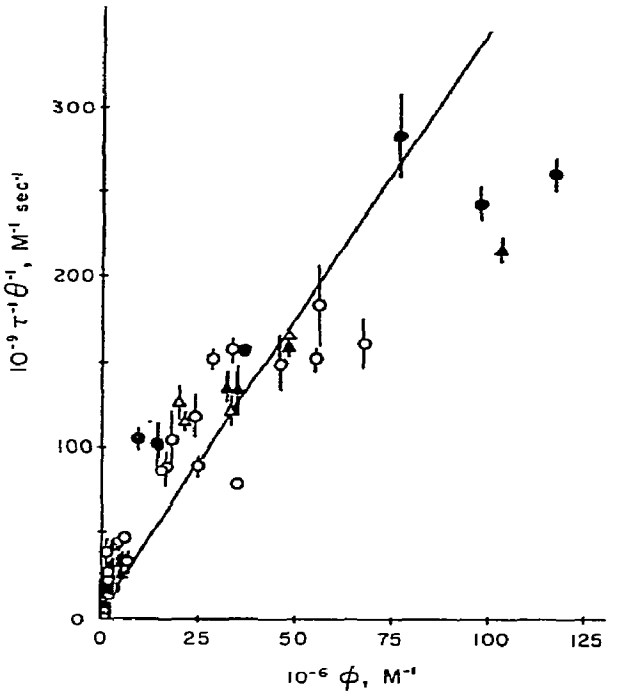

Fig. 1. Relaxation data at 7°C. Key: (●) Imidazole; (○) BSA; (△) BSA + Ca(II); (▲) BSA + Gd(III). The line corresponds to the least squares calculation for the BSA data alone.

were obtained for imidazole with all of the rate data summarized in table 3, in which the least squares errors are the ones tabulated. Similar results were obtained at 15° and 25°C and these are also tabulated in table 3. At 25°, k_{12} was calculated from K_{Im} and k_{21}, and k_{23} from the hydrolysis equilibrium constant of reaction (2) coupled with k_{32}. These were not carried out at the other temperatures because K_{Im} has not been reported at these other temperatures.

At 25°, there is agreement of our BSA results compared to the literature results with imidazole. At 7°C the rate constants obtained for imidazole and for BSA in our study were within experimental error of each other. This provides strong evidence that the BSA reactions under investigation in this pH range are indeed those of the imidazole groups. In addition, for similar concentrations the relaxation magnitudes were greater for BSA than for imidazole, consistent with the existence of many imidazole groups in the protein.

The proposed mechanism, which assumes the proton dissociation and recombination step is more rapid for the indicator systems than for the BSA or imidazole systems, must be further examined to test the assumption. At 13° for imidazole [11] and chlorophenol red [13], respectively, $10^{-10}k_{21}$ equals 1.5 and 2.3 $M^{-1}sec^{-1}$ and $10^{-3}k_{12}$ equals 1.5 and 19 sec^{-1}. Considering only reaction (3) to be present would result in a relaxation equation given by:

$$\tau^{-1} = k_{21} + k_{12}([H^+] + [In^-]). \quad (9)$$

For the range of indicator concentrations of 10^{-5} to 10^{-6}M, τ^{-1} would be in the range of (50 to 250) $\times 10^3$ sec^{-1}, which is about an order of magnitude greater than the observed relaxation times for each experimental solution. Hence, the assumption that reaction (3) can be treated as a rapid equilibrium reaction coupled to (1) and (2) is consistent with calculated and experimental results.

The results reported above do not answer the ini-

Table 3
Kinetic summary

	τ (°C)	$10^{-10}k_{21}$, ($M^{-1}sec^{-1}$)	$10^{-3}k_{12} = K_{Im}k_{21}$ (sec^{-1})	$10^{-3}k_{32}$ (sec^{-1})	$10^{-10}k_{23} = k_{32}K_{Im}/K_w$
BSA	7	0.40 ± 0.34		3.5 ± 1.4	
	15	1.2 ± 0.5		2.1 ± 0.7	
	25	1.8 ± 1.0	1.8 a)	2.5 ± 1.0	2.5 a)
Imidazole	7	0.85 ± 0.44		3.0 ± 1.1	
	13 b)	1.5 ± 0.5	1.5		
	25 b)			2.3 ± 0.4	2.3

a) k_{12} and k_{23} are not calculated at 7° and 15° because they are determined directly from K_{Im} which is unknown at these temperatures.
b) Reference [11].

tial questions posed, that is, do Ca(II) and lanthanide(III) ions bind at the imidazole sites in BSA, and if so, does the Ca(II) get replaced in competing reactions. If we let M^{m+} represent the complexing metal ion, a new reaction must be considered along with reactions (1) through (4). It would be expected that there would be more electrostatic binding at the neutral imidazole than at the protonated group. Therefore, the simplest complexation reaction would be:

$$M^{m+} + Im \underset{k_d}{\overset{k_f}{\rightleftharpoons}} ImM^{m+} . \qquad (10)$$

This reaction can couple to the others in three ways: it can have a relaxation time much more rapid than, much slower than, or of the same order as the rate-determining reactions in the absence of added cations. For each case, different complex relaxation time expressions, are obtained utilizing the kinetic data which are tabulated in table 4.

With Ca(II) present, a binding constant of 2 has been reported for the imidazole groups in BSA [8]. Since this binding constant, K_f, is equal to k_f/k_d, both the forward and back reactions must have similar rate constants. For most Ca(II) complexation reaction, k_f is of the order of 10^8 $M^{-1}sec^{-1}$ [16]. Unless the mechanism of Ca(II) binding is significantly different in BSA than in all simple molecules studied, k_f and hence k_d would be expected to be of the order of 10^8. Assuming only eq. (10) to be present, this will result in an equilibrium process which is more rapid than observed without the Ca(II), with τ^{-1} a factor of 10^4 greater than observed in its absence. The relaxation time expression that is valid in this case is

$$\tau^{-1} = k_{21}\{[H^+] + (\beta/\gamma)[Im] + \beta K_{Im}\}$$
$$+ k_{32}\{1 + (\beta/\gamma)[Im]/[H^+] + \beta[Im]/[ImH^+]\} , \qquad (11)$$

where

$$\beta = 1 + K_f[M^{m+}]/1 + K_f[Im] . \qquad (12)$$

By dividing both sides of eq. (11) by the coefficient of k_{32}, the experimental data can be plotted as a linear function. The calcium data does fit this experimental expression. However, the diffusion-controlled rate constant k_{21} becomes 8×10^{10} $M^{-1}sec^{-1}$, which is too large to be realistic as well as being more

Table 4
Relaxation data at 7°C for solutions containing Ca(II) or Gd(III) [b]

$10^6 Im_{total}$ (M)	10^6 [M^+] (M)	pH	10^6 [H^+] (M)	10^6 [Im] (M)	10^6 [In^-] [a] (M)	$10^{-3}\tau^{-1}$ (sec^{-1})	$10^{-9}\tau^{-1}\theta^{-1}$	ϕ (M)
Calcium containing solutions								
20.6	10,800	7.43	0.0495	13.8	2.57 M	20.2 ± 1.8	125	20.2
20.6	20,500	7.80	0.0212	17.0	5.14 M	20.5 ± 0.3	166	47.3
24.0	11,900	7.46	0.0466	16.4	2.70 M	18.5 ± 1.0	116	21.5
24.0	10,900	7.65	0.0298	18.5	3.94 M	16.7 ± 0.9	123	33.5
Gadolinium containing solutions								
1.88	10.1	6.58	0.353	0.416	29.1 C	19.3 ± 1.9	41.2	2.84
3.17	10.1	6.10	1.05	0.275	18.3 C	13.2 ± 0.9	11.2	0.95
3.17	4.02	6.37	0.565	0.476	24.7 C	11.5 ± 1.2	16.7	1.77
3.17	50.0	6.81	0.207	1.03	33.2 C	8.8 ± 0.7	26.0	4.84
6.34	10.1	6.56	0.365	1.36	28.8 C	16.5 ± 2.4	31.8	2.74
12.0	88.0	7.67	0.0283	9.36	4.10 M	17.6 ± 2.0	134	35.3
20.0	88.0	7.63	0.0309	15.3	3.83 M	17.3 ± 1.2	127	32.4
20.0	176	7.80	0.0209	16.6	5.19 M	19.6 ± 0.6	159	47.8
40.0	88.0	8.14	0.00973	36.5	8.64 M	24.1 ± 0.7	217	103

a) C = chlorophenol red; M = metracresol purple.
b) The concentrations presented here are those calculated with the assumption of no metal ion complexation at the imidazole sites.

than an order of magnitude greater than in the absence of calcium. Therefore, we conclude that this mechanism cannot be correct.

The assumption was then made that calcium does not bind to the imidazole groups at a pH less than 8. For this case, the mechanism for the observed reaction must be the same as given by the previous equations. The calcium data are plotted in fig. 1, assuming no interactions with the imidazole groups. It is evident that the data based on this assumption are within experimental error of solutions without calcium. Therefore, we have concluded that calcium does not bind to the imidazole groups in BSA between pH 6 and 8.

For those experiments where Gd(III) was used as the binding cation, the mechanism is somewhat different. The values of k_f obtained by jump techniques with different ligands have been of the order of 10^7 $M^{-1}sec^{-1}$ [16]. The expected value for K_f for the imidazole groups alone should be lower than 7700, reported for total Gd(III) binding to BSA [9]. In that same paper Reuben reported that the complex dissociation constant ($1/K_f$) was at least 120 times smaller for Ca(II) than for Gd(III) at pH = 6.3. Based on this, a reasonable lower limit for K_f at the imidazole sites should be about 120 times that reported for Ca, or approximately 240. For K_f between 240 and 7700, reaction (10) must either be the slow step or be similar in rate to reactions (1) and (2). With the assumption that the observed relaxation is characteristic of reaction (10) coupled to the more rapid equilibrium of (1) through (4), a new relaxation time expression should apply, given by

$$\tau^{-1} = k_f \left\{ [\mathrm{Im}] + \frac{[\mathrm{M}^{m+}]}{1 + \dfrac{[\mathrm{H}^+]}{K_{\mathrm{Im}} + [\mathrm{Im}]/\gamma}} \right\} + k_d .$$

Although the data can be plotted to yield the straight line given by eq. (12), this mechanism must be rejected on other grounds. With BSA and indicator, the observed relaxation times were in the range of about 5000 to 30 000 sec^{-1}. For those solutions containing Gd(III), the same relaxation time range was observed for the test solutions, indicating that if a lanthanide–imidazole interaction exists, reaction (10) must be of the same time scale as the slow steps in the sequence without Gd.

Thus, we have derived the relaxation equations for the assumption that reactions (1), (2) and (10) have approximately the same time constants. The exact solution for this problem involves the use of a five by five matrix to solve the resulting secular equations. For simplicity the assumption is made that the equilibrium involving OH^- with ImH^+ is the most rapid reaction of the three. With this simplification, the observed relaxation time equations become:

$$\tau^{-1} = \left\{ 1 + \frac{[\mathrm{ImH}^+]}{[\mathrm{ImH}^+] - \gamma} + \frac{1}{[\mathrm{ImH}^+]/\gamma[\mathrm{H}^+] - 1} \right\} k_{32}$$
$$+ k_{21}\{[\mathrm{H}^+] + (\alpha/\gamma)[\mathrm{Im}] + \alpha K_{\mathrm{Im}}\}$$
$$+ k_f\{[\mathrm{M}^{m+}] + (1-\alpha)([\mathrm{Im}] + 1/K_f)\}, \qquad (13)$$

where

$$\alpha = (K_w[\mathrm{ImH}^+]/\gamma[\mathrm{H}^+]^2 - [\mathrm{OH}^-])^{-1}(K_w/K_{\mathrm{Im}}). \qquad (14)$$

The complexity of the resulting relaxation time expression does not permit a simple graphical presentation of the data. Hence, the results for k_{21} and k_{32} in the absence of Gd(III) were used along with the equilibrium concentration data, assuming that K_f was 7700. For the nine test solutions, k_f was calculated to be in the range of 0.78 to 16.5 × 10^8 $M^{-1}sec^{-1}$, with no systematic variation in k_f obtained with Gd(III), BSA or pH. The scatter in the calculated k_f values alone makes this mechanism suspect. However, even the smallest calculated k_f is larger than has been observed for any Gd complexation reaction below 12.5°C. The highest values are at or greater than the diffusion-controlled rate expected for a reaction with the highly solvated lanthanide ion and a large molecule such as BSA. One must conclude from the experimental data that in the pH range of 6.1 to 7.8, Gd(III) does not complex with the imidazole groups in BSA at 7°C. Thus, this data was recalculated assuming no Gd(III) binding and is tabulated in table 4 and shown in fig. 1.

One of the Gd data points corresponds to a pH of 8.14, and this point does not fall on the experimental line by much more than any conceivable experimental error. This may indicate that above pH 8, Gd(III) complexation involving some of the imidazole groups may occur. Alternately, at higher pH a conformation change may exist either in BSA or upon metal ion complexation with BSA. The data for the BSA solution at pH 7.95 in the absence of Gd(III), also deviates from

the experimental line in the same manner as the high pH-Gd point. Since this type of deviation is not present in the imidazole high pH range solutions (greater than 8), it appears that an additional process is starting to develop at high pH in BSA systems consistent with the spectroscopic observations of Birnbaum and Darnell [6].

Since this investigation eliminates the possibility of significant cation binding to the imidazole groups in BSA between pH 6 and 8, the question must be asked if the temperature jump technique would indeed be sensitive to this complexation reaction when the binding constants are as small as 2 and 240 for calcium and gadolinium binding, respectively. Using a proton indicator, as in this study, and using a similar temperature jump instrument, the complexation reaction between Gd(III) and anthranilic acid in D_2O was successfully investigated even though the complexation constant was 242 [17]. Based on this result, we would have been able to detect complex formation between the imidazole groups and Gd(III), had this process occurred. Preliminary measurements on systems containing calcium and BSA at a pH greater than 8.4 have revealed that the slow relaxation observed under similar conditions in the absence of calcium totally disappears [18]. This is the prediction of eq. (11) for metal ion binding in which both k_f and k_d are large, indicating that calcium binding does occur to BSA at high pH, and that binding of this nature can be detected using the temperature jump technique. Thus, the results reported in this study require that neither Ca(II) nor Gd(III) bind to the imidazole groups in the pH range of 6 to 8.

Our experiments were derived to ignore binding at carboxyl groups, and hence we can say nothing about binding differences at these sites. However, binding is expected at the carboxyl groups for both cations [6, 12], and in future work these studies will be extended to the lower pH region. Our data suggests that Reuben's conclusion that the binding sites at pH 6.3 must be different for the two cations may not be valid. An alternate interpretation originally made in his paper, is that the binding differences result solely from the much smaller binding constant for divalent calcium than tervalent gadolinium. If this is true, when both cations are present in similar concentrations it is the Gd(III) which would successfully bind at a given site. We believe that the differences between calcium and gadolinium binding are due to differences in the magnitude of the binding constants rather than to binding at different sites for the two cations. This possibility is currently under investigation.

Acknowledgement

The author gratefully acknowledges the financial support of this project by the Research Corporation through the Cottrell Research Grants Program. The author would also like to thank Mr. Jeffry Reidler for obtaining some of the relaxation data on the imidazole system.

References

[1] L. Mela, Biochemistry 8 (1969) 2481.
[2] D.W. Darnall and E.R. Birnbaum, J. Biol. Chem. 245 (1970) 6484.
[3] T.M. Radhakrishnan, K.A. Walsh and H. Neurath, Biochemistry 8 (1969) 4020; J. Am. Chem. Soc. 89 (1970) 3059.
[4] G.E. Smolka, E.R. Birnbaum and D.W. Darnall, Biochemistry 10 (1971) 4556.
[5] P.M. Colman, L.H. Weaver and B.W. Mathews, Biochem. Biophys. Res. Comm. 46 (1972) 1999.
[6] E.R. Birnbaum, J.E. Gomez and D.W. Darnall, J. Am. Chem. Soc. 92 (1970) 5287.
[7] A.D. Sherry, E.R. Birnbaum and D.W. Darnall, J. Biol. Chem. 247 (1972) 3489.
[8] H.A. Sarnoff and M.S. Lewis, J. Phys. Chem. 67 (1963) 1211.
[9] J. Reuben, Biochemistry 10 (1971) 2834.
[10] J. Reuben, J. Phys. Chem. 75 (1971) 3164.
[11] M. Eigen, G.G. Hammes and K. Kustin, J. Am. Chem. Soc. 82 (1960) 3482.
[12] C. Tanford, S.A. Swenson and W.S. Shore, J. Am. Chem. Soc. 77 (1955) 6414.
[13] M. Eigen and G.G. Hammes, J. Am. Chem. Soc. 82 (1960) 5951.
[14] M. Eigen and L. DeMaeyer, in: Techniques of organic chemistry, Vol. VIII, Part II, ed. A. Weissberger (Interscience, New York, 1963);
E.F. Caldin, Fast Reactions in Solution (Wiley, New York, 1964).
[15] M. Eigen and R.G. Wilkins, in: Mechanisms of inorganic reactions (Amer. Chem. Soc., Washington, D.C., 1965).
[16] K. Kustin and J. Swinehart, Progr. Inorg. Chem. 13 (1970) 107.
[17] H.B. Silber, R.D. Farina and J.H. Swinehart, Inorg. Chem. 8 (1969) 819.
[18] H.B. Silber and J. Rosen, work in progress.

BIOPHYSICAL CHEMISTRY 1 (1974) 308–311. © NORTH-HOLLAND PUBLISHING COMPANY

DILATOMETRIC STUDIES OF THE DENATURATION OF IMMUNOGLOBULIN G BY GUANIDINIUM CHLORIDE *

S. LAPANJE, J. ŠKERJANC and M. VOZELJ
Department of Chemistry and Institute of Microbiology, University of Ljubljana, Ljubljana, Yugoslavia

Received 18 October 1973
Revised manuscript received 15 November 1973

The denaturation of immunoglobulin G and its light chains by guanidinium chloride at 25°C was followed using the dilatometric method. From results of the dilatometric measurements the differences between the partial molar volumes of the proteins in water and in guanidinium chloride solutions of various concentrations, respectively, have been obtained. The differences reflect the extent of unfolding as well as the denaturant binding to the protein. Several experiments were also performed in which the protein disulfide bonds were reduced by dithioerythritol.

The volume change produced by the reduction of one mole of disulfide bonds of immunoglobulin G in 6 M guanidinium chloride was found to be the same as that for oxidized glutathione; the value was −0.9 ml/mol.

1. Introduction

Among the methods which can be used for following denaturation of globular proteins dilatometry has proved to be quite useful [1–5]. The reason for this is that the extent of denaturation, i.e., unfolding is reflected in volume changes which in turn reflect various processes taking place during denaturation. In the following we report on dilatometric studies of the denaturation of immunoglobulin G (IgG) and its light chains by guanidinium chloride (GdmCl). The reason for choosing these proteins is due not only to their importance as antibodies but also to the fact that they represent very interesting complex molecules. The gross structure of IgG has been elucidated. The IgG molecule consists of two identical light chains and two identical heavy chains which are linked together by noncovalent interactions and interchain disulfide bonds. IgG in man is a heterogeneous mixture of chemically different molecules. However, the differences are relatively small. Chemically homogeneous IgG molecules are produced by certain plasma tumors, myelomas. For details, the reader is referred to the review article by Edelman and Gall [6].

In order to elucidate the role of IgG disulfide bonds in volume changes, a few experiments were also performed in which these bonds were ruptured by dithioerythritol (DTE). In parallel experiments oxidized glutathione (GTT) was reduced by the same reagent.

2. Experimental

Two preparations of IgG were used in the studies. One was isolated from pooled normal human serum by ammonium sulfate precipitation and DEAE-cellulose chromatography [7]. The other was a lyophilized myeloma protein (Co) with lambda light (L) chains, kindly provided by Dr. K.J. Dorrington and J. Ellerson of the University of Toronto. Heavy (γ) and L chains were prepared from reduced and alkylated pooled IgG by chromatography on Sephadex G–100 in 1 M propionic acid [7]. Solutions of pooled IgG and its L chains in 0.02 M NaCl–0.01 M TrisHCl, pH 7.7, prepared by dialysis were subsequently concentrated in

* A preliminary report of this work has been presented at the Third International Conference on Chemical Thermodynamics, Baden (near Vienna), September 1973.

an ultrafiltration cell (Amicon Corp.) fitted with UM–10 and XM–100 membranes, respectively. Solutions of Co IgG were prepared by dissolving the protein in the same buffer. Owing to their low solubility, γ chains are not suitable for dilatometric studies. Protein concentrations were determined spectrophotometrically at 280 nm using the following values for $E^{1\%}_{1\,cm}$: IgG, 14.0 and L chains, 12.0.

GdmCl was an ultra pure product from Schwarz/Mann. DTE and disodium salt of oxidized GTT were obtained from Sigma Chemical Co. All other reagents used were of analytical grade.

Volume changes were measured at 25°C in Linderstrøm-Lang dilatometers. They were filled by means of Hamilton syringes and weighing was deemed unnecessary. Into one arm of the dilatometer 1.00 ml of a 3 to 6% protein solution or (1–Φ) ml, i.e. 0.98 to 0.96 ml, of the solvent, 0.02 M NaCl–0.01 M Tris-HCl, was pipetted, and into the other 4.00 ml of an appropriate GdmCl solution prepared in the same solvent. Φ is the protein displacement volume which is equal to the protein weight multiplied by its partial specific volume, $\bar{v}_2 = 0.733$ ml/g [8]. This value which was obtained from density measurements actually refers to a myeloma protein but the values for pooled IgG's as well as for other myeloma proteins should be quite close. All other experimental details are the same as described previously [5]. With pooled IgG and its L chains at least four experiments were performed for each GdmCl concentration, and with myeloma IgG at least two. The absolute error of single determinations is estimated at ± 100 ml/mol and ± 15 ml/mol for IgG and its L chains, respectively.

3. Results and discussion

The volume changes determined in dilatometric experiments were analyzed by using the relation [1]

$$\Delta V_2 = \Delta V_{(1-\Phi)} + n_2 (\bar{V}_{2G} - \bar{V}_2), \qquad (1)$$

where ΔV_2 and $\Delta V_{(1-\Phi)}$ represent the volume changes produced upon mixing 1.00 ml of protein solution and (1.00–Φ) ml of buffer, respectivley, with 4.00 ml of an appropriate CdmCl solution; n_2 is the number of moles of the protein and $(\bar{V}_{2G} - \bar{V}_2)$ is the difference between the partial molar volume of the protein in the GdmCl solution and in the buffer. The values of $(\bar{V}_{2G} - \bar{V}_2)$ for pooled and myeloma IgG's are plotted in fig. 1, those for L chains in fig. 2.

Inspection of the curves in figs. 1 and 2 shows that they have a similar form. This is due to the fact that for all three proteins the value of $(\bar{V}_{2G} - \bar{V}_2)$ first increases with GdmCl concentration, reaches a maximum, then decreases, reaches a minimum, and rises again. This behavior is similar to that of proteins studied previously [4, 5]. Therefore similar interpretation appears most reasonable. Thus the initial increasing of $(\bar{V}_{2G} - \bar{V}_2)$ is

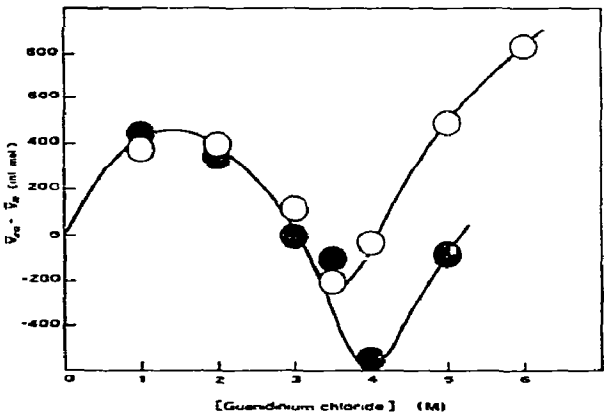

Fig. 1. Differences of the partial molar volume of pooled (○, and myeloma (●, immunoglobulin G at 25°C, as a function of guanidinium chloride concentration.

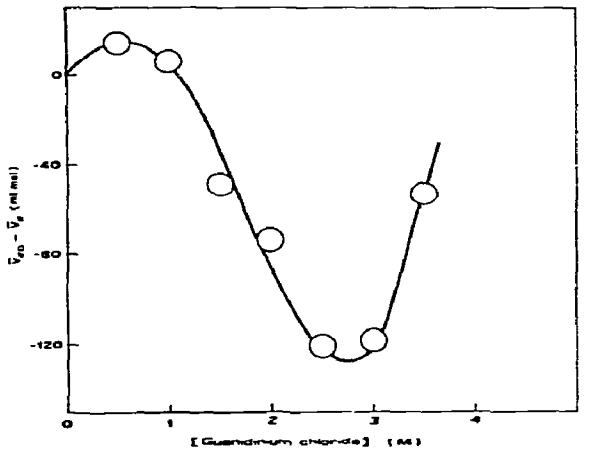

Fig. 2. Differences of the partial molar volume of immunoglobulin G light chains at 25°C, as a function of guanidinium chloride concentration.

attributed to changes of solvation of ionic groups on protein molecules, i.e., to the gradual competitive displacement of water molecules in hydration sheaths by guanidinium or chloride ions. However, just before the protein molecules begin to unfold the maximum is reached. Unfolding is accompanied by gradual filling up of the hollows in protein molecules with solvent, resulting in volume decrease which in this region apparently prevails over the volume increase due to changing solvation. In agreement with this, the minimum occurs at complete unfolding. The increase of $(\bar{V}_{2G}-V_2)$ afterwards is again due to solvation changes. Such an interpretation is corroborated by the fact that the curves though similar are not identical. A difference between the curves for pooled and myeloma IgG's is observable at GdmCl concentrations higher than 3.5 M. This also is the concentration at which unfolding as followed by optical rotatory dispersion (ORD) is complete [9]. However, from dilatometric experiments it appears that the myeloma protein is more stable and therefore unfolds at a higher GdmCl concentration. Moreover, the volume change at complete unfolding, about −550 ml/mol, is larger than that for pooled IgG, about −200 ml/mol, which could reflect the greater stability of myeloma protein. From the difference $(\bar{V}_{2G}-\bar{V}_2)$ we can naturally obtain the values of $\bar{V}_{2G}$ and $\bar{v}_{2G}$, respectively, at individual GdmCl concentrations. Let us illustrate this with pooled IgG at complete unfolding, in 3.5 M GdmCl. By subtracting 200 ml/mol from the value for native IgG ($\bar{V}_2$ = 107750 ml/mol [8]) and by dividing with m.w. = 147000 [10] we arrive at a value of 0.732 ml/g. The difference between $\bar{v}_2$'s in water and in 3.5 M GdmCl is thus 0.001 ml/g which is within the limit of experimental error of values obtained from density measurements. The value of $\bar{v}_2$ in 6 M GdmCl obtained in a similar way is 0.739 ml/g which is well outside the limit of experimental error. This is of significant importance for investigators preforming ultracentrifugal studies in GdmCl.

The maximum and the minimum of the curve for L chains appear at 0.5 M and 2.7 M GdmCl, respectively, which is in fair accord with ORD findings [9]. The L chains are undoubtedly less stable than the whole IgG molecules. The volume change at complete unfolding is −130 ml/mol (m.w. = 23400 [10]).

The proposed interpretation does by no means imply that only the above mentioned processes contribute to volume changes during denaturation by GdmCl; they appear, however, to be the dominating ones. Since a detailed discussion of various processes and their eventual contributions has been given in a previous paper [2], it need not be repeated here. However, the recent findings by Bøje and Hvidt [11] should be mentioned. The transfer of aliphatic groups from the interior of protein molecules to aqueous environment appears to be accompanied by small, but positive volume changes.

There is another point which we have not explicitly stated in previous papers dealing with dilatometric studies, namely, that in the proposed interpretation unfolding is being treated as a continuous process.

In the discussion we have not mentioned Katz's dilatometric study of the denaturation of bovine serum albumin by GdmCl which covered the concentration range between 0 to 3.8 M denaturant [12]. Namely, after completing the study of IgG we performed a study of bovine serum albumin up to 6 M GdmCl. The results obtained, which will be published separately, are qualitatively similar to those found with IgG and, where data exist, also to those of Katz.

The results of dilatometric experiments with DTE are summarized in table 1. Proper comparison of the volume changes in pooled IgG and oxidized GTT, respectively, can be made after calculating the volume change per disulfide bond. In the absence of GdmCl only the four interchain IgG disulfide bonds are reduced compared to one in GTT [7]. By dividing the value for IgG by four, we obtain the value −33 ml per mole of disulfide bonds as compared to only −2.4 ml/mol for GTT. This, in our opinion, reflects the

Table 1
Volume changes of pooled immunoglobulin G and oxidized glutathione upon reduction of disulfide bonds with dithioerythritol at 25°C and pH 7.7

Solvent	Compound	ΔV_{corr} [1] (ml/mol)
0.01 M TRIS–HCL– 0.02 M NaCl	IgG	−130 ± 30
	GTT	− 2.4 ± 0.5
6 M GdmCl	IgG	−15 ± 5
	GTT	− 0.9 ± 0.2

[1] In the calculation the m.w. of IgG was taken to be 147 000 [9]. ΔV_{corr} is the volume change corrected for dilution effects.

fact that some loosening of the IgG structure occurs after reduction of interchain disulfide bonds which has been observed also in ORD studies [9]. In 6 M GdmCl, on the other hand, all 16 disulfide bonds are reduced and the volume change per mole of bonds is −0.9 ml which is the same as for GTT. This apparently reflects the fact that the volume change accompanying the reduction of disulfide bonds in 6 M GdmCl is due to the reduction; in other words, IgG in 6 M GdmCl with disulfide bonds intact is already randomly coiled which is in agreement with ORD findings [9]. It is perhaps interesting to mention in this connection that Kupke et al. [13] recently determined by a magnetic viscodensimeter a lowering of $\bar{v}_2$ by 0.003 ml/g upon the reduction of the four disulfide bonds in ribonuclease in 6 M GdmCl by 0.1 M 2-mercaptoethanol. Their volume decrease per mole of disulfide bonds is thus about 10 times larger than ours.

In conclusion, we can say that the volume changes observed in the denaturation of IgG and its L chains by GdmCl, though small, display in accord with expectation similar behaviour as other globular proteins studied so far. However, owing to the complexity of the processes involved, only a qualitative interpretation of the changes is feasible.

Acknowledgement

The authors thank G. Trtnik for technical assistance. This work was supported by the Boris Kidrič Fund.

References

[1] S. Katz and T.G. Ferris, Biochemistry 5 (1966) 3426.
[2] J. Škerjanc, V. Doleček and S. Lapanje, Eur. J. Biochem. 17 (1970) 160.
[3] S. Lapanje, J. Škerjanc and V. Doleček, Croat. Chem. Acta 43 (1970) 65.
[4] S. Lapanje and J. Škerjanc, Biochem. Biophys. Res. Commun. 43 (1971) 682.
[5] J. Škerjanc and S. Lapanje, Eur. J. Biochem. 25 (1972) 49.
[6] G.M. Edelman and W.E. Gall, Ann. Rev. Biochem. 38 (1969) 415.
[7] G.T. Stevenson and K.J. Dorrington, Biochem. J. 118 (1970) 703.
[8] J. Pilz, G. Puchwein, O. Kratky, M. Herbst, O. Haager, W.E. Gall, and G.M. Edelman, Biochemistry 9 (1970) 211.
[9] S. Lapanje and K.J. Dorrington, Biochim. Biophys. Acta 322 (1973) 45.
[10] K.J. Dorrington and C. Tanford, Adv. Immunol. 12 (1970) 333.
[11] L. Bøje and A. Hvidt, Biopolymers 11 (1972) 2357.
[12] S. Katz, Biochim. Biophys. Acta 154 (1968) 468.
[13] D.W. Kupke, M.G. Hodgins and J.W. Beams, Proc. Natl. Acad. Sci. US 69 (1972) 2258.

BIOPHYSICAL CHEMISTRY 1 (1974) 312–317. © NORTH-HOLLAND PUBLISHING COMPANY

TRANSPORT PHENOMENA AND ION BINDING IN SOLUTIONS OF SODIUM POLYSTYRENESULPHONATE

D. DOLAR, J. ŠPAN and S. ISAKOVIĆ
University of Ljubljana, Department of Chemistry, 61001 Ljubljana, Yugoslavia

Received 18 September 1973

The results of transference and conductance measurements on solutions of sodium polystyrenesulphonate, in the concentration range from 0.0025 to 0.075 monomolar, are presented. The fraction of free counterions calculated from experimental data is found to be independent of molecular weight of the polyelectrolyte within the range of degree of polymerization from 200 to 2400. The experimental data, combined with the cell model, are used to calculate the electrostatic potential at a cylindrical surface which surrounds the polyion and divides the counterions into bound and free. The same value for this potential is found for the whole concentration range investigated, which lends support to the assumption of cylindrical distribution of counterions in polyelectrolyte solutions.

1. Introduction

It has been observed by several authors [1] that the colligative properties of polyelectrolyte solutions are independent of molecular weight, providing the latter is not too small. Although this observation cannot be generalized to all transport properties it seems to be valid for transport phenomena in polyelectrolyte solutions in an electric field. The early results of Kern [2] on solutions of polyacrylic acid and its sodium salt indicate that conductance is independent of the degree of polymerization in the range from 200 to 2000. Schindewolf [3] has found that in saltfree sodium polyphosphate solutions the equivalent conductance and transport numbers are strongly dependent on molecular weight at low degrees of polymerization but that they attain their constant values at a degree of polymerization higher than 100. A similar behaviour has been observed by Eisenberg [4] with solutions of partially neutralized polymethacrylic acid. The solutions of this polyelectrolyte having degree of polymerization 1500 or 5400 have the same conductance, but there is an increase in conductance of 10% for samples with the degree of polymerization equal to 200. Furthermore, Nagasawa and coworkers [5] have measured the electrophoretic mobility of sodium polyacrylate at different degrees of neutralization in sodium chloride solutions. They found the mobility to be independent of molecular weight within the range of degree of polymerization from 340 to 13 000.

Quite recently Nagasawa et al. [6] have found that the electrophoretic mobility of the fractionated sodium polystyrenesulphonate having degrees of polymerization between 1300 and 13 000 is not dependent on molecular weight even at low ionic strengths. This observation is not in agreement with the calculations based on the theory of Hermans and Fujita [7–9] according to which the mobility of the polyion should depend on molecular weight at low ionic strengths. In this theory the polyionic coil is assumed to have the form of a sphere with a uniform distribution of fixed charges throughout its volume. Thus, the ionic atmosphere, consisting of counterions and coions, should also have spherical symmetry. According to Nagasawa et al. [6] the assumption that there is a spherical distribution of counterions around the polyion should be the main reason for disagreement between theory and experiment. It seems that a more realistic model for the polyion is an expanded random coil whose skeleton is surrounded by a cylindrical ionic atmosphere. It has been shown by some simplified calculations [6] that this model is more suitable for the interpretation of the electrophoretic mobility.

The purpose of this paper is to give additional sup-

port to the idea of the cylindrical distribution of counterions mentioned above. Thus, the fraction of free counterions obtained from conductance and transference measurements will be interpreted in the light of the cell model [10]. Furthermore, some results will be presented in order to show to what extent the conductance and transference numbers in solutions of sodium polystyrenesulphonate depend on molecular weight in the range of degree of polymerization lower than that investigated by Nagasawa et al. [6].

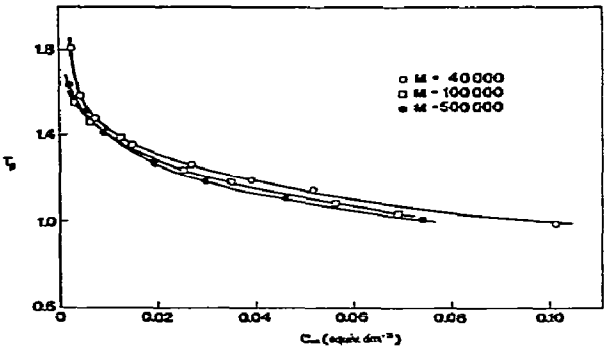

Fig. 1. The concentration dependence of the polyion constituent transference number in sodium polystyrenesulphonate solutions at 25°C with molecular weight as indicated.

2. Experimental

2.1. Material

Two samples of sodium polystyrenesulphonate (NaPSS) with nominal molecular weights of about 100 000 and 500 000 were used in this investigation. The first was purchased from Polysciences, Inc., Rydal, Pennsylvania, and the second was kindly supplied by Down Chemical Co., Midland, Michigan. The samples were purified by dialysis as described elsewhere [11]. The degree of substitution was found to be 1.00.

2.2. Transference numbers

The polyion constituent transference number was determined by the indirect moving boundary method [12, 13]. The rising boundary cell consisted of a 30 cm long tube with an internal diameter of 5 mm, a stopcock on each end of the tube, and two electrodes. The cathode was made of platinum gauze and the anode of a silver wire. The stopcocks on both ends of the tube make possible the isolation of a column of the adjusted Kohlrausch solution [14]. This solution was removed from the tube by a fine pipet and the concentration of NaPPS was determined spectrophotometrically at 261.5 nm using a Hilger–Watts, Uvispek MK9 spectrophotometer. Sodium chloride was used in the leading solution as its transference numbers have been precisely determined [15].

2.3. Conductance

The conductance bridge, built around a Campbell–Shackleton ratio box, has been described previously [16]. In order to eliminate polarization errors the resistance was measured at several frequencies and extrapolated to infinite frequency. All measurements were made at 25.0 ± 0.01°C with an average accuracy of 0.1%.

3. Results

The transference number of the polyion constituent, T_p, in NaPSS solutions was calculated from the Kohlrausch relation [17, 18]

$$T_p = t_{Cl}\, c_{NaPSS}/c_{NaCl}\,, \qquad (1)$$

where t_{Cl} is the transference number of chloride ion in the leading solution of sodium chloride, of concentration c_{NaCl}, and c_{NaPSS} is the adjusted concentration of the following solution of NaPSS. Both concentrations are expressed in equiv./dm^3 which is, for the polyelectrolyte, equal to monomolarity, c_m. For t_{Cl} in eq. (1) the values obtained by Allgood and Gordon [15] were used. The solvent and volume corrections as described by Spiro (ref. [13], p. 259) were applied throughout.

In fig. 1 a plot of T_p versus c_m is presented for samples having the following molecular weights: 40 000, 100 000, and 500 000, corresponding to approximate degrees of polymerization 200, 480, and 2400, respectively. For a better comparison the results obtained with the first sample, taken from a previous study [11], have also been included. The differences between the values of T_p corresponding to different molecular weights are very small, not exceeding 5%

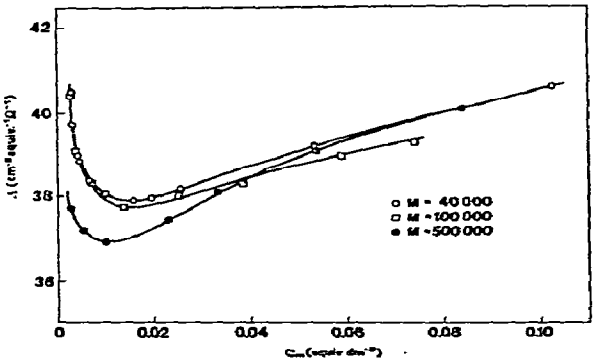

Fig. 2. The concentration dependence of the equivalent conductance in sodium polystyrenesulphonate solutions at 25°C with molecular weight as indicated.

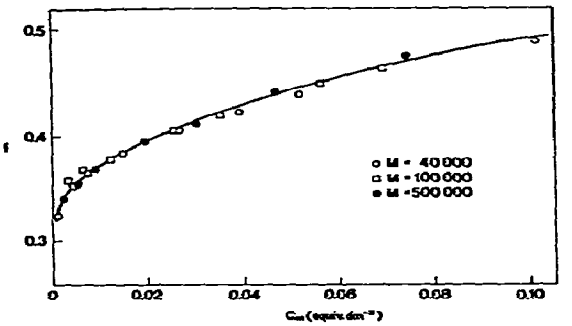

Fig. 3. The concentration dependence of the fraction of free counterions in sodium polystyrenesulphonate solutions at 25°C with molecular weight as indicated.

(the difference between the values of the upper and lower curves in fig. 1). It is necessary to emphasize that the estimated error for the measurement of T_p is about 1%. Furthermore, the curves for the two highest molecular weights intersect at a low concentration and are very close to each other at higher concentrations. Therefore, it may be concluded that in order to investigate the dependence of transference numbers on molecular weight one has to choose samples with degrees of polymerization lower than 200.

The variation of equivalent conductance with concentration is shown in fig. 2 for the same samples as described above. The values on the left side of the minima are not very reliable since carbon dioxide was not excluded from solutions. In spite of this deficiency it is possible to see that the maximal difference in conductance between samples with different molecular weight is about 2%.

Wall and coworkers [19] have proposed a method for the evaluation of the fraction of free counterions, which is based on conductance and transference data. Their expression written in a more convenient form [20] is

$$f = \Lambda/(\lambda_p + \lambda_c)\,, \qquad (2)$$

where f is the fraction of free counterions, Λ the equivalent conductance of the polyelectrolyte, λ_p and λ_c the equivalent conductances of the polyion and counterion, respectively. The equivalent conductance of the polyion is related to the measured transference number T_p, defined by eq. (1), through the equation

$$\lambda_p = \Lambda T_p\,. \qquad (3)$$

In order to evaluate the unknown quantity λ_c in eq. (2) the assumption [19] was adopted that λ_c is equal to the equivalent conductance of the counterion in a solution of 1,1 electrolyte at a concentration corresponding to that of the free counterions in the polyelectrolyte solution. It has been shown [21] that the error introduced by this assumption is not significant for dilute solutions.

The concentration dependence of the fraction of free sodium ions obtained with three different samples of NaPSS is shown in fig. 3. It is clear that the fraction of free counterions is, within experimental error, independent of molecular weight in the range of degree of polymerization investigated. In figs. 1 and 2 one can observe a slight increase in T_p and Λ for the sample with the degree of polymerization equal to 200. The fraction f is insensitive to these variations in T_p and Λ, as seen in fig. 3, since they partially compensate each other. This can also be demonstrated by writing the expression for the fraction of free counterions in a different way

$$f = (T_p + \lambda_c/\Lambda)^{-1} \qquad (4)$$

which follows from eqs. (2) and (3).

In a previous paper [16] we have reported the fraction of free hydrogen ions in solutions of polystyrenesulphonic acid, obtained from conductance and transference measurements. The concentration dependence of f is very similar to that of NaPSS but the values are about 10% higher.

Jordan et al. [22] have also derived the fraction of free counterions from conductance and transference data on solutions of NaPSS. A direct comparison with their results is not possible since they used the polymer with a higher degree of sulphonation and investigated a lower concentration range. However, in a very narrow overlapping concentration range a reasonable agreement can be observed.

4. Discussion

The fraction of free counterions in a polyelectrolyte solution or the charge-fraction, as it is called by Kurucsev and Steel [20], is the formal analogue of the degree of ionization in simple electrolyte solutions. It is necessary to emphasize, however, that the applied method of determination does not make any assumption concerning the nature of binding of those counterions which are not "free". The method is applicable to any type of binding occurring in polyelectrolyte solutions. For interpretation of the results obtained with this method, the type of binding becomes, of course, very important. It seems that in solutions of polystyrenesulphonates the so-called atmospheric binding has the predominant role [23]. Consequently, the results obtained for the fraction of free counterions, as shown in fig. 3, will be interpreted in terms of pure electrostatic interaction between polyion and counterions. We shall apply the cell model [10] which assumes a cylindrical distribution of counterions around the polyion.

For a detailed description of the model the reader is referred to an article by Lifson and Katchalsky [24]; their basic expressions and symbols will be reproduced here. The polyion represented by a negatively charged cylinder of radius a and length h, has ν monomer units of length b ($= h/\nu$) and each monomer unit, in turn, has one monovalent ionized group. The positive monovalent counterions are distributed symmetrically around the polyion in a cylinder with the radius R. The Poisson–Boltzmann equation applied to this system has the solution

$$\psi = \frac{kT}{e_0} \ln \frac{(1+\beta^2) r^2 \sin^2(\beta \ln Ar)}{\beta^2 R^2}, \tag{5}$$

where ψ is the potential, e_0 the protonic charge, r the distance from the axis of the polyion, β and A the integration constants, and k and T have their usual meaning. In eq. (5) it is supposed that $\psi(R) = 0$. The constants β and A are determined by the boundary conditions from which it follows

$$1 + \beta \operatorname{ctg}(\beta \ln AR) = 0, \tag{6}$$

$$1 + \beta \operatorname{ctg}(\beta \ln Aa) = \lambda. \tag{7}$$

λ in eq. (7) is the charging parameter defined by

$$\lambda = e_0^2 / \epsilon kTb, \tag{8}$$

where ϵ is the dielectric constant of the solvent. From eqs. (6) and (7) it follows that

$$\lambda = (1+\beta^2)/(1 + \beta \operatorname{ctg} \beta\gamma), \tag{9}$$

where γ is the concentration parameter related to monomolarity, c_m, by

$$\gamma = \ln \frac{R}{a} = \frac{1}{2} \ln \frac{10^3}{\pi a^2 b N_A} - \tfrac{1}{2} \ln c_m. \tag{10}$$

N_A in eq. (10) is Avogadro's number. The eqs. (5–7) and (9) retain their form if condition $\lambda \geq \gamma/(1+\gamma)$ is satisfied, i.e., they are valid for polyions with high charge density.

The classification of counterions into bound and free is a useful simplification of the involved physical situation. Since no general agreement exists about the criterion for a theoretical distinction between both groups of counterions, many definitions are acceptable [25]. In every case a cylindrical surface surrounding the polyion can be found which divides the counterions into bound and free. Denoting the distance from the axis of the polyion to this surface by d, the fraction of free counterions,

$$f = \frac{1}{\nu} \int_d^R n^0 \exp(-e_0 \psi / kT) \, \mathrm{d}V, \tag{11}$$

where $dV = 2\pi hr\,dr$, and

$$n^0 = [(1+\beta^2)/\lambda]\ (\nu/2\pi hR^2)\,. \tag{12}$$

Taking into account eqs. (5), (6), and (12) we obtain after integration

$$f = (1/\lambda)[1 + \beta\,\mathrm{ctg}(\beta \ln Ad)]\,. \tag{13}$$

This eq. can be solved for d which gives after elimination of A with the aid of eqs. (7) and (10)

$$\ln(d/a) = \frac{1}{\beta}\,\mathrm{arctg}\,\frac{\beta\lambda(1-f)}{\beta^2+(f\lambda-1)(\lambda-1)}, \quad \text{for } f\lambda \geqslant 1\,; \tag{14}$$

$$\ln(d/a) = \gamma - \frac{1}{\beta}\,\mathrm{arctg}\,\frac{\beta f\lambda}{1+\beta^2-f\lambda}, \quad \text{for } f\lambda \leqslant 1\,.$$

Thus, the distance d or the fraction d/a can be calculated. The experimental values of f should be substituted on the right-hand side of eq. (14).

The potential at the distance d could be evaluated from eq. (5), but it can also be calculated directly from the expression

$$-\frac{e_0\psi(d)}{kT} = 2\gamma + \ln\frac{(f\lambda-1)^2+\beta^2}{1+\beta^2} - \frac{2}{\beta}\,\mathrm{arctg}\,\frac{\beta\lambda(1-f)}{\beta^2+(f\lambda-1)(\lambda-1)}, \quad \text{for } f\lambda \geqslant 1\,;$$

$$-\frac{e_0\psi(d)}{kT} = \ln\frac{(f\lambda-1)^2+\beta^2}{1+\beta^2} + \frac{2}{\beta}\,\mathrm{arctg}\,\frac{\beta f\lambda}{1+\beta^2-f\lambda}, \quad \text{for } f\lambda \leqslant 1\,; \tag{15}$$

which follows from eqs. (5), (10), (13), and (14).

For the calculations presented below the following values of the parameters were applied: $a = 8$ Å, $b = 2.55$ Å, $\epsilon = 78.54$ and $T = 298.15$°K. According to eq. (8) the structural value of the parameter $\lambda = 2.8$.

In fig. 4 the concentration dependence of the relative distance, d/a, is presented. The increase of the distance with decreasing concentration indicates that an expansion of the ionic atmosphere occurs in diluting the polyelectrolyte solution. It is interesting to

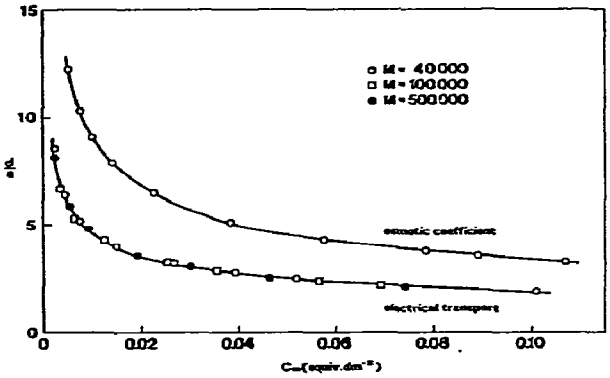

Fig. 4. The concentration dependence of the relative distance, d/a [eq. (14)].

compare the values of d/a derived from different experimental data. Such a comparison between thermodynamic and transport measurements is made in fig. 4. The values of the osmotic coefficient, which is also considered as a measure for the fraction of free counterions, are taken from ref. [26].

More striking are the results presented in fig. 5, showing that the dimensionless potential $e_0\psi(d)/kT$ is not dependent on concentration. A slight bending of the curve upwards at low concentrations is probably insignificant and cannot influence the interpretation which follows below. From many experimental and theoretical studies of electrical transport phenomena [10] it may be concluded that the mobility of a counterion depends on its location in the ionic atmosphere. The condensed counterions lose part of their mobility perpendicular to the surface of the polyion axis. The free counterions are much less restricted in their mo-

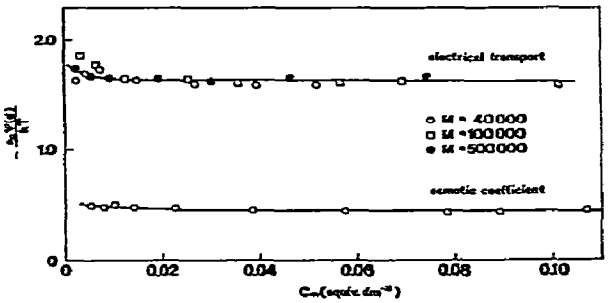

Fig. 5. The dimensionless potential [eq. (15)] at a cylindrical surface surrounding the polyion and dividing the counterions into bound and free.

vement in all directions and their mobility is practically the same as in solutions of simple electrolytes. It is obvious that the transition between these extreme groups of ions should be continuous. How much a counterion is restricted in its movement very likely depends on its potential energy which is due to its instant location in the ionic atmosphere. Since from experiment information is available about the distribution of counterions between the two groups, there should also exist a definite value of the electric energy which can be used as a criterion for the separation of counterions into bound and free. The value of this energy, more precisely its ratio to the thermal energy, was found to be independent of concentration which lends support to the model adopted for these calculations.

In order to have a comparison we have also plotted in fig. 5 the values of $e_0\psi(d)/kT$ obtained from the osmotic coefficient of solutions of NaPSS [26] of molecular weight 100 000. In this case the potential $e_0\psi(d)/kT$ is lower and the relative distance d/a is greater, see fig. 4, which means that less counterions are found outside the boundary surface mentioned above. This is in agreement with the well known fact that the osmotic coefficient is always smaller than the fraction of free counterions obtained from transport phenomena.

Acknowledgement

The partial financial support of the Boris Kidrič Fund, Ljubljana, is gratefully acknowledged.

References

[1] R.W. Armstrong and U.P. Strauss, in: Encyclopedia of polymer science and technology, Vol. 10, eds. H.F. Mark and N.G. Gaylord (Interscience, New York, 1969) pp. 781–861.
[2] W. Kern, Z. Physik. Chem. A 181 (1938) 249.
[3] U. Schindewolf, Z. Physik. Chem. (Frankfurt) 1 (1954) 134.
[4] H. Eisenberg, J. Polymer Sci. 30 (1958) 47.
[5] J. Noda, M. Nagasawa and M. Ota, J. Am. Chem. Soc. 86 (1964) 5075.
[6] M. Nagasawa, J. Noda, T. Takahashi and N. Shimamoto, J. Phys. Chem. 76 (1972) 2286.
[7] J.J. Hermans and H. Fujita, Kon. Ned. Akad. Wetensch. Proc. Ser. B 58 (1955) 182.
[8] J.J. Hermans, J. Polymer Sci. 18 (1955) 529.
[9] J.J. Hermans, in: The structure of electrolytic solutions, ed. W.J. Hamer (Wiley, New York, 1959) pp. 308–318.
[10] A. Katchalsky, Pure Appl. Chem. 26 (1971) 327.
[11] J. Špan and A. Gačeša, Z. Physik. Chem. (Frankfurt), in press.
[12] G.S. Hartley, E. Drew and B. Collie, Trans. Faraday Soc. 30 (1934) 648.
[13] M. Spiro, in: Physical methods of chemistry, Vol. I, Part IIA, eds. A. Weissberger and B.W. Rositer (Interscience, New York, 1971) pp. 205–295.
[14] D.R. Muir, J.R. Graham and A.R. Gordon, J. Am. Chem. Soc. 76 (1954) 2157.
[15] R.W. Allgood and A.R. Gordon, J. Chem. Phys. 10 (1942) 124.
[16] D. Dolar, J. Špan, and A. Pretnar, J. Polymer Sci. C16 (1968) 3517.
[17] F. Kohlrausch, Ann. Physik 62 (1897) 209.
[18] L.G. Longsworth, J. Am. Chem. Soc. 52 (1930) 1897.
[19] J.R. Hiuzenga, P.F. Grieger and F.T. Wall, J. Am. Chem. Soc. 72 (1950) 2636.
[20] T. Kurucsev and B.J. Steel, Rev. Pure Appl. Chem. 17 (1967) 149.
[21] R.L. Darskus, D.O. Jordan and T. Kurucsev, Trans. Faraday Soc. 62 (1966) 2876.
[22] D.O. Jordan, T. Kurucsev and M.L. Martin, Trans. Faraday Soc. 65 (1969) 606.
[23] U.P. Strauss and Y.P. Leung, J. Am. Chem. Soc. 87 (1965) 1476.
[24] S. Lifson and A. Katchalsky, J. Polymer Sci. 13 (1954) 43.
[25] D. Dolar and A. Peterlin, J. Chem. Phys. 50 (1969) 3011.
[26] D. Kozak, J. Kristan and D. Dolar, Z. Physik. Chem. (Frankfurt) 76 (1971) 85.

BIOPHYSICAL CHEMISTRY 1 (1974) 319–324. © NORTH-HOLLAND PUBLISHING COMPANY

CALORIMETRY OF DNA–DYE INTERACTIONS IN AQUEOUS SOLUTION. I. PROFLAVINE AND ETHIDIUM BROMIDE

F. QUADRIFOGLIO, V. CRESCENZI*, and V. GIANCOTTI
Laboratory of Macromolecular Chemistry, Institute of Chemistry, University of Trieste, Trieste, Italy

Received 11 December 1973
Revised manuscript received 11 February 1974

The results of an investigation on the interaction of proflavine and of ethidium bromide with DNA (calf thymus) in dilute aqueous solution are reported. The binding of the two dyes by DNA has been studied by means of microcalorimetric and of equilibrium dialysis measurements. Data on the thermodynamics of dimerization of both proflavine and ethidium bromide in aqueous solution obtained on the basis of spectroscopic and/or calorimetric experiments are also reported.

The enthalpy data show that dye-dimerization and dye "strong" interaction with DNA are energetically favourable and quite similar while only in the latter case the phenomenon is also entropy driven. This is taken as further evidence in support of the concept that "strong" interaction of both proflavine and ethidium bromide with DNA means dye molecules intercalation into the native, double helical structure of the biopolymer.

1. Introduction

A vast number of studies have been carried out on the binding of cationic dyes by DNA in aqueous solution. Many of these studies aimed at an understanding of the mechanisms through which the "binding" of certain dyes capable of affecting the biological activity of DNA may eventually take place (see, e.g., ref. [1]). In particular, using proflavine (PF) and ethidium bromide (EB) different authors have reported spectroscopic, viscometric and ultracentrifugation data pointing out convincingly that both dyes when "strongly" bound by native DNA are actually *intercalated* between adjacent base pairs along the biopolymer's double helical chains [2–15]. This would indeed be also true for a number of other dyes of suitable molecular structure with fused aromatic rings. The "strong" binding, characterized by association constants greater than 10^5 M^{-1}, is generally limited however to molar ratios (r) of bound dye per DNA nucleotide smaller than about 0.15–0.20 in dilute solutions of relatively low ionic strengths. At higher r values, when all sites available for intercalation appear to be saturated, a weaker type of binding prevails. Additional dye molecules would then interact with DNA mainly through coulombic forces and/or via self-stacking on the charged surfaces of the rod-like DNA chains [1, 16].

From a thermodynamic standpoint, however, either the strong or the weak binding of PF and EB by DNA have been characterized essentially in terms of apparent equilibrium constants K_I, i.e., of approximate standard-state free energy of binding values at near room temperature. Only a few enthalpy (and entropy) data on DNA–dye interactions have been evaluated always from van 't Hoff plots of K_I values. For instance, the enthalpy of EB strong-binding by DNA has been reported as ~0 by LePecq and Paoletti for ionic strengths lower than 0.1, approximately [10]. On the contrary, for PF an approximate enthalpic value of at least −5 kcal/mole (mole of dye strongly-bound by DNA) may be inferred from the data of Chambron

* Mailing address: Laboratorio di Chimica delle Macromolecole, Istituto di Chimica, Università di Trieste, Piazzale Europa 1, 34127 Trieste, Italy.

et al. [12]. In both instances, for the experimental conditions employed, dye *intercalation* is believed to take place.

We thus consider that a reliable, more comprehensive, thermodynamic picture of DNA–dye interactions is still badly needed. Its achievement may, in fact, help clarify undisclosed features of such interactions and may provide original evidence on the intercalation process as distinct from the "weaker" binding ones. This has prompted us to undertake an investigation of the interaction of a few dyes with DNA mainly with the aid of calorimetric measurements. To our knowledge this technique has not been applied so far to these type of studies. This is certainly not due to a lack of interest of the very type of approach but, we are inclined to believe, to a number of technical difficulties which are encountered in extending the otherwise blooming field of biochemical calorimetry to the systems of our concern. Using a sensitive flow-type calorimeter we trust to have been able to overcome such difficulties (but see section 2).

We wish to report here a few data useful for a thermodynamic description of proflavine and ethidium bromide binding by DNA in dilute aqueous solutions at 25°, in particular for dye to DNA concentration ratios for which dye intercalation takes place nearly quantitatively.

Data on the enthalpy of PF and EB dimerization in aqueous solution at 25°, evaluated by direct calorimetric measurements and/or from van't Hoff plots of spectral data (PF), are also reported as they appear to pertain to the mechanism of dye–DNA strong interactions.

2. Experimental

2.1. Samples

Proflavine hydrochloride (K & K) was purified by repeated crystallization from water. Ethidium bromide (Sigma Chemical Co.) was used without further purification. DNA from calf thymus was a Sigma Chemical Co. Sample (type I, sodium salt, highly polymerised). All other reagents were Carlo Erba RP products.

2.2. Buffer

Unless otherwise specified, the experiments were performed in the presence of 0.01 M phosphate buffer (pH = 7.0).

2.3. Procedures

2.3.1. Preparation of the solutions

The concentrations of stock solutions of proflavine and of ethidium bromide were determined by means of spectral absorption measurements after appropriate dilutions so that the amount of dye dimers could be neglected in each case. For PF a value of 42 000 M^{-1} cm^{-1} for the molar extinction coefficient at 444 nm (monomer spectrum) was used, which is close to the value reported by Schwarz et al. [17]. In the case of monomeric EB the molar extinction coefficient at 480 nm was 5120 M^{-1} cm^{-1}, a value close to that reported also by others [10, 15].

In the experiments with PF all the glassware, including of course the spectrophotometric cells, had to be carefully conditioned with the dye solutions. Absorption of PF onto even slightly rough glass surfaces as well as on plastic tubings, etc., may in fact lead to serious concentration errors.

In our experience a contact of at least five minutes of a PF solution with any given glass container, cell or pipet, followed by repeated rinsing with aliquots of fresh solution are necessary. This procedure may be avoided in the case of EB which is only very slightly adsorbed on glass.

The concentration of DNA solutions was determined spectrophotometrically using a molar extinction coefficient of 6400 M^{-1} cm^{-1} at 259 nm. Doubly distilled water was employed.

2.3.2. Determination of equilibrium constant and enthalpy of dye dimerization

The equilibrium constant and the enthalpy of dimerization of EB in water were evaluated by means of calorimetric measurements using a LKB 10700 batch microcalorimeter with glass cells. Details on the experimental procedure and on the elaboration of the experimental data have been already reported else-

where [18].

In the case of PF in water erratic results were obtained with the batch calorimeter due to dye absorption onto the glass cells, which any attempt of partial "conditioning" failed to obviate.

A LKB flow type microcalorimeter was then employed. In this case two peristaltic pumps passed initially through the apparatus only solvent and at a constant flow rate until a good base line was recorded. Then one of the pumps was made to pass a PF solution which was mixed into the flow-cell with solvent (i.e., phosphate buffer or phosphate buffer-KCl) coming from the other pump. The instrumental responses were normal, i.e., the traces of the recorder connected to the calorimeter (via a Keithley 150B amplifier) did not exhibit any anomaly.

With the flow-apparatus, once all the surfaces the dye solution enters in contact with are saturated, a steady-state would be attained and the final response of the calorimeter should only deal with the dye-dilution process. However, the reproducibility of the measurements was poor at low ionic strenghts but good at higher KCl concentrations. The average value of the enthalpy of dimerization ΔH_D of PF in 0.5 M KCl was found in this way to be -8.5 ± 0.5 kcal/mole of dimer, at 25°. The value $\Delta H_D = -7.13 \pm 0.6$ kcal/mole for the self-association of PF in 0.05 M phosphate buffer (pH = 7.8) and 0.2 M KCl at 25° has been reported by Shiao and Sturtevant [19] on the basis of flow-calorimetry measurements.

Apparently these authors have not encountered any of the experimental difficulties mentioned above even in using PF solutions as concentrated as 0.017 M. They were thus able to derive both K_D and ΔH_D for PF only by means of calorimetry (as we also did with EB [18]). In our case, having at disposal sufficiently accurate heat of dilution data for only a limitated range of PF concentrations, the calculation of ΔH_D was based on the knowledge of the equilibrium constants K_D at the ionic strengths used, and therefore on the number of moles of PF undergoing the dimer→monomer reaction in the mixing cell (the heat of dilution of the monomer and dimer PF species was considered negligible at the total stoichiometric concentrations used ($10^{-3} - 10^{-4}$M)).

These calculations require of course that K_D values be known with accuracy: furthermore, disposal of such K_D data for different temperature may allow an independent evaluation of ΔH_D (van't Hoff enthalpy of dimerization). Since the literature K_D data may not have been determined using the precautions said above in handling PF solutions and in view of the not very reproducible ΔH_D data obtained by us by calorimetry, the equilibrium constants and the enthalpy of PF dimerization in aqueous solution were determined by means of spectroscopic measurements. The procedure given in details by Schwarz et al. [17] was followed.

A Hitachi Perkin Elmer EPS-3t spectrophotometer equipped with water thermostated cells was used. The results are reported in table 1 of the discussion. Incidentally, the van't Hoff enthalpic values determined by us for PF dimerization are in very good agreement with those given by Schwarz et al. for low ionic strengths. On the contrary, for 0.5 M KCl these authors report a values of −8.5 kcal/mole which is higher than our spectroscopic value but that happens to be quite close to our calorimetric mean value. Mention must also be made of the results of Haugen and Melhuish [20] according to which ΔH_D for PF in 0.01 M phosphate or acetate buffer (pH = 4) is -5.5 ± 1.0 kcal/mole on the basis of absorption spectra and quantum efficiency of fluorescence measurements. The latter value however, may not be directly comparable to the other figures quoted above in view of the possible influence of the pH (besides of the ionic strength) on the thermodynamics of PF self-association.

2.3.3. Dialysis experiments of DNA–dye solutions

These experiments were carried out following closely the procedure of Armstrong et al. [9]. The elaboration of the dialysis equilibrium data to derive DNA-dye interaction constants (see table 1) was made accordingly. Our experiments were all performed at 25° using pretreated Kalle Aktiengesellschaft dialysis tubings. The concentrations of DNA and of dye were close to those used in the calorimetric experiments, but only dye to DNA concentration ratios smaller than 0.15 were considered.

2.3.4. Calorimetric measurements of DNA–dye interactions

An LKB flow-type microcalorimeter has been used. The way of handling the data for the calculation of enthalpy of binding values are fully described elsewhere [21]. The DNA concentration was around 10^{-3} equiv.

Table 1
Thermodynamic data on the dimerization and on the interaction with DNA of proflavine (PF) and ethidium bromide (EB) in dilute aqueous solution. (All data are for 25°C, unless indicated otherwise)

	Dimerization			Interaction with DNA [b]		
	solvent	K_D (M^{-1})	ΔH_D (kcal/mole)	solvent	K_I (M^{-1})	ΔH_I (kcal/mole)
PF [a]	H_2O	477	−6.3 ± 0.6	0.01 M phosphate buffer pH = 7 I = 0.015	9.4×10^5 [d]	−6.7 ± 0.5
	H_2O (45°)	240				
	0.5 M KCl	1837	−6.5 ± 0.6 (−8.5 ± 0.5)	0.01 M phosphate buffer + KCl I = 0.10	3.5×10^5 [d]	−7.6 ± 0.6
	0.5 M KCl	900				
EB [c]	H_2O	41	−7.6 ± 0.3	0.01 M phosphate buffer pH = 7 I = 0.015	4.0×10^6 [d]	−6.2 ± 0.6
				0.01 M phosphate buffer + KCl I = 0.10	1.1×10^6 [d]	−6.7 ± 0.5

a) ΔH_D is in kcal per mole of dye dimer. The value given in parenthesis was determined by calorimetry (see section 2).
b) The data are relative to the "strong" binding of PF or EB onto DNA (see text and fig. 1).
c) Dimerization constant and dimerization enthalpy for EB were derived by us from calorimetric data as explained elsewhere [18]. ΔH_D is in kcal per mole of dye dimer.
d) The K_I values were evaluated from dialysis equlibrium data for dye to DNA (phosphorous) molar concentration ratios, r, lower than 0.12.

P/ℓ while the concentration of PF was never greater than 10^{-4} M to avoid correction for the heat of dilution (i.e., of dimer dissociation) of this dye.

We wish to point out here that in the case of dye binding by DNA the calorimetric data were found fairly reproducible. In this case, in fact, the dye/DNA concentration ratios were always such that practically all dye molecules present in the solutions were strongly bound to the biopolymer. Evidently, dye adsorption phenomena were reduced to a minimum as the binding constant to DNA is much higher than the binding constant to the glass surface. In any case the experiments with the flow-calorimeter were carried out in this way: first DNA solution against solvent was run (baseline), then the dye solution was run against DNA solution. In this manner dye adsorption on the cell surface doesn't occur at all due to the higher affinity of the dye for DNA.

With EB the values of the enthalpy of binding to DNA derived by flow-calorimetry could be exactly reproduced using a batch type microcalorimeter, always at 25°C.

3. Results and discussion

The results of the calorimetric measurements on the interaction of PF and of EB with DNA at two ionic

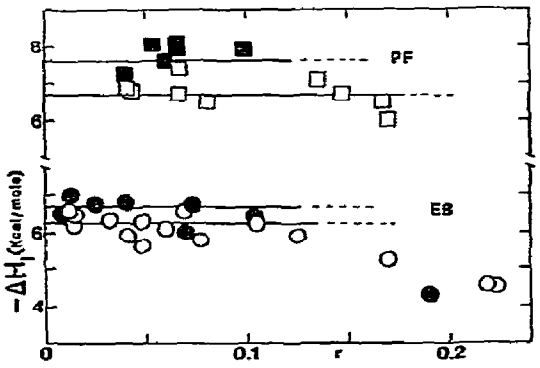

Fig. 1. Enthalpy of interaction between proflavine (PF) and ethidium bromide (EB) with calf thymus DNA as a function of stoichiometric molar ratio dye/DNA, r. Open symbols: ionic strength I = 0.015 (phosphate buffer pH = 7); full symbols: ionic strength I = 0.1 (phosphate buffer pH 7 + KCl).

strengths are reported in fig. 1.

In ordinate ΔH_I is the enthalpy of interaction in kcal per mole of dye; in abscissa r is the stoichiometric molar concentration ratio of dye to DNA phosphorous in the solutions. In view of the very high values of the association constants derived from equilibrium dialysis measurements (which are in good agreement with literature data [9, 12, 13, 15, 16]) (see table 1) for the same experimental conditions used in the calorimetric measurements, the difference between ΔH_I expressed as above or in kcal per mole of dye bound is well within the experimental errors.

In the case of EB our results show, despite some scatter in the points, that for r lower than 0.15, approximately, the ΔH_I values may be considered independent of r, while for r greater than 0.15 there is a drop in $-\Delta H_I$ which is beyond experimental errors. This feature is in qualitative agreement with evidences from other experimental approaches indicating that (under the conditions used in our work) for r lower than 0.15–0.20 EB is bound to DNA diversely than for higher r values. Our calorimetric data for PF (fig. 1) do not allow to draw a similar conclusion. We had in fact to limit the measurements to low r values because with increasing r beyond about 0.15 the quality of the data rapidly deteriorated due to a much lower extent of PF–DNA interaction and thus to the onset of dye adsorption in the calorimeter cells (see section 2).

The results which we can sufficiently rely upon (fig. 1) do show, however, that for $r < 0.12$, i.e., when "strong" dye binding would only occur according to spectroscopic and dialysis data [9, 12, 13, 16], the enthalpy of PF–DNA interaction may be considered independent of r.

The average ΔH_I calorimetric values for the "strong" binding of both PF and EB by DNA are reported in table 1 together with the binding constants $K_I(M^{-1})$ derived from dialysis equilibrium measurements. In the same table the dimerization constants and the enthalpy of dimerization of PF and EB, respectively, derived from our spectroscopic (PF) or calorimetric (EB) measurements are also given.

This set of data invites a few comments. For the possible reasons indicated in the experimental part and as it is evident by inspection of fig. 1, the dye dimerization enthalpies and the dye–DNA interaction enthalpies of table 1 have to be considered uncertain to ±15 and ±10%, respectively. Despite all this we think that our data clearly point out that self-association of the two dyes considered and their "strong" interaction with DNA are characterized by quite similar heat effects.

Indeed we believe this is not mere coincidence but, on the contrary, original evidence in favour of the widely held opinion that strong binding of both EB and PF by DNA is synonymous of dye molecules *intercalation* between adjacent bases along the biopolymer chains. Intercalation of an aromatic polycyclic molecule like PF into the *native* structure of DNA must involve interruption on stacked base-pair contact (which would require at least 5 kcal per mole of contacts, approximately [22, 23]) and the establishment of two new contacts between the intercalated molecule and the previously stacked bases.

Our data would indicate that intercalation leads to dye–base interactions energetically as favourable as base–base and/or dye–dye ring interaction per actual surface of contact*.

In the intercalation process other factors such as for instance a stiffening and/or elongation of the DNA chains, local changes in charge density of the biopolymer, etc., may contribute to the observed overall enthalpy. In our opinion, however, the associated heat effects should be of relatively small absolute values. More important, our data show that dye intercalation is a process which, as distinct from dye dimerization, is favoured also by the entropy.

It is in fact immediately evaluated from the data of table 1 that in the case of EB (for which more reliable information is available to us) dimerization in water is accompanied by a decrease in entropy (ca. −18 e.u.) while intercalation is characterized by an increase of entropy (ca. +10 e.u., at the lower ionic strength studied).

An increase of entropy in an association reaction in aqueous solution must find its origin essentially in the liberation of water molecules from the hydration sheaths of the interacting species. This is consistent with the intercalation mechanism too, and suggests a noticeable

* On this basis we have to consider wrong the result of LePecq and Paoletti according to which $\Delta H_I \approx 0$ for the EB–DNA system at low ionic strength [10]: the results of Chambron et al. [12] for PF–DNA are on the contrary in qualitative agreement with our calorimetric data.

degree of penetration into the core of DNA double helix of the intercalated dye molecules whose solvation shells would be eventually stripped off on entering the DNA "phase".

For what concerns the influence of ionic strength on the energetics of dye-binding to DNA we find that a more than sixfold increase in KCl concentration reduces K_I for both PF and EB by a factor of nearly four: on the other hand the ΔH_I's exhibit small decreases which are, however, within experimental errors. A reduction of K_I for PF and acridine-orange strong interaction with DNA has been logically ascribed to counterion's screening of the electrostatic potential along DNA chains [9]: from a thermodynamic standpoint our data would point out that this corresponds to a (slightly) smaller entropy gain upon dye–binding at the higher ionic strengths. Thus part of the observed effect (i.e., the decrease in K_I) probably stems from a diminished hydration of interacting species at relatively high KCl concentrations.

It will be most interesting to ascertain whether the thermodynamic characterization presented above for the strong interaction of both PF and EB with DNA is applicable also in the case of other compounds of biological importance (like certain antibiotics and other dyes as well) which are thought to intercalate into DNA.

Additional data on the energetics of dyes self-association should also prove useful as more has to be learned on this very type of phenomenon. Our results show, for instance, that the unitary entropy of PF and EB dimerization in water is nearly zero (PF) or negative (EB).

It is difficult to reconcile this evidence with the idea that dye dimerization may be depicted in general as a hydrophobic forces-driven process, at least within the limits of the popular version of the "hydrophobic interactions" concept.

An explanation of our finding evidently would require careful consideration of an interplay of different types of interactions, from attractive "hydrophobic" to repulsive coulombic ones, for the solvated dimeric species.

Acknowledgement

This work has been sponsored by the Italian Consiglio Nazionale delle Ricerche, Rome.

References

[1] P.H. von Hippel and J.D. McGhee, Ann. Rev. Biochem. 41 (1972) 231, and literature quoted therein; A. Blake and A.R. Peacocke, Biopolymers 6 (1968) 1225.
[2] L.S. Lerman, J. Mol. Biol. 3 (1961) 18.
[3] L.S. Lerman, J. Cellular Comp. Physiol. Suppl. 1 (1964) 1.
[4] J. Cairns, Cold Spring Harbor Symp. Quant. Biol. 27 (1962) 311.
[5] D.M. Neville, Jr. and D.R. Davies, J. Mol. Biol. 17 (1965) 57.
[6] D.S. Drummond, N.J. Pritchard, V.F.W. Simpson-Gildemeister and A.R. Peacocke, Biopolymers 4 (1966) 971.
[7] Y. Mauss, J. Chambron, M. Daune and H. Benoit, J. Mol. Biol. 27 (1967) 579.
[8] W. Bauer and J. Vinograd, J. Mol. Biol. 33 (1968) 141.
[9] R.W. Armstrong, T. Kurucsev and U.P. Strauss, J. Am. Chem. Soc. 92 (1970) 3174.
[10] J.-B. LePecq and C. Paoletti, J. Mol. Biol. 27 (1967) 87.
[11] C. Paoletti and J.-B. LePecq, J. Mol. Biol. 59 (1971) 43.
[12] J. Chambron, M. Daune and Ch. Sadron, Biochim. Biophys. Acta 123 (1966) 306.
[13] J. Chambron, M. Daune and Ch. Sadron, Biochim. Biophys. Acta 123 (1966) 319.
[14] S. Ichimura, M. Zama, H. Fujita and T. Ico, Biochim. Biochim. Biophys. Acta 190 (1969) 116.
[15] M.J. Waring, J. Mol. Biol. 13 (1965) 269.
[16] A.R. Peacocke and J.N.H. Skerrett, Trans. Faraday Soc. 52 (1956) 261.
[17] G. Schwarz, S. Klose and W. Balthasar, Eur. J. Biochem. 12 (1970) 454.
[18] V. Crescenzi and F. Quadrifoglio, Eur. Polymer J., in press.
[19] D.D.F. Shiao, J.M. Sturtevant, Biochemistry 8 (1969) 4910.
[20] G.R. Haugen and W.H. Melhuish, Trans. Faraday Soc. 60 (1964) 386.
[21] V. Crescenzi, F. Delben, S. Paoletti and J. Skerjanc, J. Phys. Chem., in press.
[22] P.L. Privalov, O.B. Ptitsyn and T.M. Birshtein, Biopolymers 8 (1969) 559.
[23] L.G. Bunville, E.P. Geiduschek, M.A. Rawitscher and M.J. Sturtevant, Biopolymers 3 (1965) 213.

BIOPHYSICAL CHEMISTRY 1 (1974) 325–337. © NORTH-HOLLAND PUBLISHING COMPANY

THE TEMPERATURE-DEPENDENT SELF-ASSOCIATION OF ADENOSINE 5'TRIPHOSPHATE IN 0.154 M NaCl *

Will E. FERGUSON, Charles M. SMITH and E.T. ADAMS, Jr.
Chemistry Department, Texas A&M University, College Station, Texas 77843, USA

and

Grant H. BARLOW
Molecular Biology Department, Abbott Laboratories, Inc., North Chicago, Illinois 60064, USA

Received 10 August 1973
Revised manuscript received 20 November 1973

The disodium salt of adenosine 5'triphosphate (ATP), dissolved in and dialyzed against isotonic saline, undergoes a temperature-dependent self-association. Self-association increases with decreasing temperature. The technical achievement that made these experiments possible was the development and availability of a hollow fiber dialyzer with a low molecular weight (200) cutoff. Several models were tested to describe the experimental data, and a monomer–dimer–trimer association seemed to describe the data best. Both the dimerization and trimerization were exothermic; values of the thermodynamic functions for these reactions are reported. The self-association reaction for ATP is much stronger than that observed for purine and cytidine, as well as for various nucleosides whose self-association in aqueous solutions has been studied.

1. Introduction

The self-association of purine, pyrimidine and several nucleosides has been studied extensively by physical methods [1–7]. In nonaqueous solutions hydrogen bonds [2] appear to play an important role in the observed self-association reactions. In aqueous solutions much evidence has been accumulated to indicate that base stacking, the layering of planar bases on one another, plays a prominent role in the observed self-association of nucleosides and nitrogen bases [1, 3, 6]. Sedimentation equilibrium studies on these small molecules have so far been restricted to water soluble, uncharged compounds, such as purine, cytidine, and various ribo- and deoxyribonucleosides [4, 5, 7]. One very good reason for this may be due to the fact that nucleotides ionize, and heretofore one could not dialyze them against supporting electrolyte(s). Thus one would have to make corrections for charge (Donnan) and other nonideal effects in a multicomponent system. It has been shown by Vrij [8, 9] and by Casassa and Eisenberg [10] that if one can dialyze the ionizable solute of interest in a multicomponent system containing supporting electrolyte (small electrolytes like NaCl or KCl) to swamp out charge effects, then the sedimentation equilibrium equation can be reduced to a form that is formally the same as that for a two component system.

With the availability of hollow fiber dialyzers having low molecular weight cutoffs, the possibility of dialyzing solutions containing low molecular weight solutes, such as the disodium salt of adenosine triphosphate (Na_2ATP) dissolved in isotonic (0.154 M) saline, became feasible. Thus we acquired a hollow fiber dialyzer (Bio-Rad Laboratories Cat. No. 751-3300) with a reported molecular weight cutoff of 200. The nominal molecular weight cutoff is defined

* This is paper VIII in the series Sedimentation Equilibrium in Reacting Systems. Presented at the 166th National Meeting of the American Chemical Society, Chicago, Illinois, Aug. 26–31, 1973. Please address all correspondence regarding this paper to Dr. E.T. Adams, Jr.

(by Bio-Rad Labs) to be the molecular weight of a solute that will be 85% retained by the hollow fiber.

We chose ATP as the first important, small molecular weight, ionizable compound to study since it is involved in so many biochemical reactions essential to life processes. Also, it has the largest molecular weight of the three adenosine nucleotides. Thus one could see if an ionizable compound exhibited more or less self-association than related, neutral compounds. If there were self-association with ATP, then one could do similar studies with the adenosine di-(ADP) and monophosphates (AMP) and study the effect of the type of phosphate group present on the self-association reaction. Another reason for studying ATP is that very little information is available about its state of aggregation in solution; this is also true of many important nucleotides, coenzymes and vitamins. Some diffusion studies on aqueous solutions of ATP have been carried out by Bowen and Martin [11]; their results show a very slight decrease in the diffusion coefficient with increasing concentration of ATP, which could indicate self-association. They have also reported on the effect of ionic strength and of various ions on the diffusion coefficient. The sedimentation equilibrium experiment is particularly well-suited for the study of self-associating solutes. Here we report on the results of our studies on the self-association of Na_2ATP dissolved in and dialyzed against isotonic saline; these experiments were performed at 10, 16, 20, 25 and 30°C.

2. Preparation of adenosine 5'triphosphate solutions

The disodium salt of adenosine 5'triphosphate (Na_2ATP) was purchased from the Sigma Chemical Co. (Lot No. 111C-7360); their highest purity grade was used in these experiments. All solutions were made up in boiled, deionized water. Glassware, ultracentrifuge cell parts and syringes were scrupulously cleaned before use. The ATP* solutions were dialyzed in a Bio-Rad Osmolyzer (Cat. No. 751–3300) which had the following characteristics: a molecular weight cutoff of 200, 10 ml volume inside the fibers, 100 ml volume outside the fibers, and 1000 cm^2 surface area for the fibers. Before use the dialyzer was rinsed for several hours with isotonic saline. A teflon-coated, magnetic stirring bar was placed in the lower part of the osmolyzer (below the plastic web) so that the outer solution (isotonic saline) could be stirred continuously while dialysis was in progress. The ATP solution was introduced into the fibers through a millipore filter. At least six changes of dialysate were used; the period between changes of the isotonic saline solution was 20 to 30 minutes. That there was a Donnan effect in these short periods was evident from the increase in volume inside the fibers. We usually removed some ATP solution from the fiber bundle as the dialysis proceeded; this was removed from the fiber bundle opposite to the one used for the introduction of the sample. Since ATP has such a large extinction coefficient in the ultraviolet—15 400 per mole of monomer at 254 nm, we could easily ascertain if the fiber membranes would hold back the ATP. After the 20–30 minute dialysis period we observed an absorbance of less than 0.010 at 254 nm in the dialysate when compared against nondialyzed, isotonic saline solutions. For very prolonged periods of about 12–14 hours more ATP would come across the membranes. The initial concentrations in this series of sedimentation equilibrium experiments ranged from 0.001 M to 0.022 M, as moles of monomer. Using the theory of multicomponent systems, we assumed that the molecular weight of the monomer, M_1, was 492.7, which is the molecular weight of the redefined solute component Na_2ATP-NaCl. At 25°C the pH of the ATP solutions varied from 3.3 to 4.6, depending on the ATP concentration. In a blank experiment, 10 ml of 0.154 M NaCl were placed inside the hollow fiber and 100 ml of Cl^- free, doubly distilled water were placed outside the fiber. We were able to show that Cl^- (and hence NaCl) passed through the membrane, since a silver nitrate test on an aliquot of the outer liquid, taken after 20 minutes to simulate a short dialysis, was positive. To rule out the possibility of metal ion effects on the self-association of the ATP, atomic absorption spectrophotometry was carried out on some ATP solutions. The results indicated negligible amounts of iron (25 ppm) and magnesium (3 ppm) per gram of ATP.

* Hereafter we shall usually refer to Na_2ATP or the redefined component, Na_2ATP-NaCl, as ATP.

3. Concentration determination and density increment

The concentration of the dialyzed ATP solution was determined by three different methods: differential refractometry at 546 nm, ultraviolet absorbance at 254 nm on carefully diluted solutions, and boundary-forming experiments in the ultracentrifuge. Boundary-forming experiments were usually performed on solutions of lower ATP concentration (20 fringes or less). Since refractometric optics (Rayleigh and schlieren optics) were used in our ultracentrifuges, the concentration determinations were always converted to the number of fringes that would be produced in an ultracentrifuge cell with a 12 mm thick, double-sector centerpiece when light having a wavelength of 546 nm was used. The number of fringes, J, is the number of wavelengths difference in optical path between the solution and the solvent. From the three methods for determining concentration, we were able to establish the following relation between the number of fringes (12 mm), J, and c, the ATP concentration in grams per liter; at 20°C we obtained $J = 4.2155\ c$. Concentration values at other temperatures were calculated by using procedures advocated by Adams and Filmer [12].

In order to obtain the weight (M_{wc}) or the apparent weight (M_{wa}) average molecular weights, it is necessary to know the partial specific volume, $\bar{v}$, of the solute and the density of the ATP solutions, ρ, or else it is necessary to know the density increment [8, 10], which we used in these experiments. For ATP concentrations in grams per liter, c, the density increment is given by $1000(\partial\rho/\partial c)_\mu$. The subscript μ means that all diffusible solutes which can pass through the dialysis membrane have the same chemical potential; this condition is achieved by dialysis. Density increments were determined from careful density measurements of ATP solutions; these measurements were carried out on an Anton Paar Digital Precision Density Meter Model DMA 02C. Values of the density increment ranged from 0.309 at 10°C to 0.297 at 37°C, and they gave a very good straight line when plotted against temperature. Linear regression analysis gave the following equation for the variation of the density increment with temperature:

$$1000(\partial\rho/\partial c)_\mu = 0.313 - 4.42 \times 10^{-3}\, t\,. \qquad (1)$$

Here t is the temperature in degrees Celsius. The correlation coefficient was 0.999.

4. Ultracentrifugation

Sedimentation equilibrium experiments were carried out in two Beckman/Spinco Model E analytical ultracentrifuges that were equipped with Rayleigh and schlieren optics. Both ultracentrifuges had electronic speed controls, and both were equipped with temperature control systems, so that temperature control of about ± 0.05°C could be obtained. The Rayleigh and schlieren patterns were photographed on Kodak Type II-G spectroscopic plates in one of the ultracentrifuges. The other ultracentrifuge was modified to accept a 70 mm film magazine, and the Rayleigh and schlieren patterns were photographed on Kodak IV–F 70 mm film, which had a polyester film base. This ultracentrifuge was also modified to accept a helium-neon laser ($\lambda = 632.8$ nm) light source, in addition to the usual water cooled, mercury vapor lamp.

For these experiments the solute concentrations were measured in terms of 12 mm fringes produced at 546 nm. We could convert the red laser light fringes to green (546 nm) fringes by the relation

$$J(\text{red}) = 0.8487\ J(\text{green})\,. \qquad (2)$$

This relation was established by comparing differential refractometry experiments at 546 nm and boundary-forming experiments at 546 and 628.3 nm. In all of these experiments carbon-filled, epoxy resin, double-sector centerpieces were used. The ultracentrifuge cell filling procedures described by Adams and Lewis [13] were scrupulously followed. At lower solute concentrations ($J = 10$ or lower) 30 mm centerpieces were used. We could convert 30 mm fringes to 12 mm fringes of the same wavelength by the relation

$$J(12\text{ mm}) = J(30\text{ mm})/2.5\,. \qquad (3)$$

At higher solute concentrations (30 fringes or more) we had to use red fringes or schlieren patterns produced by the green light. The experiments described in this work were performed at 34 000 rpm. The solution column thicknesses used in these experiments ranged from 4.5 to 6 mm. Photographic data were collected at the beginning of the experiment and about 36 hours later. The photographic films and plates were read on a Nikon Model 6C comparator.

5. Quantities needed for the analysis

It has been shown by Vrij [8,9] and by Casassa and Eisenberg [10] that the sedimentation equilibrium equation for a macromolecular solute in a multicomponent system can be reduced to a form that is formally the same as that for a two component system, provided that the solution is dialyzed against solvent so that the chemical potential of the small (diffusible) solutes is the same on both sides of the membrane. Since our material was dialyzed, it will be assumed that the Vrij–Overbeek [9] or Casassa–Eisenberg [10] conventions apply, and we will use equations for two component systems. The average molecular weights, the equilibrium constants (K_i), and the second virial coefficients (BM_1) will refer to an associating solute constituent or component defined by these conventions.

In order to obtain the apparent weight average molecular weight (M_{wa}), it is necessary to make the following assumptions regarding the self-associating species: 1) The refractive increments, ψ_i, are the same. 2) The density increments, $1000(\partial\rho/\partial c)_{\mu,T}$, are the same. 3) The natural logarithm of the activity coefficient, y_i, on the c-scale (g/ℓ) can be represented by

$$\ln y_i = BM_1 c\,, \quad i = 1, 2, \ldots\,. \tag{4}$$

Here BM_1 is the second virial coefficient. With the aid of these assumptions, M_{wa} is obtained [8, 10] from

$$\frac{\mathrm{d}\ln c}{\mathrm{d}(r^2)} = AM_{wa}\,, \tag{5}$$

where

$$A = 1000(\partial\rho/\partial c)_{\mu,T}\omega^2/2RT\,. \tag{6}$$

The quantity ω^2 is the square of the angular velocity of the rotor ($\omega = 2\pi$ rpm/60), R is the gas constant (8.314×10^7 ergs/deg-mole) and T is the absolute temperature. In eq. (5) c is the concentration in g/ℓ of the associating solute at any radial position, r, in the solution column of the ultracentrifuge cell. M_{wa}, the apparent weight average molecular weight, is related [14, 15] to the true weight average molecular weight, M_{wc}, by the relation

$$\frac{M_1}{M_{wa}} = \frac{M_1}{M_{wc}} + BM_1 c\,. \tag{7}$$

The quantity M_{wc} is the same as M_{wr} [14], the weight average molecular weight at any radial position r in the solution column of the ultracentrifuge cell. It has been shown that M_{wr} and also M_{wa} are functions of c for self-associating solutes, hence the symbol M_{wc} is used with self-associating solutes [14, 15]. In order to analyze self-associations it is necessary to do experiments at several different initial concentrations, c_0, calculate M_{wa}, and make a plot of M_{wa} vs. c from all the experimental data [12–16]. Fig. 1 shows such a plot for ATP at two different temperatures, 10 and 30°C. The increase in M_{wa} with c (or J) is characteristic of a self-association; the rapid rise of M_{wa} in the very low concentration region indicates the presence of a strong association. In order to proceed with the analysis for the type of self-association that is present it is necessary to calculate M_1/M_{na} from plots of M_1/M_{wa} vs. c. Here one notes that M_{na} is the apparent number average molecular weight, and M_1/M_{na} is obtained [16] from

$$\frac{M_1}{M_{na}} = \frac{1}{c}\int_0^c \frac{M_1}{M_{wa}}\,\mathrm{d}c = \frac{M_1}{M_{nc}} + \frac{BM_1 c}{2}\,. \tag{8}$$

M_{nc} is the true number average molecular weight. With the aid of eqs. (7) and (8), and with the observation that the sum of the weight fractions, f_i, of the self-associating species must be one, i.e.,

$$\sum_{i=1}^{n} f_i = 1\,, \tag{9}$$

we can proceed with the analysis.

6. Test for the type of association present

6.1. Monomer–n–mer association

Could the observed self-association be described by

$$nP_1 \rightleftharpoons P_n\,, \quad n = 2, 3, \ldots\,, \tag{10}$$

where P represents the self-associating solute? First of all note that a monomer–dimer ($n = 2$) self-association cannot exist, since values of M_{wa} much greater than the molecular weight of dimer ($M_2 = 985.4$) are encountered; this is evident in fig. 1. The quantities M_1/M_{na} and M_1/M_{wa} can be used to analyse for other

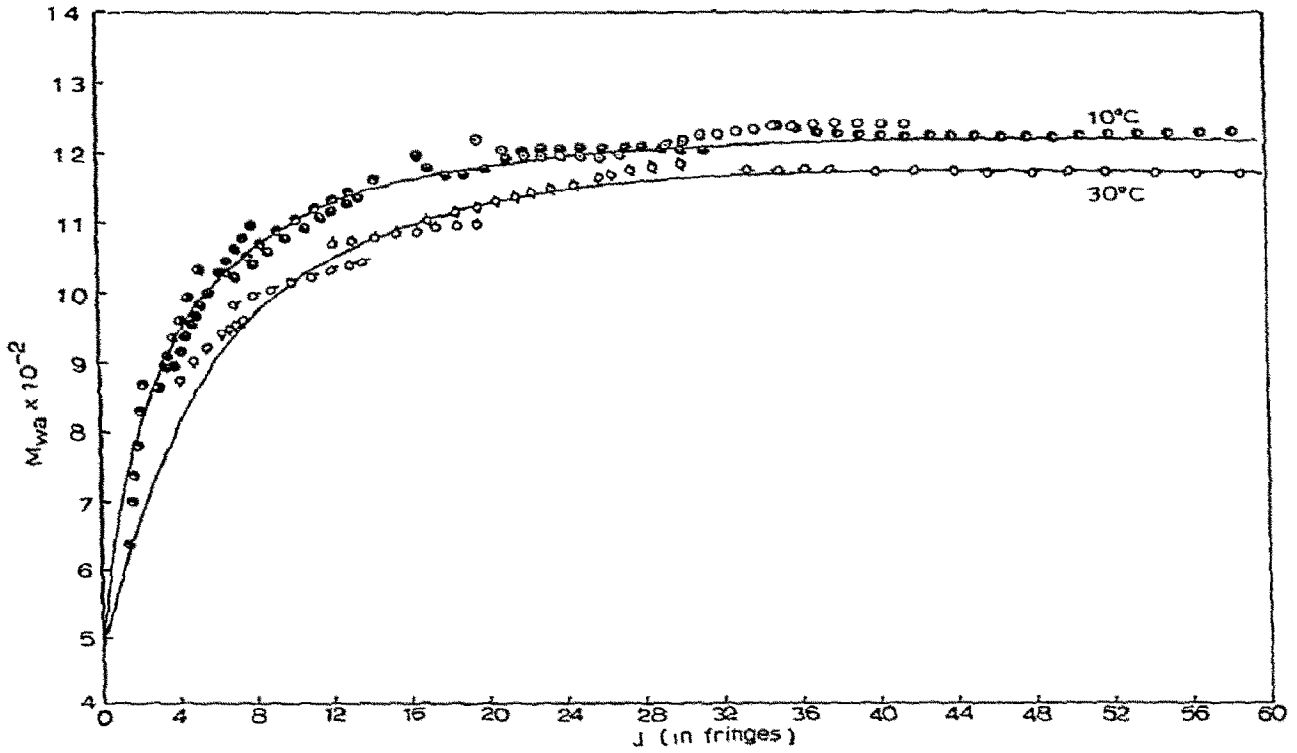

Fig. 1. Plot of M_{wa} vs. J for ATP in isotonic saline at 10°C (upper curve) and at 30°C (lower curve). The various symbols represent values of M_{wa} obtained with solutions of different initial ATP concentration. Note that the association is stronger at 10°C. The solid line in both plots represents the curve generated from values of K_2, K_3 and BM_1 reported in table 3.

monomer–n–mer associations. Note that whenever eq. (4) applies, it is possible to combine equations (7) and (8) to give [17–19]

$$\xi = \frac{2M_1}{M_{na}} - \frac{M_1}{M_{wa}} = \frac{2M_1}{M_{nc}} - \frac{M_1}{M_{wc}}. \tag{11}$$

In obtaining the quantity ξ, we have eliminated the nonideal terms; for a monomer–n–mer self-association we can show, with the aid of eq. (9), that [17, 19]

$$\xi = \frac{2+2f_1(n-1)}{n} - \frac{1}{n+f_1(1-n)}, \tag{12}$$

since $f_n = 1-f_1$. Eq. (12) is quadratic in f_1, and one can use the standard quadratic formula to obtain f_1. The proper root to use in the one that contains the negative square root of the discriminant. Knowing f_1, the equilibrium constant, K_n, for the association reaction can be obtained from the relation [17–19]

$$\frac{1}{f_1} = 1 + K_n(cf_1)^{n-1} \tag{13}$$

or

$$1 - f_1 = K_n c^{n-1} f_1^n .$$

Here a plot of $1/f_1$ vs. $(cf_1)^{n-1}$ or $1-f_1$ vs. $c^{n-1}f_1^n$ has a slope of K_n. We tried this procedure on several models from $n = 3$ to $n = 8$. The plots based on eq. (13) are shown in fig. 2. Although the plot for $n = 3$ has only slight curvature, we can impeach this model, since if it were correct, it would have to satisfy a plot based on eq. (7) to obtain BM_1. Here one notes that

$$\frac{M_1}{M_{wa}} - \frac{M_1}{M_{wc}} = BM_1 c , \tag{14}$$

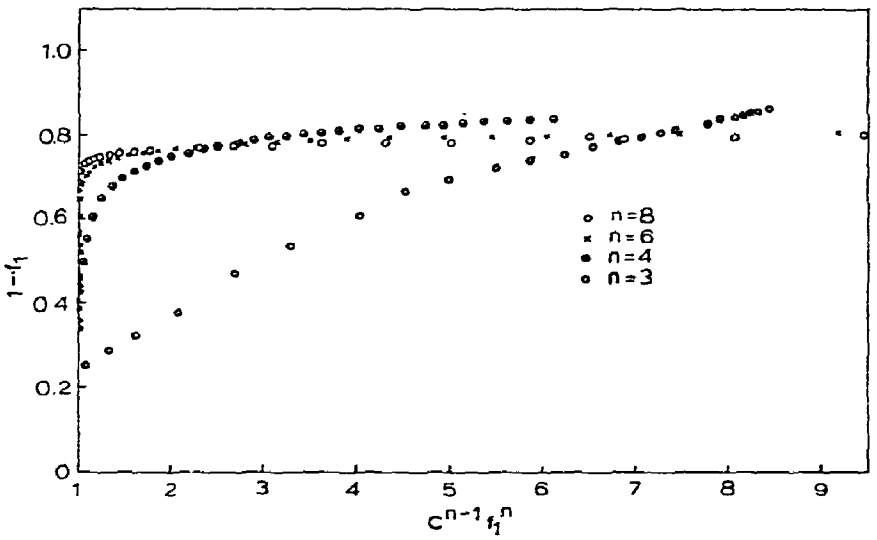

Fig. 2. Test for monomer–n–mer association. Values of f_1 were calculated from eq. (12) for several possible monomer–n–mer associations (n = 3, 4, 6, 8). These values of f_1 were then used in plots based on eq. (13). If one of these choices is correct the plot should give a straight line whose slope is K_n. None of the models seem to describe the observed self-association. The abscissa is in arbitrary units. One unit (the distance from 0 to 1, 1 to 2, etc.) has the following values: 0.04 (g/ℓ)^2 for n = 3, 0.4 (g/ℓ)^3 for n = 4, 4 (g/ℓ)^5 for n = 6 and 40 (g/ℓ)^7 for n = 8. The data collected at 10°C were used here.

and $M_1/M_{wc} = 1/[n + f_1(1-n)]$ for a monomer–n–mer self-association. The plot of $(M_1/M_{wa} - M_1/M_{wc}$ vs. c would give a straight line whose slope is BM_1; this plot failed for n = 3. Fig. 2 indicates that the plot based on eq. (13) is not satisfied for n = 4, 6 or 8 also. So, it appears a monomer–n–mer self-association is absent.

6.2. Sequential indefinite self-association

In this situation several multiple equilibria are present, and the overall result appears to be

$$nP_1 \rightleftharpoons qP_2 + mP_3 + hP_4 + \ldots . \qquad (15)$$

Such associations which appear to continue without limit are known as sequential, indefinite self-associations. If the usual assumptions about these indefinite self-associations are made, then it can be shown [17, 19] that

$$\xi = \frac{2M_1}{M_{na}} - \frac{M_1}{M_{wa}} = 2\sqrt{f_1} - \frac{\sqrt{f_1}}{2-\sqrt{f_1}}, \qquad (16)$$

$$\sqrt{f_1} = (1/4)\{(\xi+3) - \sqrt{(\xi+3)^2 - 16\xi}\}, \qquad (17)$$

and

$$1 - \sqrt{f_1} = kCf_1 . \qquad (18)^*$$

Eqs. (16) and (17) were applied to the experimental data, and the values of f_1 or $\sqrt{f_1}$ so obtained were used in eq. (18). The plot of $1 - \sqrt{f_1}$ vs. Cf_1 based on eq. (18) should give a straight line whose slope is k, the intrinsic equilibrium constant, if the model be correct. Fig. 3 shows the plot based on eq. (18); the extreme curvature rules out this model. We also used methods developed by Tang [20] to see if an indefinite self-association of the type $nP \rightleftharpoons qP_2 + hP_4 + lP_6 + \ldots$ were present, and our tests indicated this association was absent.

6.3. Monomer–dimer–trimer and monomer–dimer–tetramer associations

The last two models tested were the monomer–dimer–trimer and the monomer–dimer–tetramer self-associations. These associations can be represented as

$$nP_1 \rightleftharpoons qP_2 + mP_3 \qquad (19)$$

* Here C is the total concentration of the associating solute in g/ml. $C = c/1000$.

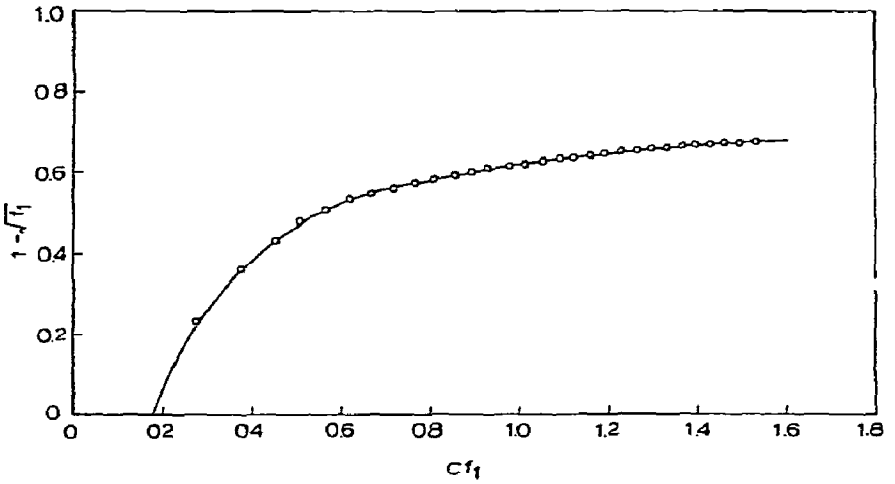

Fig. 3. Test for sequential, indefinite self-association. Eqs. (16–18) were used here. This plot is based on eq. (18). If the model were correct, the plot of $1-\sqrt{f_1}$ vs. Cf_1 should give a straight line whose slope is k, the intrinsic equilibrium constant. The data collected at 10°C were used here.

and

$$nP_1 \rightleftharpoons qP_2 + hP_4 \,. \tag{20}$$

Besides obtaining the quantities M_1/M_{wa} and M_1/M_{na}, it is also possible to evaluate the quantity $\ln f_a$ from the plot of M_1/M_{wa} vs. c, since [15, 21]

$$\ln f_a = \int_0^c \left(\frac{M_1}{M_{wa}} - 1\right)\frac{dc}{c}. \tag{21}$$

It should be noted that this is a proper integral since the

$$\lim_{c\to 0}\left(\frac{M_1}{M_{wa}} - 1\right)/c = -K_2 + BM_1$$

if dimer is present, or BM_1 if dimer is absent. The quantity f_a is the apparent weight fraction of monomer and is defined by $f_a = f_1 \exp(BM_1 c)$. We can combine M_1/M_{wa}, M_1/M_{na}, c and f_a to develop the following equation in one unknown, BM_1, for a monomer–dimer–trimer association [15]:

$$\frac{6M_1}{M_{na}} = 5 + 2f_a e^{-BM_1 c} + 3BM_1 c - \frac{1}{M_1/M_{wa} - BM_1 c}. \tag{22}$$

An analogous equation can be developed for a monomer–dimer–tetramer association. These equations may not be too reliable with strong self-associations, since the largest contribution to the integral in eq. (21) comes from the region of lowest concentration (from about 3 fringes to zero fringes). Thus the accumulated error reduces the usefulness of eq. (22) or its analogs. How did we overcome this problem? First we tried a direct Monte Carlo method ‡ on the appropriate expressions for M_1/M_{wa}, such as

$$\frac{M_1}{M_{wa}} = \frac{1 + K_2 c_1 + K_3 c_1^2}{1 + 2K_2 C_1 + 3K_3 C_1^2} + BM_1 c \tag{23}$$

for a monomer–dimer–trimer association. Unfortunately this leads to a trap. We can vary K_2 and K_3 considerably in eq. (23) with compensating variations in BM_1, so that the calculated and observed values of M_1/M_{wa} are in good agreement.

Our next thought was to see if we could get rid of the noisy part of the quantity $\ln f_a$ (see eq. (21)). This can be done. Note that

$$\ln f_a/f_{a_*} = \int_{c_*}^{c}\left(\frac{M_1}{M_{wa}} - 1\right)\frac{dc}{c} = \int_{c_*}^{c}\left(\frac{M_1}{M_{wa}} - 1\right)\frac{dJ}{J}. \tag{24}$$

‡ The Monte Carlo methods used here were developed by Mr. Charles M. Smith and will be reported in a later publication.

Here c_* is a concentration greater than zero and f_{a_*} is the value of f_a at c_*. The choice of c_* is arbitrary, but we wish to choose it so that we reduce the noise in eq. (21). Thus we could choose $J_* = 2$, for example. Eq. (22) can be modified to give f_1/f_{1_*}. Then if we multiply the equation for f_1/f_{1_*} by exp $[BM_1(c-c_*)]$ we obtain

$$\frac{f_a}{f_{a_*}} \equiv \frac{f_1}{f_{1_*}} e^{BM_1(c-c_*)} = \frac{\left[\frac{6M_1}{M_{na}} - 5 - 3BM_1c + \frac{1}{(M_1/M_{wa} - BM_1c)}\right] e^{BM_1(c-c_*)}}{\left[\frac{6M_1}{M_{na_*}} - 5 - 3BM_1c_* + \frac{1}{(M_1/M_{wa_*} - BM_1c_*)}\right]} \quad (25)$$

The asterisk means that the quantities so subscripted are evaluated at $c = c_*$. The analogous equation for the monomer–dimer–tetramer association is

$$\frac{f_a}{f_{a_*}} = \frac{\left[\frac{8M_1}{M_{na}} - 6 - 4BM_1c + \frac{1}{(M_1/M_{wa} - BM_1c)}\right] e^{BM_1(c-c_*)}}{\left[\frac{8M_1}{M_{na_*}} - 6 - 4BM_1c_* + \frac{1}{(M_1/M_{wa_*} - BM_1c_*)}\right]} \quad (26)$$

Now we can use an array of data from c_* to the highest concentration and evaluate BM_1 by a Monte Carlo method, since it is the only unknown. We are on firmer grounds trying to evaluate one unknown by a Monte Carlo method than to try and evaluate three unknowns at once. Once BM_1 is known, then $f_1 = c_1/c$ can be evaluated at each concentration since

$$f_1 = \frac{1}{2}\left[\frac{6M_1}{M_{na}} - 5 - 3BM_1c + \frac{1}{(M_1/M_{wa} - BM_1c)}\right] \quad (27)$$

for a monomer–dimer–trimer association, or

$$f_1 = \frac{1}{3}\left[\frac{8M_1}{M_{na}} - 6 - 4BM_1c + \frac{1}{(M_1/M_{wa} - BM_1c)}\right] \quad (28)$$

for a monomer–dimer–tetramer association. Since $c_1 = f_1 c$, one notes that the following linear equations can be obtained for the two self-associations:

$$Y = \frac{c - c_1}{c_1^2} = K_2 + K_3C_1 \quad (29)$$

and

$$Y = \frac{c - c_1}{c_1^2} = K_2 + K_4C_1^2 \,. \quad (30)$$

In eq. (29) a plot of Y vs. C_1 has a slope of K_3 and an intercept of K_2; in eq. (30) a plot of Y vs. C_1^2 has a slope of K_4 and an intercept of K_2. The results of a linear regression analysis of our data at 10 and 30°C are summarized in table 1. Since the correlation coefficient was so much better for the monomer–dimer–trimer association, this then is the better model to describe the observed self-association. Table 2 lists the observed values of M_1/M_{wa} and M_1/M_{na} used in these tests. The last two columns in table 2 give the

Table 1
Data used to distinguish between a monomer–dimer–trimer and a monomer–dimer–tetramer association

Monomer–dimer–trimer association			Monomer–dimer–tetramer association		
Temperature	10°C	30°C	Temperature	10°C	30°C
BM_1 a)	2.31×10^{-3}	3.17×10^{-3}	BM_1 c)	6.79×10^{-3}	7.66×10^{-3}
Sum of absolute value of error	0.293	0.298	Sum of absolute value of error	1.47	1.07
K_2(ℓ/g) b)	0.966	0.157	K_2(ℓ/g) d)	8.26	2.40
K_3(ℓ/g)^2	4.141	1.502	K_4(ℓ/g)^3	0.211	0.605
Correlation coefficient	0.902	0.891	Correlation coefficient	0.051	0.638

a) A Monte Carlo method based on eq. (25) was used here. The error reported is the sum of $|(f_a/f_{a_*})_{obs} - (f_a/f_{a_*})_{calc}|$ over the array of data used.

b) K_2 and K_3 were evaluated from eq. (29). The correlation coefficients were obtained from a linear regression analysis.

c) A Monte Carlo method based on eq. (26) was used here. The error reported here is summed over the same number of data points used in the previous model.

d) K_2 and K_4 were evaluated from eq. (30). The correlation coefficients were obtained from a linear regression analysis.

Table 2
Observed values of M_1/M_{wa} and M_1/M_{na} and the percent error between the calculated and observed values of M_1/M_{wa} at 10° and 30°C for a 1, 2, 3 and a 1, 2, 4 self-association

A. 10°C					B. 30°C				
			$100\,\Delta(M_1/M_{wa})_{calc}/(M_1/M_{wa})_{obs}$					$100\,\Delta(M_1/M_{wa})_{calc}/(M_1/M_{wa})_{obs}$	
J	$\frac{M_1}{M_{wa(obs)}}$	$\frac{M_1}{M_{na(obs)}}$	1–2–3	1–2–4	J	$\frac{M_1}{M_{wa(obs)}}$	$\frac{M_1}{M_{na(obs)}}$	1–2–3	1–2–4
2	0.6189	0.7644	−1.04	− 1.01	2	0.7493	0.8562	−0.40	+ 5.77
4	0.5252	0.6652	−0.75	−12.95	4	0.5972	0.7664	+1.67	− 7.18
6	0.4851	0.6109	−0.61	−19.57	6	0.5275	0.6960	+2.98	−14.30
8	0.4652	0.5768	+0.04	−23.20	8	0.5007	0.6503	+1.34	−15.30
10	0.4503	0.5529	+0.03	−26.39	10	0.4839	0.6186	+0.14	−15.34
12	0.4387	0.5348	−0.27	−29.23	12	0.4719	0.5951	−0.61	−15.12
14	0.4303	0.5205	−0.48	−31.48	14	0.4622	0.5768	−0.96	−14.96
16	0.4236	0.5088	−0.70	−33.44	16	0.4539	0.5619	−1.02	−14.93
18	0.4186	0.4990	−0.84	−35.06	18	0.4475	0.5495	−1.06	−14.79
20	0.4145	0.4908	−0.97	−36.48	20	0.4416	0.5390	−0.90	−14.84
22	0.4112	0.4837	−1.09	−37.75	22	0.4364	0.5299	−0.66	−14.97
24	0.4087	0.4775	−1.16	−38.85	24	0.4322	0.5219	−0.44	−15.06
26	0.4068	0.4721	−1.16	−39.77	26	0.4284	0.5149	−0.18	−15.21
28	0.4051	0.4674	−1.21	−40.67	28	0.4251	0.5086	+0.11	−15.40
30	0.4039	0.4632	−1.21	−41.47	30	0.4232	0.5029	+0.14	−15.32
32	0.4028	0.4594	−1.23	−42.23	32	0.4216	0.4979	+0.21	−15.31
34	0.4021	0.4561	−1.22	−42.90	34	0.4207	0.4934	+0.17	−15.20
36	0.4018	0.4531	−1.14	−43.45	36	0.4198	0.4893	+0.19	−15.18
38	0.4015	0.4504	−1.09	−43.99	38	0.4196	0.4856	+0.09	−15.05
40	0.4015	0.4479	−1.00	−44.46	40	0.4193	0.4823	+0.08	−15.04
42	0.4015	0.4457	−0.94	−44.94	42	0.4196	0.4793	−0.07	−14.89
44	0.4020	0.4437	−0.80	−45.28	44	0.4200	0.4766	−0.19	−14.80
46	0.4021	0.4419	−0.75	−45.73	46	0.4207	0.4742	−0.36	−14.67
48	0.4023	0.4403	−0.70	−46.17	48	0.4214	0.4720	−0.50	−14.58
50	0.4026	0.4387	−0.65	−46.59	50	0.4223	0.4700	−0.67	−14.49
52	0.4033	0.4374	−0.52	−46.87	52	0.4232	0.4682	−0.81	−14.43
54	0.4040	0.4361	−0.41	−47.17	54	0.4243	0.4665	−0.98	−14.36
56	0.4045	0.4350	−0.33	−47.51	56	0.4254	0.4650	−1.14	−14.32
58	0.4053	0.4339	−0.23	−47.79	58	0.4265	0.4637	−1.28	−14.31
60	0.4059	0.4330	−0.17	−48.13	60	0.4280	0.4625	−1.49	−14.23

percent error in M_1/M_{wa} for the monomer–dimer–tetramer (1, 2, 4) self-associations. It is clear from these data and the data in table 1, that the monomer–dimer–trimer association is the better choice. To finish the analysis we assumed a linear relation between BM_1 and temperature and obtained a first approximation for BM_1 at the other temperatures; these were used in the Monte Carlo program to obtain the final values of BM_1. These values of BM_1 were held constant, and values of K_2 and K_3 were floated by a Monte Carlo method so that a better fit (as measured by the sum of the absolute value of the error) to the M_{wa} vs. J was obtained. The final values we obtained are listed in table 3. The solid lines in fig. 1 show how well the values of K_2, K_3 and BM_1 fit the experimental data at 10 and 30°C. A monomer–dimer–trimer association can be considered to be a simultaneous monomer–dimer and monomer–trimer association. Figs. 4 and 5 show the plots of $\ln K_2$ vs. $1/T$ and $\ln K_3$ vs. $1/T$, respectively; the slope in each plot gives $-\Delta H^\circ/R$ for each reaction. For the dimerization reaction the standard enthalpy change was $\Delta H^\circ =$

Table 3
Association equilibrium constants and second virial coefficients for the self-association of ATP in isotonic saline

Temp. (°C)	K_2 (ℓ/g)	K_3 (ℓ/g)^2	BM_1 (ℓ/g)
10	0.966	4.14	2.31×10^{-3}
16	0.607	3.00	2.45
20	0.411	2.11	2.58
25	0.285	1.45	2.64
30	0.165	1.25	3.17

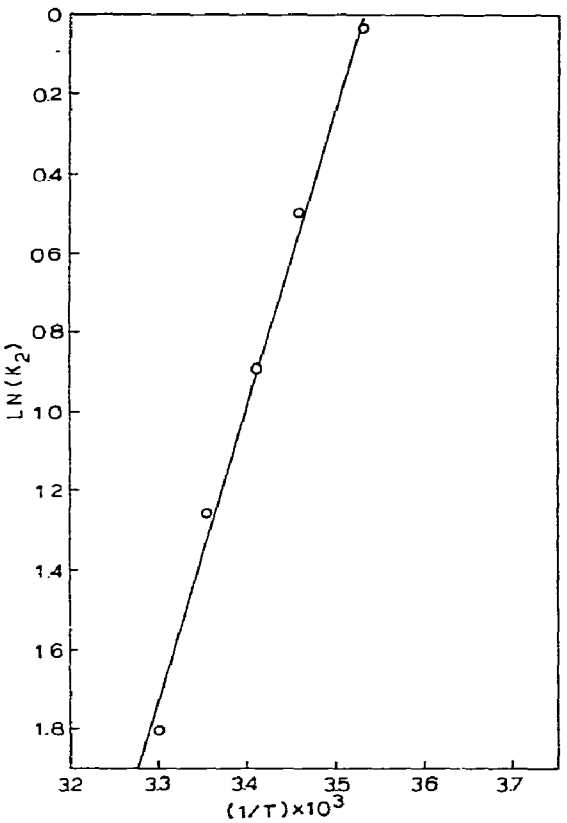

Fig. 4. Plot of $\ln K_2$ vs. $1/T$. This is the Van't Hoff plot for the dimerization reaction. Since the molar association constant $k_2 = (M_1/2)K_2$, the slope of the plot of $\ln K_2$ vs. $1/T$ is the same as $d \ln k_2/d\,(1/T) = -\Delta H^\circ/R$. The least squares slope for this plot was $7.49_8 \times 10^3$, and the correlation coefficient was 0.997.

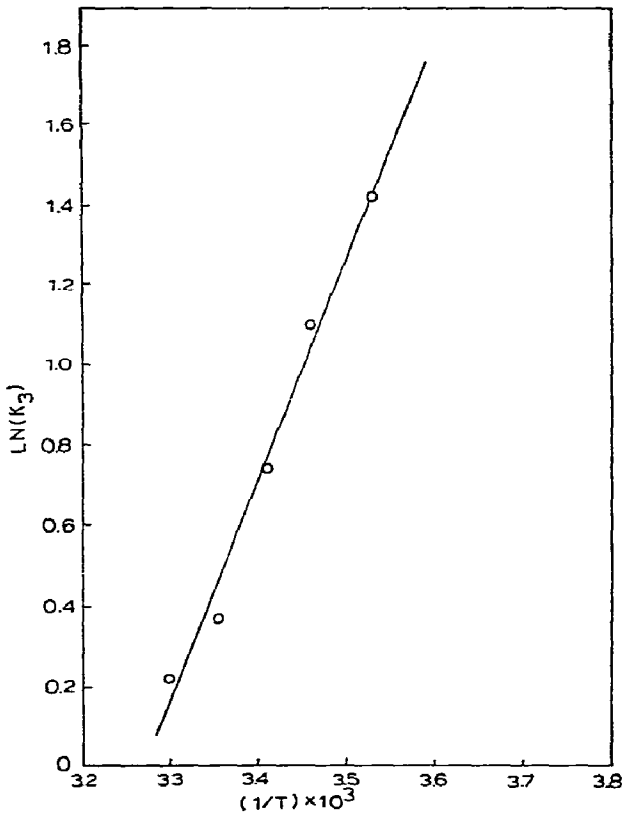

Fig. 5. Plot of $\ln K_3$ vs. $1/T$. This is the Van't Hoff plot for the trimerization reaction. Since the molar association constant $k_3 = (M_1/3)K_3$, the slope of this plot is $d \ln k_3/d\,(1/T) = d \ln K_3/d\,(1/T) = -\Delta H^\circ/R$. The least squares slope for this plot was $5.45_6 \times 10^3$, and the correlation coefficient was 0.991.

-14.9 kcal/mole, and for the trimerization reaction $\Delta H^\circ = -10.8$ kcal/mole. Table 4 lists the molar association constants, k_i ($i = 2$ or 3), the standard Gibbs free energy change, ΔG°, and the standard entropy change, ΔS°, for both reactions.

7. Discussion

It should be emphasized that these experiments would not have been feasible without the availability of hollow fiber dialyzers with a low molecular weight (200 g) cutoff. The availability of this device should

Table 4
Molecular association equilibrium constants and thermodynamic functions for the self-association of ATP in isotonic saline

Monomer–dimer association				Monomer–trimer association			
T (°K)	k_2 (ℓ/mole)	ΔG° (kcal/mole)	ΔS° (cal/deg mole)	T (°K)	k_3 (ℓ/mole)^2	ΔG° (kcal/mole)	ΔS° (cal/deg mole)
283.15	2.38×10^2	−3.08	−41.7	283.15	3.35×10^5	−7.16	−13.0
289.15	1.49	−2.88	−41.6	289.15	2.43	−7.12	−12.9
293.15	1.01	−2.69	−41.7	293.15	1.71	−7.02	−13.0
298.15	0.702	−2.52	−41.5	298.15	1.17	−6.92	−13.1
303.15	0.406	−2.23	−41.7	303.15	1.01	−6.94	−12.9

$k_2 = (M_1/2)K_2$, $M_1 = 492.7$,
$\Delta H^\circ = -14.9$ kcal/mole (obtained from fig. 4),
$R = 1.9872$ cal/mole deg.

$k_3 = (M_1^2/3)K_3$,
$\Delta H^\circ = -10.8$ kcal/mole (obtained from fig. 5).

encourage further studies on small, ionizable, biologically important molecules, such as coenzymes.

Our work has clearly demonstrated the presence of a temperature-dependent self-association reaction for solutions of ATP in isotonic saline. It is interesting to note that the diffusion experiments on ATP by Bowen and Martin [11] give very little indication of a self-association (see their table 5). The self-association reaction observed by us with ATP is much stronger than the self-association observed by others with purine and various nucleosides [4–7]. Note that our experiments covered a range of 0 to 0.03 M (as monomer) of ATP. In other sedimentation equilibrium experiments [4, 5, 7] on purine and various nucleosides much higher concentration ranges have been used – up to 0.7 M (as monomer) for cytidine [7] and up to 1 M (as monomer) for purine [4, 7]. It is interesting to compare our results with the work of others. At 25°C Van Holde, Rossetii and Dyson [7] obtained values of $k_2 = 0.64$ to 0.82 ℓ/mole and $k_{23} = 0.53$ to 1.50 ℓ/mole for cytidine, depending on the association model chosen; our results for ATP were $k_2 = 70.2$ and $k_{23} = 1.67 \times 10^3$. The quantity $k_{23} = k_3/k_2$. The work of Solie and Schellman [5] indicated that the order of self-association at 25°C was deoxyadenosine > deoxythymidine > inosine > purine riboside. The highest concentrations they observed was 0.0524 molal for deoxyadenosine and 0.1316 molal for purine riboside. Their dimerization equilibrium constant ranged from $k_2 = 1.2$ molal^{-1} for purine riboside to $k_2 = 10$ molal^{-1} for deoxyadenosine. Ts'o [6] has summarized the association constants, which he and his associates obtained by vapor pressure osmometry on purine and various nucleosides. Their values at 25°C ranged from k_2 or k (the intrinsic equilibrium constant) of 0.61 for uridine to 22.2 for N-6-dimethyl adenosine. Clearly we are observing a much stronger self-association with ATP; this enhancement of the self-association may be due to the triphosphate group.

From the thermodynamic functions listed in table 4 one notes that ΔH° is negative (exothermic) for the dimerization and the trimerization reactions. It appears that ΔH° is the major contributor to the ΔG° values. The negative values of ΔS° may reflect in part the increase in order due to the association reactions. One wonders why an ionizable solute like ATP undergoes self-association; one would think that the ATP^{-2} ions would repel each other? The tendency to associate must be much stronger than the electrostatic repulsion. A similar behavior has been noted with proteins at acidic pH which is below the isoionic or isoelectric point. Insulin [22] self-associates at pH ca. 2; the β-lactoglobulins A, B and C undergo self-association at low pH (between 2 and 3) also [18–20, 23, 24].

It has been suggested by a referee that pH changes due to the temperature variations involved in these studies might influence the self-association of ATP. To test this hypothesis we measured the pH of three different dialyzed solutions of ATP at 10, 20, and 30°C using a Radiometer Model TTT2 pH meter. The results of these measurements are listed in table 5. The highest concentration used here is about 3 times greater than the highest intial concentration used in

Table 5
Results of pH measurements of three different dialyzed solutions of ATP at three different temperatures

ATP concentration	pH		
(mole of monomer)	10°C	20°C	30°C
0.0016 M	4.79	4.70	4.61
0.0120 M	3.70	3.68	3.65
0.0651 M	3.00	2.99	2.99

the sedimentation equilibrium experiments. Clearly, there is a much greater pH change over the concentration range used in these experiments than there is due to temperature alone. In fig. 1 it is evident that the self-association, as reflected in the values of M_{wa}, was much greater at 10°C than at 30°C. This is most likely due to a temperature effect on K_2 and K_3. The studies reported here are preliminary results; we have demonstrated that one can successfully study the self-association of small ionizable molecules of biological importance. More studies on compounds of this type should appear in the future. In future work with ATP we plan to study the effects of ionic strength, of divalent ions like Mg^{2+} and of pH on the self-association of ATP. The important thing was to demonstrate the feasibility of the kind of study reported here; the technical achievement which made this possible was the availability of a hollow fiber dialyzer with a low molecular weight (200) cutoff. It is quite evident from the plots of M_{wa} vs. c in fig. 1 that one cannot analyze self-associations from one or two experiments in the low concentration range. In fig. 1 it would be possible to take data from experiments covering the range 0 to 8 fringes in concentration and draw all sorts of M_{wa} vs. c curves with this data.

One possible biological role for the self-association of ATP is suggested by the work of Nichol, Smith and Ogston [25]. They have pointed out that allosteric effects can be produced by a small self-associating ligand (like ATP) that binds to a larger acceptor molecule such as an enzyme. They have also shown that this allosteric behavior could also be encountered when both the ligand and acceptor molecules self-associate. Since ATP is involved in many enzyme reactions, their arguments could be applied to this situation.

Acknowledgments

This work was supported in part by grants (to ETA) from the National Science Foundation, GB 32242, and the Robert A. Welch Foundation, A485. Will E. Ferguson is a Robert A. Welch Foundation Postdoctoral Fellow. We thank Drs. Dale Swindle and Emile Schweikert of the Center for Trace Characterization, Texas A&M University for their help in the atomic absorption spectrophotometry measurements. The laser and the film magazine used with the ultracentrifuge were obtained through funds provided by the Research Council of Texas A&M University.

References

[1] P.O.P. Ts'o, I.S. Melvin and A.C. Olson, J. Am. Chem. Soc. 85 (1963) 1289.
[2] R. Hamlin, R.C. Lord and A. Rich, Science 148 (1965) 1734.
[3] A.D. Broom, M.P. Schweiger and P.O.P. Ts'o, J. Am. Chem. Soc. 89 (1967) 3612.
[4] K.E. Van Holde and G.P. Rossetti, Biochemistry 6 (1967) 2189.
[5] T.N. Solie and J.A. Schellman, J. Mol. Biol. 33 (1968) 61.
[6] P.O.P. Ts'o, Ann. N.Y. Acad. Sci. 153 (1969) 785.
[7] K.E. Van Holde, G.P. Rossetti and R.D. Dyson, Ann. N.Y. Acad. Sci. 164 (1969) 279.
[8] A. Vrij, Ph.D. Dissertation, University of Utrecht, 1959.
[9] A. Vrij and J.Th.G. Overbeek, J. Colloid Sci. 17 (1962) 570.
[10] E.F. Casassa and H. Eisenberg, Advan. Protein Chem. 19 (1964) 287.
[11] W.J. Bowen and H.L. Martin, Arch. Biochem. Biophys. 107 (1964) 30.
[12] E.T. Adams, Jr. and D.L. Filmer, Biochemistry 5 (1966) 2971.
[13] E.T. Adams, Jr. and M.S. Lewis, Biochemistry 7 (1968) 1044.
[14] E.T. Adams, Jr. and H. Fujita, in: Ultracentrifugation in theory and experiment, ed. J.W. Williams (Academic Press, New York, 1963) p. 119.
[15] E.T. Adams, Jr., Fractions No. 3 (1967).
[16] E.T. Adams, Jr., Biochemistry 4 (1965) 1646.
[17] P.W. Chun, S.J. Kim, J.D. Williams, W.T. Cope, L.-H. Tang and E.T. Adams, Jr., Biopolymers 11 (1972) 197.
[18] J. Visser, R.C. Deonier, E.T. Adams, Jr. and J.W. Williams, Biochemistry 11 (1972) 2634.
[19] L.-H. Tang and E.T. Adams, Jr., Arch. Biochem. Biophys. 157 (1973) 520.

[20] L.-H. Tang, Ph.D. Dissertation, Illinois Inst. of Tech., Chicago, 1971.
[21] E.T. Adams, Jr. and J.W. Williams, J. Am. Chem. Soc. 86 (1964) 3454.
[22] P.D. Jeffrey and J.H. Coates, Biochemistry 5 (1966) 3820.
[23] S.N. Timasheff and R. Townend, J. Am. Chem. Soc. 83 (1961) 470.
[24] J.L. Sarquis and E.T. Adams, Jr., unpublished data.
[25] L.W. Nichol, G.D. Smith and A.G. Ogston, Biochem. Biophys. Acta 184 (1969) 1.

BIOPHYSICAL CHEMISTRY 1 (1974) 338–348. © NORTH-HOLLAND PUBLISHING COMPANY

STUDIES ON THE STRUCTURE OF CHEMICALLY METHYLATED DNA

E. BAUER, H. BERG, G. LÖBER, K. WELLER

Akademie der Wissenschaften der DDR, Forschungszentrum für Molekularbiologie und Medizin, Zentralinstitut für Mikrobiologie und experimentelle Therapie Jena, Abteilung Biophysikochemie, 69 Jena, DDR

and

M. HARTMANN and Ch. ZIMMER

Akademie der Wissenschaften der DDR, Forschungszentrum für Molekularbiologie und Medizin, Zentralinstitut für Mikrobiologie und experimentelle Therapie Jena, Abteilung Biochemie, 69 Jena, DDR

Received 2 January 1974

CD and melting temperature measurements on the nature of DNA with chemically methylated guanine-rich sites indicate that the stable secondary structure of DNA depicted by Ramstein et al. involves considerable distortions resulting from decreased base–base stacking interaction. Besides that quantum chemical data gained from PPP calculations are in favor of a weaker hydrogen bonding interaction in the methylated guanine–cytosine base pair. CD measurements demonstrate that methylated DNA-regions differ from the nonmethylated helical structure, since formation of a condensed conformation as occurs in the transition from B to the C-like structure is prevented by positively charged methylated guanine residues. An increase in helix winding angle, however, can not be excluded.

Binding ability of the dyes acridine orange, phenosafranine, and the antibiotic actinomycin C is lowered for methylated DNA, while binding of proflavine is, in accordance with the results of Ramstein and Leng, slightly enhanced. The reason for the opposite behavior of proflavine is at present not fully understood. In particular changes in the binding ability with dyes could not be correlated with base specificity of complex formation. It is discussed that structural changes in DNA towards a loose conformation decrease the binding tendency for acridine orange, phenosafranine, and actinomycin C.

1. Introduction

Physicochemical properties of methylated DNA have been reported in recent papers [1–3]. Chemical methylation decreases the thermal stability and increases the flexibiltiy of the DNA molecule. Changes in the interaction of methylated DNA with ligands such as spermine and poly-L-lysine were also observed [1]. It was of further interest to investigate dye binding to methylated DNA with respect to possible alterations in GC selective binding effects. The nature of structural changes of the double helix caused by methylation are important in understanding biological effects, especially those producing inhibition of enzymatic processes [4].

2. Materials and methods

2.1. Methylated DNA

DNA samples employed in these studies are those described earlier [5, 6]. Methylation has been performed according to Pochon and Michelson [2] with some modifications: dimethylsulphate saturated with *n*-tributylamine was added to DNA (0.88 mg/ml) in 1 N or 2 N NaCl. *n*-tributylamine was removed by ether extraction and exhaustive dialysis. The degree of methylated guanine residues has been analysed by hydrolysis [7] with 1 N HCl during 20 min at 100°C. Elution was performed with 1 N HCl using columns of Dowex 50 W X 8 or IR 120. The compositions of

Table 1
Degree of methylation of DNA's employed in these studies

DNA	GC content (mole %)	7-methylguanine (MeG) (mole %)
calf thymus	42	28.0 67.0
streptomyces chrysomallus	72	17.9 25.6 45.8

methylated DNAs are given in table 1; the accuracy of determinations was within ± 2%. No methylated adenine could be detected in the samples by this method.

2.2. Dyes

3,6-Diaminoacridinium·HSO_4 (proflavine) was prepared according to the method described by Albert [8]. 3,6-Dimethylaminoacridine (acridine orange) was purified by Achtert [9], from the commercial product acridine orange·HCl·$ZnCl_2$, Bayer Leverkusen. Origin of other dyes: phenosafranine, Bayer Leverkusen; actinomycin C, isolated in our institute [10].

2.3. Circular dichroism (CD)

CD measurements were carried out in a Roussel–Jouan dichrograph Model CD-185 using cells of 5 mm light path. Ellipticities were calculated on the bases of $E^{1\%}_{1\,cm} = 180$ for *streptomyces chrysomallus* DNA and $E^{1\%}_{1\,cm} = 200$ for calf thymus DNA [3, 4]. [ψ]-values are expressed in units of degrees ml dm^{-1} g^{-1}.

2.4. Fluorescence

Fluorescence spectra were measured with a fluorescence spectrophotometer using 1 cm cuvettes as described elsewhere [11]; the concentrations of methylated DNAs were 0.09% corresponding to 2.8×10^{-3} M phosphate. Conditions are SSC buffer, pH 7, dye concentration of stock solutions 2×10^{-6} M. In the case of proflavine and acridine orange binding, studies were performed at low dye concentrations and higher ionic strength, thus ensuring application of the mass action law as considered in ref. [12].

2.5. Polarography

Polarographic measurements were done with the aid of a tast-polarograph, Atlaswerke Bremen, under application of the tast method which is well suitable at low substance concentrations [13]. The temperature of the polarographic cell was kept constant within the limits of ± 0.01°C. Mercury pool at the bottom of the cell was used as a reference electrode. The dropping time of the mercury electrode was 5 sec. Stock solution of calf thymus DNAs was 2×10^{-4} M DNA-phosphate in phosphate buffer ionic strength 0.0228 M. Stock solutions of phenosafranine were 1.5 and 6×10^{-4} M in phosphate buffer of same ionic strength as used for DNA. Measurements were performed at 3, 15, 25, 35 and 45°C.

Binding curves for complex formation of actinomycin C with DNA were obtained by means of a pulse polarograph A 3100, Southern Instruments. The antibiotic was dissolved in 0.16 M phosphate buffer to ensure a stock concentration not greater than 5×10^{-6}M.

2.6. Evaluation of binding data

Binding of phenosafranine with DNA, as followed by aid of polarographic technique was considered as a cooperative process according to refs. [14, 15]. The model employed assumes DNA as a linear homogeneous chain, neglecting differences in base composition. Moreover, only one binding mechanism was taken into consideration. For total dye and DNA concentrations C^t_A and C^t_p, respectively, corresponding mass-conservation equations can be written as follows:

$$C^t_A = C_A + C_{Ab}, \tag{1}$$

$$C^t_p = C_p + \alpha C_{Ab}, \tag{2}$$

where C_A = free dye concentration, C_{Ab} = bound dye concentration, C_p = concentration of nonoccupied phosphates, α = number of phosphates per binding site.

Polarographic step height, or fluorescence intensity F, should be linearly related to $C_A + qC_{Ab}$, where q equals the ratio of F_b to F_0 for totally bound and free dye, respectively. If this linear relationship does not hold as it is true for low C^t_A values and using pulse polarographic technique, F has to be substituted by a calibra-

tion function:

$$F = F(C_A + q C_{Ab}). \quad (3)$$

Nevertheless, C_A can be calculated from

$$C_A = \{C(F) - q C_A^t\}/(1-q), \quad (4)$$

where $C(F)$ is the inverse calibration function. The model gives for the degree of coverage θ:

$$\theta = \frac{\alpha C_{Ab}}{C_p^t} = \frac{1}{2} + \frac{C_A s - 1}{4\{\frac{1}{4}(C_A s - 1)^2 + C_A s\sigma\}^{1/2}} \quad (5)$$

where s and σ denote the equilibrium constants of microscopic cooperative binding and the parameter of cooperativity, respectively. By means of a comparison of (4) and (5) in a suitable transformation one gets an iterative improvement of α, s, and σ if q is known from experiments. Assuming $\sigma = 1$, i.e., non-cooperativity, eq. (5) can be transformed by a simple calculation into the mass action law,

$$s = K = \frac{C_{Ab}}{C_A C_p/\alpha}, \quad (6)$$

which is used for the determination of binding data for the complex formation of proflavine, acridine orange, and actinomycin C with normal and methylated calf thymus DNA. In eq. (6), K is the equilibrium constant for noncooperative binding.

2.7. *Quantum chemical calculations*

Electron distributions and binding orders for G and MeG were mostly found by different quantum chemical procedures [16–18]. Therefore it seems difficult to confirm possible differences between both due to their different electronic behaviors. For this reason quantum chemical parameters of 9-methylguanine and 7,9-dimethylguanine (see formula) instead of guanosine and 7-methylguanosine (MeG), respectively, were gained from PPP calculations. Atom coordinates were taken from X-ray diffraction measurements done with guanosine and protonated 9-methylguanosine instead of 9-methylguanosine and 7,9-dimethylguanosine, respectively. Two-center integrals were evaluated with the aid of the approximation given by Ohno.

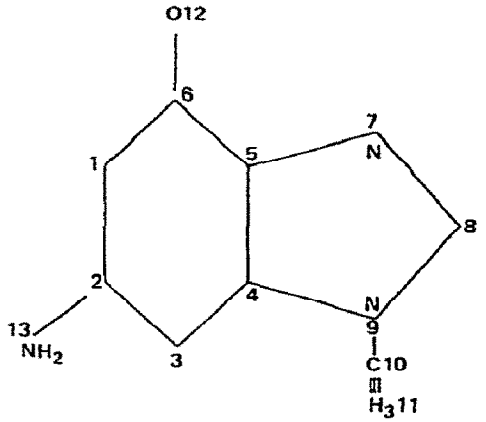

3. Results

3.1. *Thermal and acid denaturation*

The melting temperature of DNA decreases linearly with increasing amount of methylated guanine bases [1] which indicates alterations in the base–base interactions and in the repulsion forces between phosphate residues due to the formation of positively charged MeG sites. We obtained further insight into the nature of those changes involved in the disturbed methylated DNA structure by thermal melting in the presence of 7.2 M $NaClO_4$. As shown in table 2 at 25.6 mole % MeG, T_m decreases by 12.8°C in 7.2 M $NaClO_4$ compared to ΔT_m of 4.3°C in 0.02 M $NaClO_4$; at 45.8 mole % MeG DNA is strongly denatured in the presence of 7.2 M $NaClO_4$ at 25°C indicated by the residual hyperchromicity of 8%. Concentrated $NaClO_4$ solution [19] is effective as an hydrophobic interaction breaking agent and affects dispersion forces of the type of van der Waals attractions. Lowering of those interaction forces is markedly enhanced by formation of MeG within the DNA double helix. The acidic denaturation of methylated DNA (fig. 1) also exhibits a pronounced destabilization (decrease of pH_m) with increasing degree of methylation. As shown by the insert in fig. 1 the characteristic pH_m value is lowered linearly with increasing MeG in a way similar to that observed in the thermal melting behavior [1]. As indicated by the absorbance changes at 260 nm around pH 3.4 (fig. 1) the extent of stable protonated GH^+C regions [20] is diminished with increasing MeG.

Table 2
Thermal melting of methylated DNA of *streptomyces chrysomallus*

Mole%	7-Methylguanine (MeG) T_m (°C)		Hyperchromicity (%)	
	0.02 M $NaClO_4$	7.2 M $NaClO_4$	0.02 M $NaClO_4$	7.2 M $NaClO_4$
0	83.7	53.5	31.8	23.0
17.9	81.1	43.1	30.5	23.2
25.6	79.4	40.7	29.5	23.0
45.8	73.7	denatured	27.6	8.0

3.2. Conformational transitions caused by methylation of DNA

CD results of methylated DNA have been previously reported [1]. However, no conclusions on DNA conformation were drawn. CD data of methylated DNA obtained in the presence of 7.2 M $NaClO_4$ and ethylene glycol solutions make it possible to give a preliminary interpretation of structural alterations. CD spectra of GC-rich DNA with increasing MeG in 0.02 M NaCl and in 7.2 M $NaClO_4$ are presented in fig. 2. The positive CD maximum at 268 nm and the negative band at 243 nm are diminished with increasing degree of methylation. Depression of the positive band of native DNA indicates alteration of the normal B conformation. On the other hand the lowering of the negative band is similar to that observed for denatured DNA. However, the shape of intact methylated DNA is quite different from that of the denatured form (curves 1 to 5). Thus CD spectra may be tentatively explained by loosening of the B conformation involving base twisting and diminished base–base interactions (table 2). Results in 7.2 M $NaClO_4$ are compatible with this interpretation. In the presence of 7.2 M $NaClO_4$ the positive CD amplitude of DNA is reduced and the maximum appears at 267 nm [21], which has been attributed to C-like structural changes. However, these salt induced changes are less pronounced in $NaClO_4$ in comparison to NaCl or Na acetate [21]. An alternative explanation by a direct interaction of ClO_4 ions with methylated guanine residues is also possible on the basis of anionic effects as reported by Robinson and Grant [22]. As indicated in fig. 2 the positive and negative CD maxima are depressed while at 45.8 mole% MeG a denatured form is obtained in agreement with the melting behavior (table 2).

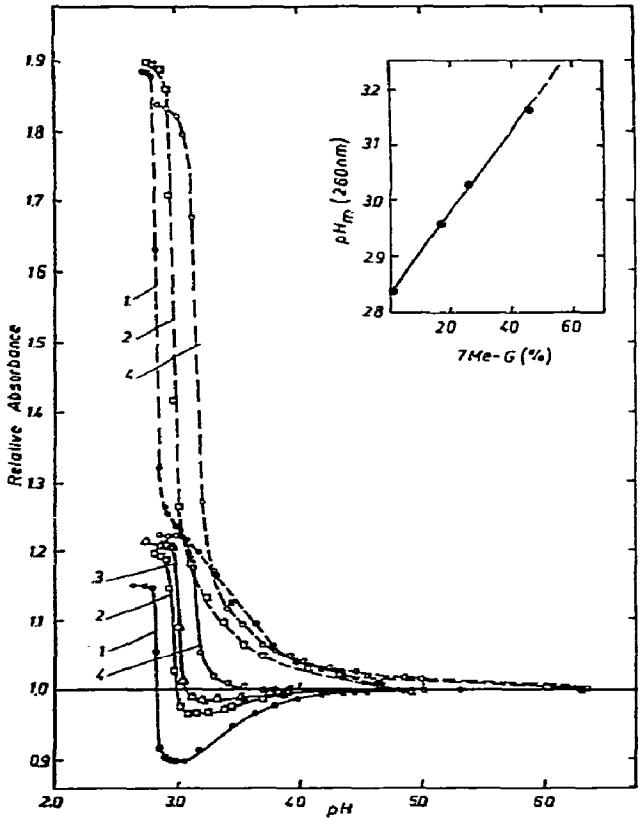

Fig. 1. Spectrophotometric acidic titration of methylated *streptomyces chrysomallus* DNA in 0.2 M NaCl; numbers indicating increasing amount of methylated guanine residues: 1, 0 mole%; 2, 17.9 mole%; 3, 25.6 mole%; 4, 45.8 mole%; full lines at 260 nm, broken lines at 280 nm, insert: dependence of pH_m on degree of methylation, MeG-content.

Comparison with the copper(II) complex of non-methylated DNA (curve 6) suggests interesting similarities in the CD spectrum to the methylated DNA (curve 3). Copper(II) preferentially affects the GC pairs in DNA due to the affinity to N-7 of guanine,

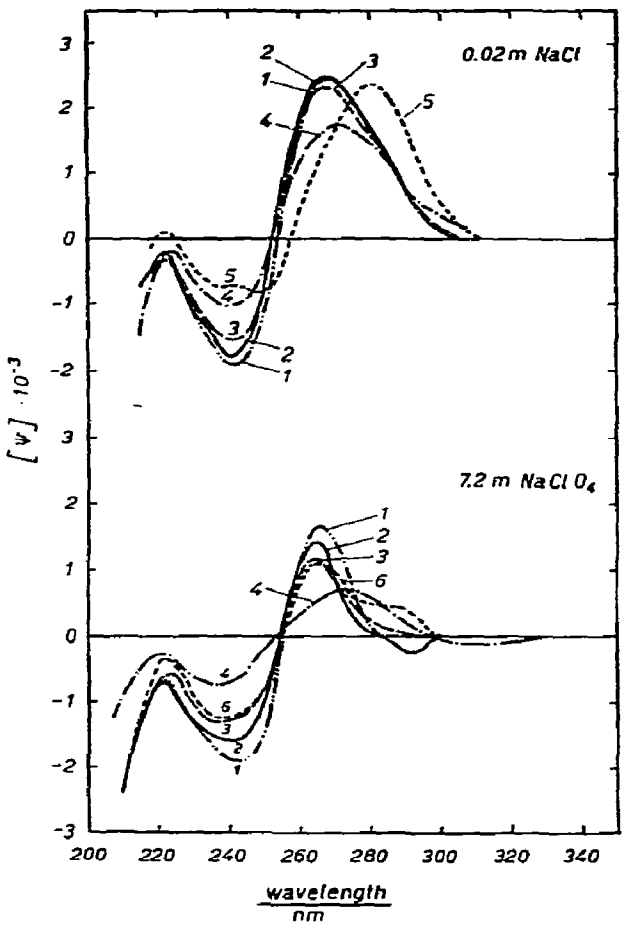

Fig. 2. CD spectra of methylated *streptomyces chrysomallus* DNA in the presence of low and extremely high salt concentrations: 1, native nonmethylated DNA; 2, 18 mole% methylguanine (MeG); 3, 25.6 mole% MeG; 4, 45.8 mole% MeG; 5, nonmethylated heat denatured 5 min at 100°C; 6, copper(II) complex at 0.3 Cu^{2+}/DNA-phosphate.

the same site at which methylation occurs. This selective complex formation of the transition metal ions Cu^{2+}, Zn^{2+} or Mn^{2+} with native DNA in 7.2 M $NaClO_4$ [23] results in loosening and initial unwinding of the DNA helix due to binding to N-7 of guanine bases.

The CD results obtained in the presence of ethylene glycol (fig. 3) demonstrate considerably less changes for methylated DNA compared to nonmethylated DNA (fig. 3b). The decrease of the positive CD maximum of nonmethylated DNA with increasing ethylene glycol concentration is compatible with a similar monotonic transition from B to C-like structures induced by salts [21, 24–26]. This is accompanied by an increased winding angle and by a shortening of stacked base distances [26, 27]. As demonstrated in fig. 3b no CD changes are observed for methylated DNA between 10% and 50% ethylene glycol, first at 70% solvent variation of the positive and negative bands occurs while 80% glycol produces initial denaturation effects. This is indicated by the characteristic displacement of the positive CD maximum towards longer wavelengths which is associated with a pronounced decrease of the negative CD band. The plot of $[\psi]$ versus increasing ethylene glycol concentration (fig. 4) clearly shows the different behavior between methylated and nonmethylated DNA. The nonmethylated DNA is more sensitive to ethylene glycol induced conformational changes while methylated DNA is restricted to undergo changes from B to C-like structures. This means that the shortening of the base distance is prevented by repulsion forces involved in positively charged methylated GC-sites. Since high concentration of the organic solvent causes dehydration and destabilization of the DNA helix [28] 80 and 90% ethylene glycol initiates denaturation of the loosely structured methylated GC-rich DNA. This means that positively charged sites such as protonated GC-regions in DNA prevent the formation of compact structures. In fact the disruption of a compact state of DNA in polyethylene glycol upon protonation has been observed recently [29].

3.3. Quantum chemical data

Remarkable enhancements of electron densities result after methylation of the N-7 atom preferentially at the 4, 8, and 13 positions of the guanine residue. In contrast to this, electron densities are decreased in the 5 and 9 positions. Methylation yielded an increase of binding orders between atoms 2–3, 4–9, 5–7, 6–1, and 8–9, while they are decreased between the atoms 2–13, 3–4, 5–6, and 7–8.

Of particular interest are positions 1, 12, and 13, since they are responsible for the formation of three hydrogen bonds in the GC-base pair. Positions 1 and 13 act as proton donors, position 12 as an proton acceptor. Thus electron density changes caused by methylation may be interpreted with respect to hydrogen bond formation in the following manner. Position 12 (proton acceptor site): decrease of electron density

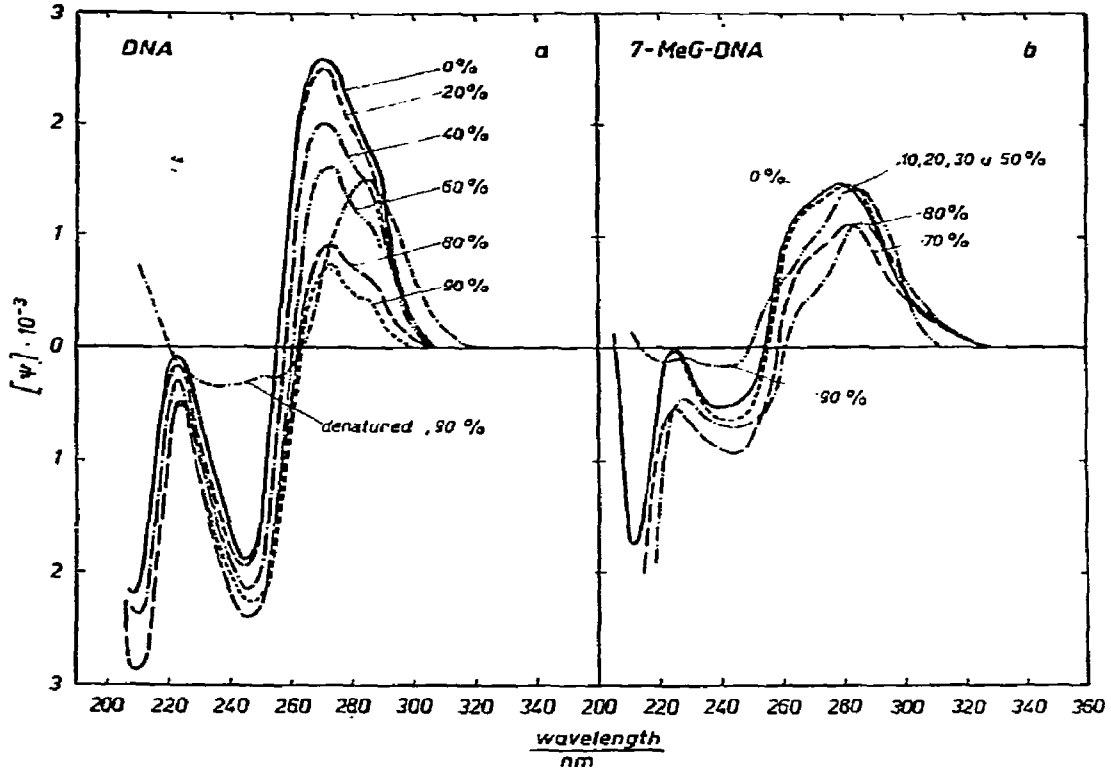

Fig. 3. Variation of CD spectra of methylated and nonmethylated *streptomyces chrysomallus* DNA with increasing ethylene glycol concentration (V%) at 0.02 M $NaClO_4$ + 10^{-3} M EDTA, 26°C: (a) nonmethylated DNA; (b) methylated DNA with 53 mole% MeG.

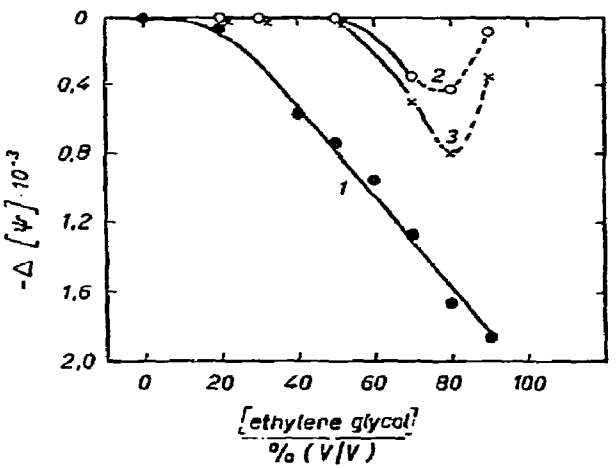

Fig. 4. Dependence of the CD amplitudes on the ethylene glycol concentration. Nonmethylated DNA: 1, at 272 nm, methylated DNA (53 mole% MeG): 2, at 282 nm; 3, at 272 nm; ionic conditions correspond to that of fig. 3.

by about + 0.00315 means slight weakening of hydrogen bonding; position 1 (proton donor site): decrease of electron density by about + 0.00986 means slight strengthening of hydrogen bonding; position 13 (proton donor site): increase of electron density by about −0.01367 means strong weakening of hydrogen bonding. Thus the overall effect of changes in charge distribution may cause a weakening of hydrogen bonded GC-base pairs after methylation. Likewise bulky methyl groups might support the destabilization effect for steric reasons.

3.4. Binding of dyes with normal and methylated calf thymus DNA

3.4.1. Proflavine and acridine orange

Binding of a fluorescent molecule with DNA is accompanied by changes in fluorescence intensity [30, 31] which are used for estimation of binding data

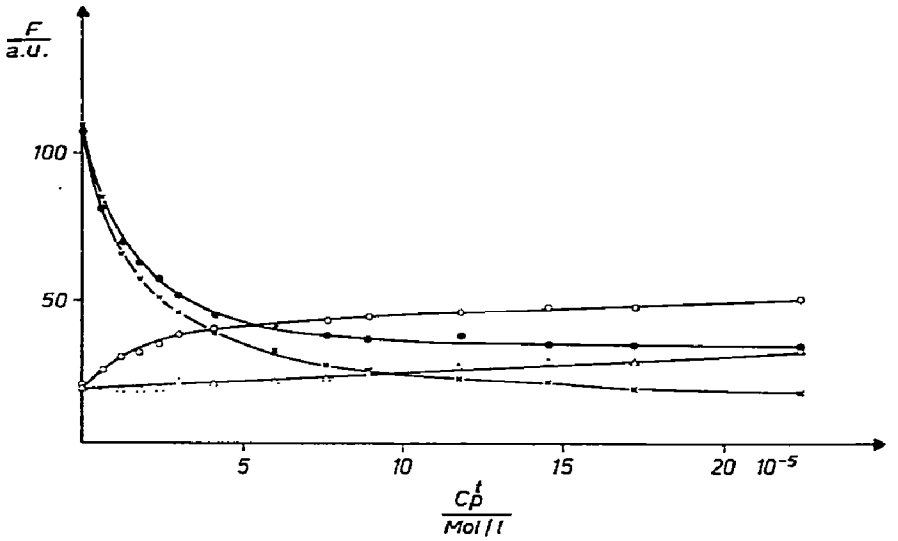

Fig. 5. Variation of fluorescence intensity (F) after addition of DNA to solution of dyes in SSC buffer; DNA concentration is given in moles phosphate per ℓ (c_p^t); dye concentration 2×10^{-6} M; ××× proflavine + calf thymus DNA (nonmethylated); ooo acridine orange + calf thymus DNA (nonmethylated); ●●● proflavine + calf thymus DNA (67 mole% MeG); ΔΔΔ acridine orange + calf thymus DNA (67 mole% MeG).

[32–37]. The experimental conditions chosen (low dye concentration, high ionic strength) ensure that binding occurs mainly in terms of type I-complexes. This binding process quenches fluorescence of amino acridines (i.e., proflavine) [30, 38, 40, 41], while fluorescence of dialkylamino acridines (i.e., acridine orange) is enhanced [30, 31, 35–40]. Fig. 5 demonstrates the influence of added nonmethylated and methylated DNA on fluorescence intensities of proflavine and acridine orange. Assuming the noncooperative model as valid, q, α, and K can be gained for proflavine binding from a Klotz plot and a Scatchard plot (table 3). Binding curves of acridine orange yielded for nonmethylated calf thymus DNA: $q = 2.47$ and $K/\alpha = 4 \times 10^4$ ℓ/mole, α could not be determined separately. The linear in-

Table 3
Binding parameter of the complex formation of proflavine with nonmethylated and methylated (67 mole% MeG) calf thymus DNA as obtained from fluorescence measurements

Nonmethylated DNA	Methylated DNA
q = 0.164	q = 0.324
K/α 1.0×10^5 ℓ/mole	K/α 2.2×10^5 ℓ/mole
α = 10	α = 10
K = 1.0×10^6 ℓ/mole	K = 2.2×10^6 ℓ/mole

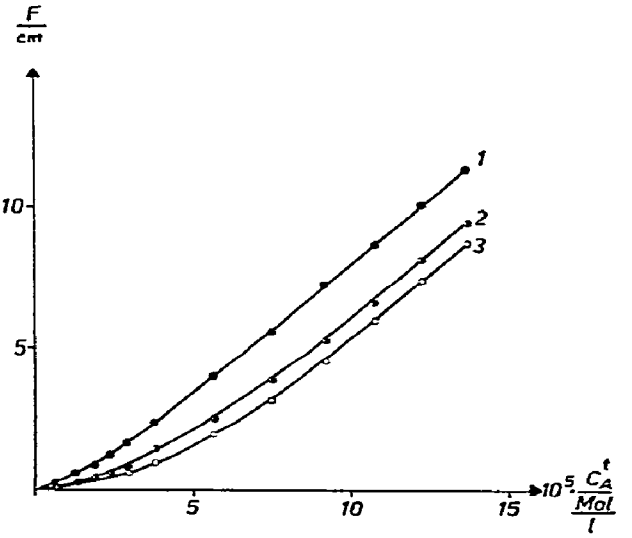

Fig. 6. Variation of polarographic wave height (F) of phenosafranine with increasing dye concentration; 25°C; phosphate buffer, pH 7, ionic strength 0.0228 mole/ℓ; DNA concentration: 2×10^{-4} mole phosphate/ℓ; 1, without DNA; 2, in presence of methylated calf thymus DNA (67 mole% MeG); 3, in presence of nonmethylated calf thymus DNA.

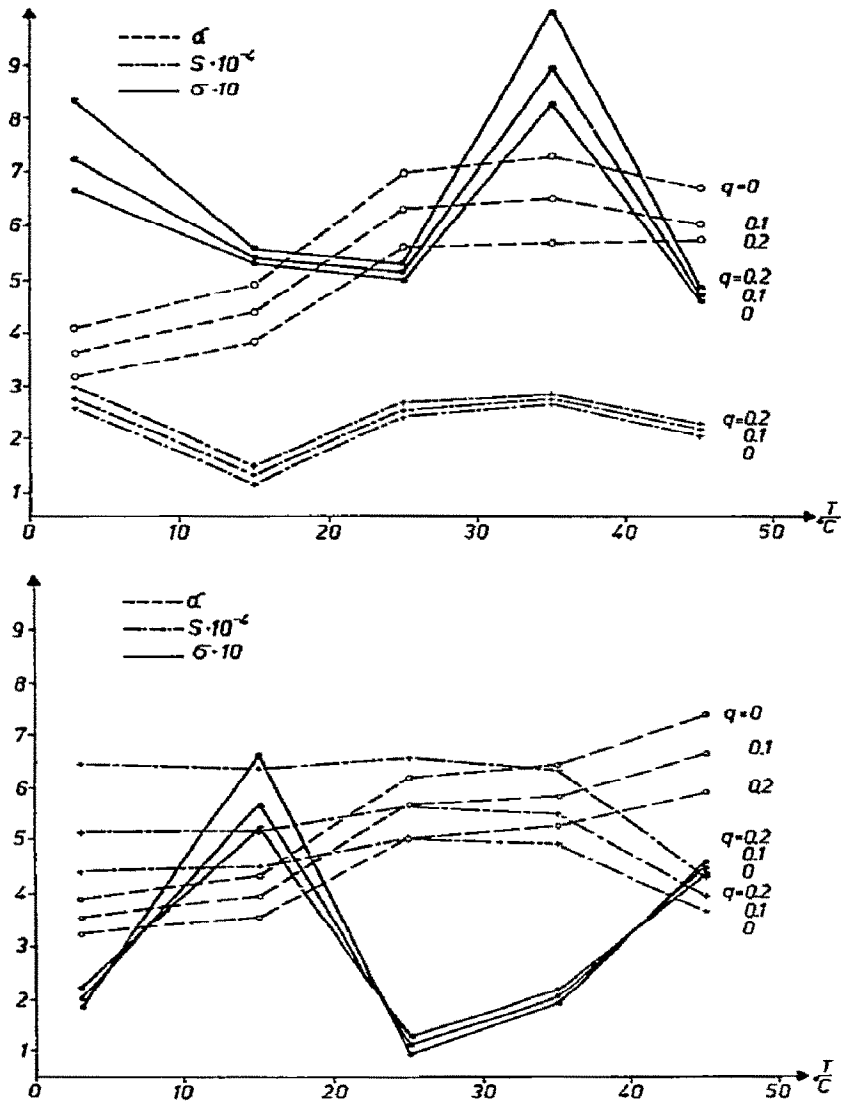

Fig. 7. (a) Parameter α, s, and σ of the complex formation of phenosafranine with calf thymus DNA as function of temperature. (b) Parameters α, s, and σ of the complex formation of phenosafranine with methylated calf thymus DNA (67 mole% MeG) as function of temperature. The curves were calculated for three assumed values of q together with experimental data. The obvious deviation of σ can be explained by the fact, that the error of the parameter σ is strongly dependent on the value of σ in the model used.

crease in the binding curve for same dye with methylated DNA supports the idea of an essentially lower value K/α compared with that of nonmethylated DNA.

3.4.2. *Phenosafranine*

Fig. 6 demonstrates that methylated DNA induces in favor of a weaker binding a smaller decrease of the polarographic reduction step. Binding data calculated from binding curves led to the following conclusion (fig. 7). (i) α increases with temperature for both types of DNAs; (ii) α was found to be higher and s lower when methylated DNA was used; (iii) the parameter of cooperativity σ is higher for methylated DNA indi-

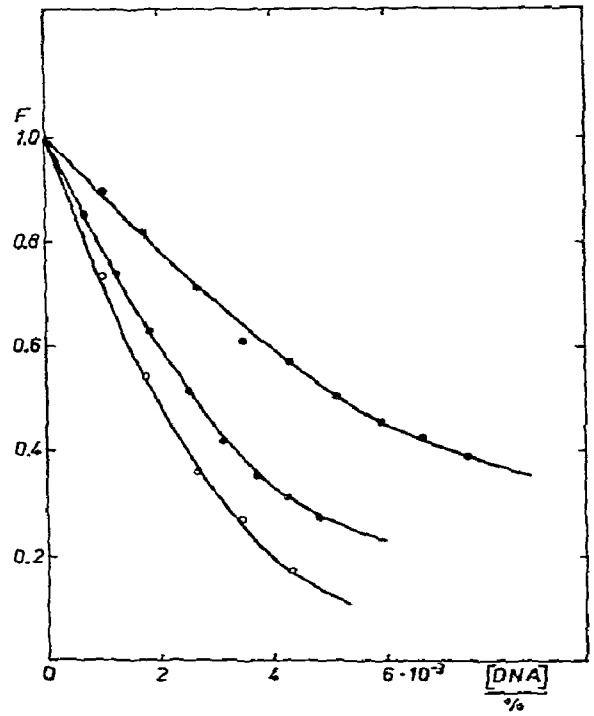

Fig. 8. Complex formation of actinomycin C with DNA as registrated with the aid of a pulse polarograph; dye concentration 5×10^{-6} M; 0.16 M phosphate buffer, pH 7; oo native calf thymus DNA (nonmethylated); •• methylated calf thymus DNA (28 mole% MeG); •• methylated calf thymus DNA (67 mole% MeG).

cating that neighbour sites of an already occupied binding site cannot be occupied as easily as in the case of nonmethylated DNA.

3.4.3. Actinomycin-C

Complexing of actinomycin C with DNA was reported previously [42, 43]. Typical for the binding is a pronounced GC specificity of intercalation process of the chromophor while the peptide rings are fixed at the DNA surface through contributions of hydrophobic interaction. Recently it was shown [44, 45] that the binding constant K (noncooperative model) obtained polarographically is in rather good accordance with that obtained form spectrophotometric measurements. $q \rightarrow 0$ indicates that the actinomycin C–DNA complex is not fully reducible at the mercury electrode. This indicates a steric inhibition of electron uptake by the intercalated chromophor. Guanine

Table 4
Dependence of complex constant of actinomycin C with DNA on MeG content

MeG (mole %)	K/α (ℓ/mole)
0	1.4×10^5
28	8.8×10^4
67	6.1×10^4

methylation decreases actinomycin C binding with increasing degree of methylation (see fig. 8 and table 4).

4. Discussion

The present results are suggestive for the nature of structural distortions in the intact DNA double helix of methylated guanine-rich sites. Loosening and lowering of base–base interactions of the methylated regions is inferred from CD- and melting temperature measurements. Melting curves at 7.2 M $NaClO_4$ and acidic titration indicate that the stable secondary structure of methylated DNA depicted earlier [1] involves considerable distortions resulting from possible decreasing base–base interactions of positively charged guanine regions and their neighbours. CD measurements demonstrate a loose conformation, which is different from the normal B structure, but does not contain denatured regions. The methylated state is restricted to change the conformation to C-like structures and therefore methylation of DNA prevents the formation of compact structures in those regions. However, an increase of the winding angle between base pairs may occur as in the case of the C-like conformation but with loosening of methylated pairs. Quantum chemical calculations are in accordance with reported measurements on thermal stability of methylated DNA. As demonstrated above introduction of a positive charge into the guanine residue by methylation leads to a loosening of the hydrogen bonded GC base pair. In connection with those results it needs to be mentioned that cytosine in methylated DNA accepts electrons more easily than in the case of native DNA [46].

The binding of acridine orange, phenosafranine, and actinomycin C is weakened in using methylated DNA however, in accordance with recent results [3] a stronger binding affinity was found for the complex proflavine-methylated DNA. The greater q-value ob-

Table 5
Base specificity of binding of various dyes with DNA and the effect of guanine methylation

Dye	Base specificity	Effect of methylation on dye binding
proflavine	AT [41,48,49]	strengthening
acridine orange	AT [39,48,50]	weakening
phenosafranine	no significance [51]	weakening
actinomycin C	GC [42,52]	weakening

tained for this complex is in favor of the fact that, as opposed to guanine [34], MeG acts as a worse fluorescence quencher. Table 5 points out that a relationship with current ideas on base specificity of dye binding obviously does not exist. From thermodynamic data it cannot be decided at present whether the decreased binding of the majority of dyes comes from steric or energetic contributions.

The increase of acridine fluorescence after binding with DNA is generally ascribed to AT-rich centers in double helical DNA [38, 39, 41]. Denaturation of DNA depresses the fluorescence increase and type-I binding as well. However, denatured regions were not detectable in methylated DNA. Possibly, enhanced flexibility of methylated DNA found by Ramstein et al. [1] changes binding properties towards the denatured state of DNA. This would be in favor of the known fact that acridine orange [39, 47] is a much better indicator of transitions in the secondary structure of DNA than proflavine or the related dye, acriflavine [34]. Concerning actinomycin C a considerably lower binding affinity was reported for denatured DNA and RNA [53–55]. Therefore it seems possible that the observed conformational transition of methylated DNA from the B form towards a loosened structure described above on the one hand, and the positively charged bulky MeG on the other hand might be reasons for the decrease in actinomycin C complexing ability. However, cooperative effects as found in the case of phenosafranine are to be taken into account for further studies [56].

The results on the conformational behavior and dye binding properties of methylated DNA might be of importance for variations of modified DNA in loosely structured (e.g., after UV damage) or condensed states, as occur in the DNA–histone complex of chromatin.

Acknowledgement

We are greatly indebted to Dr. J. Fabian, Sektion Chemie der Technischen Universität Dresden, for performance of quantum chemical calculations. Moreover authors are grateful to Mrs. R. Klarner, Mrs. U. Fiedler, and Miss Ch. Radtke for their valuable technical assistance in the experimental work and Miss Chem.-Ing. E. Sarfert for isolation of DNA samples. For valuable advice concerning CD measurements we thank Dr. G. Luck.

References

[1] J. Ramstein, C. Helene and M. Leng, European J. Biochem. 21 (1971) 125.
[2] F. Pochon and M.A. Michelson, Biochim. Biophys. Acta 149 (1967) 99.
[3] J. Ramstein and M. Leng, Biochim. Biophys. Acta 281 (1972) 18.
[4] L. Boule-Charest and M.D. Namet-Bradley, Biochim. Biophys. Acta 277 (1972) 276.
[5] E. Sarfert and H. Venner, Hoppe-Seyler's Z. Physiol. Chem. 340 (1965) 157.
[6] E. Sarfert and H. Venner, Z. Allg. Mikrobiol. 9 (1969) 153.
[7] P.D. Lawley and P. Brookes, Biochem. J. 89 (1963) 127.
[8] A. Albert, J. Chem. Soc. (1941) 121.
[9] G. Achtert, Diplomarbeit, Friedrich-Schiller-Universität Jena (1967).
[10] K.H. Zepf and H. Berg, Pharmazie 14 (1959) 396.
[11] G. Löber, Z. Physik. Chem. (Leipzig) 223 (1963) 90.
[12] G. Löber, V. Kleinwächter and H. Schütz, Biopolymers 11 (1972) 2439.
[13] K. Kronenberger, H. Strehlow and A.W. Elbel, Polarograph. Ber. 5 (1957) 62.
[14] G. Schwarz, European J. Biochem. 12 (1970) 442.
[15] E. Bauer and K. Weller, Studia Biophys. 24/25 (1970) 111.
[16] B. Pullman and A. Pullman, Quantum Biochemistry TCA5 (1966) 53; TCA7 (1967) 110.
[17] A Denis and H. Berthod, J. Chim. Phys. 65 (1968) 1815.
[18] A. Pullman, Intern. J. Quantum Chem. (1968) 187.
[19] K. Hamaguchi and E.P. Geiduschek, J. Am. Chem. Soc. 84 (1962) 1329.
[20] Ch. Zimmer and H. Venner, Biopolymers 4 (1966) 1073.
[21] Ch. Zimmer and G. Luck, Biochim. Biophys. Acta 312 (1973) 215.
[22] D.R. Robinson and M.E. Grant, J. Biol. Chem. 241 (1966) 4030.
[23] Ch. Zimmer and G. Luck, Proc. IV. Intern. Biophys. Congr., Moscow, to be published.

[24] M.-J.B. Tunis-Schneider and M.F. Maestre, J. Mol. Biol. 10 (1970) 73.
[25] D.S. Studdert, M. Patroni and R.C. Davis, Biopolymers 11 (1972) 761.
[26] V.I. Ivanov, T.E. Minchenkova, A.K. Stschelkina and A.J. Poletajev, Biopolymers 12 (1973) 891.
[27] A. Arnott, Progr. Biophys. Mol. Biol. 21 (1970) 265.
[28] T.T. Herskovits, Arch. Biochem. Biophys. 97 (1962) 474.
[29] Ch. Zimmer, G. Burckhardt and G. Luck, Studia Biophys. 40 (1973) 57.
[30] G. Löber, Z. Chem. 9 (1969) 252.
[31] G. Löber, Z. Chem. 11 (1971) 135.
[32] G. Oster, Trans. Faraday Soc. 47 (1951) 660.
[33] H.G. Heilweil and Q. van Winkle, J. Phys. Chem. 59 (1955) 939.
[34] K.R. Tubbs, E.W. Ditmars Jr. and Q. van Winkle, J. Mol. Biol. 9 (1964) 545.
[35] G. Löber, Studia Biophys. 2 (1967) 79.
[36] G. Löber and G. Achtert, Biopolymers 8 (1969) 595.
[37] G. Löber, Photochem. Photobiol. 9 (1968) 23.
[38] G. Weill and M. Calvin, Biopolymers 1 (1963) 401.
[39] O.F. Borisova and L.A. Tumerman, Biofizika 9 (1964) 537.
[40] G. Löber, Photochem. Photobiol. 4 (1965) 607.
[41] B. Weisblum and P.L. de Haseth, Proc. Natl. Acad. Sci. USA 69 (1972) 629.
[42] H. Berg and F.A. Gollmick, in: Electrochemische Prinzipien und Methoden in der Molekularbiologie, ed. H. Berg (Akademie Verlag, Berlin, 1966) p. 533.
[43] W. Müller and D.M. Crothers, J. Mol. Biol. 35 (1968) 251.
[44] H. Berg and K. Eckardt, Z. Naturforsch. 25b (1970) 362.
[45] H. Berg, H. Bär and A. Walter, Studia Biophys. 24/25 (1970) 103.
[46] J. Ramstein, J. Renaud and M. Leng, Compt. Rend. Acad. Sci. (Paris) 273D (1971) 2643.
[47] R. Rigler, Acta Physiol. Scand. 67 suppl. 267 (1966) 1.
[48] V. Kleinwächter, Z. Balcarová and J. Bohaček, Biochim. Biophys. Acta 174 (1969) 188.
[49] N.F. Gersch and D.O. Jordan, J. Mol. Biol. 13 (1965) 138.
[50] V. Kleinwächter and J. Koudelka, Biochim. Biophys. Acta 91 (1964) 539.
[51] V. Böckel and G. Löber, unpublished.
[52] I.H. Goldberg, M. Rabinowitz and E. Reich, Proc. Natl. Acad. Sci. USA 48 (1962) 2094.
[53] R. Haselkorn, Cold Spring Harbor Symp. Quant. Biol. 28 (1963) 91.
[54] E. Reich, in: The role of chromosomes in development, ed. M. Locke (Academic Press, New York, 1964) p. 73.
[55] C.E. Gellert, G. Smith and G. Felsenfeld, J. Mol. Biol. 11 (1965) 445.
[56] H. Berg and H. Schütz, unpublished.

BIOPHYSICAL CHEMISTRY 1 (1974) 349–357. © NORTH-HOLLAND PUBLISHING COMPANY

HEAT DENATURATION OF RIBONUCLEASE

E.I. TIKTOPULO and P.L. PRIVALOV

Institute of Protein Research, Academy of Sciences of the USSR, Poustchino, Moscow Region, USSR

Received 30 July 1973
Revised manuscript received 17 January 1974

One of the main and, chronologically, perhaps one of the first questions in the study of globular protein heat denaturation is that of the applicability of the "all or none" principle to this process, i.e., whether the transition of globular protein from the native into the denaturated state occurs abruptly, without intermediate, thermodynamically stable forms or there are several successive transitions. Despite an intensive study of the process of denaturation this question still remains unsettled. Moreover, its actuality has greatly increased lately with the accumulation of contradictory data.

1. Introduction

Originally, the possibility of describing denaturation of globular proteins by an abrupt process was sooner postulated than demonstrated [1, 2]. Such a consideration gave great advantages since it offered the possibility of a simple quantitative analysis reducing denaturation to a usual monomolecular reaction. At the same time, a simultaneous change of several properties of protein in a rather narrow temperature interval rendered such an interpretation highly probable [3].

However, later, with the increase of the number of parameters recorded in a heated protein solution the validity of the proposed assumption was put to question [4]. These doubts were supported by numerous reports according to which the change of some parameters observed in the heated protein solution proceeded in a considerably larger temperature interval and did not seem to be as simultaneous as it was thought. It follows then that the change of the protein state under the influence of temperature is a considerably more complicated process than it was presumed in the first approximation and is probably not reduced to only an abrupt process. An impression was created that the protein molecule undergoes several successive changes with heating and it was not clear whether it was possible at all to distinguish a qualitatively different stage among these changes which we could consider as denaturational.

In the present paper this question is examined on the example of ribonuclease A, the most popular object in the study of the denaturation process. Up to the present, most experiments on denaturation have been carried out on it because of its exceptional reversibility to different influences and, correspondingly, it is here that the majority of contradictory data and opinion has accumulated [5–22]. Unfortunately, their analysis by a comparison of functional dependences of different parameters on temperature is very complicated by the fact that the data were obtained on different preparations and in different conditions and, moreover, with a precision far insufficient for a quantitative analysis. This compelled us to carry out a new series of more precise measurements to ensure a more reliable accuracy of the compared functions than done before. We hope to show on the example of their analysis that in fact there are no contradictions in thermal properties of ribonuclease.

2. Methods

Studies were carried out on pancreatic ribonuclease A. The commercial preparation was separated on the SE Sephadex C-25 column equilibrated by 0.1 M phosphate buffer, pH 6.5. To remove phosphate ions, the solution was passed through a Sephadex G-25 column equilibrated by 0.1 M sodium perchlorate. The homogeneity of the preparation was controlled by gel filtra-

tion of Sephadex G-75 and by electrophoresis on polyacrylamide gel. To avoid formation of aggregates the column preparation was not lyophilized and purification on the column was carried out directly before the experiment to reduce storage time. The necessary solutions were obtained by dialysis against 0.04 M glycin buffer with a corresponding pH value. The protein concentration in the solution was determined spectrophotometrically by the extinction coefficient $E^{0.1}_{278} = 0.738$.

Spectrophotometrical measurements were carried out on a Hitachi-124 instrument with differential thermostated cells. During plotting of the melting curves one of the cells was thermostated at 10°C.

Measurement of the optical activity was done on a Perkin–Elmer 141-M spectropolarimeter. The circular dichroism was measured on a Jasco J-20 spectropolarimeter. Calorimetric measurements were performed on the new precision model of the scanning microcalorimeter designed at the Institute of Protein Research [23].

All the measurements connected with temperature scanning were performed automatically at continuous heating at a same constant rate of 1 deg/min for all the methods. Differential spectra curves were obtained by a step-wise heating with a 15 min delay at each temperature.

3. Results

3.1. Spectrophotometric data

For many technical reasons they are perhaps the most frequently used in studying the process of heat denaturation in general and of heat denaturation of ribonuclease in particular [5–8].

Under the influence of temperature the absorption spectrum of ribonuclease actually undergoes extremely important changes. As seen from the given differential curves plotted at different temperatures (fig. 1a) the changes are particularly great in the 236, 278 and 285 nm region.

Here three circumstances attract attention: (a) the change of the spectrum starts from the lowest temperatures and proceeds up to the highest; (b) the character of the change of the differential spectrum alters abruptly starting at some definite temperature (46°C for the given solution with pH 4.0); (c) at the first stage of changes of the differential spectrum there are

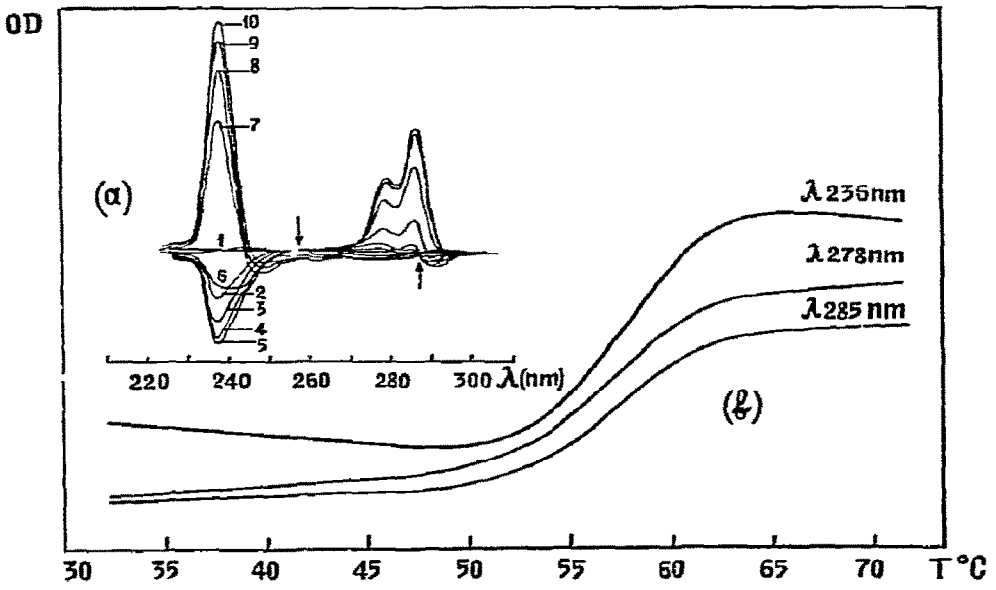

Fig. 1. (a) Differential spectra of RNase in solution with pH 4.0 at different temperatures. 1–20°C, 2–27°C, 3–35°C, 4–41°C, 5–46°C, 6–52°C, 7–56°C, 8–61°C, 9–67°C, 10–72°C. (b) Change of the RNase optical density in solution at pH 4.0 at three wavelengths.

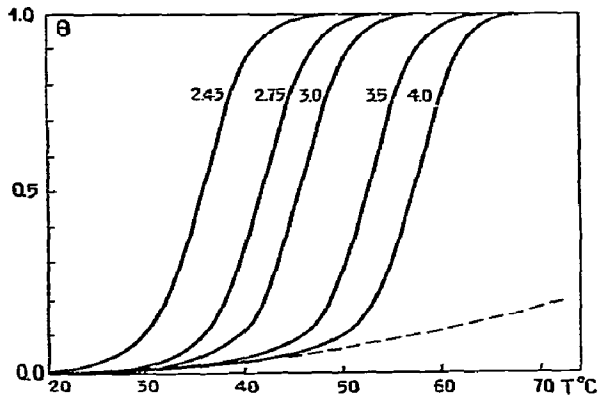

Fig. 2. Relative changes of the RNase optical density at λ 285 nm at different pH values.

two indistinct isosbestic points at 256 and 285 nm.

Fig. 1 shows that temperature functions of spectral characteristics taken at different wavelengths will be different. At the isosbestic points (256 and 285 nm) no essential changes of optical density will be observed up to the temperature of 46°C (fig. 1b). At 278 nm changes in both temperature regions occur in the same direction but in quite a different way. The question arises: which of these wavelengths should be taken for a thermodynamical analysis of the process of protein temperature transformations?

It is clear that the simplest curve obtained at 285 nm has a certain advantage since it sees only a part of the complicated process and it must be easier to interprete. However, the obtained curves at different pH at this wavelength also differ noticeably from symmetrical sigmoids characteristic for simple processes by a very extended low-temperature slope (fig. 2) which is connected with non-ideality of the isosbestic points. We can attempt to take into account the introduced distortion by extrapolating the initial changes on the main stage of the process and considering the change at this stage only from the extrapolated line. Naturally, the shape of the curve thus isolated for the main stage of the curve will considerably depend on the function by which the extrapolation of the initial changes into the temperature region of the main stage was carried out. By extrapolating different functions it can be seen that the most symmetrical sigmoid curve describing the main stage will be obtained in the case when the parabolic function has been taken for extrapolation of the initial changes (fig. 2, dotted line). However, it is much easier to carry out the separating operation if we do not use the optical density temperature dependence curve itself for analysis but its temperature derivative (see fig. 3). In this case the initial part of the changes will be represented with good precision by a linear function easily extrapolated in the region of the peak describing the main stage. Applying the same separating operation to the curves obtained at other wavelengths it is convincingly seen that in all the cases the complicated curves characterizing changes of the protein state will separate into two simple and completely similar functions: a parabolic function (linear for the derivative curve) and an almost symmetrical sigmoid (an almost symmetrical peak for the derivative) (figs. 4a, b). If a van 't Hoff plot is drawn by these sigmoid curves (i.e., the dependence of $R\ln K$ on $1/T$), practically identical lines will be obtained for all the wavelengths (at corresponding pH) with a hardly noticeable constant curvature (fig. 4c) evidencing a small asymmetry of the isolated curves. At any other division of the observed complicated curves we shall not obtain a constant curvature of the line on van 't Hoff plots.

3.2. Data on circular dichroism

Data on circular dichroism also point to the complex character of ribonuclease changes with temperature. This was noted for the first time in ref. [15] according to which temperature changes in ribonuclease proceed in two clearly divided stages – from 15 to 50°C and from 50°C. A more thorough analysis, how-

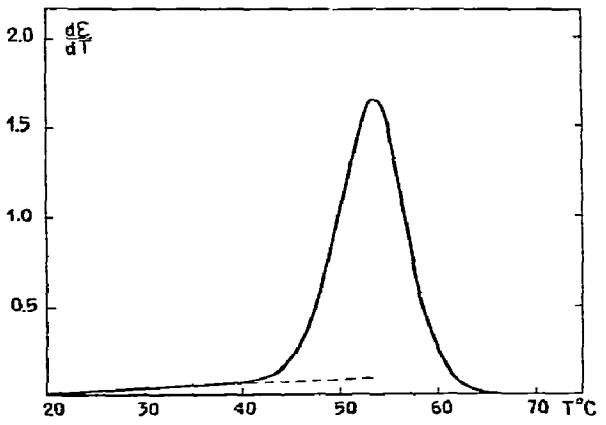

Fig. 3. Temperature derivative of the change of the RNase optical density at pH 3.5.

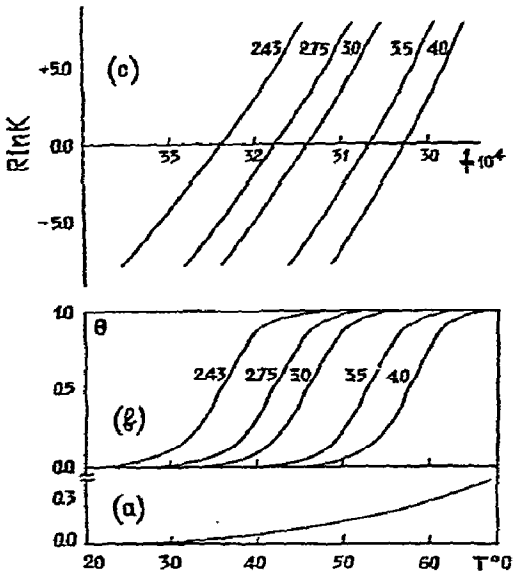

Fig. 4. Division of complex curves of the optical absorption at different pH values in two components: the parabolical (a), the sigmoidal (b) and van 't Hoff plots of sigmoidal functions (c).

ever, has shown (see fig. 5) that in fact we cannot separate a distinct interval of the first stage since changes start from the very beginning of heating regardless of the initial temperature of heating and wavelengths. But at different wavelengths the sensitivity is not the same. On the whole, the picture differs little from that observed spectrophotometrically: the relative change of circular dichroism with temperature also appears as a complex function consisting of a monotonous component not depending on pH and a sigmoid component, the position of which is directly determined by the pH value (fig. 6).

By separating sigmoid parts and plotting van 't Hoff graphs for them (see fig. 7) we also obtain curves with a hardly noticeable curvature indicating to the slight asymmetry of sigmoid components.

3.3. Data on optical activity

Data on optical activity are also very similar to those of spectrophotometry (see fig. 8). Wavelengths are also seen here at which changes of the protein molecule state are practically not observed at the ini-

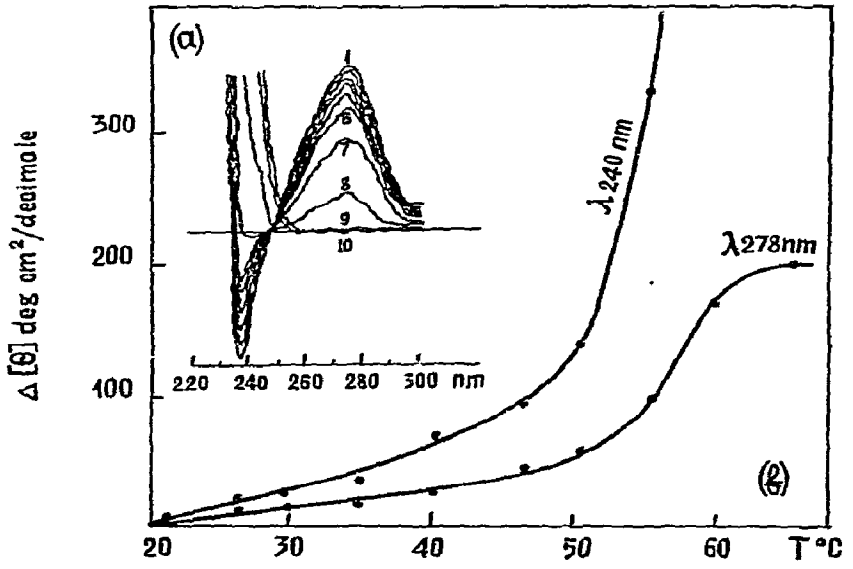

Fig. 5. Changes of circular dichroism with temperature in the RNase solution at pH 4.0. (a)The circular dichroism spectra at different temperatures: 1 – 21.0°C, 2 – 26°C, 3 – 29.6°C, 4 – 35°C, 5 – 40.5°C, 6 – 46.7°C, 7 – 51.6°C, 8 – 55.5°C, 9 – 59.5°C, 10 – 64.5°C. (b) Changes of circular dichroism at two wavelengths.

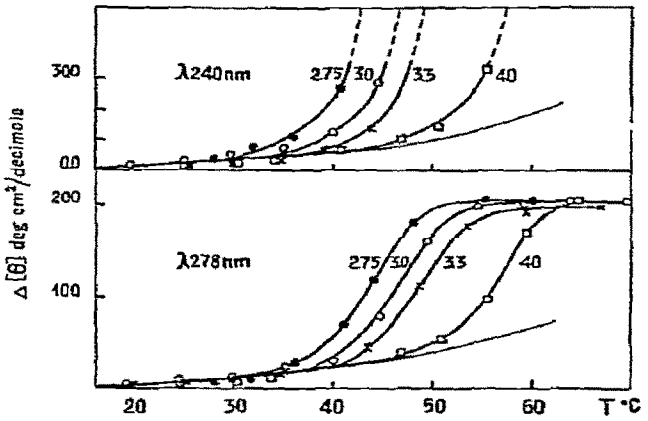

Fig. 6. Temperature changes of RNase circular dichroism at different pH values of solutions at two wavelengths.

tial stage of heating and there are spectrum regions in which distinct changes are observed from the very start (see also ref. [8]). Using simpler regularities obtained at 302 nm we derive transition curves at different pH values (fig. 9a) the van't Hoff plots of which are also represented by lines with a hardly noticeable constant curvature (fig. 9b).

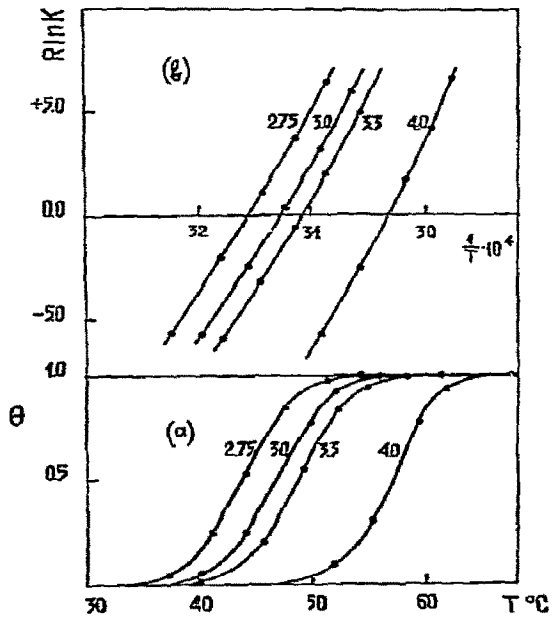

Fig. 7. Sigmoidal component of RNase circular dichroism change (a) at different pH values and its van't Hoff plot (b).

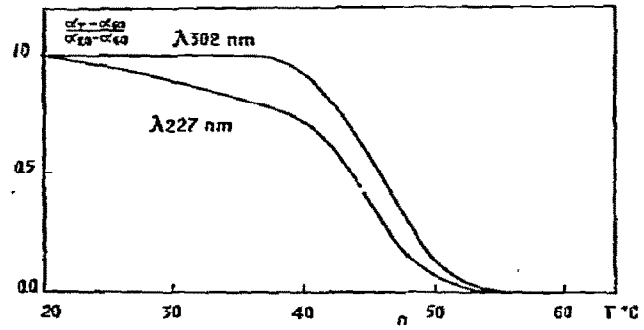

Fig. 8. Relative change of RNase optical activity at different wavelengths in solution at pH 3.0.

3.4. Calorimetric investigations

Calorimetric investigations of the heated ribonuclease solutions were the subject of a great number of papers [16–22] since it was obvious that these data must play the main role in solution of the problem. However, the precision achieved in the majority of

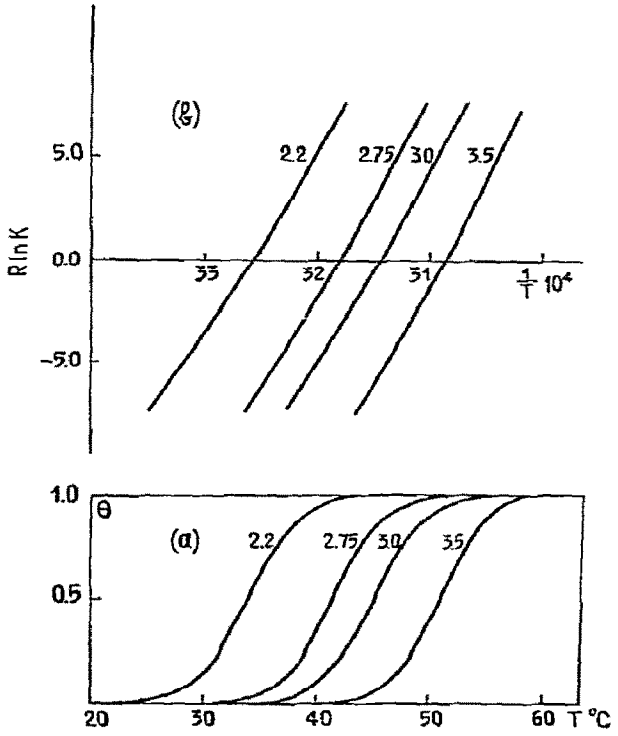

Fig. 9. Relative change of RNase optical activity at 302 nm with a different pH value of solution (a) and its van't Hoff plot (b).

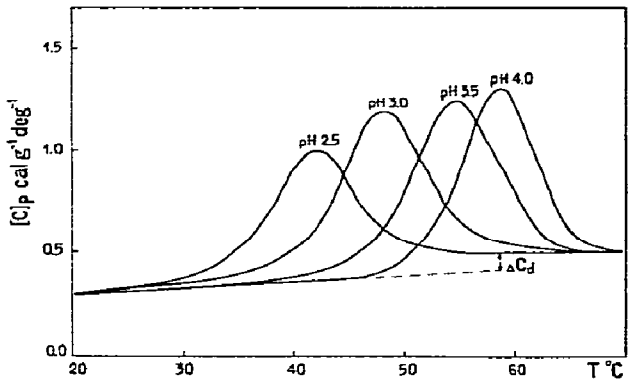

Fig. 10. Temperature dependence of the RNase partial heat capacity at different pH values.

these studies proved to be insufficient to realize the set task. The most reliable results were obtained in refs. [17, 19] with the main difference that in the first the results were obtained in integral form, i.e., as enthalpy dependence on temperature, while in the second paper they were in differential form – heat capacity dependence on temperature. Though certain thermal effects of denaturation proved to be very similar in both cases (see fig. 11) the difficulties of analysis and interpretation of the integral form of recording led to some misunderstanding connected with determination of effective parameters. To eliminate these misunderstandings fig. 10 gives the temperature dependence of the enthalpy derivative on temperature or the ribonuclease partial heat capacity at different pH values.

It is seen from fig. 10 that the heat capacity change which occurs at the start of the heating (from 20°C) is also very nearly to linear. Deviations from linearity start only from the temperatures where the character of the change of the optical properties is modified. The thermal effect of this process can be separated by a linear extrapolation of the initial and final course of heat capacity to the middle of the intensive peak of heat absorption designated as T_d.

Linear extrapolation of the course of the initial and final heat capacity to the middle of *the peak* shows that as a result of the process connected with heat absorption, the partial heat capacity of protein increases considerably by an amount of ≈ 0.09 cal/g (see fig. 1[illegible]). Data of ref. [17] are given in the same figure.

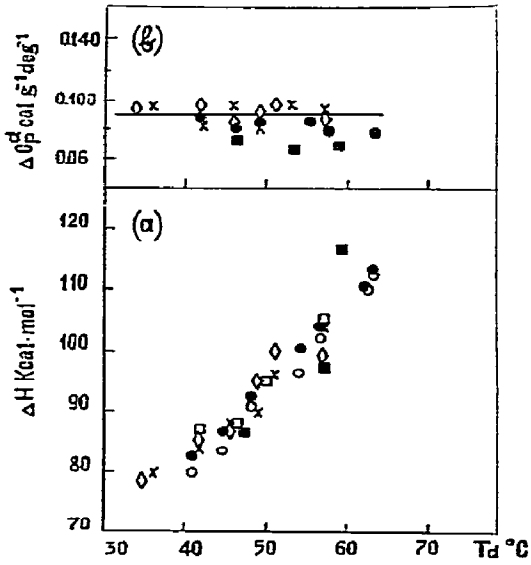

Fig. 11. Dependence of molar denaturational enthalpy (a) and denaturational change of partial heat capacity (b) of RNase at different pH values on the temperature of transition. Calorimetric values: • – (19); ■ – (17). Effective values: ○ – from calorimetry; × – from optical absorption; ◇ – from optical activity; □ – from circular dichroism.

The area outlined by the heat absorption curve and extrapolation lines corresponds to the heat absorbed as a result of the process proceeding at these temperatures. Multiplied by a mole of protein it will represent the calorimetric or real enthalpy of this process. It is easy to see that the molar enthalpy increases with the growth of the protein thermostability (fig. 11a), but increase of the area occurs only at the expense of peak sharpening.

From the sharpening of the heat absorption peak it is possible to determine the effective enthalpy of the process using the van't Hoff equation (see ref. [24]). For the midpoint, where

$$\Delta H_t = 4RT^2 \, d\vartheta/dT$$

having in mind that for the calorimetric curve $d\vartheta/dT$ is height of the peak ΔC_p divided by the enthalpy (per mole), we have:

$$\Delta H_t^{\text{eff}} = 2\,R^{1/2}T(\Delta C_p)^{1/2}.$$

The values of effective enthalpies of the process corresponding to the peak are given in fig. 11a as a

function of midpoint temperature T_T. (For an asymmetric peak T_T does not coincide with the temperature of the peak maximum, but for ribonuclease the difference is rather small - 0.6°.)

4. Discussion

From the above it is clearly seen that the structural changes of ribonuclease with temperature are indeed of a quite complicated character. But the impression is created that the complicated function describing these changes is a combination of two simpler functions, a parabolic one (linear for the derivative curve) and a sigmoid (peak on the derivative curve). Most intriguing is that the shape of those function(s) is similar for all indices by which the change of protein was registered; only the relative contribution of these functions to the resulting curve is different. The easiest way to show this for the sigmoids is to compare the parameters of their van 't Hoff plots, i.e., the slope at the midpoint and its curvature. The advantage of using van 't Hoff plots here is that their slope corresponds to the enthalpy of the process if it represents a two-state transition. As for the curvature it corresponds to the temperature dependence of enthalpy, or, in other words, to the heat capacity change at transition inasmuch as $d\Delta H_t/dT = \Delta C_p^t$.

It can be seen that the effective enthalpies of transition, or slopes of the van 't Hoff plot determined by all the used parameters are temperature dependent and at all temperatures their slopes and their curvatures coincide within error of determination (see figs. 11a, b).

This coincidence of effective enthalpies is a very essential indication of the two-state transition character of the process responsible for the sigmoid change of protein properties (see ref. [3]). But much more indicative here is the coincidence of effective enthalpies with the real calorimetric ones. Unfortunately the spread of points in fig. 11 is too great (about 10%). Thus, we can speak about the adequacy of the two-state model for the considered process only in this approximation. But it is possible to achieve a higher resolution here if only calorimetric data will be used. The greatest advantage of calorimetry in solving this problem is that the effective as well as the real calorimetric enthalpy can be obtained from the same experimental curve of heat absorption and hence their comparison can be made with a much greater accuracy. Fig. 12 gives the ratio of $\Delta H^{cal}/\Delta H^{eff}$ obtained by calorimetry at different pH versus the corresponding transition temperature. The spread of points here is much less (only 3%) and it is clearly seen that the ratio of calorimetric and effective enthalpies is not a strict unity

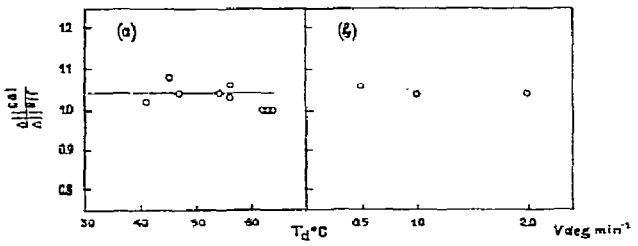

Fig. 12. The ratio of calorimetric and effective enthalpies (a) at different pH versus transition temperature at a heating rate of 1 deg/min; (b) at different heating rates and the same pH versus heating rate.

$$\Delta H^{cal}/\Delta H^{eff} = 1.05 \pm 0.03.$$

This deviation is not dependent on the heating rate (see fig. 12b), so it cannot be due to the non-homogeneity of the temperature field in the cell at continuous heating. Thus we have to conclude that this deviation is the measure of inadequacy of the two-state model for the considered process. In other words this deviation proves that there are some intermediate states. But as the deviation is rather small (only 5%) the concentration of proteins in the intermediate states must be small too, i.e., these states are fairly unstable thermodynamically and during transition the protein passes them too rapidly (see also ref. [25]) Thus, in many cases, when the mechanism of transition is not under question, we can consider this process as a two-state transtition from one microscopic state to another essentially different in enthalpy. Since this qualitatively different state is usually called denatured, we can call this process, which we separated out from the overall thermal change of protein, denaturation.

Having thus defined denaturation as a strongly cooperative transition we consider all the changes taking place with the protein before denaturation as non- de-

naturational or predenaturational changes of the native protein. The main difference of these changes from the denaturational one is that they are not the result of a cooperative transition between macroscopic states substantially different in enthalpy. Naturally, the question arises as to the origin of these gradual changes of the protein molecule.

At present there are some facts which should be taken as starting points in solving this problem.

The change in partial heat capacity of protein increases in the predenaturational region of temperatures [17, 19]; simultaneously the partial volume increases [9] and there is an increase in the rate of hydrolysis by proteases [8] and in the rate of proton exchange [26, 27]. However, the most noteworthy is that at the same time only a monotonous change of chemical shifts of the proton resonance lines proceeds for separate groups without a change of their area and shape [12, 13]. (The situation is analogous to another protein, lysozyme, the best studied by the NMR method [28].) It is perhaps this property that most clearly distinguishes the predenaturational process from the denaturational one at which new resonance lines appear and the development of the process is accompanied by an increase of their area at the expense of the previous ones. Hence it follows that denaturational and predenaturational changes are connected with exchange processes proceeding at qualitatively different rates. If denaturational changes are defined by comparatively slow transitions between two clearly defined macroscopic protein states, the predenaturational ones are connected with exchange processes of several orders faster. Judging by the different influence of temperature on different histidines [12, 13] it is most probable that these processes are local fluctuations of the native structure at its weak points increasing with temperature. Such a fluctuational mechanism explains many properties of globular proteins, in particular, the proton exchange which increases with temperature [26, 27] and the isosbestic points observed in the differential spectrum (see fig. 1). The presence of isosbestic points indicates that the chromophores responsible for absorption in this region of the spectrum have two states and that the population of the second state increases with the growth of temperature. If this second state represents local defects of the native structure, it is clear that the rate of their formation and disappearance will be high, while the concentration will be low since their formation is not accompanied by a substantial entropy gain at the expense of conformational mobility and a considerable shift of complementary groups in space. At the same time it is apparent that due to a high rate of transitions between microscopic states, an averaging of practically all the experimentally observed parameters must take place, and therefore we can consider predenaturational protein changes as gradual changes of its macroscopic native state similar to a usual thermal expansion of solids.

References

[1] M.A. Eizenberg and G.W. Schwert, J. Gen. Physiol. 34 (1951) 583.
[2] J.A. Schellman, Compt. Rend. Trav. Lab. Carlsberg 29 (1955) 230.
[3] R. Lumry, R. Biltonen and J.F. Brandts, Biopolymers 4 (1966) 917.
[4] D.C. Poland and H.A. Scheraga, Biopolymers 3 (1965) 401.
[5] J. Hermans Jr. and H.A. Scheraga, J. Am. Chem. Soc. 83 (1961) 3283.
[6] R.A. Scott and H.A. Scheraga, J. Am. Chem. Soc. 85 (1963) 3866.
[7] J.F. Brandts and L. Hunt, J. Am. Chem. Soc. 89 (1967) 4826.
[8] W.A. Klee, Biochemistry 6 (1967) 3736.
[9] D.N. Holcomb and K.E. van Holde, J. Phys. Chem. 66 (1962) 1999.
[10] J.P. Cohen Addad, J. Mol. Biol. 50 (1970) 595.
[11] G.C.R. Roberts and O. Jardetzky, Advan. Protein Chem. 24 (1970) 448.
[12] O. Zaborsky and G.E. Millman, Biochim. Biophys. Acta 271 (1972) 274.
[13] D.G. Westmoreland and C.R. Matthews, Proc. Natl. Acad. Sci. U.S. 70 (1973) 914.
[14] T.Y. Tsong, R.L. Baldwin and P. McPhie, J. Mol. Biol. 63 (1972) 453.
[15] E.R. Simons, E.G. Schneider and E.R. Blout, J. Biol. Chem. 244 (1969) 4023.
[16] K. Beck, S.J. Gill and M. Downing, J. Am. Chem. Soc. 87 (1965) 901.
[17] T.Y. Tsong, R.P. Hearn, D.P. Wrathall and J.M. Sturtevant, Biochemistry 9 (1970) 2666.
[18] P.L. Privalov, N.N. Khechinashvili and B.P. Atanasov, Biopolymers 10 (1971) 1865.
[19] P.L. Privalov, E.I. Tiktopulo and N.N. Khechinashvili, Intern. J. Peptide Protein Res. 5 (1973) 229.
[20] G.G. Kresheck and H.A. Scheraga, J. Am. Chem. Soc. 88 (1966) 4588.
[21] F. Delben, V. Crescenzi and F. Quadrifoglio, Intern. J. Protein Res. 1 (1969) 145.
[22] B.G. Winchester, A.P. Mathias and B.R. Rabin, Biochem. J. 117 (1970) 299.

[23] P.L. Privalov, V.V. Plotnikov and V.V. Filimonov, Chemical thermodynamics (1974), to be published.
[24] P.L. Privalov, Biofizika (USSR) 15 (1970) 206.
[25] T.Y. Tsong and R.L. Baldwin, J. Mol. Biol. 69 (1972) 149.
[26] S.J. Leach and P.H. Springell, Australian J. Chem. 15 (1962) 350.
[27] C.K. Woodward and A. Rosenberg, J. Biol. Chem. 246 (1971) 4105.
[28] C.C. McDonald, W.D. Phillips and D. Glickson, J. Am. Chem. Soc. 93 (1971) 235.

BIOPHYSICAL CHEMISTRY 1 (1974) 358–366. © NORTH-HOLLAND PUBLISHING COMPANY

A MECHANICAL MODEL FOR THE HALF-OF-THE-SITES REACTIVITY OF OLIGOMERIC ENZYMES

P.L. LUISI
Swiss Federal Institute of Technology (E.T.H.) Zürich, Switzerland

and

M. ZANDOMENEGHI
Istituto di Chimica Fisica, Università di Pisa, Italy

Received 18 October 1973
Revised manuscript received 18 January 1974

We developed a model which is able to provide a rationalization of the half-of-the-sites reactivity of oligomeric enzymes. According to this model, a dimeric enzyme is considered as a system of two coupled oscillators, which are able to transmit energy (information) to each other via a weak elastic coupling. In such a system, the energy may fluctuate between the two coupled elements so as to accumulate in one of the two at a time, i.e., at one time a certain energy state will be present in *only one* of the two elements. If this energy state (protomer conformation) is relevant for the chemical reaction, the conditions of half-of-the-sites reactivity may be fulfilled. The limits, and possible generalization, of this model are discussed.

1. Introduction

In the last few years the term "half-of-the-sites reactivity" has been introduced [1–3] in relation to those oligomeric enzymes which, under certain conditions, display chemical reactivity at only one half of the active sites. Among the systems which, in one way or another, seem to possess this feature, one finds dimeric enzymes such as alkaline phosphatase [4, 5], malic dehydrogenase [6, 7], horse liver alcohol dehydrogenases [3, 8, 9]; tetrameric enzymes such as glyceraldehyde-3--phosphate dehydrogenase from yeast [2, 10] and muscle [12], exameric enzymes such as uridin-6-phosphate-1C-dehydrogenase [13], and octameric enzymes such as glutamine synthetase [14] and aceto-acetate decarboxylase [15]. A more detailed list can be found in the recent works by Landunsky [16], and Koshland [1].

Although at the present time some aspects of the phenomenon are still unclear (in particular the relation between the kinetic and the thermodynamic (binding) aspects *), there is no doubt that the half-site reactivity is experimentally a well ascertained property of several oligomeric enzymes, and one which deserves attention for its implications about the mechanism of subunit interaction. At the present, the half-of-the-sites reactivity is often attributed to a negative cooperativity [2, 17], and to an alternating model [7] ("flip-flop" mechanism [5, 16]) as far as the kinetics of the enzyme turnover is concerned.

Part of the skepticism that the half-of-the-sites reactivity still encounters is certainly due to the difficulty of envisioning the possible thermodynamic and/or physiological driving forces responsible for it. What is the rationale of an enzyme machinery which works with one half (or one half at a time) of its active centers?

* For instance, some enzymes (yeast glyceraldehyde-3-phosphate dehydrogenase is an example) show the half-site reactivity only in binding. Other enzymes (for example horse liver alcohol dehydrogenase) display the half-site reactivity only in transient kinetics, while binding is normal.

In this study we have attempted to see whether an answer – at least partial and preliminary – could be given to such a question. For this, we examine the mechanical behaviour of the oligomeric enzyme, considered as an assembly of elements bound by forces which can be represented as elastic forces. In particular, we consider the subunits as coupled oscillators, in which the coupling corresponds to the subunits interaction. We will show that, when mechanical energy flows along the system, the two oscillators (subunits) pass through a set of energy states (protomer-conformations) in an antiphasic manner, namely only one subunit at a time possesses a given energy state. The limits and the possible implication of this mechanical analogy will be discussed.

2. The model

We assume that the cooperative phenomena characterizing some oligomeric enzymes are a direct consequence of the transmission of energy from one protomer to the other. We believe that the simplest and most reasonable way to describe the *dynamic properties* of these molecular systems is with models, in which each protomer is seen as an assembly of masses bound by elastic forces. Depending upon the degree of information that one desires, there are several models of various degrees of sophistication that in principle could be proposed. Restricting ourselves to dimeric proteins, the model illustrated in fig. 1 is certainly the simplest: two coupled oscillators of equal mass m, characterized by equal elastic force constants k, the oscillators weakly interacting through the element with a force constant $k_b \ll k$.

The equation of motion of this system takes the well known form [18] (under the appropriate starting conditions):

$$x_A = A \cos\tfrac{1}{2}(\omega' + \omega_0)t \cos\tfrac{1}{2}(\omega' - \omega_0)t\,,$$

$$x_B = A \sin\tfrac{1}{2}(\omega' + \omega_0)t \sin\tfrac{1}{2}(\omega' - \omega_0)t\,, \qquad (1)$$

where $\omega_0 = \sqrt{k/m}$, $\omega' = \sqrt{\omega_0^2 + 2k_b/m}$ and x_A and x_B are displacements of the two masses from the equilibrium position. Equation (1) indicates that, under conditions of weak coupling ($k \gg k_b$) the vibrational energy of one oscillator will be continuously transmitted to the other with a frequency $\frac{1}{2}(\omega' - \omega_0)$,

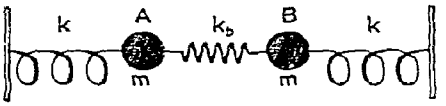

Fig. 1. The coupled oscillator. k is the elastic force constant of each oscillator, and k_b the force constant of the elastic linking element (which simulates subunits interaction).

whereas the conversion of potential into kinetic energy in each oscillator takes place with a frequency * $\frac{1}{2}(\omega' + \omega_0) \approx \omega_0$. The time dependence of the total energy in each of the two oscillators is illustrated in fig. 2a. Each oscillator receives and gives away cyclically the total energy, so that the maximum of energy of one oscillator is coupled with the minimum of energy in the other one. In any real system, due to dissipation of energy by the environment (damping), the intensity of the motion will decrease with time. This, however, does not modify the alternating behaviour (provided that the damping is not exceedingly large).

Models based on oscillators are utilized in many different fields of chemistry and physics: many cases of weakly interacting particles can be treated in terms of oscillators. The most well known examples are in classical spectroscopy [19] ‡, in the theory of viscoelasticity in solids [20], in the theory of optical activity [21], and in the propagation of light in the crystals [22]. Recently a model based on two connected springs has been utilized by Hopfield for describing the free energy of binding within the hemoglobin protomer [23]. In a somewhat related line of reasoning, Volkenstein proposed elastic vibrations in a hypersonic region of the spectrum (acoustic phonons) as an explanation of positive cooperativity [24]. Also, the model presented in this paper may be considered to be related to rack mechanisms [25–27], as these mechanisms involve the utilization of mechanical energy arising from strain and distortion of bonds.

* H. Buc remarked to us that by releasing the condition $k_b \ll k$, one can generate an analogy appropriate to the case of concerted transitions. T. Keleti suggests the use of different masses (one for the protomer as apoenzyme, the other for the protomer containing the ligand) in order to use dispersion relations (which may eventually lead to the prediction of spectroscopic bands).

‡ See also any textbook on spectroscopy.

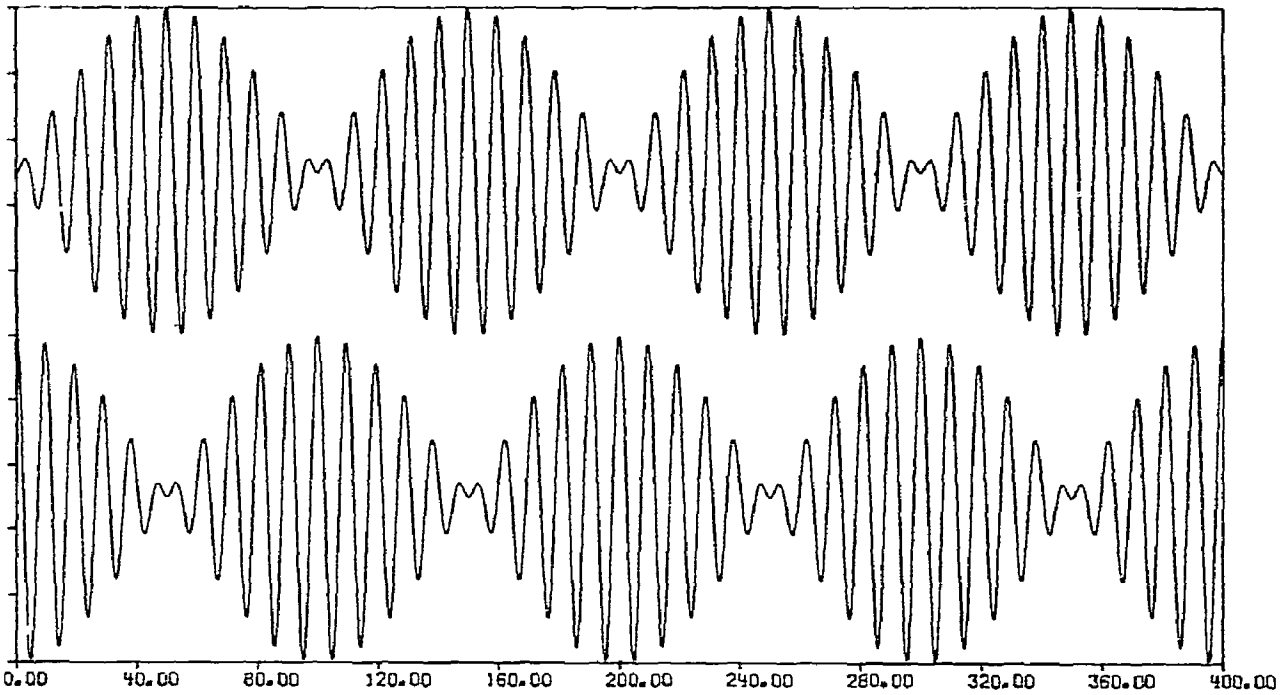
0.00
40.00
80.00
120.00
160.00
200.00
240.00
280.00
320.00
360.00
400.00
TIME (PICØSECØNDS)

(a)

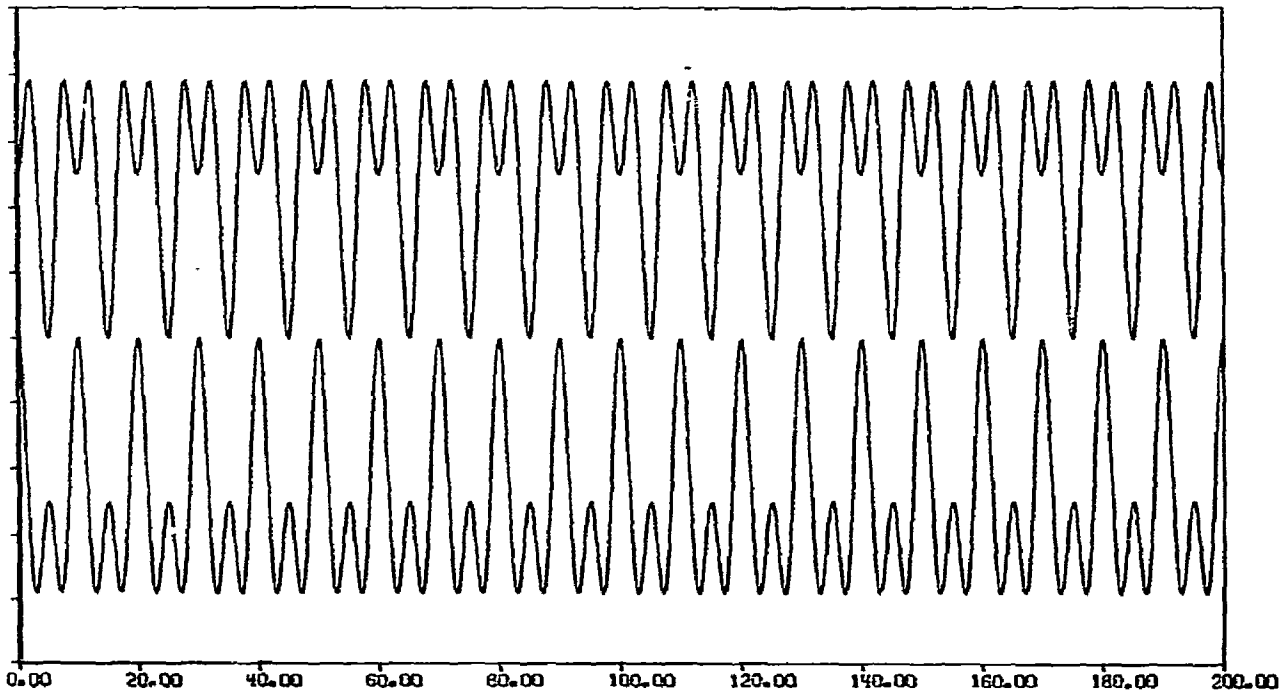
0.00
20.00
40.00
60.00
80.00
100.00
120.00
140.00
160.00
180.00
200.00
TIME (PICØSECØNDS)

(b)

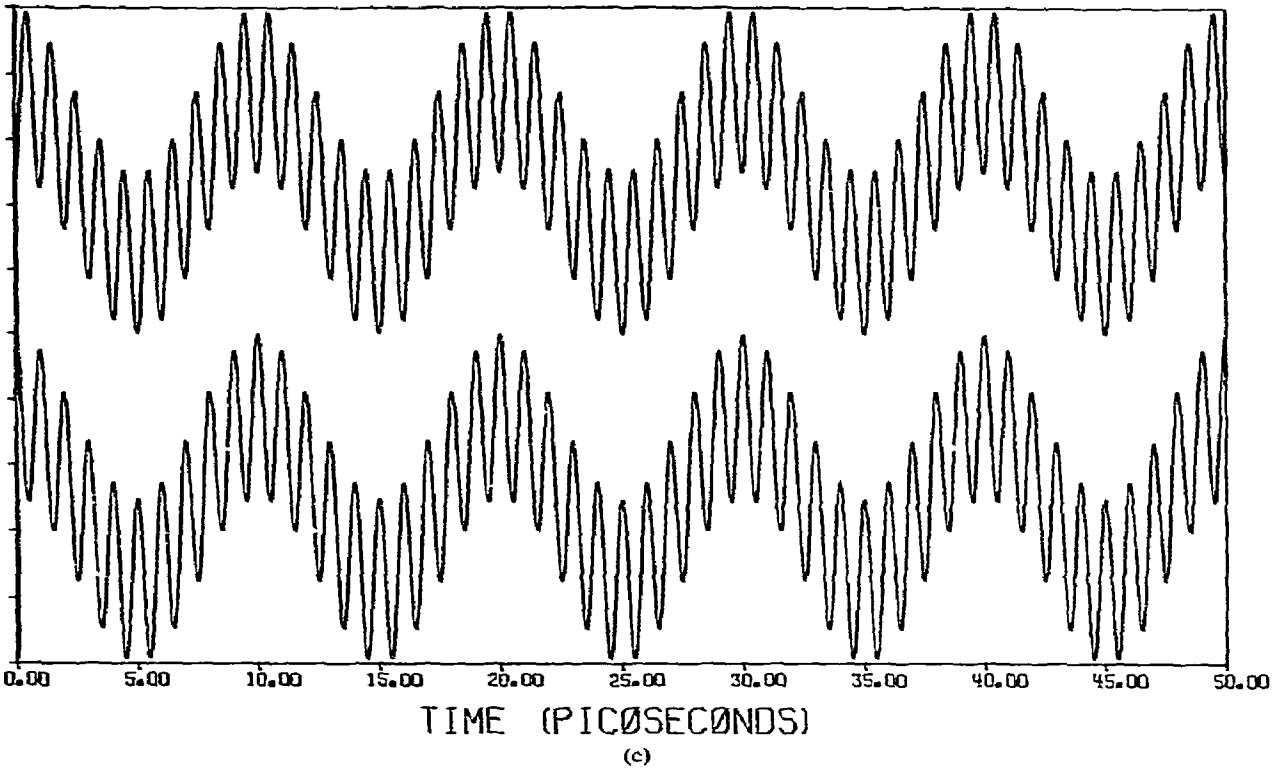

Fig. 2. Illustration of the equation of motion of the coupled oscillator of fig. 1, showing the antiphasic behaviour of the two elements. Calculations have been carried out on the basis of eq. (1), assuming $\omega_0 \approx 2\pi \times 10^{11}$ sec^{-1} and $\omega' = 1.1\omega_0$ (a); $\omega' = 2\omega_0$ (b); $\omega' = 10\omega_0$ (c). Notice that in the third case there is no more coupling (the two frequences are too far apart). The starting conditions implicit in eq. (1) are that both oscillators are at rest, one (A) being at the maximum amplitude and the other in the equilibrium position ($x_B = 0$ at $t = 0$).

There are no particular assumptions to be made about the oligomeric protein in order to consider it as a weakly interacting coupled oscillator, other than to provide for small damping. The most relevant aspect of the model is that energy flows cyclically from one active site to the other, so that *a given energy state (conformation) is present in only one subunit at a time. If only one conformation is active, reaction will therefore occur at only one site.* In our analogy with the mechanical oscillator of fig. 1, it is as if one of the two springs at a certain point of the cycle remains frozen in the extended state, so that the other spring is necessarily frozen in the compressed state. As a consequence of release of energy from the occupied site, (for instance upon chemical reaction), the energy can eventually fluctuate back to the other site. In this way, reaction at the "second" site would be rate limited by a chemical event occurring at the "first" site.

3. Further considerations on the model

One point to discuss is whether the extreme simplicity of this model is consistent with the complexity of a chemical system. For instance, in the model of fig. 1, the mass is concentrated in only two points, whereas a protein is characterized by a tridimensional and discontinuous distribution of mass. The motion of waves travelling in a discontinuous tridimensional elastic system, under definite boundary conditions, is extremely complex. Furthermore, it is questionable whether such a complex model is in keeping with the chemical system. We are concerned with the specific

energy transmission which flows from one active site to the other and not with the overall and unspecific vibrational energy of the macromolecule. It is therefore not unrealistic to use a model, as that in fig. 1, in which the flow of energy is "channelled" via particular bonds in a monodimensional pathway.

The use of more complex models would not change the basic alternating behaviour of the energy flow. Let us consider, for instance, a linear array of a very large number of coupled oscillators. In such a system, the perturbation (for instance a longitudinal or a transversal oscillation) propagates from one spring to the next one, and once having arrived at the end of the system, is reflected back (in the presence of suitable boundary conditions) with the same motion characteristics [18]. In this case an element of the system would pass cyclically through a given energy state with a certain period T.

An even more sophisticated model would be a bidimensional lattice of springs. Since for a system of two oscillators in series the elastic constant is $k_s = k_1 k_2/(k_1+k_2)$ and for two oscillators in parallel is $k = k_1 + k_2$, the overall elastic constant for the bidimensional lattice consisting of z rows, will be $k = kz/n$ (where n is the number of elastic elements in each row and all the elements of the lattice are identical). It is easy to verify that for a cubic lattice, as well as for two coupled cubic lattices, the condition of periodic energy flow is maintained.

We can also consider an elastic bar, with a variation of elasticity in the middle (which serves as a coupling between two equal parts, A and A'). In this case, the mass and the elasticity are distributed uniformely in the space. A perturbation wave which originated at an extremity of the bar will propagate with a velocity $v = \sqrt{E/\rho}$, where E is the elastic constant and ρ is the linear density of the bar [28]. If the velocity in the middle region is not too different from v (allowing for instance E and ρ to change by about the same factor), the wave will reach the second extremity and will be reflected back (and so on) with a period $T = 4\ell/v$ (where 2ℓ is the length of the bar). We are thereby achieving condition of an alternation of the energy flux.

It would be interesting to obtain an estimate of the period T characterizing the energy flow from one oscillator to the other. A straightforward solution to this problem, even when neglecting the damping, is not possible at the present, mostly because we do not have precise ideas of the values of the molecular coupling constants which are responsible for the elasticity of the chemical system. In the model of fig. 1 the rough estimation of $T \approx 2\pi\sqrt{km/k_b^2}$ can be obtained by assuming $k = 15\ k_b = 75 \times 10^5$ dyne/cm (5×10^5 dyne/cm is the order of magnitude of the force constant of molecular vibrators) and $m = 4 \times 10^{-20}$ g. We obtain therefore $T \approx 10^{-11}$ sec. For the case of two coupled cubic lattices containing 15 bonds in each row, the elastic constant of each cube is $15\ k_b$ (k_b is the elastic constant of a bond). Assuming $k_b \approx 5 \times 10^5$ dyne/cm, we obtain the same figure as before for the period T. In the case of the elastic bar previously mentioned, one may recall the velocity of wave propagation (for instance sound, or explosion waves) in a solid to be of the order of 4000 m/sec [18]. Considering a system of 40 Å in length, this implies a period $T \approx 4 \times 10^{-12}$ sec (in a liquid column we would have slightly greater values, i.e., $\sim 2 \times 10^{-12}$ sec, and in air $\sim 4 \times 10^{-11}$ sec [18]. These calculated values for the period T have to be seen as lower limits. One can envision the oscillating energy E accompanied by a specific conformational change characterized by an activation energy U larger than E (so that the amount of energy E "helps" in overcoming the energy barrier U). In this case, the appearance of the biologically active conformation might be rate limited by the exponential factor $(U-E)/kT$ and the period T could thereforefore fall in any time range.

Estimating the energy involved in the alternating motion is also of interest. In fig. 3, a rough evaluation is carried out on the basis of the model of fig. 1. Assuming appropriate molecular masses and bond force constants, one finds that the energy involved in the fluctuation should be between 1 and 10 kcal, which is chemically relevant. It is worthwhile to emphasize again that the reliability of such estimates is decidedly affected by the lack of information about the parameters characterizing vibrational energy of proteins.

It is also pertinent to speculate about the chemical nature of the forces which put the system in motion. One can envision two possibilities: (a) the alternating motion is induced by collisions or binding with ligand molecules; (b) the oscillating energy is characteristic of the oligomeric protein per se, namely a

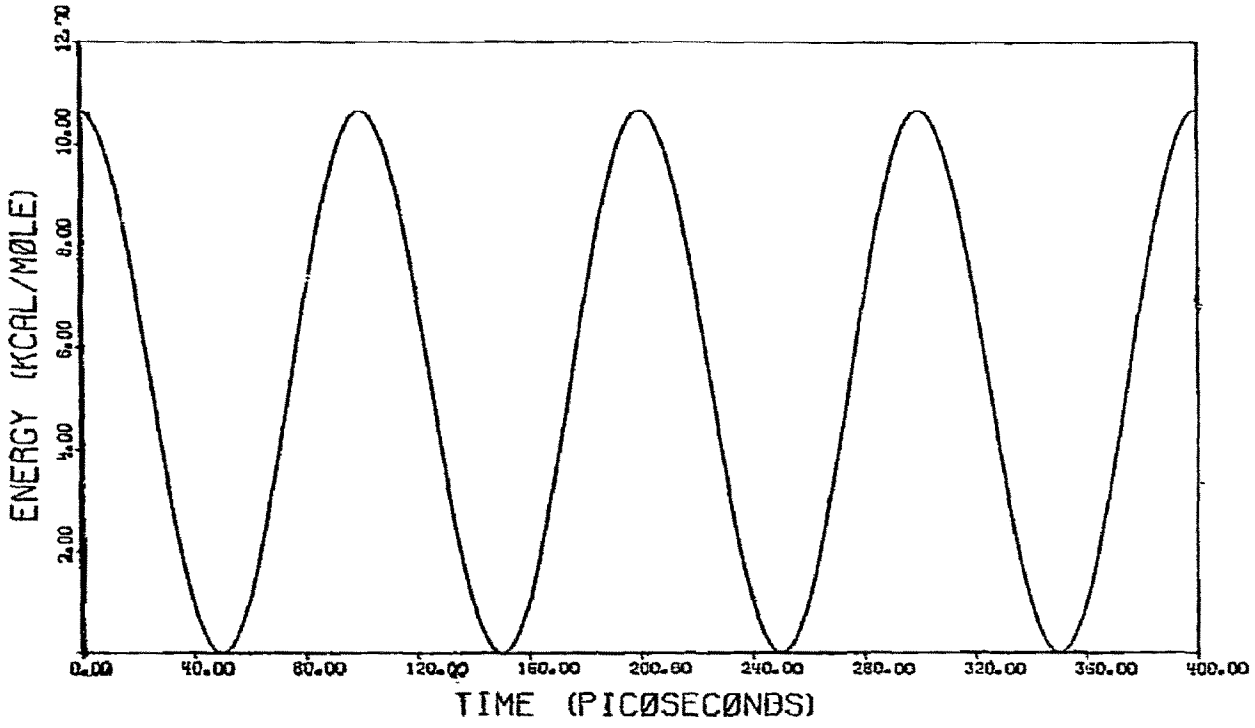

Fig. 3. The oscillating behaviour of the total energy (kinetic + potential) with time of one element of the coupled oscillator. The motion of the other element (not shown for the sake of simplicity) is antiphasic. The total energy of the system of fig. 1 is given by

$$E = \tfrac{1}{2}m(\dot{x}_A^2 + \dot{x}_B^2) + \tfrac{1}{2}k(x_A^2 + x_B^2) + \tfrac{1}{2}k_b(x_A + x_B)^2 \qquad (2)$$

Assuming a weak coupling ($k_b/k \to 0$) the two elements are unequivocally defined and the total energy of A (e.g.) is

$$E_A = \tfrac{1}{2}m_A\dot{x}_A^2 + \tfrac{1}{2}kx_A^2 = \tfrac{1}{2}mA^2\omega_0^2\cos^2\tfrac{1}{2}(\omega-\omega_0)t. \qquad (3)$$

The calculations in the figure have been carried out with $\omega_0 = 2\pi \times 10^{11}\,\mathrm{sec}^{-1}$, $\omega' = 1.1\,\omega_0$, $m = 4 \times 10^{-23}$ kg, $A = 1.0$ Å (with $A = 0.3$ Å one would obtain about 1/10 of such an energy amplitude). In order to obtain the energy in kcal/mol, the dimension factor $6.02 \times 10^{23} \times 10^{-3} \times 10^{-16}/4.18$ is utilized.

mode of existence for part of its internal energy. At the present stage of investigation, detailed analysis of this point (as well as many other questions addressed in this section) is not feasible.

To estimate energy dissipation would only be possible with very detailed models, specifying, for instance, the mass and elastic properties at the boundary between oscillators and environment (other proteic bonds, solvent molecules, etc.).

The model illustrated in fig. 1 can easily be extended to include tetramers. In order to do so, it is necessary to take into account the possible different couplings among the four oscillators (i.e., the symmetry of the subunit interactions). The simplest situation is that in which the oscillators are in a linear arrangement (as in fig. 4a) and the force constants are all equal.

A much more realistic kind of subunit coupling is that illustrated in fig. 4b, in which the tetramer is seen as two dimers coupled by the force constant k'_b, the two elements of a dimeric unit interacting through a force constant k_b. Many types of oscillations of mechanical energy are possible, (depending on the numerical relation between k, k_b, k'_b and on the phase relationship between the motions of the elements). One limiting case is that in which the two "dimers" are independent – k'_b does not allow for energy transmission – and the motions of the two dimers are in phase. This is one possibility to allow for half-of-the-sites reactivity in a tetramer.

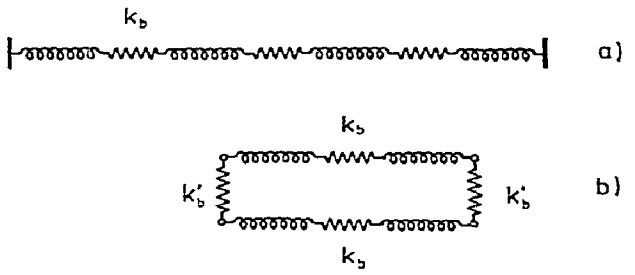

Fig. 4. Two possible mechanical analogs of a tetrameric protein, showing different types of subunit interaction.

4. Discussion

No experimental proof can be provided at the present for the occurrence of the inter-oligomeric energy fluctuation, or of the relevance of this fluctuation to enzyme chemistry. The validity of our model can be verified presently only via its capability of rationalizing sparse experimental observations into a logical scheme, and in terms of its consistency with the accepted views of subunit cooperative interactions. In this regard, we would like to point out the following:

(1) The model provides a logical way to visualize the propagation of energy states – and therefore the transmission of information – within an oligomeric assembly. In this way, the dynamics of cooperativity phenomena are attributed to the general properties of coupled oscillators. The model is sensitive to the basic features of the oligomeric assembly – such as the symmetry and the boundary interactions – which are known to play a fundamental role in cooperativity phenomena [2,29].

(2) The model readily permits a rationalization of the half-of-the-sites reactivity. The difference between enzymes displaying the half-of-the-sites reactivity and the "normal" ones, is that in the latter case the energy fluctuation does not take place (for instance because of the lack of a suitable coupling) or *is not relevant* for the chemical reaction.

(3) Once the hypothesis is accepted, that the oscillating energy is chemically relevant, is tempting to speculate that in the dimer this energy might be twice that existing in the isolated protomer and that this could provide us with a rationale for a possible "advantage" of oligomeric enzymes. In fact, the relatively large amount of energy which accumulates at one time at an active site could be utilized to reach a high activation energy level, which would not be reached in the isolated protomeric subunit. In this regard, one could also consider that most of the enzymes displaying half-of-the-sites reactivity do so with pseudosubstrates or under non physiological conditions. Since in this case, the formation of –E–E–X would very likely require more energy than with the physiological substrate under physiological conditions, one could understand that the enzyme machinery could be blocked at the level of half reactivity.

It may be useful at this point to compare our views with those already existing in the literature on the half-of-the-sites reactivity. We would like to stress again that in this work we have been dealing with *the origin* of the cooperative subunit interaction. The half-of-the-sites reactivity is seen as a *consequence* of our physical model. By contrast, most of the views presented in the literature to explain the half-of-the-sites reactivity or alternating subunit (flip-flop) mechanisms, are concerned with structure models, or structure transitions, independently of the dynamics and of the physical forces from which they originate.

However, we can compare the *results* of our model with some of the structure model description of the half-of-the-sites reactivity. Stallcup, Koshland and Levitzki [1,2] list four possible mechanisms for this phenomenon: (a) a pre-existing asymmetry due to non-identical primary structure of the subunits; (b) a pre-existing asymmetry due to conformational changes induced by the association of the subunits; (c) steric or electronic interactions between adjacent active sites; and (d) negative cooperativity among subunits induced by ligand binding.

The picture we draw from our model is consistent with the mechanism (b), in the sense that a kind of dissymmetry is present in the oligomer. However, we are dealing with a dynamic dissymmetry, as the fluctuating energy (and the corresponding conformational states) flows continuously from one subunit to the other, as shown below:

This dissymetry can be frozen only upon reaction of one of the sites. This reaction may induce a change in reactivity in the other site, due to a modification of the energy distribution within the molecule. But this step – which would correspond to the mechanism (d) of Staalcup and Koshland – is not a required corollary of our model. In other words, no negative cooperativity is required by our model to explain the half-of-the sites reactivity. Actually, any kind of cooperativity (positive, negative, or not at all) may accompany the reaction at the first site, and the consequent temporary block of chemical reactivity. In this sense, our model is not inconsistent with the allosteric models commonly accepted [30,31] to explain non-linear binding.

The last point we would like to discuss, concerns possible experimental proofs for our model. With spectroscopy, one may attempt to measure the frequency of the vibration of a macromolecule. In this regard, Peticolas and coworkers, by utilizing laser Raman spectroscopy, have shown that definite low-frequency motions exist in proteins [32]. In fact, it appears that large protions of the protein molecule are constantly undergoing a measurable coherent periodic vibration. Furthermore, the vibrations are sensitive to the protein conformation [32]. This connection with the experimental work of Peticolas and coworkers gives a more concrete understanding of the harmonic oscillator forces postulated in our model. It remains to be seen whether such motions are sensitive to the oligomeric structure, i.e., whether there is some change from the monomer to the dimer; and whether there are changes produced by going from E–E to –E–E–X or to X–E–E–X.

Further experimental investigations could be carried out to analyze the values of the activation energies characterizing some of these enzymatic reactions. On the basis of these measurements, one may be able to show that when an enzyme displays a normal behaviour with substrate A and a half-of-the-sites reactivity with substrate B, the activation energy is higher in the second case. Finally, data such as those obtained for malic dehydrogenase [6], i.e., half-reactivity in the crystalline state, can be evaluated as an indication of the functional internal asymmetry of the isolated molecule.

Acknowledgements

We are very grateful to the Swiss National Fonds for financial help (Grant Nr. 38500.72). The collaboration of Dr. U. Suter for the computer programs of figs. 2 and 3 is very much appreciated. Suggestions and criticism of W. Block, H. Buc, J. Holbrook, T. Keleti, R. McQuarrie, F. Seydoux, C. Vernon at the early stage of the manuscript have been particularly useful to the authors.

References

[1] A. Levitski, W.B. Staalcup and D.E. Koshland, Jr., Biochemistry 10 (1971) 3371.
[2] W.B. Stallcup and D.E. Koshland, Jr., Biochem. Biophys. Res. Commun. 49 (1972) 1108.
[3] S.A. Bernhard, M.F. Dunn, P.L. Luisi and P. Schack, Biochemistry 9 (1970) 185.
[4] D. Trentham and H. Gutfreund, Biochem. J. 106 (1968) 455.
[5] C. Petitclerc, C. Lazdunski, D. Chappelet, A. Molchin and M. Lazdunski, Eur. J. Bioch. 14 (1970) 30.
[6] E. Hill, D. Tsernoglu, L. Webb and L.J. Banaszak, J. Mol. Biol. 72 (1972) 577.
[7] K. Harada and R.G. Wolfe, J. Biol. Chem. 243 (1968) 4123, 4131.
[8] M.F. Dunn and S.A. Bernhard, Biochemistry 10 (1971) 4569.
[9] P.L. Luisi and R. Favilla, Biochemistry 11 (1972) 2303.
[10] D. Givol, FEBS Letters 5 (1969) 153.
[11] C. Woenckhaus, G. Dietz and E. Schättle, Hoppe-Seyler's Z. Phys. Chem. 354 (1973) 211.
[12] S.A. Bernhard and O.P. Malhotra, J. Biol. Chem. 243 (1968) 1243;
J. Batke, FEBS Letters 2 (1968) 81.
[13] J.S. Franzen, J. Kno, A.J. Eichler and D.S. Feingold, Biochem. Biophys. Res. Commun. 50 (1973) 517.
[14] S. Tate and A. Meister, Proc. Natl. Acad. Sci. US. 68 (1961) 71.
[15] M. O'Leary and F.H. Westheimer, Biochemistry 7 (1968) 913.
[16] M. Lazdunski, Current Topics in Cellular Regulation 6 (1972) 267.
[17] R.A. Cook and D.E. Koshland, Jr., Biochemistry 9 (1970) 3337, 215.
[18] A.P. French, Vibration and waves (Nelson, New York, 1972).
[19] C.W. Oseen, Anal. Phys. 48 (1915) 1.
[20] Chimie macromoleculaire, Vol. 1, ed. G. Champetier (Hermann, Paris, 1970) chap. 4.
[21] J.G. Kirkwood, J. Chem. Phys. 5 (1937) 479.
[22] M. Born, Optik (Springer, Berlin, 1933).

[23] J.J. Hopfield, J. Mol. Biol. 77 (1973) 207.
[24] M.V. Volkenstein, Biofizika 15 (1970) 215.
[25] H. Eyring, R. Lumry and J. Spikes, in: Mechanism of enzyme action, eds. W. McElroy and G. Glass (John Hopkins Univ. Press, Baltimore, 1954) p. 123.
[26] R. Lumry, A. Solbakken, J. Sullivan and L. Reyerson, J. Am. Chem. Soc. 84 (1962) 142.
[27] R. Lumry and R. Biltonen, in: Structure and stability of biological macromolecules, eds. S.N. Timasheff and G.D. Fasman (Marcel Dekker, New York, 1969) p. 146.
[28] C.A. Coulson, Waves (Oliver and Boyd, 1941) chap. 4.
[29] B.W. Matthews and S.A. Bernhard, Ann. Rev. Bioph. 2 (1973) 257.
[30] D.E. Koshland, Jr., G. Nemethy and D. Filmer, Biochemistry 5 (1966) 365.
[31] J. Monod, J. Wyman and J.P. Changeux, J. Mol. Biol. 12 (1965) 88.
[32] K.G. Brown, S.C. Erfurth, E.W. Small and W.L. Peticolas, Proc. Natl. Acad. Sci. US 69 (1972) 1467.

BIOPHYSICAL CHEMISTRY 1 (1974) 367–375. © NORTH-HOLLAND PUBLISHING COMPANY

ULTRASONIC STUDY OF THE KINETICS OF COUNTERION SITE BINDING IN AQUEOUS SOLUTIONS OF POLYELECTROLYTES

R. ZANA and C. TONDRE

C.N.R.S., Centre de Recherches sur les Macromolécules, 67083 Strasbourg-Cedex, France

Received 16 August 1973
Revised manuscript received 2 January 1974

The excess ultrasonic absorption due to counterion binding has been studied as a function of frequency for a series of polysalts in the range 1–150 MHz. All the relaxation spectra can be represented by a relaxation equation with two relaxation terms. The relaxation frequencies appear concentration independent and the relaxation amplitudes seem proportional to concentration. The low frequency relaxation process appears to depend mainly on the nature of the counterion while the high frequency relaxation process seems to be mostly dependent on the nature of the polyion. These results are quite similar to those obtained in ultrasonic studies of ion-pairing in solutions of divalent sulfates. The kinetic model used for the quantitative analysis of these results has been modified for polysalts through introducing the concept of "counterion condensation". In this modified model the excess absorption is assigned to the perturbation by the ultrasonic waves of the equilibria between the three states of hydration of the complex formed by a counterion and that part of the polyion where it is bound. Analytical expressions of the relaxation amplitudes have been derived using classical procedures for this modified kinetic model. In the case of cobalt–polyphosphate (Co–PP), the ultrasonic data together with the results of NMR measurements on either Co^{2+} or Co–PP have been used for the evaluation of the volume changes, the rate constants and the fractions of counterions in the three states of hydration involved in the binding equilibria. The volume changes obtained in this manner depend only slightly on the method of calculation and appear to be consistent with volume changes for outer-sphere and inner-sphere complex formation. These results are discussed.

1. Introduction

In a previous paper [1] the results of measurements of density changes and water proton chemical shift changes upon additions of $CoCl_2$ to aqueous solutions of tetramethylammonium (TMA) salts of various polyelectrolytes have been reported. These measurements have permitted the acquisition of: (1) the total volume changes ΔV^1 upon binding of Co^{2+} by various polyions, and (2) the fraction of Co^{2+} bound by polyphosphates with complete loss of exchangeable water molecules.

On the other hand, owing to the volume changes associated with counterion binding [1–3] in polyelectrolyte solutions, an excess ultrasonic absorption arises when sound waves are propagated through polysalt solutions [4] which may be used to obtain informations on the kinetics of counterion binding equilibria.

The purpose of this paper is to show that ultrasonic data together with the results of density and NMR measurements [1] permit the evaluation of the rate constants and volume changes for the binding equilibria, as well as the fractions of counterions in the three states of hydration of the complex formed by the counterion and the part of the polyion where it is bound. The calculations are based on a kinetic model, similar to that for ion pair formation [5], modified to take into account Manning's concept of counterion condensation [6]. The method has been used for cobalt–polyphosphate (Co–PP) only, because of the large ultrasonic effects found with this salt and the availability of density [1, 7] and NMR data on Co–PP [1, 8], and Co^{2+} [9] solutions.

2. Experimental section

The following compounds were investigated: sodium–

polyethylenesulfonate (Na–PESA), lithium, sodium, potassium, rubidium, manganese and cobalt polyphosphates (Li–PP, Na–PP, K–PP, Rb–PP, Mn–PP and Co–PP). The origin of the polyelectrolytes, the purification procedures and the preparation of the alkali metal polysalts have been previously reported [4, 7].

The Co–PP solution has been obtained by passing a K–PP solution twice through a cation exchange resin prealably saturated with Co^{2+}. The limpid Co–PP solution obtained by filtering off the exchanged solution remained limpid during storage at 5° for several weeks. Atomic spectroscopy showed that the exchange K^+–Co^{2+} was complete to within 0.1%. The concentration of the Co–PP solution has been determined as previously reported [1].

The Mn–PP solution was prepared in the same manner as the Co–PP solution but with a starting K–PP solution about four times more dilute in order to avoid precipitation during the exchange. After concentration by vacuum evaporation an opalescent Mn–PP solution was obtained and studied. This solution could be made limpid through exchanging about 10% Mn^{2+} with TMA^+, by adding a known amount of cationic exchange resin in the TMA form. Ultrasonic absorption measurements performed at frequency 1.68 MHz, where the excess absorption is quite large, showed that this partial exchange resulted in a 4% increase of absorption, which is within the experimental error.

The ultrasonic absorption coefficients α were measured in the frequency range 1–150 MHz at 25°, using

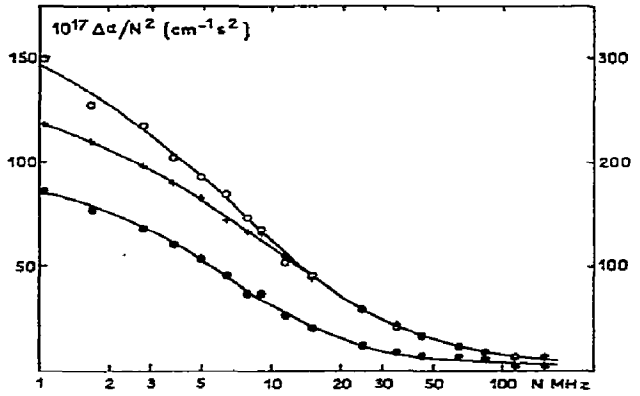

Fig. 1. Ultrasonic relaxation spectra of sodium polyphosphate at 25°. The solid lines represent the curves obeying eq. (2) and best fitting the experimental results (•, o and +). Left scale: $c_{Na-PP} = 0.033N$ (•) and $0.0617N$ (o); right scale: $c_{Na-PP} = 0.107N$ (+).

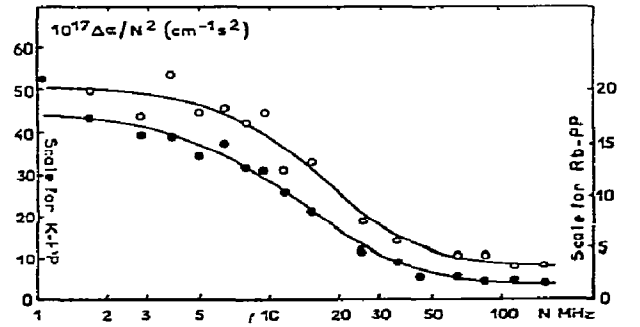

Fig. 2. Ultrasonic relaxation spectra of potassium (•) and rubidium (o) polyphosphates at 25°. The solid lines represent the theoretical curves obeying eq. (2) and best fitting the experimental results (• and o). Left scale: K–PP $0.117N$; right scale: Rb–PP $0.11N$.

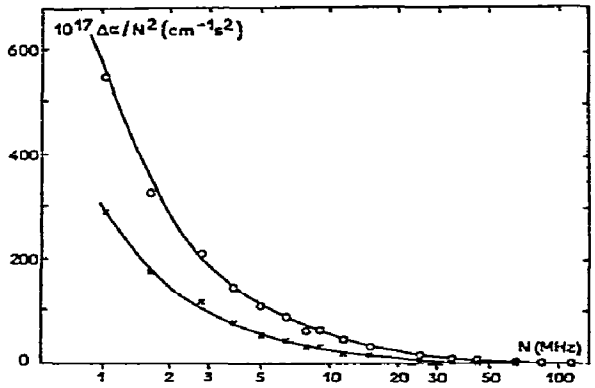

Fig. 3. Ultrasonic relaxation spectra of cobalt polyphosphate at 25°. $c_{Co-PP} = 0.125N$ (o) and $0.068N$ (×). The solid lines represent the curves obeying eq. (2) and best fitting the experimental results (o and ×).

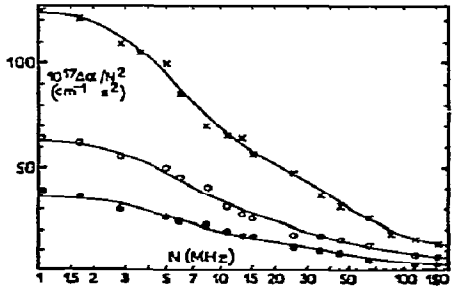

Fig. 4. Ultrasonic relaxation spectra of sodium polyethylenesulfonate at 25°. $c_{Na-PESA} = 0.095N$ (•), $0.19N$ (o) and $0.36N$ (×). The solid lines represent the theoretical curves obeying eq. (2) and best fitting the experimental results (•, o and ×).

ultrasonic interferometry [10] between 1 and 10 MHz and the standard pulse technique [11] at frequencies above 6 MHz. The overall experimental accuracy was ± 3% or ± 2 × 10^{-17} cm^{-1} sec^2 when expressed in terms of $\alpha/(\text{frequency})^2$, whichever the larger.

3. Results and discussion

3.1. Results

Figures 1 to 4 show the variation of the quantity $\Delta\alpha/N^2$, which is defined by eq. (1), as a function of the ultrasonic frequency N for Na–PESA, Na–PP, K–PP, Rb–PP and Co–PP. The results for Li–PP and Mn–PP were similar.

$$\Delta\alpha/N^2 = (\alpha_{C-P} - \alpha_{TMA-P})/N^2. \quad (1)$$

In eq. (1) α_{C-P} and α_{TMA-P} are the ultrasonic absorption coefficients for equimolar solutions of the polyelectrolyte P having the counterions C and TMA respectively. We have shown [4, 12–14] that $\Delta\alpha/N^2$ represents, to a very good approximation, the contribution of counterion site binding to the absorption of the polysalt C–P solution. This was inferred from the following facts: (1) no excess absorption was found in solutions of TMA salts of strong chelating agents [15] or when TMA^+ becomes bound by strong polyions such as PESA [14], PP [2] and polystyrenesulfonate [16], and (2) the excess absorption of polystyrenesulfonic acid [16] and PESA [14] solutions does not change upon neutralization by TMA–OH for the whole range of neutralization degrees.

Each relaxation spectrum was fitted by a relaxation equation having two relaxation terms:

$$\frac{\Delta\alpha}{N^2} = \frac{A_1}{1+N^2/N_1^2} + \frac{A_2}{1+N^2/N_2^2} + B, \quad (2)$$

$$N_{1,2} = (2\pi\tau_{1,2})^{-1}, \quad (3)$$

where τ_1 and τ_2 are the relaxation times, N_1 and N_2 the relaxation frequencies, A_1 and A_2 the relaxation amplitudes, and B a constant. The values of A_1, A_2, N_1, N_2 and B given in table 1 were determined by a trial and error procedure in order to fit the results of figs. 1 to 4 within the experimental accuracy (see section 2) in the whole frequency range. An indication of the accuracy on the values of A_1, A_2, N_1 and N_2 is given by the four sets of values of relaxation parameters for Co–PP 0.125N, which all fit the results within the experimental accuracy, with the second set giving the best fit. The values of the relaxation parameters for the alkali metal polysalts and for Mn–PP are probably less accurate than those of Co–PP.

Table 1
Values of the relaxation parameters

Polysalt	concentration (equiv./liter)	$10^{17}A_2$ (cm^{-1} sec^2)	N_2 (MHz)	$10^{17}A_1$ (cm^{-1} sec^2)	N_1 (MHz)	$10^{17}B$ (cm^{-1} sec^2)
Li–PP	0.115	10	5	30	18	8
Na–PP	0.033	53	4	32	14	3
	0.062	87	3.7	60	19	5.5
	0.107	120	4.5	105	22	10
K–PP	0.117	10	6.5	30	16	4
Rb–PP	0.110	–	–	17	17	3
Mn–PP	0.07	620	1.4	30	12	6
Co–PP	0.068	500	1.05	44	11	1
Co–PP	0.125	700	1.4	70	10	2
		950	1.05	90	10	2
		1500	0.72	100	10	2
		1000	1.05	75	12	2
Na–PESA	0.095	22	5.5	12	45	2.5
	0.19	40	6	[illegible]	40	6
	0.36	75	6	42	50	9

For all of the polysalts but Co–PP the values of B are greater than the experimental error on $\Delta\alpha/N^2$ at high frequencies ($\pm 2 \times 10^{-17}$ cm^{-1} sec^2). This may indicate either the existence of some relaxation process at $N > 100$ MHz or the failure of eq. (1) to correctly represent the contribution of counterion binding at high frequencies when this contribution becomes small and thus comparable to those of other processes [12, 13]. These processes may then make different contributions to the absorptions of equimolar solutions of C–P and TMA–P (see eq. (1)]. In either case the existence of B affects neither the discussion which follows nor the quantitative analysis of the results for Co–PP since in this instance B is close to zero.

3.2. Effect of concentration

Table 1 indicates that for Na–PESA, Na–PP and Co–PP both N_1 and N_2 are, within the experimental error, independent of the polysalt concentration c, expressed in equiv./liter, in the range of concentration investigated in this work. The relaxation amplitudes A_1 and A_2 appear to be nearly proportional to c. These results, i.e., relaxation frequencies independent of polysalt concentration and relaxation amplitudes proportional to concentration, appear to be a very general characteristic of polysalt solutions. Indeed the results of fig. 5 show that for Co–PP solutions $\Delta\alpha/N^2$ is proportional to concentration in the range where the polysalt is soluble. Also in a previous work [12] we have shown that for solutions of lithium salt of carboxymethylcellulose the absorption due to counterion binding is proportional to concentration in the range 0.03 –0.2N. Finally, an identical result has been obtained by other workers [17] for several polysalts. Such results imply that the absorption associated with counterion binding arises from monomolecular processes. It must be pointed out that the above results are strikingly similar to those obtained in ultrasonic absorption studies of ion-pair formation in aqueous solutions of divalent sulfates [18, 19]. The measured excess absorptions were found to be proportional to concentration at $c < 0.2$ M and were analyzed in terms of a multistep process with concentration independent relaxation frequencies.

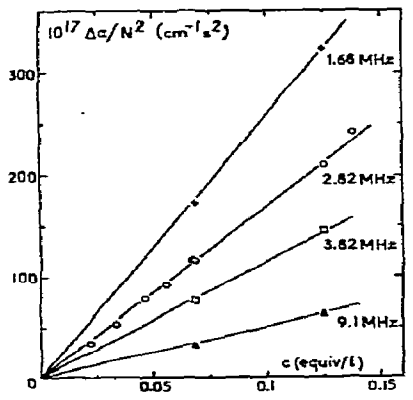

Fig. 5. Cobalt–polyphosphate: variation of $\Delta\alpha/N^2$ with concentration at 25°.

These results can be compared with those of Atkinson et al. [17] on polyacrylic acid and carboxymethylcellulose. An excess ultrasonic absorption proportional to c was observed but a distribution of relaxation frequencies was needed in order to fit the absorption data for monovalent counterions. However, these authors attributed the total excess absorption measured with respect to water to counterion site binding although it is known [2, 12, 13] that for polycarboxylate solutions this quantity also includes contributions of other chemical equilibria. This provides a reasonable explanation for the differences between their results [17] and ours for monovalent counterions. For divalent counterions the data of these authors show two relaxation bands because the contribution of counterion binding is then much greater than that due to other processes. In our work these bands are reduced to two relatively well defined relaxation frequencies because the effects superimposed on counterion binding have been eliminated by using the tetramethylammonium reference.

3.3. Effect of the nature and valency of the counterion

The results given in table 1 show that for polyphosphates the low frequency relaxation process has an amplitude, A_2, very sensitive to the nature of the counterion. These values of A_2 define the same ionic sequence as does the total volume changes upon binding [1, 7] because the relaxation amplitude is proportional to the square of the volume change [5]. On the other hand, the values of N_2 do not depend much on the counterion nature, for counterions with the same valency, and show differences much smaller than expected between monovalent and divalent counterions. The ratio of the

values of N_2 for Co–PP and Mn–PP ranges between 1 and 2 while a ratio close to 9 has been reported for $CoSO_4$ and $MnSO_4$ [19]. Our findings are similar to those of Atkinson et al. [17] who reported comparable mean N_2 values for calcium and magnesium polyacrylates while calcium and magnesium acetates show low frequency relaxation processes very far apart on the frequency scale.

Table 1 also indicates that both A_1 and N_1 depend only slightly on the nature of the counterion as compared to A_2 and N_2.

3.4. Effect of the nature of the polyion

At a given polysalt concentration table 1 shows that the solutions of Na–PP are characterized by values of A_1 and A_2 much greater than those of the Na–PESA solutions. These large differences of relaxation amplitudes reflect the much greater total volume change associated to the binding of Na^+ by PP compared to that of Na^+ by PESA [7]. The comparison between Na–PESA and Na–PP also shows that if N_2 depends only little on the nature of the polyion, N_1 is significantly increased in going from PP to PESA.

The results of sections 3.3 and 3.4 point out that the low frequency relaxation process depends primarily on the nature of the counterion while the high frequency relaxation process depends mostly on the nature of the polyion. The ultrasonic studies of ion-pairing in solutions of divalent sulfates [5, 18, 19] have led to similar conclusions. At this point it is worth recalling that the kinetic models used in the quantitative interpretation of these studies assume either a two-step [18] or a three-step equilibrium [5, 19] and that the authors [5, 18, 19] agree to assign the rate limiting step to the release of water molecules by the metal ion, i.e., to the formation of an inner-sphere complex between the metal ion and $SO_4^=$. Some authors [18] ascribe the high frequency relaxation process to the diffusion encounter of the metal ion and $SO_4^=$ followed by the formation of an outer-sphere complex between these two species, while others [19] split this step into two different ones. The three step model leads to the wrong sign for the volume change for the middle step and for this reason does not appear to be physically sound.

3.5. Kinetic model for counterion site binding

In view of the above results we shall assume that counterion binding equilibria can be represented by:

$$C + P \longrightarrow CP_1 \underset{k_2}{\overset{k_1}{\rightleftharpoons}} CP_2 \underset{k_4}{\overset{k_3}{\rightleftharpoons}} CP_3, \qquad (4)$$

where the CP_i's represent different states of hydration of the complex formed by one counterion C and that part P of the polyion where it is fixed. Only three states appear in eq. (4) because the ultrasonic absorption data in the range 1–155 MHz indicates two relaxation processes. From the data given in table 1 and by analogy with ion-pairing we shall assume that: (1) in state CP_1 the hydration shells of C and P are in contact but still intact, (2) the high frequency relaxation process is associated with the equilibrium $CP_1 \rightleftharpoons CP_2$ and corresponds to outer-sphere complex formation between C and P, and (3) the low frequency relaxation process is associated with $CP_2 \rightleftharpoons CP_3$ and corresponds to inner-sphere complex formation between C and P.

The reaction $C + P \rightarrow CP_1$ has been written as an irreversible reaction in order to include in the above model the effect of counterion condensation [6] which is specific to polyelectrolyte solutions. This effect which is similar to a phase change occurs when the charge parameter ξ is larger than 1. It brings about the "condensation" of part of the counterions on the polyion in order to lower ξ to a value just below 1. The values of the fractions ρ of condensed counterions at infinite dilution, calculated using Manning's theory [6], are generally in very good agreement with the experimental values measured at finite concentration. The condensed counterions exchange probably very rapidly with the "free" counterions. However, at any moment the fraction of condensed counterions is constant and is independent of the polyion concentration if this concentration is not too large [6]. This is thought to be the essential difference between ion-pair formation in solutions of small electrolytes and counterion binding in polyelectrolyte solutions.

It can be shown that condensed counterions identify with those in states CP_1, CP_2 and CP_3. Indeed, in Manning's treatment condensed counterions are those which are close enough to the polyion (considered as a charged thread) as to reduce its electrical charge by a charge equal to that of the condensed counterions.

Therefore, the maximum distance between a condensed counterion and the polyion part where it is condensed must be close to the sum of the radii of the hydrated counterion and polyion site, i.e., close to Bjerrum distance for ion-pair formation. Condensed counterions may therefore be identified with counterions in states CP_1, CP_2 and CP_3 given the above definition of these three states.

4. Theoretical

4.1. Analytical expressions of the relaxation parameters

In reaction (4) the four rate constants k_1, k_2, k_3 and k_4, the three concentrations $[CP_1]$, $[CP_2]$ and $[CP_3]$ and the two volume changes $\Delta V_{21} = \bar{V}_{CP_2} - \bar{V}_{CP_1}$ and $\Delta V_{32} = \bar{V}_{CP_3} - \bar{V}_{CP_2}$ (the symbol $\bar{V}$ refers to partial molal volume at infinite dilution) are unknown. However, several relationships can be derived between these nine quantities.

If c is the counterion concentration (equal to the site concentration since we are dealing with neutral salts), using Manning's fraction of condensed counterions [6], one has

$$\rho c = [CP_1] + [CP_2] + [CP_3]. \tag{5}$$

The use of the mass action law leads to the following eqs., where T is defined by eq. (10):

$$[CP_1] = \rho c k_2 k_4 / T, \qquad [CP_2] = \rho c k_1 k_4 / T,$$
$$[CP_3] = \rho c k_1 k_3 / T. \tag{6}$$

On the other hand, the total volume change ΔV^1 upon binding, obtained from density measurements [1], may be written as follows:

$$\Delta V^1 = \{\Delta V_{21}([CP_2] + [CP_3]) + \Delta V_{32}[CP_3]\}/c. \tag{7}$$

Finally, the methods developed by Eigen [5] and others [20] permit to derive analytical expressions for N_1, N_2, A_1 and A_2 in terms of the rate constants and of the volume changes. The following equations have been obtained (see appendix)

$$\tau_{1,2}^{-1} = 2\pi N_{1,2} = \tfrac{1}{2} S[1 \pm (1 - 4T/S^2)^{1/2}], \tag{8}$$

and

$$A_{1,2} = 1.18 \times 10^{-7} \times \rho c \tau_{2,1}^{-1} \times \frac{(\Delta V^1/\rho - \Delta V_{21} k_1 \tau_{2,1})^2 [T - k_1(S - \Sigma)]}{k_1 [\Sigma \tau_{1,2}^{-2} + T(\tau_{2,1}^{-1} - \tau_{1,2}^{-1} - \Sigma)]}, \tag{9}$$

with

$$T = 1/\tau_1 \tau_2 = 2\pi N_1 . 2\pi N_2 = k_1(k_3 + k_4) + k_2 k_4, \tag{10}$$

$$S = 1/\tau_1 + 1/\tau_2 = 2\pi N_1 + 2\pi N_2 = k_1 + k_2 + k_3 + k_4, \tag{11}$$

and

$$\Sigma = k_1 + k_2. \tag{12}$$

In eqs. (5) to (12) the rate constants are in sec^{-1}, the volume changes in cm^3/equiv., c in equiv./liter and the A's in cm^{-1} sec^2. Equations (8) and (9) show that the model represented by eq. (4) is characterized by concentration independent relaxation frequencies and relaxation amplitudes proportional to c, as experimentally observed.

At this point is must be emphasized that two important problems connected with the fact that we are dealing with polyelectrolyte solutions have been overlooked in the derivation of the relaxation parameters. First, when dealing with counterion–polyion interaction one should use an "effective" concentration of site rather than the stoichiometric concentration [21]. Second, polyions may be considered as small droplets of concentrated solution where activity coefficients differ from the value 1 used in the calculations. However, it is at the present time very difficult to take into account these two problems.

In the case of Co–PP, eqs. (9) contain only three unknown parameters: k_1, Σ and ΔV_{21} since ΔV^1 is known [1]. A third equation which would correspond to an additional result on the system under study is therefore required to solve these equations. We shall now examine the case of Co–PP and see how the results of NMR studies on Co^{2+} [9] or on the binding of Co^{2+} by polyphosphate [1, 8] can be used for the quantitative analysis of the ultrasonic data.

Table 2
Results of the calculations

$10^{17}A_1$ ($cm^{-1}sec^2$)	$10^{17}A_2$ ($cm^{-1}sec^2$)	N_1 (MHz)	N_2 (MHz)	$10^{-7}k_1$ (sec^{-1})	$10^{-7}k_2$ (sec^{-1})	$10^{-7}k_3$ (sec^{-1})	$10^{-7}k_4$ (sec^{-1})	ΔV_{21} (cm^3/mole)	ΔV_{32} (cm^3/mole)	$\frac{[CP_1]}{\rho c}$	$\frac{[CP_2]}{\rho c}$	$\frac{[CP_3]}{\rho c}$
(a)												
70	700	10	1.4	6.2	0.05_5	0.24	0.64	23	4.6	0.006	0.72	0.27
90	950	10	1.05	6.2	0.10	0.24	0.42	22.9	4.4	0.01	0.63	0.36
100	1500	10	0.72	6.1	0.14_5	0.24	0.21	22.3	4.2	0.01	0.47	0.52
75	1000	12	1.05	7.4	0.11	0.24	0.42	22.8	4.3	0.01	0.63	0.36
(b)												
70	700	10	1.4	6.2	0.1	0.52	0.37	22.3	3.4	0.006	0.41	0.58
90	950	10	1.05	6.1	0.17	0.39	0.28	21.9	4.3	0.01	0.41	0.58
100	1500	10	0.72	6.1	0.18	0.27	0.19	21.8	4.4	0.01	0.41	0.58
75	1000	12	1.05	7.4	0.15	0.39	0.27	22.1	3.6	0.01	0.41	0.58

(a) First method of calculation.
(b) Second method of calculation as explained in the text.

4.2. Quantitative analysis of the ultrasonic data relative to Co–PP

First method: the value of the rate constant k_{H_2O} for the exchange of a water molecule between the inner hydration sheath of Co^{2+} and the bulk water is known from NMR studies. The most reliable value of k_{H_2O} appears to be 2.4×10^6 sec^{-1} [9]. On the other hand, Eigen et al. [15] have shown that k_{H_2O} depends only slightly on the nature of the ligand which replaces the water in the inner hydration sheath, in the case of small ligands. This result will be assumed to hold true when the ligand is part of a polyion, as in the present case. Moreover we shall assume that $k_3 = k_{H_2O}$ as was done by others [17]. From eqs. (10) to (12) one obtains

$$k_1 = [\Sigma(\Sigma + k_3 - S) + T]/k_3. \quad (13)$$

Equations (9) and (13) have been solved with the help of a minicomputer using the four sets of values of the relaxation parameters given in table 1 for Co–PP $0.125N$ and the values $\rho = 0.86$ [6] and $\Delta V^1 = 20.8$ cm^3/equiv. [1]. The results of the calculations given in table 2, show that the ΔV's are rather insensitive to the values of the relaxation parameters while the fractions of bound counterions and the rate constants k_2 and k_4 are quite sensitive to these values.

Second method: recent NMR measurements [1, 8] have shown that all of the Co^{2+} ions introduced into a TMA–PP solution lose all of their hydration water, up to a ratio $r = [Co^{2+}]/[TMA–PP]$ of 0.5, while Co^{2+} ions in excess with respect to $r = 0.5$ show only little loss of hydration water. Therefore, the value 0.5 may be considered as equal to the fraction of bound ions involved in inner-sphere complex formation, i.e., in state CP_3 in reaction (4), if we assume that in the NMR experiments the TMA ions present into the PP solution have no influence on the fraction of counterions in state CP_3. This assumption is supported by the fact that the results of fig. 3 in ref. [1] can be obtained by either adding $CoCl_2$ to TMA–PP or mixing Co–PP and TMA–PP. Therefore one can write

$$r = [CP_3]/c = \rho k_1 k_3/T. \quad (14)$$

The combination of eqs. (10) to (12) and (14) yields

$$k_1 = T\Sigma r/\{[\Sigma(S-\Sigma) - T]\rho + Tr\}. \quad (15)$$

The results obtained in solving eqs. (9) and (15) are given in table 2. They do not differ much from those obtained by assuming a known value of k_3. The fractions of bound counterions appear to be independent of the set of values of relaxation parameters used in the calculations.

4.3. Discussion of the results of table 2

The two above methods of analyzing the ultrasonic data yield values of ΔV_{21} much larger than ΔV_{32}. Such a result is to be expected on the basis of recent theoretical considerations [22] on volume changes upon inner-sphere and outer-sphere complex formation. Our results are also in line with those reported for ion-pair formation in solutions of $MnSO_4$ [18]. In this case, ultrasonic measurements, analyzed in terms of a two step model, yielded values of 5 and 1 cm^3/equiv. for ΔV_{21} and ΔV_{32} respectively. The larger volume changes found for Co–PP as compared with $MnSO_4$ are due to the larger electrostriction of PP as compared with $SO_4^=$ (respectively –19.6 [1] and about –5 [23] cm^3/equiv.). A direct comparison of results for Co–PP and $CoSO_4$ would be, of course, preferable. Nevertheless, the comparison between the data for $MnSO_4$ and Co–PP is relevant because the total volume changes for ion pair formation in solutions of divalent sulfates show little dependence on the nature of the counterion [24] and similar values of ΔV_{21} and ΔV_{32} may be expected for $CoSO_4$ and $MnSO_4$.

In the previous [1] NMR-density study the total volume change ΔV^1 upon binding of Co^{2+} to polyphosphate has been split into the individual contributions of Co^{2+} ions and polyion charged sites which were found to be $\Delta V^1_{Co} = 10.3 \pm 1$ cm^3/equiv. and $\Delta V^1_p = 10.2 \pm 1$ cm^3/equiv. One may be tempted to identify ΔV_{32} and ΔV_{21} which are sometimes referred to as the "volume changes for the cation and anion desolvation steps" respectively with ΔV^1_{Co} and ΔV^1_p and wonder about the origin of the large difference which appears between the two sets of values. In fact in doing so one would be comparing physically different quantities. Indeed while ΔV^1_{Co} and ΔV^1_p do represent properties of the individual ions, ΔV_{32} and ΔV_{21} are related with the properties of the inner and outer sphere complexes. The formation of the outer sphere complex CP_2 results in the release of water molecules from the hydration shell of the polyion site and also in a reordering of the hydration shell of the Co^{2+} ion which must involve a sizable volume change, owing to the decrease of electrostatic field in this shell. Thus both the counterion and the site contribute to the formation of the outer sphere complex. The values of ΔV^1_p, ΔV^1_{Co}, ΔV_{32} and ΔV_{21} give the first experimental evidence of this fact which was theoretically predicted by Hemmes [22]. The same reasoning holds for ΔV_{32}.

Table 2 shows that the two methods of analysis yield very similar results when applied to the third set of relaxation parameters. If we now consider the results obtained by the two methods for the second set of parameters, i.e., the set of values best fitting the experimental results of fig. 4, it appears that changing k_3 from 2.4×10^6 to 3.9×10^6 sec^{-1} leads to very different values for the fractions of counterions. This emphasizes the importance of the value of k_3 chosen for the calculations in the first method. Unfortunately the values of k_3 are not accurately known. For instance, values as different as 1.4 and 2.4×10^6 sec^{-1} have been measured in two independent NMR studies [19, 25]. Thus, one can consider that, within the experimental accuracy, the kinetic model given above is consistent with the results of ultrasonic absorption, NMR and density measurements and may therefore represent to a certain extent what is really occurring into polyelectrolyte solutions.

5. Conclusions

The results obtained in this study have shown that the excess absorption associated with counterion binding has the same characteristics as that due to ion-pair formation in solutions of divalent sulfates. They can be quantitatively analyzed using a kinetic model which incorporates the features of the kinetic model for ion pair formation and Manning's theory of counterion condensation. The use of an additional NMR result on either Co^{2+} or Co–PP has permitted for the first time the calculation of the rate constants, the volume changes and the fractions of the three types of bound counterions in the case of Co–PP solutions. The values obtained for the volume changes are consistent with those for outer-sphere and inner-sphere complex formation, i.e., with the kinetic model presented in this work for counterion site binding.

This report however should be only taken as a preliminary one in this field of investigation. Indeed some important problems related with the polymeric nature of the system have been overlooked in the derivation of the expressions of the relaxation amplitudes. However, research in this field should be pursued as such studies may help understanding the more complicated interactions between metal ions and biopolyelectrolytes

such as nucleic acids. More experiments should be performed both in a larger concentration range and with a series of divalent counterions, in order to investigate more thoroughly the effect of the nature of the counterion on the values of N_2 and A_2. Also the frequency range investigated should be extended below 1MHz in order to permit more accurate determinations of N_2 and A_2. A newly developped ultrasonic technique [26] and the relaxation techniques based on fast pressure changes [5] may prove extremely useful.

Appendix

The rate equations for the two step equilibrium (4) are

$$\begin{aligned} dx_1/dt &= -(k_1 + k_2)x_1 - k_2x_3 = a_{11}x_1 + a_{12}x_3, \\ dx_3/dt &= -k_3x_1 - (k_3 + k_4)x_3 = a_{12}x_1 + a_{22}x_3, \end{aligned} \tag{A.1}$$

where x_1 and x_3 represent small changes of $[CP_1]$ and $[CP_3]$. The a_{ij} can be easily identified.

Using the matrix method one readily obtains eq. (9). On the other hand, at 25°

$$A_{1,2} = 1.18 \times 10^{-7}\, \Gamma_{1,2} \Delta V_{1,2}^2 \tau_{1,2}, \tag{A.2}$$

with

$$\Gamma_1 = \left(\frac{1}{\tau_2} - \frac{1}{\tau_1}\right)^2 \left[\left(a_{11} + \frac{1}{\tau_2}\right)^2 \left(\frac{1}{[CP_1]} + \frac{1}{[CP_2]}\right) + \frac{2a_{21}}{[CP_2]}\left(a_{11} + \frac{1}{\tau_2}\right) + a_{21}^2\left(\frac{1}{[CP_2]} + \frac{1}{[CP_3]}\right)\right]^{-1},$$

$$\Gamma_2 = \left(\frac{1}{\tau_2} - \frac{1}{\tau_1}\right)^2 \frac{a_{21}^2}{a_{11}^2} \left[\left(a_{11} + \frac{1}{\tau_1}\right)^2 \left(\frac{1}{[CP_1]} + \frac{1}{[CP_2]}\right) + \frac{2a_{21}}{[CP_2]}\left(a_{11} + \frac{1}{\tau_1}\right) + a_{21}^2\left(\frac{1}{[CP_2]} + \frac{1}{[CP_3]}\right)\right]^{-1},$$

$$\Delta V_1 = \frac{a_{21}\,\Delta V_{32} + \Delta V_{21}\,(a_{11} + 1/\tau_2)}{(1/\tau_2 - 1/\tau_1)},$$

$$\Delta V_2 = -\frac{a_{11}}{a_{21}} \frac{a_{21}\,\Delta V_{32} + \Delta V_{21}\,(a_{11} + 1/\tau_1)}{(1/\tau_2 - 1/\tau_1)}. \tag{A.3}$$

The combination of equations (6)–(8), (10)–(12) and (A.2) and (A.3) yields eqs. (9) which give A_1 and A_2 as a function of Σ, k_1 and ΔV_{21}.

References

[1] P. Spegt, C. Tondre, G. Weill and R. Zana, Biophys. Chem. 1 (1973) 55.
[2] U.P. Strauss and Y. Po Leung, J. Am. Chem. Soc. 87 (1965) 1476.
[3] A. Ikegami, Biopolymers 6 (1968) 431; J. Polymer Sci. A-2 (1964) 907.
[4] C. Tondre and R. Zana, J. Phys. Chem. 75 (1971) 3367.
[5] M. Eigen and L. de Maeyer, Techniques of organic chemistry, Vol. VIII, Part 2 (Interscience, New York, 1963).
[6] G.S. Manning, J. Chem. Phys. 51 (1969) 924, 933 and 3249; Biopolymers 9 (1970) 1543.
[7] C. Tondre and R. Zana, J. Phys. Chem. 76 (1972) 3451.
[8] P. Spegt and G. Weill, Compt. Rend. Acad. Sci. (Paris) C 274 (1972) 587.
[9] A. Chmelnik and D. Fiat, J. Chem. Phys. 47 (1967) 3986.
[10] R.S. Musa, J. Acoust. Soc. Am. 30 (1958) 215.
[11] J. Andreae, R. Bass, E. Heasell and J. Lamb, Acustica 8 (1958) 131.
[12] R. Zana, C. Tondre, M. Rinaudo and M. Milas, J. Chim. Phys., Physicochim. Biol. 68 (1971) 1258.
[13] R. Zana and B. Michels, Proc. 7th Int. Congr. Acoustics, Akademiai Kiado, Vol. 2 (Budapest, 1971) p. 41.
[14] C. Tondre and R. Zana, IUPAC Symposium, Book of Abstracts, Vol. I, Leiden (1970) p. 387.
[15] M. Eigen, Pure Appl. Chem. 6 (1963) 97; 20 (1969) 93.
[16] C. Tondre and R. Zana, unpublished results.
[17] G. Atkinson, E. Baumgartner and R. Fernandez-Prini, J. Am. Chem. Soc. 93 (1971) 6436.
[18] L.G. Jackopin and E.B. Yeager, J. Phys. Chem. 74 (1970) 3766.
[19] A. Bechtler, K. Breitschwerdt and K. Tamm, J. Chem. Phys. 52 (1970) 2975;
K. Tamm, 6th Intern. Congr. Acoustics, Tokyo (1968) paper GP-3-3.
[20] G. Hammes and A. Park, J. Am. Chem. Soc. 90 (1968) 4151.
[21] R.W. Armstrong and U.P. Strauss, Encyclopedia of polymer science and technology, Vol. 10 (Interscience, New York, 1969) p. 781.
[22] P. Hemmes, J. Phys. Chem. 76 (1972) 895.
[23] J. Padova, J. Chem. Phys. 39 (1965) 1552.
[24] F. Fischer and D. Davies, J. Phys. Chem. 69 (1965) 2595.
[25] T.J. Swift and R.E. Connick, J. Chem. Phys. 41 (1964) 2553.
[26] F. Eggers, Acustica 19 (1967) 323.

BIOPHYSICAL CHEMISTRY 1 (1974) 376–380. © NORTH-HOLLAND PUBLISHING COMPANY

HEATS OF DILUTION OF POLYACRYLIC ACID AT VARIOUS DEGREES OF IONIZATION

J. ŠKERJANC
Department of Chemistry, University of Ljubljana, 61000 Ljubljana, Yugoslavia

Received 15 August 1973
Revised manuscript received 22 January 1974

The heats of dilution of polyacrylic acid at four constant degrees of ionization (α = 0, 0.25, 0.50, and 1.00) have been measured in the concentration range 0.6 – 0.002 monomolal. The heat of dilution for pure acid (α = 0) is positive in the investigated concentration range, whereas it is negative for partially neutralized acid (α = 0.25 and 0.50). For completely neutralized acid, for sodium polyacrylate (α = 1), the measured heat effects are exothermic at concentrations above about 0.05 monomolal, while below 0.05 M they become endothermic. The experimental results have been evaluated with the help of a previously developed theoretical treatment based on the cell model.

1. Introduction

Quite recently three papers dealing with the heats of dilution of aqueous solutions of polyacrylic acid have been published [1–3]. In the work of Cartier and Daoust [1] the heats of dilution data for pure acid and for its sodium salt have been reported. Unfortunately, the dilution method and the way, in which the experimental results of these authors are presented, are quite unusual and unsuitable for the interpretation which is usually adopted in the field of simple electrolytes and polyelectrolytes.

In the work of Crescenzi et al. [2] the heat of dilution, ΔH_D, of polyacrylic acid has been presented as a function of the degree of ionization, α, for α's between about 0.05 and 0.6, and in the work of Ise et al. [3] the results of ΔH_D for solutions of sodium polyacrylate (α = 1) are reported. The experimental points in both papers are limited to a very narrow concentration range. Therefore, it seemed justified to extend these measurements to a wider concentration range for various degrees of ionization and thus accumulate more information on the thermal properties of this popular polyelectrolyte.

In this paper we shall present the heats of dilution of polyacrylic acid over a wide range of polyelectrolyte concentration (from about 0.002 to 0.6 monomolal) for four constant degrees of ionization (0, 0.25, 0.50, and 1.00) and shall evaluate these results with the help of a previously developed theoretical treatment [4, 5].

2. Materials and method

As starting material polyacrylic acid, HPA, purchased from K & K Laboratories, Inc. (Plainview, N.Y.) was used. Its molecular weight was around 10 000. Prior to use, an aqueous solution of the acid was exhaustively dialyzed against water. The concentration of the stock solution of HPA was determined by potentiometric titration. Aqueous solutions of the acid of various degrees of neutralization were prepared by adding a corresponding amount of CO_2 free NaOH to the acid solution.

In all experiments double quartz distilled water was used.

In most experiments the same calorimeter and procedure were applied as described previously [5]. A few experiments were also carried out with a LKB 10700-1 flow microcalorimeter.

3. Results and discussion

The heats of dilution, ΔH_D, in the present paper

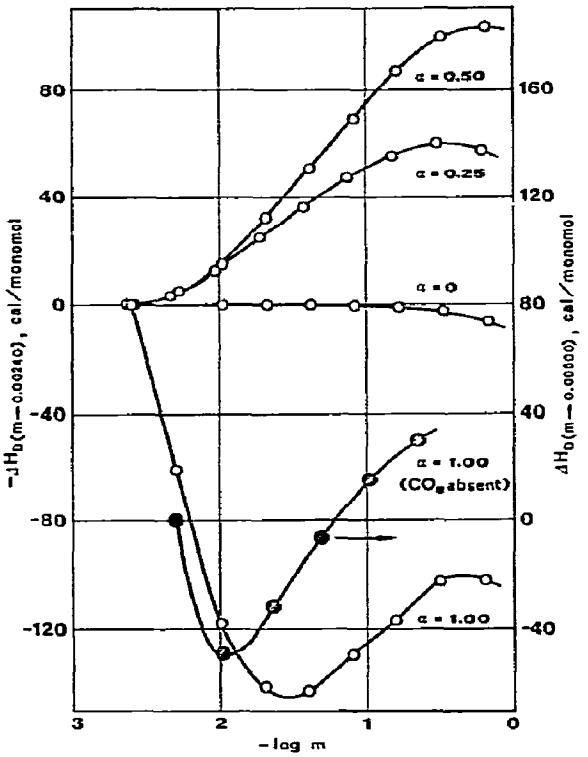

Fig. 1. Enthalpies of dilution of polyacrylic acid in water at 25°C for various degrees of ionization, α, as a function of polyelectrolyte monomolality. The solid circles (ordinate right!) represent experimental values for $\alpha = 1$ obtained in the absence of CO_2.

were obtained in experiments in which approximately the same volumes of a polyelectrolyte solution and water were mixed. The final solution from each experiment was used as the initial solution for the subsequent dilution. By summing up the heat effects accompanying successive dilutions the concentration dependence of ΔH_D over a larger concentration range was obtained.

In fig. 1 the enthalpy of dilution of HPA at 25°C for $\alpha = 0$, 0.25, 0.50, and 1.00 has been plotted against the logarithm of monomolality. ΔH_D is expressed in calories per monomole of polymer. Several interesting features may be deduced from this set of results. First of all it is evident that the experimental values for $\alpha = 0$, 0.25, and 0.50 are in agreement with expectations. Whereas for pure acid ($\alpha = 0$) ΔH_D is practically zero, the enthalpy of dilution of partially neutralized acid ($\alpha = 0.25$ and 0.50) is much larger and has the same characteristic shape as observed previously for Na, K, and Cs polystyrenesulphonates [5]. On the other hand, the shape of the ΔH_D curve for completely neutralized acid, for NaPA ($\alpha = 1$), is quite different. It can be seen that the measured heat effects for NaPA are exothermic at concentrations above about 0.05 monomolal, while below 0.05 M they become endothermic. For this, at first sight unusual behavior, one can find a complete analogy in the field of simple electrolytes. A similar concentration dependence of ΔH_D with a minimum has been found for hydrolyzing electrolytes [6]. The appearance of the minimum has been attributed to the endothermic enthalpy of hydrolysis which is superimposed on the exothermic enthalpy of dilution and which overweights the latter at high dilutions. A curve very similar to the one for NaPA in fig. 1 has been found for sodium acetate with a minimum at about 0.01 M. It is well known that except at very low α polyacrylic acid is a much weaker acid than its simple analog, acetic acid [7]. Thus, the extent of hydrolysis for sodium polyacrylate is even larger than for sodium acetate at the same concentration (the pH of 0.01 monoM NaPA, used in these experiments, was around 9.5 and the pH of 0.01 M Na acetate is around 8.4) and it seems that the same interpretation as for hydrolyzing electrolytes may be applied also in this case. The heat of ionization of acetic acid is of the order of -0.1 kcal mol^{-1} and that of polyacrylic acid at about $\alpha = 1$ is of the order of -1 kcal mol^{-1} [2]. Therefore, the overall heat effect of hydrolysis depends practically only on the energy required for ionization of a corresponding amount of water molecules which take part in the process of hydrolysis ($\Delta H_i \approx 13.3$ kcal mol^{-1} for water). Thus one can explain, at least qualitatively, the shape of the experimental curve below the concentration at which the minimum appears, while above it the curve agrees well with those observed for partially neutralized HPA ($\alpha = 0.25$ and 0.50).

Another factor which may affect considerably the heats of dilution of salts which on hydrolysis give basic solutions, is the presence of residual CO_2 in the solution and in the diluting water. The influence of CO_2 on ΔH_D values has been discussed in detail for solutions of sodium acetate [8].

In order to exclude the influence of absorbed CO_2

we performed a few heat of dilution measurements with solutions of NaPA in which care was taken to assure "CO_2 free" conditions. For this purpose the diluting water and the NaPA stock solution were prepared CO_2 free and a LKB flow microcalorimeter, which enables such conditions, was used for measurements. Results obtained are presented in fig. 1 as solid circles. Because the lowest concentration arrived at in these experiments was higher than in previous ones it was not possible to choose for this curve the same reference point as before. Nevertheless one can make a quantitative comparison of the two curves obtained for $\alpha = 1$ under different conditions. It is evident that the presence of CO_2 lowers the heat effects on dilution between the same initial and final concentrations and also moves the minimum of the ΔH_D curve to higher concentrations, a situation which has been predicted, although experimentally not yet confirmed, for solutions of sodium acetate [8].

It has to be mentioned that the reproducibility of the data obtained with the flow microcalorimeter was not very good, especially not at the lowest concentrations. One of the possible reasons for the scattering of the results is that in some runs the presence of CO_2 was not excluded completely. Therefore the measurements were not extended to lower concentrations.

The influence of CO_2 on heats of dilution of partially neutralized HPA solutions ($\alpha = 0.25$ and 0.50) is practically negligible since these solutions are acid [8].

It has been shown for sodium acetate [6] that the concentration dependence of ΔH_D above the minimum agrees reasonably well with that predicted by interionic attraction theory of Debye and Hückel. Therefore, it would be interesting to see if one can find a satisfactory agreement between theoretical and experimental values above the minimum also in the case of hydrolyzing polyelectrolytes.

For interpretation of the concentration dependence of many thermodynamic properties of solutions of those polyelectrolytes for which the charge effect plays a dominant role, the Lifson–Katchalsky polyion–counterions attraction theory [9], based on the cell model [10], has been applied successfully [11, 12]. On the basis of this theory an expression for the electrostatic enthalpy of a polyelectrolyte solution, H_e, has been derived recently [4, 5]. This expression, generalized for various degrees of ionization, α, and calculated per monomole of polyelectrolyte would read:

$$H_e = \frac{\alpha z_1 RT}{z_2 \lambda}\left[(1+\beta^2)\gamma + \ln\frac{(1-\lambda)^2-\beta^2}{1-\beta^2} + \lambda\right]\left(1+\frac{T}{\epsilon}\frac{d\epsilon}{dT}\right)$$

$$+\frac{\alpha z_1 RT}{2 z_2 \lambda}\left[1-\beta^2-\frac{2\lambda e^{2\gamma}}{e^{2\gamma}-1}\right]\left(\frac{T}{V}\frac{dV}{dT}-2\frac{T}{a}\frac{da}{dT}\right), \quad (1)$$

where z_1 and z_2 are the valencies of the ionized group on the polyion and of the counterion, respectively, γ is a concentration parameter proportional to $-\log c$, β is a constant related to γ and λ, ϵ is the dielectric constant of the solvent, V is the volume of the solution, and a is the distance between the axis of the macromolecular rod and the center of a counterion.

It should be noted that except in the pre-bracket terms, α appears also in the charge-density parameter, λ:

$$\lambda = \alpha z_1 z_2 e_0^2/\epsilon k T b\,, \quad (2)$$

where e_0 is the protonic charge, and b is the distance between the ionizable groups.

Electrostatic enthalpy of the solution, H_e, is related to the enthalpy of dilution by

$$\Delta H_D(m_{In} \to m_{Fi}) = H_e(\gamma_{Fi}) - H_e(\gamma_{In})\,. \quad (3)$$

All other details have been given previously [4, 5].

Eq. (1) has two adjustable parameters, λ and $d\ln a/d\ln T$. The first one, λ, is the principal parameter of the cell theory. It appears in theoretical expressions for all thermodynamic properties and usually has to be properly adjusted in order to bring theory and experiment into agreement. Thus a purely empirical parameter, not subject to independent evaluation, is incorporated into theory. It is found that the ratio between this empirical λ ($\lambda_{effective}$) and the structural λ, given by eq. (2), is always $\lambda_{effective}/\lambda_{structural} \geq 1.0$ and further, that this ratio is proportional to the extent of coiling of the polyion. So it is found that the ratio $\lambda_{effective}/\lambda_{structural}$ is 1 for the truly rod-like polyelectrolyte DNA [13], 1 to 1.3 for rather stiff polystyrenesulphonic acid [4, 14, 15], close to 1.5 for carboxymethylcellulose [16], and appears to have a higher value, of about 2, for flexible-chain polyelectrolytes, polyphosphates, polymethacrylates, and polyacrylates [16]. The possible reasons for the deviation of the effective value of λ from the structural one is discussed by Katchalsky et al. [16]. They

suggest that these larger effective values of λ may be consequence of macroion coiling ($b_{effective} < b_{structural}$), or of lower effective dielectric constant ($\epsilon_{effective} < \epsilon_{H_2O}$), or a combination of these effects. Naturally, one will accept this qualitative explanation and the above procedure of rationalizing the experimental values only if the same, or at least approximately the same, value of λ will satisfactorily explain experimental data of different thermodynamic properties for a given polyelectrolyte. Comparison of theoretical and experimental osmotic coefficients has shown [16], as mentioned already, that "the best fit" λ for polyacrylates is larger by a factor of 2 than the structural one, given by eq. (2) ($\lambda_{effective} = 2\lambda_{structural} = 5.66\,\alpha$). In accordance with the above, this value of λ was used in the present calculations.

The coefficient $d \ln a/d \ln T$ was assumed to be, in the first approximation, negligible and set equal to zero. The value 5 Å was taken for the macromolecular radius, a, needed for obtaining the relation between γ and concentration [9]. It was estimated from structural data on polyacrylates. For b, the distance between the ionizable groups (i.e., —COOH groups) in a macromolecule, the value 2.52 Å, typical for vinylic polyelectrolytes, was used and for parameters characteristic for the solvent, the values for water at 298.15°K were used [17].

In fig. 2 the experimental enthalpies of dilution of HPA are compared with those predicted by theory. The "CO_2 free values" are plotted for $\alpha = 1$. A reasonable agreement between theory and experiment can be seen over much of the concentration range. At high concentration, however, a negative deviation from the theoretical prediction occurs. Such a situation has also been observed with alkali [5] and alkaline-earth [18] polystyrenesulphonates and the reason for these deviations has been attributed to the increasing noncoulombic interactions among ions at high concentration. Polymer–polymer interactions, which are reflected in the endothermic enthalpy of dilution of pure polyacrylic acid ($\alpha = 0$), represent one part of these interactions. One can also notice that disagreement between theoretical and experimental heats of dilution appears at lower concentrations for $\alpha = 0.25$ than for $\alpha = 0.50$ and 1.00. This is not surprising, since it is well known [9] that at such low degrees of ionization the cell model is only roughly applicable.

Comparison of our ΔH_D values with those published

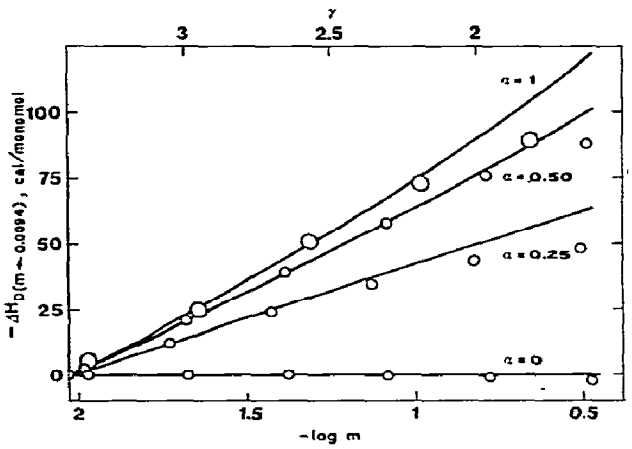

Fig. 2. Comparison of the experimental enthalpies of dilution of polyacrylic acid in water (points) with those predicted by theory (lines).

previously shows that our values agree with those of Crescenzi et al. [2] to within a few percent, whereas the values of Ise et al. [3] for $\alpha = 1$ are somewhat larger than our "CO_2 free" values. Also the interpretation of the experimental results given by the latter authors differs from that in this paper. For the theoretical interpretation of their data Ise et al. used the same eqs. (1) and (3). They found a reasonable agreement between experimental and calculated values by using the structural value of λ and an unusually large value of the coefficient $d \ln a/d \ln T$. Thus, they ignored the fact that experimental osmotic coefficients of NaPA can be explained by the cell model only if an empirical λ, which is 2 times larger than the structural one, is used in the calculations [16]. It has to be emphasized that λ is the only possible adjustable parameter in the theoretical equation for the osmotic coefficient [9]. Therefore, and also for the reasons discussed before, we used in the calculations λ obtained from osmotic coefficient measurements. As noted above this λ satisfactorily explains also the concentration dependence of ΔH_D of HPA for all degrees of ionization studied.

Acknowledgement

I am greatly indebted to Professor V. Crescenzi,

University of Trieste, Italy, for permission to perform part of the calorimetric measurements in his laboratory. I also with to express my thanks to Professor D. Dolar for reading and commenting on the manuscript.

This study was supported by the Boris Kidrič Fund and by the Federal Fund for Scientific Work.

References

[1] J.P. Cartier and H. Daoust, Can. J. Chem. 49 (1971) 3935.
[2] V. Crescenzi, F. Quadrifoglio and F. Delben, J. Polym. Sci. Part A-2 10 (1972) 357.
[3] N. Ise, K. Mita and T. Okubo, J.C.S. Faraday I 69 (1973) 106.
[4] J. Škerjanc, D. Dolar and D. Leskovšek, Z. Physik. Chem. (Frankfurt am Main) 56 (1967) 207.
[5] J. Škerjanc, D. Dolar and D. Leskovšek, Z. Physik. Chem. (Frankfurt am Main) 70 (1970) 31.
[6] E. Lange, in: The structure of electrolytic solutions, ed. W.J. Hamer (John Wiley, New York, 1959) pp. 147–149.
[7] R.W. Armstrong and U.P. Strauss, in: Encyclopedia of polymer science and technology, Vol. 10, eds. H.F. Mark, N.G. Gaylord and N.M. Bikales (Interscience, New York, 1968) p. 823.
[8] D. Leskovšek, Vestnik SKD 11 (1964) 41, 47.
[9] S. Lifson and A. Katchalsky, J. Polym. Sci. 13 (1954) 43.
[10] R.M. Fuoss, A. Katchalsky and S. Lifson, Proc. Natl. Acad. Sci. USA 37 (1951) 579;
T. Alfrey, Jr., P.W. Berg and H. Morawetz, J. Polym. Sci. 7 (1951) 543.
[11] A. Katchalsky, in: International symposium on macromolecules, ed. M.J. Voorn (Butterworths, London, 1971) p. 327.
[12] D. Dolar, Thermodynamic properties of polyelectrolyte solutions, presented at Advanced Study Institute on Charged and Reactive Polymers, Forges-les-Eaux, June 1972, to be published.
[13] H.E. Auer and Z. Alexandrowicz, Biopolymers 8 (1969) 1.
[14] D. Dolar and H. Leskovšek, Makromol. Chem. 118 (1968) 60.
[15] D. Kuzak, J. Kristan and D. Dolar, Z. Physik. Chem. (Frankfurt am Main) 76 (1971) 85.
[16] A. Katchalsky, Z. Alexandrowicz and O. Kedem, in: Chemical physics of ionic solutions, eds. B.E. Conway and R.G. Barradas (John Wiley, New York, 1966) pp. 299, 309.
[17] H.S. Harned and B.B. Owen, The physical chemistry of electrolytic solutions, 3rd Ed. (Reinhold, New York, 1958) p. 161.
[18] J. Škerjanc, S. Hočevar and D. Dolar, Z. Physik. Chem. (Frankfurt am Main) 86 (1973) 311.

BIOPHYSICAL CHEMISTRY 1 (1974) 381–386. © NORTH-HOLLAND PUBLISHING COMPANY

THERMODYNAMIC AND KINETIC PARAMETERS OF AN OLIGONUCLEOTIDE HAIRPIN HELIX

Dietmar PÖRSCHKE

Max-Planck-Institut für biophysikalische Chemie, 34 Göttingen, Germany

Received 31 July 1973
Revised manuscript received 5 November 1973

The thermodynamics of the hairpin helix–single strand transition of $A_6C_6U_6$ has been analyzed by a staggering zipper model with consideration of single strand stacking. This analysis yields an enthalpy change of +11 kcal/mole for the formation of a first, isolated base pair. The stability constant of a first (intramolecular) base pair in $A_6C_6U_6$ is around 2×10^{-5} at 25°C, whereas a first (intermolecular) base pair in an $A_6 \cdot U_6$ helix is characterised by a stability constant of about $4 \times 10^{-3} M^{-1}$ (25°C, extrapolated from $A_n \cdot U_n$ oligomer measurements). These data indicate a destabilizing effect of the C_6 loop.

The rate constant of hairpin helix formation is 2 to 3×10^4 sec^{-1} associated with an activation enthalpy of +2.5 kcal/mole. The rate of helix dissociation of the $A_6C_6U_6$ hairpin is in the range of 10^3 to 10^5 sec^{-1} with an activation enthalpy of 21 kcal/mole. A comparison with the kinetic parameters obtained for A • U oligomer helices shows a specific influence of the C_6 loop due to the stacking tendency of the cytosine residues. This influence is preferentially reflected in the relatively low value of the rate constant of helix formation.

1. Introduction

Hairpin helices are common elements in the secondary structure of nucleic acid chains [1–3]. Thus the knowledge of both thermodynamic and kinetic parameters of hairpin helices is important for an understanding of nucleic acid structure and function. Some hairpins have been analyzed previously [4–9]. The hairpin helix formed from $A_6C_6U_6$ (and from corresponding model nucleotides) is particularly suitable for investigation, since both thermodynamic and kinetic parameters of double helices formed from short A- and U-oligomers are known in detail. Thus the specific contribution of the loop structure may be evaluated quite accurately. In the present investigation the treatment of $A_6C_nU_6$-loop thermodynamics given by Uhlenbeck et al. [8] is extended by consideration of single strand stacking. Furthermore fast relaxation measurements have been performed, which allow additional insight into the nucleation process.

2. Materials and methods

$A_6C_6U_6$ was kindly supplied by O.C. Uhlenbeck. Melting curves were obtained as described previously [10]. The kinetics were investigated using a fast temperature jump technique developed by Hoffman [11]. The samples were heated in microcells of 5 mm optical pathlength containing about 100 λ of solution. Usually temperature jumps of 4.2°C were applied. The relaxation times (given in table 1) are mean values obtained from 3 to 4 jump experiments for each set of conditions, and are accurate to about ± 15%. The accuracy of the thermodynamic parameters evaluated by a least squares fitting procedure is about ± 10%.

3. Results

3.1. Thermodynamics

The absorbance temperature profile for $A_6C_6U_6$

Table 1
Thermodynamic parameters of helix nucleation

		ΔH (kcal)	ΔS (e.u.)	Stability constant (25°C)
First base pair in $A_6C_6U_6$	($\beta_L s_{AU}$)	+10.9	+15.4	2.3×10^{-5}
First base pair in $A_n \cdot U_n$	($\beta_{AU} s_{AU}$)	−3.3	−21.7	$4.4 \times 10^{-3}\,M^{-1}$
Partial nucleation parameters of the C_6 loop	(β_L/β_{AU})	+14.2	+37.1	5.2×10^{-3} M

in 1 M NaCl, 0.05 M Na-cacodylate pH 6.9 obtained in the present investigation is identical to the one given by Uhlenbeck et al. [8]. Thus a difference in the evaluated parameters is due to a difference in the data treatment. The basis for the elucidation of thermodynamic parameters from absorbance measurements has been discussed previously [8]. In the present investigation the absorbance corresponding to the coil form has been obtained by extrapolation of the absorbance values measured at temperatures above the cooperative transition to the region of the helix–coil transition. The absorbance of the hairpin helix was assumed to be independent of the temperature (providing that the six cytosine residues do not have much conformational freedom within the loop and thus do not show any considerable temperature dependence of the absorbance).

Fitting of the $A_6C_6U_6$ absorbance data according to an all or none model, with the enthalpy change ΔH_t, entropy change ΔS_t and the hypochromicity h as adjustable parameters, lead to results similar to those given by Uhlenbeck et al. [8] ($\Delta H_t = -18.3$ kcal/mole, $\Delta S_t = -61.7$ e.u., h (= absorbance of hairpin helix)/(absorbance of the coil at 50°C) = 0.83).

These thermodynamic parameters allow a reasonable description of the conformational transition in $A_6C_6U_6$. However, an accurate analysis of the conformational transition, in particular an analysis of the nucleation process requires a more detailed description. Among the different effects that influence the conformation of $A_6C_6U_6$, the stacking equilibrium in the single strands is very important. A simple calculation shows that the single strand stacking equilibrium will contribute considerably to the free energy change. For the free energy change of A · U base pair formation the term due to coupling of the adenylic acid stacking equilibrium is given by [12]

$$RT \ln\{1 + \exp[-(\Delta H_A - T\Delta S_A)/RT]\},$$

where ΔH_A and ΔS_A are the enthalpy and entropy changes associated with the stacking reaction of adenylic acid residues. Using the thermodynamic data evaluated previously [12] ($\Delta H_A = -7900$ cal/mole, $\Delta S_A = -25.5$ e.u.), this free energy term is around 1 kcal at 0°C. The enthalpy of A · U base pair formation given at 78°C (T_m value of poly A · poly U in 1 M salt) will be different by about 4 kcal at 0°C. Thus the single strand stacking equilibrium should not be neglected, if meaningful thermodynamic parameters are to be evaluated.

The present evaluation is based upon a set of thermodynamic parameters, which has been derived from polymer data and has proved successful in the description of melting curves over a range of chain lengths going from polymers down to helices with 8 base pairs [12]. The equilibrium constant for formation of a single A · U base pair adjacent to a helix s_{AU} is calculated according to

$$s_{AU} = \exp(-G_{AU}/RT),$$

$$\Delta G_{AU} = \Delta H_{AU} - T\Delta S_{AU} + RT \ln\{1 + \exp[-(\Delta H_A - T\Delta S_A)/RT]\},$$

where ΔG_{AU}, ΔH_{AU} and ΔS_{AU} are the free energy change, enthalpy change and entropy change for the formation of A · U base pairs adjacent to a preexisting helix in the absence of stacking in the adenylic acid single strand ($\Delta H_{AU} = -10.9$ kcal/mole, $\Delta S_{AU} = -30.7$ e.u.).

The nucleation process is described by a nucleation parameter β_L, with the product $\beta_L s_{AU}$ assigning the stability constant of a first isolated base pair. β_L is calculated according to

$$\beta_L = \exp(-\Delta G_L/RT),$$

$$\Delta G_L = \Delta H_L - T\Delta S_L - RT \ln\{1 + \exp[-(\Delta H_A - T\Delta S_A)/RT]\},$$

where ΔH_L and ΔS_L are the nucleation enthalpy and entropy. Note, that the stacking correction term cancels for the first base pair (cf. ref. [12]). Intermediate helical species were considered according to a staggering zipper model. Any dependence of the nucleation parameter upon the loop size has not been considered, since reliable information about this dependence is not available. A prediction according to a gaussian distribution will not be reliable in the present case, since single strand stacking seems to be a critical factor in the loop conformation.

ΔH_L, ΔS_L and the hypochromicity were fitted to the experimental data yielding the following values: $\Delta H_L = 21.8$ kcal/mole, $\Delta S_L = 46.1$ e.u. and $h = 0.81$. The resulting thermodynamic parameters for the formation of a first, isolated base pair are presented in table 1 together with some comparable parameters for the helix initiation in oligo A · oligo U helices.

3.2. Kinetics

The relaxation signal observed in temperature jump experiments with $A_6C_6U_6$ exhibits two different relaxation phases. A fast relaxation process appears at times shorter than 1 μsec and mainly reflects the single strand stacking reaction [13]. The amplitude of this process increases with increasing temperature. The second process is observed in the time range of 5 to 50 μsec. Its amplitude shows maximal values around 20°C (the T_m of the hairpin helix). The relaxation time is independent of the nucleotide concentration, but depends very much upon the temperature (cf. table 2). Obviously this relaxation time represents the helix–coil transition of the hairpin. The kinetics of this transition may be conveniently described by using an all or none formalism

$$\text{Hairpin} \underset{k_D}{\overset{k_R}{\rightleftharpoons}} \text{Coil},$$

with the relaxation time

$$1/\tau = k_R + k_D .$$

Thus the rate constants k_R and k_D can be readily evaluated using the all or none stability constant $K = k_R/k_D$ (cf. table 2). Arrhenius plots of the rate constants yield the following enthalpies of activation:

Hairpin formation: $AE_R = 2.5$ kcal/mole,

Hairpin dissociation: $AE_D = 21$ kcal/mole .

Table 2
Kinetic parameters of the $A_6C_6U_6$ hairpin helix–coil transition (in 1 M NaCl, 0.05 M Na-cacodylate pH 6.9)

T (°C)	τ (μsec)	K "all or none"	k_R (sec^{-1})	k_D (sec^{-1})
4.2	46	8.7	2×10^4	2.2×10^3
14.2	34	2.7	2.2×10^4	7.9×10^3
24.2	20	0.93	2.4×10^4	2.6×10^4
34.2	7.5	0.34	3.4×10^4	1.0×10^5

4. Discussion

4.1. Thermodynamics

The thermodynamic parameters obtained in the present investigation support the conclusion of Uhlenbeck et al. [8], that helix nucleation in the $A_6C_6U_6$ hairpin is associated with a positive enthalpy change. However, the magnitudes of the thermodynamic parameters obtained for the nucleation process are quite different. The rather high enthalpy for the formation of a first base pair (21–24 kcal/mole) reported by Uhlenbeck et al. [8] has been explained by an unstacking reaction of cytosine residues in the hairpin loop. Thus the influence of the single strand stacking potential has been recognised but has not been directly considered in the data evaluation. The present results demonstrate that the thermodynamic potential due to single strand stacking has a great influence in quantitative data evaluation.

In a comparison of the nucleation parameters obtained for $A_6C_6U_6$ with those derived for $A_n \cdot U_n$ oligomer helices [12] (table 1) it should be noted that the $A_6C_6U_6$ nucleation proceeds intramolecularly whereas the $A_n \cdot U_n$ nucleation is an intermolecular process. Moreover the $A_6C_6U_6$ nucleation parameters were obtained in 1 M salt, whereas those for

$A_n \cdot U_n$ were measured in 0.05 M salt. Nevertheless the "partial quantities" obtained by subtraction of the enthalpy changes (and entropy changes resp.) evaluated for the $A_6C_6U_6$ and the $A_n \cdot U_n$ nucleation (cf. table 1) will reflect the specific contribution of the C_6 loop to the nucleation process in $A_6C_6U_6$. These "partial quantities" are rather similar to the thermodynamic parameters obtained for the dissociation of single strand stacks [14], suggesting the dissociation on average of about two cytosine stacks in the hairpin loop formation.

The overall thermodynamic stability of the $A_6C_6U_6$ hairpin helix may be compared to that of an $A_6 \cdot U_6$ double helix. Certainly the T_m value of an $A_6 \cdot U_6$ double helix at a strand concentration of 10^{-4} M is lower than that of the $A_6C_6U_6$ hairpin helix. However, if the stability constant of an $A_6 \cdot U_6$ double helix at 1 M salt is extrapolated from previous oligomer measurements [12], a value of about 200 M^{-1} is obtained at 25°C. Thus a solution containing 10^{-2} M A_6 and U_6 will exhibit the same T_m as the $A_6C_6U_6$ helix. This comparison illustrates, that the "effective local concentration" of the complementary sites in $A_6C_6U_6$ is lower than might be expected. This is due to the specific stacking effect of the C_6 loop (cf. discussion of the recombination rate constant).

4.2. Kinetics

The nucleation process may be further characterised by an analysis of the kinetic parameters. As has been shown previously [13] the value of the activation enthalpy may be used to elucidate the number of base pairs required for helix nucleation. The helix nucleus is defined as the smallest helix species, to which addition of a further base pair is faster than the dissociation of a base pair at the helix end. According to this definition the nucleus formation is the rate determining step in the helix formation. The analysis of nucleation may be performed by consideration of the following different kinetic models:

(1) If the formation of the first base pair is the rate determining step in helix formation, i.e., $k_R = k_{01}$, the rate constant for the formation of the second base pair k_{12} should be higher than that for the dissociation of the first base pair k_{10}. A simple calculation using the stability constant of the first base pair $K_{01} = 2 \times 10^{-5}$ and the rate constant of recombination $k_R = 2 \times 10^4$ sec^{-1} yields for k_{10} a value of 10^9 sec^{-1}. This rate constant is much higher than that expected for base pair addition k_{12}, which has been determined previously from oligomer measurements [13] to be around 10^7 sec^{-1}. Thus the formation of the first base pair cannot be the rate determining step, although the value of the activation enthalpy measured for $A_6C_6U_6$ helix formation, $AE_R = 2.5$ kcal/mole, would be consistent with such a mechanism.

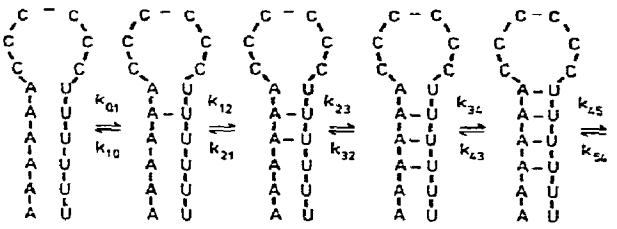

Fig. 1. Schematic representation of the hairpin helix formation in $A_6C_6U_6$.

(2) Because of the rather high positive enthalpy change for the formation of the first base pair, $\Delta H_{01} = 10.9$ kcal/mole, a mechanism assuming nucleation in the second step of base pair formation is not consistent with the experimental activation enthalpy.

(3) If formation of the third base pair is assumed to be rate determining, the activation enthalpy is given by the reaction enthalpy for the formation of a two base pair helix $\Delta H_{02} = \Delta H_{01} + \Delta H_{12} = 10.9 - 6 = 4.9$ (kcal/mole) increased by the activation enthalpy (2 to 3 kcal/mole) for the formation of the third base pair. Thus the activation enthalpy calculated for this mechanism is still higher than the experimental value.

(4) The enthalpy of activation calculated for a mechanism assuming that formation of the fourth base pair is the rate determining step is given by $AE_R = \Delta H_{01} + \Delta H_{12} + \Delta H_{23} + AE_{34} \rightarrow 10.9 - 6 - 6 + (2 \text{ to } 3) \rightarrow (1 \text{ to } 2)$ (kcal/mole). This value is quite close to the experimental value and thus it may be concluded, that the formation of the fourth base pair is the rate determining step in the $A_6C_6U_6$ hairpin helix formation.

As has been discussed for the nucleation of $A_n \cdot U_n$ helices, the nucleation length observed in $A_6C_6U_6$ implies, that a correct description of the nucleation process requires more than one nucleation parameter, namely β_1 for the first base pair, β_2 for the second,

and β_3 for the third, such that the product $\beta_1\beta_2\beta_3$ is equal to β_L.

The rate of nucleation in the $A_6C_6U_6$ hairpin helix $k_R = 2$ to 3×10^4 sec^{-1} is rather low compared with the nucleation rate observed in $A_n \cdot U_n$ oligomer helices [13] ($k_R \approx 10^6$ M^{-1} sec^{-1} at 0.05 M salt; estimated to be around 10^7 M^{-1} sec^{-1} in 1 M salt). Obviously this low rate constant is correlated to the low value of the nucleation parameter. The low nucleation rate may be explained by the conformation of the $A_6C_6U_6$ nucleotide. Both the adenosine and the cytidine residues are characterized by a strong stacking tendency which leads to the formation of a single stranded helical structure. In this structure the contact between the complementary adenine and uracil bases is inhibited. Thus the helix nucleation is dependent upon the dissociation of at least one stacked pair. This preequilibrium will reduce the rate of helix nucleation, as is demonstrated by the experimental rate constants.

In a comparison of the dissociation rate constants, it is quite interesting to observe that the dissociation rate of the $A_6C_6U_6$ loop is rather similar to that expected for a $A_6 \cdot U_6$ double helical complex. Extrapolation of the dissociation rates measured for higher oligomer helices [13] to the hexamer helix leads to values between 10^4 and 10^5 in the range of 0 to 20°C in 0.05 M salt. Evidence has been obtained previously that the dissociation rate of short oligomer helices is almost independent of the ionic strength [15] (whereas a strong ionic strength dependence is observed for the recombination rates). Thus, the comparison demonstrates that the specific influence of the loop is not reflected in the dissociation rate, but is preferentially indicated in the rate constants of hairpin helix formation.

4.3. Comparison of different loops

The present investigations suggest that the thermodynamic and kinetic properties of hairpin helices specifically depend upon the structure of the loop. Due to this specific influence it will be rather difficult to predict the properties of different hairpin helices accurately. For instance, the nucleation parameter of a $A_6(CUC_4)U_6$ hairpin is probably quite different from that found in $A_6C_6U_6$, since the U residue may allow free rotation of the nucleotide chain within the loop.

In spite of the specific properties of some loops a close correspondence of the properties of different loops is reflected in the rate constants. Among the loops that have been analysed to date, all rate constants of hairpin formation, measured in the temperature range of the conformational transition, are around 1 to 5×10^4 sec^{-1}. This includes hairpins of widely different thermodynamic stabilities, such as a hairpin helix containing 4 GC base pairs (which melts at 84°C) [7], hairpin helices containing mixed AU and GC pairs (melting at 58 or 70°C) [5], the present hairpin helix with AU base pairs exclusively and also hairpin helices formed from oligouridylic acids (melting around 5°C) [6]. The rate of loop formation k_R is determined by the rate of helix nucleation, which is given as the product of a pre-equilibrium constant $\kappa\beta s^\nu$ and a rate constant of base pair formation k_f

$$k_R = (\kappa\beta s^\nu) k_f ,$$

where ν is the number of base pairs in the preequilibrium complex and $\nu+1$ corresponds to the "nucleation length" and κ is a statistical factor describing the number of possible nucleus arrangements. The rate constant of base pair formation (adjacent to preformed base pairs) is probably associated with a relatively low positive activation enthalpy. Thus the value of k_f is probably similar for the different hairpin helices. Accordingly the preequilibrium constants $\kappa\beta s^\nu$ seem to be almost identical for the different hairpin helices in the temperature range of their conformational transition. A low nucleation parameter β may be compensated either by a high chain growth parameter s or by an increased number of base pairs ν in the preequilibrium complex. Although the value of k_R is quite similar for different hairpin helices, the nucleation process, e.g., the number of base pairs within the nucleus, may be different. Differences in the nucleation processes may be indicated by the corresponding activation enthalpies. Actually the activation enthalpies for loop formation are quite different in the various loops analyzed to date, ranging from −22 kcal/mole [7], to +2.5 kcal/mole ($A_6C_6U_6$).

Acknowledgement

Thanks are due to Drs. R. Römer, C. and R.S.

Taylor for reading the manuscript and to Mr. J. Ronnenberg for technical assistance.

References

[1] J.R. Fresco, B.M. Alberts and P. Doty, Nature 188 (1960) 98.
[2] M. Staehelin, Experientia 27 (1971) 1; W. Min Jou, G. Haegeman, M. Ysebaert and W. Fiers, Nature 237 (1972) 82.
[3] M. Eigen, Naturwissensch. 58 (1971) 470.
[4] R.L. Baldwin, Accounts Chem. Res. 4 (1971) 265, and references cited therein.
[5] R. Römer, D. Riesner, G. Mass, W. Wintermeyer, R. Thiebe and H.G. Zachau, FEBS Letters 5 (1969) 15.
[6] M. Doulent, J.C. Thrierr, F. Brun and M. Leng, Biochem. Biophys. Res. Commun. 41 (1970) 1590.
[7] S.M. Coutts, Biochim. Biophys. Acta 232 (1971) 94.
[8] O.C. Uhlenbeck, P.N. Borer, B. Dengler and I. Tinoco, Jr., J. Mol. Biol. 73 (1973) 483.
[9] J. Gralla and D.M. Crothers, J. Mol. Biol. 73 (1973) 497.
[10] M. Eigen and D. Pörschke, J. Mol. Biol. 53 (1970) 123.
[11] G.W. Hoffman, Rev. Sci. Instr. 42 (1971) 1643.
[12] D. Pörschke, Biopolymers 10 (1971) 1989.
[13] D. Pörschke, Thesis, Univ. Braunschweig (1968); D. Pörschke and M. Eigen, J. Mol. Biol. 62 (1971) 361.
[14] J. Brahms, J.C. Maurizot and A.M. Michelson, J. Mol. Biol. 25 (1967) 465.
[15] D. Pörschke, O.C. Uhlenbeck and F.H. Martin, Biopolymers 12 (1973) 1313.

BIOPHYSICAL CHEMISTRY 1 (1974) 387–395. © NORTH-HOLLAND PUBLISHING COMPANY

SOLUBILITY RELATIONSHIPS IN BINARY MIXTURES OF HEMOGLOBIN VARIANTS. APPLICATION TO THE "GELATION" OF SICKLE-CELL HEMOGLOBIN

Allen P. MINTON

Laboratory of Biophysical Chemistry, National Institute of Arthritis, Metabolism, and Digestive Diseases, National Institutes of Health, Bethesda, Maryland 20014, USA

Received 22 August 1973
Revised manuscript received 12 November 1973

A thermodynamic treatment of solubility in binary mixtures of hemoglobin variants is presented. It is shown that the reported dependence of the minimum gelling concentration in five binary mixtures of the variants S, C_{Harlem}, Korle-Bu and A may be satisfactorily accounted for using the derived solubility relations together with simple models relating structure to interaction energies in the condensed phase.

1. Introduction

According to a recently proposed model [1], the process of aggregation commonly referred to as the gelation of sickle-cell hemoglobin takes place in two steps: the formation of microtubular fibers by a process of microprecipitation, and the spontaneous alignment of these fibers to form a highly viscous nematic phase commonly (but incorrectly) referred to as gel. It has been theoretically shown that the volume fraction of fiber required to initiate spontaneous alignment decreases as the axial ratio of fiber increases. In the limit of large fiber axial ratio, it follows that the minimum "gelling" concentration (or MGC) experimentally determined by measurement of viscosity will be very close to (but slightly greater than) the solubility of isolated hemoglobin molecules (i.e., that concentration of non-associated hemoglobin which is in equilibrium with fiber). To a good approximation, therefore, we may treat the MGC as an expression of hemoglobin solubility, or alternatively, the free energy of fiber formation.

Bookchin et al. [2–4] have measured the dependence of the MGC upon composition in binary mixtures of the hemoglobin variants S (β_6 glu → val) [5], C_{Harlem} or C_H (β_6 glu → val; β_{73} asp → asn) [2], Korle-Bu or KB (β_{73} asp → asn) [6], and normal hemoglobin A. In section 2 a thermodynamic treatment of hemoglobin solubility in binary mixtures is presented which takes into account the formation of hybrid tetramers in such mixtures [7]. In section 3 three models relating amino-acid substitutions in the several variants to changes in the interactions between tetramers in the fiber array (and hence the free energy of fiber formation) are presented. The ability of each of these models to account for the data of Bookchin et al. is assessed using the relations developed in section 2. Finally, in section 4 the implications of the results obtained in section 3 for the structure of the microtubular fiber are discussed.

In the following treatment we refer to a region on the surface of a hemoglobin tetramer as *variable* if it contains a site which is varied by mutation in at least one of the set of variants [A, S, C_H, KB] and as *constant* if it does not contain such a site. The β-chain characteristic of a particular variant is denoted by one of the lower case letters a, s, c, or k, and a particular tetrameric species is defined by specifying both of the β-chains. For example, the tetrameric species $\alpha_2\beta_2^A$ is denoted by aa, and the hybrid species $\alpha_2\beta^A\beta^S$ in solution is denoted by (sa), where the parentheses indicate that the order of specification is immaterial.

2. Thermodynamics of hemoglobin solubility in binary mixtures

The treatment of this section is based upon the following assumptions:

(1) All (tetrameric) hemoglobin molecules in the fiber are equivalently oriented in the fiber array. This assumption has been made (usually tacitly) in previous studies of the structure of hemoglobin fibers [8–11], and is equivalent to the statement that the smallest structural unit participating in every class of interactions occurring in the array is a single hemoglobin molecule.

(2) Variable surface regions on neighboring molecules in the microtubular array do not interact with each other, but only with constant surface regions. This assumption permits us to express the total free energy of the array as a sum of energies associated with individual molecules, and is probably valid if all molecules in the array are equivalently oriented as assumed above and in the literature [8–11].

(3) The gross three-dimensional conformation (tertiary/quaternary structure) of non-associated hemoglobin molecules in solution is largely unaffected by the presence of amino acid substitutions at the surface of the tetramer. Moreover, the gross three-dimensional conformation of constituent hemoglobin molecules in the microtubular array is largely unaffected by the presence of these substitutions and changes in intermolecular interactions arising from them. These assumptions permit the definition of internal energies associated with hemoglobin molecules in the solution and condensed (fiber) phases. The chemical potential of a molecular species in the microtubule array may consequently be represented by the sum of its internal and interaction energies.

In the following formulation the two components of the binary mixture are designated P and Q and their β-chains p and q. Non-associated hemoglobin will contain the tetrameric species pp, qq, and (pq). If the total hemoglobin concentration is in excess of the solubility, these species will also be found in the condensed phase (fiber). Since the hybrid species (pq) lacks the two-fold symmetry of pp and qq, it may assume either of two distinguishable orientations in the microtubular lattice, denoted by pq and qp. We shall proceed by calculating the chemical potential of each species in the condensed phase and in the solution. The solubility will then be determined by the equilibrium condition that the chemical potential of each species be the same in both phases.

2.1. Condensed phase

We may write a partition function Γ for a microtubular array consisting of N_{pp} tetramers of species pp, N_{pq} tetramers of species pq, and so forth, which is valid providing $N \equiv N_{pp} + N_{pq} + N_{qp} + N_{qq}$ is large in the thermodynamic sense.

$$\Gamma = g_{pp}^{N_{pp}}\, g_{pq}^{N_{pq}}\, g_{qp}^{N_{qp}}\, g_{qq}^{N_{qq}}\, (N!/N_{pp}!N_{pq}!N_{qp}!N_{qq}!) \times \exp[-(N_{pp}w_{pp} + N_{pq}w_{pq} + N_{qp}w_{qp} + N_{qq}w_{qq})/kT], \quad (1)$$

where the g_{ij} are internal partition functions and the w_{ij} are lattice interaction energies associated with each of the indicated species, k is Boltzmann's constant and T the absolute temperature. We may define the internal energy of a tetramer in the condensed phase as

$$\mu_{ij}^{CI} \equiv -kT \ln g_{ij}. \quad (2)$$

μ_{ij}^{CI} may be written as the sum of two terms

$$\mu_{ij}^{CI} \approx \mu_{ij}^{\Sigma} + \mu', \quad (3)$$

where μ_{ij}^{Σ} is the sum of the standard state chemical potentials of the isolated amino acids in a molecule of species ij, and μ' is the free energy of assembling these amino acids into an isolated hemoglobin molecule with the conformation found in the fiber. According to assumption 3 above, μ' is species independent. If we denote by μ_{ij}^{C} the chemical potential of species ij in the condensed phase, then

$$\mu_{ij}^{C}/kT = -\partial \ln \Gamma/\partial N_{ij} = (w_{ij} + \mu_{ij}^{\Sigma} + \mu')/kT + \ln f_{ij}, \quad (4)$$

where $f_{ij} \equiv N_{ij}/N$.

2.2. Solution phase

If we denote by μ_{ij}^{S} the chemical potential of non-associated species ij in the solution, then in the ideal approximation

$$\mu_{ij}^{S}/kT = \mu_{ij}^{SI}/kT + \ln c_{ij}, \quad (5)$$

where c_{ij} is the concentration of species ij in solution in units of g/dl, and μ_{ij}^{SI} is a standard state chemical potential of ij at a concentration of 1 g/dl. μ_{ij}^{SI} may be written as a sum of terms

$$\mu_{ij}^{SI} = \mu_{ij}^{\Sigma} + \mu_{ij}^{0}, \tag{6}$$

where μ_{ij}^{Σ} is the sum of standard state chemical potentials of the isolated amino acids in a molecule of species ij and μ_{ij}^{0} is the free energy of assembling the isolated amino acids into an isolated hemoglobin molecule in solution. The hybrid species (pq), lacking the two-fold symmetry of pp and qq, has accessible to it in solution twice as many distinguishable rotational quantum states as either of the two homogeneous species. From this consideration [12] and from approximation 3 above, it follows that

$$\mu_{pp}^{0} \approx \mu_{qq}^{0} \approx \mu_{(pq)}^{0} + kT \ln 2 \equiv \mu^{0}. \tag{6a}$$

The assumption of equilibrium between the homogeneous species pp and qq on one hand and the hybrid (pq) on the other hand imposes the condition

$$\mu_{pp}^{S} + \mu_{qq}^{S} = 2\,\mu_{(pq)}^{S}. \tag{7}$$

Substitution of relations (5) and (6) into (7) yields

$$c_{(pq)}^{2} = 4\,c_{pp}\,c_{qq}. \tag{8}$$

The total concentration of hemoglobin present, c, and fraction of component Q, x_2, are given by

$$c = c_{pp} + c_{(pq)} + c_{qq}, \qquad x_2 = [c_{qq} + \tfrac{1}{2}\,c_{(pq)}]/c. \tag{9}$$

Combining relations (8) and (9) we obtain

$$\begin{aligned} c_{pp} &= c\,(1 - x_2)^2, \\ c_{(pq)} &= 2\,c\,x_2\,(1 - x_2), \\ c_{qq} &= c\,x_2^2. \end{aligned} \tag{10}$$

Substitution of relations (6) and (10) into (5) yields

$$\begin{aligned} \mu_{pp}^{S}/kT &= \mu_{pp}^{\Sigma}/kT + \mu^{0}/kT + \ln c + 2\ln(1-x_2), \\ \mu_{(pq)}^{S}/kT &= \mu_{(pq)}^{\Sigma}/kT + \mu^{0}/kT + \ln c + \ln[x_2(1-x_2)], \\ \mu_{qq}^{S}/kT &= \mu_{qq}^{\Sigma}/kT + \mu^{0}/kT + \ln c + 2\ln x_2. \end{aligned} \tag{11}$$

2.3. Equilibrium between solution and condensed phases

At equilibrium

$$\mu_{ij}^{S}/kT = \mu_{ij}^{C}/kT. \tag{12}$$

By substitution of relations (4) and (11) into (12) and rearrangement we obtain

$$\ln c + 2\ln(1 - x_2) = (w_{pp} + \mu' - \mu^{0})/kT + \ln f_{pp}, \tag{13a}$$

$$\begin{aligned} \ln c + \ln[x_2(1 - x_2)] &= (w_{pq} + \mu' - \mu^{0})/kT + \ln f_{pq} \qquad (13b) \\ &= (w_{qp} + \mu' - \mu^{0})/kT + \ln f_{qp}, \qquad (13c) \end{aligned}$$

$$\ln c + 2\ln x_2 = (w_{qq} + \mu' - \mu^{0})/kT + \ln f_{qq}, \tag{13d}$$

where c and f_{ij} now specifically denote the values of c and f_{ij} at equilibrium.

The solubility of pure species P, denoted by c_0, is given by eq. (13a) evaluated for $x_2 = 0, f_{pp} = 1$:

$$\ln c_0 = (w_{pp} + \mu' - \mu^{0})/kT. \tag{14}$$

We define the following lattice interaction parameters

$$\begin{aligned} W_{12} &\equiv (w_{pq} - w_{pp})/kT, \\ W_{21} &\equiv (w_{qp} - w_{pp})/kT, \\ W_{22} &\equiv (w_{qq} - w_{pp})/kT. \end{aligned} \tag{15}$$

By subtracting eq. (14) from eqs. (13a–d) and making the substitutions indicated in (15), the following set of relations is obtained

$$\ln(c/c_0) + 2\ln(1 - x_2) = \ln f_{pp}, \tag{16a}$$

$$\begin{aligned} \ln(c/c_0) + \ln[x_2(1 - x_2)] &= W_{12} + \ln f_{pq} \qquad (16b) \\ &= W_{21} + \ln f_{qp}, \qquad (16c) \end{aligned}$$

$$\ln(c/c_0) + 2\ln x_2 = W_{22} + \ln f_{qq}.$$

The definition of f_{ij} [eq. (4)] is equivalent to the expression

$$f_{pp} + f_{pq} + f_{qp} + f_{qq} = 1. \tag{17}$$

Given the values of c_0, x_2, W_{12}, W_{21}, and W_{22}, relations (16) and (17) constitute a set of five equations

which may be solved for the remaining five unknown variables:

$$c = c_0/(A + B + C + D), \tag{18a}$$

$$f_{pp} = A/(A + B + C + D), \tag{18b}$$

$$f_{qq} = B/(A + B + C + D), \tag{18c}$$

$$f_{pq} = C/(A + B + C + D), \tag{18d}$$

$$f_{qp} = D/(A + B + C + D), \tag{18e}$$

where

$$A \equiv (1 - x_2)^2,$$

$$B \equiv x_2^2 \exp(-W_{22}),$$

$$C \equiv x_2(1 - x_2) \exp(-W_{12}),$$

$$D \equiv x_2(1 - x_2) \exp(-W_{21}).$$

Relations (18), in particular (18a), are the main results of this section and will be utilized subsequently in the analysis of experimental data. It will therefore be helpful at this point to group together and restate the definitions of the variables appearing in these relations.

Input:

c_0 – the solubility of component P in homogeneous solution;

x_2 – the fraction of component Q in the binary mixture $P + Q$;

W_{22} – the energy of interaction of species qq with its neighbors in the microtubular array, relative to that of pp (units of kT);

W_{12}, W_{21} – the energies of interaction of two distinguishable orientations of the hybrid species (pq) with their neighbors in the microtubular array, relative to that of pp (units of kT).

Output:

f_{ij} – the fractional abundance of species ij in the microtubule in equilibrium with non-associated hemoglobin.

c – the solubility of a mixture of hemoglobins P and Q, composition denoted by x_2, with respect to the formation of a condensed phase of composition denoted by the set of f_{ij}. c is expected to be nearly equal to the viscosity-defined MGC.

3. Analysis of gelling data

Bookchin et al. [2–4] have measured the viscosity-defined minimum "gelling" concentration (MGC) of the binary mixtures S + A, S + C_H, S + KB, C_H + A, and C_H + KB as a function of mixture composition. According to the results obtained in the preceding section, the composition dependence of the solubility (or MGC) in a single binary mixture may be interpreted in terms of the three interaction parameters W_{12}, W_{21}, and W_{22}, totalling fifteen parameters for the five binary mixtures. In this section we shall show that these fifteen parameters may be expressed as functions of a considerably smaller number of independent increments of lattice interaction energy which are associated with particular amino acid substitutions or combinations thereof. For reference, the amino acid substitutions corresponding to each tetrameric species found in the condensed phase of one of these five binary mixtures are listed in table 1.

In the context of the present analysis, a model is defined as a set of assumptions relating the structure and orientation of a tetramer in the microtubular array to the free energy of interaction of that tetramer with its neighbors in the fiber (lattice interaction energy). We shall present three such models, beginning with the simplest (i.e., requiring the smallest number of independently variable parameters), and determine which of the proposed models are capable of accomodating the published observations.

(a) *Model I*: Let $u_i^{(j)}$ represent the increment of lattice interaction energy associated with an amino acid substitution at the site β_i in local environment j. Assume that the increment of lattice interaction energy associated with each of the four variable sites is independent of lattice interactions involving any other variable site. This model is characterized by the four independent parameters $u_6^{(1)}$, $u_{73}^{(1)}$, $u_6^{(2)}$, and $u_{73}^{(2)}$. In table 2 are listed the lattice interaction energies of each species relative to aa (hemoglobin A) and to pp (the first-specified component in a binary mixture), calculated according to Model I.

An additional constraint, which is model-independent, is provided by the measurement of the MGCs

Table 1
Amino acid substitutions (relative to hemoglobin A) characterizing tetrameric species occurring in gelling binary mixtures of the hemoglobin variants A, S, C_H, and KB. The superscript index refers to one of two possibly non-identical local environments for the β-chain in the microtubular array

P + Q (*pp*) (*qq*)	*pp*	*pq*	*qp*	*qq*
S + A	$\beta_6^{(1)}, \beta_6^{(2)}$	$\beta_6^{(1)}$	$\beta_6^{(2)}$	
S + C_H	$\beta_6^{(1)}, \beta_6^{(2)}$	$\beta_6^{(1)}, \beta_6^{(2)}, \beta_{73}^{(2)}$	$\beta_6^{(1)}, \beta_{73}^{(1)}, \beta_6^{(2)}$	$\beta_6^{(1)}, \beta_{73}^{(1)}, \beta_6^{(2)}, \beta_{73}^{(2)}$
S + KB	$\beta_6^{(1)}, \beta_6^{(2)}$	$\beta_6^{(1)}, \beta_{73}^{(2)}$	$\beta_{73}^{(1)}, \beta_6^{(2)}$	$\beta_{73}^{(1)}, \beta_{73}^{(2)}$
C_H + A	$\beta_6^{(1)}, \beta_{73}^{(1)}, \beta_6^{(2)}, \beta_{73}^{(2)}$	$\beta_6^{(1)}, \beta_{73}^{(1)}$	$\beta_6^{(2)}, \beta_{73}^{(2)}$	
C_H + KB	$\beta_6^{(1)}, \beta_{73}^{(1)}, \beta_6^{(2)}, \beta_{73}^{(2)}$	$\beta_6^{(1)}, \beta_{73}^{(1)}, \beta_{73}^{(2)}$	$\beta_{73}^{(1)}, \beta_6^{(2)}, \beta_{73}^{(2)}$	$\beta_{73}^{(1)}, \beta_{73}^{(2)}$

Table 2
Lattice interaction energies calculated according to Model I

P + Q (*pp*) (*qq*)	Lattice interaction energies (units of *kT*) relative to aa W_{pp}	W_{pq}	W_{qp}	W_{qq}	relative to *pp* W_{12}	W_{21}	W_{22}
S + A	$u_6^{(1)} + u_6^{(2)}$	$u_6^{(1)}$	$u_6^{(2)}$	0	$-u_6^{(2)}$	$-u_6^{(1)}$	$-u_6^{(1)} - u_6^{(2)}$
S + C_H	$u_6^{(1)} + u_6^{(2)}$	$u_6^{(1)} + u_6^{(2)} \div u_{73}^{(2)}$	$u_6^{(1)} + u_{73}^{(1)} + u_6^{(2)}$	$u_6^{(1)} + u_{73}^{(1)} + u_6^{(2)} + u_{73}^{(2)}$	$u_{73}^{(2)}$	$u_{73}^{(1)}$	$u_{73}^{(1)} + u_{73}^{(2)}$ (0.401)
S + KB	$u_6^{(1)} + u_6^{(2)}$	$u_6^{(1)} + u_{73}^{(2)}$	$u_{73}^{(1)} + u_6^{(2)}$	$u_{73}^{(1)} + u_{73}^{(2)}$	$-u_6^{(2)} + u_{73}^{(2)}$	$-u_6^{(1)} + u_{73}^{(1)}$	$-u_6^{(1)} + u_{73}^{(1)} - u_6^{(2)} + u_{73}^{(2)}$
C + A	$u_6^{(1)} + u_{73}^{(1)} + u_6^{(2)} + u_{73}^{(2)}$	$u_6^{(1)} + u_{73}^{(1)}$	$u_6^{(2)} + u_{73}^{(2)}$	0	$-u_6^{(2)} - u_{73}^{(2)}$	$-u_6^{(1)} - u_{73}^{(1)}$	$-u_6^{(1)} - u_{73}^{(1)} - u_6^{(2)} - u_{73}^{(2)}$
C_H + KB	$u_6^{(1)} + u_{73}^{(1)} + u_6^{(2)} + u_{73}^{(2)}$	$u_6^{(1)} + u_{73}^{(1)} + u_{73}^{(2)}$	$u_{73}^{(1)} + u_6^{(2)} + u_{73}^{(2)}$	$u_{73}^{(1)} + u_{73}^{(2)}$	$-u_6^{(2)}$	$-u_6^{(1)}$	$-u_6^{(1)} - u_6^{(2)}$

of homogeneous solutions of hemoglobin S (24.2_5 g/dl under the experimental conditions employed by Bookchin et al. [2–4]) and hemoglobin C_H (36.2 g/dl under the same conditions). These two solutions correspond to the compositional extremes $x_2 = 0$ and $x_2 = 1$ respectively of the binary mixture S + C_H. Substituting the values $x_2 = f_{qq}^T = 1$ into eq. (16d) we obtain the following completely general expression for the interaction energy of cc relative to ss:

$$W_{22} = \ln (c/c_0) \approx \ln (\text{MGC } C_H/\text{MGC S}) = 0.401. \quad (19)$$

As shown in table 2, this result reduces the number of independently variable parameters in Model I to three.

Upon examination of table 2 we observe that according to Model I, the energy parameters W_{12}, W_{21}, and W_{22} are identical for the two binary mixtures S + A and C_H + KB. According to relation (18a) the

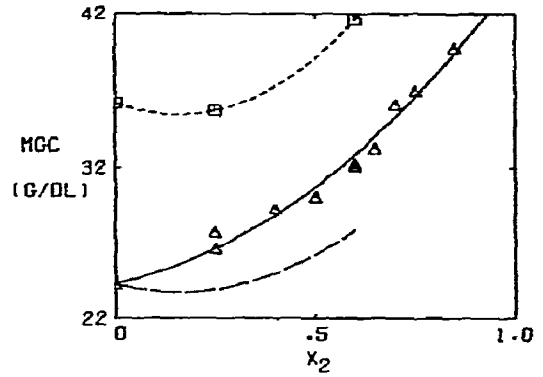

Fig. 1. MGC versus composition for the binary mixtures S + A and C_H + KB. Data points are from refs. [2–4]. (△) data, S + A; (▫) data, C_H + KB. (——) quadratic curve fitted to data, S + A; (– – –) quadratic curve fitted to data, C_H + KB; (— — —) curve for S + A assuming composition dependence equivalent to that of C_H + KB (Model I).

dependence of c/c_0 upon x_2 should therefore be identical for these two mixtures. The data presented in fig. 1 show that this is not the case. We may therefore conclude that the lattice interactions associated with the β_6 and β_{73} positions are not entirely independent as postulated in Model I.

(b) *Model II*: According to the X-ray model of deoxyhemoglobin [13, 14] the 6 and 73 positions on a single β-chain are relatively close together (~18 Å) and separated by a considerably greater distance (> 40 Å) from the 6 and 73 positions on the other β-chain. It is therefore reasonable to postulate that the lattice interaction associated with a site on one β-chain is independent of lattice interactions involving sites on the other β-chain, but is *not* independent of lattice interactions involving sites not far removed in space on the same β-chain. This model requires the addition of two parameters to the four already encountered in Model I ($u_6^{(1)}$, $u_{73}^{(1)}$, $u_6^{(2)}$, and $u_{73}^{(2)}$). The two additional parameters, $u_{6,73}^{(1)}$ and $u_{6,73}^{(2)}$, represent increments of lattice interaction energy associated with a double substitution at sites 6 and 73 on the same β-chain in local environments 1 and 2 respectively. "Interaction" between the 6 and 73 positions on the same β-chain will be expressed as non-additivity of the lattice interaction energy increments; in general $u_{i,j}^{(k)}$ will not be equal to $u_i^{(k)} + u_j^{(k)}$. Lattice interaction energies calculated for this model are listed in table 3.

Because of the constraint given by eq. (19) the number of independently variable parameters in Mod-

Table 3
Lattice interaction energies calculated according to Model II

P +Q	Lattice interaction energies (units of kT) relative to aa				relative to *pp*		
(*pp*) (*qq*)	W_{pp}	W_{pq}	W_{qp}	W_{qq}	W_{12}	W_{21}	W_{22}
S + A	$u_6^{(1)} + u_6^{(2)}$	$u_6^{(1)}$	$u_6^{(2)}$	0	$-u_6^{(2)}$	$-u_6^{(1)}$	$-u_6^{(1)} - u_6^{(2)}$
S + C_H	$u_6^{(1)} + u_6^{(2)}$	$u_6^{(1)} + u_{6,73}^{(2)}$	$u_{6,73}^{(1)} + u_6^{(2)}$	$u_{6,73}^{(1)} + u_{6,73}^{(2)}$	$-u_6^{(2)} + u_{6,73}^{(2)}$	$-u_6^{(1)} + u_{6,73}^{(1)}$	$-u_6^{(1)} + u_{6,73}^{(1)}$ $-u_6^{(2)} + u_{6,73}^{(2)}$ (0.401)
S + KB	$u_6^{(1)} + u_6^{(2)}$	$u_6^{(1)} + u_{73}^{(2)}$	$u_{73}^{(1)} + u_6^{(2)}$	$u_{73}^{(1)} + u_{73}^{(2)}$	$-u_6^{(2)} + u_{73}^{(2)}$	$-u_6^{(1)} + u_{73}^{(1)}$	$-u_6^{(1)} + u_{73}^{(1)}$ $-u_6^{(2)} + u_{73}^{(2)}$
C_H + A	$u_{6,73}^{(1)} + u_{6,73}^{(2)}$	$u_{6,73}^{(1)}$	$u_{6,73}^{(2)}$	0	$-u_{6,73}^{(2)}$	$-u_{6,73}^{(1)}$	$-u_{6,73}^{(1)} - u_{6,73}^{(2)}$
C_H + KB	$u_{6,73}^{(1)} + u_{6,73}^{(2)}$	$u_{6,73}^{(1)} + u_{73}^{(2)}$	$u_{73}^{(1)} + u_{6,73}^{(2)}$	$u_{73}^{(1)} + u_{73}^{(2)}$	$u_{73}^{(2)} - u_{6,73}^{(2)}$	$u_{73}^{(1)} - u_{6,73}^{(1)}$	$u_{73}^{(1)} - u_{6,73}^{(1)}$ $+ u_{73}^{(2)} - u_{6,73}^{(2)}$

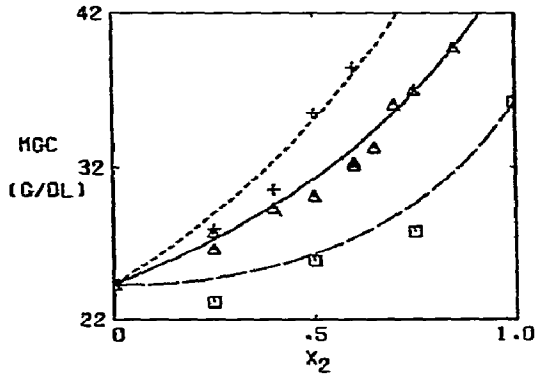

Fig. 2. MGC versus composition for the binary mixtures S + A, S + C_H, and S + KB. Data points are from refs. [2–4]. Curves are calculated from Model II using best-fit parameter values given in legend to table 4. (△;——) S + A, (□;– – –) S + C_H, (+;– – – –) S + KB.

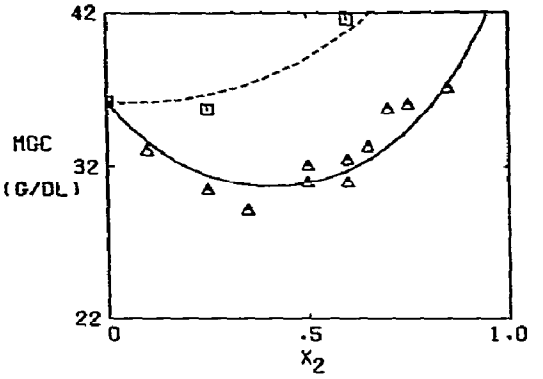

Fig. 3. MGC versus composition for the binary mixtures C_H + A and C_H + KB. Data points are from refs. [2–4]. Curves are calculated from Model II using best-fit parameter values given in legend to table 4. (△;——) C_H + A, (□;– – – –) C_H + KB.

el II reduces to five. These five parameters were varied so as to obtain the best least-squares fit of eq. (18a) to the data of Bookchin et al. for all five binary hemoglobin mixtures simultaneously. Only one well-defined set of parameter values yielded a fit which could be judged satisfactory. The results obtained using this set of best-fit parameter values are shown in figs. 2 and 3 listed in table 4.

As judged by the magnitude of the sum of squared residuals (denoted by F), the fit appears to be fairly good. For comparison, a quadratic polynomial of the form $c(x_2) = A_1 + A_2 x_2 + A_3 x_2^2$ (with A_1 fixed at either 24.25 or 36.2 as appropriate) was fitted to the data set for each binary mixture individually. For the set of five binary mixtures, a minimum value of F = 20.2 (g/dl)^2 was obtained with ten independently variable parameters. By simultaneously fitting the five binary mixtures using Model II, a minimum value of F = 34.5 (g/dl)^2 was obtained with only five independently variable parameters. An attempt was made to obtain a simultaneous fit of eq. (18a) to all five data sets with the additional constraints $u_6^{(1)} = u_6^{(2)}$, $u_{73}^{(1)} = u_{73}^{(2)}$, and $u_{6,73}^{(1)} = u_{6,73}^{(2)}$, but this was not possible.

Table 4
Values of the lattice interaction energies in Model II calculated using the following set of best-fit parameter values: $u_6^{(1)} = 0.068$, $u_6^{(2)} = -0.692$, $u_{73}^{(1)} = 0.437$, $u_{73}^{(2)} = -0.244$, $u_{6,73}^{(1)} = 0.938$, $u_{6,73}^{(2)} = -1.167$

P +Q	Lattice interactions energies (units of kT) relative to pp		
(pp) (qq)	W_{12}	W_{21}	W_{22}
S + A	0.692	-0.068	0.624
S + C_H	-0.475	0.876	(0.401)
S + KB	0.447	0.375	0.822
C_H + A	1.167	-0.938	0.229
C_H + KB	0.922	-0.501	0.421

(c) *Model III*: If no assumptions are made regarding additivity or equivalence of interactions associated with the β_6 or β_{73} sites, then a total of fifteen different energy parameters becomes possible — four for single substitutions, six for double substitutions, four for triple substitutions, and one for a quadruple substitution. This number may be reduced somewhat by assuming that microscopic environments 1 and 2 are equivalent. Then the following energy increments may be defined: $u_6, u_{73}, u_{6,6}, u_{73,73}, u_{6,73}^{(1)}$ (both substitutions on same β-chain), $u_{6,73}^{(2)}$ (substitutions on different β-chains), $u_{6,6,73}$, $u_{6,73,73}$, and $u_{6,6,73,73}$. The interaction energies calculated according to this model are listed in table 5. The constraint imposed by eq. (19) reduces the number of independently variable parameters in Model III by one to a total of eight.

In view of the large number of independently variable parameters in this model, there can be little doubt that a satisfactory fit to the data may be achieved. However, for the same reason, the numerical significance of

Table 5
Lattice interaction energies calculated according to Model III

P + Q (pp) (qq)	Lattice interaction energies (units of kT) relative to aa			relative to pp	
	W_{pp}	$W_{pq} = W_{qp}$	W_{qq}	$W_{12} = W_{21}$	W_{22}
S + A	$u_{6,6}$	u_6	0	$u_6 - u_{6,6}$	$-u_{6,6}$
S + C_H	$u_{6,6}$	$u_{6,6,73}$	$u_{6,6,73,73}$	$u_{6,6,73} - u_{6,6}$	$u_{6,6,73,73} - u_{6,6}$ (0.401)
S + KB	$u_{6,6}$	$u^{(2)}_{6,73}$	$u_{73,73}$	$u^{(2)}_{6,73} - u_{6,6}$	$u_{73,73} - u_{6,6}$
C_H + A	$u_{6,6,73,73}$	$u^{(1)}_{6,73}$	0	$u^{(1)}_{6,73} - u_{6,6,73,73}$	$-u_{6,6,73,73}$
C_H + KB	$u_{6,6,73,73}$	$u_{6,73,73}$	$u_{73,73}$	$u_{6,73,73} - u_{6,6,73,73}$	$u_{73,73} - u_{6,6,73,73}$

best-fit parameter values which would be obtained through a least-squares fitting procedure would be highly doubtful. It is likely that many combinations of parameter values would yield approximately equal local minimum values of F, and therefore we will not pursue the numerical aspects of this model further.

4. Discussion

We have shown that the experimentally observed dependence of the MGC upon composition in five binary mixtures of four hemoglobin variants may be satisfactorily accounted for by a straightforward solubility analysis together with simple models relating structural features to the free energy of fiber formation. It is important to stress that because of the simplified physical picture upon which the thermodynamic treatment is based, and because of approximations made in the treatment itself (most notably the neglect of nonideality), quantitative conclusions may not be drawn with any degree of confidence from the results reported in section 3. On the other hand, the major qualitative factors appear to be properly taken into account, permitting the following *qualitative* conclusions to be drawn from these results:

(1) Changes in the interaction energy between hemoglobin tetramers in the microtubular array due to amino acid substitutions at β_6 and/or β_{73} are of the order of kT or smaller.

(2) In view of the large degree of non-additivity observed for interactions associated with the 6 and 73 positions on the same β-chain, it is probable that both of these sites are involved in a single constellation of interacting groups at one interface between neighboring tetramers in the microtubular array.

(3) The simplest interpretation of the mixture gelling data (Model II) suggests that the environment of the two β-chains in the microtubular array are non-equivalent. This suggestion contradicts two recently published speculations about the orientation of hemoglobin molecules in the fiber [9, 10], but is consistent with the orientational constraints imposed by recent measurements of the linear dichroism of sickle-cell hemoglobin fibers [11]. The equivalence of the two β-chain environments cannot be ruled out on the basis of the present solubility analysis, but such an interpretation (Model III) would require the invocation of a substantially more complex set of interactions between surface sites on different β-chains as well as on the same β-chain.

(4) The final point to be made is so tentative as to be more in the nature of a speculation than a conclusion, and derives from the observation that according to the simplest satisfactory model accounting for the mixture data (Model II), the interaction energy increment associated with one of the two β_6 sites is ten times as great as that associated with the other β_6 site. This may conceivably indicate that one of the two β_6 sites does not directly participate in an interaction between neighboring tetramers in the fiber, as suggested by Bookchin and Nagel [4].

Acknowledgement

I thank Dr. H.A. Saroff for his support of this work and Dr. H.J. Hofrichter for helpful suggestions and for critically reading and checking preliminary drafts of this report.

References

[1] A.P. Minton, J. Mol. Biol. 82 (1974) 483.
[2] R.M. Bookchin, R.L. Nagel and H.M. Ranney, J. Biol. Chem. 242 (1967) 248.
[3] R.M. Bookchin, R.L. Nagel and H.M. Ranney, Biochim. Biophys. Acta 221 (1970) 373.
[4] R.M. Bookchin and R.L. Nagel, J. Mol. Biol. 60 (1971) 263.
[5] V.M. Ingram, Nature 180 (1957) 326.
[6] F.I.D. Konotey-Ahulu, E. Gallo, H. Lehmann and B. Ringelhann, J. Med. Genet. 5 (1968) 107.
[7] R.M. Macleod and R.J. Hill, J. Biol. Chem. 248 (1973) 100.
[8] M. Murayama, Science 153 (1966) 145.
[9] J.T. Finch, M.F. Perutz, J.F. Bertles and J. Dobler, Proc. Natl. Acad. Sci. US 70 (1973) 718.
[10] S.J. Edelstein, J.N. Telford and R.H. Crepeau, Proc. Natl. Acad. Sci. US 70 (1973) 1104.
[11] J. Hofrichter, D.G. Hendricker and W.A. Eaton, Proc. Natl. Acad. Sci. US 70 (1973) 3604.
[12] T.L. Hill, Introduction to statistical thermodynamics (Addison–Wesley, Reading, Mass., 1960) Ch. 8, Sec. 3.
[13] A.F. Cullis, H. Muirhead, M.F. Perutz, M.G. Rossman and A.C.T. North, Proc. Roy. Soc. A265 (1962) 161.
[14] H. Muirhead, J.M. Cox, L. Mazzarella and M.F. Perutz, J. Mol. Biol. 28 (1967) 117.

BIOPHYSICAL CHEMISTRY 1 (1974) 396. © NORTH-HOLLAND PUBLISHING COMPANY

ERRATUM

R.J.M. Tausk, J. van Esch, J. Karmiggelt, G. Voordouw and J.Th.G. Overbeek, Physical chemical studies of short-chain lecithin homologues. II. Micellar weights of dihexanoyl- and diheptanoyllecithin, Biophys. Chem. 1 (1974) 184.

On page 198 an error was made in eq. (25). This equation should read:

$$v = 54.8 + 26.9 \times 2 \times n \text{ Å}^3. \qquad (25)$$

All calculations performed with the help of this equation are also slightly in error.

The following corrections should be made:

page 198: 2nd column, 1st line: $v = 296.4$ Å^3 should read $v = 323.$ Å^3;
2nd column, 7th line: 11.2 Å should read 10.9 Å;
fig. 12: 42 Å and 3.5 Å should read 46.8 Å and 3.1 Å respectively;
legend to fig. 12, 2nd line: 6.8 monomers should read 6.2 monomers;

page 200: 7th line from below: $Q = 2.1$ and $Q = 2.0$ respectively should read $Q = 2.2$ and $Q = 2.0^6$ respectively.

The corrections for nonideality based on model II are somewhat too small (figs. 13—15 and 17). The largest errors occur at high concentrations of diC_7- lecithin. The average micellar weight at 17 mg ml^{-1} and $R = 19$ Å for instance should be 9% higher than given in fig. 15 (curve III). At $R = 16$ Å the plotted result at the same concentration is 7% too small (curve II).

AUTHOR INDEX TO VOLUME 1

SUBJECT INDEX TO VOLUME 1

Each page number refers to the first page of a given reference